Universidad Autónoma de Madrid
Programa de Doctorado de Biociencias Moleculares

Papel de la proteasa MT4-MMP como modulador de los monocitos patrulleros en el contexto inflamatorio

Cristina Clemente Toribio

Madrid 2020

Departamento de Biología Molecular
Facultad de Ciencias
Universidad Autónoma de Madrid

Papel de la proteasa MT4-MMP como modulador de los monocitos patrulleros en el contexto inflamatorio

Doctoranda: Cristina Clemente Toribio (Licenciada en Biología, UAM)
Directora de la Tesis: Alicia García Arroyo
Centro Nacional de Investigaciones Cardiovasculares-Carlos III (Madrid, ESP)

RESUMEN

Los monocitos patrulleros son una población de leucocitos circulantes en la sangre encargados de rastrear el endotelio de los vasos, detectando daño celular y captando partículas nocivas tanto en condiciones de homeostasis como durante procesos inflamatorios. En nuestro trabajo hemos caracterizado el papel de la proteasa de matriz MT4-MMP (MMP17) en los monocitos patrulleros y los macrófagos en el contexto de inflamación.

Tras confirmar la expresión de MT4-MMP en macrófagos durante peritonitis estéril y aterosclerosis, observamos que la ausencia de MT4-MMP conllevaba una acumulación de macrófagos tanto en la membrana peritoneal inflamada como en la placa de ateroma y que estos macrófagos expresan el factor de transcripción MafB y su gen diana AIM/CD5L. Asimismo, demostramos que los macrófagos carentes de MT4-MMP expresan mayores niveles del receptor CD36 y son más activos captando lípidos modificados lo que resulta en una aceleración de la aterosclerosis. En cuanto al mecanismo celular, la ausencia de MT4-MMP incrementa el número de monocitos patrulleros adheridos a la placa de ateroma incipiente y el bloqueo de dicho reclutamiento previene el acúmulo de macrófagos MafB+AIM/CD5L+, el depósito de lípidos y la aceleración de la aterosclerosis. Por tanto MT4-MMP parece regular primariamente la adhesión y reclutamiento temprano de los monocitos patrulleros durante el proceso inflamatorio. En este sentido, observamos que en ausencia de MT4-MMP hay una acumulación de la integrina αMβ2 en la membrana de los monocitos patrulleros y de los macrófagos peritoneales. Mediante ensayos *in silico* y de digestión *in vitro* determinamos que MT4-MMP es capaz de procesar la cadena αM de la integrina αMβ2, modulando así sus niveles en la membrana de los monocitos y macrófagos. Finalmente, mediante microscopía intravital demostramos *in vivo* que la ausencia de MT4-MMP aumenta el número de monocitos patrulleros capaces de rastrear el endotelio inflamado de manera dependiente de la integrina αMβ2.

En resumen, este trabajo identifica a MT4-MMP como un nuevo regulador de la función de los monocitos patrulleros en el contexto inflamatorio mediante el procesamiento de la integrina αM. Como consecuencia, la ausencia de MT4-MMP aumenta el número de monocitos patrulleros que rastrean el endotelio inflamado que podría ser beneficioso en patologías como la enfermedad de Alzheimer, las metástasis pulmonares o las infecciones.

SUMMARY

Patrolling monocytes are a population of circulating leukocytes in the blood responsible for tracking the endothelium of the vessels, detecting cellular damage and capturing harmful particles both in homeostasis conditions and during inflammatory processes. In our work we have characterized the role of the MT4-MMP matrix protease (MMP17) in patrollling monocytes and macrophages in the context of inflammation.

After confirming the expression of MT4-MMP in macrophages during sterile peritonitis and atherosclerosis, we observed that the absence of MT4-MMP involved an accumulation of macrophages both in the inflamed peritoneal membrane and in the atheroma plaque and that these macrophages express the MafB transcription factor and its target gene AIM/CD5L.We also show that macrophages lacking MT4-MMP express higher levels of the receptor CD36 and are more active in capturing modified lipids, resulting in an acceleration of atherosclerosis. The absence of MT4-MMP also increases the number of patrolling monocytes attached to the incipient atheroma plaque and blocking this recruitment prevents the accumulation of MafB+AIM/CD5L+macrophages, lipid deposits and acceleration of atherosclerosis. Therefore MT4-MMP seems to regulate primarily patrolling monocyte early adhesion and recruitment during inflammation. In this sense, we observe that in the absence of MT4-MMP there is an accumulation of the αMβ2 integrin in the membrane of the patrolling monocytes and the peritoneal macrophages. By *in silico* and *in vitro* digestion tests we determine that MT4-MMP is able to process the αM chain of the αMβ2 integrin, thus modulating its levels in the monocyte and macrophage membrane. Finally, through intravital microscopy we demonstrate *in vivo* that the absence of MT4-MMP increases the number of patrolling monocytes able to crawl on the inflamed endothelium in a manner dependent on the integrin αMβ2.

In summary, this work identifies MT4-MMP as a new regulator of the function of patrolling monocytes through the processing of integrin αM. As a consequence, the absence of MT4-MMP increases the number of patrolling monocytes that crawl on the inflamed endothelium which could be beneficial in pathologies such as Alzheimer's disease, lung metastasis or infections.

ÍNDICE

ÍNDICE DE FIGURAS

CLAVE DE ABREVIATURAS

AcLDL	Lipoproteína de baja densidad acetilada
ADAMTS4	Desintegrina y metaloproteinasa con motivo trombospondina 4
AIM	Inhibidor de apoptosis de macrófagos
ARN	Ácido Ribonucleico
B220	Marcador general de célula B
CCL	Quimioquina (motívo C-C) ligando
CCR	Receptor de quimioquinas
CX3CL1	Quimioquina (motivo C-X3-C) ligando 1
CX3CR1	Receptor 1 de quimioquinas CX3C
C/EBPβ	Proteínas CCAAT-potenciadoras de unión beta
CD	Grupo de diferenciación
cMaf	Protooncogén de fibrosarcoma músculoaponeurótico (MAF)
CMP	Progenitor mieloide común
CMOP	Progenitor común de monocitos
CR3	Receptor del complemento 3
CSF1R	Receptor del factor estimulante de colonias 1
DCs	Células dendríticas
Dll1	Ligando delta 1
EEM	Error estándar de la media
EGFR	Receptor del factor de crecimiento epidérmico
GFP	Proteína verde fluorescente
GM-CSF	Factor estimulante de colonias de granulocitos y macrófagos
GMP	Progenitor de granulocitos y macrófagos
GPI	Glicosilfosfatidilinositol
HIF-1α	Factor inducible de hipoxia 1-alpha
HSC	Célula originaria hematopoyética
ICAM	Molécula de adhesión intercelular
IMF	Intensidad media de fluorescencia
iNOS	Sintasa de óxido nítrico inducible

CLAVE DE ABREVIATURAS

IFN-γ	Interferón-gamma
IL	Interleuquina
IRF8	Factor de regulación de Interferón 8
JNK	Quinasa c-Jun N-terminal
KLF4	Factor 4 tipo Kruppel
FLT3	Tirosina Quinasa tipo Fms 3
LDL	Lipoproteína de baja densidad
LDLR	Receptor de lipoproteína de baja densidad
LFA-1	Antígeno asociado a función de linfocitos 1
LPM	Macrófagos peritoneales grandes
LPS	Lipopolisacárido
LRP	Proteinas Relacionadas con el receptor de lipoproteínas
Ly6C	Complejo de antígeno de linfocitos 6
Mac1	Antígeno de macrófago 1
Mafb	Homólogo B del oncogén de fibrosarcoma músculoaponeurótico (MAF)
MAPK	Proteína quinasas activadas por mitógenos
MCP-1	Poteína quimiotáctica de monocitos 1
M-CSF	Factor estimulante de colonias de macrófagos
MDP	Progenitor de células dendríticas y macrófagos
MHC II	Complejo mayor de histocompatibilidad II
MMP17	Metaloproteinasa de Matriz 17
MRV	Maraviroc
Msr1	Receptor de basura macrofágico 1
MT1-MMP	Metaloproteinasa de Matriz de membrana 1
MT4-MMP	Metaloproteinasa de Matriz de membrana 4
NK	Asesina natural
NOD2	Proteína 2 con domínio de oligomerización por unión de nucleótidos
Notch2	Proteína Homóloga 2 del locus neurogénico notch
Nr4a1	Receptor Nuclear de la subfamilia 4 grupo A miembro 1
OxLDL	Lipoproteína de baja densidad oxidada
PCR	Reacción en cadena de la polimerasa
PFA	Paraformaldehido

PI3K	Fosfoinositol 3-quinasa
PMA	Forbol 12-miristato 13-acetato
PU.1	Factor de transcripción PU.1
RelB	Factor de transcripción RelB
ROS	Especies reactivas de oxígeno
SCA-1	Antígeno de célula originaria-1
SCF-R	Receptor del Factor de células originarias
SETD1A	Subunidad SET1 del complejo de histonas Metiltransferasa Set1/Ash2
SFM	Sistema fagocítico mononuclear
SMA	Actina de músculo liso
SPM	Macrófagos peritoneales pequeños
TG	Tioglicolato
TGF-β	Factor de crecimiento trasformante-beta
TIMP-1	Inhibidor tisular de metaloproteinasas-1
TIMP-2	Inhibidor Tisular de Metaloproteinasas-2
TK	Tirosina Quinasa
TLR7	Receptor tipo toll 7
TNF-α	Factor de necrosis tumoral-alpha
TSP2	Trombospondina 2
VCAM-1	Proteína de adhesión de células vasculares 1
VLA-4	Antígeno 4 muy tardío
VEGF	Factor de crecimiento endotelial vascular

INTRODUCCIÓN

1. SISTEMA FAGOCÍTICO MONONUCLEAR (SFM)

El sistema fagocítico mononuclear se definió originalmente en los años 70 como una familia de células derivadas de progenitores pluripotentes de la médula ósea y que incluía a dichos progenitores en vías de diferenciación, a los monocitos circulantes y a los macrófagos tisulares[1]. A lo largo de los años se han incluido otros linajes en el SFM como las células dendríticas y se ha determinado que comparten un progenitor común en la médula ósea, el progenitor de Células Dendríticas y Macrófagos (MDP).La diferenciación y proliferación de las células del SFM está regulada por la citoquina M-CSF e IL-34, mediante su receptor común CSF1R (CD115)[1]

Las células del SFM se caracterizan por su actividad fagocítica así como por su plasticidad génica en respuesta a señales del entorno siendo por tanto difícil definirlas por la expresión demarcadores concretos en la superficie celular. Son por ello células esenciales en el mantenimiento de la homeostasis tisular y en contextos fisiopatológicos como la inflamación, infecciones, respuestas autoinmunes o cáncer[2].

En este trabajo nos centramos en el análisis de las poblaciones de monocitos y de macrófagos por lo que procedemos a describirlas a continuación en más detalle.

1.1. **Monocitos**

Son leucocitos pertenecientes al SFM que circulan en sangre. Representan entre el 3-10% en humanos, y entre el 2-3% en ratón de todos los leucocitos circulantes[3]. Se caracterizan por la expresión común de CD115 (CSF-1R) y de la integrina αMβ2 (también denominada CD11b/CD18, CR3 y Mac1). Aunque clásicamente se consideraban células precursoras de macrófagos y de células dendríticas (DCs) en los tejidos[4], en los últimos años se ha demostrado que los monocitos desempeñan funciones propias en la respuesta inmune. De hecho se han identificado subpoblaciones de monocitos circulantes con diferentes fenotipos y funciones celulares [5, 6].

1.1.1. **Origen de las subpoblaciones de monocitos**

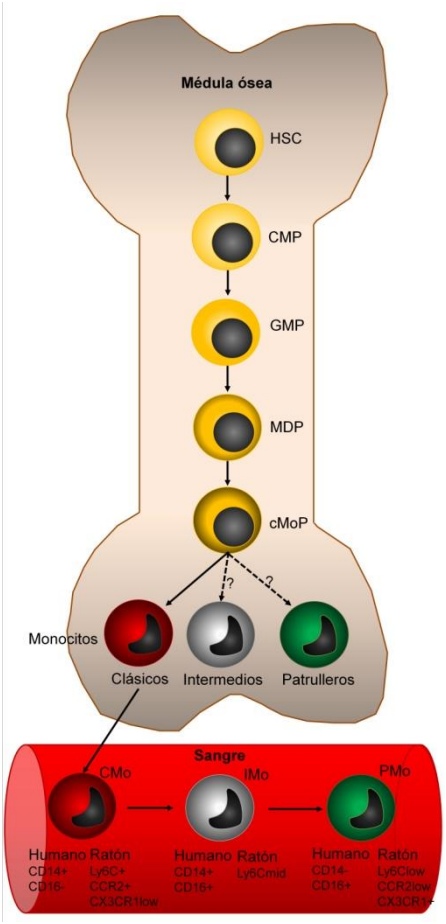

Figura 1: Diferenciación de los monocitos: En la etapa adulta los progenitores de la médula ósea dan lugar a los monocitos cásicos (CMo) que circulan en el torrente sanguíneo donde pueden diferenciarse a monocitos patrulleros (PMo) pasando por un estadio de monocitos intermedios (IMo).

Los monocitos se originan a partir de progenitores de la médula ósea y del bazo[7] en la edad adulta. El primer precursor es la célula originaria hematopoyética (HSC), que posteriormente se diferencia al precursor mieloide común (CMP), el cual expresa CD34, pero no Sca-1, y que se diferencia posteriormente a los precursores de granulocitos/monocitos (GMP), adquiriendo la expresión de CD16 y CD32. Dentro de esta subpoblación, se describe una población de precursores de monocitos/células dendríticas (MDP), que adquieren la expresión de CD115, CX3CR1 y Flt3, que dan lugar a los progenitores comunes de monocitos (cMoP), que pierden la expresión de Flt3 y ganan la de Ly6C, manteniendo los marcadores CD115 y CX3CR1 (**figura1**)[8, 9].

El modelo actual propone que la subpoblación de monocitos clásicos derivan de los progenitores cMoP y tras circular en el torrente sanguíneo durante unas horas, si no se extravasan reprimen su programa transcripcional y aumentan la expresión de los factores de transcripción C/EBPβ, KLF4 y Nr4a1 (o Nur77) dando lugar a la los monocitos patrulleros[9]. Este factor es crítico para la supervivencia/diferenciación de los monocitos patrulleros por lo que los ratones deficientes en Nr4a1 carecen casi totalmente de estos monocitos y se han utilizado clásicamente para la caracterización de sus funciones [10].

Se ha descrito recientemente que en homeostasis esta diferenciación de monocitos clásicos a monocitos patrulleros se produce en determinados nichos vasculares de la médula ósea y del bazo víainteracción de Notch2 en los monocitos clásicos con Dll1

expresado en el endotelio de dichos nichos[11]. En situaciones patológicas se puede aumentarla diferenciación de monocitos clásicos a monocitos patrulleros mediante por ejemplo la estimulación del receptor NOD2 durante procesos inflamatorios o durante las metástasis por señales procedentes de tumores como los exosomas[12, 13].Del mismo modo se conoce que las señales de estrés por estimulación adrenérgica aumentaban la circulación de los monocitos patrulleros[14]. Todo ello indica que en situaciones de daño, estrés o inflamación el organismo pone en marcha mecanismos para aumentar la abundancia o disponibilidad de monocitos patrulleros en la circulación. Sin embargo, se ha visto que en ausencia de los factores de transcripción IRF8 y KLF4, hay una disminución de los monocitos clásicos, sin afectar al número de monocitos patrulleros, indicando que quizá existan otras rutas de diferenciación de los monocitos patrulleros independientes de las anteriores y de los monocitos clásicos[15, 16].

1.1.2. **Fenotipo y función de las subpoblaciones de monocitos**

Los **monocitos clásicos** se caracterizan por la expresión alta en membrana de CD14 y la falta de expresión de CD16 en humano, y por la expresión alta de Ly6C y del receptor de quimioquinas CCR2 y baja de CX3CR1 en ratón[5, 6, 17, 18],siendo la población de monocitos mayoritaria en sangre. En humano se ha demostrado que en condiciones basales los monocitos clásicos tienen una vida media de 1 día[19].

Pese a que generalmente se encuentran circulando por el torrente sanguíneo, pueden interaccionar con el endotelio vascular y extravasarse a los tejidos tanto en condiciones basales como ante una respuesta inflamatoria. Una vez en el tejido dañado los monocitos clásicos se comportan principalmente como células proinflamatorias mediante la producción de citoquinas y quimioquinas tales como IL6, IL8, CCL2 CCL3 y CCL5[20]y la diferenciación a macrófagos mayoritariamente proinflamatorios como por ejemplo macrófagos que expresan CD11c y MHC II en el peritoneo inflamado [18].

Los monocitos clásicos interaccionan con el endotelio siguiendo el modelo canónico de extravasación de leucocitos con una serie de pasos bien definidos[21]. Primero ocurre una adhesión de los monocitos al endotelio, que viene determinado por la interacción de las selectinas E y P, ICAM1 y VCAM1 del endotelio con los receptores PSGL-1, VLA-4 (integrina α4β1) y CD44 en el monocito. Tras este contacto inicial, el monocito hace un movimiento de rodamiento en el endotelio a favor de flujo sanguíneo, que va

reduciendo su velocidad. Este movimiento de rodamiento viene orquestado por la familia de las quimioquinas C-C y C-X-C. Finalmente, los monocitos son capaces de hacer un movimiento de rastreo lateral sobre el endotelio, hasta localizar una zona por la que extravasarse. Este movimiento lateral viene determinado por ICAM1 y ICAM2 en el endotelio y por las integrinas αLβ2 y αMβ2 (LFA1 y Mac1 respectivamente) en los monocitos [22].

En el proceso de diferenciación de los monocitos clásicos a los monocitos patrulleros, se ha descrito una subpoblación de monocitos intermedios que expresan tanto CD14 como CD16 en humano, y niveles intermedios de Ly6C en ratón. Aunque se ha observado que esta población aumenta en enfermedades inflamatorias y se ha propuesto su utilización cómo indicador de enfermedades cardiovasculares[23], los datos actuales sugieren que esta población constituye un estadio intermedio de diferenciación de monocito clásico a patrullero, más que una población independiente[24].

Los **monocitos patrulleros**, tienen una expresión alta de CD16 y baja de CD14 en humano, y una expresión alta de CX3CR1 y baja de CCR2 y Ly6C en ratón[5, 6, 17, 18]. Son capaces de permanecer en el torrente sanguíneo en humano entre 5-7 días en condiciones basales. Los monocitos patrulleros constituyen alrededor del 2-8% y el 26-50% del total de monocitos circulantes en sangre, en humano y en ratón respectivamente [25].La abundancia de los monocitos patrulleros puede variar en condiciones de daño mediante la movilización de los monocitos adheridos al endotelio, incremento de su vida media e incremento de la diferenciación desde monocitos clásicos[1, 26].

A diferencia de la función típicamente proinflamatoria asignada a los monocitos clásicos, los monocitos patrulleros desempeñan funciones de vigilancia intravascular y por ello se les ha considerado monocitos antiinflamatorios o reparadores[1]. Los estudios pioneros del grupo de Geissman identificaron que los monocitos patrulleros ejercían su función de vigilancia mediante un movimiento característico y singular de rastreo luminal sobre el endotelio de los vasos. Dicho rastreo es diferente al que realizan los monocitos clásicos y otros leucocitos que se da principalmente en el sentido del flujo sanguíneo. El rastreo de los monocitos patrulleros si bien necesita de la presencia del flujo sanguíneo[27], se realiza mediante movimientos en forma de bucle, horquilla y ondas a lo largo del endotelio sin seguir la dirección o el sentido del flujo [28].

Este movimiento de rastreo se da en condiciones basales tal como se ha observado mediante microscopia intravital en lechos vasculares de diversos tejidos y órganos como piel, corazón, músculo cremaster, mesenterio y riñón[28] entre otros. Dicho rastreo da como resultado que al menos 1/3 de los monocitos totales en sangre están en contacto con el endotelio vascular[27], siendo particularmente abundantes estos monocitos en el pulmón por la alta producción de fractalquina o CX3CL1, ligando del receptor CX3CR1, por el endotelio pulmonar[29]. Además, durante el rastreo los monocitos patrulleros pueden captar partículas de hasta un tamaño de 2 μm sin que ello conlleve una finalización del rastreo, indicando que la monitorización del endotelio vascular y la captación de partículas en sangre son sus principales funciones[28].

Las características del movimiento de rastreo cambian según el contexto y así durante la inflamación o el daño inducido se hace más ´lento´ y ´prolongado' tal como se ha demostrado *in vivo* tras la activación con agonistas de TLR7 en el riñón de ratón o con patrulleros humanos *in vitro*[17, 28]. Además se ha visto recientemente que los monocitos no solo rastrean los capilares y vénulas sino también las arterias inflamadas durante la aterosclerosis de forma dependiente de las integrinas LFA1/αLβ2 y VLA4/α4β1[30]. En todos estos contextos se ha analizado el papel regulador de diversos receptores de adhesión y de quimioquinas en el movimiento de rastreo de los monocitos patrulleros. El rastreo en condiciones basales depende tanto en los monocitos patrulleros de ratón como en los humanos de la interacción del receptor de adhesión celular integrina αLβ2 (LFA-1) con ICAM1 e ICAM2 en el endotelio[17] y se modula por CX3CR1[18]ya que, aunque este receptor no es esencial, estabiliza el movimiento. Tal como se demostró induciendo una señal de daño con un agonista de TLR7 en riñón, en un escenario inflamatorio los monocitos patrulleros requieran la expresión de la integrina αMβ2 y de CX3CR1para su rastreo sobre el endotelio inflamado[28, 31]. En este contexto, los monocitos inducen el reclutamiento de neutrófilos que modulan la apoptosis de las células endoteliales dañadas siendo posteriormente eliminadas por los monocitos patrulleros acabando así con el daño y restaurando la homeostasis[28]. Dada la relevancia de la función de vigilancia intravascular por parte de los monocitos patrulleros se han descrito recientemente nuevos reguladores de dicho rastreo como por ejemplo la proteína matricelular CCN1/Cyr61 en inflamación vascular o la vía de CD36/Syk en aterosclerosis[32, 33].

Si bien los monocitos patrulleros se han considerado típicamente anti-inflamatorios o reparadores tras la fase inflamatoria desempeñada por los monocitos clásicos, se sabe

que pueden reclutarse de forma temprana en distintos escenarios en los que por tanto sus acciones no parecen ser tan claramente resolutivas de inflamación. Por ejemplo, tras inyección del patógeno *Listeria monocytogenes* en el peritoneo, se observa un pico temprano de reclutamiento de los monocitos patrulleros en las dos primeras horas de infección, seguido varias horas más tarde del reclutamiento de los monocitos clásicos[27]. Los monocitos patrulleros en dicho contexto secretan TNF-α al medio, y presentan un aumento de la expresión génica de factores implicados en el reclutamiento de otras células inflamatorias, como IL-1, lisozimas y TLRs entre otros. Además, los monocitos patrulleros extravasados son capaces a su vez de diferenciarse a macrófagosmediante elincremento de la expresión de los factores de transcipción cMaf y Mafb; a diferencia de los monocitos clásicos reclutados que se diferencianvía Relb y Pu.1 [27], sugiriendo funciones relacionadas con la inflamación de los monocitos patrulleros en este contexto. De forma similar, durante la aterosclerosis, los monocitos patrulleros se reclutan a la placa incipiente de modo dependiente de CCR5 e independiente de CCR2 y CX3CR1, con funciones propuestas relacionadas con fagocitosis, angiogénesis y diferenciación a células dendríticas[34, 35], pero sin estar todavía bien definidas aún hoy sus funciónes.

Dada su capacidad de captar partículas en el torrente sanguíneo también se ha descrito recientemente el papel esencial de los monocitos patrulleros en la prevención de metástasis tumorales al pulmón, en cooperación con células NK [29] así como en el aclaramiento de depósitos intravasculares de β-amiloide durante la angiopatía de la enfermedad de Alzheimer[36]. Por ello se ha propuesto como posibles nuevas terapias para estas patologías la potenciación de la actividad de rastreo y fagocitosis intravascular por parte de los monocitos patrulleros sin haberse identificado hasta el momento ninguna diana molecular para ello.

1.2. **Macrófagos**

Los macrófagos son células fagocíticas diferenciadas presentes en los tejidos. Su origen varía a lo largo del desarrollo. En estadios embrionarios se originan a partir de progenitores presentes en el saco vitelino, para posteriormente diferenciarse desde progenitores del hígado fetal, y finalmente establecerse la hematopoyesis en la médula ósea en periodos perinatales y post-natales... Los macrófagos generados en el periodo embrionario se diseminan por los diversos órganos anidando en los tejidos y adquiriendo fenotipos específicos en cada uno de ellos[37]. Si bien los macrófagos

embrionarios llegan a todos los tejidos durante el desarrollo pudiendo mantenerse en la edad adulta mediante proliferación local, existe también un recambio de dichos macrófagos desde de monocitos circulantes en la edad adulta. Dicho recambio es más pronunciado en unos tejidos que en otros, resultando finalmente en una heterogeneidad de poblaciones macrofágicas en los diversos tejidos[38]. De este modo, por ejemplo, la microglía en el cerebro está compuesta principalmente por macrófagos embrionarios, existiendo un reemplazamiento bajo, mientras que los macrófagos embrionarios intestinales son sustituidos en alto porcentaje por macrófagos derivados de monocitos de médula ósea durante la edad adulta [37].

Los macrófagos desempeñan un amplio espectro de funciones, tanto durante el desarrollo embrionario como en homeostasis y en condiciones patológicas en el adulto, pudiendo variar dichas funciones dependiendo del contexto en el que se hallen. De este modo se describieron inicialmente dos tipos de macrófagos mediante su inducción *in vitro* por distintas citoquinas y que mostraban diferente expresión demarcadores de superficie, producción de citoquinas y actividades biológicas. Se denominaron macrófagos pro-inflamatorios o M1 y anti-inflamatorios o M2 (**Figura 2**).

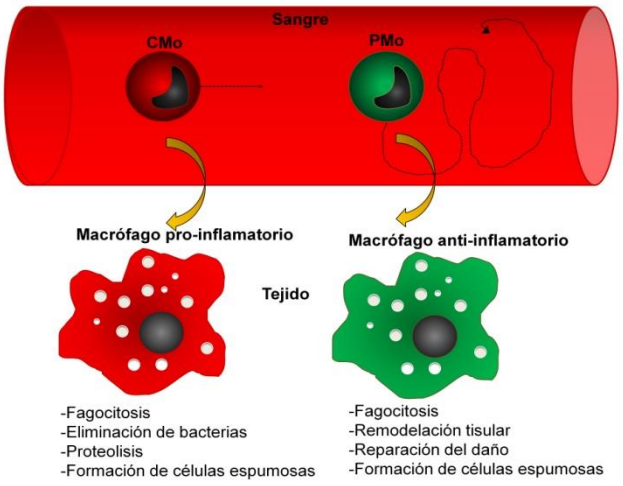

Figura 2: Función de los monocitos: Los monocitos clásicos (CMo) en el torrente sanguíneo hacen un movimiento de rodamiento en dirección de flujo, extravasándose al tejido dañado y diferenciándose a macrófagos pro-inflamatorios. Los monocitos patrulleros (PMo) realizan un movimiento de rastreo sobre el endotelio vascular, detectando y reparando el daño en el lumen de los vasos, pudiendo extravasarse a los tejidos inflamados donde dan lugar a macrófagos anti-inflamatorios.

Los macrófagos pro-inflamatorios responden a estímulos como TNF-α, IFN-γ y LPS, produciendo citoquinas proinflamatorias como las interleuquinas IL-1β, IL-6, IL-12, IL-23 eIL-27; CXCL-9, CXCL-10, CXCL-11 CXCL-16 y CCL5, así como Arginasa (Arg-2), la sintasa de óxido nítrico inducible (iNOS) y especies reactivas de oxígeno (ROS); mientras que los macrófagos anti-inflamatorios responden a las interleuquinas IL-4, IL-10 eIL-15 produciendo a su vez IL-10, TGF-β, CCL16, CCL-17, CCL-18, CCL-22 y CCL-24 y VEGF. De este modo los macrófagos pro-inflamatorios actúan en la

resistencia a infecciones (víricas, bacterianas, fúngicas y de protozoos) así como en enfermedades autoinmunes entre otras, mientras que las funciones de los macrófagos anti-inflamatorios están más relacionadas con reparación tisular y angiogénesis[39]. Dada la plasticidad mostrada por los macrófagos *in vivo*, esta clasificación ha quedado obsoleta y se considera que los macrófagos pueden mostrar subtipos en un amplio espectro fenotípico y funcional dependiendo de las señales del entorno[40].

Dada la heterogeneidad de los macrófagos, no sólo por su origen, sino también por su plasticidad en la respuesta a citoquinas locales, la búsqueda de un marcador universal para su detección es un aspecto todavía abierto. Si bien clásicamente se han utilizado marcadores como F4/80 por su expresión en gran variedad de macrófagos tisulares incluyendo la microglía y los macrófagos peritoneales, así como los macrófagos derivados de monocitos adultos; sin embargo, en otras poblaciones de macrófagos residentes, como los macrófagos alveolares, su expresión es baja[1]. Otros marcadores utilizados para la detección de macrófagos son las lectinas (como CD169 o CD206), los receptores basureros (*scavengers*) implicados en los procesos de eferocitosis (como SRA o CD36),los receptores de Fc e integrinas[41], si bien aunque su expresión es diferente en los distintos subtipos de macrófagos, se expresan también en otros leucocitos, como monocitos y células dendríticas.Mediante elanálisis transcriptómico de macrófagos de diversos tejidos de ratón se pudo observar que existían unos cientos de transcritos que diferenciaban macrófagos de células dendríticas, pero no todos ellos estaban presenten en todos los macrófagos estudiados. A pesar de ello se ha logrado identificar los marcadores Mertk y CD64 como expresados en macrófagos maduros y ausentes en células dendríticas[42].

De este modo hay un creciente interés en entender la plasticidad fenotípica y funcional de los macrófagos en distintos contextos inflamatorios.

2. MODELOS DE INFLAMACIÓN ESTÉRIL

El proceso inflamatorio es una respuesta mediada por los leucocitos en cooperación con otros tipos celulares inducida por la presencia de un agente externo o por daño tisular, y encaminada a la eliminación de dicho agente o daño y a la restauración de la homeostasis. Cuando la respuesta inflamatoria se origina por daño celular o tisular

directo sin la presencia de agentes patógenos externos se denomina inflamación estéril. En este trabajo de tesis doctoral hemos empleado dos modelos de inflamación estéril, uno agudo (peritonitis estéril inducida por tioglicolato) y otro crónico (aterosclerosis inducida por dieta grasa) que pasamos a comentar a continuación.

2.1. **Peritonitis estéril**

La cavidad peritoneal es un espacio virtual localizado en el abdomen de los mamíferos, y que está separado de los órganos internos (intestino, hígado, riñones entre otros) por la membrana denominada membrana peritoneal. En la cavidad peritoneal habitan multitud de células del sistema inmune tanto en condiciones basales como inflamatorias, entre las que se encuentran los macrófagos. Existen dos poblaciones mayoritarias de macrófagos, los LPM (del inglés *large peritoneal macrophages*/macrófagos peritoneales grandes) y los SPM (del inglés *small peritoneal macrophages*/ macrófagos peritoneales pequeños)[43]. En condiciones basales, los LPM son mayoritarios, constituyendo aproximadamente un 90% del total de los macrófagos peritoneales, ysiendo los SPM únicamente un 10% [43]; estas proporciones en contexto inflamatorio. Los macrófagos LPM expresan altos niveles de la integrina αMβ2 y del marcador F4/80 a diferencia de los SPM que muestranuna expresión intermedia, siendo estos marcadores útiles para su distinción, aun existiendo diferencias también en otros[43, 44, 45].

La inducción de la peritonitis estéril se realiza mediante la inoculación en la cavidad peritoneal de agentes proinflamatorios como el tioglicolato y el zimosán A [46], siendo un modelo accesible y ampliamente utilizado para el estudio del reclutamiento de los monocitos y su diferenciación a macrófagos.

Tras la inducción de la peritonitis (**figura 3**), se produce un rápido reclutamiento de leucocitos en la cavidad peritoneal, principalmente durante los primeros 3 días, disminuyendo su número posteriormente. Las primeras células reclutadas son los neutrófilos, los cuales alcanzan su máxima acumulación el primer día tras el estímulo. Los monocitos son las células mayoritariamente reclutadas hasta el día 7 tras la estimulación, siendo las principales responsables del incremento celular en el peritoneo. Por último, los linfocitos son las células mayoritarias desde los 7 días en adelante tras el estímulo[47].

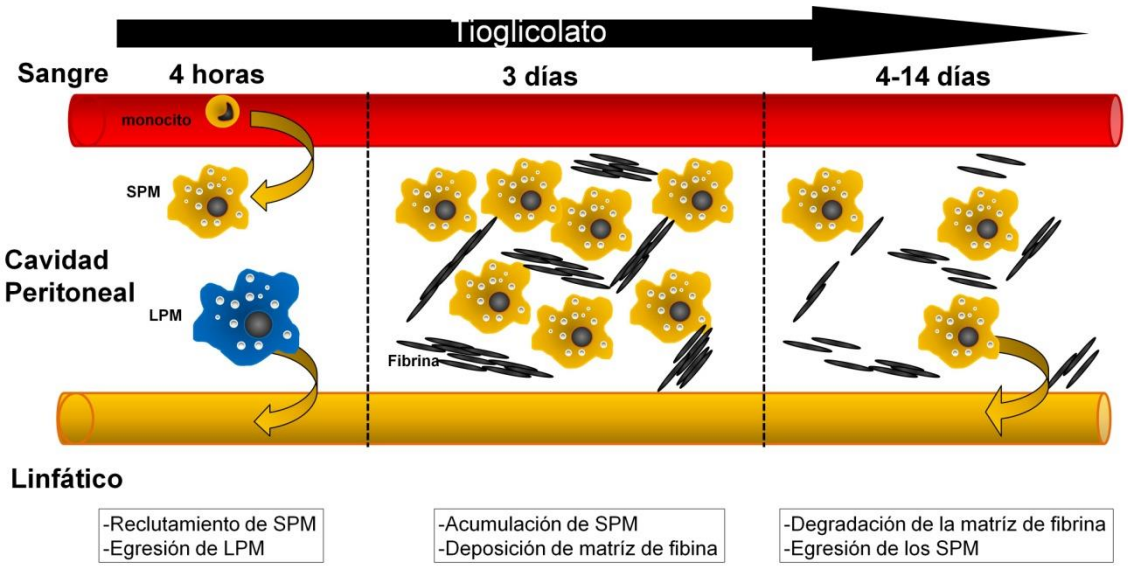

Figura 3: Evolución de la peritonitis: Tras un estímulo inflamatorio como la inoculación de tioglicolato en la cavidad peritoneal, los monocitos se reclutan al peritoneo desde las primeras 4 horas, diferenciándose a SPM (Small Peritoneal Macrophages), mientras que los macrófagos residentes, los LPM (Large Peritoneal Macrophages) egresan de la cavidad peritoneal. A tres días hay mayor número de SPMs en la cavidad peritoneal, que generando también una matriz de fibrina. Entre los días 4 y 14 se produce la fase de resolución, en la cual la matriz de fibrina se degrada y se produce la egresión de los SPMs de la cavidad peritoneal.

Los monocitos reclutados en el peritoneo tras la estimulación con tioglicolato dan lugar a los SPM, siendo este reclutamiento dependiente fundamentalmente de la quimioquina MCP-1/CCL2[48]asícomo de la expresión de L-selectina en los monocitos[49]. Tras la inflamación, los LPM emigran del peritoneo en las 4 primeras horas, mientras que los SPM aumentan en número hasta llegar a un máximo a los 3-4 días de la estimulación, y posteriormente emigrar del peritoneo desde el día 4 hasta el día 14[47, 50]. Se ha observado que ambos procesos de emigración son dependientes de la integrína αMβ2 [50]. Se ha postulado que los monocitos clásicos son los reclutados en el peritoneo inflamado, dando lugar a los SPM, mientras que los monocitos patrulleros podrían ser responsables del reemplazamiento de los LPM en condiciones basales[51].

2.2. **Aterosclerosis**

La aterosclerosis es una enfermedad que cursa por una desregulación metabólica que da lugar a una respuesta inflamatoria crónica en la pared vascular de las arterias y a la consiguiente formación de placas de ateroma constituidas por varios tipos celulares

[52].En estadios tardíos, la placa de ateroma o bien trombos formados sobre ella pueden desprenderse de la pared arterial bloqueando las arterias. Por ello la aterosclerosis es la mayor responsable de eventos cardiovasculares severos como el infarto de miocardio y los accidentes cerebrovasculares isquémicos[52].

Las regiones arteriales más susceptibles al desarrollo de aterosclerosis son aquellas donde se produce un flujo turbulento de la sangre ya que el flujo laminar es protector del endotelio mediante la represión de señales inflamatorias[53]. Dichas regiones son principalmente las válvulas aórticas, la curvatura menor del cayado aórtico y las ramificaciones a lo largo de la aorta, donde se forman inicialmente las placas de ateroma.

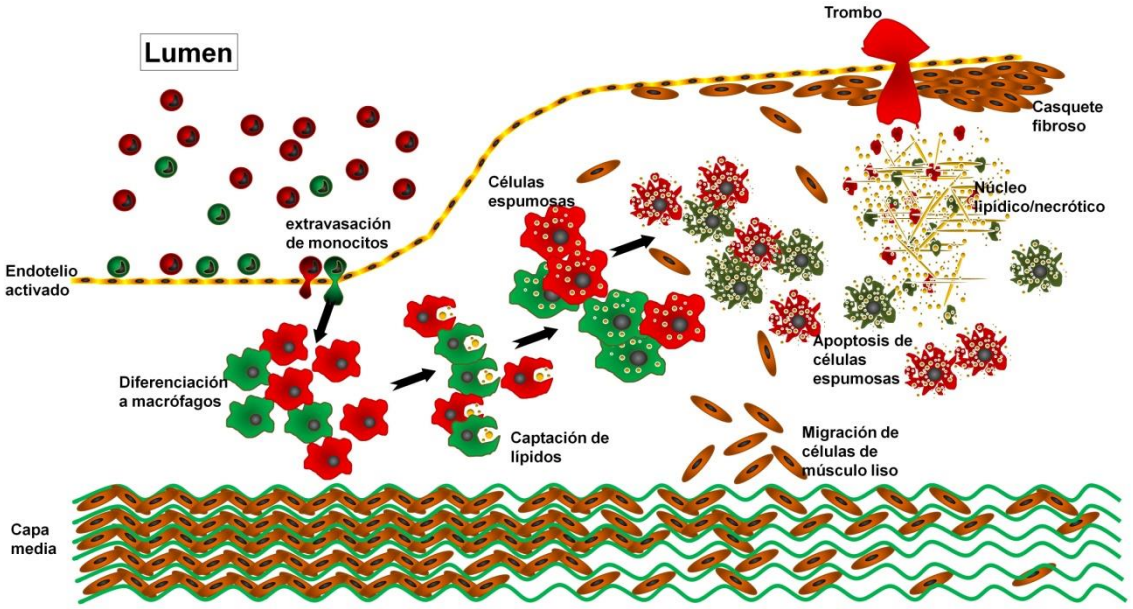

Figura 4: Evolución de la aterosclerosis: Los monocitos clásicos y patrulleros interacciona con el endotelio activado, extravasándose a la capa íntima de la aorta donde se diferencian a macrófagos. Dichos macrófagos en la placa de ateroma pueden proliferar y captar lípidos, acumulándolos y diferenciándose a células espumosas. En estadios tardíos las células espumosas entran en apoptosis, liberando los lípidos al exterior creando el núcleo lipídico/necrótico. Paralelamente las células del músculo liso de la capa media pueden migrar a la superficie de la placa y formar el casquete fibroso. Finalmente la placa de ateroma puede romperse, originándose un trombo.

El inicio de la aterosclerosis se produce por una acumulación en las arterias de lípidos (principalmente colesterol asociado a LDL modificadas por ejemplo por oxidación) que inducen un daño en las células endoteliales que conforman la íntima de las arterias. El endotelio responde al daño expresando moléculas como ICAM1 en la membrana, y

secretando citoquinas, como M-CSF y GM-CSF, que posteriormente inducirán la diferenciación de los monocitos a macrófagos [54]. El daño endotelial es detectado por los monocitos, mediante receptores como las integrinas αMβ2 o αLβ2 y α4β1, acumulándose en dichas regiones y desencadenando la respuesta inflamatoria. Al igual que en la peritonitis, la quimioquina principal del reclutamiento de monocitos en aterosclerosis es MCP1/CCL2[55]. Los monocitos reclutados en la zona de daño migran atravesando la íntima y se diferencian a macrófagos (**Figura 4**), los cuales captan los lípidos, los acumulan en su interior y se diferencian a células espumosas, quedándose localizadas entre la íntima y la media. Las células espumosas de la placa producen factores que inducen el reclutamiento de otras células inflamatorias, incrementando así el crecimiento de la placa. A su vez, las células de músculo liso que conforman la pared vascular se desdiferencian en respuesta a factores como por ejemplo OxLDL, pudiendo proliferar y migrar desde la media hacia la región luminal de la placa en estadios avanzados de la enfermedad, creando el casquete fibroso[56]. En estadios avanzados las células espumosas entran en apoptosis en la placa, liberando al exterior los lípidos, acumulándose y formando el núcleo lipídico/necrótico en la placa.

1.1.1. **Monocitos patrulleros en aterosclerosis**

El reclutamiento de monocitos y su posterior diferenciación a macrófagos en la placa es un proceso fundamental para el desarrollo de la enfermedad, de modo que cuando se inhibe, no se produce la enfermedad[57].

En cuanto a las acciones selectivas de las dos subpoblaciones de monocitos, se sabe que los clásicos participan de la respuesta inflamatoria que conlleva a la formación de la placa y se ha propuesto que los patrulleros serían protectores de aterosclerosis. Esto se ha fundamentado en estudios con ratones deficientes en Nur77/Nr4a1 que desarrollaban más aterosclerosis, pero dado estos ratones que también tenían un fenotipo de macrófagos más proinflamatorios no queda claro si los patrulleros son protectores o contribuyen a la formación de la placa. En este sentido, se ha visto en modelos de ratón que los monocitos patrulleros pueden reclutarse tempranamente a la placa de manera dependiente del receptor CCR5[34]mientras que los clásicos emplean los tres receptores de quimioquinas CX3CR1, CCR2 y CCR5[58]. Los monocitos patrulleros rastrean el endotelio dañado de las arterias durante la aterosclerosis de manera dependiente de LFA-1 e integrinas α4. Este rastreo se intensifica con la dieta grasa y dado que en el ratón deficiente en Nur77/Nr4a1se detecta más daño vascular

se ha sugerido que los monocitos patrulleros podían tener un papel protector del daño vascular.[30]

Además, los monocitos patrulleros expresan receptores basureros como CD36 capaz de captar LDL-oxidadas (OxLDL), y el estímulo con dieta grasa produce un incremento del rastreo de los monocitos en el endotelio dependiente de CD36[59, 60, 61]. Por tanto los monocitos patrulleros podrían ser claves en la eliminación de lípidos.

1.1.2. **Acumulación y diversidad de los macrófagos en la aterosclerosis**

Dentro de la placa de ateroma, los macrófagos constituyen el 30-50% de todas las células mieloides presentes[62]. Generalmente se ha asumido que los macrófagos presentes en la placa procedían de monocitos circulantes que se diferenciaban a macrófagos en la placa, pero actualmente se ha visto que pueden proceder de distinta ontogenia, incluyendo macrófagos residentes, dando lugar a una variedad de fenotipos de macrófagos dependiendo de las señales del ambiente

La abundancia de macrófagos en la placa aterosclerótica determina la evolución de la enfermedad[63]. Esta abundancia se regula sobre todo en las fases iniciales por el reclutamiento de los monocitos circulantes y en estadios más avanzados por la proliferación, apoptosis y egresión de los macrófagos en la placa [64, 65, 66, 67]. La proliferación es determinante para la progresión de la placa ya que su inhibición reduce la formación de placa[68]. Sin embargo, la apoptosis de los macrófagos en la placa desempeña un papel dual a lo largo del proceso [69]. En estadios tempranos de la aterosclerosis, cuando el contenido de células inflamatorias es bajo, la apoptosis de los macrófagos en la placa es beneficiosa ya que esos macrófagos apoptóticos son fagocitados por otros en la placa, y como resultado el tamaño de la placa disminuye. Sin embargo, en estadios avanzados de la enfermedad, cuando se acumulan abundantes células espumosas en la placa, la muerte masiva de las mismas hace que el resto de células fagocíticas no sean capaces de eliminarlas, produciéndose una acumulación de dichas células apoptóticas, la inducción de la muerte de otras célulasy por tanto la formación de un núcleo necrótico[64]. Este núcleo necrótico está principalmente compuesto por los lípidos antes contenidos en el interior de las células espumosas que son liberados al espacio extracelular tras la muerte de dichas células[70]. Respecto a la egresión de los macrófagos de la placa con la consiguiente reducción del tamaño de ésta [65], [71] aunque se ha propuesto como mecanismo de regulación actualmente se piensa que su contribución al número final de macrófagos de la placa

es bastante limitada[72, 73].

Hasta ahora se han caracterizado seis subtipos de macrófagos en las placas de ateroma, en función del estímulo que induce su diferenciación, de sus marcadores y de las citoquinas que producen[74]. Los macrófagos M1 son aquellos macrófagos proinflamatorios que responden a lípidos presentes en la placa como colesterol y OxLDL y que expresan TLR4 y NF-kB y secretan TNFα, IL-6 e IL-22. Los macrófagos M(Hb) se diferencian en respuesta a la presencia de hemoglobina y haptoblobina, adquieren la expresión de CD163 y secretan IL-10. Los macrófagos Mhem son aquellos que responden al hierro tipo hemo, expresan LXR-α y LXR-β y secretan IL-10 y HMOX-1. Los macrófagos M2 (separados actualmente en M2a, M2b, M2c y M2d), los típicamente anti-inflamatorios, se diferencian en respuesta a IL-4 e IL-10, expresan LXR-α y producen a su vez IL-10 e IL-4. Los macrófagos Mox se diferencian respondiendo a fosfolípidos oxidados, expresan TLR-2 y NFE2L2 y producen IL-1β y Cox-2. Finalmente, los macrófagos M4, son aquellos que se diferencian en respuesta a CXCL4 y producen IL-6, TNF y MMP7[74].Dadas las señales que inducen su diferenciación estos macrófagos se diferencian en distintos estadios a lo largo de la aterosclerosis localizándose además en distintas zonas de la placa de ateroma.[75].Si bien clásicamente se ha considerado a los macrófagos M1 como pro-inflamatorios y a los M2 como anti-inflamatorios, se ha incluido a los macrófagos M4 dentro de los inflamatorios y a los macrófagos M(Hb) y Mhem como antiinflamatorios[74]. Estudios más recientes de RNASeq están contribuyendo a entender la heterogeneidad fenotípica y funcional de los macrófagos en la placa[76].

2. MT4-MMP

MT4-MMP (también denominada MMP17) es un miembro del grupo de las metaloproteinasas de matriz (MMP), perteneciente al subgrupo de las de tipo de membrana (MT-MMP). Las MMPs son endopeptidasas dependientes de Zn que comparten un mismo motivo en el sitio catalítico[77]. MT4-MMP muestra poca similitud de secuencia con el resto de miembros de la subfamilia; tan solo un 40% de similitud en el dominio catalítico con el resto de MT-MMPs[78]. Fue la primera MT-MMP descrita que presenta una unión a la membrana celular mediante un puente glicosil-

fosfatidilinositol (GPI) [78], siendo posteriormente identificada MT6-MMP con el mismo anclaje a la membrana.

MT4-MMP fue clonada en 1996 de células de carcinoma de mama humano[79], y ha sido ampliamente estudiada en el contexto tumoral. Sin embargo desde el inicio se describió también su expresión en células de linaje mieloide y en particular en macrófagos[79, 80, 81, 82, 83], lo que indicaban posibles funciones de esta proteasa en inflamación.

2.1. **Dominios de MT4-MMP**

MT4-MMP posee la estructura típica de las MMPs (**Figura 5**). Muestra en su amino terminal un dominio pro-peptídico que mantiene la conformación inactiva de la proteasa y que se une al resto de la proteína mediante 9 residuos típicos de la familia MT-MMP. Este motivo (R-X-R/K-R) es procesado por furina en el transGolgi, liberando el dominio pro-peptídico y dando lugar a la confirmación madura y potencialmente activa de la proteasa [79].

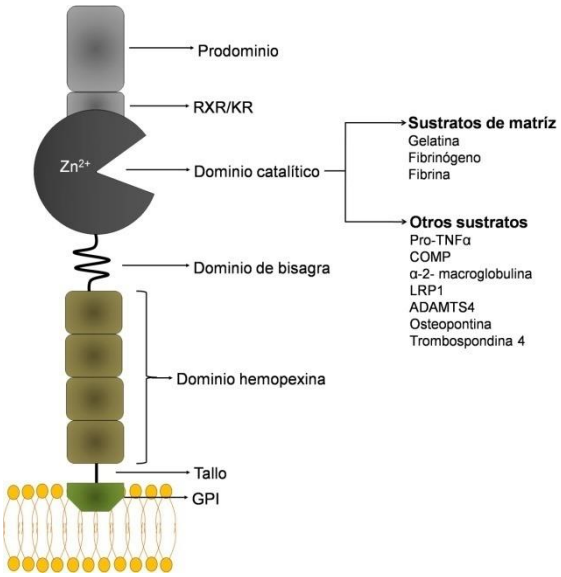

Figura 5: Estructura esquemática de MT4-MMP

Tras el dominio pro-peptídico, MT4-MMP consta de un dominio catalítico, que muestra las características propias de las MMPs replegándose en presencia de Zn^{2+} y Ca^{2+} mediante su unión a la secuencia consenso “HEXXHXXGXXH”, siendo por tanto su actividad dependiente de Zn^{2+}como en el resto de las MMPs [84].A continuación se encuentra el dominio hemopexina, que está unido al dominio catalítico mediante la región de bisagra y contribuye a la especificidad de sustrato. Cuando se cambia este dominio hemopexina en MT1-MMP por el dominio hemopexina de MT4-MMP, MT1-MMP pierde la capacidad de procesar pro-MMP2, que es un sustrato típico de la proteasaMT1-MMP[85], lo que sugiere que MT4-MMP puede tener especificidades de sustrato distintas a las del resto de MT-MMP, haciéndola una metaloproteinasa única en su actividad y función[86].

Tras el dominio hemopexina, MT4-MMP muestra una pequeña región de denominada tallo,parte de la cual es procesada por una transamidasa durante la ruta secretoria permitiendo la adición del anclaje hidrofóbico GPI. Esta región posee dos cisteínas, una de las cuales, la Cys564, es susceptible de ser N-glicosilada, pero no O-glicosilada, y parece estar implicada en la dimerización y oligomerización de MT4-MMP, mediante interacciones no covalentes [87].Esta unión a la membrana mediante un puente GPI le confiere a MT4-MMP una localización en dominios lipídicos específicos de la membrana plasmática [87], permitiéndole co-localizar con otras proteínas que contengan dicho anclaje tales como el receptor de folato, CD14 o uPAR[88, 89] ;o bien con proteínas también presentes en estos dominios como caveolina-1o integrinas[90].

2.2. **Sustratos de MT4-MMP**

Como ya se ha comentado, el dominio catalítico de MT4-MMP es el menos homólogo con el resto de MMPs, mostrando una similitud en aminoácidos de menos del 40% [80, 84, 85].

En cuanto a los sustratos reconocidos de MT4-MMP, en un principio se pensó que era capaz de procesar gelatina pero no se le considera una MMP clásicamente procesadora de proteínas de la matriz extracelular como colágeno o fibronectina. Los estudios con sustratos o péptidos sintéticos *in vitro* han identificado algunos sustratos componentes de la matriz extracelular inflamatoria como el fibrinógeno y la fibrina[80, 91] y otros sustratos como el factor de necrosis tumoral-alfa (pro-TNF-α), ADAMTS-4, α2-macroglobulina, la proteína relacionada al receptor de lipoproteínas de baja densidad (LRP1) y la proteína de matriz de cartílago oligomérica (COMP)[94, 95, 96, 79, 83, 91, 92]. La relevancia del procesamiento de estos sustratos *in vivo* no ha podido demostrarse. Más recientemente nuestro laboratorio ha identificado trombospondina-4 y osteopontina [92] como nuevos sustratos de MT4-MMP mediante estudios de proteómica y de validación *in vitro* demostrando además la relevancia del procesamiento de osteopontina *in vivo* en modelos de ratón. MT4-MMP también sería potencialmente capaz de autoprocesar se en la superficie celular [93].

La actividad catalítica de MT4-MMP puede ser inhibida de forma endógena por los inhibidores tisulares TIMP-1 y TIMP-2 [85], y también por inhibidores químicos generales de metaloproteinasas como el ilomastat (también conocido como galardina o GM6001)[94]. Hasta el momento no se han descrito inhibidores específicos de MT4-MMP.

2.3. Expresión y función de MT4-MMP

Además de su expresión en diversos tumores (como carcinoma de mama) [79], MT4-MMP se expresa en una variedad de líneas y tipos celulares, en concreto en leucocitos se ha descrito su expresión en macrófagos, eosinófilos y linfocitos B [81, 83, 95].

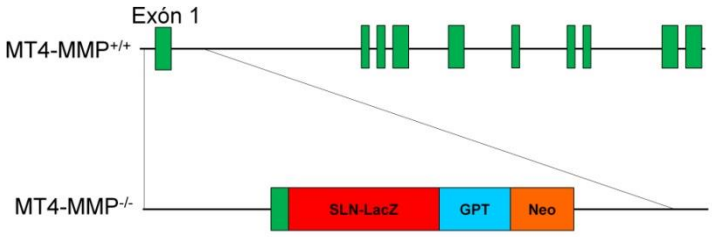

Figura 6: Diseño del ratón MT4-MMP-LacZ: El ratón deficiente en MT4-MMP se generó en el laboratorio del Dr. Seiki[80] mediante la inserción de un casete LacZ con una señal de localización nuclear (SNL) en el locus del gen de MT4-MMP (Mmp17) eliminando parte del exón 1. De este modo, se previene la expresión del gen de MT4-MMP, adquiriéndose en su lugar la capacidad de expresar LacZ (β-galactosidasa) en el núcleo.

Para la caracterización tanto de su expresión como de su función ha sido particularmente útil la generación por el grupo del Prof. Seiki en 2007 del modelo de ratón reportero deficiente para MT4-MMP [81].Dicho ratón fue generado mediante la inserción *'in-frame'* de una secuencia *LacZ* (que codifica para la proteína bacteriana β-galactosidasa, unido a una señal de localización nuclear) eliminando el final del primer exón y parte del primer intrón (**Figura 6**) [81]. Esto conlleva la ausencia de expresión del gen de MT4-MMP (MMP17) y a su vez la expresión de β-galactosidasa bajo el promotor endógeno de MT4-MMP (MMP17. De esta manera se puede analizar la expresión endógena de MT4-MMP en ratones heterocigotos mientras que los ratones homocigotos lacZ/lacZ son deficientes en MT4-MMP. Esta deficiencia no produce efectos en el desarrollo embrionario, la viabilidad o la fertilidad y sólo se reportó inicialmente un defecto leve en la regulación del centro de la sed a nivel del sistema nervioso central[81, 96]. Dada la ausencia de buenos anticuerpos contra MT4-MMP, en particular contra la de ratón, este modelo ha permitido analizar la expresión endógena de MT4-MMP mediante tinción enzimática con X-gal (sustrato de β-galactosidasa),con anticuerpos específicos contra β-galactosidasa o mediante PCR para el gen lacZ [81, 92, 97]. También ha permitido identificar nuevas funciones de MT4-MMP mediante un análisis más detallado del fenotipo de los ratones deficientes tanto en condiciones de homeostasis como tras la inducción de distintas patologías[92, 96].

2.3.1. **MT4-MMP en condiciones fisiológicas**

El análisis de los ratones reporteros adultos mostró que MT4-MMP se expresa abundantemente en células de músculo liso tanto vascular (en arterias como la aorta) como visceral (p.ej. en útero) y en neuronas de diversas regiones del cerebro[92, 96]. Esta expresión correlaciona con los defectos reportados en la organización y función de las células de músculo liso en la aorta[92] y con la alteración del centro de la sed[96]. También se observó su expresión en otros tejidos como ovarios y testículos y [79, 81]. En cuanto a su expresión en células del linaje mieloide, se ha confirmado en el ratón reportero la expresión del gen de MT4-MMP en los macrófagos alveolares del pulmón y en los macrófagos peritoneales en condiciones basales. En estos últimos, la expresión de MT4-MMP baja tras ocho horas de estimulación con LPS, y después vuelve a aumentar[81]. Dado que se había propuesto pro-TNFα como sustrato de MT4-MMP, se cuantificó la producción de TNFα en macrófagos peritoneales estimulados con LPS y se vio que en los ratones deficientes en MT4-MMP la producción era normal con lo que no se considera que ésta sea una función esencial ni selectiva de MT4-MMP. Por ello se postulan funciones alternativas para MT4-MMP en macrófagos en procesos inflamatorios.

Durante el desarrollo embrionario se ha descrito que MT4-MMP se expresa mayoritariamente en determinados lechos vasculares, como el endotelio del endocardio y durante la formación de la aorta, en regiones del tejido nervioso, como el bulbo olfativo e hipocampo y médula ósea, así como durante el desarrollo del ojo, y durante el desarrollo de las patas[92, 97]. También se ha demostrado, utilizando tanto el ratón deficiente en MT4-MMP como el modelo de pez cebra, que la ausencia de MT4-MMP durante el desarrollo afecta a la correcta disposición de las células de músculo liso en la aorta, así como a la migración de las células de la cresta neural[92, 98].

2.3.2. **MT4-MMP en condiciones patológicas**

Las acciones y función de MT4-MMP se ha estudiado mayoritariamente en el contexto tumoral, dada su expresión incrementada en distintos tumores, principalmente en aquellos que mostraban mayor invasividad[93, 99, 100]. Así el incremento de expresión de MT4-MMP correlaciona con la disminución de trombospondin-2, lo cual es indicativo de tumores tumorales metastáticos[101]. La expresión de MT4-MMP en el contexto tumoral se puede regular por hSETD1A [102] y a través de la vía inducida por hipoxia

HIF-1α y SLUG [103]. En cuanto a la función de MT4-MMP en tumores, la sobreexpresión de MT4-MMP en células tumorales incrementa su proliferación así como la angiogénesis con vasos que son más permeables por la alteración en el recubrimiento por pericitos perivasculares. El resultado era un incremento del crecimiento tumoral y de las metástasis[104, 105].En cuanto al mecanismo se ha propuesto queMT4-MMP interacciona y regula la actividad del receptor EGFR de forma independiente de su actividad catalítica lo que resulta en una activación de las vías de señalización de MAPK y PI3K[93, 101, 104, 105]. Recientemente se ha sugerido también un papel de MT4-MMP en la regulación de la motilidad e invasión de células tumorales mediante su asociación con PDGFRα y Tks5 y la señalización vía Src y las GTPasas Rho y Cdc42 sin definir el requerimiento o no de su actividad catalítica [106].

La expresión de MT4-MMP se regula también en contextos inflamatorios como durante infección bacteriana[107] o tras la estimulación con IL7 [108]. También en osteoartritis, una enfermedad inflamatoria donde la degradación del cartílago es crucial, se ha observado que la expresión de MT4-MMP se encuentra incrementada, lo cual sugiere su función como agrecanasa[109, 110].

En nuestro laboratorio hemos caracterizado recientemente las acciones de MT4-MMP en las células de músculo liso de las arterias durante la remodelación vascular patológica[92, 111]. Los ratones deficientes en MT4-MMP tienen una mayor incidencia de aneurismas aórticos inducidos mediante angiotensina II así como y una mayor formación de neoíntima tras la ligación permanente de la carótida todo ello relacionado con el defecto en el fenotipo de las células de músculo liso vasculares mencionado anteriormente. En cuanto al mecanismo, pudimos demostrar que el procesamiento de osteopontina por MT4-MMP, y en concreto el fragmento N-terminal generado, es necesario para la correcta activación de la vía de JNK durante la diferenciación de las células de músculo liso de la aorta.

OBJETIVOS

MT4-MMP se expresa en células del sistema inmune y en concreto en macrófagos alveolares y en macrófagos peritoneales donde sus niveles se regulan por estímulos inflamatorios como LPS y PMA[80, 81] Sin embargo, aunque la expresión de MT4-MMP se regula en contextos inflamatorios y se propuso que era necesaria para el procesamiento y liberación de la citoquina proTNFα [81], los ratones deficientes en dicha proteasa producen cantidades normales de este factor proinflamatorio lo que sugiere funciones alternativas desconocidas para MT4-MMP en inflamación y en particular en macrófagos.

Teniendo en cuenta estos antecedentes este trabajo se propuso como objetivo principal el estudio del papel de MT4-MMP en los monocitos y en los macrófagos en el contexto inflamatorio con los siguientes objetivos específicos:

1. Analizar la expresión de la proteasa MT4-MMP en los macrófagos en contextos de inflamación estéril aguda (peritonitis) y crónica (aterosclerosis).

2. Estudiar el impacto de la ausencia de MT4-MMP, global o específica en leucocitos, en la abundancia y fenotipo de los macrófagos en dichos contextos de inflamación estéril y en la progresión de la aterosclerosis.

3. Caracterizar el papel de MT4-MMP en la adhesión y reclutamiento de monocitos en los estadios tempranos de la inflamación estéril en el modelo de aterosclerosis.

4. Investigar la implicación de la actividad catalítica y el mecanismo por el que MT4-MMP ejerce sus acciones reguladoras en macrófagos y monocitos *in vivo*.

.

MATERIALES Y MÉTODOS

1. Reactivos

Los reactivos utilizados se detallan en la siguiente tabla:

ANTICUERPOS	CASA COMERCIAL	REFERENCIA	USO
CD16/CD32	BD Pharmingen	553142	Citometría de flujo
B220-biotinilado	BD Pharmingen	51.01122J	Citometría de flujo
CD3-biotinilado	BD Pharmingen	51.01082J	Citometría de flujo
Ly6G-PE	BD Biosciences	551461	Citometría de flujo
NK1.1-PE	BD Biosciences	553165	Citometría de flujo
CD11b-Alexa647	eBiosciences	51-0112-82	Citometría de flujo e Inmunofluorescencia
CD11b-biotinilado	BD Pharmingen	51.01712J	Citometría de flujo
CD45-v450	eBiosciences	48-0451-82	Citometría de flujo
Ly6C-FITC	BD Biosciences	553104	Citometría de flujo
Ly6C-APC	BD Pharmingen	560596	Citometría de flujo
CCR5-PE	eBiosciences	12.1951-12	Citometría de flujo
CCR2-FITC	Biolegend	150607	Citometría de flujo
F4/80-PEcy7	Biolegend	123114	Citometría de flujo
CD115-PE	Biolegend	135505	Citometría de flujo
Estreptavidina-PE	BD Biosciences	554061	Citometría de flujo
Anti-Macrofágo Clon PM-2K	Abcam	Ab58822	Inmunofluorescencia
Mac3	Santa Cruz Biotechnology	sc-19991	Inmunofluorescencia
MT4-MMP	Abnova	PAB4785	Inmunofluorescencia
MT4-MMP	GeneTex	GTX105268	Inmunofluorescencia
Beta-galactosidasa	Abcam	ab4761	Inmunofluorescencia
SMA	Sigma	A5228	Inmunofluorescencia
Ki67	Abcam	ab16667	Inmunofluorescencia
Caspasa-3	Cell Signalling	9661S	Inmunofluorescencia

Procesada			
CD11c	eBiosciences	11-014-81	Inmunofluorescencia
Mafb	Santa Cruz Biotechnology	sc-10022	Inmunofluorescencia
AIM	GeneTex	GTX37448	Inmunofluorescencia
Adipofilina	Novus Biologicals	NB110-40887	Inmunofluorescencia
GFP	Abcam	Ab13970	Inmunofluorescencia
CD36	Cascade BioScience	ABM-5525	Citometría de flujo
MT4-MMP	Abcam	ab51075	Western Bloting
CD11b	Abcam	ab75476	Western Bloting
Caveolina-1	Cell Signalling	3267S	Western Bloting
α-actina	Dako	M0851	Western Bloting
Tubulina	Sigma	T6074	Western Bloting
donkey-anti-rabbit 800	Odyssey	P/N 925-32213	Western Bloting
donkey-anti-rabbit 680	Odyssey	P/N 925-68073	Western Bloting
donkey-anti-mouse 800	Odyssey	P/N 925-32212	Western Bloting
donkey-anti-mouse 680	Odyssey	P/N 925-68072	Western Bloting
CD11b M1/70	eBiosciences	16-0112	Bloqueo Funcional
Control de Isotipo IgG	eBiosciences	16-4031	Bloqueo Funcional
Faloidina-Texas Red	Invitrogen	T-7471	Inmunofluorescencia
Hoechst 33342	Sigma	861526	Inmunofluorescencia
Hoechst 33258	Sigma	861405	Citometría de flujo

Tabla 1: Lista de anticuerpos utilizados

OTROS REACTIVOS	CASA COMERCIAL	REFERENCIA
Dieta grasa	ssniff	e15721-34
Maraviroc (Celsentri)	Dra Mª Ángeles Muñoz, Hospital Universitario del Gregorio Marañón Madrid	
Lympholyte	Cedarlane	CL5031
Oil Red-O	Sigma	O0625
Fluoromont-G	SouthernBiothech	0100-01
DNAsa-I	Sigma	D5025
SYRB green	Applied Biosystem	4309115
cebador*hMMP17*	TaqMan	Hs00211754_m1
cebador*hTBP*	TaqMan	Hs9999991_m1
hrMT4-MMP	Thermo Fisher Scientific	RP-77535
pkh26	Sigma	MINI26
pkh67	Sigma	MINI67
Cicloheximida	Sigma	C104450

Tabla 2: Lista de otros reactivos utilizados

2. Modelos animales y experimentos *in vivo*

2.1. Modelos animales

Los ratones deficientes en MT4-MMP se generaron como se ha descrito previamente en el laboratorio del doctor Seiki [81]. Brevemente, se produjo la deficiencia en MT4-MMP mediante la inserción de un casete LacZ eliminando parte del primer exón y el primer intrón del gen, evitando así la expresión del gen de MT4-MMP y generando la expresión de la beta-gactosidasa bajo el promotor de MT4-MMP permitiendo así la visualización de la activación de su expresión. Los ratones deficientes en LDLR y los ratones reporteros CX3CR1$^{GFP/WT}$ fueron obtenidos de Jackson Laboratories. Todos los ratones fueron mantenidos en el fondo genético C57BL6/J. Los ratones dobles deficientes para MT4-MMP y LDLR y los deficientes para MT4-MMP y CX3CR1$^{GFP/WT}$ fueron generados mediante cruce de las líneas en el Centro Nacional de Investigaciones Cardiovasculares Carlos III (CNIC) en la zona libre de patógenos según las guías de la institución. Todos los estudios animales fueros realizados con la aprobación del comité ético local (Comité ético para el bienestar animal del CNIC con

el número de procedimiento CNIC-01/13 y con el número de permiso del gobierno local de Madrid PROEX 34/13) y conforme a la directiva 2010/63EU y la recomendación 2007/526/EC relativas a la protección de animales utilizados para experimentación y otros propósitos científicos. No se utilizó ningún análisis estadístico para la estimación del tamaño muestral, y los individuos fueros distribuidos de modo aleatorio entre los grupos de experimentación.

Para la inducción de la placa de ateroma, ratones macho de 3 meses de edad fueron alimentados con dieta grasa durante los tiempos indicados.

Para los experimentos de trasplante de médula, los ratones deficientes en LDLR fueron letalmente irradiados con 9Gy en una dosis única, y reconstituidos con médula ósea total obtenida de las tibias y los fémures de ratones silvestres y deficientes en MT4-MMP. Para la reconstitución se inyectó un total de 10^7 células vía intravenosa por la vena de la cola. Tras 4 semanas de reconstitución, los ratones se alimentaron con dieta grasa durante los tiempos indicados.

Para los experimentos de bloqueo de CCR5, se administró intragástricamente el compuesto Maraviroc (MRV, 25 µg/g) o el vehículo (5% DMSO y 0.5% HCl 1N en agua destilada) a los ratones $LDLR^{-/-}$ trasplantados con médula ósea. La primera dosis fue administrada 12 horas antes de alimentar los ratones con la dieta grasa, y durante el experimento se administró cada 12 horas durante la primera semana, y cada 24 horas las restantes, siendo la última administración 2 horas antes del sacrifico.

Para los experimentos de transferencia adoptiva de los monocitos patrulleros, se aislaron monocitos de bazos de ratones MT4-$MMP^{+/+}$/$CX3CR1^{GFP/+}$ y MT4-$MMP^{-/-}$ /$CX3CR1^{GFP/+}$ en el citómetro de flujo. Se seleccionó la población Linaje negativa (Lin-: negativa para los marcadores B220, CD3, Ly6G y NK1.1), y dentro de ella, las células GFP positivas y Ly6C negativas. Se transfirió un total de $5x10^5$ células vía intravenosa a ratones deficientes en LDLR y estos se sacrificaron tras 3 días de dieta grasa para su análisis.

2.2. **Genotipado de los ratones trasplantados con médula ósea**

Se obtuvieron muestras de sangre de los ratones trasplantados tras 4 semanas del trasplante. Las células blancas fueron obtenidas utilizando Lympholyte según especificaciones del fabricante, y el ADN fue extraído mediante digestión con

proteinasa K y precipitación con Isopropanol. La PCR se realizó utilizando los siguientes cebadores: MT4-MMP$^{+/+}$: 5´-TCAGACACAGCCAGATCAGG-3´, LacZ: 5´-AATATGCGAAGTGGACCTGG-3´ y común: 5´-AGCAACACCGGCATCCACTAC-3´. El programa utilizado para la PCR fue 94ºC por 2 minutos, seguido de 40 ciclos de 95ºC durante 40 segundos, 58ºC durante 49 segundos y 72ºC durante 1 minuto, y un ciclo final de elongación a 72ºC durante 10 minutos.

2.3. **Análisis bioquímicos**

Los niveles de colesterol, triglicéridos y glucosa en la sangre de los ratones se determinaron utilizando el Dimensions RxL Max system (Siemens Healthineers).

2.4. **Transducción de los macrófagos peritoneales *in vivo***

Se generaron los lentivirus codificantes para la proteína total de MT4-MMP (Secuencia Completa, SC) y su mutante catalítico (MT4-MMP E248A, EA) así como el control de GFP (*mock*) tal como se ha descrito [92]. Los virus fueron inyectados i.p. en ratones MT4-MMP$^{+/+}$ y MT4-MMP$^{-/-}$ a una concentración aproximada de 1x10^{8} pfu/ml. Tras 5 días los macrófagos peritoneales se extrajeron para su análisis.

2.5. **Microscopía intravital en el músculo cremaster**

La microscopía intravital en el músculo cremaster se realizó como previamente se ha descrito [112]. En resumen, se anestesiaron los ratones y el músculo cremaster fue limpiado de tejido externo y expuesto en un pedestal transparente para su visión óptica. El músculo se cortó longitudinalmente con cautela y se extendieron los extremos con suturas quirúrgicas para exponer el tejido. Para el mantenimiento correcto de la temperatura en condiciones fisiológicas, el músculo se perfundió continuamente con buffer Tyrode (NaCl 134 mM, KCl 2.68 mM, $CaCl_2$ 1.80 mM, $MgCl_2$ 1.05 mM, NaH_2PO_4 417 µM, $NaHCO_3$ 11.9 mM, Glucosa 5.56 mM, pH 5.6) templado. 4 horas antes de la cirugía, a los animales se les administró intraescrotalmente 345 ng de CCL2/MCP-1. Los monocitos se marcaron mediante inyección intravenosa de los anticuerpos contra CD115-PE, Ly6C-APC o Ly6G-PE. Para los experimentos de bloqueo funcional de la integrina αM (CD11b), se inyectaron el anticuerpo bloqueante M1/70 o su correspondiente control de isotipo vía intravenosa (4mg/Kg) antes de la microscopia intravital. La microcirculación del cremaster se observó con un microscopio intravital

Leica DM6000-FS acoplado a una cámara DFC350-FX con un objetivo de inmersión en agua Apo 40x NA 1.0. Se analizaron entre 3 y 5 vénulas seleccionas aleatoriamente (de 25-40 µm de diámetro) por ratón, y las interacciones leucocito-endotelio se cuantificaron en segmentos de vasos de 350 µm durante 5 minutos. Se utilizó el programa LAS-AF (Leica Application Suite Advanced Fluorescence) para la adquisición y el procesamiento de las imágenes.

3. Obtención y procesamiento de las muestras humanas

Las arterias coronarias humanas fueron obtenidas de extirpaciones de corazón durante operaciones de trasplante en el Hospital de la Santa Creu i Sant Pau (HSCSP, Barcelona, España). El estudio fue aprobado por el comité ético del Hospital de la Santa Creu i Sant Pau (04/2016) y fue realizado acuerdo a la Declaración de Helsinki. El consentimiento escrito fue obtenido por cada paciente. Inmediatamente después de la operación quirúrgica, las arterias fueron diseccionadas, limpiadas de tejido conectivo y examinado bajo el microscopio de disección. Las muestras de vasos fueron congeladas en nitrógeno líquido y guardadas a -80ºC para posterior extracción de proteína y ARN, o alternativamente, fueron fijadas con PFA al 4% e incluidos en parafina para su análisis histológico. Las muestras fueron clasificadas como lesiones tempranas (las cuales presentaban únicamente engrosamiento de la íntima) y lesiones de aterosclerosis avanzadas (las cuales presentaban células de músculo liso en la íntima).

4. Análisis histológico y tinción de inmunofluorescencia de tejido

4.1. Tinción de ORO (Red Oil-O)

Las aortas procedentes de ratones eutanasiados fueron fijadas con 4% de PFA toda la noche a 4ºC. La grasa y el tejido conectivo fueron eliminados de las aortas bajo el microscopio de disección. Se abrió longitudinalmente la aorta en su totalidad dejando expuesta la parte luminal y se tiñó con 0.2% Oil Red-O en 78% metanol. Se adquirieron las imágenes utilizando una lupa Nikon SMZ800 con una cámara Nikon Coolpix 4500 acoplada. El área positiva para Oil red-O fue cuantificada utilizando el programa Image J (National Institutes of Health, https://imagej.net/Welcome).

4.2. **Análisis histológico y tinción de inmunofluorescencia**

Los corazones de ratones eutanasiados se perfundieron con PBS, se extrajeron y se fijaron con 4% de PFA toda la noche a 4ºC. Posteriormente se embebieron en parafina y se cortaron en secciones de 5 µm para su uso para tinciones con H&E e inmunofluorescencia.

Para las tinciones con H&E las muestras fueron desparafinadas, re-hidratadas, y teñidas con hematoxilina de Harris y eosina, tras lo cual fueron des-hidratadas y montadas con DPX. Las fotos se obtuvieron utilizando el microscopio Leica DM2500 con el programa LAS-AF. Las imágenes fueron analizadas utilizando Image J.

Para las tinciones de inmunofluorescencia las muestras fueron desparafinadas, re-hidratadas, y posteriormente se procedió al desenmascaramiento utilizando buffer citrato (Citrato sódico 10 mM, 0.05% Tween 20, pH6; se utilizó para la mayoría de las tinciones) o buffer Tris-EDTA (Tris base 10 mM, EDTA 1mM, 0.05% Tween 20, pH9; únicamente para las tinciones para Caspasa-3) durante 20 minutos a 95ºC y posterior enfriamiento durante 2 horas a temperatura ambiente. Las secciones se bloquearon y permeabilizaron durante 1 hora a temperatura ambiente con PBS 0.3% Tx100, 5% BSA y 5% suero de cabra. Se incubaron los siguientes anticuerpos primarios toda la noche a 4ºC en buffer de bloqueo: anti-Mac3, anti-MT4-MMP, anti-betagalactosidasa, anti-Ki67, anti-Caspasa 3 procesada, anti-CD11c, anti-Mafb y anti-AIM. Posteriormente las muestras se lavaron con PBS 0,1%Tx100, e incubaron durante 2 horas a temperatura ambiente con los correspondientes anticuerpos secundarios conjugados. Finalmente, las muestras fueron montadas con Fluoromont conteniendo Hoechst 33342. Las imágenes fueron adquiridas utilizando el microscopio confocal LSM700 de Zeiss (Carl Zeiss), utilizando un objetivo de 25x. Las imágenes fueron procesadas utilizando el programa Zen2009 Light Edition system (Carl Zeiss) y se cuantificaron utilizando el programa Image J o el Cell Profiler (Broad institute).

4.3. **Tinción *in toto* de inmunofluorescencia**

La membrana peritoneal mesentérica se obtuvo de ratones tras 72 horas de tioglicolato, y las aortas se obtuvieron de ratones tras 3 días de dieta grasa. Los tejidos se limpiaron bajo la lupa de disección y las aortas fueron abiertas en longitudinal. Posteriormente los tejidos fueron fijados durante una noche a 4ºC con 4% PFA.

Posteriormente las muestras fueron bloqueadas y permeabilizadas utilizando PBS con 0,3% TX100, 5% BSA, 5% suero de cabra y 1:100 anti-CD16/CD32 durante 1 hora a temperatura ambiente. Las muestras fueron teñidas toda la noche a 4ºC con anti-CD11b-Alexa647, anti-Ly6C, Anti-CD115, anti-CD31 o anti-GFP, y posteriormente con los correspondientes anticuerpos secundarios y Hoechst 33342 durante 2 horas a temperatura ambiente. Finalmente, las muestras fueron montadas con Fluoromont. Las imágenes fueron adquiridas utilizando el microscopio confocal LSM700 de Zeiss (Carl Zeiss), utilizando un objetivo de 10x. Las imágenes fueron procesadas utilizando el programa Zen2009 Light Edition system (Carl Zeiss) y se cuantificaron utilizando el programa Image J.

5. Cultivos y experimentos celulares *in vitro*

5.1. **Análisis de los macrófagos peritoneales**

Los macrófagos peritoneales primarios se obtuvieron de ratones MT4-MMP$^{+/+}$ y MT4-MMP$^{-/-}$ mediante lavado peritoneal con 10 ml de PBS frio tras 3 días de la inducción de peritonitis mediante inyección intraperitoneal (i.p.) de 3% de tioglicolato (TG). Posteriormente se contaron los macrófagos, se resuspendieron en medio RPMI-1640 suplementado con 2.5% de suero fetal bovino, 10mM de HEPES, 50 UI/ml de penicilina, 50 µg/ml de estreptomicina, 1mM de piruvato sódico y 0.1 mM de aminoácidos no esenciales y se cultivaron sobre plástico para la obtención de proteína y ARN o sobre cristales con fibrinógeno para las tinciones de inmunofluorescencia. Para los estudios de citometría de flujo se utilizaron macrófagos recién extraídos de la cavidad peritoneal.

Para los análisis de inmunofluorescencia, los macrófagos se sembraron sobre cubreobjetos (500,000 células por cada cubreobjetos de 12 mm de diámetro), con matriz de fibrinógeno. Tras 3 ó 24 horas de adhesión de los macrófagos, estos fueron fijados con 4% PFA durante 10 minutos a temperatura ambiente para su posterior tinción. Se bloquearon y permeabilizaron las muestras utilizando PBS con 0.3% TX100, 5% BSA, 5% suero de cabra y 1:100 del anti-CD16/CD32 durante 1 hora a temperatura ambiente. Posteriormente las células se incubaron durante toda la noche a 4ºC con los siguientes anticuerpos primarios: anti-Mafb, anti-AIM y anti-Caspasa 3. Al día siguiente se incubaron durante 2 horas a temperatura ambiente con los

correspondientes anticuerpos secundarios marcados, y con anti-CD11b-Alexa 647 y faloidina-Texas Red. Las muestras fueron montadas utilizando Fluoromont con Hoechst 33342 y las imágenes fueron adquiridas utilizando el microscopio confocal Nickon A1R, utilizando un objetivo de 20x. Las imágenes fueron procesadas y analizadas utilizando el programa Image J.

Para el estudio de la afinidad por el componente C3 del complemento (C3) y el estudio de apoptosis, los macrófagos peritoneales se sembraron sobre cubreobjetos y tras 24 horas se incubaron con eritrocitos opsonizados con C3 durante los tiempos indicados o con cicloheximida (100 µg/ml) durante 6 horas (para la inducción de la apoptosis). Posteriormente se fijaron y se tiñeron y analizaron como anteriormente se ha descrito.

Para analizar la afinidad por AcLDL, los macrófagos en suspensión se incubaron con AcLDL marcadas con FITC durante los tiempos indicados y la intensidad de fluorescencia de AcLDL-FITC fue analizada mediante citometría de flujo.

Para los experimentos de egresión, los macrófagos peritoneales procedentes de ratones MT4-MMP$^{+/+}$ y MT4-MMP$^{-/-}$ tras peritonitis fueron marcados con las sondas PKH26 y PKH67 respectivamente según indicaciones del suministrador. Las células marcadas se mezclaron en ratio 1:1 y se transfirió un total de 500.000 células i.p. a ratones silvestres pre-estimulados con TG durante 3 días. Posteriormente se indujo la egresión mediante la inyección de 1µg de LPS o PBS como control vía i.p., y tras 4 horas se sacrificaron los ratones y se analizó el lavado peritoneal y los bazos mediante citometría de flujo.

5.2. **Citometría de flujo**

Las muestras de sangre, médula ósea y los macrófagos peritoneales se bloquearon durante 15 minutos a 4ºC con PBS conteniendo 5% FBS y 1:100 de anti-CD16/CD32. Posteriormente se tiñeron durante 20 minutos a 4ºC con los siguientes anticuerpos: anti-CD11b-Alexa647 o biotinilado, anti-CD45-V450, anti-Ly6C-FITC o APC, anti-CCR5-PE, anti-CCR2-FITC, anti-F4/80-PeCy7, anti-AIM/CD5L y anti-CD36. Tras ello se incubaron otros 20 min a 4ºC con los correspondientes anticuerpos secundarios. Para la cuantificación de las células muertas de añadió Hoechst 33258 5 minutos antes del análisis. Las muestras de sangre y médula se incubaron con el buffer de lisis de eritrocitos (Buffer ACK; 150 mM NH_4CL, 10 mM $KHCO_3$, 0.1 mM Na_2EDTA, pH 7.2-7.4) durante 7 minutos a temperatura ambiente tras la tinción. Los datos fueron

adquiridos utilizando el citómetro FACSCanto III (BD) y analizados utilizando el programa FlowJo (Tree Star).

6. Técnicas bioquímicas

6.1. PCR cuantitativa (qPCR)

El ARN total fue extraído utilizando TRIzol (Invitrogen) con columnas de alta densidad Maxtract (Quiagen, 1038988). El ARN aislado fue tratado con DNAsa I y la retrotranscripción se realizó con el kit de transcripción reversa de cDNA de alta capacidad (Applied Biosystems). Para las muestras de ratón, la qPCR fue realizada utilizando la mezcla maestra SYBR Green PCR, en el sistema de detección CFX384 (Biorad). Los cebadores utilizados se detallan en la **Tabla 3**. Los datos fueron normalizados utilizando los niveles de expresión de 36b4 y ciclofilina en cada muestra individual. Para las muestras humanas la qPCR se realizó utilizando los cebadores de TaqMan para el gen *MMP17*, incluyendo *TBP* para normalizar los niveles de expresión. Todas las muestras fueron analizadas por triplicado, y los niveles de ARN fueron analizados utilizando Biogazelle qBase PLUS.

GEN	CEBADORES
Itgam	5'-TGCCATAATGCAAGTTGCTG-3'
	5'-ATCACCAGCAAAGTGGAAGC-3'
Mmp17	5´-ACTGTCCAAAGCGATTACTGC-3´
	5´-GCATCGAGGGGTTTTCATCAG-3´
Il6	5´-TAGTCCTTCCTACCCCAATTTCC-3´
	5´-TTGGTCCTTAGCCACTCCTTC-3´
Tnfa	5´-CCAGACCCTCACACTCAGATC-3´
	5´-CACTTGGTGGTTTGCTACGAC-3´
Il1b	5´-GCTGAAAGCTCTCCACCTCA-3´
	5´-AGGCCACAGGTATTTTGTCG-3´
Il10	5´-TGAATTCCCTGGGTGAGAAG-3´
	5´-TCACTCTTCACCTGCTCCACT-3´
Tgfb	5´-GCTAATGGTGGACCGCAAC-3´
	5´-CGAATGTCTGACGTATTGAAGAA-3´

Mafb	5´-AGGACCGCTTCTCTGATGA-3´
	5´-GAGCTGCGTCTTCTCGTTCT-3´
Cd5l	5´-GGAAGACACGTTGGCTCAAT-3´
	5´-AGACGCACATCCTCTGGAAT-3´
Cd36	5´-GAGCAACTGGTGGATGGTTT-3´
	5´-GCAGAATCAAGGGAGAGCAC-3´
Ccr5	5´-TGCAGTCCTCATTTTCCACA-3´
	5´-CCTACAGCGAAACAGGGTGT-3´
Ccr2	5´-ACACCCTGTTTCGCTGTAGG-3´
	5´-CCTGGAAGGTGGTCAAGAAG-3´
Cx3cr1	5´-AAGTTCCCTTCCCATCTGCT-3´
	5´-CGAGGACCACCAACAGATTT-3´
Cyclophilin	5´-ACAGGTCCTGGCATCTTGTC-3´
	5´-CATGGCTTCCACAATGTTCA-3´
36b4	5´-GCGACCTGGAAGTCCAACTA-3´
	5´-ATCTGCTGCATCTGCTTGG-3´

Tabla 3: Lista de los cebadores utilizados para la qPCR.

6.2. **Western blotting**

Para las muestras humanas las proteínas se extrajeron de las arterias coronarias, con el buffer de lisis (50 mM Tris-HCL pH 7,5, 1% Tritón X-100, 150 mM NaCl, 1mM DTT e inhibidores de proteasas) en frío. Las proteínas de aortas con aterosclerosis de ratón se obtuvieron a partir de muestras embebidas en parafina, a las que se les quitó la parafina externa, se las desparafinó y se las rehidrató; posteriormente se lisaron estas muestras en 20mM Tris-HCL pH7,5 y 2% SDS e inhibidores de proteasas y se incubaron a 100ºC durante 20 minutos y a 60ºC durante 2 horas. Para la extracción de proteínas de macrófagos peritoneales, se utilizó un buffer de lisis que contenía 10mM Tris-HCL pH7,5, 1% Tx114, 150mM NaCl e inhibidores de proteasas, y se incubaron las muestras a 30ºC durante 5 minutos para la separación de las fases lipofílica e hidrofílica.

Las proteínas se separaron en gel SDS-PAGE al 10% y se transfirieron a membranas de nitrocelulosa de 0.45 µm de poro, para su posterior bloqueo con 5% de leche

desnatada en TBST durante 1 hora a temperatura ambiente. Los siguientes anticuerpos primarios usados se incubaron toda la noche a 4ºC: anti-MT4-MMP, anti-CD11b, anti-caveolina1, anti-α actina, anti-tubulina. Posteriormente se lavaron con TBST, se revelaron mediante incubación con anticuerpos secundarios de Odyssey durante 1 hora a temperatura ambiente, y se visualizaron utilizando el Odyssey Infrared Imaging System (LI-COR Biosciences).

7. Análisis *in silico*

7.1. Modelado *in silico* del dímero de MT4-MMP con el heterodímero de la integrina αMβ2

Las secuencias FASTA de las proteínas maduras de MT4-MMP/MMP17 y la integrina αMβ2 fueron analizadas con I-Tasser v4.4 implementado localmente para modelado en cadena. Los modelos seleccionados fueron aquellos que presentaban un plegamiento correcto con una mínima energía (el mejor alineamiento estructural respecto a los patrones). En dicho modelos, los dominios transmembrana (TM) se encontraban contenidos en el centro de la proteína. Por ello los ángulos de dichas regiones (los transmembrana y los C-terminales) fueron fijados acorde a la estructura secundaria predicha, y se hizo un ciclo de refinamiento con la estructura de membrana en la Rosetta suite v3.5 release 2015.23.58158 (www.rosettacommons.org). Para encajar el dímero de MT4-MMP con el dímero de la integrina, los monómeros modelados previamente fueron posicionados de acuerdo a lo previamente publicado de dimerización en interfase usando pymol v1.8 (www.pymol.org), y el modelo dimérico nuevo fue usado como patrón inicial. Usando este modelo como entrada, con la misma restricción anterior, se generó un nuevo modelo del dímero usando la aplicación *mp_dock* de la estructura de membrana Rosetta suite v3.5 release 2015.23.58158 en cada caso. Finalmente utilizando los modelos obtenidos, el complejo MT4-MMP-itgam-itb2 fue modelado con una aproximación similar.

7.2. Identificación del sitio de corte de la integrina αM por MT4-MMP y validación mediante digestión *in vitro*.

Los sitios de corte de la integrina αMβ2 por MT4-MMP se identificaron utilizando Cleavpredict (http://cleavpredict.sanfordburnaham.org/) y los sitios predichos y expuestos fueron filtrados de acuerdo a la matriz de procesamiento peptídico en la base de datos MEROPS (http://merops.sanger.ac.uk/). La conservación de los sitios de corte en las cadenas de la integrina αL y β2 en ratón y en humano fue testada utilizando Uniprot (http://www.uniprot.org/aling/). El péptido correspondiente al sitio de corte en la cadena αM identificado uniendo los datos de las bases de datos y del modelado *in silico* (RPQVTFSENLSSTCHTKER), fue generado en el Centro de Investigaciones Biológicas (CIB, CSIC, Madrid) e incubado con la proteína recombinante humana de MT4-MMP (hrMT4-MMP) correspondiente al dominio catalítico, durante 2 horas a 37ºC en agua. Los péptidos resultantes se analizaron mediante reacción paralela monitorizada de alta resolución en el aparato Easy nLC 1000 nano-HRLC (Thermo Fisher Scientific), acoplado a un espectrómetro de masas cuádruple-orbital (Q Exactive, Thermo Scientific). Los péptidos fueron separados a 200 nL/min en un gradiente continuo consistente en 8-30% B por minuto y 30-90% B por 2 minutos (B= 90% acetonitrilo, 0.1% ácido fórmico) e ionizado utilizando una aguja de emisión de nanospray Picotip (New Objetive, Woburn, MA, USA). Cada carrera de espectrometría de masas consiste en un espectro de resolución FT aumentado (resolución de 15,000) en el rango de 400-1400 m/z seguido por un espectro independiente de datos MS/MS de 7 iones parientes adquiridos durante la carrera cromatográfica. El valor de búsqueda AGC en el Orbitrap para la supervivencia del escaneo fue seleccionada como 1,500,000 y la fragmentación se realizó con un 27% de la energía de colisión normalizada con un valor de búsqueda de 250,000 iones. Los datos fueron analizados utilizando Xcalibur 2.2 (Thermo Fisher Scientific).

8. Análisis estadístico

Todos los resultados se han analizado y representado gráficamente utilizando el software GraphPad Prism 4.0 (GraphPad Software, La Jolla, USA). Para comparar dos grupos muestrales de igual varianza se utilizó el método de la t de Student de dos colas. Cuando las varianzas eran significativamente diferentes, se aplicó el método de

Welch. En los casos en los que se compararon más de dos grupos muestrales se utilizó ANOVA de una cola o dos colas combinado con el método de comparación múltiple de Bonferroni en los casos en los que las muestras se ajustaron a una distribución paramétrica, y el método de Kruskal-Wallis combinado con el método de comparación múltiple de Dunn cuando no se ajustaron. En aquellos casos donde las muestras control se normalizaron a uno se usó el método de la t de Student de un grupo para su análisis estadístico. En los casos en los que se compararon frecuencias se utilizó el método de Chi-cuadrado cuando había más de 2 rangos y la prueba exacta de Fisher cuando había únicamente 2 rangos.

En todos los casos se representó la media ± el error estándar de la media (EEM) y se consideraron las diferencias significativas cuando el valor p del correspondiente análisis estadístico era inferior a 0.05. Se representó el grado de significación con uno, dos, tres o cuatro asteriscos, siendo: * $p<0.05$, ** $p< 0.01$, *** $p< 0.001$, **** $p< 0,0001$.

RESULTADOS

Los macrófagos deficientes en MT4-MMP se retienen en la membrana peritoneal inflamada y presentan mayores niveles de la integrina αM en la membrana celular

Tal como se ha mencionado, MT4-MMP se expresa en líneas y células mieloides y en macrófagos [80, 81, 83], se regula en procesos inflamatorios[107] y aunque puede procesar pro-TNF-α los ratones deficientes en la proteasa liberan cantidades normales de esta citoquina[80]. Todo ello indica que MT4-MMP podría estar desempeñando funciones alternativas durante la inflamación, y en particular en los macrófagos.

Dado que la ausencia de MT4-MMP afecta a la migración de otros tipos celulares [92, 98], investigamos en primer lugar su efecto en la movilización de los monocitos y macrófagos a las zonas de inflamación. Para ello utilizamos el modelo de peritonitis inducido por tioglicolato (TG), para el cual se administra TG vía intraperitoneal en ratones lo que produce el reclutamiento de células inmunes, y en concreto de monocitos que se diferencian a macrófagos en los primeros días. (**Figura 7a**). Comprobamos que en condiciones basales la población mayoritaria en el peritoneo eran macrófagos residentes (denominados LPM de las siglas en inglés "*large peritoneal macrophages*") y tras 3 días de peritonitis la población mayoritaria eran los macrófagos SPM (de las siglas en inglés "*small peritoneal macrophages*") derivados de monocitos circulantes (**Figura 7b**).

De este modo indujimos peritonitis estéril con TG en ratones deficientes en MT4-MMP y en sus correspondientes controles de genotipo silvestre (a partir de ahora nos referiremos a ellos como $MT4^{-/-}$ y $MT4^{+/+}$ respectivamente). Observamos que los macrófagos peritoneales obtenidos tras 3 días de TG de ratones $MT4^{+/+}$ pero no los de los ratones $MT4^{-/-}$ expresan MT4-MMP, tanto a nivel de proteína (**Figura 7c**) como a nivel de ARN mensajero (**Figura 7d**).

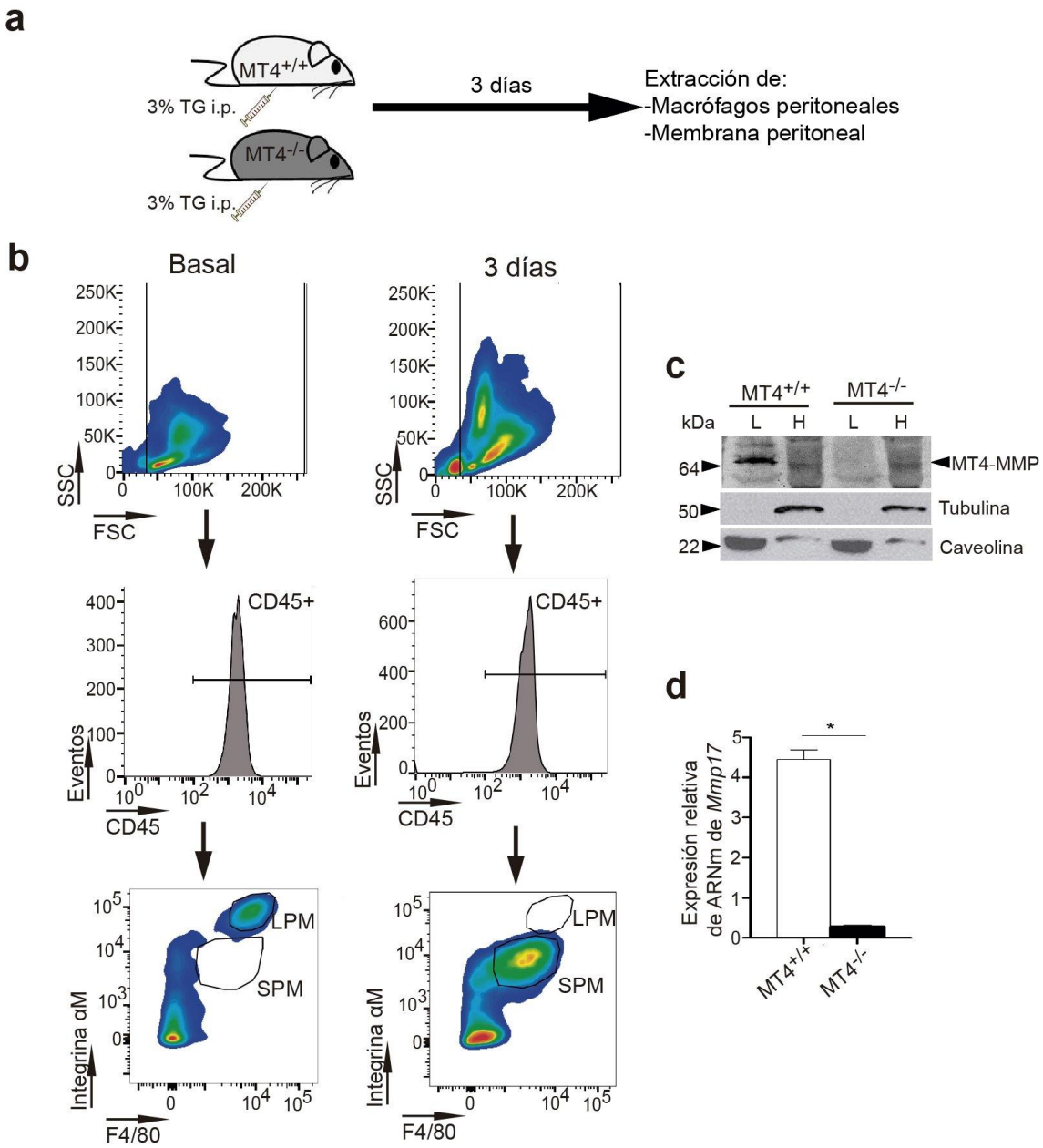

Figura 7: MT4-MMP se expresa en macrófagos peritoneales durante peritonitis. a. Esquema del diseño experimental de inducción de peritonitis en ratones MT4-MMP$^{+/+}$ y MT4-MMP$^{-/-}$ mediante inyección intraperitoneal (i.p.) de tioglicolato (TG). **b.** Gráfica denubes de puntos representativos de los lavados peritoneales de ratones en condiciones basales (panel superior) y tras 3días de TG (panel inferior).LPM indica "Large Peritoneal Macrophages" y SMP indica "Small Peritoneal Macrophages".**c.** Western blot representativo de lisados de Tx114 de macrófagos peritoneales de ratones MT4-MMP$^{+/+}$ y MT4-MMP$^{-/-}$tras peritonitis. L indica fracción lipofílica y H indica fracción hidrofílica. **d.** Expresión relativa de ARNm de MT4-MMP (*Mmp17*) de macrófagos peritoneales de ratones MT4-MMP$^{+/+}$ y MT4-MMP$^{-/-}$ tras peritonitis. n=6 ratones por genotipo en 2 experimentos independientes. Los datos fueron analizados mediante el método de la t de Student. *p<0.05.

En este modelo el número de macrófagos (definidos como células positivas para CD45, la cadena αM de la integrina αMβ2 y el marcador F4/80) era significativamente menor en el exudado peritoneal de los ratones MT4$^{-/-}$ que en el de los ratones MT4$^{+/+}$ (**Figura 8a**). Esta disminución de macrófagos en el exudado correlaciona con un incremento en el número de células positivas para la integrina αM (principalmente monocitos y macrófagos) adheridos en la membrana peritoneal mesentérica de los ratones MT4$^{-/-}$ (**Figura 8b**). Todo ello nos indica que la ausencia de MT4-MMP produce una retención de los macrófagos en el tejido inflamado.

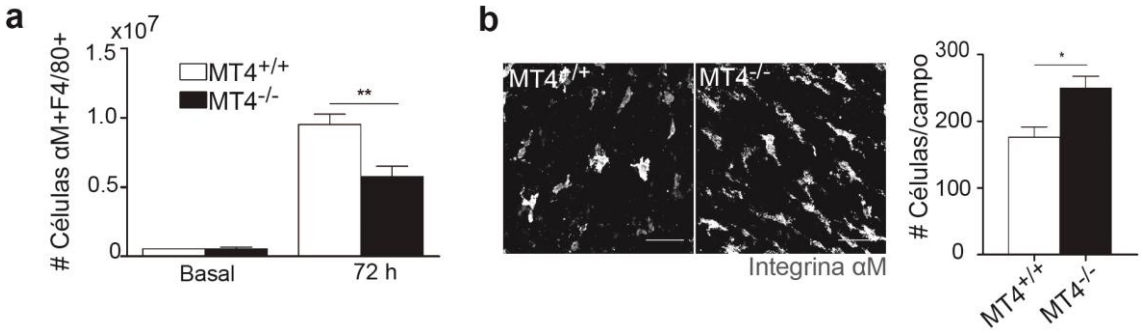

Figura 8: La ausencia de MT4-MMP en macrófagos peritoneales aumenta su retención en la membrana peritoneal inflamada. a. Cuantificación del número de macrófagos (células positivas para CD45, integrina αM y F4/80) obtenidos en los lavados peritoneales de ratones MT4-MMP$^{+/+}$ y MT4-MMP$^{-/-}$ en condiciones basales y tras peritonitis. n= 3 ratones por genotipo en basal y 12 en peritonitis en 1 y 4 experimentos independientes. Los datos se analizaron mediante ANOVA de una cola seguido del post-test de Bonferroni. **p<0.001. **b.** Imágenes representativas de membranas peritoneales de ratones MT4-MMP$^{+/+}$ y MT4-MMP$^{-/-}$ tras 3 días de tioglicolato, y teñidas para la integrina αM. La barra de escala equivale a 50μm. **c.** Cuantificación del número de macrófagos adheridos a la membrana peritoneal de ratones tratados como en **b**. n= 6 ratones por genotipo de 2 experimentos independientes. Los datos se analizaron mediante el método de la t de Student. *p<0.05.

En el análisis de citometría de flujo observamos además que, tras la inducción de peritonitis, los macrófagos MT4$^{-/-}$ expresaban niveles mayores de la integrina αM en la superficie celular que los macrófagos MT4$^{+/+}$ (**Figura 9a**), sin mostrar diferencias en los niveles de ARN mensajero (**Figura 9b**). Las integrinas son glicoproteínas heterodiméricas de membrana celular importantes para la adhesión de las células a proteínas de la matriz extracelular o a ligandos de membrana de otras células [113]. La integrina αMβ2 (también denominada CD11b/CD18, CR3, o Mac1) se expresa mayoritariamente en células mieloides[114]. Dicha integrina está implicada en la adhesión a diversos ligandos tales como fibrinógeno (en la matriz extracelular provisional tras daño) o ICAM1 (en la superficie de las células endoteliales), cuya

expresión aumenta en procesos inflamatorios[113]. Las integrinas se expresan en la membrana celular en conformaciones de distinta afinidad por el ligando [115], de modo que puede haber un aumento del heterodímero sin que esto implique un incremento en su actividad. Para investigar si el aumento en la integrina αMβ2 en los macrófagos deficientes en MT4-MMP implica también un aumento en su actividad, aislamos macrófagos peritoneales tras peritonitis por TG y analizamos su unión a dos de sus ligandos, el componente 3 del complemento (C3) y el fibrinógeno.

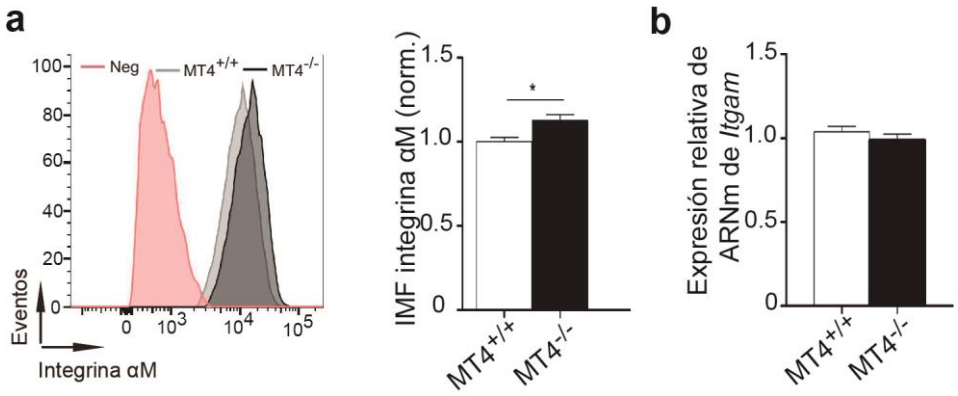

Figura 9: Los niveles de la integrina αM en la membrana de los macrófagos peritoneales tras peritonitisestán incrementados en ausencia de MT4-MMP. a. Histogramas representativos de la expresión de la integrina αM en los macrófagos peritoneales tras peritonitis de ratones MT4-MMP$^{+/+}$ y MT4-MMP$^{-/-}$ (izquierda) y cuantificación de la intensidad media de fluorescencia (IMF) normalizada (derecha). n=20 ratones por genotipo en 4 experimentos independientes. Los datos fueron analizados mediante el método de la t de Student. *p<0.05. **b.** Niveles de expresión de ARNm de la integrina αM (*Itgam*) de macrófagos peritoneales tras peritonitis de ratones MT4-MMP$^{+/+}$ y MT4-MMP$^{-/-}$. n= 6 ratones por genotipo en 2 experimentos independientes. Los datos fueron analizados mediante el método de la t de Student.

En primer lugar, incubamos los macrófagos peritoneales MT4$^{-/-}$ y MT4$^{+/+}$ con eritrocitos opsonizados con C3, y cuantificamos el número de eritrocitos captados por macrófago tras 5, 10 y 15 minutos de incubación mediante microscopía (**Figura 10a**). Lo que pudimos observar es que en ausencia de MT4-MMP desde el minuto 5, había más eritrocitos captados, y este aumento se mantenía hasta el minuto 15 (**Figura 10b**), lo que nos indica que los macrófagos deficientes en MT4-MMP son más activos captando partículas vía la integrina αMβ2.

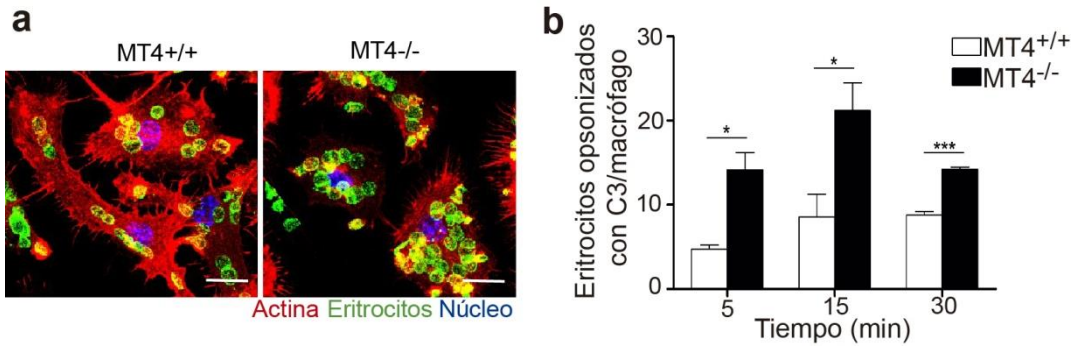

Figura 10: Los macrófagos peritoneales deficientes en MT4-MMP son más activos captando eritrocitos opsonizados con C3. a. Imágenes representativas de macrófagos peritoneales tras peritonitis de ratones MT4-MMP$^{+/+}$ y MT4-MMP$^{-/-}$ en presencia de eritrocitos opsonizados con el componente 3 del complemento (C3). En rojo se muestra la actina (faloidina), en verde los eritrocitos y en azul los núcleos (Hoechst). La barra de escala equivale a 15 µm. **b.** Cuantificación del número de eritrocitos opsonizados con C3 por macrófago como en **a** tras 5, 10 y 15 minutos de incubación. n=6 muestras por genotipo en 2 experimentos independientes. Los datos fueron analizados mediante ANOVA de dos colas seguido del post-test de Bonferroni. *p<0.05, ***p< 0.001.

Complementariamente, cultivamos los macrófagos peritoneales tras peritonitis sobre fibrinógeno, otro ligando de la integrina αMβ2, y tras adhesión durante 3 y 24 horas los analizamos mediante microscopía (**Figura 11a**). No observamos diferencias entre los genotipos en el número de macrófagos adheridos ni en su circularidad (**Figura 11b-c**) a ninguno de los tiempos, sin embargo el área celular tras 3 horas era mayor en ausencia de MT4-MMP, manteniéndose la diferencia tras 24 horas de adhesión (**Figura 11a-b**). Además, el anticuerpo bloqueante de unión a ligando de la integrina αM, M1/70, eliminaba el incremento en área de los macrófagos deficientes en MT4-MMP, indicando que este incremento en el área celular sobre fibrinógeno es dependiente de la integrina αMβ2 (**Figura 11a-d**).

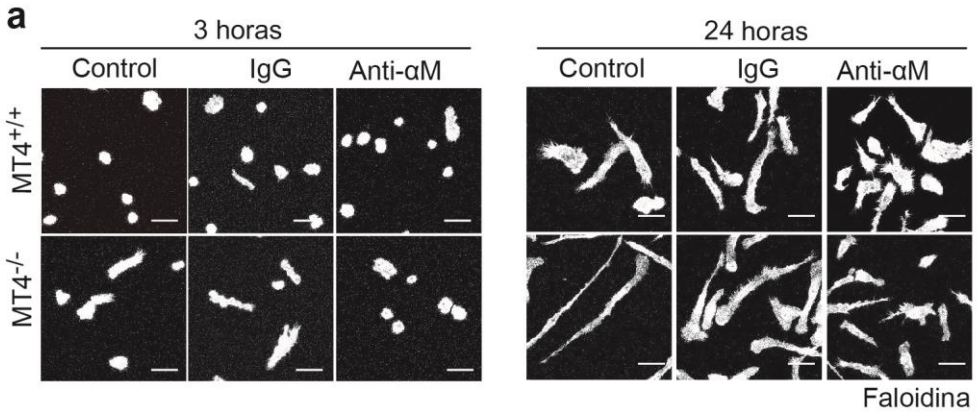
a
3 horas
24 horas
Control
IgG
Anti-αM
Control
IgG
Anti-αM
MT4+/+
MT4-/-
Faloidina

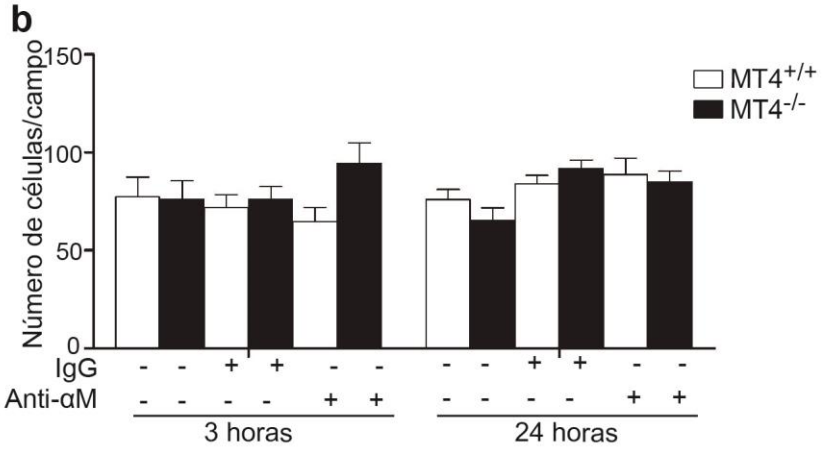
b
Número de células/campo
150
100
50
0
MT4+/+
MT4-/-
IgG
Anti-αM
3 horas
24 horas

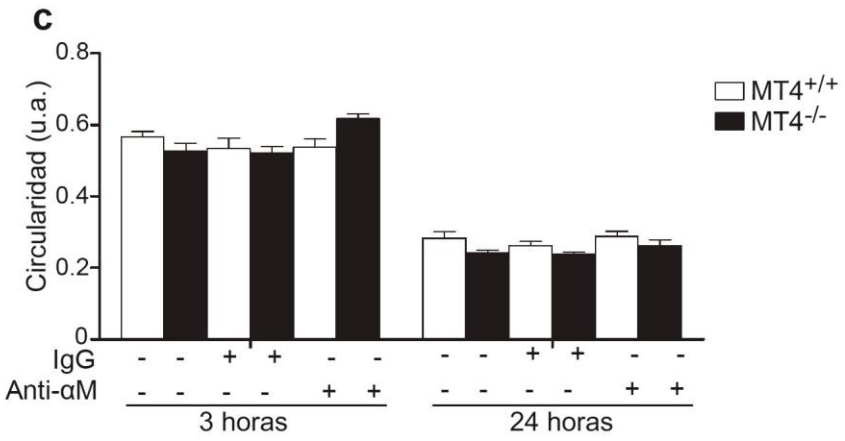
c
Circularidad (u.a.)
0.8
0.6
0.4
0.2
0
MT4+/+
MT4-/-
IgG
Anti-αM
3 horas
24 horas

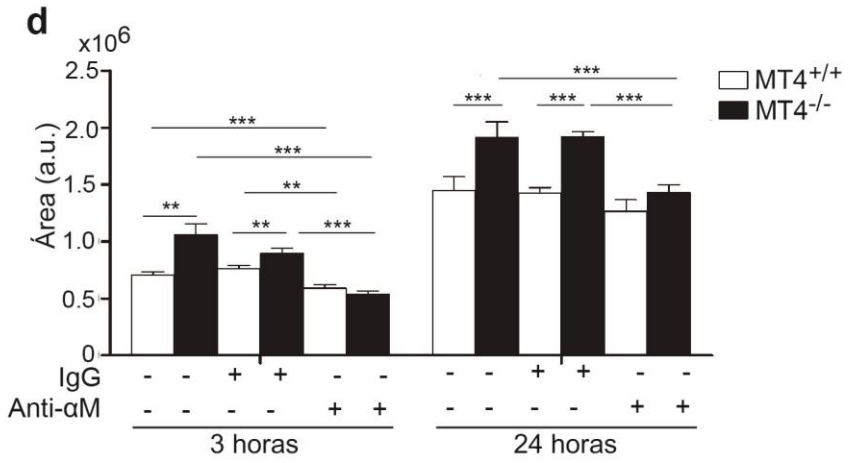
d
x10^6
Área (a.u.)
2.5
2.0
1.5
1.0
0.5
0
MT4+/+
MT4-/-
IgG
Anti-αM
3 horas
24 horas

Figura 11: La ausencia de MT4-MMP en macrófagos peritoneales tras peritonitis induce un área celular mayor sobre fibrinógeno de modo dependiente de la integrina αMβ2. a. Imágenes representativas de macrófagos peritoneales tras peritonitis de ratones MT4-MMP$^{+/+}$ y MT4-MMP$^{-/-}$ plaqueados sobre fibrinógeno y teñidos para actina tras 3 o 24 horas de adhesión en presencia o ausencia del anticuerpo bloqueante de la integrina αM (anti-αM, clon M1/70) o su correspondiente control de isotipo (IgG). La barra de escala equivale a 30μm. Cuantificación del número de células adheridas (**b**), circularidad (**c**) y área celular (**d**) de macrófagos tratados como en**a**. n=6 ratones por genotipo en 2 experimentos independientes. Los datos fueron analizados mediante ANOVA de una cola seguido del post-test de Bonferroni. **p<0.01, ***p<0.001.

MT4-MMP se expresa en los macrófagos de las placas de aterosclerosis

Para investigar si MT4-MMP se expresaba también en los macrófagos en un contexto de inflamación estéril crónica utilizamos el modelo de aterosclerosis en ratón. Para ello utilizamos ratones deficientes en el receptor de LDL (LDLR$^{-/-}$) que desarrollan placas ateroscleróticas en la aorta cuando se alimentan con dieta grasa [116]. Cruzamos estos ratones con los deficientes en MT4-MMP, generando l ratones LDLR$^{-/-}$MT4$^{-/-}$, y sus correspondientes controles LDLR$^{-/-}$ MT4$^{+/+}$.

En primer lugar, analizamos los niveles de MT4-MMP a nivel de proteína por Western blot en lisados obtenidos de la aorta ascendente de ratones LDLR$^{-/-}$MT4$^{+/+}$ y LDLR$^{-/-}$ MT4$^{-/-}$ en condiciones basales, así como en estadios tempranos y tardíos de la enfermedad (0, 8 y 16 semanas de dieta grasa respectivamente) (**Figura 12a-c**). Pudimos observar que en condiciones basales hay altos niveles de expresión de MT4-MMP, mientras que tras 8 semanas de dieta grasa la expresión de MT4-MMP es prácticamente indetectable, volviendo a incrementarse tras16 semanas de dieta grasa. En todos los estadios se pudo comprobar que MT4-MMP estaba ausente en los ratones LDLR$^{-/-}$MT4$^{-/-}$ (**Figura 12b-c**). Por inmunofluorescencia observamos que MT4-MMP se expresa en los diversos tipos celulares (células de músculo liso, endoteliales y macrófagos) que componen las placas de aterosclerosis tras 8 semanas de dieta grasa (**Figura 12d**).

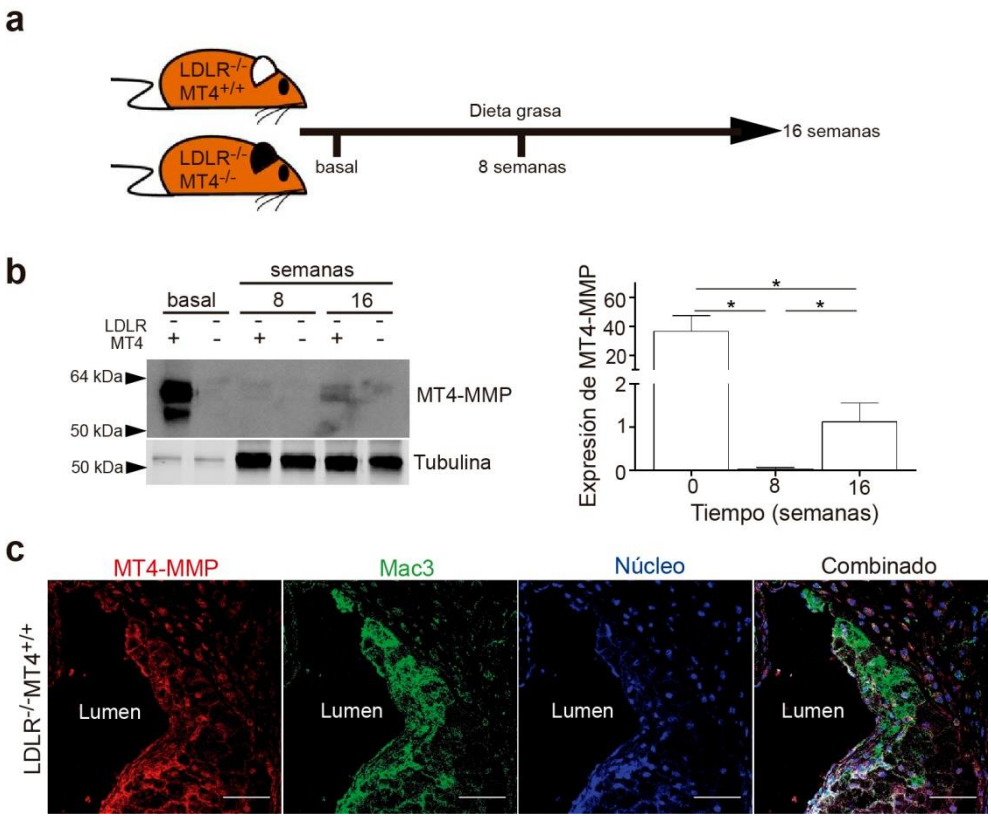

Figura 12: MT4-MMP se expresa en los macrófagos presentes en la placa durante la aterosclerosis en ratón. a. Esquema del diseño experimental de inducción de aterosclerosis en ratones LDLR$^{-/-}$MT4-MMP$^{+/+}$ y LDLR$^{-/-}$MT4-MMP$^{-/-}$. **b.** Western blot representativo de lisados de aortas de ratones LDLR$^{-/-}$MT4-MMP$^{+/+}$ y LDLR$^{-/-}$MT4-MMP$^{-/-}$ tras 0, 8 y 16 semanas de dieta grasa (izquierda) y cuantificación de la cantidad de proteína de MT4-MMP en los ratones LDLR$^{-/-}$MT4-MMP$^{+/+}$(derecha). n=4 ratones independientes por condición. Los datos fueron analizados mediante ANOVA de una cola seguido del post-test de Bonferroni. *p<0.05. **c.** Imágenes representativas de válvulas aórticas de ratones LDLR$^{-/-}$MT4-MMP$^{+/+}$ tras 8 semanas de dieta grasa. En rojo se muestra MT4-MMP, en verde Mac3 y en azul los núcleos (Hoechst). La barra de escala equivale a 50 µm.

Para investigar si los macrófagos que expresaban MT4-MMP en la placa de ateroma derivaban de monocitos circulantes, se trasplantaron ratones LDLR$^{-/-}$ con células de médula ósea de ratones deficientes en MT4-MMP. Como ya se ha comentado, estos ratones expresan β-galactosidasa bajo el promotor de MT4-MMP, y mediante la tinción con anti-β-galactosidasa observamos macrófagos positivos en la placa tanto a 1 como a 8 semanas tras dieta grasa (**Figura 13**), indicando que los macrófagos que expresan MT4-MMP en la placa de ateroma derivan de monocitos circulantes.

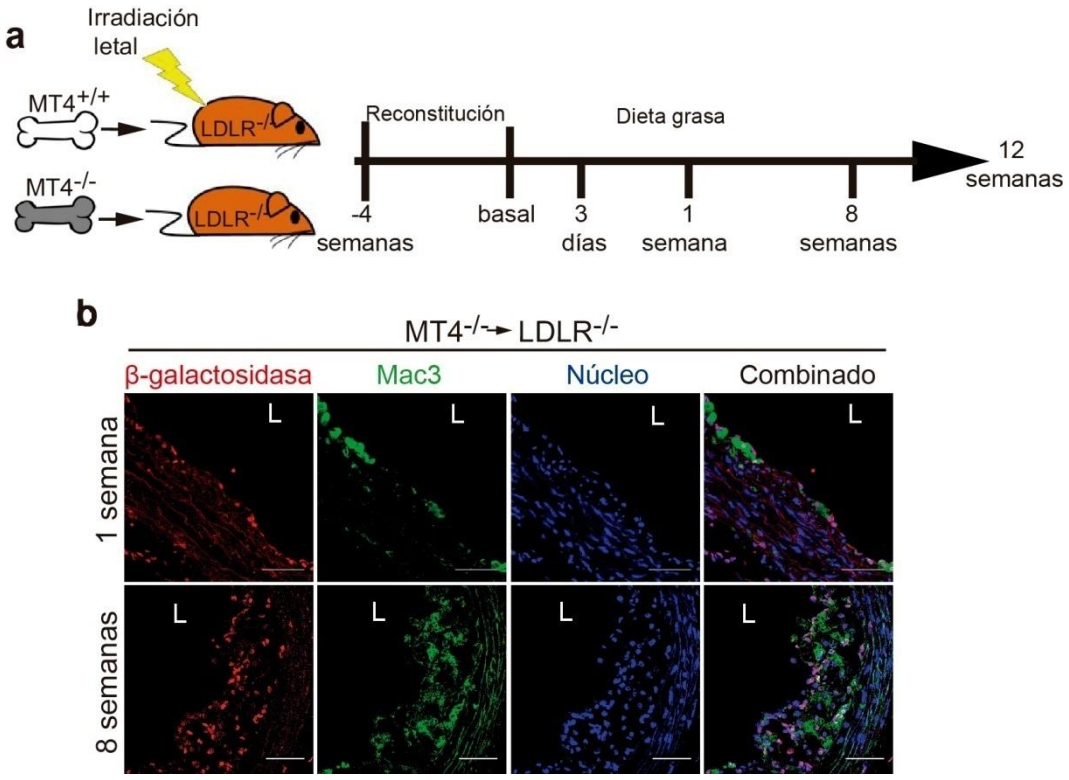

Figura 13: MT4-MMP se expresa en macrófagos derivados de monocitosen la placa de ateroma. a. Esquema del diseño experimental de inducción de aterosclerosis en ratones LDLR$^{-/-}$ irradiados y trasplantados con médula ósea de ratones MT4-MMP$^{+/+}$ o MT4-MMP$^{-/-}$. **b.**Imágenes representativas de válvulas aórticas de ratones LDLR$^{-/-}$ irradiados y trasplantados con médula MT4-MMP$^{-/-}$ (LacZ+) y alimentados con dieta grasa durante 1 u 8 semanas. En rojo se muestra β-galactosidasa, en verde Mac3 y en azul los núcleos (Hoechst). La barra de escala equivale a 50µm. L indica lumen.

Dada la relevancia de la aterosclerosis en patología humana como causante de la mayoría de los eventos de infarto de miocardio, analizamos si el patrón de expresión de MT4-MMP en placas ateroscleróticas humanas se asemejaba a lo observado en ratón. Para ello analizamos arterias humanas con aterosclerosis incipiente (engrosamiento de la íntima, lo equivalente a 8 semanas en ratón) o avanzada (con placas patentes, lo equivalente a 16 semanas en ratón). Observamos, que MT4-MMP se expresaba a bajos niveles en las placas incipientes, y su expresión aumentaba en las placas avanzadas, tanto a nivel de proteína como a nivel de RNA mensajero (**Figura 14a-b**). Este aumento de expresión de MT4-MMP correlacionaba con un mayor contenido de macrófagos en la placa, sugiriendo que este subtipo celular era el principal responsable de la expresión de MT4-MMP observada en estadios avanzados (**Figura 14c**).

Por ello pudimos concluir que los niveles de MT4-MMP se regulan durante la progresión de la aterosclerosis, incrementándose en placas avanzadas, y que los macrófagos derivados de monocitos circulantes presentes en la placa aterosclerótica expresan MT4-MMP.

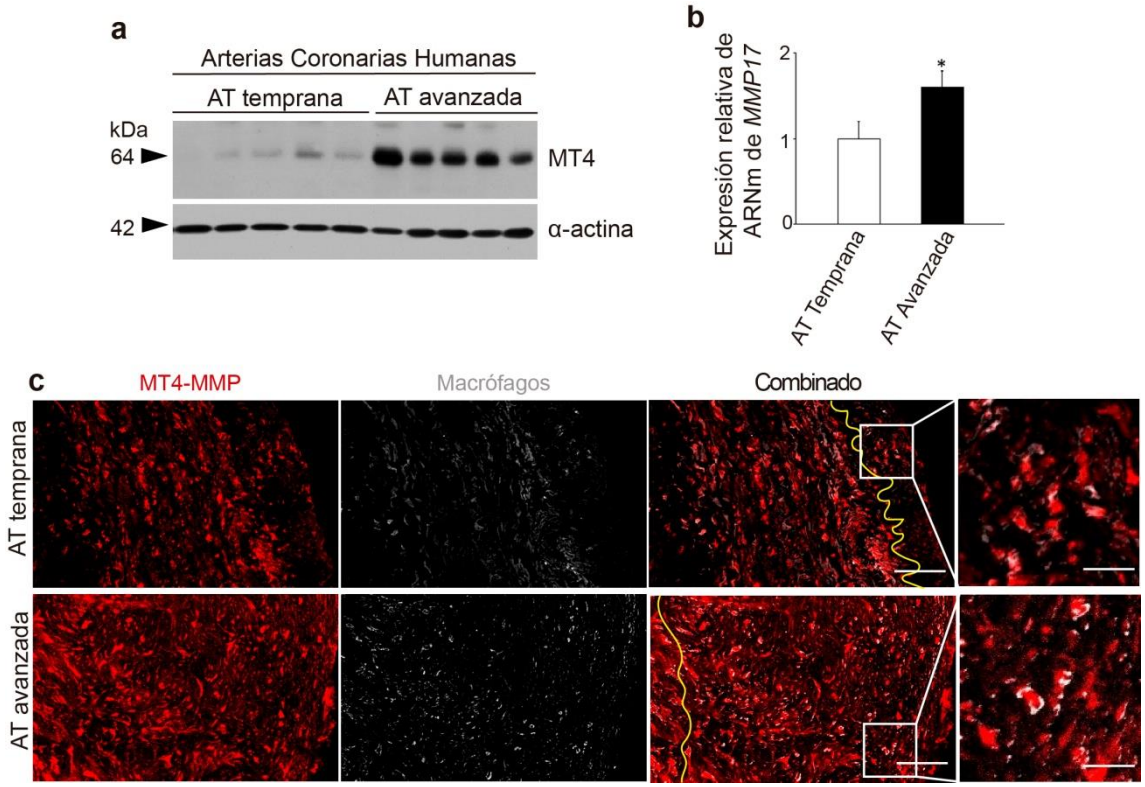

Figura 14: La expresión de MT4-MMP se incrementa en estadios avanzados de aterosclerosis en humano. a. Western blot representativo de lisados de arterias coronarias humanas con placa de ateroma temprana o avanzada. **b.** Expresión relativa de ARNm de MT4-MMP (*MMP17*) de arterias coronarias humanas con placa de ateroma temprana o avanzada. n= 10 y 15 muestras independientes respectivamente. Los datos fueron analizados mediante el método de la t de Student. *p<0.05.**c.** Imágenes representativas de arterias coronarias humanas con placa de ateroma temprana o avanzada teñidas para MT4-MMP en rojo, el marcador macrofágico en gris y los núcleos en azul (Hoechst). A la derecha se muestra la magnificación. La barra de escala equivalea 100 µm y 25 µm en la magnificación. En amarillo se indica lamembrana elástica interna.

La ausencia de MT4-MMP en el compartimento hematopoyético produce una mayor acumulación de macrófagos en la placa de ateroma

Puesto que en la aorta tanto las células de músculo liso de la capa media como algunas células endoteliales de la íntima expresan MT4-MMP, decidimos analizar el

papel de MT4-MMP en monocitos y macrófagos utilizando el modelo de ratones LDLR$^{-/-}$ trasplantados con médula ósea. Para ello irradiamos letalmente ratones deficientes en LDLR, y los trasplantamos con médula ósea procedente de ratones MT4$^{-/-}$ o MT4$^{+/+}$. Tras 4 semanas evaluamos la correcta reconstitución de los ratones mediante el genotipado de MT4-MMP de los leucocitos circulantes en la sangre (**Figura 14a y 15a**) e indujimos la aterosclerosis mediante alimentación con dieta grasa, monitorizando el incremento de peso y los niveles en plasma de glucosa, colesterol y triglicéridos durante 12 semanas. No detectamos diferencias en dichos parámetros entre genotipos (**Figura 15b-c**).

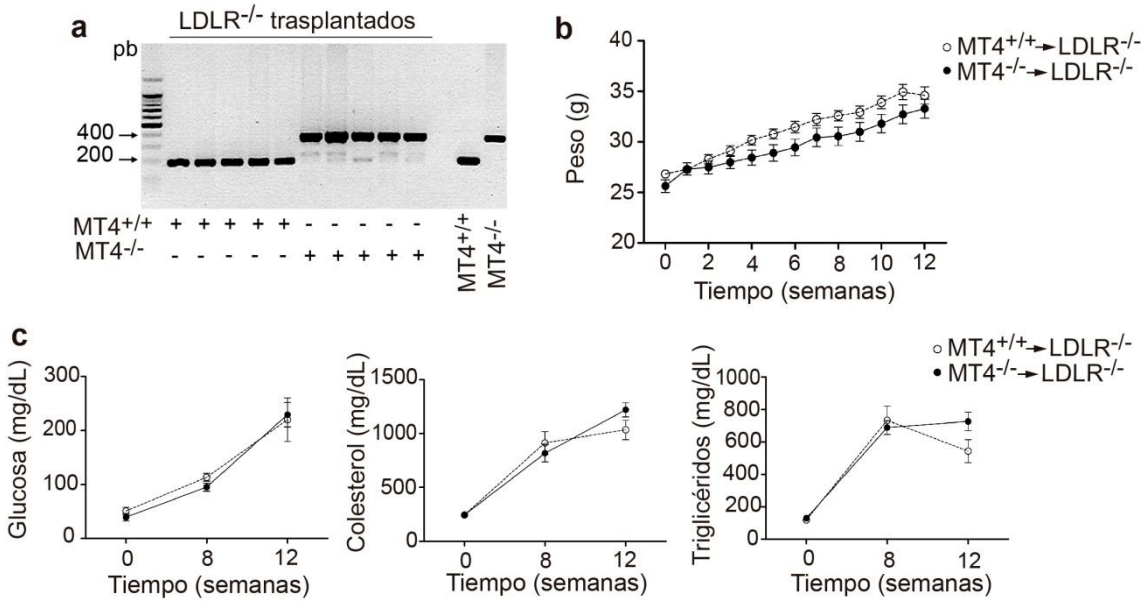

Figura 15: La ausencia de MT4-MMP en las células de médula ósea no afecta al incremento de peso ni de los niveles de glucosa, colesterol ni triglicéridos durante la aterosclerosis. a. PCR representativa de células de médula ósea de ratones LDLR$^{-/-}$ irradiados y trasplantados con médula ósea MT4-MMP$^{+/+}$ o MT4-MMP$^{-/-}$ tras 4 semanas de reconstitución. Peso (**b**) y niveles de glucosa, colesterol y triglicéridos en suero (**c**) de ratones LDLR$^{-/-}$ irradiados y trasplantados con médula MT4-MMP$^{+/+}$ o MT4-MMP$^{-/-}$ y alimentados con dieta grasa durante los tiempos indicados. n= 6 y 16 ratones por genotipo a 8 y 12 semanas en 2 y 3 experimentos independientes. Los datos fueron analizados mediante ANOVA de dos colas seguido de un post-test de Bonferroni.

Puesto que habíamos observado un aumento en la retención de macrófagos MT4$^{-/-}$ en la membrana peritoneal inflamada, cuantificamos el número de macrófagos presentes en las placas ateroscleróticas mediante tinción para el marcador Mac3, proteína también conocida como CD107b y LAMP-2, que se expresa en las membranas lisosomal y plasmática de macrófagos[117]. Tras 8 semanas de dieta grasa, tanto el área ocupada por los macrófagos (**Figura 16a-b**) como el número de macrófagos (**Figura 16c-d**) eran significativamente mayores en la placa de las válvulas aórticas de los ratones LDLR$^{-/-}$ trasplantados con médula ósea de ratones MT4$^{-/-}$ que en los trasplantados con células MT4$^{+/+}$. Esto nos indicaba que la ausencia de MT4-MMP en las células derivadas de médula ósea produce una mayor acumulación de los macrófagos en la placa de ateroma.

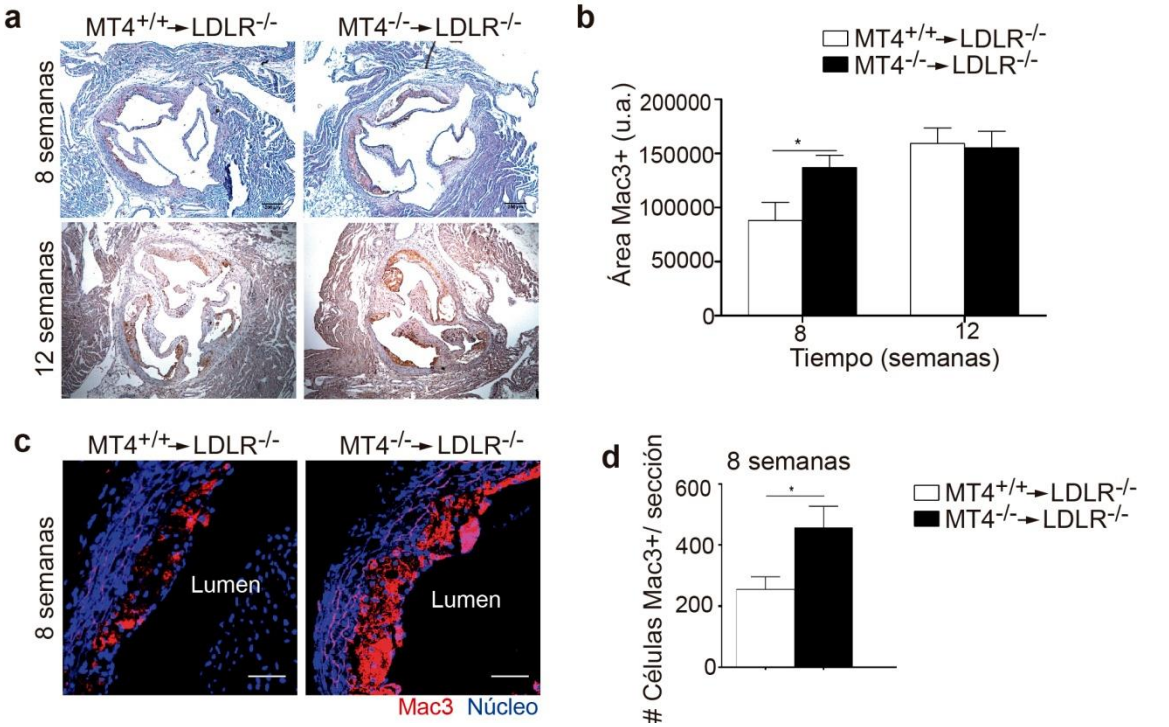

Figura 16: La ausencia de MT4-MMP en células de médula ósea produce un incremento de la acumulación de macrófagos en la placa durante la aterosclerosis. Imágenes representativas de válvulas aórticas de ratones LDLR$^{-/-}$ irradiados y trasplantados con médula ósea MT4-MMP$^{+/+}$ o MT4-MMP$^{-/-}$, alimentados con dieta grasa durante los tiempos indicados y teñidos para Mac3. La barra de escala equivale a 100µm. **b.** Cuantificación del área de Mac3 en placa en los ratones mostrados en **a**. n= 6 y 16 ratones por genotipo a 8 y 12 semanas en 2 y 3 experimentos independientes. Los datos fueron analizados mediante ANOVA de 2 colas seguido de un post-test de Bonferroni. *p<0.05. **c.** Imágenes representativas de válvulas aórticas de ratones LDLR$^{-/-}$ irradiados y trasplantados con médula ósea MT4-MMP$^{+/+}$ o MT4-MMP$^{-/-}$, alimentados con dieta grasa durante 8 semanas. En rojo se muestra Mac3 y en azul los núcleos (Hoechst). La barra de escala equivale a 20µm. **d.** Cuantificación del número de macrófagos en ratones mostrados en **c**. n=6 ratones por genotipo en 2 experimentos independientes. Los datos fueron analizados mediante el método de la t de Student. *p<0.05.

Los macrófagos son capaces de captar lípidos, acumulándolos en su interior y convirtiéndose en células espumosas en la placa [118]. Por ello, analizamos el contenido en lípidos de las placas ateroscleróticas de los ratones LDLR$^{-/-}$ trasplantados mediante la tinción *de ORO in toto (Red-Oil-O*, colorante que marca lípidos hidrofóbicos y neutros cómo triglicéridos y diacilglicéridos y ésteres de colesterol)[119]. En los ratones LDLR$^{-/-}$ trasplantados con médula MT4$^{-/-}$ había un aumento en el área de los depósitos de lípidos en el cayado aórtico tras 8 semanas que se hacía significativo tras 12 semanas de dieta grasa (**Figura 17a-b**). No observamos diferencias sin embargo en el área de la íntima (capa luminal de las arterias formada por células endoteliales que se engrosa durante la aterosclerosis) a 8 ni a 12 semanas (**Figura 17c-d**).

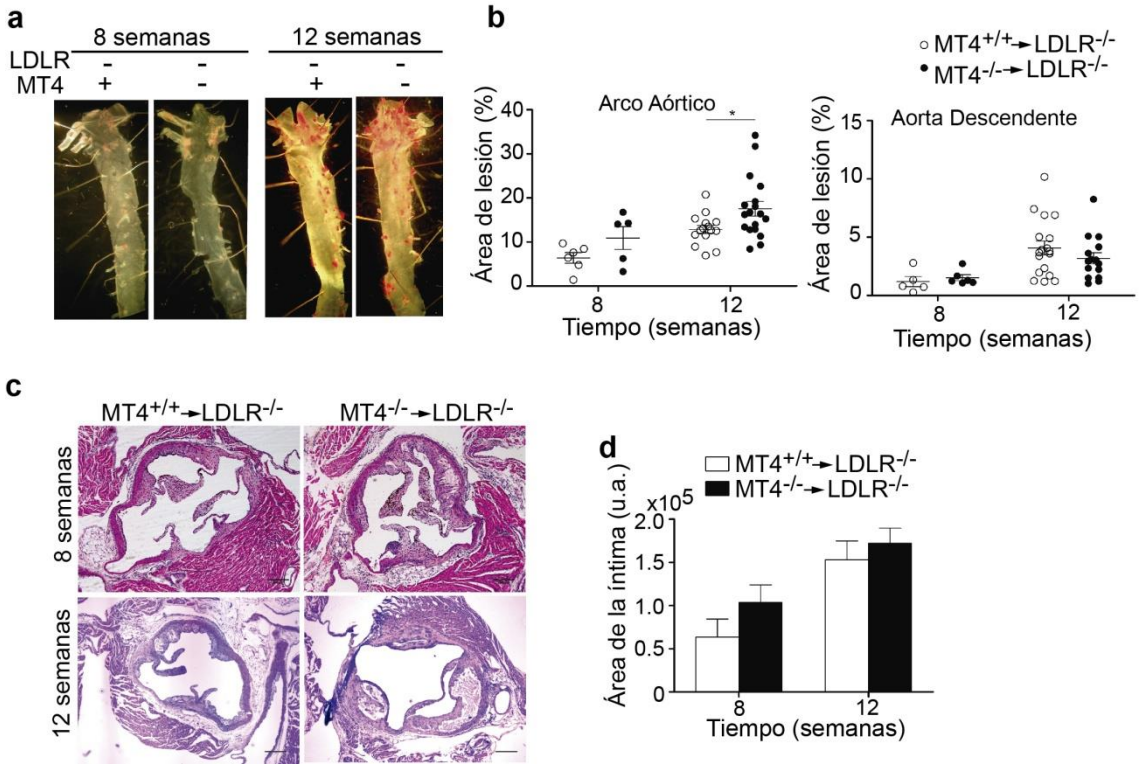

Figura 17: La ausencia de MT4-MMP en células de médula ósea produce un incremento en la acumulación de lípidos en la placa durante aterosclerosis.a. Imágenes representativas de aortas de ratones LDLR$^{-/-}$ irradiados y trasplantados con médula ósea MT4-MMP$^{+/+}$ o MT4-MMP$^{-/-}$, alimentados con dieta grasa durante los tiempos indicados y teñidos con ORO (Red Oil-O) *in toto*. b. Cuantificación del porcentaje de área de ORO positiva en el arco aórtico y en la aorta descendente de ratones tratados como ena. n= 6 ratones por genotipo en 2 experimentos independientes a 8 semanas y 16 ratones por genotipo en 3 experimentos independientes a 12 semanas. Los datos fueron analizados mediante ANOVA de dos colas seguido de un post-test de Bonferroni. *p<0.05. c. Imágenes representativas de válvulas aórticas de ratones LDLR$^{-/-}$ irradiados y trasplantados con médula ósea MT4-MMP$^{+/+}$ o MT4-MMP$^{-/-}$, alimentados con dieta grasa durante los tiempos indicados y teñidos con H&E. La barra de escala equivale a 100µm. d. Cuantificación del área de la íntima de ratones tratados como en c. n= 6 ratones por genotipo en 2 experimentos independientes a 8 semanas y 16 ratones por genotipo en 3 experimentos independientes a 12 semanas. Los datos fueron analizados mediante ANOVA de dos colas seguido de un post-test de Bonferroni.

Para caracterizar la evolución de la aterosclerosis, clasificamos las placas de acuerdo a su progresión siguiendo la clasificación de Stary [52]. Las placas se clasifican en rangos de severidad del I al VI de menos a más avanzadas de acuerdo a los siguientes parámetros histológicos: presencia de macrófagos aislados (placas de tipo I), presencia de células espumosas en la placa (placas de tipo II), presencia de pequeñas acumulaciones de lípidos extracelulares (placa de tipo III), presencia de un núcleo de lípidos extracelulares (placa de tipo IV o ateroma), presencia de un casquete fibroso (placa de tipo V o fibroateroma) y presencia de hemorragia (placa de tipo VI o lesión complicada, trombo)(**Figura 18a**). Los ratones LDLR$^{-/-}$ trasplantados con médula ósea MT4$^{-/-}$ mostraban placas más avanzadas a 8 y 12 semanas que los ratones con médula ósea MT4$^{+/+}$ (**Figura 18b**). Del mismo modo, tras 12 semanas de dieta grasa había un mayor porcentaje de ratones LDLR$^{-/-}$ trasplantados con médula ósea MT4$^{-/-}$ con el área necrótica más extensa en la placa y con un casquete fibroso más grueso (**Figura 18c-d**). En conjunto estos resultados indicaban que la ausencia de MT4-MMP en el compartimento hematopoyético induce una acumulación de macrófagos y lípidos en las placas y una aceleración de la aterosclerosis.

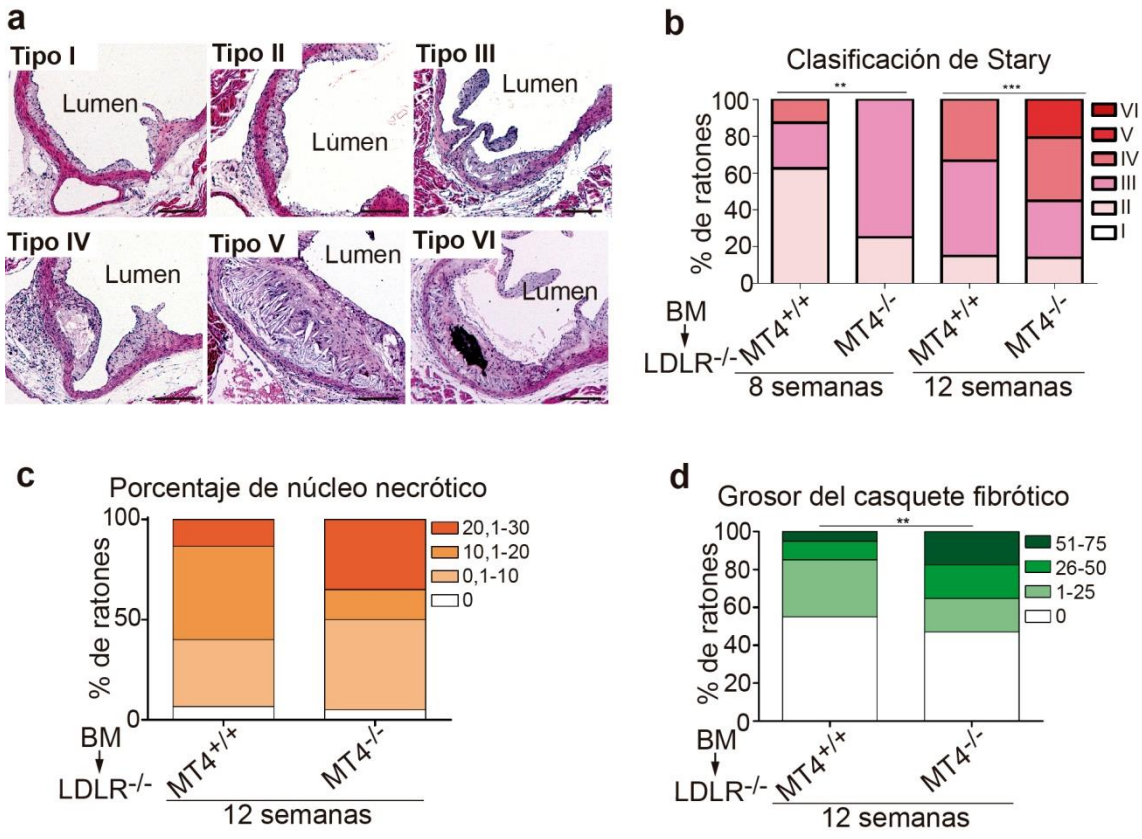

Figura 18: La ausencia de MT4-MMP en células de médula ósea acelera la progresión de la aterosclerosis. a. Imágenes representativas de válvulas aórticas de ratones $LDLR^{-/-}$ alimentados con dieta grasa y teñidas con H&E, mostrando los diferentes estadios de la clasificación de Stary. La barra de escala equivale a 200µm. **b.** Porcentaje de ratones$LDLR^{-/-}$ irradiados y trasplantados con médula ósea $MT4\text{-}MMP^{+/+}$ o $MT4\text{-}MMP^{-/-}$, alimentados con dieta grasa durante los tiempos indicados, en cada estadio de la clasificación de Stary. n= 6 ratones por genotipo en 2 experimentos independientes a 8 semanas y 16 ratones por genotipo en 3 experimentos independientes a 12 semanas. Los datos fueron analizados mediante el método de Chi cuadrado. ***p<0.001. Porcentaje en los rangos de tamaño de núcleo necrótico (**c**) y del grosor del casquete fibrótico (**d**) de ratones $LDLR^{-/-}$ irradiados y trasplantados con médula ósea $MT4\text{-}MMP^{+/+}$ o $MT4\text{-}MMP^{-/-}$, alimentados con dieta grasa durante los tiempos indicados. n= 6 ratones por genotipo en 2 experimentos independientes a 8 semanas y 16 ratones por genotipo en 3 experimentos independientes a 12 semanas. Los datos fueron analizados mediante el método de Chi cuadrado. **p<0.01.

Dado que MT4-MMP se expresa también en las células de músculo liso y en el endotelio de las placas de ateroma, investigamos si la deficiencia total de MT4-MMP afectaba al desarrollo de la aterosclerosis del mismo modo que lo hacía su deficiencia en células de médula ósea. Para ello utilizamos los ratones dobles-deficientes $LDLR^{-/-}$ /$MT4^{-/-}$. Tras alimentarlos con dieta grasa, no observamos diferencias entre genotipos en el peso ni en los niveles de glucosa, colesterol y triglicéridos en sangre (**Figura 19a-b**), al igual que ocurría con los ratones trasplantados. Tras 16 semanas de dieta grasa observamos que los ratones $LDLR^{-/-}$ deficientes en MT4-MMP presentaban mayor área de lesión lipídica en el cayado aórtico (**Figura 19c-d**) y placas más avanzadas según la clasificación de Stary (**Figura 19e-f**) comparados con los ratones $LDLR^{-/-}$/$MT4^{+/+}$. La similitud del fenotipo de los ratones dobles deficientes con el de los ratones trasplantados nos indica que MT4-MMP ejerce su función principal en la aterosclerosis mediante sus acciones en las células derivadas de médula ósea.

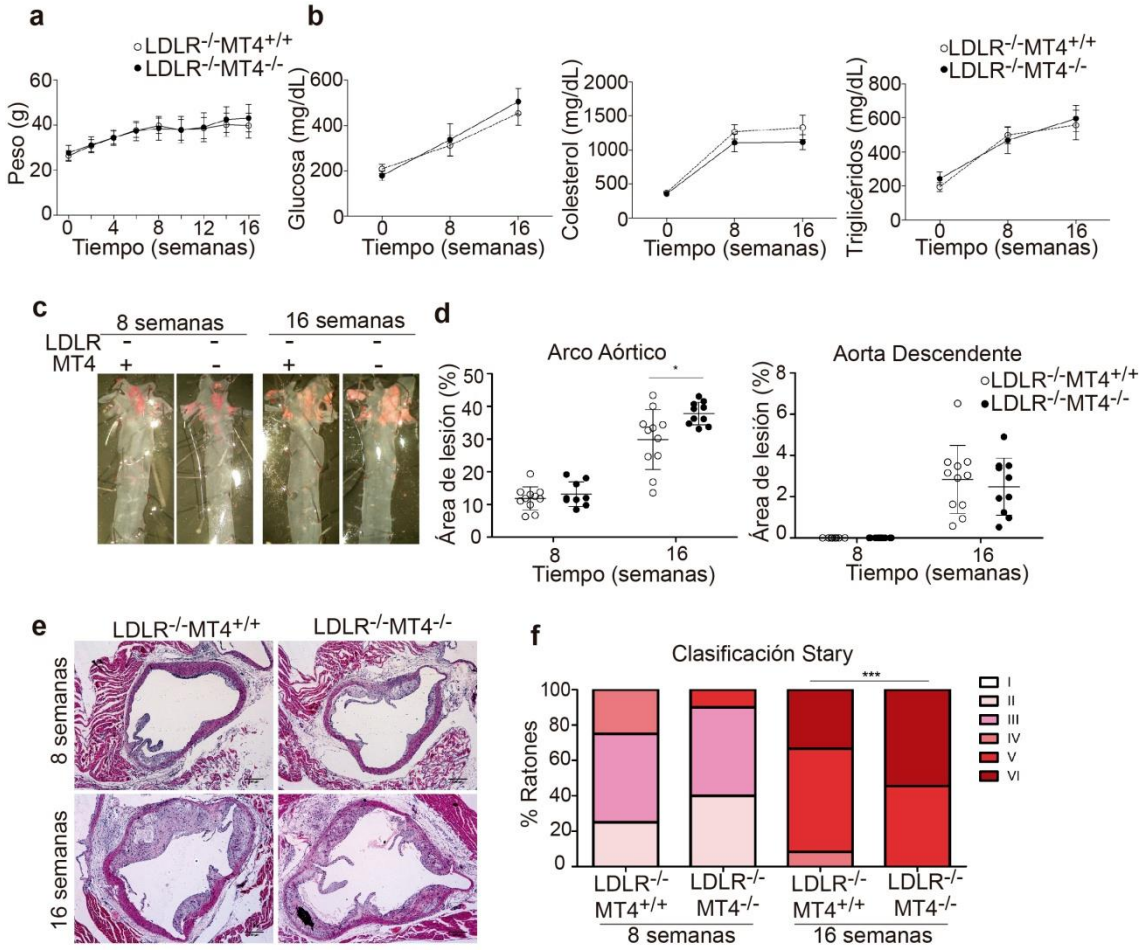

Figura 19: La ausencia total de MT4-MMP acelera la progresión de la aterosclerosis. Peso (**a**) y niveles de glucosa, colesterol y triglicéridos (**b**) en suero de ratones LDLR$^{-/-}$MT4-MMP$^{+/+}$ o LDLR$^{-/-}$MT4-MMP$^{-/-}$ y alimentados con dieta grasa durante los tiempos indicados. n= 8 y 12 ratones por genotipo a 8 y 12 semanas en 2 experimentos independientes. Los datos fueron analizados mediante ANOVA de dos colas seguido de un post-test de Bonferroni. **c.** Imágenes representativas de aortas de ratones LDLR$^{-/-}$MT4-MMP$^{+/+}$ o LDLR$^{-/-}$MT4-MMP$^{-/-}$ y alimentados con dieta grasa por los tiempos indicados y teñidos para ORO (Red Oil-O) *in toto*. **d.** Cuantificación del porcentaje de área de ORO positiva en el arco aórtico y en la aorta descendente en ratones tratados como en **c**. n=8 y 12 ratones por genotipo a 8 y 12 semanas en 2 experimentos independientes. Los datos fueron analizados mediante ANOVA de dos colas seguido de un post-test de Bonferroni. *p<0.05. **e.** Imágenes representativas válvulas aórticas de ratones LDLR$^{-/-}$MT4-MMP$^{+/+}$ o LDLR$^{-/-}$MT4-MMP$^{-/-}$, alimentados con dieta grasa durante los tiempos indicados y teñidos con H&E. La barra de escala equivale a 100µm. **f.** Porcentaje de ratones LDLR$^{-/-}$MT4-MMP$^{+/+}$ o LDLR$^{-/-}$MT4-MMP$^{-/-}$ alimentados con dieta grasa durante los tiempos indicados, en cada estadio de la clasificación de Stary. n=8 y 12 ratones por genotipo a 8 y 12 semanas en 2 experimentos independientes. Los datos fueron analizados mediante el método de Chi cuadrado. ***p<0.001.

La acumulación de macrófagos MT4-MMP$^{-/-}$ en la placa aterosclerótica no depende de su egresión, apoptosis ni proliferación

Quisimos investigar entonces cual podría ser el mecanismo por el que se estaban acumulando más macrófagos en la placa aterosclerótica en ausencia de MT4-MMP. Está establecido que la cantidad de macrófagos en la placa depende principalmente del balance entre la llegada y reclutamiento inicial de monocitos circulantes a la pared vascular inflamada y la egresión, apoptosis y proliferación de los macrófagos en la placa [72].

Primero, investigamos si había diferencias en la egresión de los macrófagos desde el tejido inflamado. Dada la dificultad metodológica para abordar este análisis en la placa aterosclerótica, decidimos investigar el proceso de egresión en el modelo de peritonitis inducida por TG. Para ello, se aislaron macrófagos peritoneales de ratones MT4$^{+/+}$ y MT4$^{-/-}$ tras 3 días de TG, se marcaron con sondas fluorescentes de distinto color y se inyectaron en proporción 1:1 intraperitonealmente en ratones control con peritonitis. Tras la transferencia de los macrófagos, se indujo su egresión con LPS inyectado vía intraperitoneal y se analizó tras 4 horas (**Figura 20a**). No se observaron diferencias en el número de macrófagos MT4$^{-/-}$ y MT4$^{+/+}$ presentes en el exudado peritoneal (**Figura 20b-d**), ni en el bazo (**Figura 20e-f**), lo cual indica que su egresión no estaba afectada por la ausencia de MT4-MMP. Dado que el LPS puede inducir muerte celular, se investigaron los niveles de apoptosis de los macrófagos MT4$^{+/+}$ y MT4$^{-/-}$ en la cavidad peritoneal tras LPS, no observándose diferencias (**Figura 20g-h**).

Figura 20: La ausencia de MT4-MMP no afecta a la egresión de los macrófagos del área de inflamación. a. Esquema del diseño experimental de egresión de macrófagos peritoneales MT4-MMP$^{+/+}$ y MT4-MMP$^{-/-}$ marcados. **b.** Gráficas de nube de puntos representativas de lavados peritoneales de ratones MT4-MMP$^{+/+}$en peritonitis y tras la inyección de macrófagos marcados y extraídos tras 4 horas de estimulación con LPS o PBS como control. **c.** Imagen representativa de macrófagos peritoneales MT4-MMP$^{+/+}$ y MT4-MMP$^{-/-}$ tras peritonitis y teñidos con las sondas PKH67 (verde) y PKH26 (rojo) respectivamente. La barra de escala equivale a 100 µm.**d.** Cuantificación del número de macrófagos marcados en ratones tratados como en **b**. n= 6 ratones por genotipo en 2 experimentos independientes. Los datos fueron analizadosmediante ANOVAde una cola seguido de un post-test de Bonferroni. ***p<0.001.**e.** Gráficas de nube de puntos representativas de bazos de ratones tratados como en **b** y la cuantificación del número de células marcadas presentes (**f**). n= 6 ratones por genotipo en 2 experimentos independientes. Los datos fueron analizados mediante ANOVA de una cola seguido de un post-test de Bonferroni. **g.** Histogramas representativos de de los macrófagos marcados con Hoechst 33258 (Ho58) de ratones tratados como en **b**, y la cuantificación del número de macrófagos marcados muertos (**h**). n= 6 ratones por genotipo de 2 experimentos independientes. Los datos fueron analizados mediante ANOVA de una cola seguido de un post-test de Bonferroni.

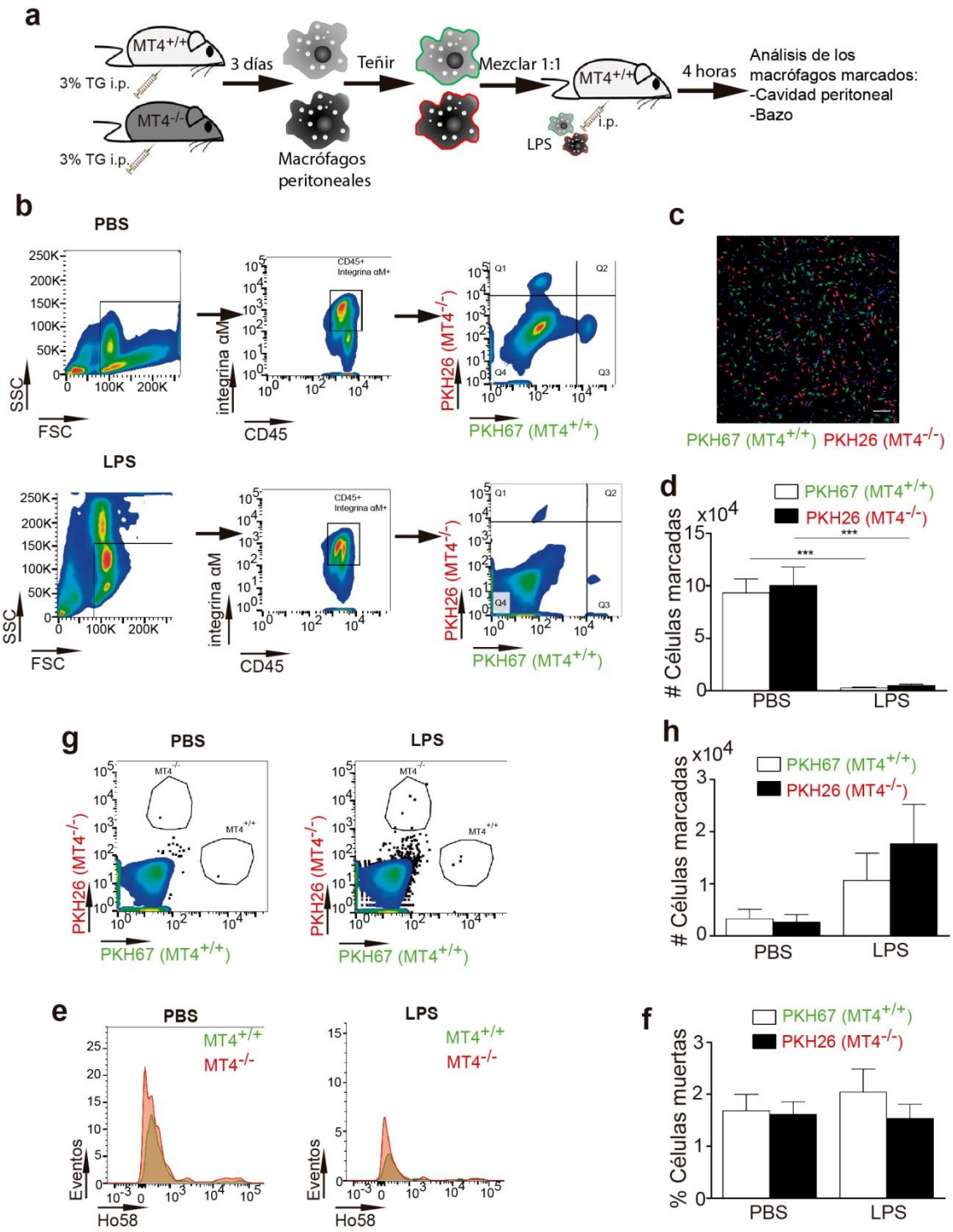
a
MT4+/+
3% TG i.p.
MT4-/-
3% TG i.p.
3 días
Macrófagos peritoneales
Teñir
Mezclar 1:1
MT4+/+
LPS
i.p.
4 horas
Análisis de los macrófagos marcados:
-Cavidad peritoneal
-Bazo
b
PBS
LPS
SSC
FSC
integrina αM
CD45
CD45+ Integrina αM+
PKH26 (MT4-/-)
PKH67 (MT4+/+)
Q1
Q2
Q3
Q4
c
PKH67 (MT4+/+) PKH26 (MT4-/-)
d
PKH67 (MT4+/+)
PKH26 (MT4-/-)
Células marcadas
x10^4
***
PBS
LPS
g
PBS
LPS
MT4-/-
MT4+/+
PKH26 (MT4-/-)
PKH67 (MT4+/+)
h
PKH67 (MT4+/+)
PKH26 (MT4-/-)
Células marcadas
x10^4
PBS
LPS
e
PBS
LPS
MT4+/+
MT4-/-
Eventos
Ho58
f
PKH67 (MT4+/+)
PKH26 (MT4-/-)
% Células muertas
PBS
LPS

Seguidamente investigamos si había diferencias en apoptosis o proliferación de los macrófagos en la placa. Para ello teñimos para caspasa-3 procesada (marcador de apoptosis) y Ki67 (marcador de proliferación) placas de ateroma de ratones trasplantados tras 8 semanas de dieta grasa (**Figura 21a y c**), sin detectarse diferencias significativas entre genotipos en la apoptosis ni en la proliferación de los macrófagos (**Figura 21b y d**).

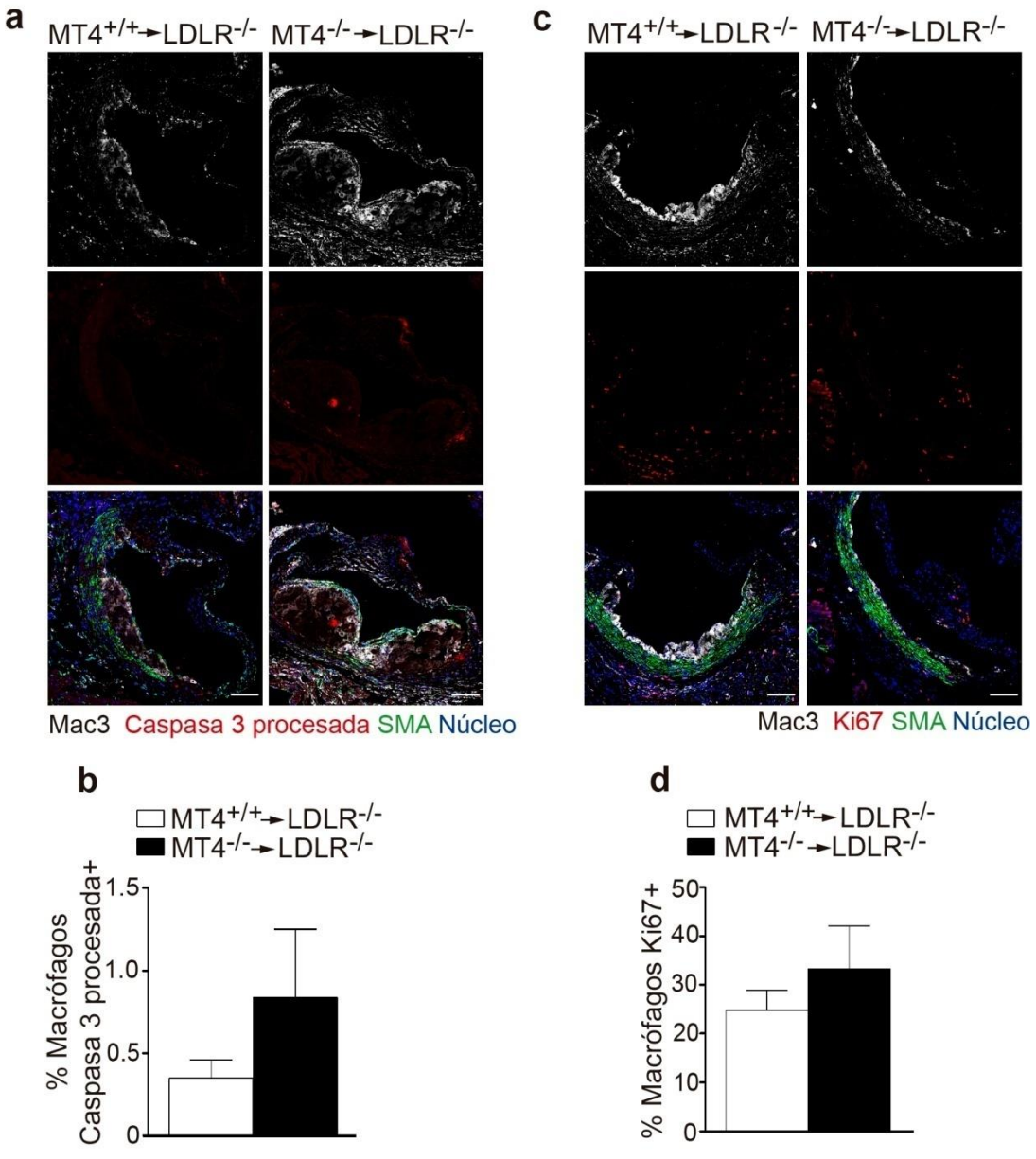

Figura 21: La ausencia de MT4-MMP en células de médula ósea no afecta a la muerte ni proliferación de los macrófagos en la placa de ateroma. a. Imágenes representativas de válvulas aorticas de ratones LDLR$^{-/-}$ irradiados y trasplantados con médula ósea MT4-MMP$^{+/+}$ o MT4-MMP$^{-/-}$, alimentados con dieta grasa durante 8 semanas y teñidos para Mac3 (gris), caspasa 3 procesada (rojo), SMA (verde) y los núcleos (Hoechst) en azul. La barra de escala equivale a 100µm. **b.** Cuantificación del porcentaje de macrófagos positivos para caspasa 3 procesada en la placa de ratones tratados como en **a**. n=6 ratones por genotipo en 2 experimentos independientes. Los datos fueron analizados mediante el método de la t de Student. **c.** Imágenes representativas de válvulas aorticas de ratones LDLR$^{-/-}$ irradiados y trasplantados con médula ósea MT4-MMP$^{+/+}$ o MT4-MMP$^{-/-}$, alimentados con dieta grasa durante 8 semanas y teñidos para Mac3 (gris), Ki67 (rojo), SMA (verde) y los núcleos (Hoechst) en azul. La barra de escala equivale a 100 µm. **d.** Cuantificación del porcentaje de macrófagos Ki67+ en laplaca de ratones tratados como en **c**. n=6 ratones por genotipo en 2 experimentos independientes. Los datos fueron analizados mediante el método de la t de Student.

La ausencia de MT4-MMP induce un mayor reclutamiento de monocitos patrulleros al endotelio inflamado durante la aterosclerosis incipiente

Puesto que no se observaron diferencias en la egresión, apoptosis ni proliferación de los macrófagos, procedimos a investigar si había diferencias en el reclutamiento de los monocitos.

Durante el reclutamiento de monocitos a los tejidos inflamados hay dos componentes celulares fundamentales, el endotelio luminal de los vasos, que en situación de inflamación incrementa la expresión en membrana de proteínas como ICAM1; y los monocitos circulantes en la sangre, que expresan en la membrana determinados receptores, como las integrinas αMβ2 (Mac1) o αLβ2 (LFA1), que son capaces de reconocer los ligandos en el endotelio, y a través de ellos adherirse y transmigrar al tejido inflamado[120]. Investigamos la activación del endotelio durante aterosclerosis mediante tinción con ICAM1 (**Figura 22a**) en ratones LDLR$^{-/-}$ trasplantados con médula MT4$^{+/+}$ o MT4$^{-/-}$ tras 8 semanas de dieta grasa, no observando diferencia entre los genotipos (**Figura 22b**).

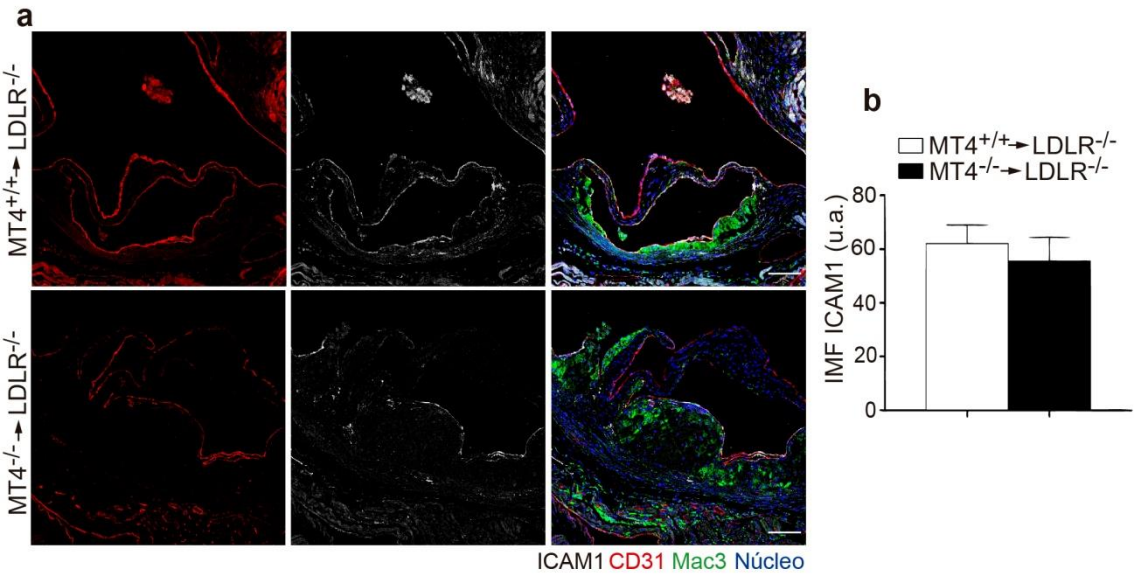

Figura 22: La ausencia de MT4-MMP en las células de médula ósea no afecta a la activación del endotelio durante la aterosclerosis. a. Imágenes representativas de válvulas aorticas de ratones LDLR$^{-/-}$ irradiados y trasplantados con médula ósea MT4-MMP$^{+/+}$ o MT4-MMP$^{-/-}$, alimentados con dieta grasa durante 8 semanas y teñidos para ICAM1 (gris), CD31 (rojo), Mac3 (verde) y los núcleos (Hoechst) en azul. La barra de escala equivale a 100 µm. **b.** Cuantificación de la intensidad media de fluorescencia (IMF) de ICAM1 en el endotelio de ratones tratados como en**a**. n=6 ratones por genotipo en 2 experimentos independientes. Los datos fueron analizados mediante el método de la t de Student.

Seguidamente investigamos el componente monocítico durante la aterosclerosis. Para ello analizamos las principales poblaciones de monocitos circulantes (clásicos, y patrulleros) utilizando los marcadores CD45, integrina αM y Ly6C, y discriminando por tamaño y complejidad; esta estrategia daba los mismos resultados la utilización del marcador canónico de monocitos CD115 (**Figura 23a-b**). No observamos diferencias en el porcentaje de monocitos clásicos (CD45+integrina αM+Ly6+) en los ratones LDLR$^{-/-}$ trasplantados con médula ósea MT4$^{-/-}$ (**Figura 23c**), mientras que si había un menor porcentaje de monocitos patrulleros (CD45+integrina αM+Ly6C-) en ausencia de MT4-MMP (**Figura 23d**). Además, tanto los monocitos clásicos como los patrulleros expresaban niveles más elevados en la membrana de la integrina αMβ2 en ausencia de MT4-MMP (**Figura 23c-d**), al igual que ocurría en los macrófagos peritoneales tras peritonitis (**Figura 9a**).

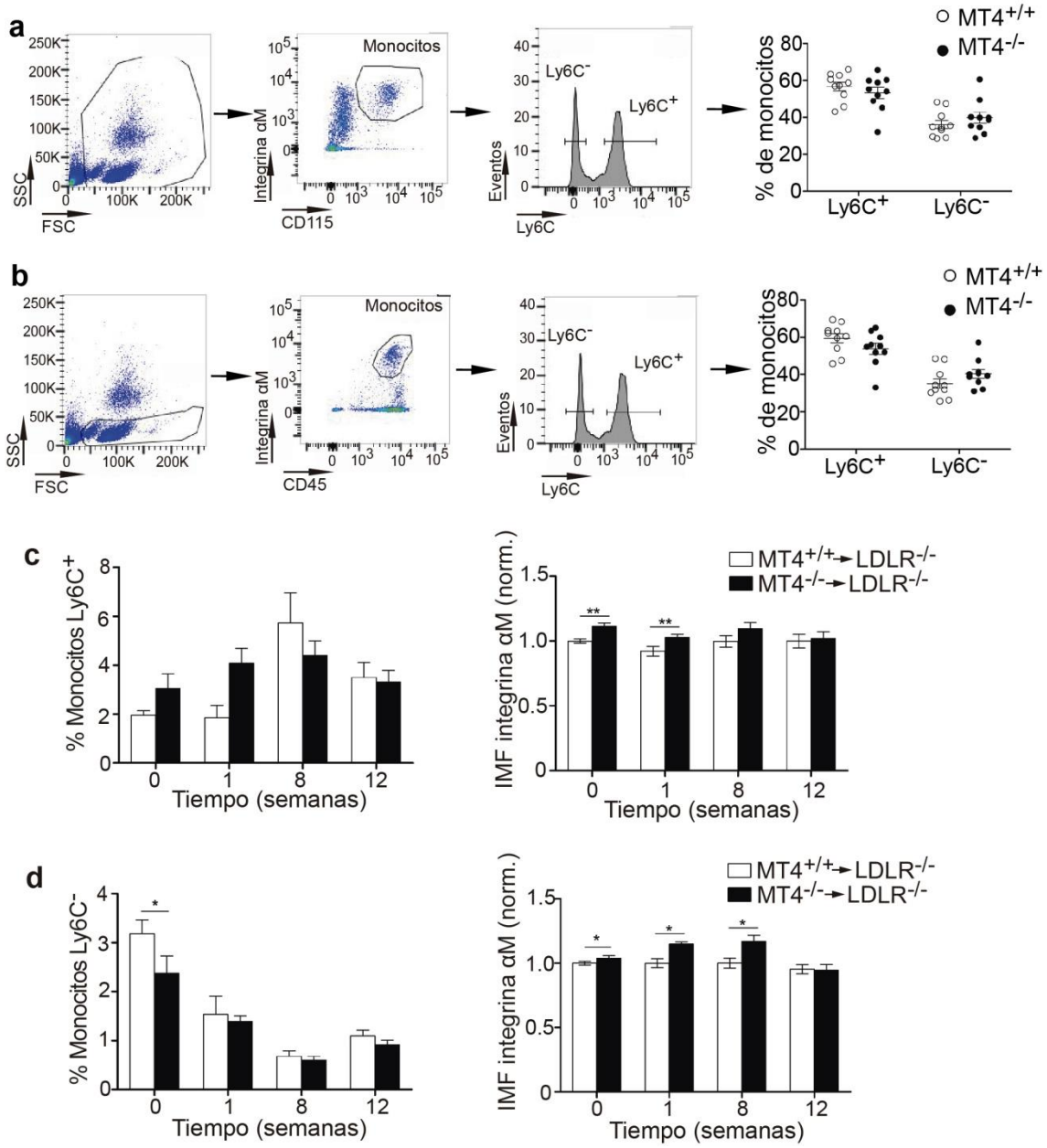

Figura 23: La ausencia de MT4-MMP en células de médula ósea incrementa los niveles de la integrina αMβ2 en la superficie de los monocitos durante la aterosclerosis. a. Estrategia de análisis y cuantificación de monocitos clásicos (Ly6C+) y monocitos patrulleros (Ly6C-) en la sangre de ratón utilizando el marcador de monocitos CD115.**b.** Estrategia de análisis y cuantificación de monocitos clásicos (Ly6C+) y monocitos patrulleros (Ly6C-) en la sangre de ratón utilizando la restricción por tamaño y complejidad. Cuantificación del porcentaje de monocitos clásicos (**c**)y de monocitos patrulleros (**d**) circulantes en sangre de ratones LDLR$^{-/-}$ irradiados y trasplantados con médula MT4-MMP$^{+/+}$ o MT4-MMP$^{-/-}$, alimentados con dieta grasa durante los tiempos indicados. Las IMF de la integrina αM (αM) se muestran en los paneles derechos. n= 6-12ratones por condición en 2-4 experimentos independientes. Los datos fueron analizados mediante ANOVA de dos colas seguido de un post-test de Bonferroni. *p<0.05, **p<0.01.

Tras ello analizamos el número de monocitos reclutados inicialmente a la aorta inflamada de ratones LDLR$^{-/-}$ trasplantados y alimentados con dieta grasa durante 3 días, mediante la tinción de la curvatura menor del cayado aórtico *in toto* con CD115 y Ly6C (**Figura 24a**). A pesar del bajo número de monocitos que se reclutan en estos estadios a la placa, pudimos observar que había un incremento significativo en el número de monocitos patrulleros en ausencia de MT4-MMP, sin variar el número de monocitos clásicos (**Figura 24b**), indicando que a pesar de que la ausencia de MT4-MMP incrementa los niveles de la integrina αMβ2 en ambas poblaciones de monocitos, únicamente los patrulleros reclutamiento al endotelio inflamado en ausencia de MT4-MMP.

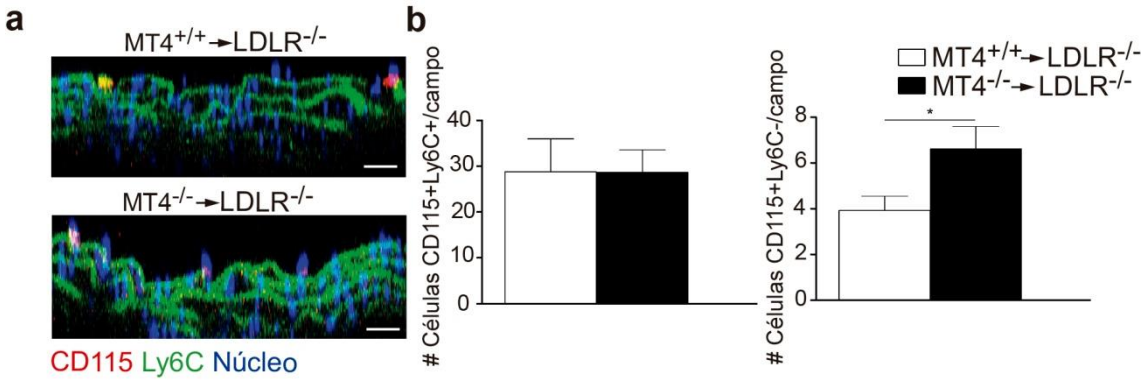

Figura 24: La ausencia de MT4-MMP en células de médula ósea incrementa la acumulación de monocitos patrulleros en las placas incipientes de ateroma. a. Imágenes ortogonales representativas del cayado aórtico de ratones LDLR$^{-/-}$ irradiados y trasplantados con médula ósea MT4-MMP$^{+/+}$ o MT4-MMP$^{-/-}$, alimentados con dieta grasa durante 3 días y teñidos *in toto* para CD115 (rojo) y Ly6C (verde). Los núcleos se muestran en azul (Hoechst) y en verde también se observa la elastina (autofluorescencia). La barra de escala equivale a 20µm. **b.** Cuantificación del número de monocitosclásicos (panel izquierdo) y de monocitos patrulleros (panel derecho) presentes en los ratones tratados como en **a**. n=6 ratones por genotipo en 2 experimentos independientes. Los datos fueron analizados mediante el método de la t de Student. *p<0.05.

Para confirmar que el efecto de la ausencia de MT4-MMP en el incremento de los monocitos patrulleros en la placa de ateroma a 3 días de dieta grasa se ejercía directamente por la acción de MT4-MMP en dichos monocitos, y que no se veía afectado por su ausencia en otras células hematopoyéticas, realizamos un experimento de transferencia adoptiva. Para ello aislamos monocitos patrulleros de ratones MT4$^{+/+}$ y MT4$^{-/-}$ cruzados con el ratón reportero CX3CR1$^{GFP/WT}$, y se trasfirieron

a ratones deficientes en LDLR (**Figura 25a**). Tras 3 días de dieta grasa, se analizó el número de células transferidas (GFP positivas) que estaban adheridas al endotelio inflamado del arco menor del cayado aórtico (**Figura 25b**), observando que había un número mayor de monocitos patrulleros deficientes en MT4-MMP comparado con los $MT4^{+/+}$ (**Figura 25c**).

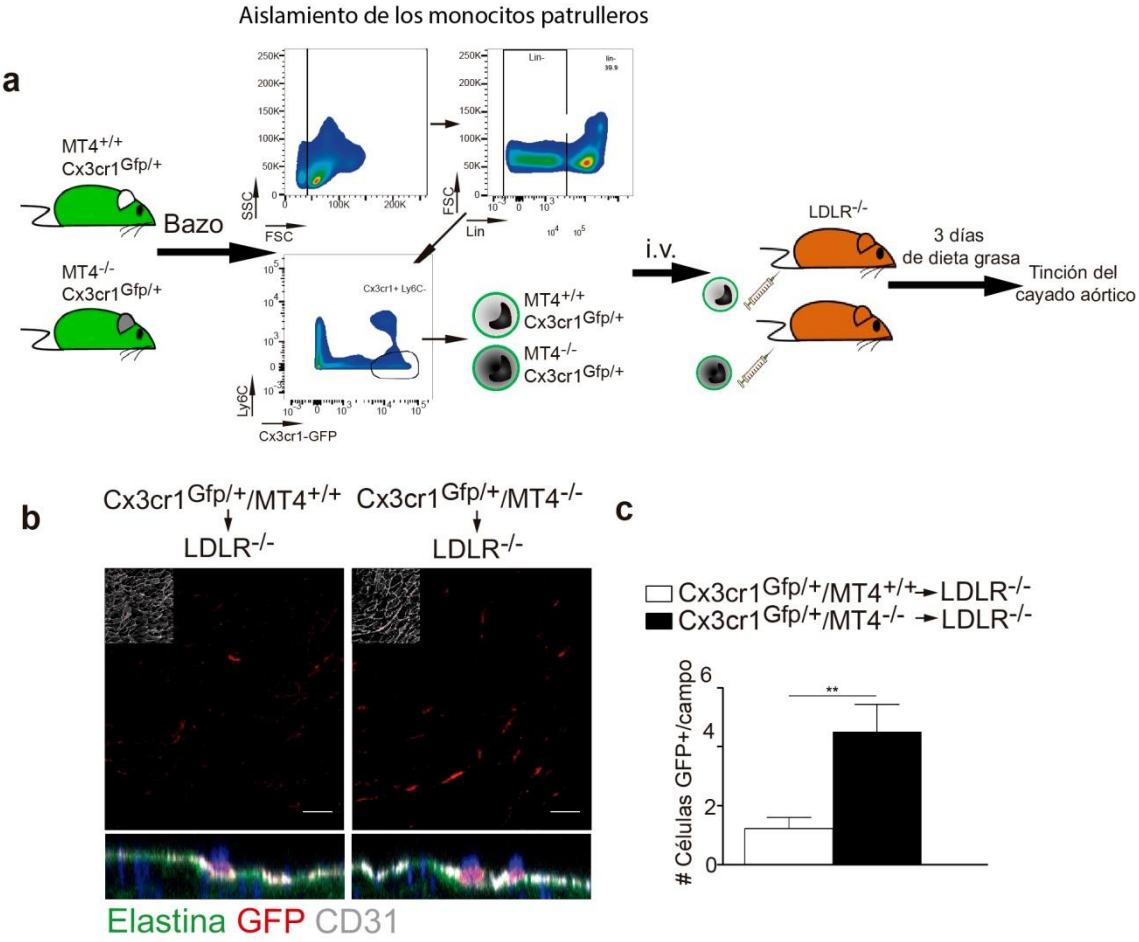

Figura 25: El incremento de los monocitos patrulleros adheridos a la placa de ateroma incipiente depende de la acción de MT4-MMP en dichos monocitos. a. Esquema del diseño experimental de la transferencia adoptiva de células $CX3CR1^{GFP/+}$ en ratones $LDLR^{-/-}$. **b.** Imágenes ortogonales representativas del cayado aórtico de ratones $LDLR^{-/-}$inyectados i.v. con monocitos patrulleros de ratones $CX3CR1^{GFP/+}MT4\text{-}MMP^{+/+}$ o $CX3CR1^{GFP/+}MT4\text{-}MMP^{-/-}$, alimentados con dieta grasa durante 3 días y teñidos *in toto* para GFP (rojo) y CD31 (gris), los núcleos se muestran en azul (Hoechst) y en verde se observa la elastina (autofluorescencia). La barra de escala equivale a 20µm. **c.** Cuantificación del número de monocitos patrulleros GFP+ adheridos al endotelio de ratones tratados como en **b**. n=6 ratones por genotipo en 2 experimentos independientes. Los datos fueron analizados mediante el método de la t de Student. **p<0.01.

Estos resultados nos indicaban que la ausencia de MT4-MMP en los monocitos patrulleros incrementaba su acumulación en las zonas de daño vascular.

En ausencia de MT4-MMP hay un incremento de macrófagos CD11c+ en placas de aterosclerosis incipientes

Mediante microscopía analizamos entonces el número de macrófagos en las placas incipientes tras 7 días de dieta grasa y no observamos diferencias significativas entre genotipos (**Figura 26a-b**). Puesto que en las placas de ateroma hay un conjunto heterogéneo de macrófagos, con distintos marcadores y funciones, analizamos si la ausencia de MT4-MMP en estos estadios tempranos podía afectar al fenotipo de los macrófagos aunque no cambiara su abundancia total. Dado que los monocitos patrulleros pueden dar lugar a macrófagosCD11c+ en el pulmón y en la placa de ateroma[14, 27, 34], analizamos este marcador y observamos que hay un mayor número de macrófagos (Mac3+) que expresan CD11c en las placas tras 7 días de dieta grasa de los ratones LDLR$^{-/-}$ trasplantados con médula ósea MT4$^{-/-}$ (**Figura 26a,c**).

Puesto que en ausencia de MT4-MMP se observaba una mayor acumulación de lípidos en placas más avanzadas (**Figura 17a-b**), y los monocitos patrulleros son capaces de captar lípidos en la placa [33], analizamos la capacidad de los macrófagos CD11c+ deficientes en MT4-MMP de acumular lípidos mediante tinción con adipofilina, que es una proteína presente en la membrana de las gotas de lípidos intracelulares de las células espumosas [121] (**Figura 26a**). Pese a que había más macrófagos con lípidos en su interior en los ratones trasplantados con células deficientes en MT4-MMP tras 7 días de dieta grasa (**Figura 26d**), una menor proporción de macrófagos CD11c+ contenían lípidos (**Figura 26e**). Ello nos indicaba que en ausencia de MT4-MMP había un incremento de macrófagos CD11c+, pero que esta población no parecía ser la implicada en el incremento posterior de lípidos en las placas.

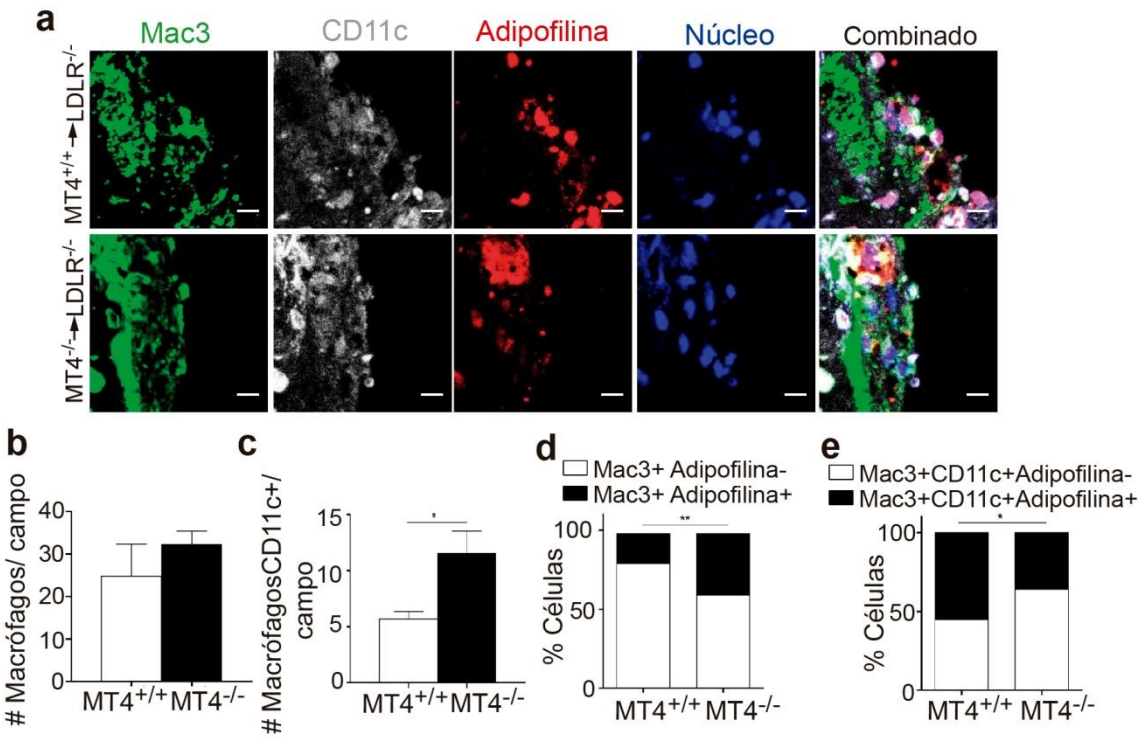

Figura 26: La ausencia de MT4-MMP en células de médula ósea incrementa la acumulación de macrófagos CD11c+ en placas incipientes de ateroma. a. Imágenes representativas de las válvulas aórticas de ratones LDLR$^{-/-}$ irradiados y trasplantados con médula ósea MT4-MMP$^{+/+}$ o MT4-MMP$^{-/-}$, alimentados con dieta grasa durante 1 semana y teñidos con Mac3 (verde), adipofilina (rojo), CD11c (gris) y los núcleos se muestran en azul (Hoechst). La barra de escala equivale a 10µm. **b.** Cuantificación del número de macrófagos (células positivas para Mac3) en ratones tratados como en **a.** n=7 ratones por genotipo en 2 experimentos independientes. Los datos fueron analizados mediante el método de la t de Student. **c.** Cuantificación del número de macrófagos CD11c+ en ratones tratados como en **a.** n=7 ratones por genotipo en 2 experimentos independientes. Los datos fueron analizados mediante el método de la t de Student. *p<0.05.**d.**Porcentaje de macrófagos positivos y negativos para adipofilina en ratones tratados como en **a**. n=7 ratones por genotipo en 2 experimentos independientes. Los datos fueron analizados mediante la prueba exacta de Fisher. **p<0.01. **e.** Porcentaje de macrófagos CD11c+, positivos y negativos para adipofilina en ratones tratados como en **a**. n=7 ratones por genotipo en 2 experimentos independientes. Los datos fueron analizados mediante la prueba exacta de Fisher. *p<0.05.

En ausencia de MT4-MMP se acumulan macrófagos Mafb+AIM/CD5L+ en placas incipientes de aterosclerosis y en peritonitis estéril, que son más resistentes a apoptosis y más activos captando lípidos pero no más inflamatorios

En otros contextos se ha visto que los monocitos patrulleros pueden activar un programa de diferenciación a macrófago vía la expresión del factor de transcripción Mafb [27], el cual a su vez puede inducir la expresión en macrófagos de genes diana tales como AIM (del inglés '*apoptosis inhibitor of macrophages´* y también denominado CD5L). Mediante tinciones de inmunofluorescencia de placas tras 7 días de dieta grasa detectamos un aumento significativo en el número de macrófagos que expresaban Mafb y AIM/CD5L en lesiones incipientes de ratones $LDLR^{-/-}$ trasplantados con médula ósea $MT4^{-/-}$ (**Figura 27a-c**), con una mayor proporción de los mismos con lípidos en su interior (**Figura 27d-e**).

La función primaria de AIM/CD5L es la inhibición de la apoptosis de macrófagos. De este modo observamos una tendencia a un menor número de macrófagos apoptóticos (positivos para caspasa-3 procesada) en las lesiones tempranas tras 7 días de dieta grasa de los ratones $LDLR^{-/-}$ trasplantados con médula ósea $MT4^{-/-}$ (8.1±3.8% en $MT4^{+/+}$ vs 6±1.6% en $MT4^{-/-}$). Este incremento en los macrófagos AIM/CD5L+ no se observa sin embargo a 8 y 12 semanas tras dieta grasa (**Figura 28a-b**).

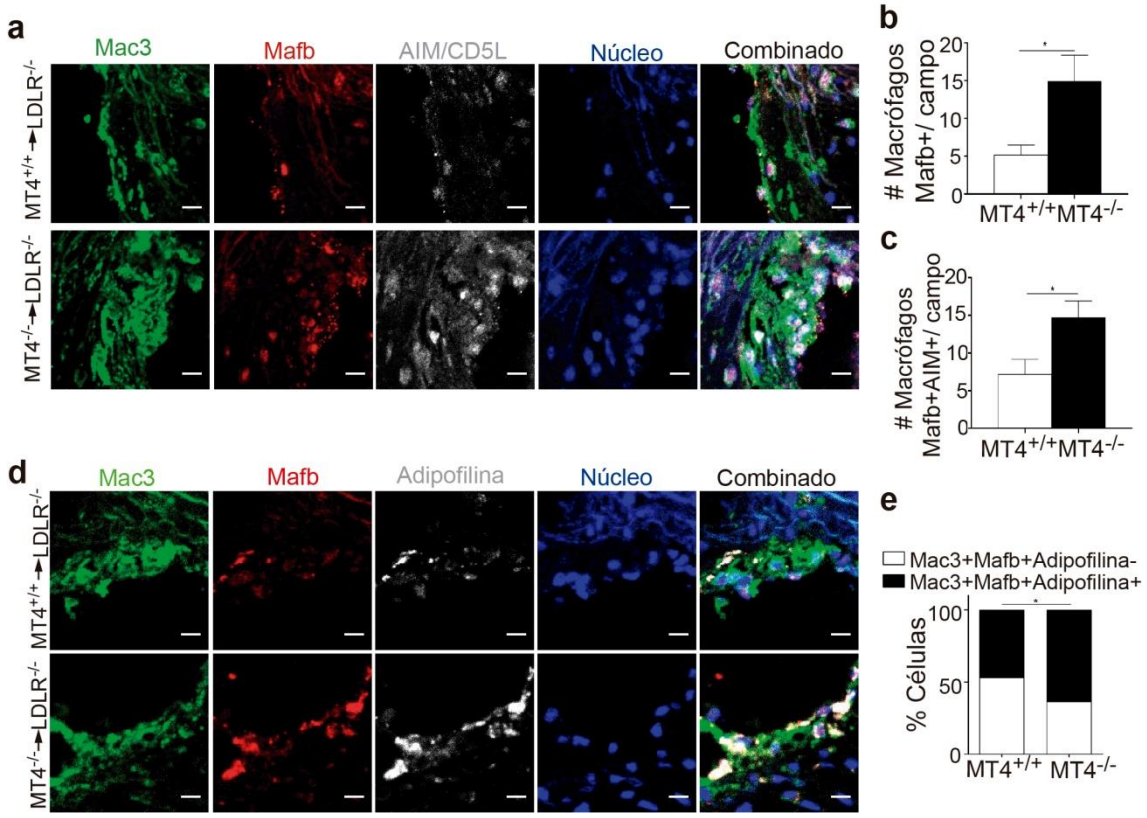

Figura 27: La ausencia de MT4-MMP en células de médula ósea incrementa la acumulación de macrófagos Mafb+AIM/CD5L+ que captan lípidos en las placas incipientes de ateroma. a. Imágenes representativas de válvulas aórticas de ratones LDLR$^{-/-}$ irradiados y trasplantados con médula ósea MT4-MMP$^{+/+}$ o MT4-MMP$^{-/-}$, alimentados con dieta grasa durante 1 semana y teñidos para Mac3 (verde), Mafb (rojo), AIM/CD5L (gris) y los núcleos se muestran en azul (Hoechst). La barra de escala equivale a 10µm. **b.** Cuantificación del número de macrófagos Mafb+ en ratones tratados como en **a.** n=7 ratones por genotipo en 2 experimentos independientes. Los datos fueron analizados mediante el método de la t de Student. *p<0.05. **c.** Cuantificación del número de macrófagos Mafb+AIM+ en ratones tratados como en **a.** n=7 ratones por genotipo en 2 experimentos independientes. Los datos fueron analizados mediante el método de la t de Student. *<p0.05.**d.** Imágenes representativas de válvulas aórticas de ratones LDLR$^{-/-}$ irradiados y trasplantados con médula ósea MT4-MMP$^{+/+}$ o MT4-MMP$^{-/-}$, alimentados con dieta grasa durante 1 semana y teñidos para Mac3 (verde), Mafb (rojo), adipofilina (gris) y los núcleos se muestran en azul (Hoechst). La barra de escala equivale a 10µm. **e.** Porcentaje de macrófagos Mafb+, positivos y negativos para adipofilina en ratones tratados como en **d**. n=7 ratones por genotipo en 2 experimentos independientes. Los datos fueron analizados mediante la prueba exacta de Fisher. *p<0.05.

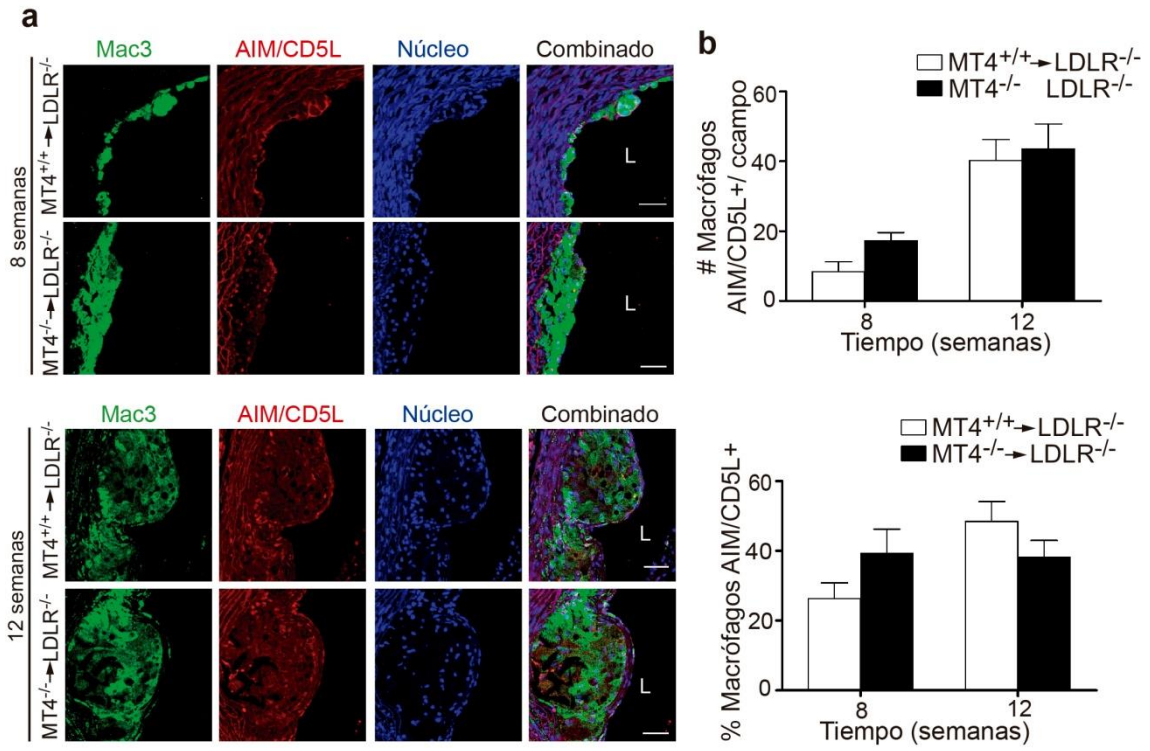

Figura 28: El incremento de macrófagos AIM/CD5L+ en la placa de ateroma en ausencia de MT4-MMP en células de médula ósea no se mantiene en estadios avanzados de la aterosclerosis. a. Imágenes representativas de válvulas aórticas de ratones LDLR$^{-/-}$ irradiados y trasplantados con médula ósea MT4-MMP$^{+/+}$ o MT4-MMP$^{-/-}$, alimentados con dieta grasa durante los tiempos indicados y teñidos para Mac3 (verde), AIM/CD5L (rojo), y los núcleos se muestran en azul (Hoechst). La barra de escala equivale a 10µm. Número (**b**) y porcentaje (**c**) de macrófagos AIM/CD5L+ en ratones tratados como en **a.** n=6 ratones por genotipo en 2 experimentos independientes. Los datos fueron analizados mediante el método estadístico de la t de Student.

Para entender mejor las propiedades funcionales de los macrófagos Mafb+AIM/CD5L+ utilizamos de nuevo el modelo de peritonitis inducida por TG.

Primero confirmamos que tras inducir peritonitis los ratones MT4$^{-/-}$ tenían también un porcentaje significativamente mayor de macrófagos peritoneales que expresaban Mafb (**Figura 29a-b**), similar al fenotipo observado en las placas de ateroma incipientes (**figura 27a-c**). Estos macrófagos mostraban también niveles de expresión de AIM/CD5L más altos analizado tanto por tinción de inmunofluorescencia (**Figura 29c**) como por citometría de flujo (**Figura 29d**). No se detectaron sin embargo diferencias en los niveles de ARN mensajero de Mafb ni de AIM (Cd5l) entre genotipos (**Figura 29e**).

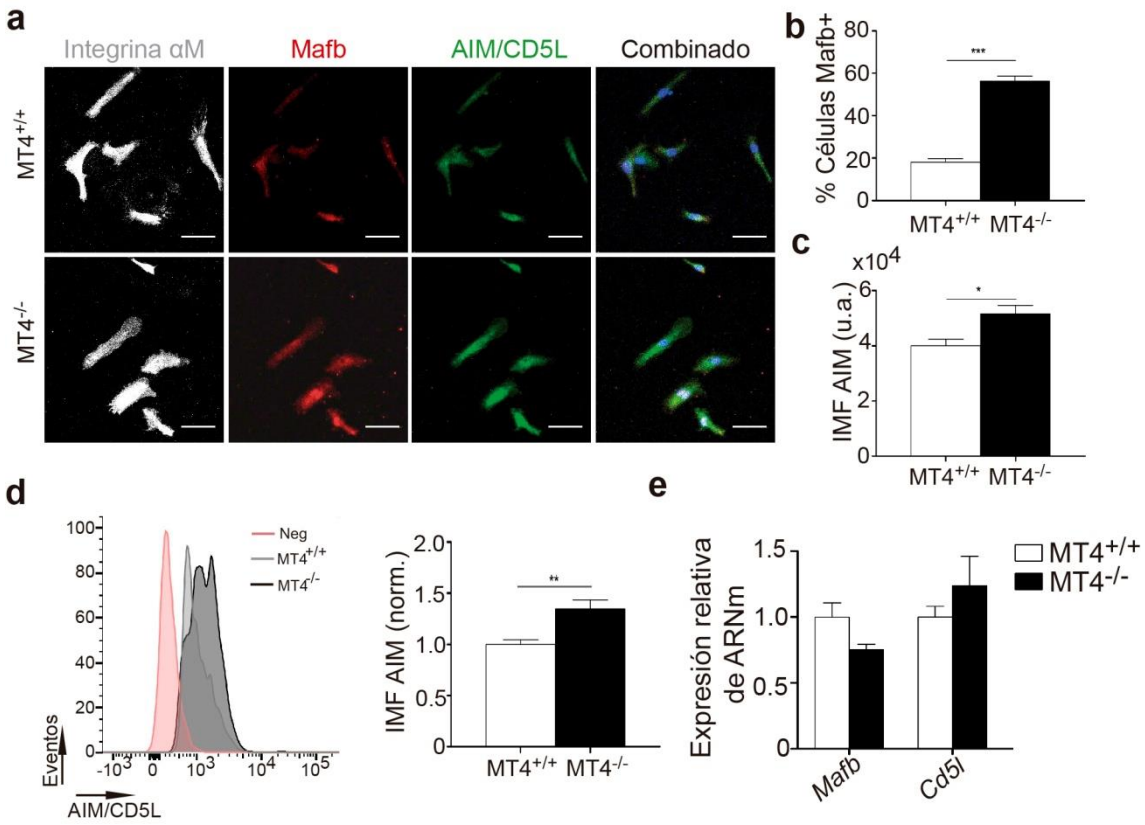

Figura 29: La ausencia de MT4-MMP incrementa el porcentaje de macrófagos Mafb+ y su expresión de AIM/CD5L en peritonitis. a. Imágenes representativas de macrófagos peritoneales de ratones MT4-MMP$^{+/+}$ y MT4-MMP$^{-/-}$ tras peritonitis y teñidos parala integrina αM (gris), Mafb (rojo), AIM/CD5L (verde) y los núcleos en azul (Hoechst). La barra de escala equivale a 20µm. **b.** Cuantificación del número de células Mafb+ en muestras tratadas como en **a**. n=6 muestras por genotipo en 2 experimentos independientes. Los datos fueron analizados mediante el método de la t de Student. *p<0.05. **c.** Cuantificación de la intensidad media de fluorescencia (IMF) de AIM/CD5L en muestras tratadas como en **a**. n=6 muestras por genotipo en 2 experimentos independientes. Los datos fueron analizados mediante el método de la t de Student. *p<0.05. **d.** Histogramas representativos de la expresión en membrana de AIM/CD5L en macrófagos peritoneales de ratones MT4-MMP$^{+/+}$ y MT4-MMP$^{-/-}$ tras peritonitis (panel izquierdo) y la cuantificación de su IMF (panel derecho). n=6 muestras por genotipo en 2 experimentos independientes. Los datos fueron analizados mediante el método de la t de Student. *p<0.05. **d.** Expresión relativa de ARNm de *Mafb* y *Cd5l* de macrófagos peritoneales de ratones MT4-MMP$^{+/+}$ y MT4-MMP$^{-/-}$ tras peritonitis. n=6 muestras por genotipo en 2 experimentos Independientes. Los datos fueron analizados mediante el método de la t de Student.

En relación con la mayor expresión de AIM/CD5L, demostramos que los macrófagos peritoneales tras TG deficientes en MT4-MMP eran más resistentes a la apoptosis inducida por cicloheximida (**Figura 30a-b**). AIM/CD5L regula también la captación de lípidos, principalmente aumentando los niveles del receptor de LDL modificadas CD36[33, 122]. Confirmamos que los macrófagos peritoneales deficientes en MT4-MMP

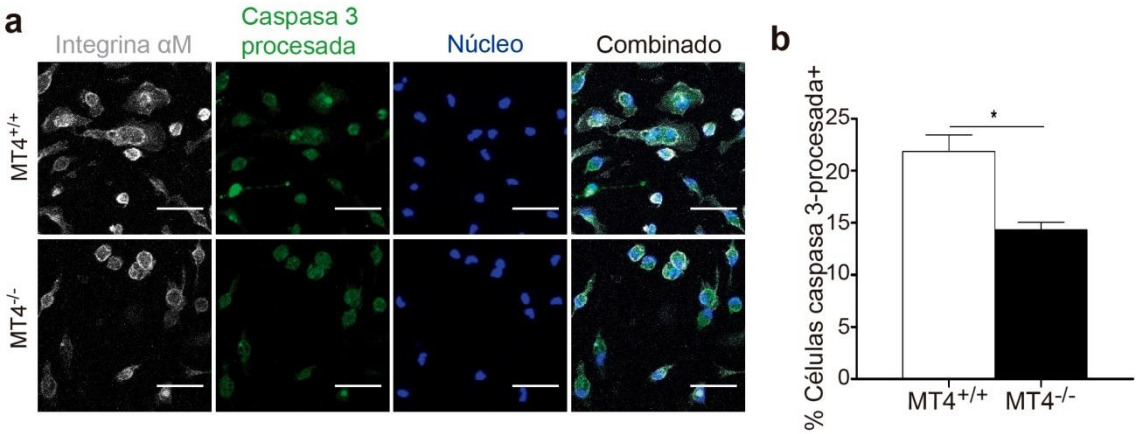

Figura 30: La ausencia de MT4-MMP en macrófagos peritoneales aumenta su resistencia a la muerte celular. a. Imágenes representativas de macrófagos peritoneales de ratones MT4-MMP$^{+/+}$ y MT4-MMP$^{-/-}$ tras peritonitis, tratados con cicloheximida y teñidos para la integrina αM (gris), caspasa 3 procesada (verde) y los núcleos en azul (Hoechst). La barra de escala equivale a 20µm. **b.** Porcentaje de los macrófagos positivos para caspasa 3 procesada en muestras tratadas como en **a**. n=6 muestras por genotipo en 2 experimentos independientes. Los datos fueron analizados mediante el método de la t de Student. *p<0.05.

expresan mayores niveles de CD36 en la membrana (**Figura 31a**) sin mostrar variaciones a nivel de ARN mensajero (**Figura 31b**). Este aumento correlaciona con una mayor captación de LDL acetiladas (AcLDL) por los macrófagos peritoneales deficientes en MT4-MMP a distintos tiempos, siendo significativa tras 3 horas de incubación (**Figura 31c**).

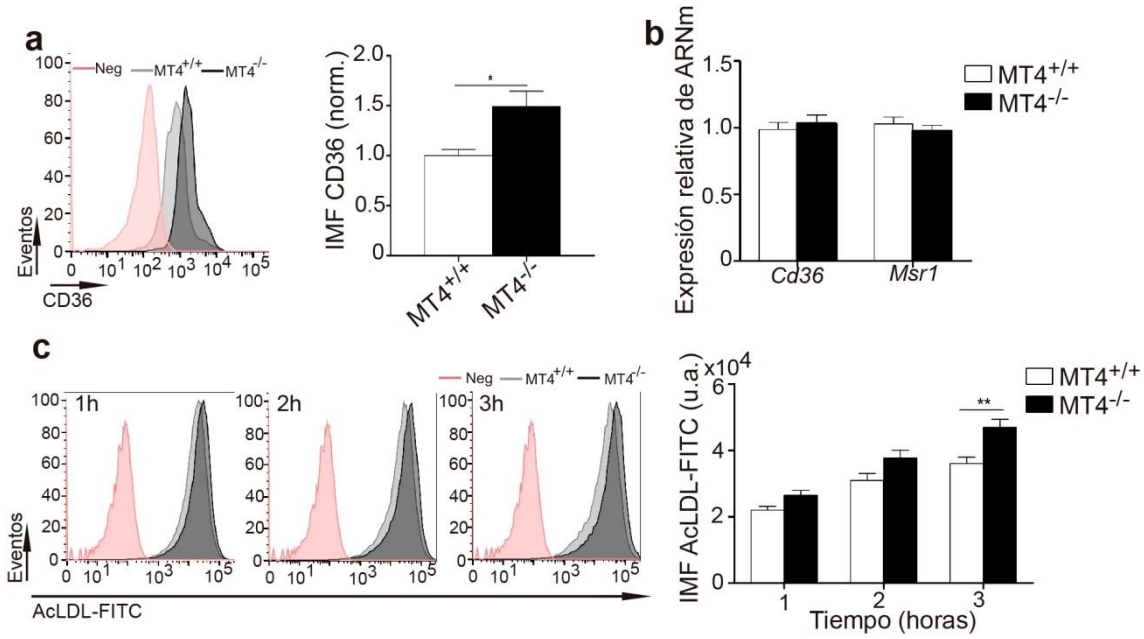

Figura 31: La ausencia de MT4-MMP en los macrófagos peritoneales incrementa los niveles de CD36 en superficie y su capacidad para captar lípidos. a. Histogramas representativos de la expresión en membrana de CD36 en macrófagos peritoneales de ratones MT4-MMP$^{+/+}$ y MT4-MMP$^{-/-}$ tras peritonitis (panel izquierdo) y la cuantificación de la IMF de CD36 (panel derecho). n=6 muestras por genotipo en 2 experimentos independientes. Los datos fueron analizados mediante el método de t de Student. *p<0.05.**b.** Expresión relativa de ARNm de *Cd36* y *Msr1* en macrófagos peritoneales de ratones MT4-MMP$^{+/+}$ y MT4-MMP$^{-/-}$ tras peritonitis. n= 6 muestras por genotipo en 2 experimentos independientes. Los datos fueron analizados mediante el método de la t de Student. **c.** Histogramas representativos de la señal de AcLDL-FITC de macrófagos peritoneales de ratones MT4-MMP$^{+/+}$ y MT4-MMP$^{-/-}$ tras peritonitis (panel izquierdo) y cuantificación de la IMF de AcLDL-FITC (panel derecho). n=6 muestras por genotipo en 2 experimentos independientes. Los datos fueron analizados mediante ANOVA de una cola seguido de un post-test de Bonferroni. *p<0.05

A pesar de que los macrófagos peritoneales deficientes en MT4-MMP son más resistentes a la apoptosis y mejores captadores de lípidos, no muestran un fenotipo más pro-inflamatorio ya que los niveles de ARN mensajero de las citoquinas pro-inflamatorias interleuquinas 1b (*Il1b*) y 6(*Il6*) y TNFα (*Tnfa*) similares a los de los macrófagos MT4$^{+/+}$ (**Figura 32a**). Tampoco se detectaron diferencias en la abundancia de ARN mensajero de las citoquinas anti-inflamatorios TGFβ (*Tgfb*) e interleuquina 10 (*Il10*), ni en los receptores de quimioquinas CCR5 (*Ccr5*), CCR2 (Ccr2) y CX3CR1 (*Cx3cr1*) (**Figura 32a y 32b**).

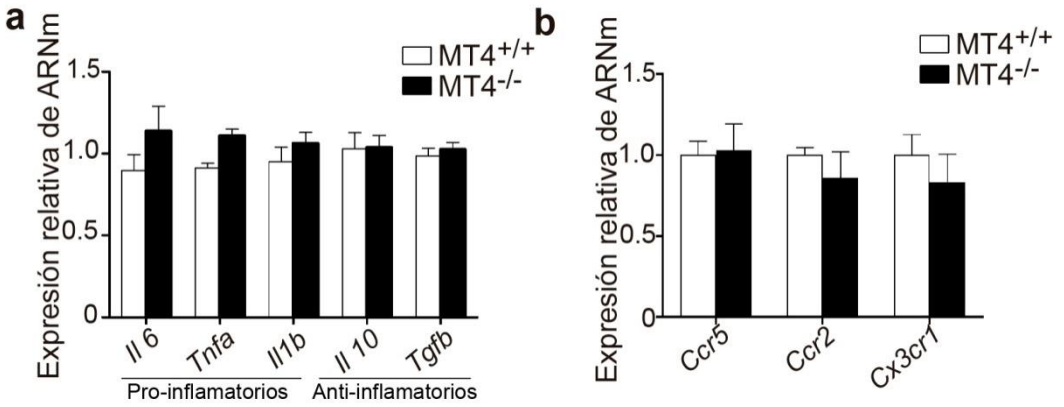

Figura 32: MT4-MMP en macrófagos peritoneales no modula la producción de citoquinas ni de receptores de quimioquinas. Expresión relativa de ARNm de las citoquinas pro-inflamatorias (*Il6*, *Tnfa* y *Il1b*) y anti-inflamatorias (*Il10* y *Tgfb*) (**a**) y de los receptores *Ccr5, Ccr2* y *Cx3cr1* (**b**) en macrófagos peritoneales de ratones MT4-MMP$^{+/+}$ y MT4-MMP$^{-/-}$ tras peritonitis. n=6 muestras por genotipo en 2 experimentos independientes. Los datos fueron analizados mediante el método de la t de Student.

La inhibición del reclutamiento temprano de monocitos patrulleros suprime la acumulación de macrófagos y lípidos así como la aceleración de la aterosclerosis en ausencia de MT4-MMP

Puesto que el impacto primario de la ausencia de MT4-MMP en aterosclerosis parece ser el aumento del reclutamiento temprano de los monocitos patrulleros al endotelio inflamado, quisimos investigar si inhibiendo ese reclutamiento se revertía el fenotipo en la progresión de la aterosclerosis.

Como ya se ha comentado, los receptores de quimioquinas implicados el reclutamiento de monocitos a la pared vascular inflamada son principalmente CX3CR1, CCR2 y CCR5. En el contexto aterosclerótico, el bloqueo de cualquiera de los tres receptores afecta al reclutamiento de los monocitos clásicos, mientras que el reclutamiento de los patrulleros únicamente se encuentra disminuido sólo cuando se bloquea CCR5, pero no se afecta por el bloqueo de CX3CR1 o CCR2[34]. Por ello para inhibir el reclutamiento de los monocitos patrulleros decidimos bloquear CCR5. Para este abordaje utilizamos el fármaco Maraviroc (MRV), un antagonista de CCR5, empleado en clínica para el tratamiento de pacientes infectados con VIH [123, 124]. Utilizamos el modelo de ratones $LDLR^{-/-}$ trasplantados con médula ósea $MT4^{+/+}$ o $MT4^{-/-}$ que tras 4 semanas de reconstitución, se alimentaron con dieta grasa. Desde el día 0 de dieta hasta el fin del experimento se administró intragástricamente MRV o vehículo (como control), desde las 12 horas previas hasta 2 horas antes del sacrificio. El MRV se administró cada 12 horas durante la primera semana y cada 24 horas durante las restantes. Los ratones se analizaron a los 3 días, y a 1 y 8 semanas de dieta grasa (**Figura 33a**).

Tras 3 días de dieta grasa se tiñó el arco menor de los cayados aórticos para CD115 y Ly6C y se contaron los monocitos clásicos y patrulleros adheridos (**Figura 33b-d**). Tras el tratamiento con MRV, hay una disminución de los monocitos reclutados, tanto clásicos como patrulleros, en presencia y en ausencia de MT4-MMP, igualando el número de monocitos patrulleros adheridos entre genotipos. Esta diferencia en el reclutamiento no correlacionaba con variaciones en los niveles de los receptores de quimioquinas CCR2 y CCR5 en la membrana de los monocitos patrulleros, que eran similares entre genotipos y tratamientos (**Figura 33e**)

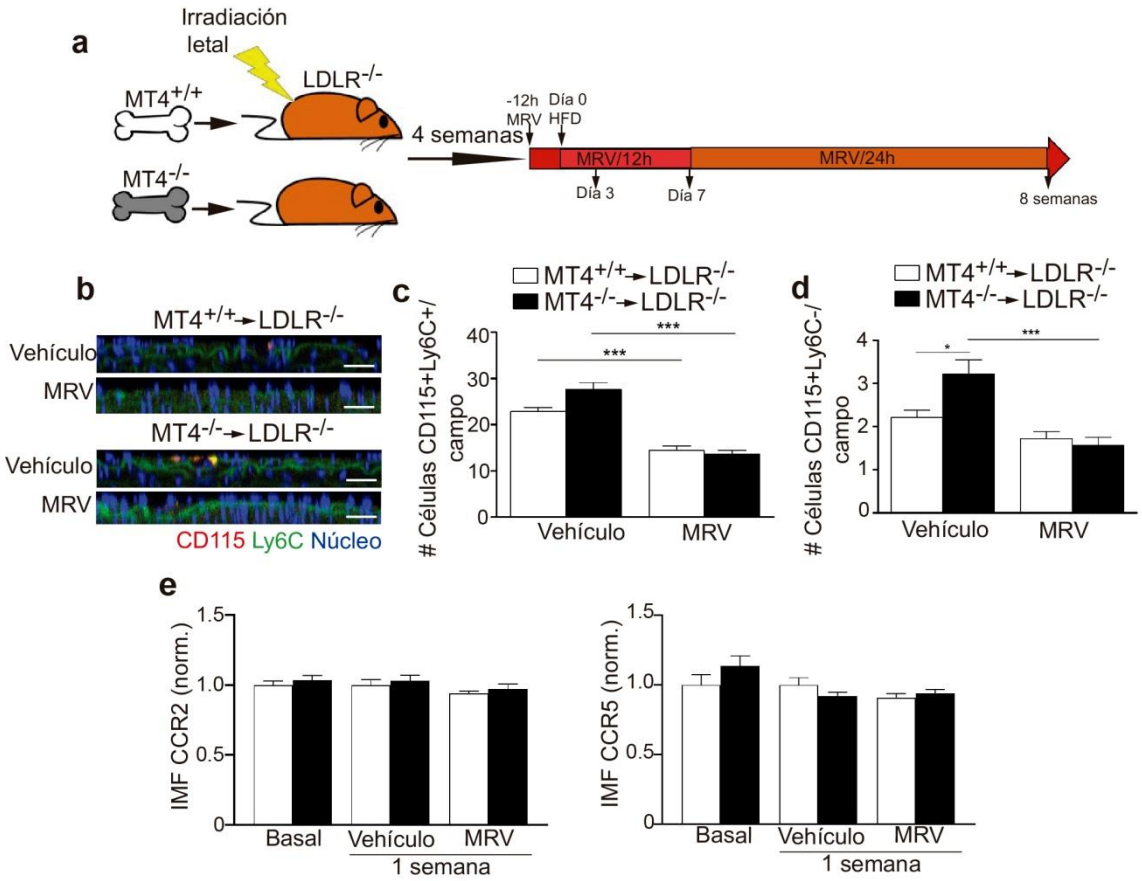

Figura 33: El bloqueo del reclutamiento de monocitos patrulleros a la placa incipiente iguala la adhesión temprana de monocitos patrulleros en ratones LDLR$^{-/-}$ trasplantados con médula ósea MT4-MMP$^{-/-}$ y MT4-MMP$^{+/+}$. a. Esquema del diseño experimental de tratamiento con maraviroc (MRV) durante aterosclerosis en ratones LDLR$^{-/-}$ irradiados y trasplantados con médula ósea MT4-MMP$^{+/+}$ o MT4-MMP$^{-/-}$. **b.** Imágenes ortogonales representativas del cayado aórtico de ratones LDLR$^{-/-}$ irradiados y trasplantados con médula ósea MT4-MMP$^{+/+}$ o MT4-MMP$^{-/-}$, alimentados con dieta grasa durante 3 días y tratados con MRV o vehículo, y teñidos *in toto*paraCD115 (rojo) y Ly6C (verde). Los núcleos se muestran en azul (Hoechst) y en verde también se observa la elastina (autofluorescencia). La barra de escala equivale a 20µm. Cuantificación del número de monocitos clásicos (**c**) y de monocitos patrulleros (**d**) adheridos en ratones tratados como en **b**. n=7-8 ratones por genotipo y condición en 2 experimentos independientes. Los datos fueron analizados mediante ANOVA de una cola seguido de un post-test de Bonferroni. *p<0.05.**e.** Niveles de IMF en membrana de los receptores CCR2 (panel izquierdo) y CCR5 (panel derecho) de monocitos patrulleros de ratones LDLR$^{-/-}$ irradiados y trasplantados con médula ósea MT4-MMP$^{+/+}$ o MT4-MMP$^{-/-}$, alimentados con dieta grasa durante 1 semana y tratados con MRV o vehículo. n=8 ratones por genotipo y condición en 2 experimentos independientes. Los datos fueron analizados mediante ANOVA de una cola seguido de un post-test de Bonferroni.

Tras corroborar el efecto del MRV en el reclutamiento temprano de los monocitos patrulleros tras 3 días de dieta grasa, analizamos si este efecto repercutía en las poblaciones de macrófagos observadas a 1 semana. El tratamiento con MRV resultaba en un descenso del número de macrófagos totales en placa (**Figura 34a-b**),

y del número de macrófagos positivos para Mafb y AIM/CD5L (**Figura 34c-d**), igualando los valores de macrófagos Mafb+AIM/CD5L+ entre genotipos.

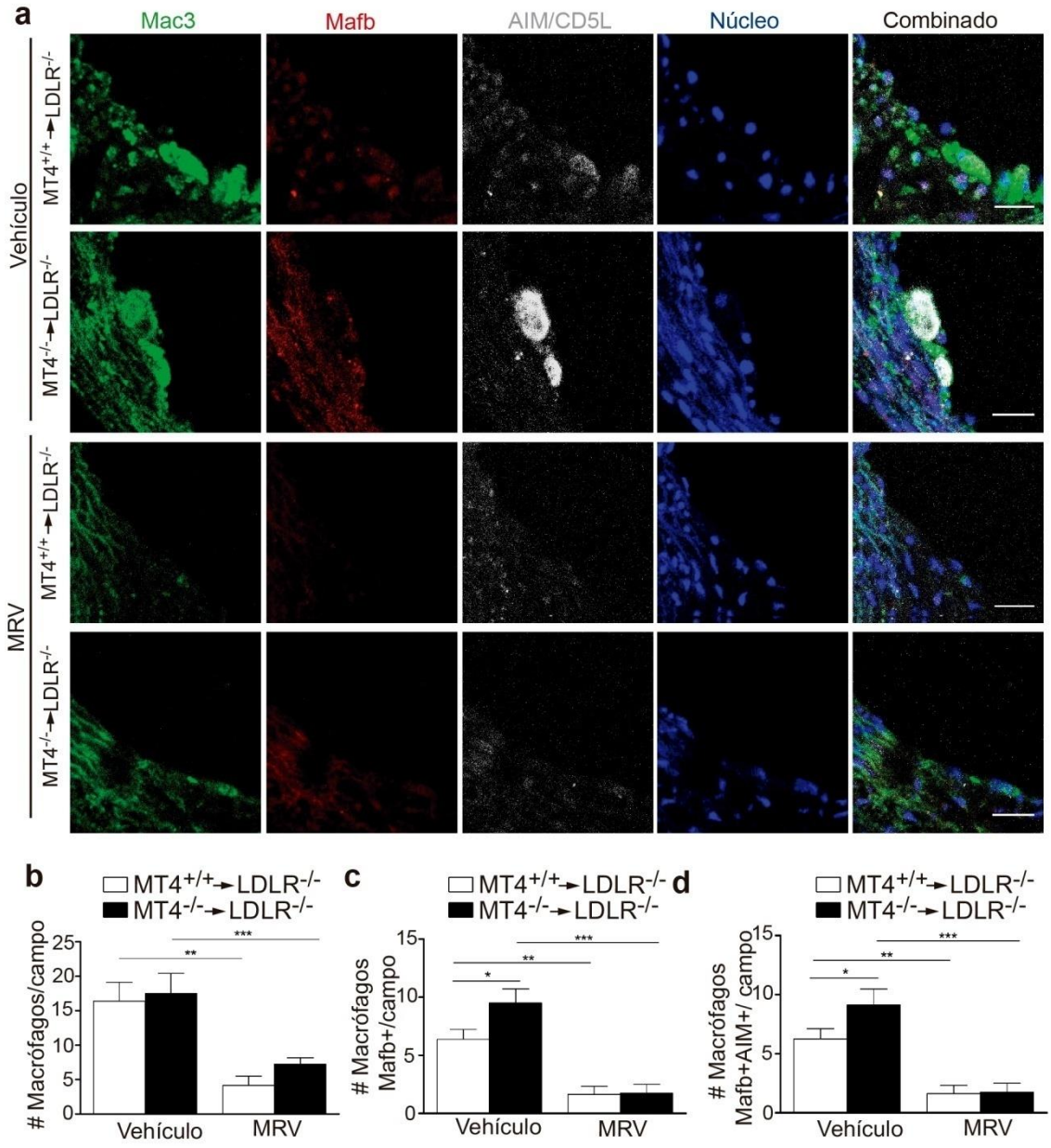

Figura 34: El bloqueo del reclutamiento de monocitos patrulleros a la placa incipiente iguala el número de macrófagos Mafb+AIM/CD5L+ en estadios tempranos entre ratones LDLR$^{-/-}$ trasplantados con médula ósea MT4-MMP$^{-/-}$ y MT4-MMP$^{+/+}$. a. Imágenes representativas de válvulas aórticas de ratones LDLR$^{-/-}$ irradiados y trasplantados con médula ósea MT4-MMP$^{+/+}$ o MT4-MMP$^{-/-}$ y tratados con MRV o vehículo, alimentados con dieta grasa durante 1 semana y teñidos para Mac3 (verde), Mafb (rojo), AIM/CD5L (gris) y los núcleos se muestran en azul (Hoechst). La barra de escala equivale a 10µm. Cuantificación del número de macrófagos (**b**), macrófagos Mafb+ (**c**) y macrófagos Mafb+AIM/CD5L+ (**d**) en ratones tratados como en **a.** n=8 ratones por genotipo y condición en 2 experimentos independientes. Los datos fueron analizados mediante ANOVA de una cola seguido de un post-test de Bonferroni.*p<0.05, **p<0.01, **p<0.001.

Finalmente analizamos el impacto del MRV en la aterosclerosis a 8 semanas de dieta grasa. El tratamiento con MRV producía una disminución en el número global de macrófagos en las placas de los ratones (**Figura 35a-b**), que correlacionaba con un descenso en el acúmulo de lípidos y en la aceleración de la aterosclerosis (**Figura 35c-g**), igualando los genotipos.

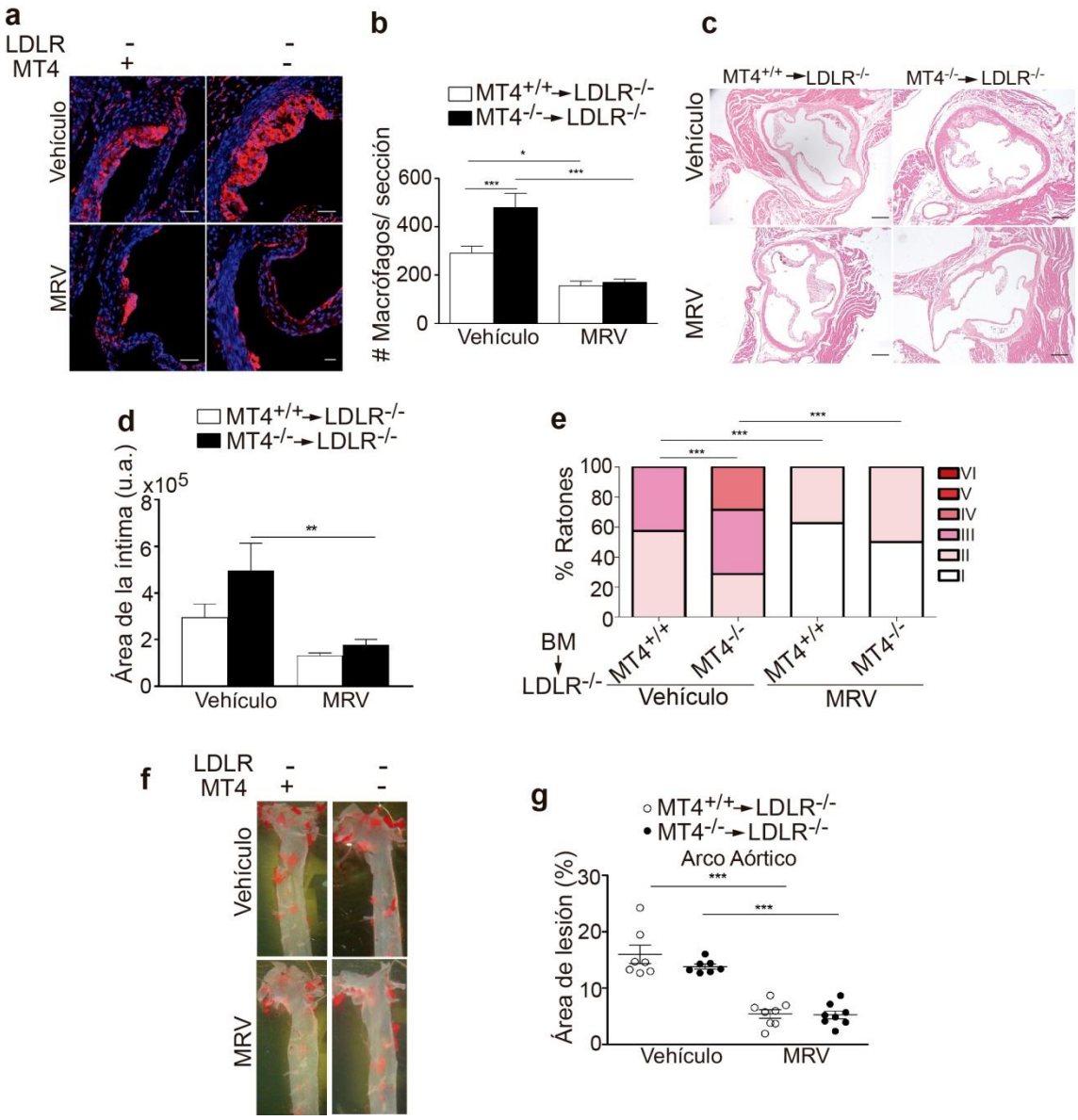

Figura 35: El bloqueo del reclutamiento de monocitos patrulleros a la placa incipiente iguala el número de macrófagos y la evolución de la aterosclerosis en estadios tardíos entre ratones LDLR$^{-/-}$ trasplantados con médula ósea MT4-MMP$^{-/-}$ y MT4-MMP$^{+/+}$. a. Imágenes representativas de válvulas aórticas de ratones LDLR$^{-/-}$ irradiados y trasplantados con médula ósea MT4-MMP$^{+/+}$ o MT4-MMP$^{-/-}$ y tratados con MRV o vehículo, alimentados con dieta grasa durante 8 semanas y teñidos para Mac3 (rojo) y los núcleos se muestran en azul (Hoechst). La barra de escala equivale a 50µm. **b.** Cuantificación del número de macrófagos en ratones tratados como en **a.** n=7-8 ratones por genotipo y condición en 2 experimentos independientes. Los datos fueron analizados mediante ANOVA de una cola seguido de un post-test de Bonferroni.*p<0.05, **p<0.01. **c.** Imágenes representativas de las válvulas aórticas de ratones LDLR$^{-/-}$ irradiados y trasplantados con médula ósea MT4-MMP$^{+/+}$ o MT4-MMP$^{-/-}$ y tratados con MRV o vehículo, alimentados con dieta grasa durante 8 semanas y teñidos con H&E. La barra de escala equivale a 100µm. Cuantificación del área de la íntima (**d**) y del porcentaje de ratones según la clasificación de Stary (**e**) en ratones tratados como en **c**.n=7-8 ratones por genotipo y condición en 2 experimentos independientes. Los datos fueron analizados mediante ANOVA de una cola seguido de un post-test de Bonferroni (**d**) o utilizando el método de la Chi cuadrado (**e**). **p<0.01, ***p<0.001. **f.** Imágenes representativas de aortas de ratones LDLR$^{-/-}$ irradiados y trasplantados con médula ósea MT4-MMP$^{+/+}$ o MT4-MMP$^{-/-}$ y tratados con MRV o vehículo, alimentados con dieta grasa durante 8 semanas y teñidas *in toto*con ORO(Red Oil-O). **g.** Cuantificación del área de depósito de lípidos en el arco aórtico en ratones tratados como en **f.** n=7-8 ratones por genotipo y condición en 2 experimentos independientes. Los datos fueron analizados mediante ANOVA de una cola seguido de un post-test de Bonferroni.**p<0.01, ***p<0.001.

Estos resultados nos indican que el fenotipo de aceleración de aterosclerosis en ausencia de MT4-MMP se debe a un incremento inicial del reclutamiento de monocitos patrulleros, los cuales dan lugar en la placa temprana preferentemente a macrófagos Mafb+AIM/CD5L+. A su vez, dichos macrófagos, en ausencia de MT4-MMP son más resistentes a la apoptosis y más eficaces captando lípidos, lo que finalmente resulta en estadios posteriores de la aterosclerosis en una mayor acumulación de macrófagos y de lípidos en la placa y en placas más avanzadas.

La actividad catalítica de MT4-MMP es necesaria para la regulación de los niveles de la integrina αMβ2 en la membrana de los macrófagos

Como hemos comentado anteriormente, las integrinas, y en concreto las integrinas β2, son importantes en los eventos de adhesión y transmigración de monocitos en el contexto inflamatorio. De hecho la integrina αMβ2 es el receptor responsable del rastreo por monocitos patrulleros sobre el endotelio inflamado [28]. Hemos determinado que tanto los macrófagos peritoneales deficientes en MT4-MMP tras peritonitis como

los monocitos patrulleros circulantes en ratones LDLR$^{-/-}$ trasplantados con médula ósea de ratones MT4$^{-/-}$ presentan mayores niveles de la integrina αMβ2 en la superficie celular.

La ausencia de cambios en los niveles de ARNm de la integrina αM en los macrófagos peritoneales sugería un mecanismo de regulación post-traslacional por MT4-MMP. Dado que ésta es una proteasa, la primera hipótesis a testar fue si MT4-MMP podía procesar la integrina αMβ2 en la membrana de los macrófagos y/o monocitos patrulleros. Para ello y dado que MT4-MMP al estar anclada por puente GPI se encuentra presente en dominios lipídicos específicos de la membrana, analizamos si la integrina αM podía localizarse en estos dominios y por tanto ser accesible a MT4-MMP en macrófagos peritoneales. Mediante subfraccionamiento proteico con el detergente Tx114 de lisados de los macrófagos peritoneales tras peritonitis, observamos que en ausencia de MT4-MMP había un incremento de la integrina αM en la fracción liposoluble (**Figura 36a-b**), la cual está enriquecida en dominios lipídicos ricos en proteínas GPI [125], y es donde se encuentra localizada MT4-MMP (**Figura 7c)**.

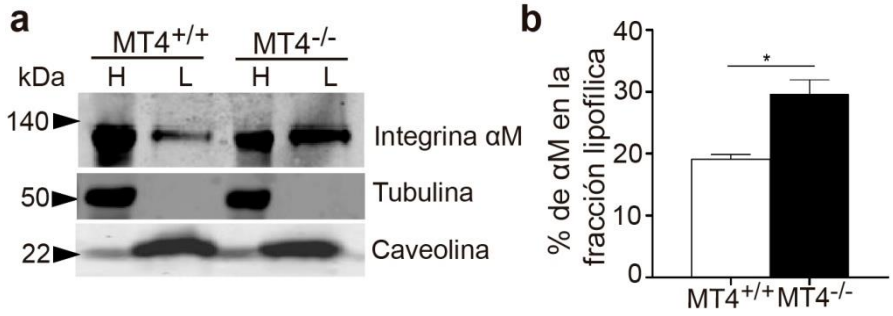

Figura 36: Los macrófagos peritoneales deficientes en MT4-MMP acumulan la integrina αM en los dominios lipídicos de la membrana plasmática. a. Western blot representativo de lisados de Tx114 de macrófagos peritoneales de ratones MT4-MMP$^{+/+}$ y MT4-MMP$^{-/-}$ tras peritonitis. Se incluyen la tubulina y caveolina como marcadores de las fracciones. L indica lipofílico y H hidrofólico. **b.** Cuantificación de la integrina αM en la fracción lipofílicade muestras tratadas como en**a**. n=6 muestras por genotipo en dos experimentos independientes. Los datos fueron analizados mediante el método de la t de Student. *p<0.05.

Tras ello investigamos si la actividad catalítica de MT4-MMP era necesaria para modular los niveles de expresión de la integrina αM en la membrana de los macrófagos. Utilizamos lentivirus (LV) que expresan la proteína nativa de MT4-MMP (secuencia completa, SC) o su mutante catalítico E248A (EA, en el cual se sustituye el glutámico E248 por una alanina, inactivando su capacidad catalítica), que además

codificaban también la expresión de la proteína fluorescente GFP como reportero (**Figura 37a**).

Se inocularon intraperitonealmente los LV en ratones $MT4^{-/-}$, utilizando como controles ratones $MT4^{+/+}$ y $MT4^{-/-}$ inyectados con LV que sólo expresaban GFP (*mock*), y se analizó el fenotipo de los macrófagos peritoneales a los 5 días. En este modelo se obtenía un menor número de macrófagos en el peritoneo que en el caso de la peritonitis inducida por TG (hasta 3 órdenes de magnitud menor) (**Figura 37b**).Los macrófagos de los ratones $MT4^{-/-}$ inyectados con LV que codificaban para GFP (*mock*) tenían niveles de expresión de la integrina αM en la membrana mayores que los de los ratones $MT4^{+/+}$ inyectados con dichos virus (**Figura 37c**), al igual que lo observado con la peritonitis por TG en ratones $MT4^{-/-}$ y $MT4^{+/+}$ (**Figura 9a**). Los macrófagos peritoneales de ratones $MT4^{-/-}$ inyectados con LV que codificaban para MT4-MMP SC mostraban niveles de expresión de la integrina αM en membrana similares a los de los macrófagos de ratones $MT4^{+/+}$ (**Figura 37c**), mientras que los macrófagos transducidos con MT4-MMP catalíticamente inactiva mantenían niveles de membrana de la integrina αM similares a los vistos en los macrófagos $MT4^{-/-}$ transducidos únicamente con el *mock* (**Figura 37c**). Estos resultados nos indicaban que la actividad catalítica de MT4-MMP es necesaria para regular los niveles de la integrina αM en la membrana de los macrófagos.

Analizamos entonces si en los macrófagos transducidos con LV la regulación de los niveles de la integrina αMβ2 en la membrana correlacionaba con un su funcionalidad como habíamos visto en los macrófagos obtenidos tras inyección de TG (**Figura 8 y 11**). Aunque no observamos diferencias en el número de macrófagos en la cavidad peritoneal en ninguna de las condiciones (**Figura 37b**), sí pudimos observar mayor número de células adheridas a la membrana del mesenterio en el caso de los ratones $MT4^{-/-}$ inyectados con virus GFP, y que en sus correspondientes controles $MT4^{+/+}$ inyectados con virus GFP (**Figura 37d-e**). De modo similar, los ratones $MT4^{-/-}$ inyectados con LV que expresaban la proteína completa de MT4-MMP, mostraba una tendencia a tener menos células adheridas al mesenterio, mimetizando el fenotipo de ratones $MT4^{+/+}$, mientras que aquellos ratones inyectados con virus que expresaban la proteína catalíticamente inactiva, tendían a mostrar más células adheridas al mesenterio, mimetizando el fenotipo de ratones $MT4^{-/-}$ (**Figura 37d-e**), aunque sin llegar a ser significativo. De igual modo, al adherir los macrófagos sobre fibrinógeno durante 3 y 24 horas (**Figura 37f**) se observó que los macrófagos $MT4^{-/-}$ transducidos

con LV codificantes de la proteína intacta de MT4-MMP, tenían menor área (similar a los macrófagos control transducidos con GFP), que aquellos transducidos con la proteína catalíticamente inactiva, los cuales tenían un área más similar a la de los macrófagos deficientes en MT4-MMP a las 24 horas, sin mostrar diferencias en el número de células adheridas ni en su circularidad (**Figura 37h-i**).

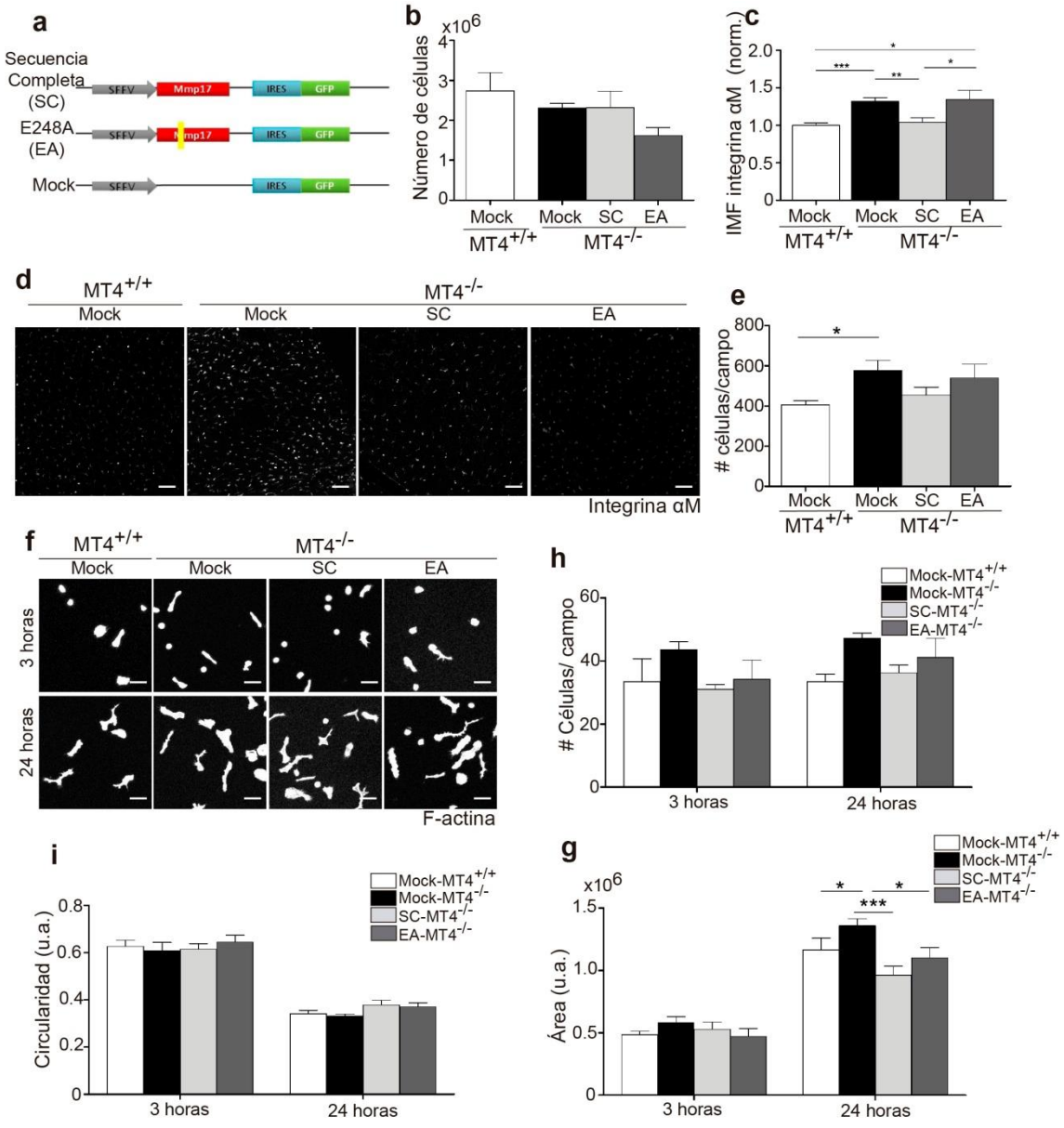

Figura 37: Los niveles dela integrina αM en la membrana de los macrófagos peritoneales es dependiente de la actividad catalítica de MT4-MMP. a. Esquema de la construcción del lentivirus codificante para la proteína total de MT4 (Secuencia Completa, SC), su mutante catalítico (E248A, EA), y el control (Mock). Cuantificación del número de macrófagos peritoneales (**b**) y de laIMF de la integrina αM en su membrana (**c**), extraídos tras 5 días de inyección de los virus mostrados en**a**, en ratones MT4-MMP$^{+/+}$ y MT4-MMP$^{-/-}$ como se indica. n=6 ratones por genotipo y condición en 2 experimentos independientes. Los datos fueron analizados mediante ANOVA de una cola seguido de un post-test de Bonferroni. *p<0.05, **p<0.01, ***p<0.001. **d.** Imágenes representativas de membranas peritoneales de ratones MT4-MMP$^{+/+}$ y MT4-MMP$^{-/-}$ tras 5 días de la inyección con los virus indicados en **a** y teñidos parala integrina αM. La barra de escala equivale a 100 µm. **e.** Cuantificación del número de células del experimento mostrado en**d**. n=6 ratones por genotipo y condición en 2 experimentos independientes. Los datos fueron analizados mediante ANOVA de una cola seguido de un post-test de Bonferroni. *p<0.05, **p<0.01, ***p<0.001. **f.** Imágenes representativas de macrófagos peritoneales de ratones MT4-MMP$^{+/+}$ y MT4-MMP$^{-/-}$ tras 5 días de la inyección con los virus indicados en **a,** plaqueados sobre fibrinógeno y teñidos para actina tras 3 o 24 horas de adhesión. . La barra de escala equivale a 30 µm. Cuantificación del número de células por campo (**g**), circularidad (**h**) yárea (**i**), del experimento mostrado en **f.** n=6 ratones por genotipo y condición en 2 experimentos independientes. Los datos fueron analizados con ANOVA de una cola seguido de un post-test de Bonferroni.

Estos datos indican que la actividad catalítica de MT4-MMP es necesaria para modular los niveles de la integrina αM en la membrana de los macrófagos.

MT4-MMP procesa la cadena αM de la integrina αMβ2

El procesamiento de un sustrato por una proteasa MMP se suele validar mediante ensayos de digestión *in vitro* en los que se incuba la proteína recombinante del posible sustrato con el domino catalítico recombinante de la proteasa y se analiza la generación de fragmentos proteolíticos mediante bioquímica, comúnmente mediante Western blot. En el caso de la integrina αMβ2 dicho abordaje no es posible pues al ser una proteína heterodimérica y transmembrana es extremadamente difícil la obtención de la proteína recombinante completa, con correcto plegamiento y conformación. Procedimos por tanto a un primer análisis *in silico* para la identificación de posibles sitios de procesamiento en las cadenas αM y β2 de la integrina por la proteasa MT4-MMP. Para ello se utilizó el software Cleavpredict (http://cleavpredict.sanfordburnaham.org/[126]). Cleavpredict identifica los sitios susceptibles de ser cortados en determinadas proteínas por distintas metaloproteinasas, en nuestro caso por MT4-MMP, y los clasifica según su accesibilidad y probabilidad de corte. Esta lista fue refinada mediante el modelado *in*

silico del dímero de MT4-MMP en aposición con la integrina αMβ2 y con ambas aproximaciones se pudo detectar la posición EN^{977}LSS como la única en la que el sitio de corte predicho para la cadena αM era accesible al centro catalítico de MT4-MMP (**Figura 38a-b** y **Tabla Suplementaria 1**). Confirmamos mediante la base de datos MEROPS (http://merops.sanger.ac.uk/) que el corte entre asparagina (N) y leucina (L) es frecuente para MT4-MMP.

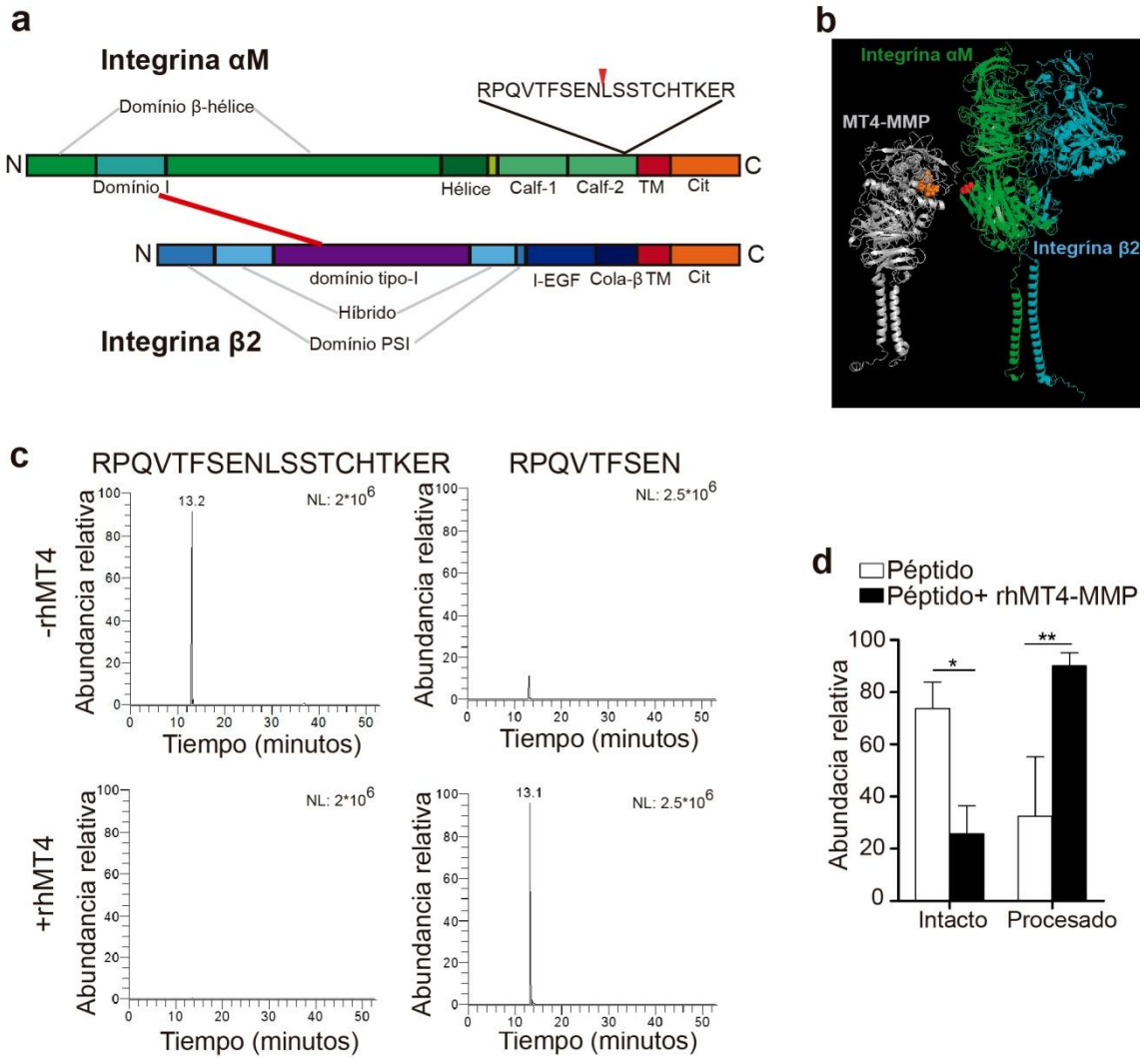

Figura 38: MT4-MMP es capaz de procesar la cadena αM de la integrina αMβ2 in vitro. a. Esquema de la integrina αMβ2 indicando el sitio de corte de αM predicho *in silico* en rojo. **b.** Representación de MT4-MMP (gris) con la integrina αMβ2 (verde y azul) indicando la posición del dominio catalítico de MT4-MMP (naranja) y el sitio de corte de la integrina αM teórico (rojo). **c.** Extractos de espectometría de masas representativos de los péptidos obtenidos de la incubación in vitro del péptido predicho de la integrina αM en presencia y ausencia del dominio catalítico recombinante de MT4-MMP. **d.** Cuantificación de la abundancia relativa del péptido de la integrina αM intacto y de su fragmento del experimento descrito en **c**. n=4 experimentos independientes. Los datos fueron analizados mediante ANOVA de una cola seguido de un post-test de Bonferroni. *p<0.05, **p<0.01.

Para corroborar el procesamiento de la cadena αM de la integrina por MT4-MMP sintetizamos un péptido que contenía la secuencia predicha del sitio de corte (RPQVTFSENLSSTCHTKER) y lo incubamos en presencia o ausencia de la proteína recombinante correspondiente al dominio catalítico de MT4-MMP humana, tras lo cual se analizó por espectometría de masas la presencia del péptido íntegro y de su correspondiente fragmento N-terminal (RPQVTFSEN) (**Figura 38c**). Pudimos comprobar que en presencia del dominio catalítico de MT4-MMP había mayor abundancia del fragmento procesado (**Figura 38d**). Por tanto pudimos concluir que MT4-MMP es capaz de cortar la cadena αM de la integrina αMβ2 en la posición $N^{977}L$.

La ausencia de MT4-MMP induce un incremento del número de monocitos patrulleros que rastrean el endotelio inflamado de modo dependiente de la integrina αMβ2

Los monocitos patrulleros se caracterizan por un patrón de adhesión y migración único en el que son capaces de desplazarse sobre el endotelio en un movimiento de rastreo para detectar daño endotelial y favorecer la restauración de la homeostasis[28]. Aunque la integrina αLβ2 es la encargada de este rastreo de los monocitos patrulleros sobre el endotelio en condiciones homeostáticas, la integrina implicada en situación de daño o inflamación es la integrina αMβ2[27, 127].

Por ello, y dado que habíamos visto un incremento de la integrina αMβ2 en los monocitos patrulleros y un aumento de su reclutamiento temprano al endotelio inflamado durante la aterosclerosis incipiente, analizamos si su comportamiento de rastreo intravascular *in vivo* estaba afectado en ausencia de MT4-MMP. Utilizamos el modelo de microscopía intravital en el músculo cremaster del ratón en el que activamos el endotelio mediante la inyección intratesticular de la quimioquina CCL2 (MCP1), clave en el reclutamiento de monocitos durante la aterosclerosis, y se tiñeron los monocitos para CD115 y Ly6C, con el fin de poder discriminar entre monocitos clásicos y patrulleros, positivos y negativos para Ly6C respectivamente, (**Figura 39a**). En ausencia de MT4-MMP, había un número significativamente mayor de monocitos patrulleros rastreando el endotelio activado (**Figura 39b-c**), sin cambios en la

velocidad, distancia ni coeficiente de confinamiento de dichos monocitos (**Figura 40a-c**). En una aproximación complementaria se marcaron las células circulantes para CD115 y Ly6G y se observó que en ausencia de MT4-MMP hay una disminución en el número de neutrófilos (CD115-Ly6G+) rodando sobre el endotelio en ausencia de MT4-MMP (**Figura 40e**).

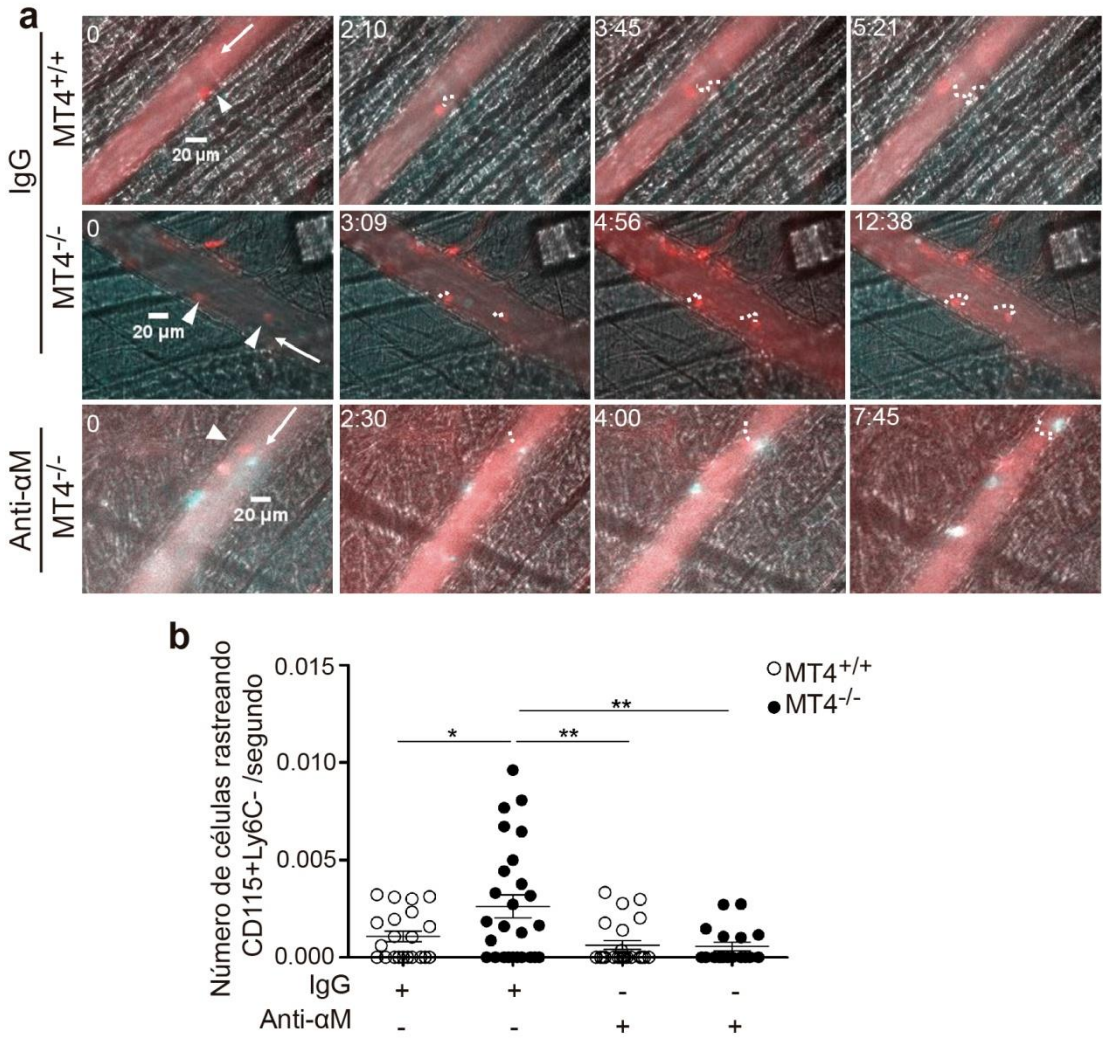

Figura 39: La ausencia de MT4-MMP incrementa el número de monocitos patrulleros que rastrean el endotelio inflamado de modo dependiente de la integrina αM. a. Imágenes representativas de microscopía intravital de músculo cremaster de ratones MT4-MMP$^{+/+}$ y MT4-MMP$^{-/-}$, tras 4 horas de estimulación con CCL2/MCP1 intratesticular y teñidos para CD115 en rojo y Ly6C en verde y en presencia del anticuerpo bloqueante de la integrina αM (anti-αM) o su control de isotipo (IgG). **b.** Cuantificación del número de monocitos patrulleros rastreando el endotelio activado en ratones tratados como en **a**. Se muestran las vénulas de una n=5 ratones por genotipo y condición en 2 experimentos independientes. Los datos fueron analizados mediante ANOVA de una cola seguido de un post-test de Bonferroni. *p<0.05, **p<0.01.

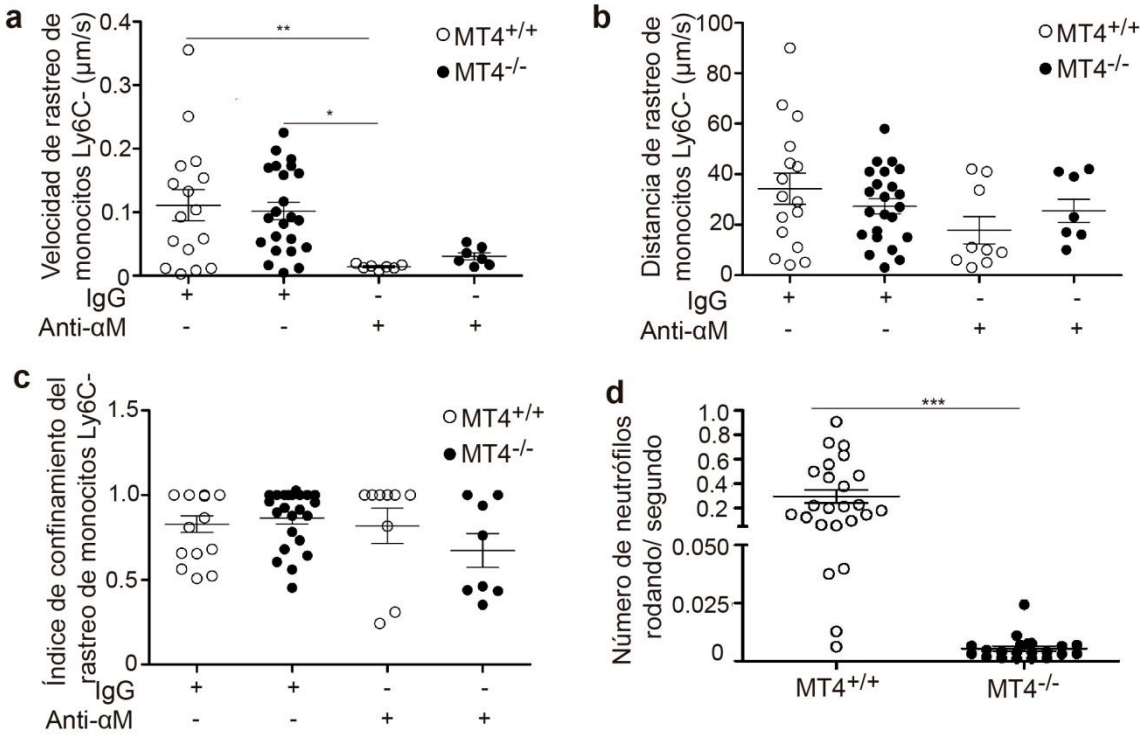

Figura 40: La ausencia de MT4-MMP no afecta a la velocidad, distancia ni índice de confinamiento de los monocitos patrulleros, pero disminuye el número de neutrófilos que ruedan sobre en el endotelio activado. Cuantificación de la velocidad (**a**), distancia recorrida (**b**) e índice de confinamiento (**c**) de los monocitos patrulleros en el músculo cremaster de ratones MT4-MMP$^{+/+}$ y MT4-MMP$^{-/-}$, tras 4 horas de estimulación con CCL2/MCP1 intratesticular y teñidos para CD115 en rojo y Ly6C en verde, en presencia del anticuerpo bloqueante de la integrina αM (anti-αM) o su control de isotipo (IgG). Se muestran las vénulas independientes de n=5 ratones por genotipo y condición en 2 experimentos independientes. Los datos fueron analizados mediante ANOVA de una cola seguido de un post-test de Bonferroni. *p<0.05, **p<0.01. **d.** Número de neutrófilos rodando en el endotelio activado del músculo cremaster de ratones MT4-MMP$^{+/+}$ y MT4-MMP$^{-/-}$, tras 4 horas de estimulación con CCL2/MCP1 intratesticular. Se muestran las vénulas individuales de n=8 ratones por genotipo en 2 experimentos independientes. Los datos fueron analizados mediante el método de la t de Student. ***p<0.001.

Por último, para comprobar si el incremento en el número de monocitos patrulleros rastreando el endotelio inflamado en ausencia de MT4-MMP era dependiente de la integrina αMβ2, inyectamos intravenosamente el anticuerpo bloqueante de unión a ligando para la integrina αM (clon M1/70). El bloqueo de la integrina αM producía una disminución de los monocitos patrulleros rastreando el endotelio, tanto en los ratones MT4$^{+/+}$ como en los MT4$^{-/-}$ (**Figura 39b-c**). Dicha disminución era significativa en el caso de la ausencia de MT4-MMP, resultando en la eliminación de diferencias entre genotipos (**Figura 39c**). El bloqueo de la integrina αM también disminuyó la velocidad de rastreo en ambos genotipos, sin afectar la distancia de rastreo ni el índice de

confinamiento (**Figura 40a-c**).

Estos experimentos indican que la ausencia de MT4-MMP induce un mayor rastreo intravascular por parte de los monocitos patrulleros sobre el endotelio inflamado *in vivo*, de modo dependiente de la integrina αM.

DISCUSIÓN

La ausencia de MT4-MMP acelera la progresión de la aterosclerosis mediante el incremento del número de monocitos patrulleros en la placa incipiente

Los monocitos patrulleros desempeñan su actividad de vigilancia en el interior de la vasculatura, donde reconocen el posible daño endotelial y promueven su reparación [28]. La mayoría de los estudios donde se ha estudiado la función de esta población de monocitos han utilizado el modelo de ratón deficiente en Nur77/Nr4a1 (Nur77$^{-/-}$). Estos ratones Nur77$^{-/-}$ carecen prácticamente de la totalidad de la población de monocitos patrulleros, pues Nur77 es un factor de transcripción fundamental para la diferenciación de dichos monocitos [128]. En este modelo Nur77$^{-/-}$ se observaba un aumento de la aterosclerosis en ratón[14, 129, 130], lo cual parecía indicar que los monocitos patrulleros tenían una función protectora de la vasculatura durante la inflamación. Sin embargo, aunque Nur77 no se expresa en los monocitos clásicos, cuando estos se diferencian a macrófago activan su expresión, y la ausencia de Nur77 les confiere un fenotipo proinflamatorio, que puede ser en parte responsable del aumento de aterosclerosis observado[129]. Otro estudio sin embargo no observaba cambios en la formación de placa de aterosclerosis en ratones LDLR$^{-/-}$ trasplantados con médula ósea Nur77$^{-/-}$, en este caso analizado únicamente mediante la acumulación de lípidos [10]. Estos datos contrapuestos han mantenido abierto el debate sobre el papel de los monocitos patrulleros durante la aterosclerosis una vez en la placa. Sin embargo, su función en el torrente sanguíneo sí está más clara, y se ha demostrado un papel protector de aterosclerosis de los monocitos patrulleros mediante la captación de lípidos circulantes y la disminución por tanto del daño endotelial durante la aterosclerosis [30, 131].

Más recientemente, se ha observado que el modelo de ratón deficiente en Nur77 utilizado en los estudios clásicos, incluyendo los comentados anteriormente, desarrollan inflamación sistémica espontánea en edad avanzada[132], y que este fenotipo no se debe a la ausencia de los monocitos patrulleros, sino a la transcripción de una proteína Nur77 truncada, correspondiente a la región N-terminal, que señaliza a través de HIF-1α, promoviendo un fenotipo inflamatorio[133]. Esto indica que el papel de los monocitos patrulleros en inflamación, y en particular en aterosclerosis, tiene que

ser reevaluado.

En los últimos años, se ha descrito que el gen Nur77 cuenta con distintas regiones activadoras de su promotor, siendo uno de estos activadores, el denominado E2, fundamental para la diferenciación de los monocitos patrulleros[134]. En dicho estudio, generan un nuevo modelo de ratón en el que se ha mutado la región activadora E2 del promotor de Nur77, fundamental para la diferenciación de los monocitos patrulleros, de modo que se eliminan estos monocitos, pero se preserva la expresión de Nur77 en macrófagos, tanto residentes como inflamatorios[134]. Este nuevo modelo ayudará a diseccionar de modo más preciso la contribución de los monocitos patrulleros ad daño tisular, como por ejemplo en la placa de aterosclerosis.

Sin embargo, tanto el modelo de ratón deficiente en Nur77 como el nuevo modelo de eliminación de la región activadora E2, son modelos en los que se estudia la función de los monocitos patrulleros mediante los efectos que produce su ausencia, no existiendo así, ningún modelo en el que se investigue la acción de los monocitos patrulleros mediante su activación.

En nuestro modelo observamos que al estar ausente la proteasa MT4-MMP, los monocitos patrulleros están más activos en situación de daño, pudiendo ser una herramienta más para poder investigar su función en otros contextos, además de la aterosclerosis, aquí estudiada. Asimismo, utilizando los ratones deficientes en MT4-MMP mostramos la primera evidencia de la posible contribución de los monocitos patrulleros a una población de macrófagos Mafb+AIM/CD5L+ (captadora de lípidos) en estadios tempranos de la aterosclerosis y en peritonitis estéril.

También describimos, mediante microscopía intravital y tinciones de zonas proaterogénicas de la aorta, que la ausencia de MT4-MMP en células de médula ósea hace que los monocitos patrulleros estén en mayor número adheridos al endotelio activado. Puesto que se ha descrito que el reclutamiento de los monocitos patrulleros en aterosclerosis depende del receptor CCR5, decidimos utilizar su inhibición para ver si revertíamos el efecto de la ausencia de MT4-MMP. Mediante la inhibición de CCR5 conseguimos reducir parcialmente el reclutamiento de monocitos patrulleros a la placa. Esta disminución equipara los números de los monocitos patrulleros adheridos en estadios tempranos obtenidos en presencia y ausencia de MT4-MMP, resultando en una abolición de la acumulación de macrófagos Mafb+AIM/CD5L+ y de lípidos en la placa y del consiguiente fenotipo acelerado de aterosclerosis. Estos resultados indican

que el principal efecto responsable del fenotipo observado de aceleración de aterosclerosis en ausencia de MT4-MMP se debe al incremento inicial del reclutamiento de monocitos patrulleros a la placa, y a su posterior diferenciación a macrófagos Mafb+AIM/CD5L+. Sin embargo, no se pueden descartar mecanismos adicionales de regulación de la aterosclerosis por MT4-MMP en monocitos patrulleros como por ejemplo el posible papel de los macrófagos CD11c+, también incrementados en la placa incipiente en ausencia de MT4-MMP y que probablemente son proinflamatorios dada la función descrita para esta subpoblación en otros contextos [135]. En este sentido, se han descrito recientemente por citometría de masas subpoblaciones de monocitos patrulleros en humanos que es posible que en respuesta a distintas señales del entorno puedan diferenciarse a poblaciones de macrófagos diferentes como Mafb+AIM/CD5L+ o CD11c+[136]. La determinación de si los macrófagos derivados de los monocitos patrulleros desempeñan un papel pro-resolutivo en estadios tardíos de la aterosclerosis requeriría de nuevos estudios que incluyan estrategias más específicas y de depleción inducible de esta subpoblación de monocitos.

La ausencia de MT4-MMP produce una acumulación diferencial de macrófagos Mafb+AIM/CD5L+, resistentes a apoptosis y captadores de lípidos, en las placas incipientes de ateroma y en peritonitis estéril

La acumulación de macrófagos en la placa depende principalmente del reclutamiento de monocitos en los estadios tempranos y de la proliferación local de los macrófagos en las fases avanzadas de aterosclerosis[66, 137]. Nosotros observamos que los ratones LDLR$^{-/-}$ trasplantados con células de médula ósea deficiente en MT4-MMP muestran una acumulación de macrófagos mayor en lesiones avanzadas de ateroma, sin observar diferencias en su proliferación, apoptosis ni egresión, indicando que posiblemente esta acumulación se debía a un incremento en el reclutamiento de monocitos a la placa. Del mismo modo, también observamos que en ratones con ausencia de MT4-MMP en las células derivadas de médula ósea, hay un incremento inicial de macrófagos Mafb+ AIM/CD5L+, indicando un desbalance en las poblaciones de macrófagos que componen la placa incipiente.

Aparte de su abundancia está cada vez más claro que los macrófagos presentan una alta plasticidad lo que les permite adoptar fenotipos y funciones claramente diferenciadas en respuesta a las señales del entorno [138]. A los dos subtipos clásicos demacrófagos, M1 y M2, o pro-inflamatorios y anti-inflamatorios respectivamente [26] que se definieron por su diferenciación *in vitro* con determinadas citoquinas (IFN-γ, TNF-α y GM-CSF o con IL-4, IL-10 y M-CSF entre otros)[26, 139], se han añadido en la placa de ateroma nuevos subtipos como los Mox y M4 (dentro de los pro-inflamatorios) y los M(Hb) y Mhem (dentro de los anti-inflamatorios) [3]. Estas poblaciones de macrófagos también cuentan con marcadores y funciones específicas dentro de la lesión. Se ha descrito por ejemplo que los Mhem y M(Hb) se inducen por la exposición al grupo hemo y al complejo hemoglobina-haptoglobina, los M4 se inducen por la quimioquina CXCL4, y los Mox se inducen por la exposición a fosfolípidos oxidados[3]. Del mismo modo, no todos responden igual a los lípidos, siendo por ejemplo los Mhem, M(Hb) y Mox resistentes a la captación de lípidos[140], lo cual indica que cumplen distintas funciones en la placa, por lo que variaciones en las proporciones de las distintas poblaciones de macrófagos podría modular, positiva o negativamente, el desarrollo de la placa.

En cuanto a la contribución de los monocitos patrulleros a la heterogeneidad de los macrófagos en la placa de aterosclerosis, se había descrito que los monocitos patrulleros eran capaces de diferenciarse a células que expresaban CD11c+ en la placa y que los monocitos CD11c+ migran a la placa componiendo una población de macrófagos CD11c+ en la placa [34, 141]. Se ha visto también, que en ausencia de CD11c, los monocitos patrulleros adheridos al endotelio se reduce, de modo dependiente de E-selectina, y del mismo modo, que su ausencia produce una reducción de la placa de ateroma [141]. En nuestro trabajo observamos que pese a no detectar diferencias en el número total de macrófagos en la placa incipiente, hay un incremento de macrófagos CD11c+ en dichas placas en ausencia de MT4-MMP en las células de médula ósea. Es probable que estos macrófagos CD11c+ deriven de monocitos patrulleros, aunque no lo hemos analizado en los ratones tratados con Maraviroc, pero podrían también derivar de los monocitos clásicos, que también pueden dar lugar a macrófagos CD11c+ en la placa[142]. Dado que no detectamos un incremento de captación de lípidos en los macrófagos CD11c+ en ausencia de MT4-MMP, es probable que esta subpoblación de macrófagos desempeñe funciones proinflamatorias en la progresión de la aterosclerosis como las descritas previamente en tejido adiposo[135].

Es interesante que en ausencia de MT4-MMP los macrófagos presentes en la placa sean mayoritariamente positivos para Mafb, lo que observamos también en los macrófagos peritoneales tras tioglicolato. Dado que se había visto que los monocitos patrulleros se diferencian a macrófagos mediante la activación del factor de transcripción Mafb en un modelo de infección peritoneal [27], Mafb podría ser un actor fundamental en la diferenciación de monocito patrullero a macrófago independientemente del contexto inflamatorio. La presencia de macrófagos Mafb+ se había detectado en las placas de ateroma establecidas de ratón y humano y se había demostrado que la ausencia de Mafb promovía la progresión de la aterosclerosis mediante la inducción de la expresión del gen diana de Mafb, AIM (del inglés "Apoptosis Inhibitor of Macrophages", también conocido como CD5L) [143]. Además de inhibir la muerte celular de los macrófagos en la placa, AIM/CD5L también está implicado en la captación de OxLDL[143, 144, 145]. Nuestro estudio confirma estas acciones de los macrófagos Mafb+AIM/CD5L+ e indica además que probablemente derivan de los monocitos patrulleros.

En el modelo de peritonitis inducida por tioglicolato observamos que los macrófagos deficientes en MT4-MMP expresaban también mayores niveles en membrana de AIM/CD5L (como los macrófagos de la placa incipiente) y de CD36, receptor de basura también expresado por los monocitos patrulleros[72] e implicado en la captación de lípidos. Estos datos correlacionaban con que en ausencia de MT4-MMP estos macrófagos unan de un modo más activo LDL modificadas (en este caso acLDL)[146], en concordancia con el papel descrito para AIM/CD5Len favorecer la captación de OxLDL mediada por CD36 y la posterior formación de células espumosas en la placa[144]. Si bien es cierto que se requerirían nuevos experimentos bloqueando CD36 para demostrar fehacientemente que es el principal receptor implicado en dicha acumulación de lípidos, sin duda el eje Mafb→AIM/CD5L→CD36 es un buen candidato para explicar el fenotipo observado en ausencia de MT4-MMP.

Es interesante reseñar que la población Mafb+AIM/CD5L+, y en concreto la deficiente en MT4-MMP, parece ser única dentro de la heterogénea población que componen los macrófagos en la placa de ateroma[147], ya que son macrófagos más resistentes a apoptosis y fagocíticos pero no muestran un fenotipo más pro- ni anti-inflamatorio al menos con las citoquinas analizadas. En este sentido, en un contexto infeccioso, se ha descrito que la cooperación de la integrina αMβ2 con CD36 y TLR2 en la membrana de los macrófagos promueve la captación y acumulación de lípidos pero sin aumentar

la respuesta inflamatoria [148]. Estudios futuros podrán ver si esta cooperación se da lugar también en los macrófagos Mafb+AIM/CD5L+ y particularmente en ausencia de MT4-MMP en la que hay un incremento de la integrina αMβ2 en la membrana de los macrófagos. Del mismo modo, la relación de esta población con las previamente descritas en la placa de ateroma (Mox, M(Hem), M(Hb) y M4)[74] necesitará de análisis futuros. Dada la diversidad de poblaciones de macrófagos que componen la placa de ateroma, estrategias que actúen sobre ambas poblaciones de macrófagos Mafb+ y Mafb- podrían ser más efectivas en la reducción de la evolución de la placa de ateroma.

Todo ello nos lleva a la conclusión de que en efecto la ausencia de MT4-MMP en células de médula ósea produce un desequilibrio en las poblaciones de macrófagos en las placas de ateroma incipientes, viéndose incrementado el número de macrófagos CD11c+ y Mafb+AIM/CD5L+, siendo estos últimos más ávidos en la captación de lípidos en la placa.

MT4-MMP es capaz de procesar la cadena αM de la integrina αMβ2 modulando el rastreo de monocitos patrulleros sobre el endotelio activado

En este estudio describimos la primera función de MT4-MMP en los monocitos y macrófagos, no relacionada con la previamente propuesta de procesamiento de pro-TNFα [80, 81, 83]. Identificamos un nuevo sustrato para MT4-MMP, la cadena αM (integrina Itgam, CD11b, αM) del heterodímero αMβ2, que puede localizarse en dominios lipídicos específicos de la membrana plasmática, al igual que MT4-MMP[149, 150, 151], lo que podría regular su reciclaje y actividad [152]. La subfamilia de las integrinas β2 está formada por αLβ2 (CD11a/CD18), αMβ2 (CD11b/CD18), αXβ2 (CD11c/CD18) y αDβ2 (CD11d/CD18), todas ellas presentes en los monocitos y macrófagos[113]. La integrina αMβ2 presenta multitud de ligandos, tanto proteínas extracelulares (por ejemplo fibrinógeno o el componente 3 del complemento) como ligandos presentes en otras células (por ejemplo los miembros de la familia ICAM)[113]. Esta variedad de ligandos hace que la integrina αMβ2 esté implicada en multitud de funciones en monocitos y macrófagos, tales como adhesión, migración y fagocitosis entre otras.

En cuanto al procesamiento proteolítico como mecanismo de regulación de la expresión y actividad de integrinas β2 en células mieloides, se ha descrito que la cadena β2 de la integrina puede ser procesada por la proteasa MMP9 en macrófagos y que αM puede cortarse por serprocidinas en neutrófilos modulando su adhesión, separación y transmigración a través de fibrinógeno [153, 154, 155]. Del mismo modo, se ha reportado que las formas solubles de la integrina β2 generadas mediante procesamiento por metaloproteinasas y que se incrementan en inflamación, mantienen la capacidad de unir ligandos, actuando como antagonistas de la integrina no procesada, lo que unido a la reducción de sus niveles de expresión en la superficie podría facilitar el despegamiento de las células durante la quimiotaxis o migración y favorecer procesos como la egresión de los macrófagos del peritoneo, [50, 156]. Nosotros observamos *in vivo* que tanto los monocitos patrulleros como los macrófagos peritoneales tras tioglicolato deficientes en MT4-MMP mostraban una acumulación en la superficie celular de la integrina αMβ2, y mediante la estrategia lentiviral pudimos concretar que es la actividad catalítica de MT4-MMP la que regula los niveles de membrana de la integrina αMβ2 en los monocitos patrulleros y los macrófagos *in vivo*. También identificamos el sitio de procesamiento mediado por MT4-MMP en la cadena αM de la integrina en la posición $N^{997}L$. Este residuo está conservado tanto en ratón como en humano, pero que no guarda homología con la secuencia de la cadena αL de la integrina LFA-1, en ambas especies. Aunque esto indicaría que el procesamiento de la integrina αM por MT4-MMP es selectivo y los datos de bloqueo con anticuerpos anti-integrina αM sugieren que sería el principal responsable del fenotipo observado en los monocitos patrulleros deficientes en la proteasa (**Figura 40**), datos previos de proteómica del laboratorio identificaron otros posibles sustratos para MT4-MMP en macrófagos entre los que se encuentra CD36, proteína que reside en dominios lipídicos ricos en GPI [157]. Dados los niveles más elevados de CD36 en macrófagos deficientes en MT4-MMP y el papel asignado recientemente a CD36 en monocitos patrulleros de captar lípidos modificados durante la aterosclerosis y de modular su rastreo sobre el endotelio dañado [131], no podemos descartar que CD36 o el procesamiento por parte de MT4-MMP de otras proteínas de membrana, contribuya al menos en parte al fenotipo observado en ausencia de MT4-MMP en inflamación estéril (peritonitis y aterosclerosis).

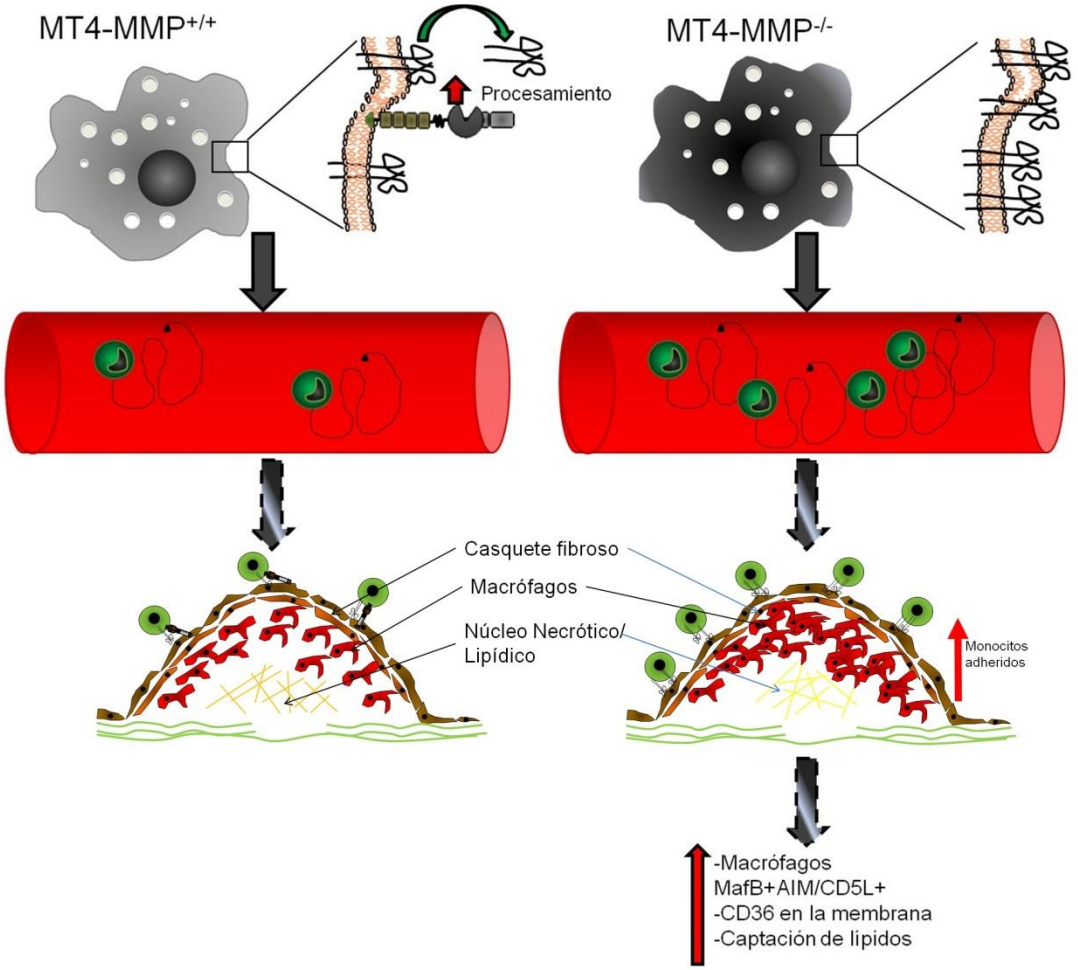

Figura 41: Modelo de las consecuencias de la ausencia de MT4-MMP en monocitos y macrófagos: MT4-MMP puede procesar la cadena αM de la integrina αMβ2 modulando los niveles de la integrina αMβ2 en macrófagos y en monocitos patrulleros, en los que regula su rastreo sobre el endotelio inflamado. En el modelo de aterosclerosis, la ausencia de MT4-MMP produce un aumento de la adhesión de los monocitos patrulleros al endotelio inflamado en las placas de ateroma incipientes. En la aorta inflamada, este aumento de monocitos patrulleros reclutados produce una acumulación de macrófagos MafB+AIM/CD5L+que son más activos captando lípidos, lo que finalmente resulta en una aceleración de la aterosclerosis.

Dado que durante el daño vascular, los monocitos patrulleros cambian su patrón de rastreo dependiente de αLβ2 a un rastreo más exhaustivo del endotelio vascular activado dependiente de la integrina αMβ2 [27, 28, 127], el procesamiento de la integrina αM por MT4-MMP podría producir la desestabilización del heterodímero de la integrina αMβ2[158], permitiendo la separación de los monocitos patrulleros y constituyendo un mecanismo clave de regulación de este proceso. Aunque el papel de la integrina αMβ2 en aterosclerosis no está suficientemente claro [159, 160, 161], nuestros resultados indican que la integrina αMβ2 es un regulador importante del rastreo de los monocitos patrulleros en contextos inflamatorios mediados por CCL2, pudiendo serlo también durante los estadios iniciales de la aterosclerosis, junto con LFA-1 (αLβ2) y VLA-4 (α4β1), descritos recientemente mediante microscopia intravital en arterias inflamadas durante la aterosclerosis [30]. Además, la interacción de la integrina αMβ2 con ICAM-1, von Willebrand factor, fibrinógeno o CCN1/Cyr61 en los sitios propensos a ateroma[32, 162, 163, 164] podría señalizar e inducir, por ejemplo, la bajada de los niveles de Foxp1 con la consiguiente inducción de la expresión de M-CSF[165]. Este factor aumenta la expresión de MT4-MMP (datos no mostrados) y Mafb [166] y podría contribuir a la regulación de la diferenciación de los monocitos patrulleros a macrófagos Mafb+.

Está aceptado que los monocitos patrulleros son reclutados a las placas de ateroma en estadios tempranos de una manera dependiente de CCR5 [167], sin embargo en nuestro estudio vemos que hay un aumento del reclutamiento de los patrulleros a la placa incipiente en ausencia de MT4-MMP que no parece depender de cambios en los niveles de expresión de los receptores de quimioquinas en los monocitos patrulleros. Pese a no haber bloqueado este reclutamiento con anti-integrina αM, los experimentos de transferencia adoptiva demuestran que las acciones de MT4-MMP se ejercen directamente sobre este tipo celular sugiriendo quela integrina αMβ2 es un actor relevante en el reclutamiento temprano de monocitos patrulleros a la placa incipiente de ateroma.

Perspectivas futuras

En nuestro estudio nos centramos en el papel que tiene MT4-MMP modulando el

papel de los monocitos patrulleros en el contexto inflamatorio y su repercusión en aterosclerosis principalmente; pero dado que en el modelo utilizado eliminamos MT4-MMP de todas las células procedentes de médula ósea, no podemos descartar que MT4-MMP pueda estar ejerciendo otras funciones en otras células inflamatorias. Si bien vemos mediante transferencia adoptiva que el incremento de monocitos patrulleros deficientes en MT4-MMP en la placa incipiente es autónomo del tipo celular, indicándonos que el fenotipo inicial es específico de los monocitos patrulleros, no podemos descartar que en el fenotipo de incremento de placa en que estadios tardíos no haya implicación de otros leucocitos donde también se ha descrito la expresión de MT4-MMP, como los eosinófilos o los linfocitos B [95].

Para poder investigar de modo más selectivo el papel de MT4-MMP en los monocitos patrulleros, tanto en aterosclerosis como en otros contextos, sería importante utilizar nuevas herramientas como el ratón condicional de MT4-MMP generado recientemente en nuestro laboratorio. De este modo podríamos delecionar la expresión de la proteasa mayoritariamente en los monocitos patrulleros utilizando líneas Cre selectivas de dicha población, como la CX3CR1-CreERT2 [168]. Utilizando estos modelos podríamos diseccionar la función de MT4-MMP en los monocitos patrulleros en estadios más tardíos de la aterosclerosis, y además evitaríamos los modelos de trasplante de médula, en los cuales la irradiación ejerce un daño sobre el endotelio vascular que puede afectar a la evolución del proceso patológico y sobre todo al fenotipo de los monocitos patrulleros, dado que una de sus funciones primarias es la detección de células endoteliales dañadas[28].

Nuestro estudio podría tener implicaciones traslacionales relacionadas con la acción ateroprotectora de MT4-MMP cuando está presente en los monocitos patrulleros. Hemos observado que la expresión de MT4-MMP se incrementa temporalmente en la placa de ateroma durante la evolución de la enfermedad en la aorta de ratón. También detectamos un incremento de MT4-MMP en las arterias coronarias humanas durante aterosclerosis, aunque en este caso es difícil diferenciar si el incremento se debe a su expresión en células inflamatorias o a su expresión en otro tipo celular. Del mismo modo que en estudios previos del laboratorio encontramos una mutación puntual en MT4-MMP (*MMP17*), que evitaba su expresión, en un paciente con aneurisma aórtico[92], pruebas genéticas similares podrían ayudar a determinar si mutaciones en el gen de MT4-MMP (*MMP17*) podrían correlacionar con un incremento en la predisposición al desarrollo de placas de ateroma.

La ausencia de MT4-MMP en los monocitos patrulleros conlleva un incremento en la superficie celular de la integrina αMβ2 y de su rastreo intravascular sobre el endotelio activado y al mismo tiempo los macrófagos derivados de dichos monocitos muestran mayor nivel en membrana de CD36, y consecuentemente mayor avidez en captar partículas. En el modelo de aterosclerosis, que nosotros hemos investigado, este incremento del rastreo y reclutamiento de los monocitos patrulleros y de la fagocitosis por los macrófagos derivados de ellos produce una aceleración de la enfermedad, puesto que incrementa la acumulación de estos macrófagos cargados de lípidos en la placa, quedándose retenidos. Sin embargo, estas características podrían ser de utilidad en patologías como infecciones, metástasis pulmonares y angiopatía amiloidea de la enfermedad de Alzehimer en las que los monocitos patrulleros desempeñan acciones beneficiosas [14, 29, 36]. En estos contextos se ha observado que los monocitos patrulleros son capaces de captar partículas perjudiciales en la vasculatura, como las células metastáicas circulantes o las placas β-amiloides depositadas en la parte luminal de los vasos; de hecho, la ausencia de monocitos patrulleros correlaciona con un incremento en las metástasis pulmonares así como en los depósitos amiloides intravasculares [29, 36]. Además,CD36 está implicado en el reconocimiento de todas estas partículas, por lo que el aumento de expresión de CD36 en los macrófagos deficientes en MT4-MMP en contextos como infección bacteriana, células tumorales apoptóticas o placas β-amiloides, podría contribuir también a su eliminación una vez en los tejidos y por tanto a la resolución de la enfermedad[169].

Por todo esto ha aumentado recientemente el interés en caracterizar los mecanismos que regulan los monocitos patrulleros para poder potenciar su actividad intravascular en estas patologías. En los últimos años se han identificado algunos reguladores de su abundancia como el estrés adrenérgico, la activación de NOD2, exosomas tumorales, etc [12, 13, 170]. Nuestros resultados identifican la primera diana molecular, MT4-MMP, cuyo bloqueo a corto plazo podría incrementar estas funciones intravasculares en los monocitos patrulleros, ofreciendo nuevas estrategias para el tratamiento de dichas enfermedades. En la actualidad no existen inhibidores químicos específicos de MMPs, ya que los que existen son generales e inhiben varios miembros de la familia, por lo que su utilización no es recomendable dados los efectos secundarios deletéreos [171]. Sin embargo, un bloqueo de la función catalítica de MT4-MMP con anticuerpos monoclonales daría la especificidad necesaria para poder ser utilizado sin efectos en otras metaloproteinasas y nuestro laboratorio ha generado estas herramientas que

están siendo testadas *in vivo* en la actualidad. Esta estrategia estaría en línea con estudios recientes en los que el bloqueo de la proteasa MT1-MMP con anticuerpos monoclonales específicos generados también por nuestro grupo ha sido eficaz en reducir la severidad de patologías infecciosas e inflamatorias[172, 173].

CONCLUSIONES

- MT4-MMP se expresa en macrófagos durante procesos inflamatorios estériles agudos como la peritonitispor TG y crónicos como la aterosclerosis por dieta grasa.
- La ausencia de MT4-MMP produce una acumulación de la integrina αMβ2 en la membrana de los macrófagos peritoneales y su retención en la membrana peritoneal inflamada.
- La ausencia de MT4-MMP en los leucocitos produce una mayor acumulaciónde macrófagos y de lípidos en la vasculatura inflamada y una aceleración de la aterosclerosis.
- La ausencia de MT4-MMP en los leucocitos resulta en un incremento de la abundancia de macrófagos Mafb+AIM/CD5L+ en la placa de ateroma incipiente y en la peritonitis estéril.
- Los macrófagos Mafb+AIM/CD5L+ deficientes en MT4-MMP son más resistentes a apoptosis, expresan más CD36 en la membrana, y captan máslípidos modificados.
- La ausencia de MT4-MMP aumenta los niveles de la integrina αMβ2 en la superficie de los monocitos patrulleros e incrementa la adhesión de estos al endotelio inflamado en los estadios iniciales de aterosclerosis.
- El bloqueo del reclutamiento de los monocitos patrulleros mediante la inhibición de CCR5 en estadios iniciales de la aterosclerosis iguala la situación deficiente en MT4-MMP a la situación silvestre previniendo la mayor acumulación de macrófagos Mafb+AIM/CD5L+ y de lípidos en las placas y la aceleración de la aterosclerosis.
- La actividad catalítica de MT4-MMP es necesaria para la regulación de los niveles de la integrina αMβ2 en macrófagos peritoneales siendo MT4-MMP capaz de procesar la cadena αM de dicha integrina en la posición $N^{977}L$.
- La ausencia de MT4-MMP produce un aumento del número de monocitos patrulleros que rastrean el endotelio inflamado *in vivo* de manera dependiente de la integrina αM.

BIBLIOGRAFÍA

1. Gordon S, Pluddemann A. The Mononuclear Phagocytic System. Generation of Diversity. *Front Immunol* 2019, **10:** 1893.

2. Fogg DK, Sibon C, Miled C, Jung S, Aucouturier P, Littman DR*, et al.* A clonogenic bone marrow progenitor specific for macrophages and dendritic cells. *Science* 2006, **311**(5757)**:** 83-87.

3. Hristov M, Heine GH. Monocyte subsets in atherosclerosis. *Hamostaseologie* 2015, **35**(2)**:** 105-112.

4. Auffray C, Sieweke MH, Geissmann F. Blood monocytes: development, heterogeneity, and relationship with dendritic cells. *Annu Rev Immunol* 2009, **27:** 669-692.

5. Ingersoll MA, Spanbroek R, Lottaz C, Gautier EL, Frankenberger M, Hoffmann R*, et al.* Comparison of gene expression profiles between human and mouse monocyte subsets. *Blood* 2010, **115**(3)**:** e10-19.

6. Wong KL, Tai JJ, Wong WC, Han H, Sem X, Yeap WH*, et al.* Gene expression profiling reveals the defining features of the classical, intermediate, and nonclassical human monocyte subsets. *Blood* 2011, **118**(5)**:** e16-31.

7. van Furth R, Cohn ZA. The origin and kinetics of mononuclear phagocytes. *J Exp Med* 1968, **128**(3)**:** 415-435.

8. Geissmann F, Manz MG, Jung S, Sieweke MH, Merad M, Ley K. Development of monocytes, macrophages, and dendritic cells. *Science* 2010, **327**(5966)**:** 656-661.

9. Hettinger J, Richards DM, Hansson J, Barra MM, Joschko AC, Krijgsveld J*, et al.* Origin of monocytes and macrophages in a committed progenitor. *Nat Immunol* 2013, **14**(8)**:** 821-830.

10. Chao LC, Soto E, Hong C, Ito A, Pei L, Chawla A*, et al.* Bone marrow NR4A expression is not a dominant factor in the development of atherosclerosis or macrophage polarization in mice. *J Lipid Res* 2013, **54**(3)**:** 806-815.

11. Gamrekelashvili J, Giagnorio R, Jussofie J, Soehnlein O, Duchene J, Briseno CG*, et al.* Regulation of monocyte cell fate by blood vessels mediated by Notch signalling. *Nat Commun* 2016, **7:** 12597.

12. Lessard AJ, LeBel M, Egarnes B, Prefontaine P, Theriault P, Droit A*, et al.* Triggering of NOD2 Receptor Converts Inflammatory Ly6C(high) into Ly6C(low) Monocytes with Patrolling Properties. *Cell Rep* 2017, **20**(8)**:** 1830-1843.

13. Plebanek MP, Angeloni NL, Vinokour E, Li J, Henkin A, Martinez-Marin D*, et al.* Pre-metastatic cancer exosomes induce immune surveillance by patrolling monocytes at the metastatic niche. *Nat Commun* 2017, **8**(1)**:** 1319.

14. Thomas G, Tacke R, Hedrick CC, Hanna RN. Nonclassical patrolling monocyte function in

the vasculature. *Arterioscler Thromb Vasc Biol* 2015, **35**(6)**:** 1306-1316.

15. Alder JK, Georgantas RW, 3rd, Hildreth RL, Kaplan IM, Morisot S, Yu X*, et al.* Kruppel-like factor 4 is essential for inflammatory monocyte differentiation in vivo. *J Immunol* 2008, **180**(8)**:** 5645-5652.

16. Kurotaki D, Yamamoto M, Nishiyama A, Uno K, Ban T, Ichino M*, et al.* IRF8 inhibits C/EBPalpha activity to restrain mononuclear phagocyte progenitors from differentiating into neutrophils. *Nat Commun* 2014, **5:** 4978.

17. Cros J, Cagnard N, Woollard K, Patey N, Zhang SY, Senechal B*, et al.* Human CD14dim monocytes patrol and sense nucleic acids and viruses via TLR7 and TLR8 receptors. *Immunity* 2010, **33**(3)**:** 375-386.

18. Geissmann F, Jung S, Littman DR. Blood monocytes consist of two principal subsets with distinct migratory properties. *Immunity* 2003, **19**(1)**:** 71-82.

19. Patel AA, Zhang Y, Fullerton JN, Boelen L, Rongvaux A, Maini AA*, et al.* The fate and lifespan of human monocyte subsets in steady state and systemic inflammation. *J Exp Med* 2017, **214**(7)**:** 1913-1923.

20. Kapellos TS, Bonaguro L, Gemund I, Reusch N, Saglam A, Hinkley ER*, et al.* Human Monocyte Subsets and Phenotypes in Major Chronic Inflammatory Diseases. *Front Immunol* 2019, **10:** 2035.

21. Ley K, Laudanna C, Cybulsky MI, Nourshargh S. Getting to the site of inflammation: the leukocyte adhesion cascade updated. *Nat Rev Immunol* 2007, **7**(9)**:** 678-689.

22. Gerhardt T, Ley K. Monocyte trafficking across the vessel wall. *Cardiovasc Res* 2015, **107**(3)**:** 321-330.

23. Rogacev KS, Cremers B, Zawada AM, Seiler S, Binder N, Ege P*, et al.* CD14++CD16+ monocytes independently predict cardiovascular events: a cohort study of 951 patients referred for elective coronary angiography. *J Am Coll Cardiol* 2012, **60**(16)**:** 1512-1520.

24. Mildner A, Schonheit J, Giladi A, David E, Lara-Astiaso D, Lorenzo-Vivas E*, et al.* Genomic Characterization of Murine Monocytes Reveals C/EBPbeta Transcription Factor Dependence of Ly6C(-) Cells. *Immunity* 2017, **46**(5)**:** 849-862 e847.

25. Yang J, Zhang L, Yu C, Yang XF, Wang H. Monocyte and macrophage differentiation: circulation inflammatory monocyte as biomarker for inflammatory diseases. *Biomark Res* 2014, **2**(1)**:** 1.

26. Das A, Sinha M, Datta S, Abas M, Chaffee S, Sen CK*, et al.* Monocyte and macrophage plasticity in tissue repair and regeneration. *Am J Pathol* 2015, **185**(10)**:** 2596-2606.

27. Auffray C, Fogg D, Garfa M, Elain G, Join-Lambert O, Kayal S*, et al.* Monitoring of blood vessels and tissues by a population of monocytes with patrolling behavior. *Science* 2007, **317**(5838)**:** 666-670.

28. Carlin LM, Stamatiades EG, Auffray C, Hanna RN, Glover L, Vizcay-Barrena G*, et al.* Nr4a1-dependent Ly6C(low) monocytes monitor endothelial cells and orchestrate their disposal. *Cell* 2013, **153**(2)**:** 362-375.

29. Hanna RN, Cekic C, Sag D, Tacke R, Thomas GD, Nowyhed H*, et al.* Patrolling monocytes control tumor metastasis to the lung. *Science* 2015, **350**(6263)**:** 985-990.

30. Quintar A, McArdle S, Wolf D, Marki A, Ehinger E, Vassallo M*, et al.* Endothelial Protective Monocyte Patrolling in Large Arteries Intensified by Western Diet and Atherosclerosis. *Circ Res* 2017, **120**(11)**:** 1789-1799.

31. Finsterbusch M, Hall P, Li A, Devi S, Westhorpe CL, Kitching AR*, et al.* Patrolling monocytes promote intravascular neutrophil activation and glomerular injury in the acutely inflamed glomerulus. *Proc Natl Acad Sci U S A* 2016, **113**(35)**:** E5172-5181.

32. Imhof BA, Jemelin S, Ballet R, Vesin C, Schapira M, Karaca M*, et al.* CCN1/CYR61-mediated meticulous patrolling by Ly6Clow monocytes fuels vascular inflammation. *Proc Natl Acad Sci U S A* 2016, **113**(33)**:** E4847-4856.

33. Marcovecchio PM, Thomas GD, Mikulski Z, Ehinger E, Mueller KAL, Blatchley A*, et al.* Scavenger Receptor CD36 Directs Nonclassical Monocyte Patrolling Along the Endothelium During Early Atherogenesis. *Arterioscler Thromb Vasc Biol* 2017, **37**(11)**:** 2043-2052.

34. Tacke F, Alvarez D, Kaplan TJ, Jakubzick C, Spanbroek R, Llodra J*, et al.* Monocyte subsets differentially employ CCR2, CCR5, and CX3CR1 to accumulate within atherosclerotic plaques. *J Clin Invest* 2007, **117**(1)**:** 185-194.

35. Swirski FK, Weissleder R, Pittet MJ. Heterogeneous in vivo behavior of monocyte subsets in atherosclerosis. *Arterioscler Thromb Vasc Biol* 2009, **29**(10)**:** 1424-1432.

36. Michaud JP, Bellavance MA, Prefontaine P, Rivest S. Real-time in vivo imaging reveals the ability of monocytes to clear vascular amyloid beta. *Cell Rep* 2013, **5**(3)**:** 646-653.

37. Varol C, Mildner A, Jung S. Macrophages: development and tissue specialization. *Annu Rev Immunol* 2015, **33:** 643-675.

38. Gordon S, Pluddemann A, Martinez Estrada F. Macrophage heterogeneity in tissues: phenotypic diversity and functions. *Immunol Rev* 2014, **262**(1)**:** 36-55.

39. Saqib U, Sarkar S, Suk K, Mohammad O, Baig MS, Savai R. Phytochemicals as modulators of M1-M2 macrophages in inflammation. *Oncotarget* 2018, **9**(25)**:** 17937-17950.

40. Shapouri-Moghaddam A, Mohammadian S, Vazini H, Taghadosi M, Esmaeili SA, Mardani F*, et al.* Macrophage plasticity, polarization, and function in health and disease. *J Cell Physiol* 2018, **233**(9)**:** 6425-6440.

41. Gordon S, Pluddemann A. Tissue macrophages: heterogeneity and functions. *BMC Biol* 2017, **15**(1)**:** 53.

42. Gautier EL, Shay T, Miller J, Greter M, Jakubzick C, Ivanov S*, et al.* Gene-expression profiles and transcriptional regulatory pathways that underlie the identity and diversity of mouse tissue macrophages. *Nat Immunol* 2012, **13**(11)**:** 1118-1128.

43. Ghosn EE, Cassado AA, Govoni GR, Fukuhara T, Yang Y, Monack DM*, et al.* Two physically, functionally, and developmentally distinct peritoneal macrophage subsets. *Proc Natl Acad Sci U S A* 2010, **107**(6)**:** 2568-2573.

44. Cassado Ados A, D'Imperio Lima MR, Bortoluci KR. Revisiting mouse peritoneal macrophages: heterogeneity, development, and function. *Front Immunol* 2015, **6:** 225.

45. Schif-Zuck S, Gross N, Assi S, Rostoker R, Serhan CN, Ariel A. Saturated-efferocytosis generates pro-resolving CD11b low macrophages: modulation by resolvins and glucocorticoids. *Eur J Immunol* 2011, **41**(2)**:** 366-379.

46. Cohn ZA. Activation of mononuclear phagocytes: fact, fancy, and future. *J Immunol* 1978, **121**(3)**:** 813-816.

47. Hermida MDR, Malta R, de SSM, Dos-Santos WLC. Selecting the right gate to identify relevant cells for your assay: a study of thioglycollate-elicited peritoneal exudate cells in mice. *BMC Res Notes* 2017, **10**(1)**:** 695.

48. Takahashi M, Galligan C, Tessarollo L, Yoshimura T. Monocyte chemoattractant protein-1 (MCP-1), not MCP-3, is the primary chemokine required for monocyte recruitment in mouse peritonitis induced with thioglycollate or zymosan A. *J Immunol* 2009, **183**(5)**:** 3463-3471.

49. Tedder TF, Steeber DA, Pizcueta P. L-selectin-deficient mice have impaired leukocyte recruitment into inflammatory sites. *J Exp Med* 1995, **181**(6)**:** 2259-2264.

50. Gomez IG, Tang J, Wilson CL, Yan W, Heinecke JW, Harlan JM*, et al.* Metalloproteinase-mediated Shedding of Integrin beta2 promotes macrophage efflux from inflammatory sites. *J Biol Chem* 2012, **287**(7)**:** 4581-4589.

51. Tacke F, Randolph GJ. Migratory fate and differentiation of blood monocyte subsets. *Immunobiology* 2006, **211**(6-8)**:** 609-618.

52. Stary HC, Chandler AB, Dinsmore RE, Fuster V, Glagov S, Insull W, Jr*., et al.* A definition of advanced types of atherosclerotic lesions and a histological classification of atherosclerosis. A report from the Committee on Vascular Lesions of the Council on Arteriosclerosis, American Heart Association. *Circulation* 1995, **92**(5)**:** 1355-1374.

53. Davies PF, Civelek M, Fang Y, Fleming I. The atherosusceptible endothelium: endothelial phenotypes in complex haemodynamic shear stress regions in vivo. *Cardiovasc Res* 2013, **99**(2)**:** 315-327.

54. Stremmel C, Stark K, Schulz C. Heterogeneity of Macrophages in Atherosclerosis. *Thromb Haemost* 2019, **119**(8)**:** 1237-1246.

55. Lin J, Kakkar V, Lu X. Impact of MCP-1 in atherosclerosis. *Curr Pharm Des* 2014, **20**(28)**:** 4580-4588.

56. Chistiakov DA, Orekhov AN, Bobryshev YV. Vascular smooth muscle cell in atherosclerosis. *Acta Physiol (Oxf)* 2015, **214**(1)**:** 33-50.

57. Xu H, Jiang J, Chen W, Li W, Chen Z. Vascular Macrophages in Atherosclerosis. *Journal of immunology research* 2019, **2019:** 4354786.

58. Combadiere C, Potteaux S, Rodero M, Simon T, Pezard A, Esposito B*, et al.* Combined inhibition of CCL2, CX3CR1, and CCR5 abrogates Ly6C(hi) and Ly6C(lo) monocytosis and almost abolishes atherosclerosis in hypercholesterolemic mice. *Circulation* 2008, **117**(13)**:** 1649-1657.

59. Febbraio M, Guy E, Silverstein RL. Stem cell transplantation reveals that absence of macrophage CD36 is protective against atherosclerosis. *Arterioscler Thromb Vasc Biol* 2004, **24**(12)**:** 2333-2338.

60. Febbraio M, Podrez EA, Smith JD, Hajjar DP, Hazen SL, Hoff HF*, et al.* Targeted disruption of the class B scavenger receptor CD36 protects against atherosclerotic lesion development in mice. *J Clin Invest* 2000, **105**(8)**:** 1049-1056.

61. Moore KJ, Kunjathoor VV, Koehn SL, Manning JJ, Tseng AA, Silver JM*, et al.* Loss of receptor-mediated lipid uptake via scavenger receptor A or CD36 pathways does not ameliorate atherosclerosis in hyperlipidemic mice. *J Clin Invest* 2005, **115**(8)**:** 2192-2201.

62. Cole JE, Park I, Ahern DJ, Kassiteridi C, Danso Abeam D, Goddard ME*, et al.* Immune cell census in murine atherosclerosis: cytometry by time of flight illuminates vascular myeloid cell diversity. *Cardiovasc Res* 2018, **114**(10)**:** 1360-1371.

63. De Meyer I, Martinet W, De Meyer GR. Therapeutic strategies to deplete macrophages in atherosclerotic plaques. *Br J Clin Pharmacol* 2012, **74**(2)**:** 246-263.

64. Andres V, Pello OM, Silvestre-Roig C. Macrophage proliferation and apoptosis in atherosclerosis. *Curr Opin Lipidol* 2012, **23**(5)**:** 429-438.

65. Llodra J, Angeli V, Liu J, Trogan E, Fisher EA, Randolph GJ. Emigration of monocyte-derived cells from atherosclerotic lesions characterizes regressive, but not progressive, plaques. *Proc Natl Acad Sci U S A* 2004, **101**(32)**:** 11779-11784.

66. Robbins CS, Hilgendorf I, Weber GF, Theurl I, Iwamoto Y, Figueiredo JL*, et al.* Local proliferation dominates lesional macrophage accumulation in atherosclerosis. *Nat Med* 2013, **19**(9)**:** 1166-1172.

67. Rosenfeld ME. Macrophage proliferation in atherosclerosis: an historical perspective.

Arterioscler Thromb Vasc Biol 2014, **34**(10)**:** e21-22.

68. Tang J, Lobatto ME, Hassing L, van der Staay S, van Rijs SM, Calcagno C*, et al.* Inhibiting macrophage proliferation suppresses atherosclerotic plaque inflammation. *Sci Adv* 2015, **1**(3).

69. Kockx MM, Herman AG. Apoptosis in atherosclerosis: beneficial or detrimental? *Cardiovasc Res* 2000, **45**(3)**:** 736-746.

70. Seimon T, Tabas I. Mechanisms and consequences of macrophage apoptosis in atherosclerosis. *J Lipid Res* 2009, **50 Suppl:** S382-387.

71. Feig JE, Parathath S, Rong JX, Mick SL, Vengrenyuk Y, Grauer L*, et al.* Reversal of hyperlipidemia with a genetic switch favorably affects the content and inflammatory state of macrophages in atherosclerotic plaques. *Circulation* 2011, **123**(9)**:** 989-998.

72. Randolph GJ. Mechanisms that regulate macrophage burden in atherosclerosis. *Circ Res* 2014, **114**(11)**:** 1757-1771.

73. Feig JE, Pineda-Torra I, Sanson M, Bradley MN, Vengrenyuk Y, Bogunovic D*, et al.* LXR promotes the maximal egress of monocyte-derived cells from mouse aortic plaques during atherosclerosis regression. *J Clin Invest* 2010, **120**(12)**:** 4415-4424.

74. Chinetti-Gbaguidi G, Colin S, Staels B. Macrophage subsets in atherosclerosis. *Nat Rev Cardiol* 2015, **12**(1)**:** 10-17.

75. Johnson JL, Newby AC. Macrophage heterogeneity in atherosclerotic plaques. *Curr Opin Lipidol* 2009, **20**(5)**:** 370-378.

76. Cochain C, Vafadarnejad E, Arampatzi P, Pelisek J, Winkels H, Ley K*, et al.* Single-Cell RNA-Seq Reveals the Transcriptional Landscape and Heterogeneity of Aortic Macrophages in Murine Atherosclerosis. *Circ Res* 2018, **122**(12)**:** 1661-1674.

77. Myasoedova VA, Chistiakov DA, Grechko AV, Orekhov AN. Matrix metalloproteinases in pro-atherosclerotic arterial remodeling. *J Mol Cell Cardiol* 2018, **123:** 159-167.

78. Itoh Y, Kajita M, Kinoh H, Mori H, Okada A, Seiki M. Membrane type 4 matrix metalloproteinase (MT4-MMP, MMP-17) is a glycosylphosphatidylinositol-anchored proteinase. *J Biol Chem* 1999, **274**(48)**:** 34260-34266.

79. Puente XS, Pendas AM, Llano E, Velasco G, Lopez-Otin C. Molecular cloning of a novel membrane-type matrix metalloproteinase from a human breast carcinoma. *Cancer Res* 1996, **56**(5)**:** 944-949.

80. English WR, Puente XS, Freije JM, Knauper V, Amour A, Merryweather A*, et al.* Membrane type 4 matrix metalloproteinase (MMP17) has tumor necrosis factor-alpha convertase activity but does not activate pro-MMP2. *J Biol Chem* 2000, **275**(19)**:** 14046-14055.

81. Rikimaru A, Komori K, Sakamoto T, Ichise H, Yoshida N, Yana I*, et al.* Establishment of an MT4-MMP-deficient mouse strain representing an efficient tracking system for MT4-MMP/MMP-17 expression in vivo using beta-galactosidase. *Genes Cells* 2007, **12**(9)**:** 1091-1100.

82. Kajita M, Kinoh H, Ito N, Takamura A, Itoh Y, Okada A*, et al.* Human membrane type-4 matrix metalloproteinase (MT4-MMP) is encoded by a novel major transcript: isolation of complementary DNA clones for human and mouse mt4-mmp transcripts. *FEBS Lett* 1999, **457**(3)**:** 353-356.

83. Gauthier MC, Racine C, Ferland C, Flamand N, Chakir J, Tremblay GM*, et al.* Expression of membrane type-4 matrix metalloproteinase (metalloproteinase-17) by human eosinophils. *Int J Biochem Cell Biol* 2003, **35**(12)**:** 1667-1673.

84. English WR, Velasco G, Stracke JO, Knauper V, Murphy G. Catalytic activities of membrane-type 6 matrix metalloproteinase (MMP25). *FEBS Lett* 2001, **491**(1-2)**:** 137-142.

85. Atkinson SJ, Roghi C, Murphy G. MT1-MMP hemopexin domain exchange with MT4-MMP blocks enzyme maturation and trafficking to the plasma membrane in MCF7 cells. *Biochem J* 2006, **398**(1)**:** 15-22.

86. Wang P, Nie J, Pei D. The hemopexin domain of membrane-type matrix metalloproteinase-1 (MT1-MMP) Is not required for its activation of proMMP2 on cell surface but is essential for MT1-MMP-mediated invasion in three-dimensional type I collagen. *J Biol Chem* 2004, **279**(49)**:** 51148-51155.

87. Sohail A, Marco M, Zhao H, Shi Q, Merriman S, Mobashery S*, et al.* Characterization of the dimerization interface of membrane type 4 (MT4)-matrix metalloproteinase. *J Biol Chem* 2011, **286**(38)**:** 33178-33189.

88. Metzner C, Salmons B, Gunzburg WH, Dangerfield JA. Rafts, anchors and viruses--a role for glycosylphosphatidylinositol anchored proteins in the modification of enveloped viruses and viral vectors. *Virology* 2008, **382**(2)**:** 125-131.

89. Kojima S, Itoh Y, Matsumoto S, Masuho Y, Seiki M. Membrane-type 6 matrix metalloproteinase (MT6-MMP, MMP-25) is the second glycosyl-phosphatidyl inositol (GPI)-anchored MMP. *FEBS Lett* 2000, **480**(2-3)**:** 142-146.

90. Truong A, Yip C, Paye A, Blacher S, Munaut C, Deroanne C*, et al.* Dynamics of internalization and recycling of the prometastatic membrane type 4 matrix metalloproteinase (MT4-MMP) in breast cancer cells. *Febs J* 2016, **283**(4)**:** 704-722.

91. Walzog B, Weinmann P, Jeblonski F, Scharffetter-Kochanek K, Bommert K, Gaehtgens P. A role for beta(2) integrins (CD11/CD18) in the regulation of cytokine gene expression of polymorphonuclear neutrophils during the inflammatory response. *Faseb J* 1999, **13**(13)**:** 1855-1865.

92. Martin-Alonso M, Garcia-Redondo AB, Guo D, Camafeita E, Martinez F, Alfranca A*, et al.*

Deficiency of MMP17/MT4-MMP proteolytic activity predisposes to aortic aneurysm in mice. *Circ Res* 2015, **117**(2)**:** e13-26.

93. Host L, Paye A, Detry B, Blacher S, Munaut C, Foidart JM*, et al.* The proteolytic activity of MT4-MMP is required for its pro-angiogenic and pro-metastatic promoting effects. *Int J Cancer* 2012, **131**(7)**:** 1537-1548.

94. Liou JT, Sum DC, Liu FC, Mao CC, Lai YS, Day YJ. Spatial and temporal analysis of nociception-related spinal cord matrix metalloproteinase expression in a murine neuropathic pain model. *J Chin Med Assoc* 2013, **76**(4)**:** 201-210.

95. Bar-Or A, Nuttall RK, Duddy M, Alter A, Kim HJ, Ifergan I*, et al.* Analyses of all matrix metalloproteinase members in leukocytes emphasize monocytes as major inflammatory mediators in multiple sclerosis. *Brain* 2003, **126**(Pt 12)**:** 2738-2749.

96. Srichai MB, Colleta H, Gewin L, Matrisian L, Abel TW, Koshikawa N*, et al.* Membrane-type 4 matrix metalloproteinase (MT4-MMP) modulates water homeostasis in mice. *PLoS One* 2011, **6**(2)**:** e17099.

97. Blanco MJ, Rodriguez-Martin I, Learte AIR, Clemente C, Montalvo MG, Seiki M*, et al.* Developmental expression of membrane type 4-matrix metalloproteinase (Mt4-mmp/Mmp17) in the mouse embryo. *PLoS One* 2017, **12**(9)**:** e0184767.

98. Leigh NR, Schupp MO, Li K, Padmanabhan V, Gastonguay A, Wang L*, et al.* Mmp17b is essential for proper neural crest cell migration in vivo. *PLoS One* 2013, **8**(10)**:** e76484.

99. Rizki A, Weaver VM, Lee SY, Rozenberg GI, Chin K, Myers CA*, et al.* A human breast cell model of preinvasive to invasive transition. *Cancer Res* 2008, **68**(5)**:** 1378-1387.

100. Wang Y, Yu SJ, Li YX, Luo HS. Expression and clinical significance of matrix metalloproteinase-17 and -25 in gastric cancer. *Oncol Lett* 2015, **9**(2)**:** 671-676.

101. Chabottaux V, Ricaud S, Host L, Blacher S, Paye A, Thiry M*, et al.* Membrane-type 4 matrix metalloproteinase (MT4-MMP) induces lung metastasis by alteration of primary breast tumour vascular architecture. *J Cell Mol Med* 2009, **13**(9B)**:** 4002-4013.

102. Salz T, Deng C, Pampo C, Siemann D, Qiu Y, Brown K*, et al.* Histone Methyltransferase hSETD1A Is a Novel Regulator of Metastasis in Breast Cancer. *Mol Cancer Res* 2015, **13**(3)**:** 461-469.

103. Huang CH, Yang WH, Chang SY, Tai SK, Tzeng CH, Kao JY*, et al.* Regulation of membrane-type 4 matrix metalloproteinase by SLUG contributes to hypoxia-mediated metastasis. *Neoplasia* 2009, **11**(12)**:** 1371-1382.

104. Chabottaux V, Sounni NE, Pennington CJ, English WR, van den Brule F, Blacher S*, et al.* Membrane-type 4 matrix metalloproteinase promotes breast cancer growth and metastases. *Cancer Res* 2006, **66**(10)**:** 5165-5172.

105. Paye A, Truong A, Yip C, Cimino J, Blacher S, Munaut C*, et al.* EGFR activation and

signaling in cancer cells are enhanced by the membrane-bound metalloprotease MT4-MMP. *Cancer Res* 2014, **74**(23)**:** 6758-6770.

106. Yan X, Cao N, Chen Y, Lan HY, Cha JH, Yang WH*, et al.* MT4-MMP promotes invadopodia formation and cell motility in FaDu head and neck cancer cells. *Biochemical and biophysical research communications* 2019.

107. Dong Z, Katar M, Alousi S, Berk RS. Expression of membrane-type matrix metalloproteinases 4, 5, and 6 in mouse corneas infected with P. aeruginosa. *Invest Ophthalmol Vis Sci* 2001, **42**(13)**:** 3223-3227.

108. Ching S, Zhang H, Chen Q, Quan N. Differential expression of extracellular matrix and adhesion molecule genes in the brain of juvenile versus adult mice in responses to intracerebroventricular administration of IL-1. *Neuroimmunomodulation* 2007, **14**(1)**:** 46-56.

109. Clements KM, Flannelly JK, Tart J, Brockbank SM, Wardale J, Freeth J*, et al.* Matrix metalloproteinase 17 is necessary for cartilage aggrecan degradation in an inflammatory environment. *Ann Rheum Dis* 2011, **70**(4)**:** 683-689.

110. Gao G, Plaas A, Thompson VP, Jin S, Zuo F, Sandy JD. ADAMTS4 (aggrecanase-1) activation on the cell surface involves C-terminal cleavage by glycosylphosphatidyl inositol-anchored membrane type 4-matrix metalloproteinase and binding of the activated proteinase to chondroitin sulfate and heparan sulfate on syndecan-1. *J Biol Chem* 2004, **279**(11)**:** 10042-10051.

111. Papke CL, Yamashiro Y, Yanagisawa H. MMP17/MT4-MMP and thoracic aortic aneurysms: OPNing new potential for effective treatment. *Circ Res* 2015, **117**(2)**:** 109-112.

112. Rius C, Sanz MJ. Intravital Microscopy in the Cremaster Muscle Microcirculation for Endothelial Dysfunction Studies. *Methods Mol Biol* 2015, **1339:** 357-366.

113. Schittenhelm L, Hilkens CM, Morrison VL. beta2 Integrins As Regulators of Dendritic Cell, Monocyte, and Macrophage Function. *Front Immunol* 2017, **8:** 1866.

114. Rosetti F, Mayadas TN. The many faces of Mac-1 in autoimmune disease. *Immunol Rev* 2016, **269**(1)**:** 175-193.

115. Fan Z, Ley K. Leukocyte arrest: Biomechanics and molecular mechanisms of beta2 integrin activation. *Biorheology* 2015, **52**(5-6)**:** 353-377.

116. Getz GS, Reardon CA. Do the Apoe-/- and Ldlr-/- Mice Yield the Same Insight on Atherogenesis? *Arterioscler Thromb Vasc Biol* 2016, **36**(9)**:** 1734-1741.

117. Chen JW, Murphy TL, Willingham MC, Pastan I, August JT. Identification of two lysosomal membrane glycoproteins. *J Cell Biol* 1985, **101**(1)**:** 85-95.

118. Wang D, Yang Y, Lei Y, Tzvetkov NT, Liu X, Yeung AWK*, et al.* Targeting Foam Cell

Formation in Atherosclerosis: Therapeutic Potential of Natural Products. *Pharmacol Rev* 2019, **71**(4)**:** 596-670.

119. Andres-Manzano MJ, Andres V, Dorado B. Oil Red O and Hematoxylin and Eosin Staining for Quantification of Atherosclerosis Burden in Mouse Aorta and Aortic Root. *Methods Mol Biol* 2015, **1339:** 85-99.

120. Shi C, Pamer EG. Monocyte recruitment during infection and inflammation. *Nat Rev Immunol* 2011, **11**(11)**:** 762-774.

121. McManaman JL, Zabaronick W, Schaack J, Orlicky DJ. Lipid droplet targeting domains of adipophilin. *J Lipid Res* 2003, **44**(4)**:** 668-673.

122. Park YM, Febbraio M, Silverstein RL. CD36 modulates migration of mouse and human macrophages in response to oxidized LDL and may contribute to macrophage trapping in the arterial intima. *J Clin Invest* 2009, **119**(1)**:** 136-145.

123. Cipriani S, Francisci D, Mencarelli A, Renga B, Schiaroli E, D'Amore C*, et al.* Efficacy of the CCR5 antagonist maraviroc in reducing early, ritonavir-induced atherogenesis and advanced plaque progression in mice. *Circulation* 2013, **127**(21)**:** 2114-2124.

124. Maggi P, Bruno G, Perilli F, Saracino A, Volpe A, Santoro C*, et al.* Effects of Therapy with Maraviroc on the Carotid Intima Media Thickness in HIV-1/HCV Co-infected Patients. *In Vivo* 2017, **31**(1)**:** 125-131.

125. Maroney SA, Ellery PE, Wood JP, Ferrel JP, Bonesho CE, Mast AE. Caveolae optimize tissue factor-Factor VIIa inhibitory activity of cell-surface-associated tissue factor pathway inhibitor. *Biochem J* 2012, **443**(1)**:** 259-266.

126. Kumar S, Ratnikov BI, Kazanov MD, Smith JW, Cieplak P. CleavPredict: A Platform for Reasoning about Matrix Metalloproteinases Proteolytic Events. *PLoS One* 2015, **10**(5)**:** e0127877.

127. Sumagin R, Prizant H, Lomakina E, Waugh RE, Sarelius IH. LFA-1 and Mac-1 define characteristically different intralumenal crawling and emigration patterns for monocytes and neutrophils in situ. *J Immunol* 2010, **185**(11)**:** 7057-7066.

128. Hanna RN, Carlin LM, Hubbeling HG, Nackiewicz D, Green AM, Punt JA*, et al.* The transcription factor NR4A1 (Nur77) controls bone marrow differentiation and the survival of Ly6C- monocytes. *Nat Immunol* 2011, **12**(8)**:** 778-785.

129. Hanna RN, Shaked I, Hubbeling HG, Punt JA, Wu R, Herrley E*, et al.* NR4A1 (Nur77) deletion polarizes macrophages toward an inflammatory phenotype and increases atherosclerosis. *Circ Res* 2012, **110**(3)**:** 416-427.

130. Hamers AA, Vos M, Rassam F, Marinkovic G, Kurakula K, van Gorp PJ*, et al.* Bone marrow-specific deficiency of nuclear receptor Nur77 enhances atherosclerosis. *Circ Res* 2012, **110**(3)**:** 428-438.

131. Silverstein RL. Oxidized Lipid Uptake by Scavenger Receptor CD36 (Cluster of Differentiation 36) Modulates Endothelial Surface Properties and May Contribute to Atherogenesis. *Arterioscler Thromb Vasc Biol* 2018, **38**(1)**:** 4-5.

132. Li XM, Lu XX, Xu Q, Wang JR, Zhang S, Guo PD*, et al.* Nur77 deficiency leads to systemic inflammation in elderly mice. *J Inflamm (Lond)* 2015, **12:** 40.

133. Koenis DS, Medzikovic L, Vos M, Beldman TJ, van Loenen PB, van Tiel CM*, et al.* Nur77 variants solely comprising the amino-terminal domain activate hypoxia-inducible factor-1alpha and affect bone marrow homeostasis in mice and humans. *J Biol Chem* 2018, **293**(39)**:** 15070-15083.

134. Thomas GD, Hanna RN, Vasudevan NT, Hamers AA, Romanoski CE, McArdle S*, et al.* Deleting an Nr4a1 Super-Enhancer Subdomain Ablates Ly6C(low) Monocytes while Preserving Macrophage Gene Function. *Immunity* 2016, **45**(5)**:** 975-987.

135. Wouters K, Gaens K, Bijnen M, Verboven K, Jocken J, Wetzels S*, et al.* Circulating classical monocytes are associated with CD11c(+) macrophages in human visceral adipose tissue. *Sci Rep* 2017, **7:** 42665.

136. Collin M, Bigley V. Human dendritic cell subsets: an update. *Immunology* 2018, **154**(1)**:** 3-20.

137. Randolph GJ. Proliferating macrophages prevail in atherosclerosis. *Nat Med* 2013, **19**(9)**:** 1094-1095.

138. Locati M, Curtale G, Mantovani A. Diversity, Mechanisms, and Significance of Macrophage Plasticity. *Annu Rev Pathol* 2019.

139. Chavez-Galan L, Olleros ML, Vesin D, Garcia I. Much More than M1 and M2 Macrophages, There are also CD169(+) and TCR(+) Macrophages. *Front Immunol* 2015, **6:** 263.

140. Chistiakov DA, Kashirskikh DA, Khotina VA, Grechko AV, Orekhov AN. Immune-Inflammatory Responses in Atherosclerosis: The Role of Myeloid Cells. *J Clin Med* 2019, **8**(11).

141. Wu H, Gower RM, Wang H, Perrard XY, Ma R, Bullard DC*, et al.* Functional role of CD11c+ monocytes in atherogenesis associated with hypercholesterolemia. *Circulation* 2009, **119**(20)**:** 2708-2717.

142. Flynn MC, Pernes G, Lee MKS, Nagareddy PR, Murphy AJ. Monocytes, Macrophages, and Metabolic Disease in Atherosclerosis. *Front Pharmacol* 2019, **10:** 666.

143. Hamada M, Nakamura M, Tran MT, Moriguchi T, Hong C, Ohsumi T*, et al.* MafB promotes atherosclerosis by inhibiting foam-cell apoptosis. *Nat Commun* 2014, **5:** 3147.

144. Amezaga N, Sanjurjo L, Julve J, Aran G, Perez-Cabezas B, Bastos-Amador P*, et al.* Human scavenger protein AIM increases foam cell formation and CD36-mediated

oxLDL uptake. *J Leukoc Biol* 2014, **95**(3)**:** 509-520.

145. Arai S, Shelton JM, Chen M, Bradley MN, Castrillo A, Bookout AL*, et al.* A role for the apoptosis inhibitory factor AIM/Spalpha/Api6 in atherosclerosis development. *Cell Metab* 2005, **1**(3)**:** 201-213.

146. Kunjathoor VV, Febbraio M, Podrez EA, Moore KJ, Andersson L, Koehn S*, et al.* Scavenger receptors class A-I/II and CD36 are the principal receptors responsible for the uptake of modified low density lipoprotein leading to lipid loading in macrophages. *J Biol Chem* 2002, **277**(51)**:** 49982-49988.

147. Schultze JL. Reprogramming of macrophages--new opportunities for therapeutic targeting. *Curr Opin Pharmacol* 2016, **26:** 10-15.

148. Almeida PE, Roque NR, Magalhaes KG, Mattos KA, Teixeira L, Maya-Monteiro C*, et al.* Differential TLR2 downstream signaling regulates lipid metabolism and cytokine production triggered by Mycobacterium bovis BCG infection. *Biochim Biophys Acta* 2014, **1841**(1)**:** 97-107.

149. Fabbri M, Di Meglio S, Gagliani MC, Consonni E, Molteni R, Bender JR*, et al.* Dynamic partitioning into lipid rafts controls the endo-exocytic cycle of the alphaL/beta2 integrin, LFA-1, during leukocyte chemotaxis. *Mol Biol Cell* 2005, **16**(12)**:** 5793-5803.

150. Leitinger B, Hogg N. The involvement of lipid rafts in the regulation of integrin function. *J Cell Sci* 2002, **115**(Pt 5)**:** 963-972.

151. Sohail A, Sun Q, Zhao H, Bernardo MM, Cho JA, Fridman R. MT4-(MMP17) and MT6-MMP (MMP25), A unique set of membrane-anchored matrix metalloproteinases: properties and expression in cancer. *Cancer Metastasis Rev* 2008, **27**(2)**:** 289-302.

152. Bumba L, Masin J, Fiser R, Sebo P. Bordetella adenylate cyclase toxin mobilizes its beta2 integrin receptor into lipid rafts to accomplish translocation across target cell membrane in two steps. *PLoS Pathog* 2010, **6**(5)**:** e1000901.

153. Vaisar T, Kassim SY, Gomez IG, Green PS, Hargarten S, Gough PJ*, et al.* MMP-9 sheds the beta2 integrin subunit (CD18) from macrophages. *Mol Cell Proteomics* 2009, **8**(5)**:** 1044-1060.

154. Zen K, Guo YL, Li LM, Bian Z, Zhang CY, Liu Y. Cleavage of the CD11b extracellular domain by the leukocyte serprocidins is critical for neutrophil detachment during chemotaxis. *Blood* 2011, **117**(18)**:** 4885-4894.

155. Evans BJ, McDowall A, Taylor PC, Hogg N, Haskard DO, Landis RC. Shedding of lymphocyte function-associated antigen-1 (LFA-1) in a human inflammatory response. *Blood* 2006, **107**(9)**:** 3593-3599.

156. Drbal K, Angelisova P, Hilgert I, Cerny J, Novak P, Horejsi V. A proteolytically truncated form of free CD18, the common chain of leukocyte integrins, as a novel marker of activated myeloid cells. *Blood* 2001, **98**(5)**:** 1561-1566.

157. Lisanti MP, Scherer PE, Vidugiriene J, Tang Z, Hermanowski-Vosatka A, Tu YH*, et al.* Characterization of caveolin-rich membrane domains isolated from an endothelial-rich source: implications for human disease. *J Cell Biol* 1994, **126**(1)**:** 111-126.

158. Wang W, Fu G, Luo BH. Dissociation of the alpha-subunit Calf-2 domain and the beta-subunit I-EGF4 domain in integrin activation and signaling. *Biochemistry* 2010, **49**(47)**:** 10158-10165.

159. Yakubenko VP, Bhattacharjee A, Pluskota E, Cathcart MK. alphaMbeta(2) integrin activation prevents alternative activation of human and murine macrophages and impedes foam cell formation. *Circ Res* 2011, **108**(5)**:** 544-554.

160. Merched A, Tollefson K, Chan L. Beta2 integrins modulate the initiation and progression of atherosclerosis in low-density lipoprotein receptor knockout mice. *Cardiovasc Res* 2010, **85**(4)**:** 853-863.

161. Cao C, Lawrence DA, Strickland DK, Zhang L. A specific role of integrin Mac-1 in accelerated macrophage efflux to the lymphatics. *Blood* 2005, **106**(9)**:** 3234-3241.

162. Methia N, Andre P, Denis CV, Economopoulos M, Wagner DD. Localized reduction of atherosclerosis in von Willebrand factor-deficient mice. *Blood* 2001, **98**(5)**:** 1424-1428.

163. Nageh MF, Sandberg ET, Marotti KR, Lin AH, Melchior EP, Bullard DC*, et al.* Deficiency of inflammatory cell adhesion molecules protects against atherosclerosis in mice. *Arterioscler Thromb Vasc Biol* 1997, **17**(8)**:** 1517-1520.

164. Orr AW, Sanders JM, Bevard M, Coleman E, Sarembock IJ, Schwartz MA. The subendothelial extracellular matrix modulates NF-kappaB activation by flow: a potential role in atherosclerosis. *J Cell Biol* 2005, **169**(1)**:** 191-202.

165. Shi C, Zhang X, Chen Z, Sulaiman K, Feinberg MW, Ballantyne CM*, et al.* Integrin engagement regulates monocyte differentiation through the forkhead transcription factor Foxp1. *J Clin Invest* 2004, **114**(3)**:** 408-418.

166. Cuevas VD, Anta L, Samaniego R, Orta-Zavalza E, Vladimir de la Rosa J, Baujat G*, et al.* MAFB Determines Human Macrophage Anti-Inflammatory Polarization: Relevance for the Pathogenic Mechanisms Operating in Multicentric Carpotarsal Osteolysis. *J Immunol* 2017, **198**(5)**:** 2070-2081.

167. Gautier EL, Jakubzick C, Randolph GJ. Regulation of the migration and survival of monocyte subsets by chemokine receptors and its relevance to atherosclerosis. *Arterioscler Thromb Vasc Biol* 2009, **29**(10)**:** 1412-1418.

168. Yona S, Kim KW, Wolf Y, Mildner A, Varol D, Breker M*, et al.* Fate mapping reveals origins and dynamics of monocytes and tissue macrophages under homeostasis. *Immunity* 2013, **38**(1)**:** 79-91.

169. Febbraio M, Silverstein RL. CD36: implications in cardiovascular disease. *Int J Biochem*

Cell Biol 2007, **39**(11)**:** 2012-2030.

170. Dimitrov S, Lange T, Born J. Selective mobilization of cytotoxic leukocytes by epinephrine. *J Immunol* 2010, **184**(1)**:** 503-511.

171. Benjamin MM, Khalil RA. Matrix metalloproteinase inhibitors as investigative tools in the pathogenesis and management of vascular disease. *Exp Suppl* 2012, **103:** 209-279.

172. Udi Y, Grossman M, Solomonov I, Dym O, Rozenberg H, Moreno V*, et al.* Inhibition mechanism of membrane metalloprotease by an exosite-swiveling conformational antibody. *Structure* 2015, **23**(1)**:** 104-115.

173. Esteban S, Clemente C, Koziol A, Gonzalo P, Rius C, Martinez F*, et al.* Endothelial MT1-MMP targeting limits intussusceptive angiogenesis and colitis via TSP1/nitric oxide axis. *EMBO Mol Med* 2019**:** e10862.

MATERIAL SUPLEMENTARIO

Posición P1/ Cadena	Residuos	PWM ^ valor	Estructura secundaria*	Accesibilidad del solvente	Domínio transmembrana**	Masa-N	Masa-C
24A	QSVVQ-LQGSR	3.71	_EEEE____E	7.92 (escondido)	OOOOOOOOOO	2702.23	205198.45
37A	GAPQE-IVAAN	2.66	E_____	**52.18 (Expuesto)**	OOOOOOOOOO	4022.94	203877.74
42A	IVAAN-QRGSL	4.23	_____E	**47.81 (Expuesto)**	OOOOOOOOOO	4491.21	203409.47
61A	CEPIR-LQVPV	4.46	EEE_____	**48.46 (Expuesto)**	OOOOOOOOOO	6635.13	201265.55
70A	VEAVN-MSLGL	3.57	_____	15.92 (escondido)	OOOOOOOOOO	7584.65	200316.03
85A	TSPPQ-LLACG	0.69	____EEEEEE	16.23 (escondido)	OOOOOOOOOO	9039.38	198861.30
86A	SPPQL-LACGP	4.96	___EEEEEE_	7.01 (escondido)	OOOOOOOOOO	9152.46	198748.22
113A	LFGSN-LRQQP	1.19	EE_____	**74.09 (Expuesto)**	OOOOOOOOOO	12022.76	195877.92
124A	KFPEA-LRGCP	7.54	_____	**52.06 (Expuesto)**	OOOOOOOOOO	13345.46	194555.22
137A	SDIAF-LIDGS	5.18	EEEEEEEE__	2.28 (escondido)	OOOOOOOOOO	14777.10	193123.58
162A	STVME-QLKKS	3.25	HHHHH____	**48.29 (Expuesto)**	OOOOOOOOOO	17622.50	190278.18
163A	TVMEQ-LKKSK	5.07	HHHH_____	26.55 (escondido)	OOOOOOOOOO	17750.56	190150.12
172A	KTLFS-LMQYS	5.71	_EEEEEEEE_	0.91 (escondido)	OOOOOOOOOO	18783.17	189117.51
173A	TLFSL-MQYSE	0.77	EEEEEEEE__	0.91 (escondido)	OOOOOOOOOO	18896.25	189004.43
175A	FSLMQ-YSEEF	1.89	EEEEEE___E	0.00 (Escondido)	OOOOOOOOOO	19155.35	188745.33
197A	PNPRS-LVKPI	3.78	__HHHH___	**41.85 (Expuesto)**	OOOOOOOOOO	21923.63	185977.05

203A	VKPIT-QLLGR	1.11	_____	**38.36 (Expuesto)**	OOOOO OOOOO	22575.05	185325.63
204A	KPITQ-LLGRT	1.86	_____E	16.07 (escondido)	OOOOO OOOOO	22703.11	185197.57
224A	RELFN-ITNGA	2.44	HH_____	**42.00 (Expuesto)**	OOOOO OOOOO	24965.40	182935.28
235A	KNAFK-ILVVI	0.78	___EEEEEE	1.95 (escondido)	OOOOO OOOOO	26166.06	181734.62
304A	NNFEA-LKTIQ	3.59	___HHHHHH	17.92 (escondido)	OOOOO OOOOO	33861.94	174038.74
310A	KTIQN-QLREK	3.54	HHHHHHHHH	**57.91 (Expuesto)**	OOOOO OOOOO	34559.34	173341.34
311A	TIQNQ-LREKI	0.94	HHHHHHHHH	31.29 (escondido)	OOOOO OOOOO	34687.40	173213.28
342A	GFSAA-ITSNG	0.61	___EE_____	19.20 (escondido)	OOOOO OOOOO	38029.92	169870.76
348A	TSNGP-LLSTV	0.97	_____EEEE_	8.56 (escondido)	OOOOO OOOOO	38599.19	169301.49
350A	NGPLL-STVGS	0.94	___EEEE__	1.22 (escondido)	OOOOO OOOOO	38825.35	169075.33
364A	GGVFL-YTSKE	1.38	EEEEE____	6.06 (escondido)	OOOOO OOOOO	40265.02	167635.66
375A	STFIN-MTRVD	1.77	_EEE_____	24.91 (escondido)	OOOOO OOOOO	41563.65	166337.03
393A	GYAAA-IILRN	2.94	___EEE____	24.59 (escondido)	OOOOO OOOOO	43508.49	164392.19
402A	NRVQS-LVLGA	6.23	____EEEEE	5.04 (escondido)	OOOOO OOOOO	44588.13	163312.55
417A	IGLVA-MFRQN	1.99	__EEEEEE_	1.27 (escondido)	OOOOO OOOOO	46176.04	161724.64
418A	GLVAM-FRQNT	1.47	_EEEEEE__	2.07 (escondido)	OOOOO OOOOO	46307.08	161593.60
420A	VAMFR-QNTGM	0.95	EEEEE____	11.30 (escondido)	OOOOO OOOOO	46610.25	161290.43
507A	RFGAA-LTVLG	2.06	_E___EEEE	11.32 (escondido)	OOOOO OOOOO	55909.62	151991.06
537A	RGAVY-LFHGT	1.34	__EEEEEEE	1.74 (escondido)	OOOOO OOOOO	58949.12	148951.56

552A	SPSHS-QRIAG	0.96	_____E__E_	18.63 (escondido)	OOOOO OOOOO	60400.78	147499.90
581A	LTMDG-LVDLT	1.38	_____EEE	**45.38 (Expuesto)**	OOOOO OOOOO	63492.30	144408.38
584A	DGLVD-LTVGA	2.89	____EEEEE	1.83 (escondido)	OOOOO OOOOO	63819.48	144081.20
589A	LTVGA-QGHVL	1.01	EEEEE___E E	17.42 (escondido)	OOOOO OOOOO	64260.74	143639.94
595A	GHVLL-LRSQP	5.43	__EEEEEE_ _	9.15 (escondido)	OOOOO OOOOO	64908.11	142992.57
606A	LRVKA-IMEFN	0.78	___EEEEEE _	**42.08 (Expuesto)**	OOOOO OOOOO	66155.88	141744.80
690A	TQVLG-LTQTC	4.32	EEEE____E E	24.85 (escondido)	OOOOO OOOOO	75731.74	132168.94
699A	CETLK-LQLPN	1.87	EEEEEEEE_ _	27.44 (escondido)	OOOOO OOOOO	76749.25	131151.43
712A	DPVSP-IVLRL	0.82	_____EEEE E	5.38 (escondido)	OOOOO OOOOO	78154.92	129745.76
716A	PIVLR-LNFSL	4.91	_EEEEEEE_ _	5.25 (escondido)	OOOOO OOOOO	78636.25	129264.43
720A	RLNFS-LVGTP	1.44	EEEE_____	27.37 (escondido)	OOOOO OOOOO	79097.47	128803.21
731A	SAFGN-LRPVL	3.71	_____E_	28.11 (escondido)	OOOOO OOOOO	80154.02	127746.66
742A	EDAQR-LFTAL	3.60	_____EEEE	**37.83 (Expuesto)**	OOOOO OOOOO	81402.71	126497.97
772A	FSFMS-LDCLV	0.98	EE_____E	**52.78 (Expuesto)**	OOOOO OOOOO	84801.22	123099.46
775A	MSLDC-LVVGG	1.77	_____EE__	**36.45 (Expuesto)**	OOOOO OOOOO	85132.34	122768.34
809A	FFPLD-LSYRK	4.21	EE___EEEE _	9.18 (escondido)	OOOOO OOOOO	88988.26	118912.42
817A	RKVST-LQNQR	3.76	E_____	**62.51 (Expuesto)**	OOOOO OOOOO	89922.77	117977.91
820A	STLQN-QRSQR	4.22	_____	**82.46 (Expuesto)**	OOOOO OOOOO	90277.95	117622.73
828A	QRSWR-LACES	0.95	_____EEEE	6.46 (escondido)	OOOOO OOOOO	91362.51	116538.17

842A	EVSGA-LKSTS	4.26	_____EEEE	**37.10 (Expuesto)**	OOOOO OOOOO	92655.06	115245.62
910A	KYAVY-MVVTS	3.07	EEEE_EEEEE	10.48 (escondido)	OOOOO OOOOO	100280.85	107619.83
943A	YQVSN-LGQRS	3.64	EEEEE____ _	16.20 (escondido)	OOOOO OOOOO	104005.61	103895.07
952A	SLPIS-LVFLV	5.31	_EEEEEEEE _	9.88 (escondido)	OOOOO OOOOO	104957.14	102943.54
955A	ISLVF-LVPVR	3.30	EEEEEE___ E	21.59 (escondido)	OOOOO OOOOO	105316.36	102584.32
960A	LVPVR-LNQTV	4.56	E___EE__E E	32.11 (escondido)	OOOOO OOOOO	105880.73	102019.95
977A	TFSEN-LSSTC	2.79	E_____E	**57.11 (Expuesto)**	OOOOO OOOOO	107908.73	99991.95
997A	DFLAE-LRKAP	5.97	_HHHHHHH __	27.49 (escondido)	OOOOO OOOOO	110147.78	97752.90
1030A	EFNAT-LKGNL	1.38	__EEEEEE_ E	6.50 (escondido)	OOOOO OOOOO	113838.61	94062.07
1048A	SHNHL-LIVST	1.80	_____EEEE E	8.84 (escondido)	OOOOO OOOOO	115992.68	91908.00
1064A	DSVFT-LLPGQ	4.20	___EEE____	27.31 (escondido)	OOOOO OOOOO	117742.59	90158.09
1122B	GDPDS-IRCDT	1.31	____HHHEE _	11.15 (escondido)	OOOOO OOOOO	124075.48	83825.20
1131B	TRPQL-LMRGC	7.00	_HHHHHHH __	24.39 (escondido)	OOOOO OOOOO	125158.04	82742.64
1132B	RPQLL-MRGCA	1.31	HHHHHHH_ __	**65.08 (Expuesto)**	OOOOO OOOOO	125271.12	82629.56
1146B	MDPTS-LAETQ	1.58	E____E__E_	**39.00 (Expuesto)**	OOOOO OOOOO	126734.71	81165.97
1163B	KQLSP-QKVTL	2.41	___E___EEE	11.32 (escondido)	OOOOO OOOOO	128567.56	79333.12
1165B	LSPQK-VTLYL	1.30	_E___EEEE E	25.69 (escondido)	OOOOO OOOOO	128823.71	79076.97
1169B	KVTLY-LRPGQ	2.63	_EEEEE___ _	20.58 (escondido)	OOOOO OOOOO	129299.97	78600.71
1177B	GQAAA-FNVTF	0.90	___EEEEEE E	25.62 (escondido)	OOOOO OOOOO	130064.40	77836.28

1191B	GYPID-LYYLM	3.22	____EEEEEE	9.45 (escondido)	OOOOOOOOOO	131729.27	76171.41
1194B	IDLYY-LMDLS	4.95	_EEEEEEE__	8.56 (escondido)	OOOOOOOOOO	132168.47	75732.21
1197B	YYLMD-LSYSM	4.11	EEEEE_____	1.52 (escondido)	OOOOOOOOOO	132527.62	75373.06
1201B	DLSYS-MLDDL	1.94	E_____HHHH	19.76 (escondido)	OOOOOOOOOO	132977.82	74922.86
1205B	SMLDD-LRNVK	2.52	__HHHHH___	6.11 (escondido)	OOOOOOOOOO	133452.00	74448.68
1211B	RNVKK-LGGDL	0.92	H_____H	**47.32 (Expuesto)**	OOOOOOOOOO	134190.47	73710.21
1219B	DLLRA-LNEIT	2.79	_HHHHHH___	29.18 (escondido)	OOOOOOOOOO	134985.92	72914.76
1249B	THPDK-LRNPC	5.04	_____	30.24 (escondido)	OOOOOOOOOO	138284.59	69616.09
1266B	QPPFA-FRHVL	2.14	______EEEE	3.56 (escondido)	OOOOOOOOOO	140236.50	67664.18
1272B	RHVLK-LTNNS	5.76	EEEEEEE___	26.77 (escondido)	OOOOOOOOOO	141016.97	66883.71
1286B	TEVGK-QLISG	2.40	HHHH_____	**36.98 (Expuesto)**	OOOOOOOOOO	142577.71	65322.97
1292B	LISGN-LDAPE	1.11	_____	20.33 (escondido)	OOOOOOOOOO	143190.02	64710.66
1302B	GGLDA-MMQVA	4.42	_HHHHHHHH_	4.20 (escondido)	OOOOOOOOOO	144128.45	63772.23
1304B	LDAMM-QVAAC	4.10	HHHHHHH___	6.42 (escondido)	OOOOOOOOOO	144390.53	63510.15
1320B	RNVTR-LLVFA	1.96	_____EEEEE	13.14 (escondido)	OOOOOOOOOO	146200.42	61700.26
1340B	GKLGA-ILTPN	2.17	HHHH_____	18.24 (escondido)	OOOOOOOOOO	148232.43	59668.25
1369B	PSVGQ-LAHKL	4.08	__HHHHHHHH	9.17 (escondido)	OOOOOOOOOO	151593.97	56306.71
1373B	QLAHK-LAENN	3.97	HHHHHHHH___	10.55 (escondido)	OOOOOOOOOO	152043.24	55857.44
1388B	AVTSR-MVKTY	1.98	EE_HHHHHHH	35.84 (escondido)	OOOOOOOOOO	153697.11	54203.57

1395B	KTYEK-LTEII	2.08	HHHHHHHHH_	25.00 (escondido)	OOOOO OOOOO	154576.55	53324.13
1407B	SAVGE-LSEDS	4.61	__EEE_____	29.90 (escondido)	OOOOO OOOOO	155814.22	52086.46
1417B	SNVVQ-LIKNA	4.56	___HHH___H	35.63 (escondido)	OOOOO OOOOO	156872.70	51027.98
1418B	NVVQL-IKNAY	1.97	__HHH___HH	17.00 (escondido)	OOOOO OOOOO	156985.78	50914.90
1440B	ALPDT-LKVTY	4.38	_____EEEE_	13.40 (escondido)	OOOOO OOOOO	159483.06	48417.62
1486B	ECIQE-QSFVI	1.79	_____EEEEE	**53.09 (Expuesto)**	OOOOO OOOOO	164574.51	43326.17
1590B	DVPGK-LIYGQ	6.65	______EE__	31.65 (escondido)	OOOOO OOOOO	175878.58	32022.10
1694B	SCAEC-LKFEK	3.58	HHH_____ _	15.88 (escondido)	OOOOO OOOOO	187179.17	20721.51
1713B	ACPGL-QLSNN	3.30	_____E____	**69.34 (Expuesto)**	OOOOO OOOOO	189127.11	18773.57
1765A	PNPLP-LIVGS	6.32	_EEEE__HHH	15.24 (escondido)	OOOOO OOMMM	195108.88	12791.80
1774A	SSVGG-LLLLA	3.85	HHHHHHHHHH	**39.61 (Expuesto)**	MMMMM MMMMM	195878.30	12022.38
1777A	GGLLL-LALIT	3.29	HHHHHHHHHH	**55.49 (Expuesto)**	MMMMM MMMMM	196217.54	11683.14
1779A	LLLLA-LITAA	6.53	HHHHHHHHHH	**60.70 (Expuesto)**	MMMMM MMMMM	196401.66	11499.02
1780A	LLLAL-ITAAL	1.94	HHHHHHHHHH	**61.68 (Expuesto)**	MMMMM MMMMM	196514.74	11385.94
1784A	LITAA-LYKLG	3.86	HHHHHHHHHH	**53.13 (Expuesto)**	MMMMM MMMMM	196870.95	11029.73
1785A	ITAAL-YKLGF	1.98	HHHHHHHHHH	**66.52 (Expuesto)**	MMMMM MMMMM	196984.03	10916.65
1787A	AALYK-LGFFK	2.20	HHHHHHHHHH	**69.15 (Expuesto)**	MMMMM MMMii	197275.18	10625.50
1817B	PNIAA-IVGGT	2.44	__HHHHHHHH	**41.07 (Expuesto)**	OOMMM MMMMM	200420.66	7480.02
1833B	IGILL-LVIWK	4.78	HHHHHHHHHH	**66.77 (Expuesto)**	MMMMM MMMMi	201909.60	5991.08

1842B	KALIH-LSDLR	1.58	HHHHHHHHHH	**63.63 (Expuesto)**	iiiiiiiii	202983.26	4917.42
1845B	IHLSD-LREYR	3.99	HHHHHHHHHH	**45.91 (Expuesto)**	iiiiiiiii	203298.40	4602.28

Tabla Suplementaria 1. Lista de sitios de corte pronosticados en la integrina αMβ2 humana por la proteasa MT4-MMP determinada por CleavPredict (http://cleavpredict.sanfordburnham.org/).A y B después del número de residuo denota su presencia en las cadenas de integrina αM o β2 respectivamente. Los sitios expuestos con mayor puntuación de corte se han resaltado en gris. Se seleccionó el sitio de corte en la posición 977A para la validación (resaltado en verde).

* Estructura secundaria predicha por jnet. De acuerdo con el Diccionario de Estructura Secundaria de Proteína, el código de una letra corresponde a: E: cadena extendida en conformación de hoja β paralela y / o antiparalela. Longitud mínima 2 residuos; es decir, extendido, lámina β. H: hélice de 4 vueltas (hélice α). Longitud mínima 4 residuos; es decir, hélice α.

** Dominio transmembrana predicho por el servidor TM-HMM. El código de la letra corresponde a: O-externo, en este caso extracelular; M- dominio transmembrana; i- interno, este caso citosólico.

APÉNDICE

nature COMMUNICATIONS

ARTICLE

DOI: 10.1038/s41467-018-03351-4 OPEN

MT4-MMP deficiency increases patrolling monocyte recruitment to early lesions and accelerates atherosclerosis

Cristina Clemente[1], Cristina Rius[2,3], Laura Alonso-Herranz[4], Mara Martín-Alonso[1], Ángela Pollán[1], Emilio Camafeita[5], Fernando Martínez[6], Rubén A. Mota[1], Vanessa Núñez[4], Cristina Rodríguez[3,7], Motoharu Seiki[8], José Martínez-González[3,9], Vicente Andrés[2,3], Mercedes Ricote[4] & Alicia G. Arroyo[1,10]

Matrix metalloproteinases are involved in vascular remodeling. Little is known about their immune regulatory role in atherosclerosis. Here we show that mice deficient for MT4-MMP have increased adherence of macrophages to inflamed peritonea, and larger lipid deposits and macrophage burden in atherosclerotic plaques. We also demonstrate that MT4-MMP deficiency results in higher numbers of patrolling monocytes crawling and adhered to inflamed endothelia, and the accumulation of Mafb+ apoptosis inhibitor of macrophage (AIM)+ macrophages at incipient atherosclerotic lesions in mice. Functionally, MT4-MMP-null Mafb+AIM+ peritoneal macrophages express higher AIM and scavenger receptor CD36, are more resistant to apoptosis, and bind acLDL avidly, all of which contribute to atherosclerosis. CCR5 inhibition alleviates these effects by hindering the enhanced recruitment of MT4-MMP-null patrolling monocytes to early atherosclerotic lesions, thus blocking Mafb+AIM+ macrophage accumulation and atherosclerosis acceleration. Our results suggest that MT4-MMP targeting may constitute a novel strategy to boost patrolling monocyte activity in early inflammation.

[1] Matrix Metalloproteinases in Angiogenesis and Inflammation Group, Centro Nacional de Investigaciones Cardiovasculares Carlos III (CNIC), Melchor Fernández Almagro 3, 28029 Madrid, Spain. [2] Molecular and Genetic Cardiovascular Pathophysiology Group, Centro Nacional de Investigaciones Cardiovasculares Carlos III (CNIC), Melchor Fernández Almagro 3, 28029 Madrid, Spain. [3] CIBER de Enfermedades Cardiovasculares (CIBERCV), Madrid, Spain. [4] Nuclear Receptor Signaling Group, Centro Nacional de Investigaciones Cardiovasculares Carlos III (CNIC), Melchor Fernández Almagro 3, 28029 Madrid, Spain. [5] Proteomics Unit, Centro Nacional de Investigaciones Cardiovasculares Carlos III (CNIC), Melchor Fernández Almagro 3, 28029 Madrid, Spain. [6] Bioinformatics Unit, Centro Nacional de Investigaciones Cardiovasculares Carlos III (CNIC), Melchor Fernández Almagro 3, 28029 Madrid, Spain. [7] Institut de Recerca del Hospital de la Santa Creu i Sant Pau-Programa ICCC, IIB-Sant Pau, Sant Antoni Maria Claret 167, 08025 Barcelona, Spain. [8] Division of Cancer Cell Research, Institute of Medical Science, University of Tokyo, 4-6-1 Shirokanedai, Minato-ku, Tokyo 108-8639, Japan. [9] Instituto de Investigaciones Biomédicas de Barcelona (IIBB-CSIC), IIB-Sant Pau, Rosselló 161, 08036 Barcelona, Spain. [10] Present address: Centro de Investigaciones Biológicas (CIB-CSIC), Ramiro de Maeztu 9, 28040 Madrid, Spain. Correspondence and requests for materials should be addressed to A.G.A. (email: agarroyo@cnic.es)

Atherosclerosis (AT) is a chronic inflammatory disease with local manifestations in the vasculature in the form of complex multi-cellular atherosclerotic lesions[1]. Cells of the innate immune response, particularly monocytes recruited by the inflamed endothelium and their derived macrophages in the plaque, are essential contributors to the initiation, progression, and eventual rupture of atherosclerotic lesions by mechanisms including the engulfment of LDL particles and the formation of lipid-overloaded foam cells[2,3]. However, the view that inflammation derives from recruited monocytes differentiating into macrophages in the plaque has been challenged and a more complex scenario is envisaged[4]. Macrophages differentiate from monocytes in response to micro-environmental stimuli in the plaque, giving rise to distinct subsets that either contribute to inflammation or favor resolution[5]. Macrophage heterogeneity within atherosclerotic lesions has attracted interest due to its possible therapeutic implications. In mice, macrophages in early atherosclerotic plaques are mainly derived from recruited monocytes, whereas macrophage proliferation is more important in advanced plaques[6]. It remains unclear how macrophage heterogeneity is regulated and contributes to AT initiation and progression. The two main circulating monocyte populations, classical monocytes (Ly6C^{high} in the mouse) and patrolling monocytes (Ly6C^{low}), are recruited to the inflamed aorta via distinct chemokine-receptor pathways[7,8]. Classical monocytes have been assigned proinflammatory functions in AT, whereas patrolling monocytes have been considered to have a protective, pro-resolution role; however, it remains unclear how these monocyte populations, particularly patrolling monocytes, contribute to distinct macrophage subsets in the plaque and to AT progression[8].

Macrophages are central actors in the vascular remodeling associated with plaque progression. This vascular remodeling involves key actions of matrix metalloproteinases (MMPs) on the extracellular matrix and vascular smooth muscle cells[9,10]. Less is known, however, about the role of MMPs in regulating inflammatory cells in AT. MT4-MMP (also named MMP17) is anchored to the plasma membrane through a glycophosphatidylinositol anchor that confers distinct features to this protease by positioning it at enriched lipid membrane domains[11,12]. MT4-MMP is expressed by macrophages but its role in inflammation is ill-defined[13,14]. MT4-MMP was first proposed to process pro-TNFα, but peritoneal macrophages lacking MT4-MMP release normal amounts of TNFα[15], indicating alternative functions of MT4-MMP in inflammation. We recently reported that MT4-MMP-null mice are more prone to angiotensin II-induced thoracic aorta aneurysms and to neointima formation in response to carotid ligation[16]. Whether MT4-MMP has roles in inflammatory vascular pathologies such as AT has not been explored.

Here we show that the crawling of patrolling monocytes on the inflamed endothelium is regulated by MT4-MMP-dependent cleavage of αM integrin (Itgam/CD11b), and that this monocyte subset contributes to the accumulation of Mafb+apoptosis inhibitor of macrophage (AIM)+-expressing macrophages in incipient plaques and to overall AT progression. As patrolling monocytes have beneficial effects in infections and the prevention of lung metastasis[8,17], our results also suggest the therapeutic potential of boosting patrolling monocyte activity through MT4-MMP targeting.

Results

MT4-MMP-null macrophages accumulate in atherosclerotic plaques. The peritoneal cavity contains two main macrophage subsets: resident or large peritoneal macrophages (LPM; CD11b^{hi}/F4/80^{hi}) and inflammation-induced/monocyte-derived small peritoneal macrophages (SPM; CD11b^{med}F4/80$^{lo/med}$)[18] (Fig. 1a). MT4-MMP is not expressed in resident LPM[15] but becomes expressed in SPM, the main population present 72 h after thioglycollate (TG) injection (Supplementary Fig. 1a); the function of MT4-MMP in SPMs remains unknown. Although we observed no differences in the number of resident macrophages, fewer SPMs were collected 72 h after TG injection in the peritoneal lavage of MT4-MMP-null mice compared with wild types (Fig. 1b) in spite of similar messenger RNA levels of chemokine receptors[19] (Supplementary Fig. 1b). In parallel, significantly more macrophages were found adhered to the inflamed MT4-MMP-null peritoneum (Fig. 1c). This hyper-adhesive phenotype correlated with elevated cell-surface expression of αM integrin (CD11b/Itgam/Mac-1) in SPMs as assessed by flow cytometry (Fig. 1d). There was no change in *Itgam* mRNA expression (Fig. 1e). Significantly more C3-opsonized sheep erythrocytes were bound to MT4-MMP-deficient SPM than to wild-type cells, confirming αM integrin activity (Fig. 1f). Moreover, MT4-MMP-deficient macrophages covered a significantly larger area than wild-type cells after adhesion for 24 h to the αM integrin ligand fibrinogen, indicating accelerated cell spreading, a post-ligand binding event; this difference was abolished by the specific anti-αM integrin inhibitory antibody M1/70 (Fig. 1g).

The hyper-adhesion of MT4-MMP-null macrophages to the inflamed peritoneum prompted us to explore their behavior in other inflammatory contexts such as the inflamed aortic vessel wall during AT. To test this, low-density lipoprotein receptor-null (*Ldlr*$^{-/-}$) mice were irradiated and transplanted with bone marrow (BM) cells from either wild-type or MT4-MMP-null mice. We observed proper engraftment and no differences in BM and blood cell populations after 4 weeks on a normal diet (Supplementary Fig. 2a, b). Transplanted mice were then placed on a high-fat diet (HFD) for different periods; weight gain and serum biochemical parameters (glucose, triglycerides, and cholesterol) were similar in both groups throughout the experiment (Supplementary Fig. 2c,d). First, we confirmed that MT4-MMP was expressed in macrophages in the aortic sinus of *Ldlr*$^{-/-}$ mice transplanted with MT4-MMP-null BM cells (MT4-MMP$^{lacZ/lacZ}$ cells) after 1 and 8 weeks fed a HFD (Supplementary Fig. 2e). We next analyzed the macrophage content in atherosclerotic plaques developed 8 weeks after HFD, finding that macrophages (Mac3+) were significantly more abundant in the aortic sinus of *Ldlr*$^{-/-}$ mice transplanted with MT4-MMP-null BM cells (Fig. 2a). This increased macrophage burden at 8 weeks correlated with significantly larger lipid lesions in the aortic arch after 12 weeks on the HFD, as revealed by en face Red Oil staining (Fig. 2b). Moreover, neointima area in the aortic sinus was comparable between groups at all time points after HFD (Supplementary Fig. 2f). Analysis of Stary classification[20] revealed that *Ldlr*$^{-/-}$ mice transplanted with MT4-MMP-deficient BM cells had significantly more advanced lesions after 8 and 12 weeks on the HFD than counterparts transplanted with wild-type BM (Fig. 2c, d and Supplementary Fig. 2g); in particular, MT4-MMP-deficient BM recipients tended to have larger necrotic cores and showed significantly thicker fibrous caps after 12 weeks on HFD (Fig. 2e). Similar results were obtained in double *Ldlr*/MT4-MMP-null mice fed a HFD. These mice nearly recapitulated the phenotype of *Ldlr*$^{-/-}$ mice transplanted with MT4-MMP-null BM, showing an increased AT burden in the aortic arch and more advanced plaques after 16 weeks of HFD (Supplementary Fig. 3a–d). In this mouse model, MT4-MMP protein and mRNA expression in aorta extracts was low in early stages (8 weeks after HFD) but progressively increased in established AT (16 weeks after HFD); a similar difference was observed between human arteries with arterial intimal thickening (early lesions) and those with established atherosclerotic lesions (Supplementary Fig. 4a–c). Of note, in early mouse

atherosclerotic plaques of MT4-MMP$^{+/+}$/*Ldlr*$^{-/-}$ mice (8 weeks after HFD), MT4-MMP expression was mainly restricted to macrophages (Supplementary Fig. 4d), indicating that MT4-MMP deficiency appears to principally impact AT progression through its effect on these cells.

Macrophage burden in the atherosclerotic plaque is mostly determined by the balance between early monocyte recruitment and late macrophage proliferation/cell death[21]. After 8 weeks of HFD, plaques from *Ldlr*$^{-/-}$ mice transplanted with MT4-MMP-null BM showed variable macrophage proliferation but no

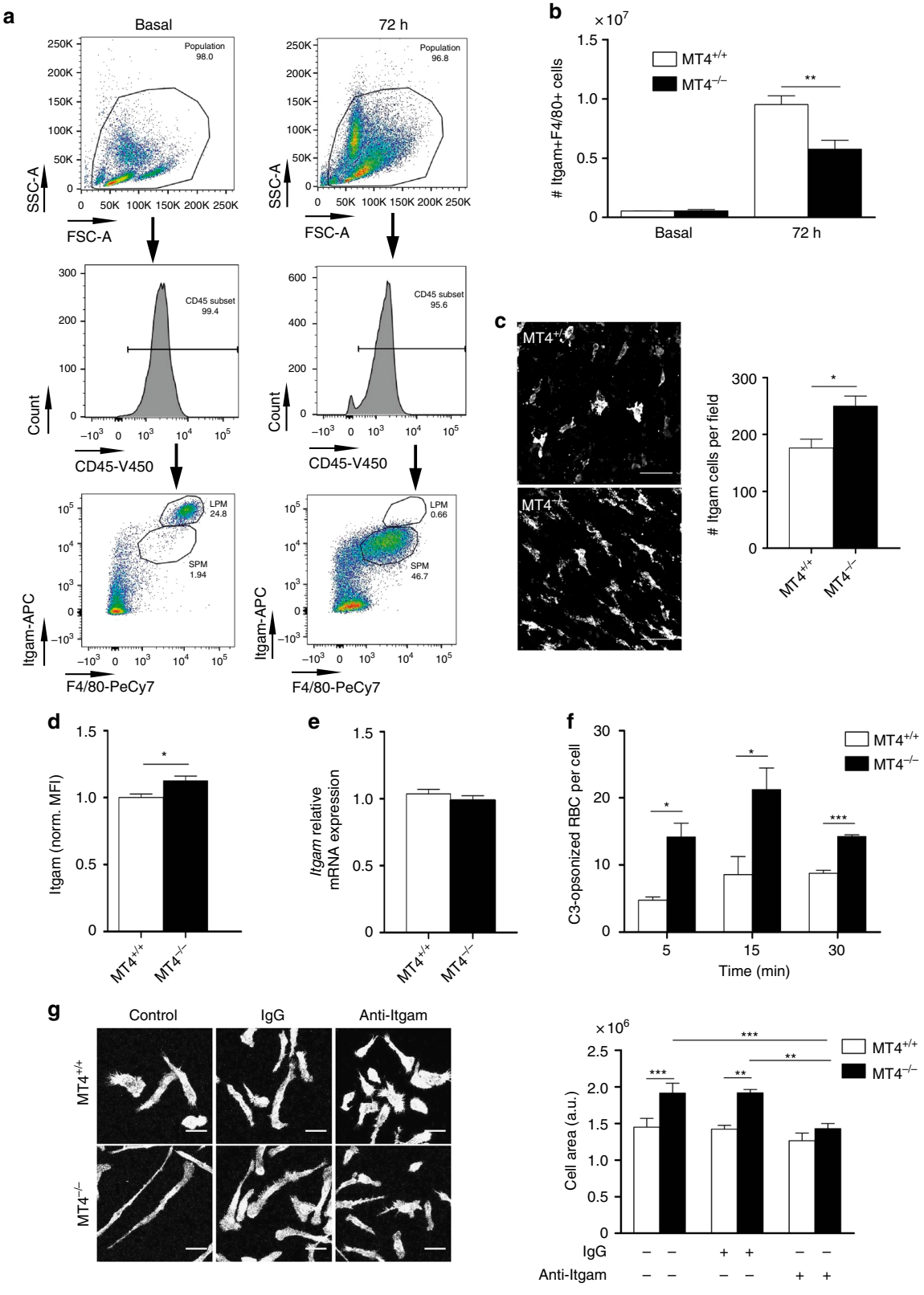

significant increase compared with wild-types (~ 33 ± 21% versus ~ 25 ± 10% Mac3+/Ki67+ cells), and cell apoptosis was a rare event (< 1% cleaved caspase-3-positive cells). We also assessed a possible influence of MT4-MMP absence in macrophage egression from inflamed tissues. TG-stimulated macrophages nearly disappeared from the peritoneal cavity in response to lipopolysaccharide (LPS), regardless the genotype with minor contribution of local death and similar numbers found of wild-type and MT4-MMP-null egressed macrophages in the spleen (Supplementary Fig. 5). These data argued in favor of enhanced monocyte recruitment during early AT as the main contributor to increased macrophage burden.

MT4-MMP absence boosts patrolling monocyte crawling. Blood monocyte abundance was similar in *Ldlr*$^{-/-}$ mice transplanted with MT4-MMP-null or wild-type BM cells (1.4% ± 0.5% and 1.3% ± 0.2%, respectively); however, before starting the HFD, lack of MT4-MMP was associated with a significantly lower percentage of circulating patrolling Ly6C^{low} monocytes and these cells displayed increased cell surface levels of αM integrin, similar to MT4-MMP-null SPMs (Figs 3a and 1c).

Increased cell-surface αM integrin in MT4-MMP-null patrolling monocytes and SPMs (Figs 3a and 1d), with no changes in mRNA expression, pointed to posttranslational regulation by MT4-MMP. Both MT4-MMP and αM integrin were located in lipid-rich domains and MT4-MMP-null peritoneal macrophages contained significantly higher levels of αM integrin in these domains (Supplementary Fig. 6a, b). MT4-MMP-null mice were then injected intraperitoneally (i.p.) with lentivirus encoding green fluorescent protein (GFP) and either full-length MT4-MMP or the catalytic dead mutant (E248A) (Fig. 3b). Analysis of peritoneal macrophages at 5 days post injection showed that expression of full-length MT4-MMP yielded normal cell-surface αM integrin levels in infected MT4-MMP-null macrophages (GFP+Itgam+F4/80+); in contrast, infection with the catalytic dead mutant yet resulted in higher surface αM integrin levels than observed in wild-type macrophages, demonstrating that MT4-MMP catalytic activity regulates αM integrin cell-surface levels in vivo (Fig. 3c). We next used the Cleavpredict software application[22] to identify possible direct MT4-MMP cleavage sites in αMβ2 integrin. The predicted and exposed sites were filtered according to the peptide cleavage matrix in the MEROPS database, and candidate cleavage sites were selected in the αM integrin chain (Itgam) between positions 970 and 1000, close to the transmembrane (TM) domain (Fig. 3d and Supplementary Data 1). In silico modeling of interaction between the human αMβ2 integrin heterodimer and the human MT4-MMP dimer confirmed EN^{977}LS as the only candidate αM integrin cleavage site accessible to the MT4-MMP catalytic center (Fig. 3d, e). This site is conserved in the mouse αM integrin chain but not in the related αL integrin chain in humans or mice. Incubation of the human recombinant MT4-MMP catalytic domain with a synthetic peptide R^{969}-R^{987} from the human αM integrin sequence resulted in significant cleavage at the αM integrin EN^{977}LS site, as assessed by mass spectrometry (Fig. 3f, g).

Crawling of patrolling Ly6C^{low} monocytes on the inflamed endothelium depends on αMβ2 integrin[23] and we therefore next analyzed the in vivo behavior of patrolling monocytes by intravital microscopy of cremaster muscle stimulated with CCL2, an essential chemokine in AT development[24,25]. Only a small number of circulating monocytes, corresponding to patrolling monocytes (CD115+Ly6C^{low}), can crawl on the inflamed endothelium[26]. MT4-MMP-null mice had significantly higher numbers of crawling monocytes on CCL2-inflamed endothelium than wild types (Fig. 4a, b and Supplementary Movies 1, 2) with no major differences in crawling velocity, distance traveled, or confinement index (Supplementary Fig. 7a). Similar total number of monocytes (CD115+Ly6G–) were observed rolling or adhered to the CCL2-inflamed endothelium (Fig. 4c), indicating a selective effect of MT4-MMP absence in patrolling monocyte behavior. Moreover, the increased crawling of MT4-MMP-null patrolling monocytes was abolished when αM integrin was blocked with the inhibitory antibody M1/70 (Fig. 4a, b and Supplementary Movies 1–4). MT4-MMP-null mice also had fewer neutrophils rolling on the inflamed endothelium, suggesting their retention by crawling patrolling monocytes, as reported in other contexts (Supplementary Fig. 7b)[23].

MT4-MMP absence increases Mafb+AIM+ macrophages in early AT. Low efficiency is a common limitation for the analysis of patrolling monocyte recruitment to the inflamed endothelium of atherosclerotic plaques[21,27]. Still, whole-mount staining showed significantly more patrolling monocytes (CD115+Ly6C–) adhered to the endothelium of the lesser curvature of the aortic arch in MT4-MMP-null BM-transplanted *Ldlr*$^{-/-}$ mice than in similar mice transplanted with wild-type cells after 3 days on the HFD (Fig. 5a); no between-genotype differences were detected in cell surface levels of CCR5, the chemokine receptor involved in patrolling monocyte recruitment[27] and CCR2 ($MFI_{CCR5} = 452 \pm 53$ and 498 ± 47, and $MFI_{CCR2} = 592 \pm 65$ and 613 ± 75 in patrolling monocytes from wild-type and MT4$^{-/-}$-BMT *Ldlr*$^{-/-}$ mice, respectively). Classical monocytes (CD115+Ly6C+) were recruited at higher proportion at this incipient stage[21,27] but similarly regardless the genotype (Fig. 5a). Notably, MT4-MMP-null sorted patrolling monocytes adoptively transferred into *Ldlr*$^{-/-}$ mice also adhered at higher numbers to the lesser curvature of the aorta after 3 days on the HFD compared with wild types confirming the cell autonomous impact of MT4-MMP absence on patrolling monocyte behavior (Fig. 5b and Supplementary Fig. 8).

Fig. 1 Enhanced trapping of MT4-MMP-null peritoneal macrophages due to increased αM integrin (Itgam) levels and activity. **a** Representative flow cytometry dot plots and histograms of mouse peritoneal macrophages stained for CD45, Itgam, and F4/80 in basal conditions (left) and 72 h after thioglycollate (TG) injection (right). **b** Number of macrophages (Itgam+F4/80+) collected in the peritoneal eluate of wild-type and MT4-MMP-null mice at the indicated times after TG injection; $n = 3$ mice in basal and $n = 12$ mice at 72 h per genotype in one in basal and four in 72 h independent experiments, respectively. **c** Representative confocal microscopy images (left) and quantification (right) of monocytes/macrophages (Itgam+) in the peritoneal membrane 72 h after TG injection; $n = 6$ mice per genotype in two independent experiments; scale bar, 50 µm. **d** Flow cytometry analysis of Itgam cell-surface levels in TG-elicited macrophages (Itgam+F4/80+) obtained 72 h after TG injection; $n = 20$ mice per genotype in four independent experiments. **e** qPCR analysis of Itgam mRNA in TG-elicited macrophages adhered to plastic overnight; $n = 6$ samples per genotype in two independent experiments. **f** Itgam integrin affinity assessed as the number of C3-opsonized red blood cells (RBCs) bound to TG-elicited peritoneal macrophages adhered to glass; $n = 6$ samples per genotype from two independent experiments. **g** Representative fluorescence images of TG-elicited macrophages adhered to fibrinogen for 24 h and labeled for F-actin in the presence or absence of Itgam blocking antibody M1/70 or IgG isotype control (left). The histogram shows quantification of the cell area (right). Scale bar, 30 µm. $n = 6$ samples per genotype in two independent experiments. Data were tested by two-way ANOVA followed by Bonferroni's post test in **f**, by two-tailed Student's *t*-test in **b**, **c**, **d**, and **e**, and by one-way ANOVA followed by Bonferroni's post test in **g**. Results are expressed as mean ± SEM. $^{*}p < 0.05$, $^{**}p < 0.01$, and $^{***}p < 0.001$

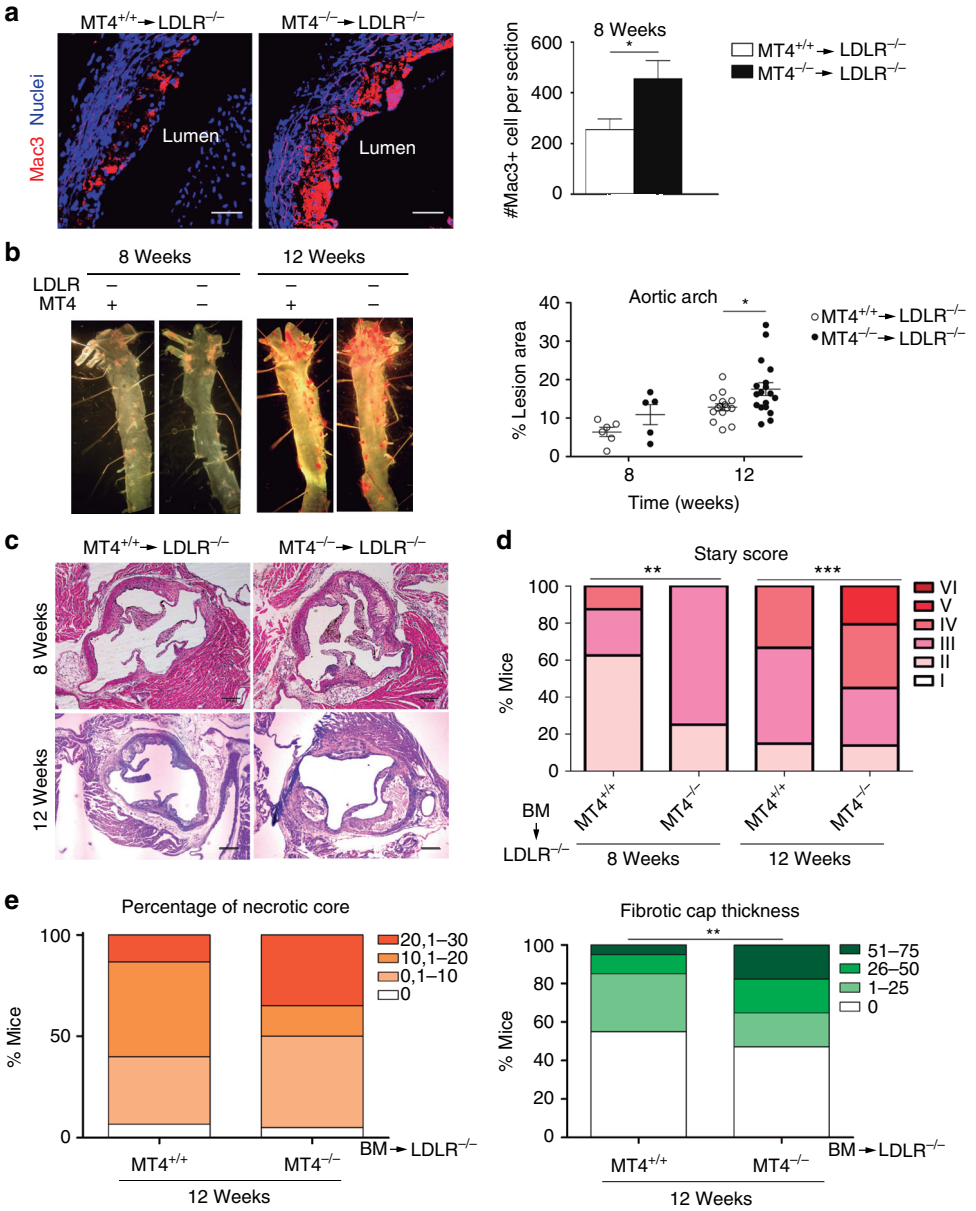

Fig. 2 Lack of MT4-MMP in BM-derived cells results in increased macrophage burden in atherosclerotic plaques and accelerated AT. **a** Representative images of Mac3 immunostaining (red; nuclei in blue) in transverse sections of aortas from *Ldlr*$^{-/-}$ mice transplanted with MT4-MMP$^{+/+}$ (MT4$^{+/+}$) or MT4-MMP$^{-/-}$ (MT4$^{-/-}$) BM cells and fed a HFD for 8 weeks; scale bar, 20 µm. The right panel shows Mac3-positive cells quantified by Image J. $n = 6$ mice per genotype in two independent experiments. **b** Representative images of en face Oil Red-stained aortas from BM-transplanted *Ldlr*$^{-/-}$ and fed a HFD for 8 or 12 weeks (left) and graph shows the area (%) of Oil Red-positive lesions in the aortic arch (right); $n = 6$ and $n = 16$ mice per genotype for 8 and 12 weeks in two and three independent experiments, respectively. **c** Representative images of transverse sections of aortic sinus stained with H&E of BM-transplanted *Ldlr*$^{-/-}$ mice; scale bar, 200 µm. **d** Stary scoring (I–VI) of aortic lesions of BM-transplanted *Ldlr*$^{-/-}$ mice, shown as a percentage of all mice for each condition after feeding a HFD for 8 or 12 weeks; $n = 6$ and $n = 16$ mice per genotype and time point in two and three independent experiments. **e** Bar graphs show the percentage of BM-transplanted *Ldlr*$^{-/-}$ mice for each range of % of necrotic area (left) and fibrotic cap thickness (right) after 12 weeks of HFD; $n = 16$ mice per genotype in three independent experiments. Data were tested by two-tailed Student's *t*-test in **a**, by two-way ANOVA followed by Bonferroni's post test in **b**, and by χ^2-test for a trend in **d**, **e**. Results are expressed as mean ± SEM. $^*p < 0.05$, $^{**}p < 0.01$, and $^{***}p < 0.001$

Although patrolling monocytes express genes related to cholesterol sensing and responses, their contribution to plaque lipid accumulation remains poorly characterized[21]. Analysis of incipient plaques after 7 days on the HFD showed no significant differences in macrophage number between *Ldlr*$^{-/-}$ mice transplanted with MT4-MMP-null or wild-type cells (Fig. 6a, b). We next explored whether increased recruitment of patrolling monocytes influences macrophage subset composition rather than their abundance.

Patrolling monocytes initiate a macrophage differentiation program in response to infection by upregulating Mafb in the peritoneal cavity[26], and this transcription factor can promote AT[26,28]. After 7 days on the HFD, incipient plaques from MT4$^{-/-}$-transplanted *Ldlr*$^{-/-}$ mice contained significantly more (~ 3-fold) Mac3+ macrophages with nuclear Mafb (49.6 ± 15%) than those from mice transplanted with wild-type cells (22.7 ± 10%; Fig. 6a, b), and this subset seemed to be more proliferative (~ 1.5-fold) in MT4$^{-/-}$-transplanted *Ldlr*$^{-/-}$ mice. All

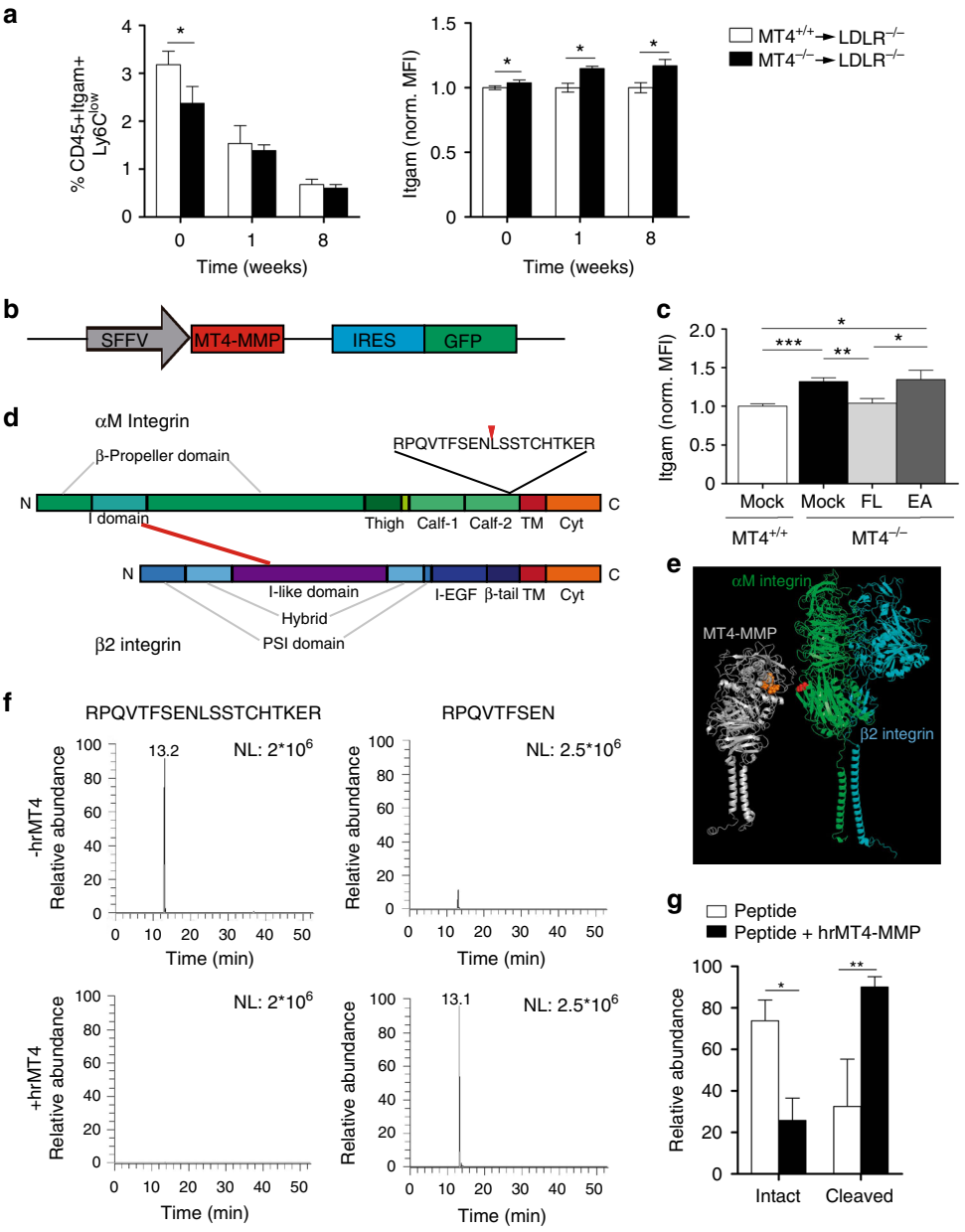

Fig. 3 The protease MT4-MMP can cleave the αM integrin chain (Itgam). **a** Percentage of circulating patrolling monocytes (CD45+Itgam+Ly6Clow, excluding granulocytes) and the normalized mean fluorescence intensity (MFI) of Itgam cell-surface levels in patrolling monocytes from *Ldlr*$^{-/-}$ mice transplanted with MT4-MMP$^{+/+}$ or MT4-MMP$^{-/-}$ BM cells and fed a HFD for 0, 1, or 8 weeks; $n = 12$, $n = 6$, and $n = 6$ mice in basal, 1 week and 8 weeks per genotype; four independent experiments in basal and two independent experiments at 1 and 8 weeks. **b** Design of lentiviral (LV) vector with SFFV-driven Mmp17 (MT4-MMP) expression and IRES-driven expression of green fluorescent protein (GFP). **c** LV encoding full-length mouse MT4-MMP (FL), the catalytic inactive mutant (E248A, EA), or GFP only (mock) were i.p. injected into MT4-MMP-null mice. Itgam cell surface levels were assessed by flow cytometry in the infected peritoneal macrophages (GFP+Itgam+F4/80+) 5 days after infection; $n = 6$ mice per condition in two independent experiments. **d** Depiction of human αMβ2 integrin domains, indicating the predicted cleavage site at position 977 in the Calf-2 domain of human αM integrin. **e** In silico model of human MT4-MMP dimer (gray) and αMβ2 integrin (αM chain, green; β2 chain, blue) showing the putative cleavage site between N977 and L978 (red) in the αM chain, and the catalytic active center in the MT4-MMP dimer (orange). **f** Representative extracted ion chromatogram of peptides obtained after incubation of the synthetic human αM integrin peptide RPQVTFSENLSSTCHTKER in the presence or absence of human recombinant MT4-MMP catalytic domain (hrMT4). **g** Quantification of the relative abundance of the intact RPQVTFSENLSSTCHTKER and N-terminal peptide fragments in each condition; $n = 4$ independent experiments. Data were tested by two-way ANOVA followed by Bonferroni's post test in **a**, by one-way ANOVA followed by Bonferroni's post test in **c**, and by two-tailed Student's *t*-test in **g**. IRES, internal ribosome entry site; SFFV, spleen focus-forming virus. Results are expressed as mean ± SEM. $^{*}p < 0.05$, $^{**}p < 0.01$, and $^{***}p < 0.001$

macrophages with nuclear Mafb also expressed AIM (apoptosis inhibitor of macrophages; Fig. 6a, b), which promotes survival of lipid-loaded macrophages[29]. In this line, a trend to reduced macrophage apoptosis (Mac3+/cleaved caspase-3+ cells) was apparent in incipient plaques of MT4$^{-/-}$-transplanted *Ldlr*$^{-/-}$ mice (~ 6 ± 2% vs ~ 8 ± 3% in those transplanted with wild-type cells). The increase in Mac3+ macrophages expressing AIM in the incipient plaques from MT4$^{-/-}$-transplanted *Ldlr*$^{-/-}$ mice

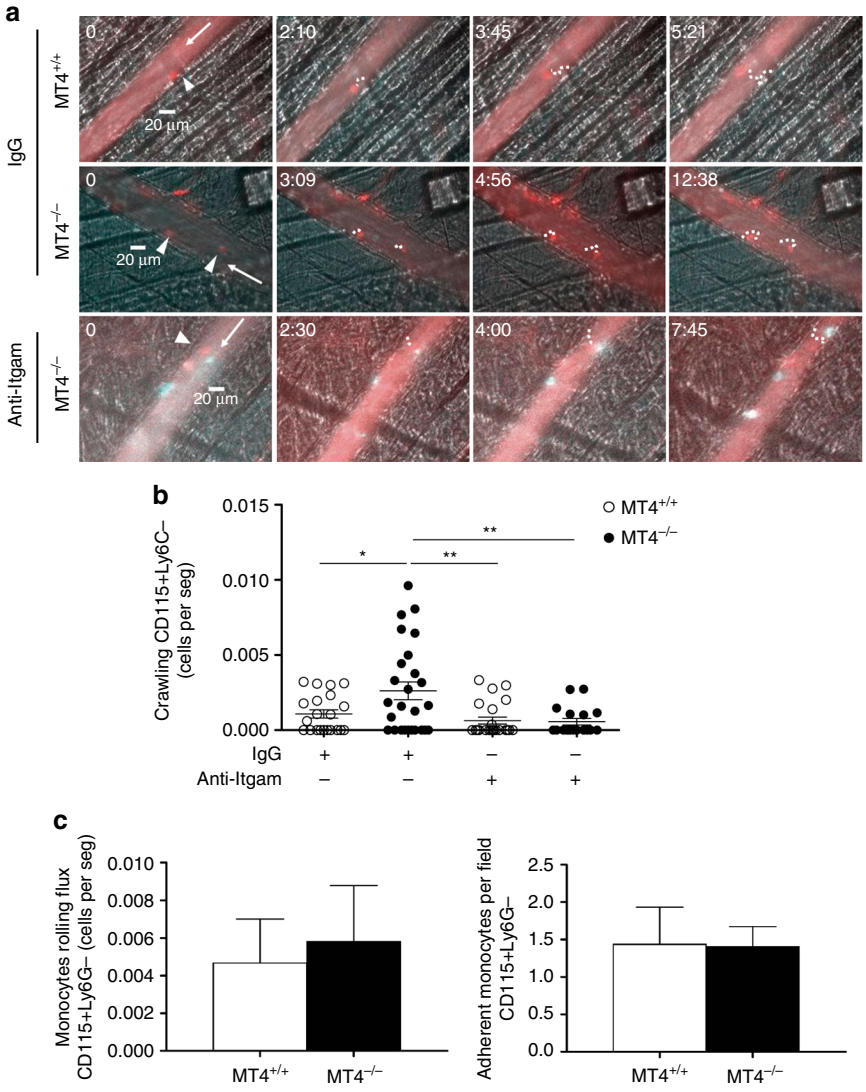

Fig. 4 Enhanced αM integrin-dependent crawling of MT4-MMP-null patrolling monocytes on CCL2-inflamed endothelium. **a** Representative intravital microscopy images of CD115+/Ly6C- patrolling monocytes (CD115 in red and Ly6C in green) crawling on the CCL2-inflamed endothelium in the cremaster muscle of wild-type ($MT4^{+/+}$) and MT4-MMP-null ($MT4^{-/-}$) mice; the recording was performed in the presence of anti-Itgam blocking antibody (M1/70) or IgG isotype control. Arrowheads, arrows, and dots respectively indicate individual patrolling monocytes, blood flow, and monocyte trajectory. Time of recording is indicated. **b** The graph shows the numbers of crawling patrolling monocytes recorded in **a** in every venule from five independent mice per genotype and condition in two independent experiments. **c** Quantification of CD115+Ly6G- rolling (left) and adherent (right) monocytes in the CCL2-inflamed endothelium in the cremaster muscle of wild-type ($MT4^{+/+}$) and MT4-MMP-null ($MT4^{-/-}$) mice. $n = 8$ mice per genotype in two independent experiments. Data were tested by one-way ANOVA followed by Bonferroni's post test in **b** and by two-tailed Student's *t*-test in **c**. Results are expressed as mean ± SEM.*$p < 0.05$, **$p < 0.01$, and ***$p < 0.001$

(39 ± 6% vs 27.6 ± 9% in those transplanted with wild-type cells) remained up to 8 weeks but was no longer observed in advanced plaques after 12 weeks on a HFD (Supplementary Fig. 9a, b). AIM also participates in oxLDL uptake[30]. Accordingly, ~ 50% of Mafb+ macrophages were positive for adipophilin in wild-type BM-transplanted $Ldlr^{-/-}$ mice and this proportion was significantly higher (~ 70%) in $Ldlr^{-/-}$ mice transplanted with MT4-MMP-null BM cells (Fig. 6c, d).

To further understand the influence of MT4-MMP absence on the functional phenotype of Mafb+AIM+ macrophages, we analyzed TG-elicited peritoneal macrophages[27]. Mirroring the accumulated subset observed in incipient atherosclerotic plaques, significantly more MT4-MMP-null macrophages contained Mafb at the nucleus (~ 60%, threefold) compared with wild types (~ 20%), and they also expressed higher levels of total and cell-surface AIM, detected by immunostaining and flow cytometry (Fig. 7a–c); *Mafb* and *Cd5l* (*Aim*) mRNA levels showed no differences (Supplementary Fig. 10a). Increased AIM expression resulted in significantly lower numbers of apoptotic MT4-MMP-null peritoneal macrophages after cycloheximide treatment (Fig. 7d). AIM also increases CD36-mediated oxLDL uptake and foam-cell formation[30]. Flow cytometry analysis revealed significantly increased cell-surface CD36 expression in TG-elicited MT4-MMP-null macrophages and these cells were more efficient at acLDL binding than wild types (Fig. 7e, f); no differences were detected in *Cd36* mRNA levels (Supplementary Fig. 10a). Further analysis showed that MT4-MMP-null peritoneal macrophages did not differ from wild types in the mRNA levels of proinflammatory cytokines (*Il1b*, *Tnfa*, and *Il6*) or anti-inflammatory cytokines (*Il10* and *Tgfb*) (Supplementary Fig. 10b).

CCR5 inhibition hinders accelerated AT in MT4-MMP absence. To prove that enhanced recruitment of patrolling monocytes in MT4-null BMT $Ldlr^{-/-}$ mice fed the HFD for 3 days

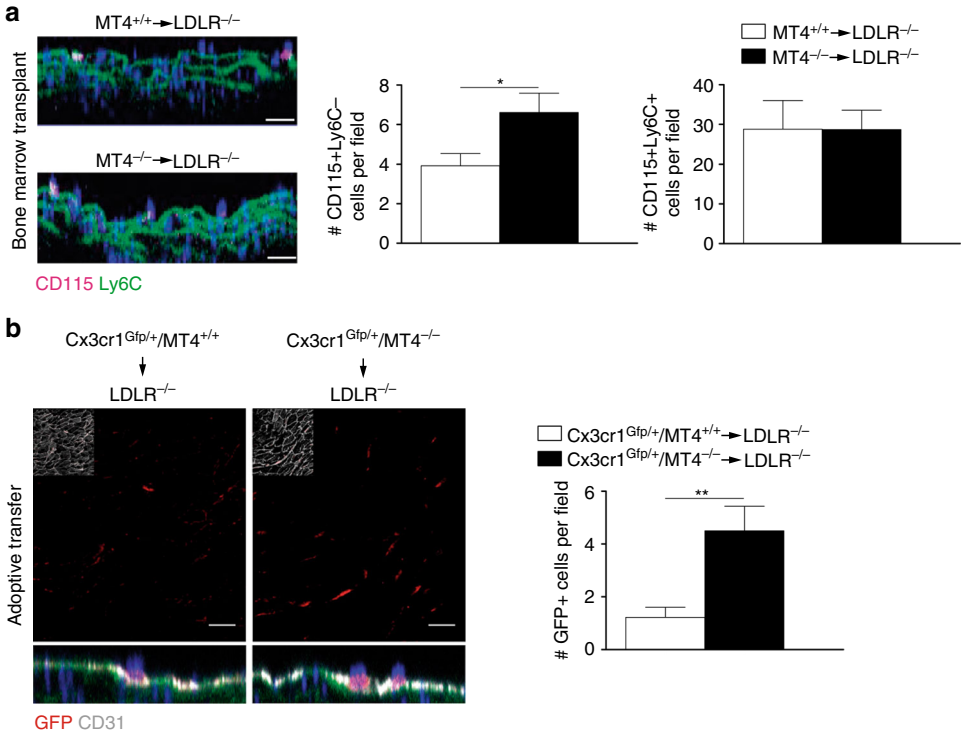

Fig. 5 Increased recruitment of MT4-MMP-null patrolling monocytes in incipient atherosclerotic lesions. **a** Representative orthogonal XZ view images of whole-mount-stained lesser curvature of the aortic arch from *Ldlr*$^{-/-}$ mice transplanted with MT4-MMP$^{+/+}$ or MT4-MMP$^{-/-}$ BM cells and fed a HFD for 3 days. Samples were stained for CD115 (magenta) and Ly6C (green); elastin autofluorescence (green) and nuclei (Hoechst, blue). The bar graph (right) shows the quantification of the number of patrolling (CD115+Ly6C−) and classical monocytes (CD115+Ly6C+) in the aorta lumen; $n = 6$ mice per genotype in two independent experiments. **b** Representative confocal microscopy images of whole-mount-stained lesser curvature of the aortic arch from *Ldlr*$^{-/-}$ mice adoptively transfer with Cx3cr1$^{Gfp/+}$ MT4-MMP$^{+/+}$ or Cx3cr1$^{Gfp/+}$ MT4-MMP$^{-/-}$ patrolling monocytes and fed a HFD for 3 days. Samples were stained for GFP (red) and CD31 (gray); elastin autofluorescence (green) and nuclei (Hoechst, blue). A z-stack of the confocal microscopy sections close to the lumen (with an inset of CD31 staining) is shown to the top and the orthogonal XZ view of the merged images to the bottom. Scale bar, 20 µm. The bar graph (right) shows the quantification of the number of transferred monocytes (GFP+) in the aorta lumen; $n = 9$ mice per genotype in two independent experiments. Data were tested by Student's *t*-test. Results are expressed as mean ± SEM.*$p < 0.05$, **$p < 0.01$

(Fig. 5a) was promoting Mafb+AIM+ macrophage accumulation and AT acceleration at later stages (Figs. 6a, b and 2), we sought to selectively block patrolling monocyte recruitment. For that, we used Maraviroc (MRV), a CCR5 antagonist used in the clinic[31], as patrolling monocyte preferentially employ this receptor to enter atherosclerotic plaques[27]. Daily treatment of mice with MRV reduced the low numbers of patrolling monocytes[27] consistent with decreased recruitment and abolished the enhanced adherence of patrolling monocytes to the aorta of MT4-null BM-transplanted *Ldlr*$^{-/-}$ mice after 3 days on the HFD (Fig. 8a). Concomitantly, MRV also led to loss of the increased abundance in Mafb+AIM+ macrophages at 7 days and in total macrophages at 8 weeks on the HFD in MT4-null BMT *Ldlr*$^{-/-}$ mice overall delaying AT progression, as shown by quantification of lipid deposits, neointima area, and Stary score, to similar levels than those observed in MRV-treated *Ldlr*$^{-/-}$ mice transplanted with wild-type cells[32] (Fig. 8b–f and Supplementary Fig. 11a–c).

The data obtained with the CCR5 antagonist demonstrate that the atherosclerotic phenotype observed in the absence of MT4-MMP is related to its primary impact on the enhanced early recruitment of patrolling monocytes to the inflamed aorta.

Discussion

Patrolling monocytes exert their surveillance activity within the vasculature, where they recognize endothelial damage and promote repair[23]. A vascular protective function for patrolling monocytes in inflammation was supported by the exacerbated AT in mice lacking the orphan nuclear receptor Nur77/Nr4a1, which present a dramatic reduction in Ly6C^{low} patrolling monocyte production[2,8,33]. These mice have, however, other defects such as a proinflammatory shift of Nur77-null macrophages, which could in part mediate the observed phenotype[33]. Moreover, a separate study did not detect changes in lipid lesions in *Ldlr*-null mice transplanted with Nur77$^{-/-}$ BM[34], and therefore debate has persisted about the atheroprotective role of patrolling monocytes. Our findings in MT4-MMP-null mice provide the first evidence for a contribution of patrolling monocytes to a proatherogenic Mafb+AIM+ macrophage subset in early plaques. The contribution of patrolling monocytes to AT may also be clarified by a recent mouse model targeting a super-enhancer that ablates Nur77-dependent Ly6C^{low} monocytes, while preserving Nur77 expression in tissue macrophages and macrophage responses to inflammation[35].

Macrophage burden mainly depends on monocyte recruitment in early plaques and on local macrophage proliferation in advanced plaques[6,36]. Established atherosclerotic lesions in MT4-MMP-null transplanted HFD-fed *Ldlr*$^{-/-}$ mice had an increased macrophage abundance unrelated to differences in proliferation. Although Ly6C^{low} patrolling monocytes are recruited early to incipient plaques in a CCR5-dependent manner[37], the mechanisms that govern their crawling, adherence, and recruitment to the plaque remain poorly defined[8]. Our study identifies MT4-MMP-mediated cleavage of αM integrin as a mechanism for fine-tuned regulation of patrolling monocyte crawling. MT4-MMP

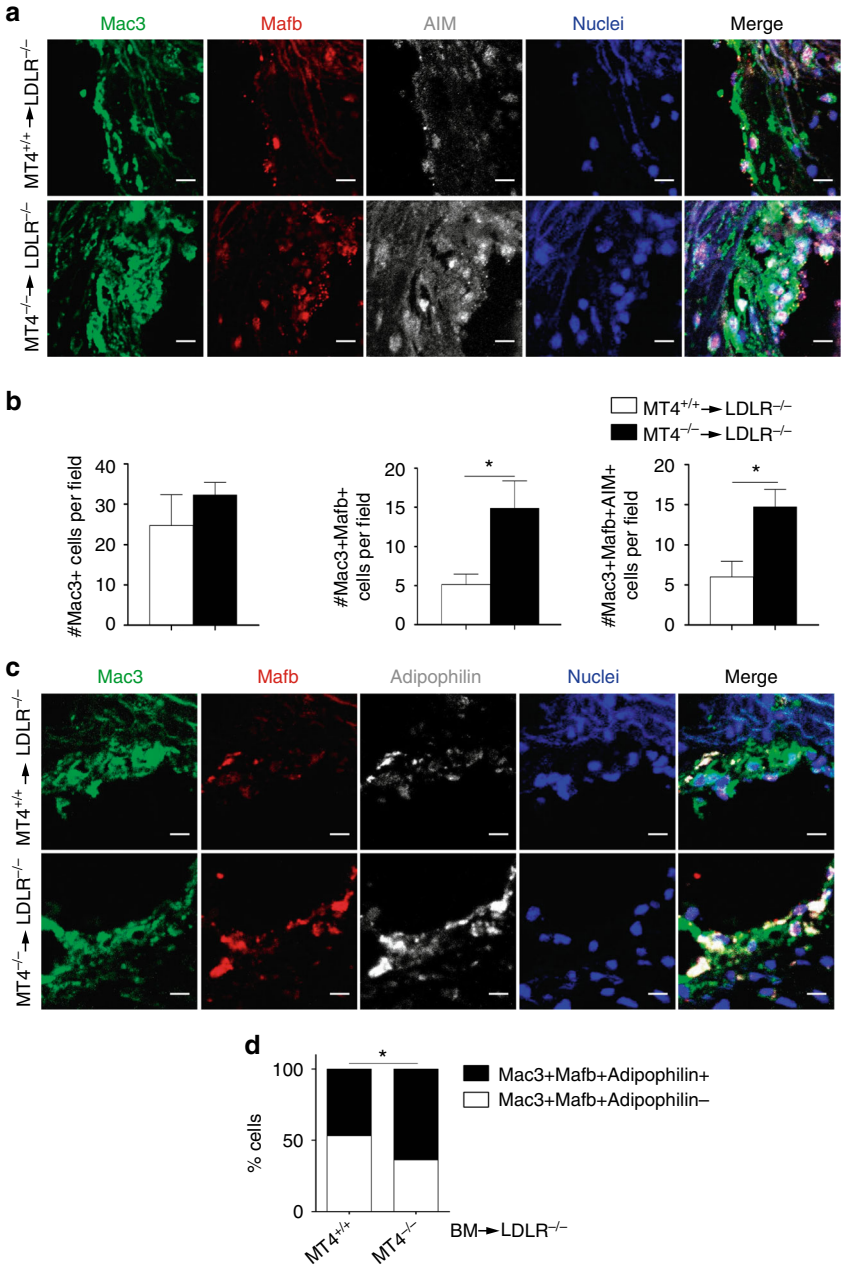

Fig. 6 Lack of MT4-MMP in patrolling monocytes leads to the accumulation of Mafb+AIM+ macrophages in incipient atherosclerotic plaques. **a** Representative images of transverse sections of aortic sinus from *Ldlr*$^{-/-}$ mice transplanted with MT4-MMP$^{+/+}$ (MT4$^{+/+}$) or MT4-MMP$^{-/-}$ (MT4$^{-/-}$) BM cells and fed a HFD for 1 week; sections were labeled for Mac3 (green), Mafb (red), and AIM (white), and with Hoechst (blue; nuclei); scale bar, 10 µm. **b** Number of Mac3+ cells (left), Mac3+Mafb+ cells (middle), and Mac3+Mafb+AIM+ cells (right) in the plaques of BM-transplanted *Ldlr*$^{-/-}$ mice fed a HFD for 1 week. **c** Representative images of transverse sections of aortic sinus from BM-transplanted *Ldlr*$^{-/-}$ mice fed a HFD for 1 week; sections were labeled for Mac3 (green), Mafb (red), and adipophilin (white), and with Hoechst (blue; nuclei); scale bar, 10 µm. **d** Relative % of adipophilin-positive and adipophilin-negative cells within the Mac3+Mafb+ population of BM-transplanted *Ldlr*$^{-/-}$ mice (1 week on HFD); $n = 7$ mice per genotype in two independent experiments. Data were tested by two-tailed Student's *t*-test in **b** and by Fisher's exact test in **d**. Results are expressed as mean ± SEM. $^{*}p < 0.05$

absence thus resulted in enhanced adhesion of patrolling monocytes on the inflamed endothelium and therefore their recruitment to incipient atherosclerotic plaques in a cell autonomous manner as shown by adoptive transfer experiments. Attention has also focused on macrophage heterogeneity in the atherosclerotic plaque, with new subsets being characterized, adding Mox, Mhem, and M4 macrophages to the established M1 and M2 categories[5]. As patrolling monocytes express genes for cholesterol sensing and response[21], it is of particular interest to determine whether their recruitment to the plaque influences macrophage composition, lipid handling, and overall AT progression. In this regard, patrolling monocytes are more prone to develop into CD11c+ cells in the plaque, but the function of these CD11c+ cells in AT was not elucidated[27,38]. We confirmed the presence of more CD11c+ cells in incipient plaques from MT4$^{-/-}$-transplanted *Ldlr*$^{-/-}$ mice (~2-fold), but these cells contained fewer lipids than CD11c+ cells in mice transplanted with wild-type BM, suggesting a limited contribution to the observed atherosclerotic phenotype (data not shown). Macrophages in MT4-MMP-null-derived plaques had an elevated accumulation of

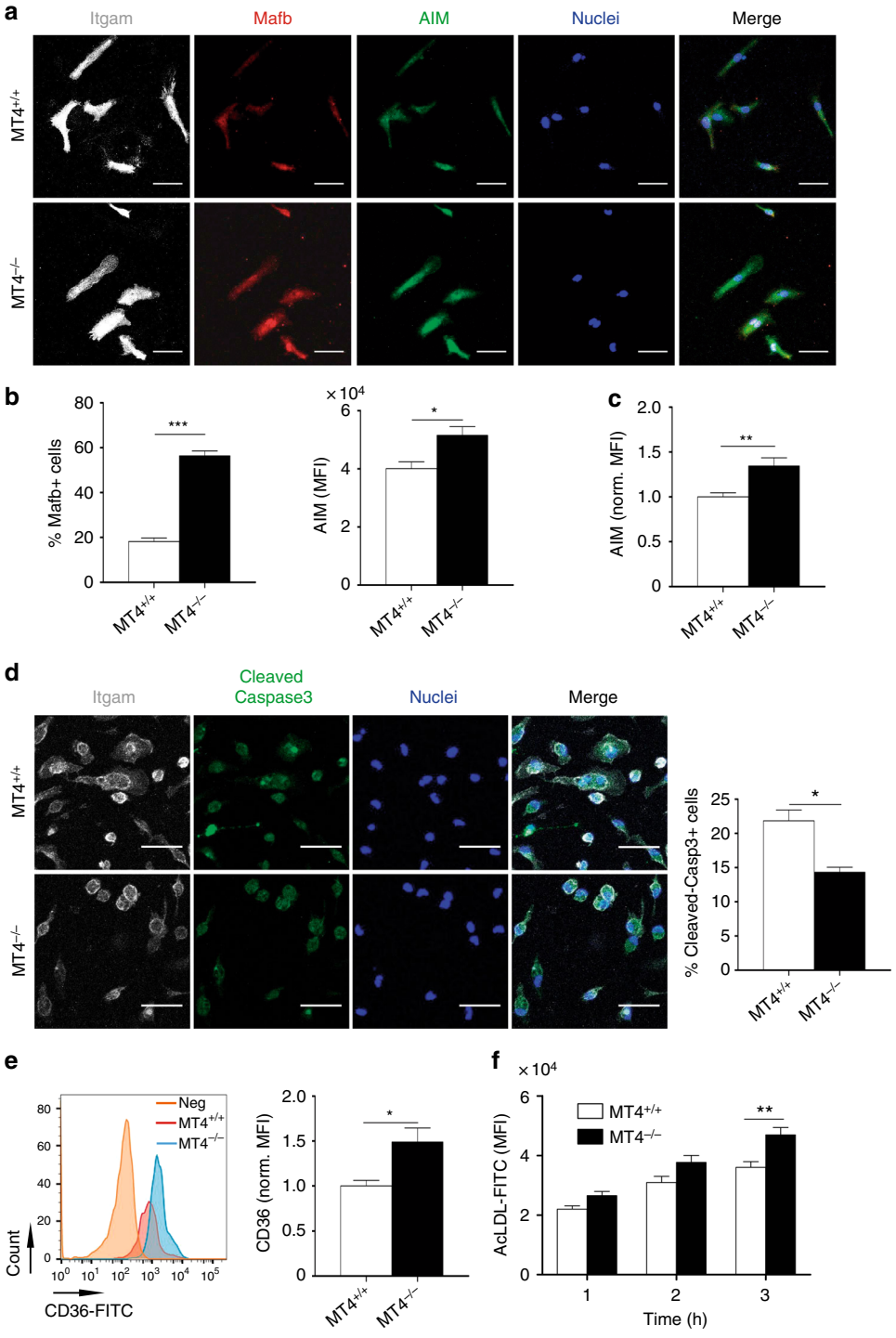

Fig. 7 MT4-MMP-null Mafb+/AIM+ peritoneal macrophages exhibit above-normal CD36 at the cell surface and enhanced acLDL binding. **a** Representative images of MT4-MMP$^{+/+}$ (MT4$^{+/+}$) or MT4-MMP$^{-/-}$ (MT4$^{-/-}$) mouse peritoneal macrophages elicited by 72 h TG stimulation and labeled for Itgam (white), Mafb (red), and AIM (green), and with Hoechst (blue, nuclei); scale bar, 20 µm. **b** Graphs show the percentage of cells Mafb+ in the nuclei (left) and the MFI of AIM within Mafb+ cells (right); $n = 6$ in two independent experiments. **c** Quantification of normalized MFI of AIM analyzed by flow cytometry in MT4$^{+/+}$ or MT4$^{-/-}$ mouse peritoneal macrophages elicited by 72-hour TG stimulation; $n = 6$ in two independent experiments. **d** Representative images of TG-elicited MT4$^{+/+}$ or MT4$^{-/-}$ mouse peritoneal macrophages treated with cycloheximide (100 µg ml^{-1}) for 6 h and labeled for Itgam (white) and cleaved-caspase 3 (green) and Hoechst (blue, nuclei); scale bar, 20 µm. Quantification of the percentage of cleaved-caspase 3-positive cells is shown on the right; $n = 3$ in one experiment. **e** Representative flow cytometry histogram plot of CD36 staining in TG-elicited MT4$^{+/+}$ or MT4$^{-/-}$ mouse peritoneal macrophages (left) and quantification of normalized MFI (right); $n = 6$ in two independent experiments. **f** MFI of AcLDL-FITC binding to TG-elicited MT4$^{+/+}$ or MT4$^{-/-}$ mouse peritoneal macrophages for the indicated times; $n = 6$ in two independent experiment. Data were tested by Student's *t*-test in **b**, **c**, **d**, and **e**, and by two-way ANOVA followed by Bonferroni's post test in **f**. Results are expressed as mean ± SEM. *$p < 0.05$, **$p < 0.01$, and ***$p < 0.001$

nuclear Mafb similar to observations in other contexts, thus supporting the idea that Mafb may be an intrinsic signature of patrolling monocyte differentiation into macrophages, regardless the inflammatory context[26]. Mafb+ lipid-loaded macrophages have been reported in mouse and human established atherosclerotic plaques, but the origin of this subset was not elucidated[28]. Mac3+Mafb+ macrophages also expressed AIM (apoptosis inhibitor of macrophages), which by inhibiting foam-cell apoptosis and favoring oxLDL uptake[28–30] may underlie the larger lipid lesions developed in the aortas of $MT4^{-/-}$-transplanted $Ldlr^{-/-}$ mice after 12 weeks on the HFD. Data obtained with the CCR5 inhibitor confirmed the dependence of patrolling monocytes on this receptor for their efficient recruitment to the plaque and the existence of non-CCR5 factors whose functional significance remains to be determined[27]. CCR5 inhibitor data also argue in favor of increased early recruitment of patrolling monocytes to athero-prone aorta areas as the primary contributor to Mafb+AIM+ macrophage abundance and AT acceleration in the absence of MT4-MMP. Notably, the phenotype was not restricted to the atherosclerotic context, since we also observed Mafb+AIM+ macrophage accumulation in TG-elicited MT4-MMP-null peritoneal macrophages. Furthermore, these macrophages exhibited higher levels of cell-surface AIM and of CD36 (a gene expressed by patrolling monocytes[21]) and bound acLDL more avidly[39], in line with the role assigned to AIM in favoring CD36-mediated oxLDL uptake and foam-cell formation[30].

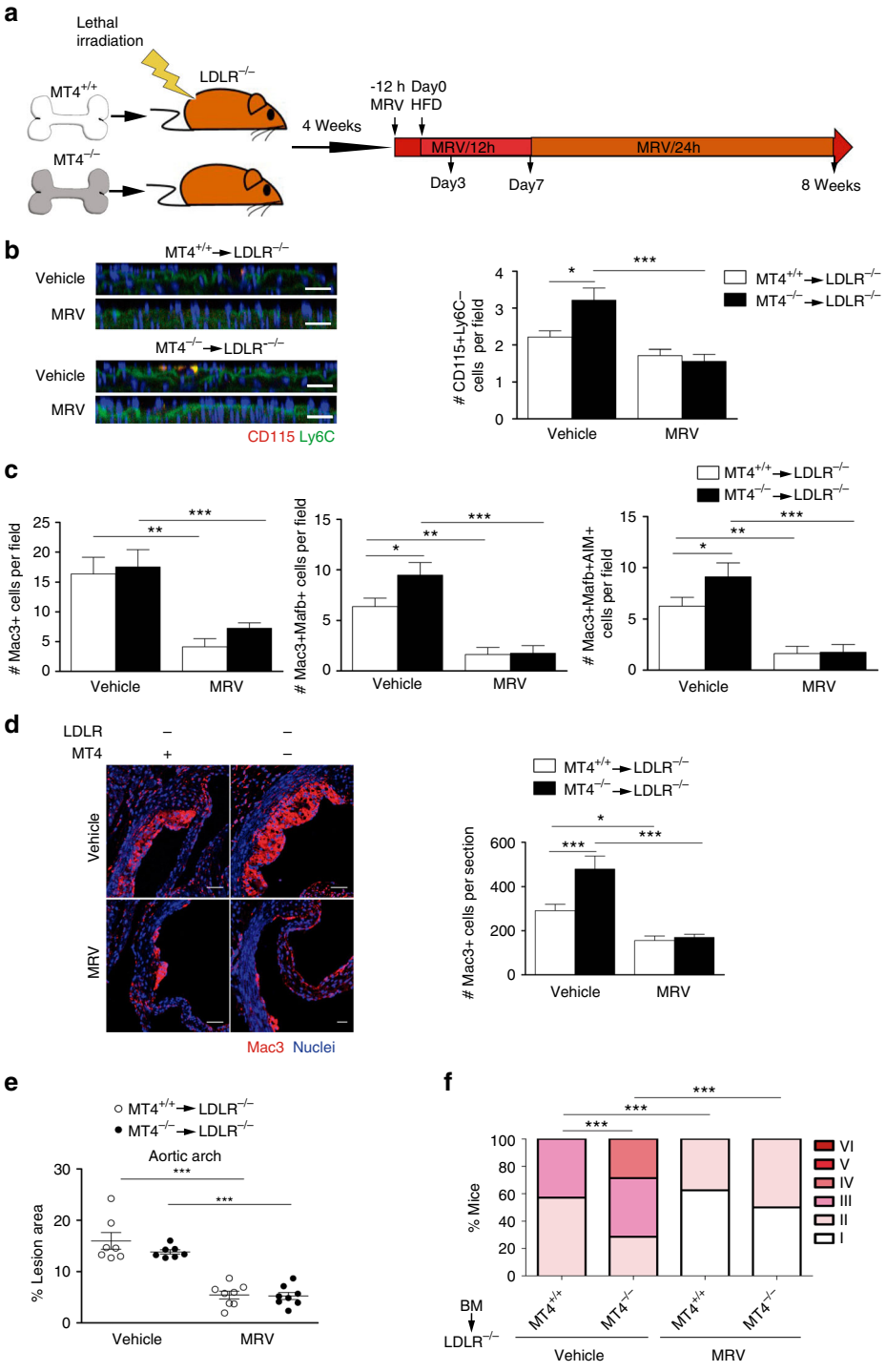

Interestingly, the functional outcome of high CD36 levels in MT4-MMP-null Mac3+Mafb+AIM+ macrophages may be further shaped by environmental factors: in a lipid-rich milieu like AT, CD36 expression would favor disease progression; however, in contexts such as bacterial infection or amyloid deposition, CD36 might promote phagocytosis and resolution[40]. The Mac3+Mafb+AIM+ subset seems to be unique within the multidimensional model of macrophage plasticity[41], with cytokine profiling indicating no shift to a proinflammatory or antiinflammatory phenotype; however, amplified αM integrin-mediated signaling in MT4-MMP-null macrophages may still produce changes in certain cytokines, such as CXCL2[42]. Cooperation of αM integrin with CD36 and TLR2 in cell-surface lipid domains on macrophages has been shown to promote lipid accumulation and downmodulate the inflammatory response[43]; future studies will elucidate whether this cooperation takes place in Mac3+Mafb+AIM+ macrophages, particularly in the absence of MT4-MMP. Our results identify a unique apoptosis-resistant, lipid-prone, and non-inflammatory Mac3+Mafb+AIM+ subset that contributes to AT progression; the relation of this subset to subsets previously reported in the atherosclerotic plaque (Mox, M(Hem), M(Hb), and M4)[5] deserves further analysis. In light of these results, combined strategies targeting Mafb+ and Mafb– macrophages may prove to be more effective at ameliorating AT progression. Determining whether patrolling monocyte-derived macrophages still have a pro-resolution role at later stages in established AT lesions would require the use of inducible depletion strategies.

This report also describes the first MT4-MMP function in monocytes/macrophages unrelated to the previously proposed pro-TNFα processing[15,13,14]. We identify the αM integrin chain (Itgam), present in lipid membrane microdomains, as a novel MT4-MMP substrate[12,44,45], and the lentiviral strategy indicates that MT4-MMP catalytic activity regulates αM integrin cell surface levels in patrolling monocytes also in vivo. Serine proteases and MMP-9 cleave the β2 integrin chain[46,47] and this shedding is thought to allow leukocyte detachment after endothelial adhesion[48,49]. We identified an MT4-MMP cleavage site at position N^{977} of the αM integrin chain, which is conserved in human and mouse αM integrin but not in the related αL integrin chains of either species. In response to vessel injury or inflammation, patrolling monocytes change their crawling pattern and shift to αMβ2 integrin dependence for vascular monitoring[23,26,50]. MT4-MMP-mediated cleavage of αM integrin would likely destabilize the integrin heterodimer[51] allowing patrolling monocytes to detach once their surveillance function on the inflamed endothelium is performed. These results thus also position αMβ2 integrin as a major regulator of patrolling monocyte behavior in AT, in which its role had remained unclear[52–54]. Interaction of αMβ2 integrin with ICAM-1, von Willebrand factor, fibrinogen, or CCN1 at athero-prone sites[55–58] might downregulate Foxp1 and induce c-fms[59], and hence influence MT4-MMP and Mafb expression (data not shown and[60]) as well as macrophage differentiation and/or proliferation.

This study has potential translational implications related to the atheroprotective action of MT4-MMP when present in BM-derived patrolling monocytes, with its expression increasing steadily with AT progression in mouse aorta and human coronary arteries. Genome-wide association studies will help to determine whether mutations in the MT4-MMP gene (*MMP17*) correlate with increased susceptibility to AT. Finally, patrolling monocytes have beneficial intravascular actions in infection, lung metastasis, and Alzheimer's disease[8,17,61], and our results suggest that short-term MT4-MMP targeting may offer a new therapeutic strategy to boost these activities.

Methods

Animal procedures. MT4-MMP-deficient mice were generated as previously described[15]. *Ldlr*-deficient and *Cx3cr1*$^{Gfp/+}$ mice[62] were obtained from Jackson Laboratories. All mouse strains were on the C57BL/6 background. MT4-MMP$^{-/-}$/*Ldlr*$^{-/-}$ and MT4-MMP$^{-/-}$/*Cx3cr1*-$^{Gfp/+}$ mice were obtained by crossing MT4-MMP-deficient mice with *Ldlr*$^{-/-}$ or *Cx3cr1*-$^{Gfp/+}$ mice. Mice used in this study included: $n = 58$ C57BL/6, $n = 67$ MT4-MMP$^{-/-}$, $n = 154$ *Ldlr*$^{-/-}$, $n = 20$ MT4-MMP$^{-/-}$/*Ldlr*$^{-/-}$, $n = 10$ *Cx3cr1*$^{Gfp/+}$, and $n = 10$ MT4-MMP$^{-/-}$/*Cx3cr1*-$^{Gfp/+}$. Mice were housed in the Centro Nacional de Investigaciones Cardiovasculares Carlos III (CNIC) Animal Facility under pathogen-free conditions and according to institutional guidelines. Animal studies were approved by the local ethics committee (CNIC Committee for Animal Welfare permit number CNIC-01/13 and local government of Madrid permit number PROEX 34/13) and conformed to directive 2010/63EU and recommendation 2007/526/EC regarding the protection of animals used for experimental and other scientific purposes, enforced in Spanish law under RD1201/2005. No statistical methods were used to pre-estimate the animal sample size and mice were randomly allocated to experimental groups. To induce atherosclerotic plaques, 3-month-old male mice were fed a HFD (ssniff, E15721-34) ad libitum for the indicated time. For BM transplantation, lethally irradiated (9 Gy) 8-week-old male *Ldlr*$^{-/-}$MT4-MMP$^{+/+}$ mice received tail vein injections of BM cells (10^7) obtained from tibias and femurs of euthanized donor *Ldlr*$^{+/+}$MT4-MMP$^{+/+}$ or *Ldlr*$^{+/+}$MT4-MMP$^{-/-}$ mice. After 4 weeks on standard chow diet, transplanted mice were placed on the HFD for the indicated time. For CCR5 blocking, MRV (25 μg/g) or vehicle (5% dimethyl sulfoxide and 0.5% HCl 0.1 N in distilled water) were administered to BM transplanted *Ldlr*$^{-/-}$ mice by oral gavage every 12 h for 3 days, 7 days, or during the first week, and then every 24 h for a further 7 weeks until the end of the experiments. MRV was first administered at the end of the day previous to HFD feeding and last administered 2 h before sacrificing the mice. For adoptive transfer experiments, patrolling monocytes were sorted from the spleen of MT4-MMP$^{+/+}$/*Cx3cr1*-$^{Gfp/+}$ and MT4-MMP$^{-/-}$/*Cx3cr1*-$^{Gfp/+}$ mice as Lin (B220 (BD Pharmingen, 51.01122J), CD3 (BD Pharmingen, 51.01082J), Ly6G (BD Biosciences, 551461), and NK1.1 (BD Biosciences, 553165))-negative, GFP-positive and Ly6C-negative cells. Patrolling monocytes (5×10^5) were injected intravenously into 3-month-old male *Ldlr*$^{-/-}$ mice; the mice were fed on the HFD for 3 days and then killed and the aortas processed for whole-mount staining. Investigators were not blinded during the analysis of mouse samples.

Fig. 8 CCR5 inhibition results in loss of enhanced recruitment of patrolling monocytes, Mafb+AIM+ macrophage accumulation and AT acceleration in MT4-MMP-null BMT *Ldlr*$^{-/-}$ mice. **a** Scheme depicts the experimental design of CCR5 blocking strategy by Maraviroc (MRV) administration as described in M&M. **b** Representative orthogonal XZ view of confocal microscopy images of whole mount-stained aortic arch from *Ldlr*$^{-/-}$ mice transplanted with MT4-MMP$^{+/+}$ or MT4-MMP$^{-/-}$ BM cells, fed the HFD for 3 days and treated with MRV or vehicle. Samples were stained for CD115 (red) and Ly6C (green); elastin autofluorescence (green) and nuclei (Hoechst, blue) are also shown. Scale bar, 20 μm. The bar graph (right) shows the quantification of the number of patrolling monocytes (CD115+Ly6C–) in the aorta lumen; $n = 7$ vehicle and $n = 8$ MRV mice per genotype in two independent experiments. **c** Bar graphs show the quantification of the number of Mac3+ cells (left), Mac3+Mafb+ cells (middle), and Mac3+Mafb+AIM+ cells (right) in the plaques of BM-transplanted *Ldlr*$^{-/-}$ mice fed a HFD for 1 week and treated with Maraviroc or vehicle. $n = 8$ mice per genotype and condition in two independent experiments. **d** Representative microscopy images of transverse sections of aortic sinus from BM-transplanted *Ldlr*$^{-/-}$ mice fed a HFD for 8 weeks and treated with Maraviroc or vehicle; sections were labeled for Mac3 (red) and Hoechst (blue; nuclei) (upper, scale bar, 50 μm) and graph shows the quantification of the number of Mac3+ cells in the plaque (lower). $n = 7$ vehicle and $n = 8$ MRV BM-transplanted mice per genotype in two independent experiments. **e** Graph showing the lesion area of aortas stained with Oil Red from BM-transplanted *Ldlr*$^{-/-}$ mice fed a HFD for 8 week and treated with MRV or vehicle. $n = 7$ and $n = 8$ mice for Vehicle and MRV mice per genotype in two independent experiments. **f** Stary scoring (I-VI) of transverse aortic H&E-stained sections from BM-transplanted *Ldlr*$^{-/-}$ mice fed a HFD for 8 weeks and treated with Maraviroc or vehicle, shown as a percentage of all mice for each score. $n = 7$ vehicle and $n = 8$ MRV BM-transplanted mice per genotype in two independent experiments. Data were tested by one-way ANOVA followed by Bonferroni's post test in **b**–**e** and by χ^2-test for a trend in **f**. Results are expressed as mean ± SEM. $^*p < 0.05$, $^{**}p < 0.01$, $^{***}p < 0.005$

Human artery sampling and preservation. Human coronary arteries ($n = 25$) were collected from freshly excised hearts during transplant operations at the Hospital de la Santa Creu i Sant Pau (HSCSP, Barcelona, Spain). The study was approved by the Hospital de la Santa Creu i Sant Pau Ethics Committee (04/2016) and was conducted according to the Declaration of Helsinki. Written informed consent was obtained from each patient. Immediately after surgical excision, arteries were dissected, cleaned of connective tissue, and examined under a dissecting microscope. Vessel samples were frozen in liquid nitrogen and stored at −80 °C for later protein or RNA extraction. Human samples were classified as early lesions (presenting only thickening of the intima) and established atherosclerotic lesions (presenting smooth muscle cells in the intima).

Genotyping of BM-transplanted mice. Blood samples were obtained from BM-transplanted mice 4 weeks after transplantation. White blood cells were isolated using Lympholyte (Cedarlane, CL5031) and DNA was extracted by isopropanol precipitation. PCR was performed using the following primers: forward WT: 5′-TCAGACACAGCCAGATCAGG-3′, forward KO 5′-AATATGCGAAGTG-GACCTGG-3′, and reverse (common to WT and KO) 5′-AGCAA-CACGGCATCCACTAC-3′. PCR was conducted at 94 °C for 2 min followed by 40 cycles of 95 °C for 40 s, 58 °C for 40 s, and 72 °C for 1 min, and a final elongation at 72 °C for 10 min.

Biochemical analysis. Total mouse serum cholesterol, triglycerides, and glucose were measured using the Dimensions RxL Max system (Siemens Healthineers).

Atherosclerotic lesion analysis. Hearts and aortas from euthanized mice were fixed with 4% of paraformaldehyde overnight at 4 °C. Adventitial fat and connective tissue were removed from aortas under a dissecting microscope. Whole aortas were opened longitudinally to expose the entire luminal surface and stained with 0.2% Oil Red O (Sigma-Aldrich, O0625) in 78% methanol. Images were acquired with a Nikon SMZ800 stereomicroscope (Nikon, Japan) coupled to a Nikon Coolpix 4500 digital color camera (Nikon). The Oil Red-positive area was measured using Image J (https://imagej.nih.gov/ij/; National Institutes of Health, Bethesda, MD).

Histological and immunohistochemical analysis. Mouse hearts and aortas were perfused with phosphate-buffered saline (PBS), extracted, fixed in 4% paraformaldehyde for 24 h at 4 °C, embedded in paraffin, and cut in 5 µm transverse sections for immunostaining or hematoxylin and eosin staining. Deparaffinized sections were rehydrated, and antigens were retrieved at 95 °C for 20 min in citrate buffer pH 6 or (for cleaved caspase-3 staining only) Tris-EDTA buffer pH 9. Sections were then left to cool to room temperature for 2 h. Antigen-retrieved paraffin sections and cryosections were blocked and permeabilized for 1 h at room temperature in PBS containing 0.3% (w/v) Triton X-100, 5% bovine serum albumin (BSA), 5% goat serum, and a 1:100 dilution of anti-CD16/CD32 (24g2, BD Pharmingen 553142). For immunofluorescence, sections were stained with anti-Mac3 (Santa Cruz Biotechnology, sc-19991), anti-MT4 (Abnova, PAB4785), anti-beta-galactosidase (rabbit, Abcam ab4761), anti-Ki67 (Abcam, ab16667), anti-cleaved caspase-3 (Cell Signaling Technology, 9661 S), anti-CD11c (eBiosciences, 11-014-81), anti-Mafb (Santa Cruz Biotechnology, sc-10022), anti-AIM (GeneTex, GTX37448), or anti-adipophilin (Novus Biologicals, NB110-40887) at 4 °C overnight or with anti-CD11b 647 (eBiosciences, 51-0112-82) for 2 h at room temperature. Primary antibodies were detected with corresponding fluorescent-labeled secondary antibodies. Samples were mounted in Fluoromount-G (SouthernBiotech, 0100-01) containing Hoechst 33342. Images were acquired on an inverted confocal microscope (LSM700, Carl Zeiss) fitted with a × 25 oil-immersion objective. Images were processed with Zen2009 Light Edition system (Carl Zeiss). Quantification was performed with Image J (https://imagej.nih.gov/ij/; National Institutes of Health) or CellProfiler software (Broad institute).

Real time quantitative PCR. Total RNA was isolated with TRIzol reagent (Invitrogen) using Maxtract high-density columns (Qiagen, ref. 1038988). Isolated RNA was treated with DNAse I (Sigma-Aldrich, D5025) and reverse transcribed using the High-Capacity cDNA Reverse Transcription Kit (Applied Biosystems). For mouse samples, quantitative PCR (qPCR) was performed with SYBR Green PCR master mix (Applied Biosystem) in a CFX384 detection system (Bio-Rad). Primers used in this study are listed in Supplementary Table 1. Data were normalized to the expression levels of 36b4 and cyclophilin mRNA within individual samples. For human samples, qPCR was performed using TaqMan probes for human *MMP17* (Hs00211754_m1) and normalized to the expression levels of TBP (Hs99999910_m1). All samples were analyzed in triplicate and RNA levels (CNRQ; calibrated normalized relative quantity) were calculated with Biogazelle qBase PLUS.

Western blotting. Protein extracts from human coronary artery samples were prepared in ice-cold lysis buffer containing 50 mM Tris-HCl pH 7.5, 1% (w/v) Triton X-100, 150 mM NaCl, and 1 mM dithiothreitol, and supplemented with protease inhibitors[63]. Mouse atheroma samples were obtained from paraffin-embedded samples, removing the paraffin, dewaxing, and rehydrating as follows: samples were placed in a tube and incubated for 30 min at 65 °C with 1 ml xylene and incubated at room temperature with rotation. Samples were then dehydrated through 100% ethanol (2 × 1 h), 96% ethanol (30 min), 70% ethanol (30 min), and PBS (2 × 20 min). Samples were lysed in 20 mM Tris-HCl, pH 7.5 containing 2% SDS and protease inhibitors for 20 min at 100 °C and 2 h at 60 °C. After centrifugation at 13,000 r.p.m. for 15 min at 4 °C, proteins from peritoneal macrophages were extracted in a buffer containing 10 mM Tris-HCl pH 7.5, 1% (w/v) Triton X-114, 150 mM NaCl, and protease inhibitors; samples were heated for 5 min at 30 °C to separate hydrophilic and lipophilic phases. Proteins were separated by 10% SDS-polyacrylamide gel electrophoresis, transferred to nitrocellulose membranes, and blocked with 5% non-fat milk. Primary antibodies used were anti-MT4-MMP (Abcam, ab51075), anti-CD11b (Abcam, ab75476), anti-caveolin1 (Cell Signaling, 3267 S), anti-α-actin (Dako, M0851), and anti-tubulin (Sigma-Aldrich, T6074). After overnight incubation at 4 °C and washes, bound primary antibody was detected by incubation for 1 h with donkey-anti-rabbit (IRDyeTM 800CW or 680CW, 1/10,000, Odyssey) or donkey-anti-mouse (IRDyeTM 800CW or 680CW, 1/10,000, Odyssey) secondary antibodies, followed by visualization with the Odyssey Infrared Imaging System (LI-COR Biosciences). Raw western blotting images are presented in Supplementary Fig. 12.

In silico modeling of MT4-MMP dimer/Itgam-Itgb2 integrin heterodimer. Fasta sequences of mature human MT4-MMP/MMP17, Itgam, and Itgb2 proteins were analyzed with locally implemented I-Tasser suite v4.4 for threading modeling[64]. Selected models were those with minimal energy and correct folding (best structural alignment to templates). In these models, the TM domain is buried in the protein core. Therefore, angles in this region (TM plus C-term) were fixed according to the predicted secondary structure and a refinement cycle was performed with the membrane framework of Rosetta suite v3.5 release 2015.38.58158 (www.rosettacommons.org)[65]. To dock dimeric MT4-MMP to Itgam-Itgb2, the monomers modeled previously were positioned according to the published dimeric interface using pymol v1.8 (www.pymol.org) and the new dimeric model was used as the initial template. Using this model as input, with the same spanfile and constraints as before, a new dimer model was generated using the *mp_dock* application from the membrane framework of Rosetta suite v3.5 release 2015.38.58158 in each case[65]. Using the obtained dimer models, the MT4-MMP-Itgam-Itb2 complex was modeled by a similar approach.

Identification of cleavage sites and in vitro digestion assay. Cleavage sites for MT4-MMP in αMβ2 integrin were identified by Cleavpredict[22] (http://cleavpredict.sanfordburnham.org/) and the predicted and exposed sites were then filtered according to the peptide cleavage matrix in the MEROPS database (http://merops.sanger.ac.uk/). Conservation of cleavage sites in the mouse and human αM and αL integrin chains was checked in Uniprot (http://www.uniprot.org/align/). The αM integrin peptide (RPQVTFSENLSSTCHTKER) was synthetized at the Centro de Investigaciones Biológicas (CIB, CSIC, Madrid) and incubated with hrMT4-MMP (RP-77535, Thermo Fisher Scientific) for 2 h at 37 °C in water. The resulting peptides were assayed by high-resolution parallel reaction monitoring on an Easy nLC 1000 nano-HPLC apparatus (Thermo Fisher Scientific) coupled to a hybrid quadrupole-orbitrap mass spectrometer (Q Exactive, Thermo Scientific). The peptides were separated at 200 nL m^{-1} in a continuous gradient consisting of 8–30% B for 15 min and 30–90% B for 2 min ($B = 90\%$ acetonitrile, 0.1% formic acid) and ionized using a Picotip emitter nanospray needle (New Objective, Woburn, MA, USA). Each mass spectrometric (MS) run consisted of enhanced FT-resolution spectra (15,000 resolution) in the 400–1400 m z^{-1} range followed by data-independent tandem MS spectra of seven parent ions acquired during the chromatographic run. The AGC target value in the Orbitrap for the survey scan was set to 1,500,000 and fragmentation was performed at 27% normalized collision energy with a target value of 250,000 ions. Data were analyzed with Xcalibur 2.2 (Thermo Fisher Scientific).

Peritoneal macrophage analysis. Primary mouse peritoneal macrophages were obtained from MT4-MMP$^{+/+}$ or MT4-MMP$^{-/-}$ mice by i.p. lavage with 10 ml cold PBS 72 h after i.p. injection of 3% (w/v) TG. Macrophages were counted, pelleted, and resuspended in RPMI-1640 (Sigma-Aldrich) supplemented with 2.5% fetal bovine serum, 10 mM HEPES, 50 UI ml^{-1} penicillin, 50 µg ml^{-1} streptomycin, 1 mM sodium pyruvate, and 0.1 mM non-essential amino acids, and plated on coverslips for spreading experiments or on plastic tissue culture dishes for mRNA or protein analyses. Freshly isolated peritoneal cells were used for flow cytometry. For MafB and AIM immunofluorescence analysis of TG-elicited peritoneal macrophages, cells were plated on glass coverslips (500,000 cells per 12 mm-diameter coverslip) for 24 h, fixed with 4% paraformaldehyde for 10 min at room temperature, and blocked and permeabilized for 30 min at room temperature in PBS containing 0.3% (w/v) Triton X-100, 5% BSA, 5% goat serum, and a 1:100 dilution of anti-CD16/CD32 (24g2, BD Pharmingen 553142). Fixed cells were stained with anti-Mafb (Santa Cruz Biotechnology, sc-10022) and anti-AIM (GeneTex, GTX37448) overnight at 4 °C, and with anti-CD11b 647 (eBiosciences, 51-0112-82) for 2 h at room temperature, followed by the corresponding fluorescent-labeled secondary antibodies. Apoptosis was assessed by treating TG-elicited peritoneal

macrophages with cycloheximide (100 μg ml^{-1}) for 6 h and staining fixed cells with anti-cleaved caspase 3 (Cell Signaling, 9661 S) as described above. Samples were mounted in Fluoromount-G (SouthernBiotech, 0100-01) containing Hoechst 33342. Images were acquired on an inverted confocal microscope (LSM700, Carl Zeiss) fitted with a × 25 oil-immersion objective. Images were processed and analyzed using Image J (https://imagej.nih.gov/ij/; National Institutes of Health). For C3 and acLDL binding assays, TG-elicited peritoneal macrophages were plated over coverslips or left in suspension and incubated with C3-opsonized sheep red blood cells (RBCs) or with 1 μg ml^{-1} acLDL-FITC (Invitrogen, L-23380) for the indicated times at 37 °C; the number of RBC per macrophage was then counted and the fluorescence intensity of AcLDL-FITC quantitated by flow cytometry. Macrophage egression was assessed as described[52]. In brief, TG-elicited peritoneal macrophages from MT4-MMP$^{+/+}$ or MT4-MMP$^{-/-}$ mice were labeled with PKH26 or PKH67 probes (Sigma-Aldrich MINI26 and MINI67), respectively, and mixed 1:1. Dual-labeled macrophages (5×10^5) were injected i.p. into C57BL6 mice previously stimulated with TG i.p. for 72 h. LPS (1 μg) or PBS was then injected i.p. and after 4 h mice were killed and peritoneal macrophages and spleen obtained for flow cytometry analysis.

In vivo macrophage infection. Lentiviruses encoding full-length mouse MT4-MMP, MT4-MMP E248A (catalytic inactive mutant), or GFP alone (mock) were generated as described[16]. Virus was i.p. injected into MT4-MMP$^{+/+}$ or MT4-MMP$^{-/-}$ mice at ~ 1×10^8 pfu ml^{-1}. After 5 days, cells were collected and analyzed by flow cytometry.

Flow cytometry. Blood and BM samples from killed mice were blocked for 15 min at 4 °C in PBS containing 5% BSA and a 1:100 dilution of anti-CD16/CD32 (24g2, BD Pharmingen, 553142). Samples were then stained for 30 min at 4 °C with anti-CD11b 647 (eBiosciences, 51-0112-82) or biotinylated (BD Pharmingen, 51.01712 J), anti-CD45 V450 (eBiosciences, 48-0451-82), anti-Ly6C FITC (BD Bioscience, 553104) or APC (BD Pharmingen, 560595), anti-CCR5 PE (eBioscience, 12.1951-12), and anti-CCR2 (Biolegend, 150607) primary antibodies and with streptavidin PE (BD Bioscience, 554061) secondary reagent. Erythrocytes in blood samples were lysed with FACS Lysis Solution (BD Biosciences, 349202) for 7 min at room temperature. Before gating, granulocytes were excluded by FCS/SSC. Peritoneal macrophages were collected on the indicated days after TG administration and blocked with BSA/anti-CD16/CD32. Macrophages were then stained for 30 min at 4 °C with anti-CD11b 647 (eBiosciences, 51-0112-82), anti-CD45 V450 (eBiosciences, 48-0451-82), anti-F4/80 Pe-Cy7 (Biolegend, 123114), anti-AIM (GeneTex, GTX37448), and anti-CD36 (Cascade BioScience, ABM-5525) antibodies; for quantification of dead cells, Hoechst 33258 (Sigma, 861405) was added 5 min previous to flow cytometry analysis. Data were acquired in a FACSCanto III cytometer (BD) and analyzed using FlowJo software (Tree Star).

Cell spreading assay. Peritoneal macrophages were plated onto fibrinogen-coated coverslips (500,000 cells per 12 mm-diameter coverslip) for 24 h, fixed with 4% paraformaldehyde for 10 min at room temperature, stained with phalloidin-texas red (Invitrogen, T-7471, 1:100) for 2 h, and mounted in Fluoromount-G (SouthernBiotech, 0100-01) containing Hoechst 33342. Images were acquired with a confocal microscope (Nikon A1R) fitted with an × 20 air objective. Images were processed and analyzed using Image J (https://imagej.nih.gov/ij/; National Institutes of Health).

Whole-mount staining of peritoneal membranes. Peritoneal membranes were collected 72 h after TG administration, cleaned under a dissecting microscope, and fixed with 4% paraformaldehyde overnight at 4 °C. Samples were blocked and permeabilized for 30 min at room temperature in PBS containing 0.1% Triton X-100, 5% BSA, 5% goat serum (Jackson, 005-000-001), and 1:100 anti-CD16/CD32 (24g2, BD Pharmingen, 553142). Samples were then incubated with anti-CD11b 647 (eBiosciences, 51-0112-82) overnight at 4 °C and mounted in Fluoromount-G (SouthernBiotech, 0100-01) containing Hoechst 33342. Images were acquired with an inverted confocal microscope (LSM700, Carl Zeiss) fitted with a × 10 air objective. Images were processed with Zen2009 Light Edition (Carl Zeiss), and quantified using Image J (https://imagej.nih.gov/ij/; National Institutes of Health).

Intravital microscopy in the cremaster muscle. Intravital microscopy in the cremaster muscle was performed as described[25]. Mice were anesthetized and the cremaster muscle was dissected free of surrounding tissues and exteriorized onto an optical clear viewing pedestal. The muscle was cut longitudinally with a cautery and held extended at the corners of the exposed tissue using surgical suture. To maintain the correct temperature and physiological conditions, the muscle was perfused continuously with warmed Tyrode's buffer. Four hours before surgery, animals were injected intrascrotally with 345 ng of CCL2 (Preprotech, 250–10)[66]. The cremasteric microcirculation was then observed using a Leica DM6000-FS intravital microscope fitted with an Apo × 40 NA 1.0 water-immersion objective and a DFC350-FX camera. LASAF software was employed for acquisition and image processing. Monocytes were stained by i.v. injection of CD115-PE (Biolegend, 135505) and Ly6C-APC (Biolegend, 128016), and in another set of experiments neutrophils were stained by injection of Ly6G-PE (BD Biosciences, 551461). Three-to-five randomly selected venules (25–40 μm diameter) were analyzed per mouse, and leukocyte-endothelium interaction was measured in 350 μm vessel segments for 5 min. When indicated, the αM integrin (Itgam) blocking antibody M1/70 (eBioscience, 16-0112) or IgG isotype control (eBioscience, 16-4031) was injected intravenously (4 mg kg^{-1}) before intravital microscopy[26].

Statistical analysis. All data are shown as mean ± SEM. Normal distribution of the values was checked and statistical analysis performed with Prism Software (GraphPad Prism 5) using the test indicated in the figure legend. Outlier values were excluded using the online GraphPad outlier test. Statistical significance was assigned at $^*p < 0.05$, $^{**}p < 0.01$, and $^{***}p < 0.001$.

Data availability. All relevant data are available from the authors upon request.

Received: 23 February 2017 Accepted: 7 February 2018
Published online: 02 March 2018

References

1. Hansson G. K. Regulation of immune mechanisms in atherosclerosis. *Ann. N. Y. Acad. Sci.* **947**, 157–165 (2001).
2. Hamers, A. A. et al. Bone marrow-specific deficiency of nuclear receptor Nur77 enhances atherosclerosis. *Circ. Res.* **110**, 428–438 (2012).
3. Hansson, G. K. & Hermansson, A. The immune system in atherosclerosis. *Nat. Immunol.* **12**, 204–212 (2011).
4. Randolph, G. J. The fate of monocytes in atherosclerosis. *J. Thromb. Haemost.* **7**, 28–30 (2009).
5. Chinetti-Gbaguidi, G., Colin, S. & Staels, B. Macrophage subsets in atherosclerosis. *Nat. Rev. Cardiol.* **12**, 10–17 (2015).
6. Robbins, C. S. et al. Local proliferation dominates lesional macrophage accumulation in atherosclerosis. *Nat. Med.* **19**, 1166–1172 (2013).
7. Soehnlein, O. et al. Distinct functions of chemokine receptor axes in the atherogenic mobilization and recruitment of classical monocytes. *EMBO Mol. Med.* **5**, 471–481 (2013).
8. Thomas, G., Tacke, R., Hedrick, C. C. & Hanna, R. N. Nonclassical patrolling monocyte function in the vasculature. *Arterioscler. Thromb. Vasc. Biol.* **35**, 1306–1316 (2015).
9. Lin, J., Kakkar, V. & Lu, X. Impact of matrix metalloproteinases on atherosclerosis. *Curr. Drug Targets* **15**, 442–453 (2014).
10. Newby, A. C. Matrix metalloproteinases regulate migration, proliferation, and death of vascular smooth muscle cells by degrading matrix and non-matrix substrates. *Cardiovasc. Res.* **69**, 614–624 (2006).
11. Itoh, Y. et al. Membrane type 4 matrix metalloproteinase (MT4-MMP, MMP-17) is a glycosylphosphatidylinositol-anchored proteinase. *J. Biol. Chem.* **274**, 34260–34266 (1999).
12. Sohail, A. et al. MT4-(MMP17) and MT6-MMP (MMP25), a unique set of membrane-anchored matrix metalloproteinases: properties and expression in cancer. *Cancer Metastas. Rev.* **27**, 289–302 (2008).
13. English, W. R. et al. Membrane type 4 matrix metalloproteinase (MMP17) has tumor necrosis factor-alpha convertase activity but does not activate pro-MMP2. *J. Biol. Chem.* **275**, 14046–14055 (2000).
14. Gauthier, M. C. et al. Expression of membrane type-4 matrix metalloproteinase (metalloproteinase-17) by human eosinophils. *Int J. Biochem Cell Biol.* **35**, 1667–1673 (2003).
15. Rikimaru, A. et al. Establishment of an MT4-MMP-deficient mouse strain representing an efficient tracking system for MT4-MMP/MMP-17 expression in vivo using beta-galactosidase. *Genes Cells* **12**, 1091–1100 (2007).
16. Martin-Alonso, M. et al. Deficiency of MMP17/MT4-MMP proteolytic activity predisposes to aortic aneurysm in mice. *Circ. Res.* **117**, e13–e26 (2015).
17. Hanna, R. N. et al. Patrolling monocytes control tumor metastasis to the lung. *Science* **350**, 985–990 (2015).
18. Ghosn, E. E. et al. Two physically, functionally, and developmentally distinct peritoneal macrophage subsets. *Proc. Natl Acad. Sci. USA* **107**, 2568–2573 (2010).
19. Gautier, E. L., Ivanov, S., Lesnik, P. & Randolph, G. J. Local apoptosis mediates clearance of macrophages from resolving inflammation in mice. *Blood* **122**, 2714–2722 (2013).
20. Stary, H. C. et al. A definition of advanced types of atherosclerotic lesions and a histological classification of atherosclerosis. A report from the Committee on Vascular Lesions of the Council on Arteriosclerosis, American Heart Association. *Arterioscler. Thromb. Vasc. Biol.* 15, 1512–1531 (1995).
21. Randolph, G. J. Mechanisms that regulate macrophage burden in atherosclerosis. *Circ. Res.* **114**, 1757–1771 (2014).

22. Kumar, S., Ratnikov, B. I., Kazanov, M. D., Smith, J. W. & Cieplak, P. CleavPredict: a platform for reasoning about matrix metalloproteinases proteolytic events. *PLoS ONE* **10**, e0127877 (2015).
23. Carlin, L. M. et al. Nr4a1-dependent Ly6C(low) monocytes monitor endothelial cells and orchestrate their disposal. *Cell* **153**, 362–375 (2013).
24. Charo, I. F. & Taubman, M. B. Chemokines in the pathogenesis of vascular disease. *Circ. Res* **95**, 858–866 (2004).
25. Rius, C. & Sanz, M. J. Intravital microscopy in the cremaster muscle microcirculation for endothelial dysfunction studies. *Methods Mol. Biol.* **1339**, 357–366 (2015).
26. Auffray, C. et al. Monitoring of blood vessels and tissues by a population of monocytes with patrolling behavior. *Science* **317**, 666–670 (2007).
27. Tacke, F. et al. Monocyte subsets differentially employ CCR2, CCR5, and CX3CR1 to accumulate within atherosclerotic plaques. *J. Clin. Invest* **117**, 185–194 (2007).
28. Hamada, M. et al. MafB promotes atherosclerosis by inhibiting foam-cell apoptosis. *Nat. Commun.* **5**, 3147 (2014).
29. Arai, S. et al. A role for the apoptosis inhibitory factor AIM/Spalpha/Api6 in atherosclerosis development. *Cell Metab.* **1**, 201–213 (2005).
30. Amezaga, N. et al. Human scavenger protein AIM increases foam cell formation and CD36-mediated oxLDL uptake. *J. Leukoc. Biol.* **95**, 509–520 (2014).
31. Pozo-Balado, M. M. et al. Maraviroc reduces the regulatory T-cell frequency in antiretroviral-naive HIV-infected subjects. *J. Infect. Dis.* **210**, 890–898 (2014).
32. Cipriani, S. et al. Efficacy of the CCR5 antagonist maraviroc in reducing early, ritonavir-induced atherogenesis and advanced plaque progression in mice. *Circulation* **127**, 2114–2124 (2013).
33. Hanna, R. N. et al. NR4A1 (Nur77) deletion polarizes macrophages toward an inflammatory phenotype and increases atherosclerosis. *Circ. Res.* **110**, 416–427 (2012).
34. Chao, L. C. et al. Bone marrow NR4A expression is not a dominant factor in the development of atherosclerosis or macrophage polarization in mice. *J. Lipid Res.* **54**, 806–815 (2013).
35. Thomas, G. D. et al. Deleting an Nr4a1 super-enhancer subdomain ablates Ly6Clow monocytes while preserving macrophage gene function. *Immunity* **45**, 975–987 (2016).
36. Randolph, G. J. Proliferating macrophages prevail in atherosclerosis. *Nat. Med.* **19**, 1094–1095 (2013).
37. Gautier, E. L., Jakubzick, C. & Randolph, G. J. Regulation of the migration and survival of monocyte subsets by chemokine receptors and its relevance to atherosclerosis. *Arterioscler. Thromb. Vasc. Biol.* **29**, 1412–1418 (2009).
38. Wu, H. et al. Functional role of CD11c+ monocytes in atherogenesis associated with hypercholesterolemia. *Circulation* **119**, 2708–2717 (2009).
39. Kunjathoor, V. V. et al. Scavenger receptors class A-I/II and CD36 are the principal receptors responsible for the uptake of modified low density lipoprotein leading to lipid loading in macrophages. *J. Biol. Chem.* **277**, 49982–49988 (2002).
40. Febbraio, M. & Silverstein, R. L. CD36: implications in cardiovascular disease. *Int J. Biochem. Cell Biol.* **39**, 2012–2030 (2007).
41. Schultze, J. L. Reprogramming of macrophages--new opportunities for therapeutic targeting. *Curr. Opin. Pharmacol.* **26**, 10–15 (2016).
42. Walzog, B. et al. A role for beta(2) integrins (CD11/CD18) in the regulation of cytokine gene expression of polymorphonuclear neutrophils during the inflammatory response. *FASEB J.* **13**, 1855–1865 (1999).
43. Almeida, P. E. et al. Differential TLR2 downstream signaling regulates lipid metabolism and cytokine production triggered by *Mycobacterium bovis* BCG infection. *Biochim. Biophys. Acta* **1841**, 97–107 (2014).
44. Fabbri, M. et al. Dynamic partitioning into lipid rafts controls the endo-exocytic cycle of the alphaL/beta2 integrin, LFA-1, during leukocyte chemotaxis. *Mol. Biol. Cell* **16**, 5793–5803 (2005).
45. Leitinger, B. & Hogg, N. The involvement of lipid rafts in the regulation of integrin function. *J. Cell Sci.* **115**, 963–972 (2002).
46. Zen, K. et al. Cleavage of the CD11b extracellular domain by the leukocyte serprocidins is critical for neutrophil detachment during chemotaxis. *Blood* **117**, 4885–4894 (2011).
47. Vaisar, T. et al. MMP-9 sheds the beta2 integrin subunit (CD18) from macrophages. *Mol. Cell Proteom.* **8**, 1044–1060 (2009).
48. Evans, B. J. et al. Shedding of lymphocyte function-associated antigen-1 (LFA-1) in a human inflammatory response. *Blood* **107**, 3593–3599 (2006).
49. Drbal, K. et al. A proteolytically truncated form of free CD18, the common chain of leukocyte integrins, as a novel marker of activated myeloid cells. *Blood* **98**, 1561–1566 (2001).
50. Sumagin, R., Prizant, H., Lomakina, E., Waugh, R. E. & Sarelius, I. H. LFA-1 and Mac-1 define characteristically different intralumenal crawling and emigration patterns for monocytes and neutrophils in situ. *J. Immunol.* **185**, 7057–7066 (2010).
51. Wang, W., Fu, G. & Luo, B. H. Dissociation of the alpha-subunit Calf-2 domain and the beta-subunit I-EGF4 domain in integrin activation and signaling. *Biochemistry* **49**, 10158–10165 (2010).
52. Cao, C., Lawrence, D. A., Strickland, D. K. & Zhang, L. A specific role of integrin Mac-1 in accelerated macrophage efflux to the lymphatics. *Blood* **106**, 3234–3241 (2005).
53. Merched, A., Tollefson, K. & Chan, L. Beta2 integrins modulate the initiation and progression of atherosclerosis in low-density lipoprotein receptor knockout mice. *Cardiovasc. Res.* **85**, 853–863 (2010).
54. Yakubenko, V. P., Bhattacharjee, A., Pluskota, E. & Cathcart, M. K. alphaMbeta(2) integrin activation prevents alternative activation of human and murine macrophages and impedes foam cell formation. *Circ. Res.* **108**, 544–554 (2011).
55. Nageh, M. F. et al. Deficiency of inflammatory cell adhesion molecules protects against atherosclerosis in mice. *Arterioscler. Thromb. Vasc. Biol.* **17**, 1517–1520 (1997).
56. Methia, N., Andre, P., Denis, C. V., Economopoulos, M. & Wagner, D. D. Localized reduction of atherosclerosis in von Willebrand factor-deficient mice. *Blood* **98**, 1424–1428 (2001).
57. Orr, A. W. et al. The subendothelial extracellular matrix modulates NF-kappaB activation by flow: a potential role in atherosclerosis. *J. Cell Biol.* **169**, 191–202 (2005).
58. Imhof, B. A. et al. CCN1/CYR61-mediated meticulous patrolling by Ly6Clow monocytes fuels vascular inflammation. *Proc. Natl Acad. Sci. USA* **113**, E4847–E4856 (2016).
59. Shi, C. et al. Integrin engagement regulates monocyte differentiation through the forkhead transcription factor Foxp1. *J. Clin. Invest.* **114**, 408–418 (2004).
60. Cuevas, V. D. et al. MAFB determines human macrophage anti-inflammatory polarization: relevance for the pathogenic mechanisms operating in multicentric carpotarsal osteolysis. *J. Immunol.* **198**, 2070–2081 (2017).
61. Michaud, J. P., Bellavance, M. A., Prefontaine, P. & Rivest, S. Real-time in vivo imaging reveals the ability of monocytes to clear vascular amyloid beta. *Cell Rep.* **5**, 646–653 (2013).
62. Jung, S. et al. Analysis of fractalkine receptor CX(3)CR1 function by targeted deletion and green fluorescent protein reporter gene insertion. *Mol. Cell Biol.* **20**, 4106–4114 (2000).
63. Mendez-Barbero, N. et al. A major role for RCAN1 in atherosclerosis progression. *EMBO Mol. Med* **5**, 1901–1917 (2013).
64. Yang, J. et al. The I-TASSER Suite: protein structure and function prediction. *Nat. Methods* **12**, 7–8 (2015).
65. Alford, R. F. et al. An integrated framework advancing membrane protein modeling and design. *PLoS Comput. Biol.* **11**, e1004398 (2015).
66. Tan, J. H. et al. Tyrosine sulfation of chemokine receptor CCR2 enhances interactions with both monomeric and dimeric forms of the chemokine monocyte chemoattractant protein-1 (MCP-1). *J. Biol. Chem.* **288**, 10024–10034 (2013).

Acknowledgements

We thank Ángel Colmenar and Laura Balonga for technical support, the BioBanco VIH (Hospital Gregorio Marañón, Madrid) for providing essential reagents, and Simon Bartlett for English editing. This study was supported by grants from the Spanish Ministry of Economy, Industry and Competitiveness (MEIC; RD12/0042/0023 [FEDER cofunded] and SAF2014-52050R and SAF2017-83229R to A.G.A., SAF2015-64287R and SAF2015-71878-REDT to M.R., RD12/0042/0053 [FEDER cofunded] and SAF2015-64767-R to J.M-G., and SAF2016-79490-R and RD12/0042/0028 [FEDER cofunded] to V.A.) and from La Marató TV3 Foundation. C.C., M.M-A., and L.A-H. were funded by fellowships from the Spanish Ministry of Education, MEIC, and La Caixa-CNIC, respectively. C.R. was funded by a competitive postdoctoral contract grant FPDI-2013-17423 from MEIC. The CNIC is supported by the Spanish MEIC and the Pro-CNIC Foundation, and is a Severo Ochoa Center of Excellence (MEIC award SEV-2015-0505).

Author contributions

C.C. performed and analyzed most of AT and macrophage experiments. A.P. and R.A. M. performed and analyzed some AT experiments in *Ldlr*$^{-/-}$ and BM-transplanted *Ldlr*$^{-/-}$ mice. V.N. helped with BM transplants and Oil Red aorta analysis. C.R. performed and analyzed intravital microscopy experiments. L.A.-H. performed and analyzed qPCR. M.M.-A. helped in digestion assays. E.C. performed and analyzed mass spectrometry experiments. F.M. performed in silico protein modeling. C.R. and J. M-G. analyzed human samples. M.S. provided MT4-MMP-deficient mice. V.A. supervised

intravital microscopy assays. M.R. provided *Ldlr*$^{-/-}$ and Cx3cr1$^{Gfp/+}$ mice, and critical suggestions. A.G.A. designed and supervised the research and wrote the paper.

Additional information

Supplementary Information accompanies this paper at https://doi.org/10.1038/s41467-018-03351-4.

Competing interests: The authors declare no competing interests.

Reprints and permission information is available online at http://npg.nature.com/reprintsandpermissions/

Publisher's note: Springer Nature remains neutral with regard to jurisdictional claims in published maps and institutional affiliations.

Article

SOURCE DATA | TRANSPARENT PROCESS | OPEN ACCESS

EMBO Molecular Medicine

Endothelial MT1-MMP targeting limits intussusceptive angiogenesis and colitis via TSP1/nitric oxide axis

Sergio Esteban[1], Cristina Clemente[1,2], Agnieszka Koziol[1], Pilar Gonzalo[1], Cristina Rius[1,3], Fernando Martínez[4], Pablo M Linares[5], María Chaparro[5], Ana Urzainqui[6], Vicente Andrés[1,3], Motoharu Seiki[7], Javier P Gisbert[5] & Alicia G Arroyo[1,2,*]

Abstract

Pathological angiogenesis contributes to cancer progression and chronic inflammatory diseases. In inflammatory bowel disease, the microvasculature expands by intussusceptive angiogenesis (IA), a poorly characterized mechanism involving increased blood flow and splitting of pre-existing capillaries. In this report, mice lacking the protease MT1-MMP in endothelial cells (MT1$^{i\Delta EC}$) presented limited IA in the capillary plexus of the colon mucosa assessed by 3D imaging during 1% DSS-induced colitis. This resulted in better tissue perfusion, preserved intestinal morphology, and milder disease activity index. Combined *in vivo* intravital microscopy and lentiviral rescue experiments with *in vitro* cell culture demonstrated that MT1-MMP activity in endothelial cells is required for vasodilation and IA, as well as for nitric oxide production via binding of the C-terminal fragment of MT1-MMP substrate thrombospondin-1 (TSP1) to CD47/αvβ3 integrin. Moreover, TSP1 levels were significantly higher in serum from IBD patients and *in vivo* administration of an anti-MT1-MMP inhibitory antibody or a nonamer peptide spanning the αvβ3 integrin binding site in TSP1 reduced IA during mouse colitis. Our results identify MT1-MMP as a new actor in inflammatory IA and a promising therapeutic target for inflammatory bowel disease.

Keywords inflammatory bowel disease; intussusceptive angiogenesis; MT1-MMP; nitric oxide; TSP1

Subject Categories Digestive System; Immunology; Vascular Biology & Angiogenesis

DOI 10.15252/emmm.201910862 | Received 10 May 2019 | Revised 5 November 2019 | Accepted 8 November 2019

EMBO Mol Med (2019) e10862

Introduction

The vasculature delivers oxygen and nutrients to all tissues and must constantly and dynamically adapt to tissue needs. Angiogenesis, the formation of new capillaries from pre-existing vessels, is required to expand the vasculature not only during development and tissue repair, but also in pathological conditions such as cancer and chronic inflammatory disease (Potente *et al*, 2011). In these contexts, the newly formed vasculature is often marginally functional and leaky, contributing to disease progression (De Bock *et al*, 2011; Parma *et al*, 2017). Angiogenesis often occurs by capillary sprouting, which is mainly triggered by hypoxia and the subsequent production of vascular endothelial growth factor (VEGF). New therapeutic interventions in cancer and other diseases have therefore focused on inhibiting sprouting angiogenesis, mostly by blocking VEGF (Potente *et al*, 2011). However, the development of resistance to this approach and its overall limited success have shifted attention to the possible existence of alternative modes of capillary expansion (Ribatti & Djonov, 2012).

Intussusceptive angiogenesis (IA) was formally recognized in the 1980s and involves the expansion of the microvasculature through the formation of intraluminal pillars, eventually resulting in capillary splitting (Burri *et al*, 2004). IA contributes to the physiological expansion of capillary beds during embryonic development and postnatal coronary vasculature remodeling (van Groningen *et al*, 1991; Djonov *et al*, 2000). IA also occurs in certain cancers and chronic diseases such as bronchopulmonary dysplasia, in which IA generates an aberrant and dysfunctional vasculature that may contribute to disease progression (Ribatti & Djonov, 2012; Giacomini *et al*, 2015; De Paepe *et al*, 2017). Sprouting and intussusception angiogenesis mechanisms can co-exist in pathophysiological settings (Konerding *et al*, 2012; Karthik *et al*, 2018).

1 Vascular Pathophysiology Area, Centro Nacional de Investigaciones Cardiovasculares (CNIC), Madrid, Spain
2 Centro de Investigaciones Biológicas (CIB-CSIC), Madrid, Spain
3 CIBER de Enfermedades Cardiovasculares (CIBER-CV), Madrid, Spain
4 Bioinformatics Unit, Centro Nacional de Investigaciones Cardiovasculares (CNIC), Madrid, Spain
5 Gastroenterology Unit, Hospital Universitario de La Princesa, Instituto de Investigación Sanitaria Princesa (IIS-IP), Centro de Investigación Biomédica en Red de Enfermedades Hepáticas y Digestivas (CIBER-EHD), Universidad Autónoma de Madrid, Madrid, Spain
6 Immunology Department, FIB-Hospital Universitario de La Princesa, Instituto de Investigación Sanitaria Princesa (IIS-IP), Madrid, Spain
7 Division of Cancer Cell Research, Institute of Medical Science, University of Tokyo, Tokyo, Japan
*Corresponding author. Tel: +34 91 837 31 12; Fax: +34 91 536 04 32; E-mail: agarroyo@cib.csic.es

IA is a dynamic, fast, and metabolically undemanding process that barely involves proliferation but instead progresses through intraluminal endothelial cell rearrangements (Burri *et al*, 2004). IA is usually driven by a persistent increase in blood flow, and it aimed to restore shear stress in the split vessels (Styp-Rekowska *et al*, 2011). However, knowledge is scarce about the cellular and molecular mechanisms underlying IA. This is partly due to the absence of *in vitro* models of IA and the limited experimental techniques to identify and quantify genuine IA events *in vivo*, apart from scanning electron microscopy and corrosion casts (Nowak-Sliwinska *et al*, 2018). Nevertheless, genes whose expression is enriched during IA have been identified in skeletal muscle, in which the vasodilator prazosin induces IA and the excision of the agonist muscle, sprouting angiogenesis (Zhou *et al*, 1998; Egginton, 2011). Upregulated genes in skeletal muscle of prazosin-treated mice included endothelial nitric oxide synthase (eNOS) and neuropilin-1 (Nrp1), suggesting a role for these pathways in IA. Analysis of eNOS (*Nos3*)-deficient mice confirmed that eNOS is required for IA but not for sprouting angiogenesis in skeletal muscle (Williams *et al*, 2006); more recently, nitric oxide (NO) has been shown to contribute to pathological IA in tumors (Vimalraj *et al*, 2018). Advanced microscopy techniques and increasing knowledge about endothelial cell responses to blood flow have together favored the recent characterization of the IA modulators endoglin and ephrinB2/EphB4 (Hlushchuk *et al*, 2017; Groppa *et al*, 2018). However, it remains unclear how these pathways are regulated and contribute to IA, particularly during disease.

IA is the mechanism of capillary expansion during intestinal inflammation, and analysis of chemically induced murine colitis (e.g., with dextran sodium sulfate; DSS) has advanced knowledge about the morphogenesis and hemodynamics underlying inflammatory IA (Mori *et al*, 2005; Ravnic *et al*, 2007; Filipovic *et al*, 2009; Konerding *et al*, 2010). These studies show that mechanical forces and changes in intraluminal blood flow drive IA and that a marked vasodilation occurs during the first stages of IA during colitis, before complete duplication of the mucosal plexus (Filipovic *et al*, 2009; Konerding *et al*, 2010). The DSS mouse model of colitis recapitulates some of the features of human inflammatory bowel disease (IBD), a chronic inflammatory disease of the intestine comprising ulcerative colitis and Crohn's disease and characterized by phases of remission and relapse (Podolsky, 2002). IBD is a multifactorial disease featuring a primary defect in intestinal epithelial barrier integrity and an exacerbated immune response to the microbiota and for which there is as yet no universal and efficient therapy (Gyires *et al*, 2014). As in other chronic inflammatory diseases, colitis progression is believed to involve angiogenesis, which is therefore regarded as a potential treatment target for human IBD (Chidlow *et al*, 2006; Koutroubakis *et al*, 2006; Danese, 2007). Attempts have been made to reduce angiogenesis and reduce colitis symptoms by targeting diverse molecular pathways, such as VEGF, TSP1/CD36, and CD40-CD40L, with limited success (Danese *et al*, 2007a,b; Punekar *et al*, 2008; Scaldaferri *et al*, 2009). There is therefore a need to decipher the molecular pathways involved in colitis-associated IA in order to design more rational therapeutic strategies.

During colitis, epithelial and mesenchymal cells, as well as other cell types, increase expression of MT1-MMP (Pender *et al*, 2000; te Velde *et al*, 2007; Alvarado *et al*, 2008), a membrane-anchored matrix metalloproteinase whose activity contributes to sprouting angiogenesis *in vitro* and *in vivo* through the combined processing of substrates such as TSP1, NID1, and CYR61 (Galvez *et al*, 2001, 2005; Koziol *et al*, 2012a). MT1-MMP also has non-proteolytic actions that contribute to the regulation of Rac1 or HIF1α signaling (Koziol *et al*, 2012b). MT1-MMP is expressed in endothelial cells (ECs) at low levels in homeostatic conditions, but it is upregulated by the pro-inflammatory cytokines TNFα and interleukin-1 (Rajavashisth *et al*, 1999; Koziol *et al*, 2012a). Despite the important role of MT1-MMP in sprouting angiogenesis, the potential contribution of endothelial MT1-MMP to IA, particularly in the context of inflammation and IBD, has not been explored previously.

In the present study, the analysis of mice specifically lacking MT1-MMP in ECs identified this protease as an actor in inflammation-driven IA whose endothelial targeting results in preserved vasculature and amelioration of colitis. Deciphering the underlying MT1-MMP/TSP1/αvβ3 integrin/NO molecular axis opens avenues for the development of new diagnostic and therapeutic interventions in IBD.

Results

MT1-MMP is required for intussusceptive angiogenesis (IA) in DSS-induced colitis

To investigate the possible role of MT1-MMP (gene name *MMP14*) in inflammation-driven IA, we used the DSS-induced colitis model, a widely recognized model of IA (Konerding *et al*, 2010). We first assessed MT1-MMP expression in ECs of the mucosa vasculature in the colon by tracking β-gal expression in $MT1^{lacZ/+}$ reporter mice. In non-treated mice, nuclear β-gal expression was present in ECs in the vessels nearby the muscularis mucosa but was barely detected in those of the mucosal plexus, the polygonal capillary network around the colonic crypts. Treatment of mice with 1% DSS significantly increased the proportion of endothelial cells expressing β-gal in the mucosal plexus after 3 days with a remaining augmented trend at 7 days (Appendix Fig S1A and B). Patches of β-gal-positive ECs were frequently detected near the Y-junctions (tri-corners) in the mucosal vascular plexus (Appendix Fig S1C). MT1-MMP was deleted in the ECs of $MT1\text{-}MMP^{f/f}$;*Cdh5*Cre^{ERT2} mice ($MT1^{i\Delta EC}$) mice by daily injections of 4-hydroxy-tamoxifen (4-OHT) for 5 days; 4-OHT injections began 3 days before DSS treatment. Isolated lung ECs were examined to confirm efficient recombination of the floxed *Mmp14* allele and the absence of MT1-MMP mRNA (Fig EV1A–C). MT1-MMP expression was also reduced in the colonic capillaries from $MT1^{i\Delta EC}$ mice examined at 7 days post-DSS (Fig EV1D).

To test the effect of prophylactic endothelial MT1-MMP deletion on DSS-induced IA, we implemented a 3D imaging method based on high-resolution confocal microscopy and Imaris® image analysis of whole-mount CD31-stained mouse intestine; this method allowed us to quantify holes in the vascular tri-corners indicating intraluminal pillars as well as capillary loops and duplications in the mucosal plexus, all hallmarks of IA (Fig EV2A). We also measured capillary bifurcation angles in the mucosal plexus, which decrease during IA (Fig EV2B; Ackermann *et al*, 2013). DSS-induced mild colitis in $MT1^{f/f}$;*Cdh5*Cre^{ERT2}-negative ($MT1^{f/f}$) control mice was associated with significantly increased IA events (holes, loops, and duplications) and smaller capillary bifurcation angles at 3 days compared

with non-treated mice (Fig 1A–C). Of note, MT1$^{i\Delta EC}$ mice showed significantly reduced numbers of DSS-induced IA capillary events (holes, loops, and duplications) at 3 and 7 days compared with MT1$^{f/f}$ mice (Fig 1A and B); intercapillary angles were also preserved in the colon mucosal plexus of MT1$^{i\Delta EC}$ mice at 3 days post-DSS treatment (Fig 1C). These findings identify MT1-MMP as a novel endothelial actor in inflammatory IA.

Loss of endothelial MT1-MMP preserves intestinal vascular perfusion and ameliorates colitis

To investigate the impact of inflammatory IA on vascular function, we analyzed vessel perfusion by intravascular injection of isolectin B4 (IB4). Perfusion decreased during colitis progression in the mucosa vascular plexus of both MT1$^{f/f}$ and MT1$^{i\Delta EC}$ mice, but it was significantly better preserved in the latter at 7 days post-1% DSS treatment (Fig 2A and B). Furthermore, 1% DSS induced vascular leakage at days 3 and 7 in the colonic mucosa of MT1$^{f/f}$ mice and at a lower extent in MT1$^{i\Delta EC}$ mice (Appendix Fig S2A).

Treatment with 1% DSS produced only subtle alterations in the intestinal mucosa after 3 days, but at 7 days, hematoxylin and eosin histology revealed better preservation of colon morphology in MT1$^{i\Delta EC}$ mice, showing fewer areas of crypt destruction than control mice (Fig 2C). Second-harmonic generation (SHG) microscopy confirmed the presence of well-structured collagen fibers surrounding crypts in MT1$^{i\Delta EC}$ mice at 7 days post-DSS, contrasting with abundant and disorganized collagen fibers in control mice (Fig 2D), an additional sign of enhanced tissue damage and fibrosis. To estimate disease severity over the 7 days of 1% DSS treatment, we calculated the disease activity index (DAI), based on a composite of weight loss, stool consistency, and hemorrhage (see Methods). The DAI was significantly lower in MT1$^{i\Delta EC}$ mice than in MT1$^{f/f}$ controls

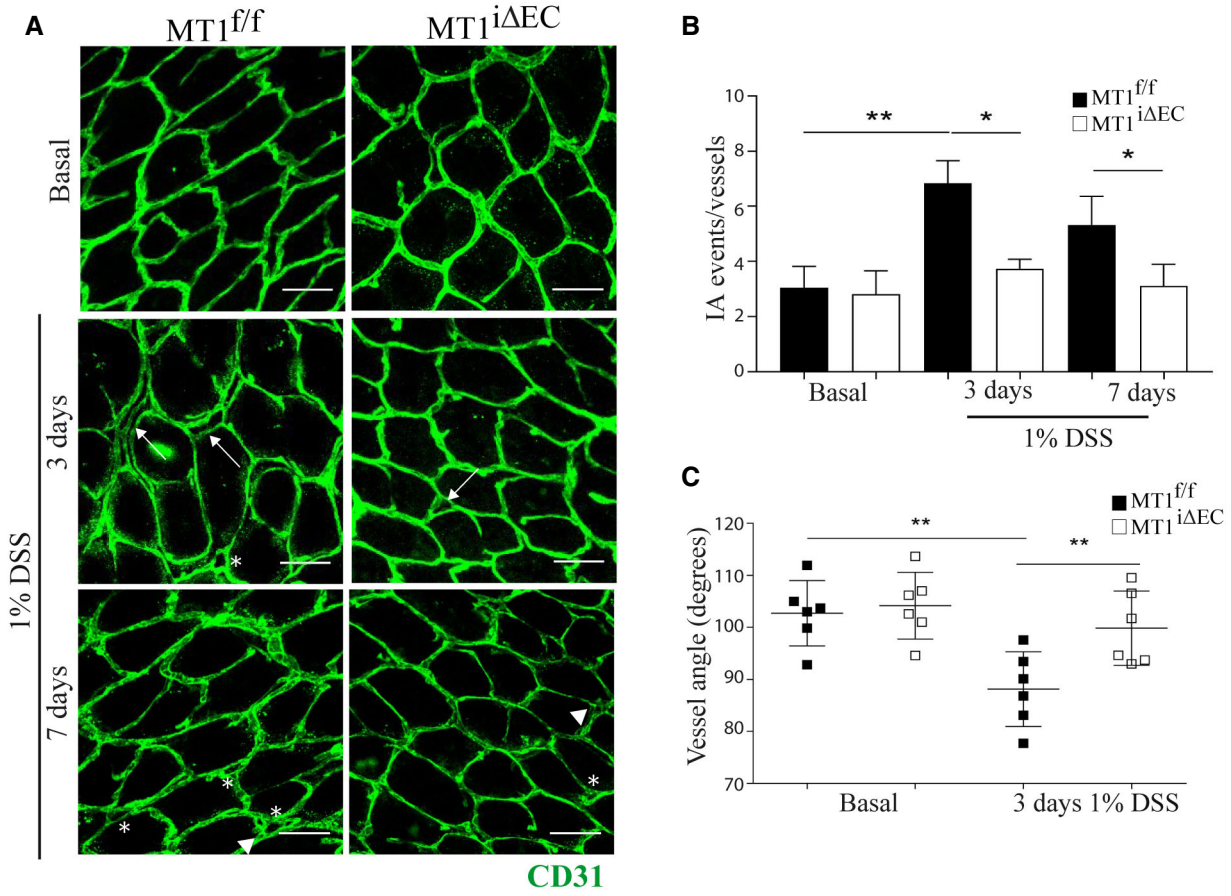

Figure 1. MT1-MMP expression in endothelial cells contributes to intussusceptive angiogenesis in colitis.

A Representative maximum-intensity projection images of colon mucosal plexus in CD31-stained (green) whole-mount distal colon from MT1$^{f/f}$ and MT1$^{i\Delta EC}$ mice left untreated (basal) or treated with 1% DSS for 3 or 7 days. Scale bar, 40 μm. Arrows, arrowheads, and asterisks indicate duplications, loops, and pillars, respectively.

B Quantification of IA events in the colon mucosal plexus of mice treated as in (A), including vascular holes, duplications, and loops; n = 9–15 mice per genotype and condition. Data are shown as mean ± SEM and were tested by one-way ANOVA with Benjamini and Hochberg post-test; *$P < 0.05$, **$P < 0.01$.

C Quantification of vascular angles at the Y-junctions in the colon mucosal plexus of mice left untreated or treated with 1% DSS for 3 days; n = 6 mice per genotype and condition. Data are shown as mean ± SEM and additionally as individual animal values and were tested by one-way ANOVA with Benjamini and Hochberg post-test; **$P < 0.01$.

Data information: Please see Appendix Table S3 for exact P-values.
Source data are available online for this figure.

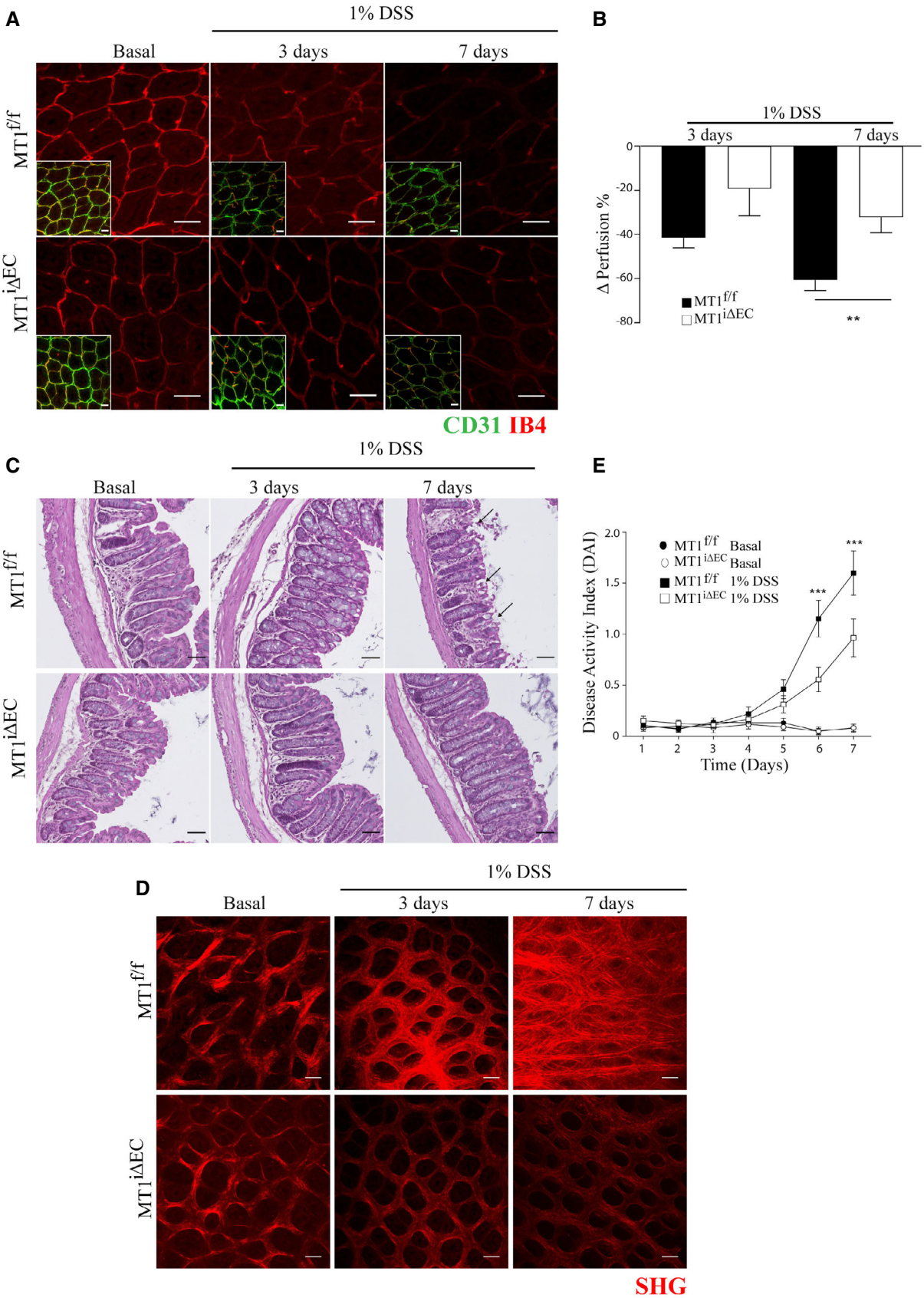

Figure 2.

Figure 2. MT1-MMP absence from endothelial cells limits deterioration of vascular perfusion and impedes colitis progression.

A Representative maximum-intensity projection images of whole-mount distal colons stained for CD31 (green) and IB4 (red) in $MT1^{f/f}$ and $MT1^{i\Delta EC}$ mice left untreated (basal) or treated with 1% DSS for 3 or 7 days. Scale bar, 40 μm.

B Perfusion decreased during 1% DSS-induced colitis in $MT1^{f/f}$ and $MT1^{i\Delta EC}$ mice; n = 8–12 mice per genotype and condition. Data are shown as mean ± SEM and were tested by one-way ANOVA with Benjamini and Hochberg post-test; $^{**}P < 0.01$.

C Representative H&E-stained colon sections from $MT1^{f/f}$ and $MT1^{i\Delta EC}$ mice left untreated (basal) or treated with 1% DSS for 3 or 7 days. Arrows indicate crypt destruction. Scale bar, 50 μm.

D Representative second-harmonic generation (SHG) microscopy images of mucosal plexus in whole-mount colons from $MT1^{f/f}$ or $MT1^{i\Delta EC}$ mice left untreated (basal) or treated with 1% DSS for 3 or 7 days. Scale bar, 40 μm.

E Disease activity index (DAI, a composite of weight change, stool consistency, and presence of fecal blood) during 1% DSS-induced colitis in $MT1^{f/f}$ and $MT1^{i\Delta EC}$ mice. Untreated mice were included as a control. n = 19–24 per genotype and condition. Data are shown as mean ± SEM and were tested by two-way ANOVA with Benjamini and Hochberg post-test; $^{***}P < 0.001$.

Data information: Please see Appendix Table S3 for exact *P*-values.
Source data are available online for this figure.

from DSS day 5 onward, indicating milder disease in the absence of endothelial MT1-MMP (Fig 2E). Numbers of $CD11b^+$ leukocytes (mostly neutrophils and monocytes) did not differ between genotypes at DSS day 3, when IA was already decreased in $MT1^{i\Delta EC}$ mice; in contrast, at DSS day 7, $CD11b^+$ leukocyte numbers in $MT1^{i\Delta EC}$ mice showed a slight but significant reduction compared with $MT1^{f/f}$ controls (Appendix Fig S2B and C). Thus, endothelium-specific MT1-MMP deletion improves 1% DSS-induced colitis progression primarily through an early impact on IA events at 3 days rather than on vascular perfusion, leukocyte traffic, and tissue alterations modulated at 7 days.

In light of these results, we next tested the therapeutic action of endothelial MT1-MMP deletion on colitis progression. Mice received five daily 4-OHT injections beginning 4 days after the initiation of 1% DSS treatment, and mice were sacrificed at DSS day 15. Therapeutic endothelial MT1-MMP deletion during established colitis significantly reduced weight loss and DAI from day 9 onward compared with $MT1^{f/f}$ control mice (Fig EV3).

MT1-MMP expression in ECs is required for vasodilation and NO production

The cellular and molecular mechanisms underlying IA are poorly defined, but there is a general consensus that it is initiated by changes in hemodynamic forces and increased blood flow (Filipovic *et al*, 2009). To investigate the role of endothelial MT1-MMP in this early step of IA that involves vasodilation (Fig 3A), we relied on intravital microscopy of the cremaster muscle and monitored arteriole vasodilation by injecting acetylcholine (ACh), which triggers EC NO secretion (Rius & Sanz, 2015; Fig 3B–D). No differences between genotypes were observed in arteriole diameter (~ 30 μm) at baseline (Fig 3C, and Movies EV1 and EV2); in contrast, maximal Ach-induced vasodilation (reached 3 min after injection) was significantly impaired in arterioles of $MT1^{i\Delta EC}$ mice compared with $MT1^{f/f}$ controls (Fig 3D, and Movies EV1 and EV2). Given the observation of IA events in colon mucosal plexus capillaries, we also analyzed the capillaries in the cremaster muscle. The diameter of cremaster capillaries did not increase in $MT1^{i\Delta EC}$ mice after Ach injection; however, this impaired response was rescued by i.v. injection of the NO donor DEANO (Fig 3E and F). These results suggest that impaired vasodilation in MT1-MMP-null ECs may be due to decreased NO production. Low NO production was confirmed by DAF-FM analysis of aortic endothelial cells (MAEC) isolated from $MT1^{i\Delta EC}$ mice (Appendix Fig S3). Furthermore, human umbilical vein endothelial cells (HUVEC) expressing MT1-MMP-targeting siRNA (siMT1) not only produced significantly lower amounts of NO (Fig 4A) but also expressed lower amounts of eNOS protein and eNOS (*Nos3*) mRNA than corresponding control ECs (Fig 4B–D).

We next implemented a protocol to assess VEGF-induced vasodilation of the colon mucosal plexus by its administration via a rectal cannula to get closer to the pathophysiology of IA during colitis (Fig EV4A and B). As shown in Fig EV4C and D, the diameter of the mucosa plexus capillaries was significantly reduced in VEGF-treated $MT1^{i\Delta EC}$ mice compared to $MT1^{f/f}$ controls.

MT1-MMP catalytic activity is required for NO production and colitis-induced IA

To determine whether inflammatory IA regulation by MT1-MMP depends on its catalytic or signaling activities (Gonzalo *et al*, 2010; Koziol *et al*, 2012a), $MT1^{f/f}$;*Cdh5*Cre^{ERT2} mice were inoculated with lentivirus (LV) encoding full-length (FL) MT1-MMP or mutated versions that abolish its catalytic (E240A) or signaling (Y573F) activities. Daily 4-OHT injections to delete endogenous endothelial MT1-MMP were started 72 h after LV injection, and 1% DSS treatment was initiated 3 days later (Fig 5A and B). Western blot analysis of GFP expression confirmed similar transduction levels in the colon regardless of the injected LV (Fig 5C). LV encoding FL and Y573F MT1-MMP increased IA events 3 days post-DSS to levels comparable to those observed in LV-mock-injected $MT1^{f/f}$ mice, whereas LV encoding E240A MT1-MMP had no effect and injected mice showed similar numbers of IA events than LV-mock-injected $MT1^{i\Delta EC}$ mice (Fig 5D–F). These results demonstrate that IA induced by 1% DSS colitis requires the catalytic activity of MT1-MMP.

MT1-MMP cleavage of TSP1 drives EC NO production

We next tested the effect of the inhibitory antibody anti-MT1-MMP LEM-2/15 (Galvez *et al*, 2001) on NO production. The inhibitory LEM-2/15 antibody significantly reduced NO amount in HUVEC transfected with control siRNA (siControl) in comparison with non-treated or isotype control-treated cells, whereas the antibody had no effect on NO production by siMT1-silenced HUVEC (Appendix Fig S4A). MT1-MMP catalytic activity is thus also required for EC NO production, which likely acts upstream of inflammatory IA (Williams *et al*, 2006).

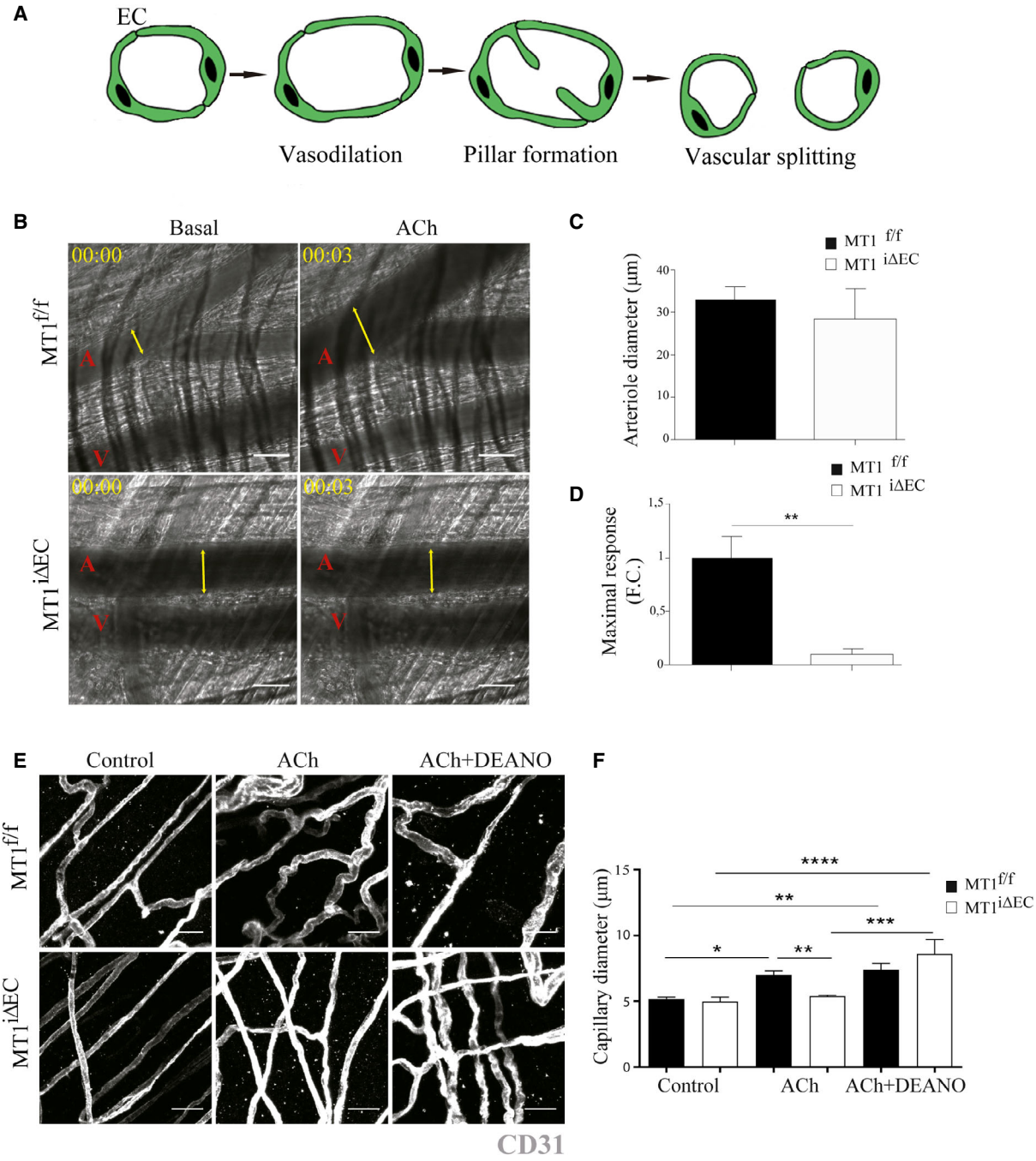

Figure 3. Endothelial cell MT1-MMP expression is required for nitric oxide-dependent vasodilation *in vivo*.

A Scheme showing IA process including vasodilatation, pillar formation, and vascular splitting. EC, endothelial cell.

B Representative intravital microscopy images of cremaster muscle from $MT1^{f/f}$ or $MT1^{i\Delta EC}$ mice before and 15 min after i.v. injection of 100 μl of 100 μM acetylcholine (ACh). A and V mark arterioles and venules, respectively, and yellow arrows indicate arteriole diameter. Elapsed time is designated as hh:mm. Scale bar, 30 μm.

C, D Cremaster arteriole diameter in basal conditions (C) and the maximum vasodilation response (diameter fold change) after 3 min of ACh stimulation (D); n = 5–6 mice per genotype. Data are shown as mean ± SEM and were tested by paired t-test; $^{**}P < 0.01$.

E Representative images of staining for CD31 (gray) in whole-mount cremaster muscle dissected from $MT1^{f/f}$ or $MT1^{i\Delta EC}$ mice before and 15 min after i.v. injection of 100 μl of 100 μM ACh alone or in combination with DEANO (100 μl of 10^{-4} M). Scale bar, 25 μm.

F Quantification of capillary diameter in mice analyzed as in (E); n = 5–8 mice per genotype and condition. Data are shown as mean ± SEM and were tested by one-way ANOVA with Benjamini and Hochberg post-test; $^{*}P < 0.05$, $^{**}P < 0.01$, $^{***}P < 0.001$, $^{****}P < 0.0001$.

Data information: Please see Appendix Table S3 for exact P-values.
Source data are available online for this figure.

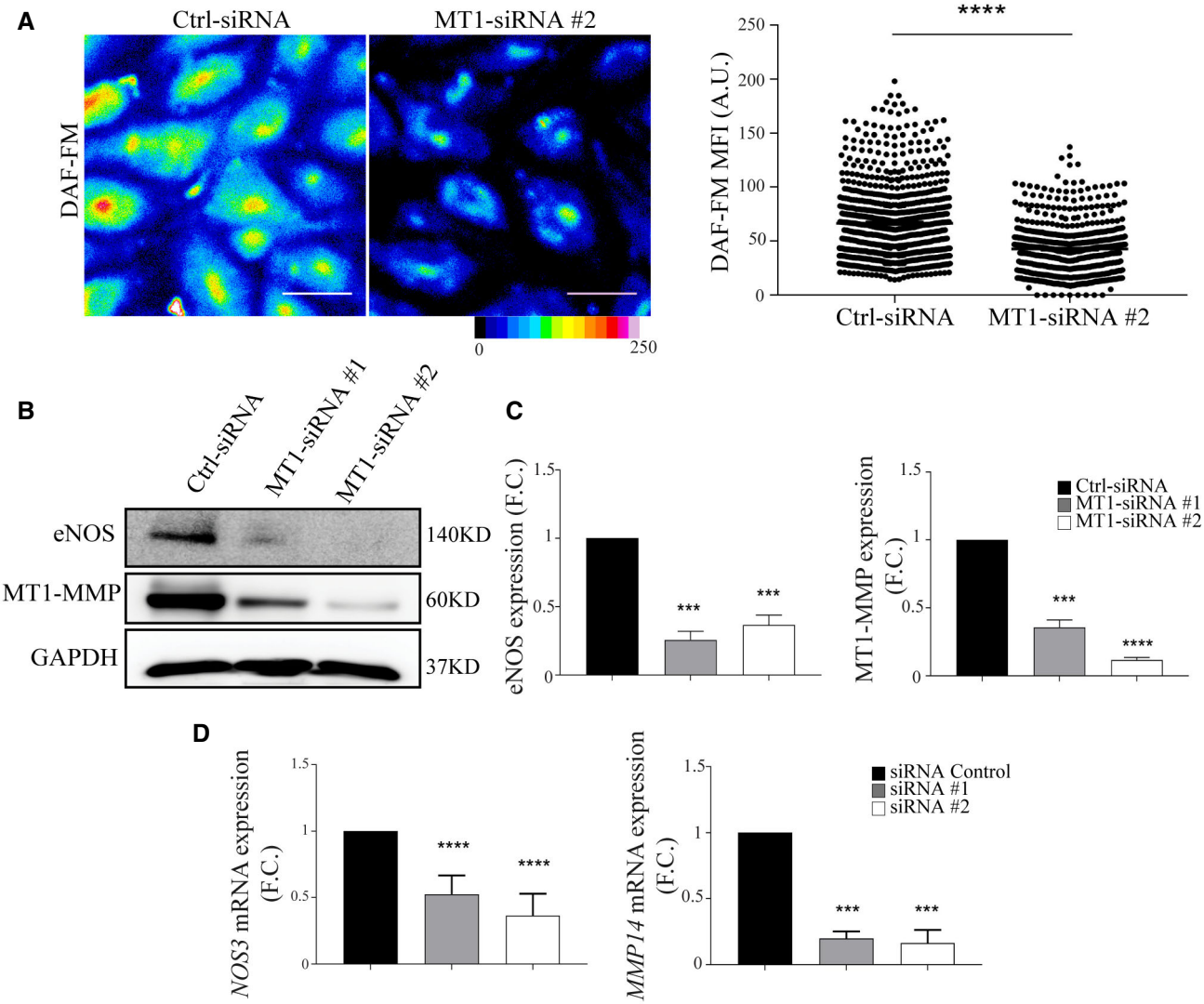

Figure 4. Decreased nitric oxide production and eNOS expression in MT1-MMP-silenced human endothelial cells.

A Representative pseudo-colored microscopy images of DAF-FM (4-amino-5-methylamino-2′,7′-difluorofluorescein diacetate) fluorescence intensity in human endothelial cells (HUVEC) expressing control or MT1-MMP siRNA (left); scale bar, 50 μm. The graph to the right shows DAF-FM mean fluorescence intensity (MFI) values obtained in n = 637–879 cells analyzed per condition in six independent experiments. Data are shown as individual cell values and mean ± SEM and were tested by the Mann–Whitney test; ****$P < 0.0001$.

B, C Representative Western blot of eNOS and MT1-MMP in HUVEC expressing control or different MT1-MMP siRNAs; GAPDH is included as a loading control (B). Bar graphs (C) show relative eNOS and MT1-MMP expression (vs. GAPDH); n = 5 independent experiments. Data are shown as mean ± SEM and were tested by one-sample t-test; ***$P < 0.001$, ****$P < 0.0001$.

D qPCR analysis of relative eNOS (*NOS3*) and MT1-MMP (*MMP14*) mRNA levels in HUVEC expressing control or MT1-MMP siRNAs; n = 4 independent experiments. F.C., fold change. Data are shown as mean ± SEM and were tested by one-sample t-test; ***$P < 0.001$, ****$P < 0.0001$.

Data information: Please see Appendix Table S3 for exact P-values.
Source data are available online for this figure.

Several angiogenesis pathways, including mechanisms involving eNOS, are suppressed by the matricellular protein thrombospondin-1 (TSP1) through its binding to CD36 (nM affinity) and/or CD47/IAP (pM affinity) (Lawler & Lawler, 2012; Resovi *et al*, 2014). We had previously identified TSP1 as a master MT1-MMP substrate and showed that loss of MT1-MMP reduced TSP1 release in TNFα-stimulated ECs (Koziol *et al*, 2012a). In the context of colitis, TSP1 serum levels increased after 7 days of 1% DSS treatment (20.27 ± 11.84 pg/ml in control vs. 37.04 ± 1.21 pg/ml in treated mice) and we sought to analyze the impact of endothelial MT1-MMP in such release. For that, we examined TSP1 intestinal distribution in DSS-treated mice, using an antibody against a sequence near the TSP1 N-terminus (Lee *et al*, 2006). Immunostained sections revealed that 1% DSS treatment upregulated TSP1 expression in the mouse colon after 3 days (Fig 6A and B). Moreover, image analysis demonstrated that TSP1 was significantly accumulated forming a

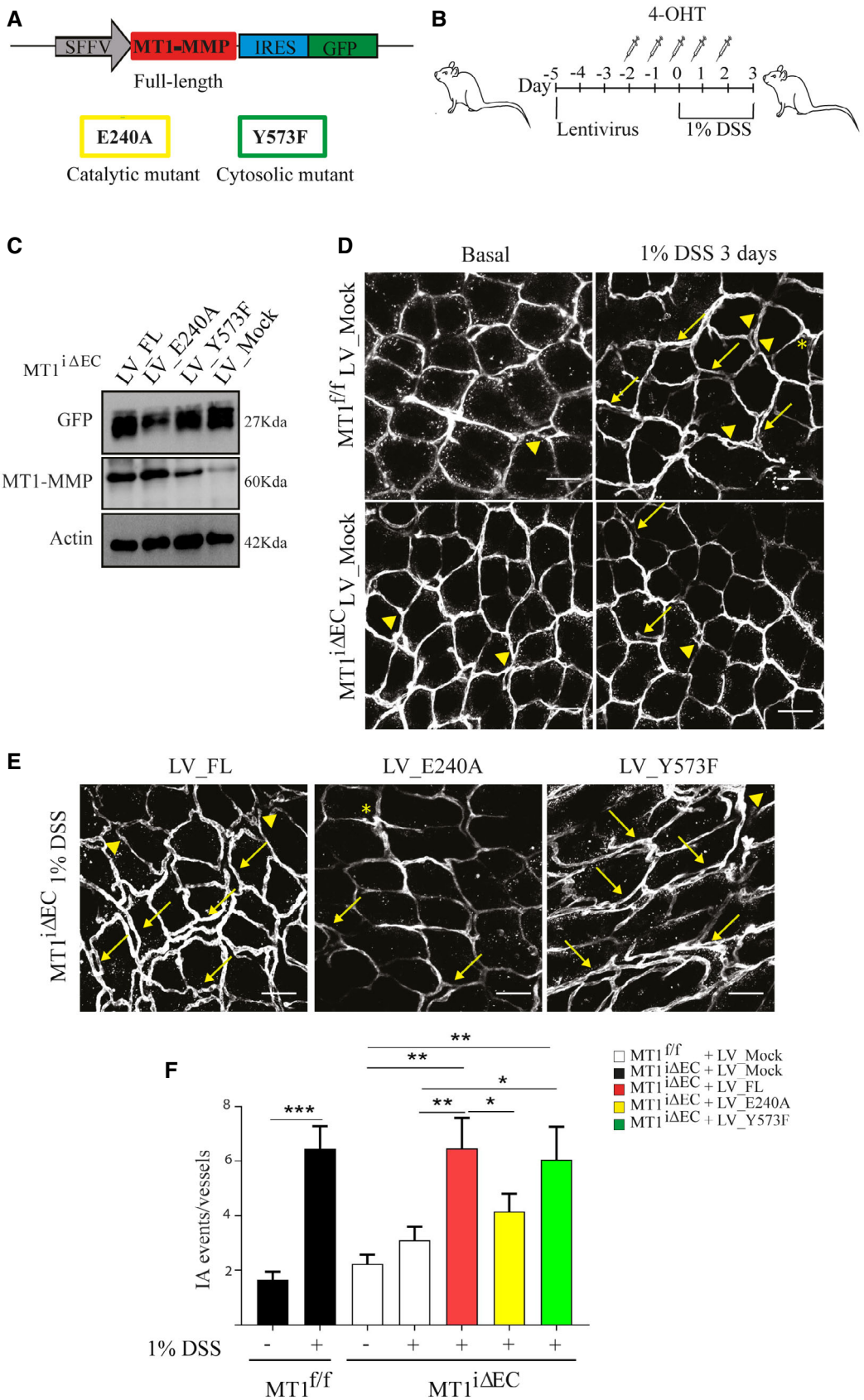

Figure 5.

Figure 5. MT1-MMP actions in intussusceptive angiogenesis during colitis depend on its catalytic activity.

A Lentivirus (LV) construct used to drive expression of MT1-MMP (*MMP14*) and green fluorescent protein (GFP) under the SFFV and IRES promoters, respectively. The point mutations introduced to obtain the catalytic (E240A) and signaling (Y573F) mutants are indicated.

B Experimental design for i.v. lentiviral injection in mice and induction of mild colitis with 1% DSS.

C Western blot of GFP and MT1-MMP protein expression in colon lysates from $MT1^{i\Delta EC}$ mice previously injected with mock LV or LV encoding full-length MT1-MMP or the E240A or Y573F mutants; mice were sacrificed 3 days after 1% DSS treatment. Actin is included as a loading control.

D, E Representative maximum-intensity projection images of staining for CD31 (gray) in whole-mount colons from $MT1^{f/f}$ or $MT1^{i\Delta EC}$ mice previously injected with mock LV (D) or LV encoding full-length MT1-MMP or the E240A or Y573F mutants (E); mice were sacrificed 3 days after 1% DSS treatment. Scale bar, 40 μm. Arrows, arrowheads, and asterisks indicate duplications, loops, and pillars, respectively.

F Quantification of IA events in mice treated as in (D and E); n = 5–8 mice per genotype and condition. Data are shown as mean ± SEM and were tested by one-way ANOVA with Benjamini and Hochberg post-test; $^{*}P < 0.05$, $^{**}P < 0.01$, $^{***}P < 0.001$.

Data information: Please see Appendix Table S3 for exact *P*-values.
Source data are available online for this figure.

thick cuff around MT1-MMP-negative vessels of the colon mucosa nearby the muscularis mucosa in $MT1^{i\Delta EC}$ mice compared with less TSP1 abundance around the MT1-MMP-expressing corresponding vessels in $MT1^{f/f}$ mice (Fig 6B and C). These data indicate that endothelial MT1-MMP contributes to perivascular TSP1 processing in the intestine.

TSP1 also accumulated in siMT1-silenced HUVEC (Fig 7A), related to defective TSP1 processing in the absence of the protease (Koziol *et al*, 2012a). Moreover, culture on TSP1-coated plates increased NO production in siControl-HUVEC significantly more than in siMT1-silenced HUVEC, suggesting that signals mediated by processed TSP1 contribute to increased NO production in MT1-MMP-expressing ECs (Appendix Fig S4B). Accordingly, we detected an N-terminal TSP1 fragment of about 50 KD in lysates from MT1-MMP-expressing HUVEC whose abundance was reduced in MT1-MMP-silenced cells, and we confirmed that TSP1 cleavage by the MT1-MMP catalytic domain yielded that N-terminal fragment by *in vitro* digestion assays (Fig EV5A and B). To decipher how MT1-MMP-mediated TSP1 processing affects NO production, we combined a CleavPredict search (Kumar *et al*, 2015) with *in silico* protein modeling. This approach identified positions $H^{441}W$ and $P^{467}Q$ in TSP1 as having good accessibility and proximity to the protease catalytic pocket, suggesting them as candidate sites for MT1-MMP cleavage (Appendix Table S1, and Fig EV5C and D), and consistent with the N-terminal TSP1 fragment observed in HUVEC lysates and by *in vitro* digestion (Fig EV5A and B). Moreover, the amino acids flanking the predicted cleavage sites (P1′:P1 positions) had high MEROPS database scores (4:1 and 8:6 for $H^{441}W$ and $P^{467}Q$ sites, respectively; https://www.ebi.ac.uk/merops/). Cleavage of TSP1 by MT1-MMP at $H^{441}W$ and/or $P^{467}Q$ would likely disrupt the CD36-binding motifs and generate a C-terminal fragment with preserved binding sites for CD47/IAP and its partner αvβ3 integrin (Lindberg *et al*, 1996), which would mediate MT1-MMP-dependent NO production in ECs. To directly validate this hypothesis, we investigated the effect of the E123CaG-1 human TSP1 fragment (aa 549–1,170; Margosio *et al*, 2008) spanning most of the predicted C-terminal TSP1 fragment after MT1-MMP processing (441/467–1,170) and containing CD47 and αvβ3 integrin binding sites. We confirmed that the E123CaG-1 TSP1 fragment induced NO production in MT1-MMP-deficient HUVEC compared with full-length TSP1 (Fig EV5E).

Interaction between CD47 and TSP1 influences NO signaling (Rogers *et al*, 2014), and we found that an anti-CD47 antibody known to block CD47 interaction with the C-terminal TSP1 domain reduced NO production by MT1-expressing ECs but had no further effect on NO production by siMT1-silenced HUVEC (Fig 7B). To determine whether CD47-driven effects involve the activity of its partner αvβ3 integrin, we blocked αvβ3 integrin binding to TSP1 with an inhibitory anti-αv integrin antibody, an RGDS peptide, or cilengitide (based on the cyclic peptide cyclo-RGDfV). All three strategies significantly decreased NO production by MT1-expressing ECs; in contrast, these treatments had negligible impact on the already reduced NO production by siMT1-silenced cells (Fig 7B–D). Similarly, NO production by siControl- and siMT1-transduced cells was unaffected by the control peptide RADS or isotype control IgG. The RGDS peptide can compete for αvβ3 integrin binding to several matrix proteins; therefore, to test for a specific effect via TSP1, we tested the effect on NO production by ECs of a selective nonamer spanning the RGD binding site for αvβ3 integrin in TSP1. The nonamer GDGRGDACK, but not the control peptide GDGRADACK, reduced NO production in MT1-MMP-expressing endothelial cells but not in siMT1-silenced cells (Fig 7E).

MT1-MMP/TSP1 signaling provides a possible diagnostic and therapeutic target in IBD

To explore the possible implications of endothelial MT1-MMP-mediated TSP1 processing in patients with IBD, we first checked MT1-MMP and TSP1 vascular expression and distribution in unaffected and affected colon areas of patients suffering from ulcerative colitis or Crohn's disease. Immunostaining on colon sections revealed more abundant capillaries in affected vs. unaffected areas that were accompanied by MT1-MMP and TSP1 upregulated expression and distinct tissue distribution; MT1-MMP was mainly located in CD31-positive vessels of the inflamed intestine while TSP1 was sparse around these vessels and mostly expressed by spiky cells resembling macrophages (Fig 8A). Since TSP1 was stained with the monoclonal antibody A6.1, which recognizes an epitope downstream of the predicted TSP1 cleavage sites for MT1-MMP (Annis *et al*, 2006), this pattern is consistent with TSP1 cleavage by endothelial MT1-MMP during DSS-induced colitis leading to TSP1 paucity around MT1-MMP-expressing vessels in $MT1^{f/f}$ mice (Fig 6B and C) and to its release to the serum. We then quantified serum TSP1 in a cohort of IBD patients scored for clinical activity, including ≥ 50 patients with ulcerative colitis or with Crohn's disease. Remarkably, TSP1 was significantly more abundant in the serum from patients with mildly active (but not with highly active) ulcerative colitis or Crohn's disease compared to healthy controls

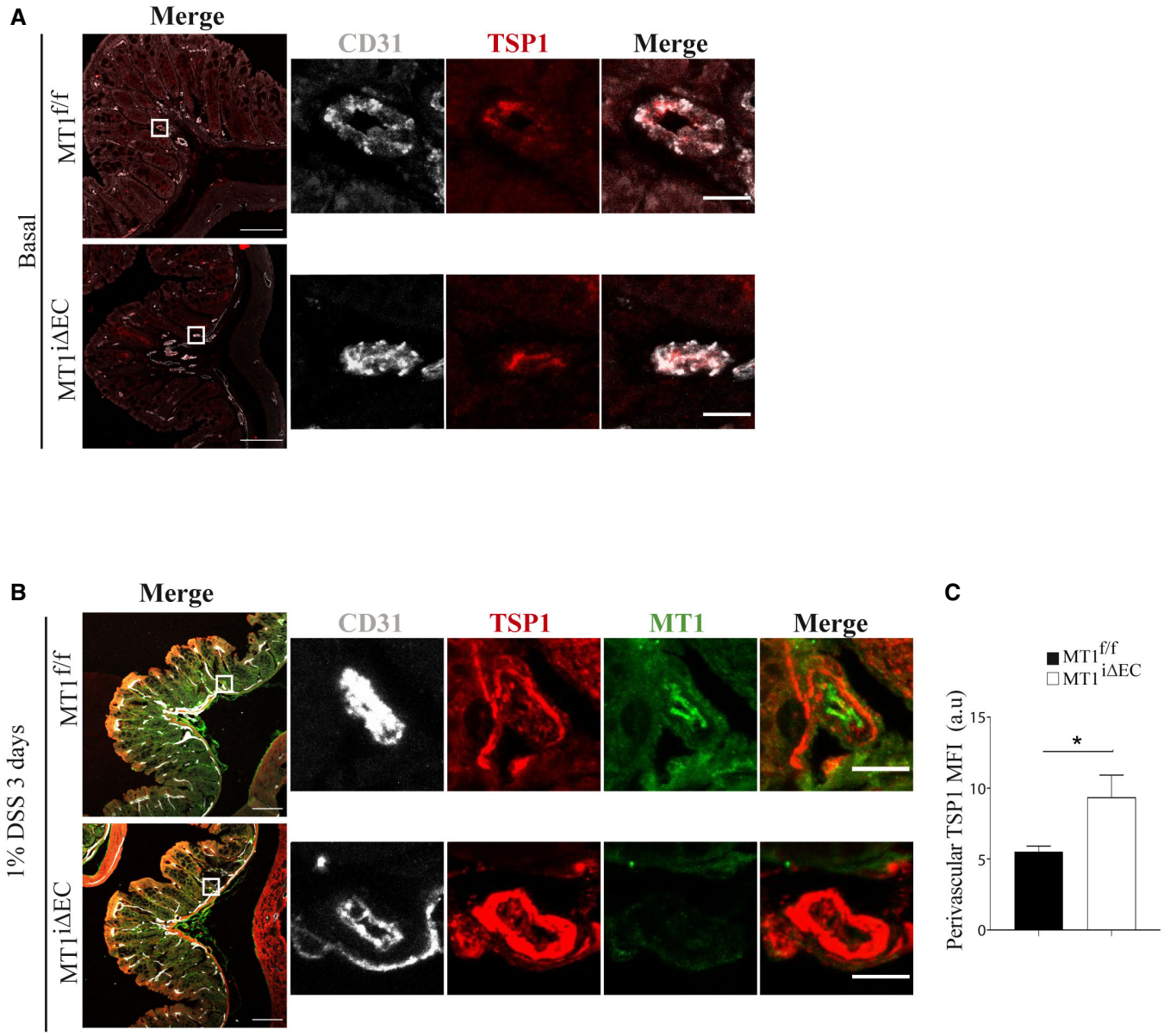

Figure 6. MT1-MMP absence in endothelial cells leads to perivascular accumulation of thrombospondin-1 (TSP1) in the inflamed colon.

A, B Representative maximum-intensity projection images of staining for TSP1 (red) and CD31 (gray) in (A) and also for MT1-MMP (green) in (B) in colon sections obtained from $MT1^{f/f}$ and $MT1^{i\Delta EC}$ mice left untreated (A) or treated with 1% DSS for 3 days (B). Magnified views are shown to the right. Scale bars, 100 μm in main panels and 10 μm in the magnified views.

C TSP1 mean fluorescence intensity (MFI) in the perivascular area of large vessels present in the colon mucosa of treated mice, as depicted in (B); $n = 4$ mice per genotype. Data are shown as mean ± SEM and were tested by *t*-test; $^*P < 0.05$.

Data information: Please see Appendix Table S3 for exact *P*-values.
Source data are available online for this figure.

(Fig 8B). This finding thus suggests that serum TSP1 may be a biomarker of early or mild IBD.

To evaluate the relevance of the MT1-MMP/TSP1/nitric oxide pathway in colitis *in vivo*, we first injected intraperitoneally the C-terminal E123CaG-1 TSP1 fragment (containing CD47 and αvβ3 integrin binding sites) into $MT1^{i\Delta EC}$ mice and observed that it significantly increased the number of IA events 3 days post-1% DSS treatment compared with mice treated with full-length TSP1 (Fig EV5F and G). Contrarily, blocking the generation of the TSP1 fragment by intraperitoneal injection of the anti-MT1-MMP inhibitory antibody LEM-2/15 significantly decreased the number of IA events in the mucosal plexus and conserved well-organized collagen fibers in $MT1^{f/f}$ control mice after 3 days of 1% DSS treatment compared to isotype control-treated mice (Fig 8C–E). Given our

finding that αvβ3 integrin binding to TSP1 drives NO production in ECs *in vitro*, we finally investigated the therapeutic potential of this pathway by selectively blocking this interaction *in vivo* and checking the impact on IA and colitis. MT1$^{f/f}$ control mice were fitted with subcutaneous minipumps allowing continuous release of a high dose of the TSP1 nonamer GDGRGDACK or the control

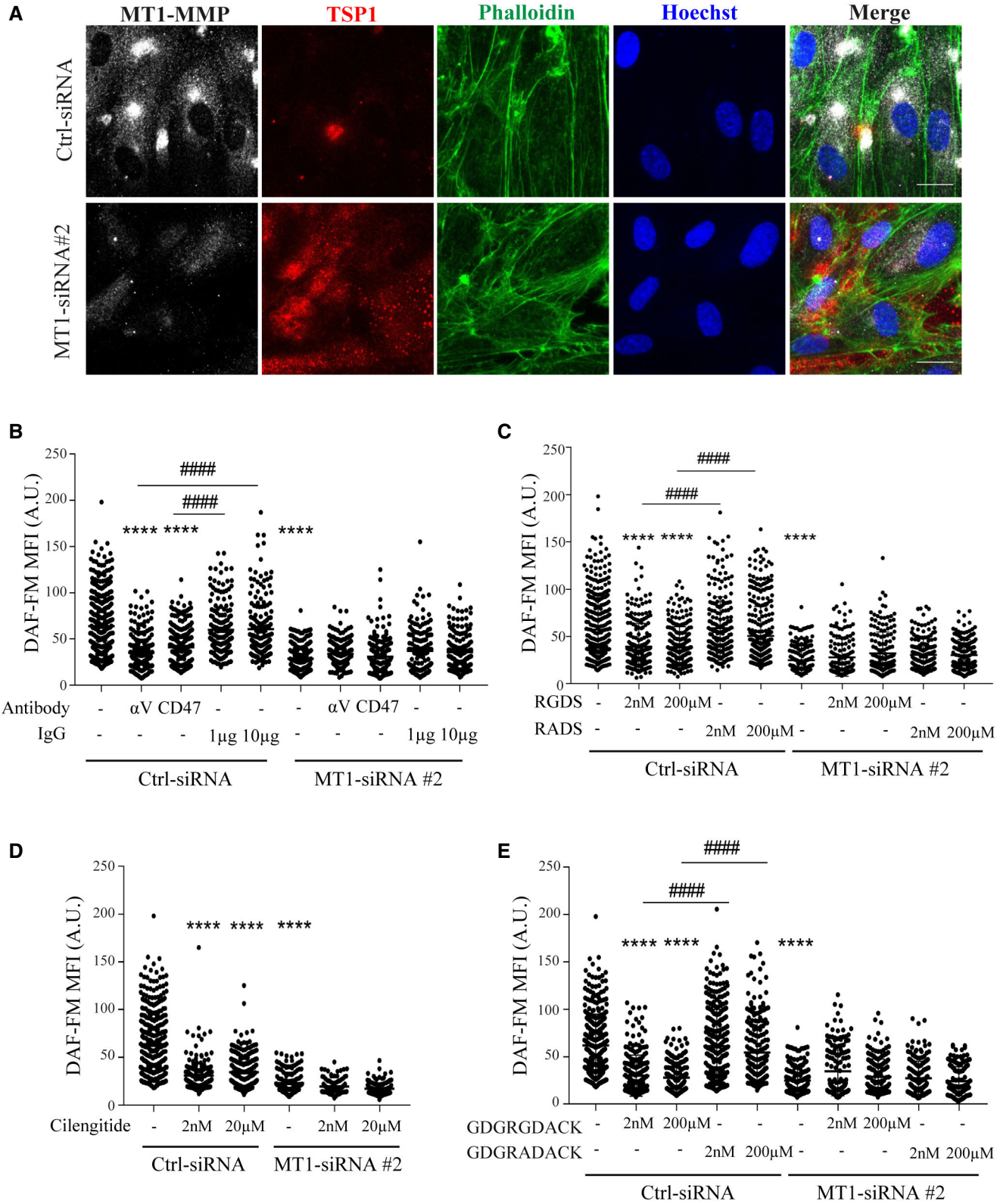

Figure 7.

Figure 7. Binding of TSP1 to CD47/IAP and αvβ3 integrin regulates nitric oxide production in MT1-MMP-expressing endothelial cells.

A Representative maximum-intensity projection images of HUVEC expressing control or MT1-MMP siRNA and stained for MT1-MMP (gray), TSP1 (red), and F-actin (phalloidin, green); nuclei are stained with Hoechst (blue). Scale bar, 20 μm.

B DAF-FM mean fluorescence intensity (MFI) in HUVEC expressing control or MT1-MMP siRNA and left untreated or treated with blocking anti-CD47 or anti-αv integrin antibodies (1 and 10 μg/ml, respectively, for 24 h) or their corresponding IgG isotype controls (IgG); n = 149–360 cells analyzed per condition in three independent experiments.

C DAF-FM mean fluorescence intensity (MFI) in HUVEC expressing control or MT1-MMP siRNA and left untreated or treated with 2 nM or 200 μM RGDS or its control peptide RADS; n = 147–385 cells analyzed per condition in three independent experiments.

D DAF-FM mean fluorescence intensity (MFI) in HUVEC expressing control or MT1-MMP siRNA and left untreated or treated with 2 nM or 20 μM of the RGD cyclic peptide cilengitide; n = 100–360 cells analyzed per condition in three independent experiments.

E DAF-FM mean fluorescence intensity (MFI) in HUVEC expressing control or MT1-MMP siRNA and left untreated or treated with 2 nM or 200 μM of the nonamer GDGRGDACK or its control peptide GDGRADACK; n = 149–337 cells analyzed per condition in three independent experiments.

Data information: Data are shown in all panels as individual cell values and mean ± SEM and were tested by the Kruskal–Wallis test; ****$P < 0.0001$, $^{\#\#\#\#}P < 0.0001$. * indicates comparison with Ctrl-siRNA, and # indicates comparison of the condition with its corresponding control. Please see Appendix Table S3 for exact P-values.
Source data are available online for this figure.

GDGRADACK (equivalent dose of 2.4 mg/mouse/day). Mice were then administered 1% DSS for 3 days, and colonic IA events were analyzed after sacrifice. Mice treated with the TSP1-nonamer GDGRGDACK had significantly fewer IA events than mice treated with the control peptide (Fig 8F and G). The reduced IA in GDGRGDACK-treated mice also resulted in better-preserved collagen fiber organization assessed by second-SHG microscopy (Fig 8H).

Discussion

In this study, we identify the protease MT1-MMP as an endothelial actor in IA, particularly during the pathogenesis of inflammatory colitis. Our results point to NO production via an MT1-MMP/TSP1/integrin αvβ3/eNOS pathway as the MT1-MMP catalytic-dependent mechanism underlying vasodilation during this mode of angiogenesis (Fig 9). Evidence from human samples confirms that this pathway is active in IBD, and blockade of DSS-induced colitis in mice with an MT1-MMP inhibitory antibody or a TSP1-targeting peptide indicates the potential of this strategy to improve IBD.

Our work also establishes that confocal microscopy of vessel-stained whole-mount colons combined with 3D-image rendering provides sufficient resolution to identify and quantify capillary holes/pillars, loops, and duplications, all hallmarks of IA, circumventing the limitations of other techniques (Nowak-Sliwinska *et al*, 2018). The use of this imaging approach in fluorescent reporter mouse lines may allow the detection of intraluminal pillars and determination of the contribution of other cell types to pathophysiological IA.

The EC-autonomous functions of MT1-MMP *in vivo* have remained poorly defined due to the unavailability, until recently, of conditionally deficient mice (Klose *et al*, 2013; Tang *et al*, 2013; Gutierrez-Fernandez *et al*, 2015; Rafii *et al*, 2015). Our results demonstrate that the specific absence of MT1-MMP in ECs decreases the number of IA events early during 1% DSS-induced mild colitis in mice and ameliorates the disease. These early IA events occur when only a minor inflammatory infiltrate is present, suggesting that the 1% DSS mild colitis model may be especially suited to dissecting the vascular IA response independently of inflammation (Chidlow *et al*, 2006). Our data also indicate that MT1-MMP endothelial targeting could be useful in other conditions that involve pathological IA, such as cancer (Ribatti & Djonov, 2012) and also bronchopulmonary dysplasia of the pre-term lung, in light of the reported role of MT1-MMP in postnatal lung expansion (De Paepe *et al*, 2017; Oblander *et al*, 2005).

Regarding the mechanism by which MT1-MMP contributes to IA and colitis, our results show that MT1-MMP EC deficiency results in decreased NO-dependent vasodilation of cremaster muscle arterioles and capillaries *in vivo* and establish that MT1-MMP catalytic activity is required for NO production by ECs *in vitro*, regulating both eNOS protein and mRNA levels. Our data therefore confirm a pathogenic role for endothelial NO in colitis in line with Beck *et al* (Beck *et al*, 2004) and contrasting its reported healing and protection actions, which are likely related to an impact on cell types other than the endothelium (Sasaki *et al*, 2003; Aoi *et al*, 2008). The dependence on endothelial MT1-MMP of colon mucosa capillary vasodilation induced by VEGF, a driver of IA and recognized activator or nitric oxide production (Cooke & Losordo, 2002), underscores the relevance of this pathway in colitis pathophysiology.

MT1-MMP may play a dual, bimodal role via NO production during IA initiation and progression. MT1-MMP-driven NO production will primarily increase blood flow in the arterioles and therefore in the downstream capillary plexus, promoting vessel splitting. This is supported by the predominant constitutive expression of MT1-MMP in arteriolar ECs rather than in the colonic mucosa capillaries. But MT1-MMP is upregulated after DSS treatment in the ECs of the mucosal plexus particularly near the Y-junctions where IA events often occur. At these sites, blood flow gradients and decreased shear stress lead to intraluminal pillar formation by undefined mechanisms (Filipovic *et al*, 2009). MT1-MMP may also drive NO production at these sites, which could then contribute to intraluminal EC rearrangements and pillar formation. Accordingly, lack of NO actions in the skeletal muscle led to reduced numbers of intraluminal filopodia, ultimately hampering cell rearrangements needed for capillary splitting (Williams *et al*, 2006). NO is also induced and required during shear stress-driven angiogenesis (Kolluru *et al*, 2010) and can regulate EC junction remodeling and directional migration (Noiri *et al*, 1998; Kevil *et al*, 2004; Thibeault *et al*, 2010; Di Lorenzo *et al*, 2013). We previously showed that NO in turn regulates MT1-MMP activity during EC migration (Genis *et al*, 2007), and our new findings thus define an additional layer of feedback NO regulation during this process.

MT1-MMP actions can rely on its catalytic or signaling capabilities (Koziol *et al*, 2012b). Although we cannot exclude a

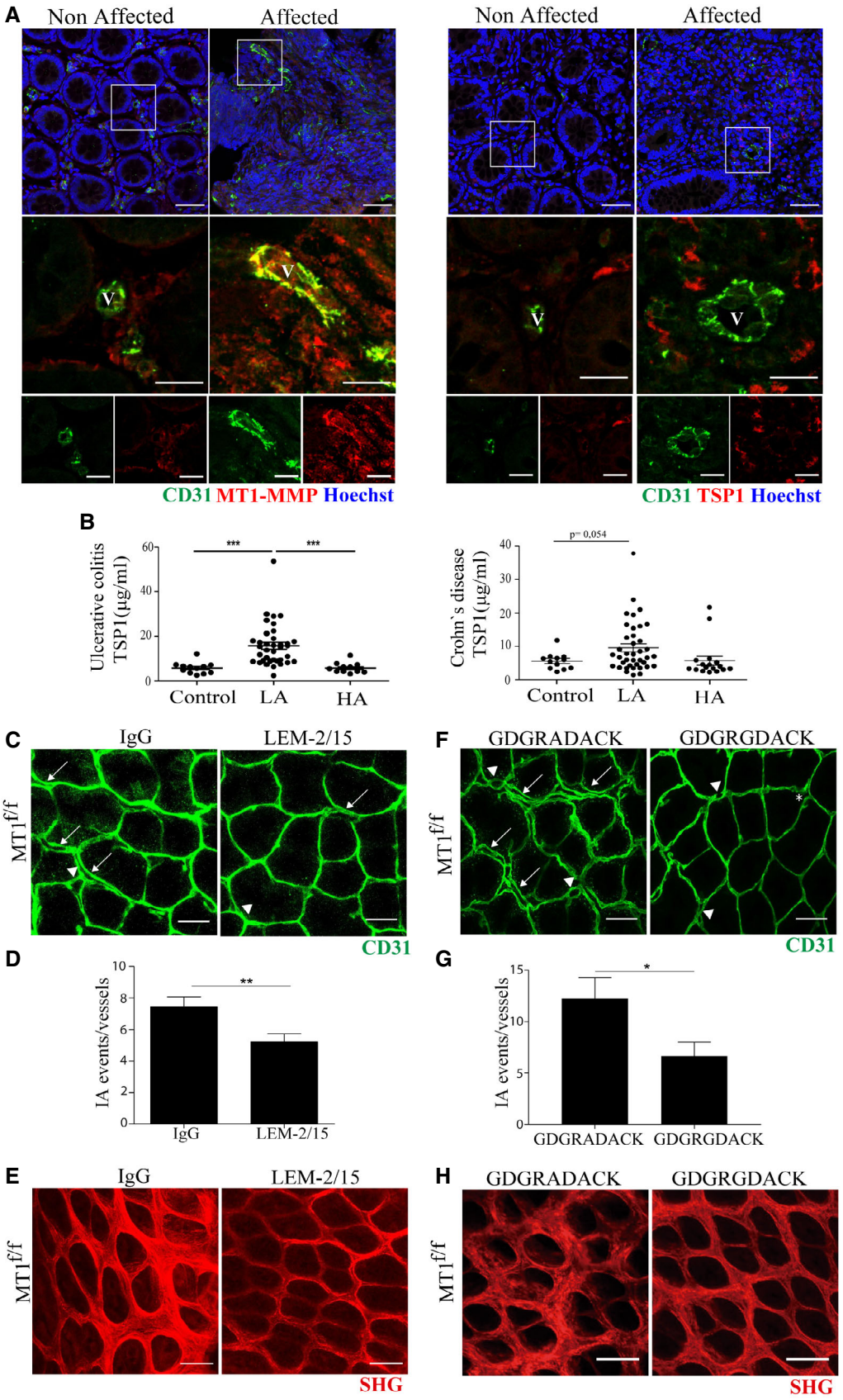

Figure 8.

Figure 8. The MT1-MMP/TSP1/αvβ3 integrin pathway is a potential biomarker and therapeutic target in inflammatory bowel disease.

A Representative maximum-intensity projection images of staining for CD31 (green), MT1-MMP or TSP1 (red), and Hoechst (blue, nuclei) in colon sections obtained from an IBD patient. Boxed areas are shown in magnified views below with merged images of green and red channels in the middle and single channels to the bottom. Non-affected and affected mucosa areas from the same patient are shown for comparison. Scale bar, 50 μm (upper panel) and 20 μm (magnified views). V, vessel.

B ELISA analysis of serum TSP1 in healthy individuals and patients affected by ulcerative colitis (left) or Crohn's disease (right). n = 12–37 individuals per condition. LA and HA indicate patients with low and high active disease based on clinical score. Data are shown as individual values and mean ± SEM and were tested by one-way ANOVA with Benjamini and Hochberg post-test; ***$P < 0.001$.

C Representative maximum-intensity projection images of CD31 staining (green) in whole-mount colon mucosal plexus of $MT1^{f/f}$ mice injected intraperitoneally with 3 mg/kg of the anti-MT1-MMP inhibitory antibody LEM-2/15 or its isotype control at day 0 and day 2 during the 3 days of treatment with 1% DSS. Scale bar, 40 μm. Arrows, arrowheads, and asterisks indicate duplications, loops, and pillars, respectively.

D Quantification of IA events in mice treated as in (C); n = 8 mice per condition in two independent experiments. Data are shown as mean ± SEM and were tested by t-test; **$P < 0.01$.

E Representative second-harmonic generation (SHG) microscopy images of whole-mount colons from $MT1^{f/f}$ mice treated as in (C). Scale bar, 40 μm.

F Representative maximum-intensity projection images of CD31 staining (green) in whole-mount colon mucosal plexus of $MT1^{f/f}$ mice treated with the TSP1 nonamer GDGRGDACK or its control peptide GDGRADACK by continuous minipump delivery (up to 2.4 mg/mouse/day) for 3 days during 1% DSS treatment. Scale bar, 40 μm. Arrows, arrowheads, and asterisks indicate duplications, loops, and pillars, respectively. Mice/n independent experiments.

G Quantification of IA events in mice treated as in (F); n = 5 and 6 mice per condition in two independent experiments. Data are shown as mean ± SEM and were tested by t-test; *$P < 0.05$.

H Representative second-harmonic generation (SHG) microscopy images of whole-mount colons from $MT1^{f/f}$ mice treated as in (F). Scale bar, 40 μm.

Data information: Please see Appendix Table S3 for exact P-values.
Source data are available online for this figure.

contribution to IA through mechanisms involving regulation of Rac1 signaling activity (Gonzalo *et al*, 2010), the lentivirus *in vivo* rescue experiments indicate the involvement of MT1-MMP catalytic activity. Our earlier work identified TSP1 as the master substrate nucleating the combinatorial proteolytic MT1-MMP program related to EC migration, invasion, and vessel formation in endothelial cells stimulated with TNFα (Koziol *et al*, 2012a), a crucial cytokine during colitis progression (Danese, 2008). TSP1 is a pleiotropic matricellular protein widely recognized as an inhibitor of angiogenesis, although certain domains can stimulate ECs (Armstrong & Bornstein, 2003). TSP1 is therefore considered a promising target in cancer and inflammatory and vascular diseases, and agonist and antagonist peptide sequences and domains have been trialed in animal models (Taraboletti *et al*, 2010; Lopez-Ramirez *et al*, 2017). TSP1 expression has been reported in the context of vascular expansion by IA, for example, in the chorioallantoid membrane and during colitis; trials of the TSP1 mimetic octapeptide ABT-898 in the mouse colitis model showed a partial decrease in microvascular density (Gutierrez *et al*, 2015). Nevertheless, to our knowledge, the role of TSP1 in IA, particularly in the inflammatory context, has not yet been directly assessed.

Interaction of TSP1 with CD36 via its type I repeat and with CD47 via its C-terminal globular domain inhibits NO signaling through several mechanisms (Isenberg *et al*, 2008a). Our data reveal that TSP1 processing by MT1-MMP contributes to NO production. Cleavage of TSP1 by MT1-MMP might disturb CD36 binding and unbrake its NO inhibition (Isenberg *et al*, 2009). However, work from Iruela-Arispe's group on TSP1 processing by Adamts1 during wound healing predicts that the cleaved N-terminal TSP1 fragment will be unstable, whereas the C-terminal fragment (able to bind CD47/αvβ3 integrin) can remain in the inflamed tissue and be released to the serum (Lee *et al*, 2006). Our results confirm the presence of TSP1 in the serum of both mice and patients affected by colitis. Moreover, we demonstrated that NO production is induced by the C-terminal TSP1 fragment in MT1-MMP-deficient ECs, and contrarily, it is reduced in MT1-MMP-expressing ECs by inhibiting the interaction of TSP1 with αvβ3 integrin or CD47 (Isenberg *et al*, 2008b), which is known to associate with and regulate β3 integrin (Chung *et al*, 1997). Our data indicate that MT1-MMP-mediated cleavage of TSP1 releases TSP1 fragments from the matrix, allowing their interaction with the CD47/αvβ3 integrin complex likely active at the dorsal plasma membrane (Lindberg *et al*, 1996). Our results also identify for the first time that interaction of αvβ3 integrin with the RGD sequence in TSP1 is crucial to the induction of NO production *in vitro* and inflammatory IA *in vivo*. αvβ3 integrin has long been recognized as a crucial regulator of vascular development and angiogenesis, with fine-tuned actions depending on the initial status of the vasculature and/or the accompanying molecular microenvironment, similar to the dual actions described for TSP1 (Armstrong & Bornstein, 2003; Robinson & Hodivala-Dilke, 2011). Danese and coworkers previously showed that treatment with the non-RGD-based peptide ATN161, which blocks both αvβ3 and α5β1 integrins, effectively decreased angiogenesis and improved colitis in the IL-$10^{-/-}$ mouse model but not in the DSS-induced model (Danese *et al*, 2007a). Our study supports integrin specificity, demonstrating that αvβ3 integrin binding to TSP1 drives NO production *in vitro* and IA *in vivo*. This is likely related to the induction of selective signals by αvβ3 but not β1 integrins (Leavesley *et al*, 1993; Yurdagul *et al*, 2013). Whether TSP1 interactions with other receptors in ECs (such as calcium channels) play additional roles in NO production will require further research (Resovi *et al*, 2014; Risher *et al*, 2018). We propose that the proteolytic processing of TSP1 enables pleiotropic actions (Iruela-Arispe, 2008). Upregulated MT1-MMP and TSP1 expression in inflammation, vascular disease, and cancer will favor cleaved TSP1-αvβ3 integrin interaction, NO production, and IA in preference to TSP1-CD36 binding, macrophage recruitment, and inflammation (Lopez-Dee *et al*, 2011). Since ECs express low levels of MT1-MMP and TSP1 under homeostatic conditions, the upregulation of endothelial MT1-MMP and thus TSP1 processing in specific disease settings may account for the reported dose or cell-type-dependent dual actions of TSP1 on NO and inflammation (Armstrong & Bornstein, 2003).

Although promotion of lymphangiogenesis by VEGF-C seems a promising strategy for colitis alleviation in mouse models

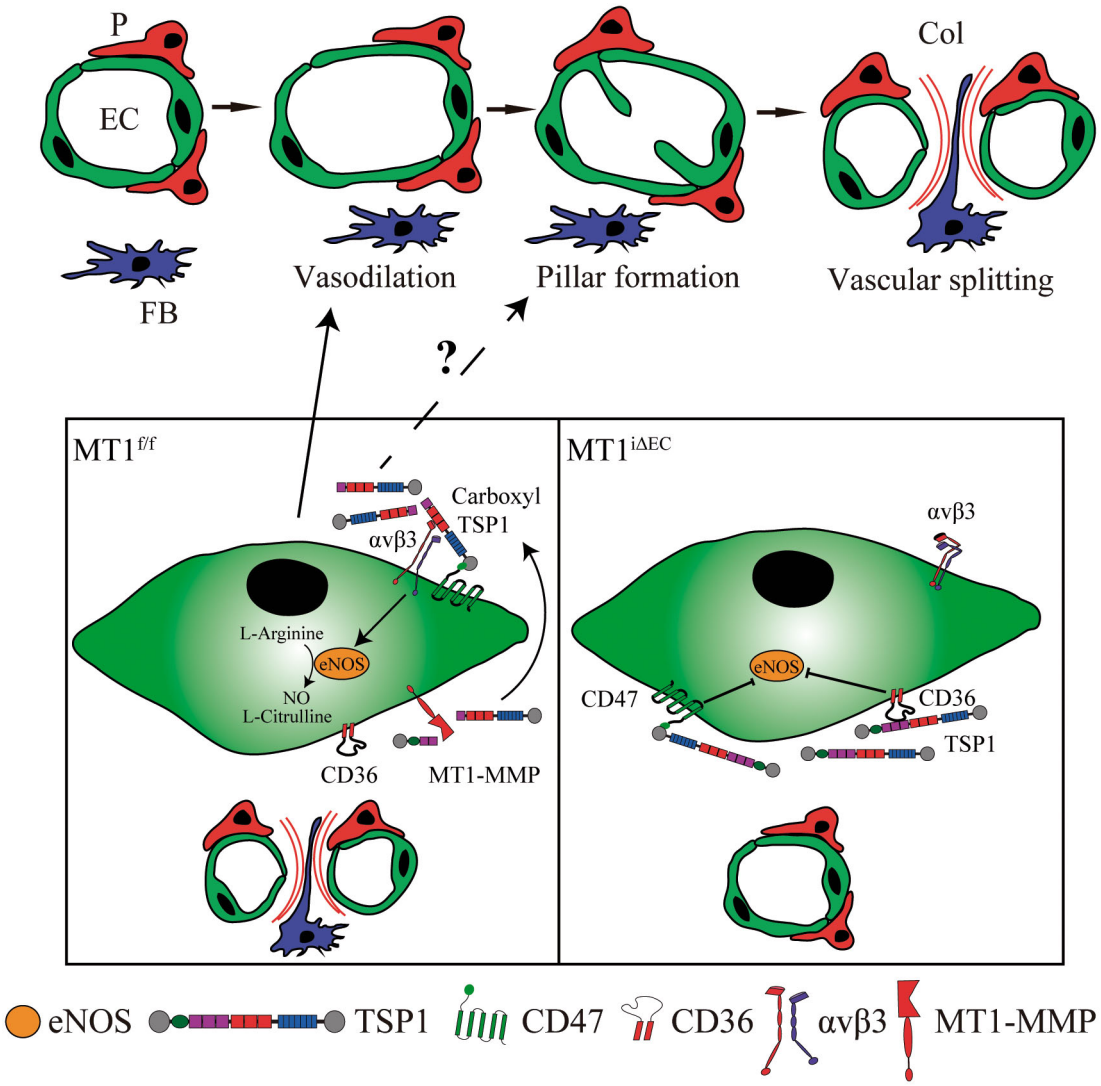

Figure 9. Working model of the role of MT1-MMP/TSP1/nitric oxide axis in IA during colitis.

The scheme depicts the role that endothelial cell MT1-MMP (left) exerts in IA during colitis by processing TSP1 and binding of the generated TSP1 C-terminal fragment to CD47/αvβ3 integrin, thus inducing nitric oxide production. This signaling cascade ultimately leads to arteriole vasodilation and endothelial cell intussusceptive remodeling in the capillary plexus of the inflamed intestinal mucosa. When MT1-MMP is absent from endothelial cells (right), this pathway is impaired, IA reduced, and colitis ameliorated. EC, endothelial cell; P, pericyte; FB, fibroblast; Col, collagen.

(D'Alessio *et al*, 2014), there is still no proven benefit for IBD patients of targeting angiogenesis, whether indirectly (inhibiting the immune response) or directly (inhibiting VEGF or other angiogenic molecules as TNFα) (Chidlow *et al*, 2006; Eder *et al*, 2015). In this regard, conflicting effects have been reported for VEGF inhibition in colitis, likely related to the kinetics and efficiency of its targeting (Tolstanova *et al*, 2009; Chernoguz *et al*, 2012). This controversy underlines the need to deepen our understanding of the mechanisms underlying IA in IBD for a more rational design of angiogenesis inhibitors. Our findings identify the MT1-MMP/TSP1/αvβ3 integrin/NO pathway as a possible therapeutic target for IA and colitis since blocking this axis by inhibiting MT1-MMP activity or competing TSP1 binding to αvβ3 integrin both diminished IA and preserved collagen fiber organization. Moreover, the *in silico* docking of the TSP1 cleavage sites with MT1-MMP could permit small-molecule screening and buildup to cell-specific strategies involving peptide-directed delivery, nanoparticles, or other modes of tissue-tailored therapeutic intervention. It is remarkable that the elevated serum TSP1 detected in patients with low-activity colitis, but not high-activity disease, correlated with the protection conferred by MT1-MMP endothelial deletion in mild mouse colitis but not severe disease (not shown). This suggests that the MT1-MMP/TSP1/NO pathway may be particularly important in early stages or mild forms of the disease, where the IA vascular response plays a predominant role in colitis progression. Finally, our data from IBD-affected patients showing elevated MT1-MMP expression in the inflamed vasculature and elevated serum TSP1 suggest their potential usefulness as surrogate biomarkers of disease activity.

Materials and Methods

Animals

C57BL/6 wild-type mice were purchased from Charles River, and MT1-MMP (*Mmp14*)-lacZ reporter mice were as previously reported (Yana *et al*, 2007). *Mmp14*$^{loxP/loxP}$ mice (Gutierrez-Fernandez *et al*, 2015) were crossed with *Cdh5*-Cre^{ERT2} mice (kindly provided by Prof. Adams' laboratory; Wang *et al*, 2010) to generate *Mmp14*$^{loxP/loxP}$;*Cdh5*-Cre$^{ERT2/+}$ mice (MT1$^{i\Delta EC}$ mice). Mice at 8–20 weeks old were injected intraperitoneally with 1 mg per mouse of 4-hydroxytamoxifen (4-OHT) on five consecutive days to induce endothelial cell-specific deletion of MT1-MMP (Monvoisin *et al*, 2006). Mice were housed and all animal experiments performed under specific pathogen-free conditions at the Animal facility of Centro Nacional de Investigaciones Cardiovasculares Carlos III (CNIC), and in strict accordance with the institutional guidelines. Mice were kept under a 12-h light/dark cycle (lights on from 07:00 to 19:00 h) and fed *ad libitum* with standard chow diet (2108 Teklad Global, Harlan Interfauna Iberica S.L.). Mice were genotyped by tail DNA PCR using the following primers: for the MT1-flox recombination, 5′-CCCTGGG TCAACTACAGCA-3′ and 5′-TTTGTGGGTGACCCTGACTTG-3′; for LacZ, 5′-ATCGTGCGGTGGTTGAA-3′ and 5′-TGCTGACGGTTAACGC CTCG-3′; and for Cre, 5′-AGGTGTAGAGAAGGCACTTAGC-3′ and 5′-CTAATCGCCATCTTCCAGCAGG-3′.

Mouse experimental colitis

Experimental colitis was induced in 8- to 20-week-old mice by supplying 1% dextran sodium sulfate (DSS) (MP Biomedicals, 0216011010) dissolved in drinking water *ad libitum* for 3 or 7 days. Daily monitoring included measuring body weight and calculating disease activity index (DAI). The baseline colitis on day 0 was scored as 0. Subsequent weight loss of 1–5% was scored as 1, 5–10% as 2, 10–20% as 3, and more than 20% as 4. For stool consistency, normal, well-formed pellets were scored as 0, semi-formed pellets not adhering to the anus were scored as 2, and liquid stools adhering to the anus were scored as 4. Similarly, no bleeding was assigned a score of 0, positive blood detection in the stool was scored as 2 (detected by hemoFEC, Cobas, 10243744), and gross rectal bleeding was scored as 4. At the end of the DSS exposure period, the whole colon was removed and cleaned with PBS. The most distal portion was fixed in 4% PFA overnight and then used directly for whole-mount staining, processed, and embedded in paraffin or frozen in OCT for histological analysis. The remaining part of the colon was homogenized for protein and RNA extraction. The anti-MT1-MMP antibody LEM-2/15 and the E123CaG-1 TSP1 fragment were administered to mice by intraperitoneal injection at 3 mg/kg and 1 μg, respectively, on day 0 and day 2 during the 3 days of 1% DSS treatment. No statistical methods were used to pre-estimate the animal sample size, and mice were randomly allocated to experimental groups. Investigators were not blinded during the analysis of mouse samples.

Lentiviral infection

The full-length MT1-MMP sequence (FL) or mutated versions to disable catalytic activity (E240A, EA) or block signaling activity (Y573F, YF) were cloned into the SFFV-IRES-GFP lentiviral backbone. Lentiviruses expressing Mock, MT1-MMP FL, EA, or YF were prepared and titered as previously described (Martin-Alonso *et al*, 2015). Lentivirus solution (100 μl) was injected intravenously into the jugular vein of adult MT1$^{i\Delta EC}$ mice at 1×10^7 pfu/ml. Mice were administered 1% DSS for 3 days and then sacrificed, and colons were processed for whole-mount staining.

Subcutaneous pump implantation

MT1-MMP$^{f/f}$ control mice were anesthetized with isoflurane and implanted with subcutaneous micro-osmotic pumps (Alzet, model 10003D) charged with 10 mg/100 μl of the peptides GDGRGDACK or GDGRADACK. Pumps released ~1 μl/h (100 μg/h), equivalent to 2.4 mg/mouse/day. Mice were administered 1% DSS for 3 days and then sacrificed, and colons were processed for whole-mount staining.

Endothelial cell culture

Human umbilical vein endothelial cells (HUVEC) were purchased from Lonza (BioWhittaker, CC-2519) and cultured on 0.5% gelatin-coated plates (unless otherwise indicated) in medium 199 supplemented with 20% FBS, 100 U/ml penicillin (Lonza), 100 μg/ml streptomycin (Lonza), 2 mM L-glutamine (Lonza), 10 mM HEPES (Lonza), and ECGS/H (Promocell, C-30120). Cells were used up to passage 5. Mouse aortic endothelial cells (MAEC) were obtained from aortas of 4-week-old mice. Briefly, after fat removal under a microscope, aortas were incubated for 5 min at 37°C in collagenase solution (collagenase type I, 3.33 mg/ml, Worthington, LS004194), thus allowing removal of the adventitia with forceps. The aortas were then cut into small pieces (1–2 mm), and a cell suspension was obtained by incubation for 45 min at 37°C in 6 mg/ml type I collagenase and 2.5 mg/ml elastase (Worthington, LS002290) diluted in DMEM. Once EC colonies were visible, they were subjected to two rounds of positive selection with anti-ICAM2 and magnetic beads. MAEC were cultured on 0.2% gelatin-coated plates in DMEM/F12 medium supplemented with 20% FBS, 100 U/ml penicillin (Lonza), 100 μg/ml streptomycin (Lonza), 2 mM L-glutamine (Lonza), 10 mM HEPES (Lonza), and ECGS/H (Promocell, C-30120).

MT1-MMP siRNA silencing

HUVEC were transfected twice with 10 nM MT1-MMP-specific siRNAs [Ambion, Thermo Fisher Scientific, MT1-ARNi#1, 8877 (4390824); MT1-ARNi#2, 8879 (4390824)] or control scramble siRNA [Ambion, Thermo Fisher Scientific, Control No. 1 (4390843)] using RNAiMAX Lipofectamine (Thermo Fisher Scientific, 13778030). Downregulation was confirmed by qPCR and Western blot.

Vascular perfusion and permeability assays

For vascular perfusion analysis, mice received intravenous injections of 100 μl of biotinylated or FITC-GSL I Isolectin B4 (Vector Labs, B1205 and FL-1201, respectively) 20 min before sacrifice. Mice were perfused under constant pressure with cold PBS, and colon samples were extracted and processed for whole-mount staining. Vascular perfusion was quantified as the percentage of the CD31-positive vascular volume containing an IB4 signal.

For vascular permeability analysis, mice received intravenous injections of 100 μl of 0.5 mg/ml (71.5 μM) Dextran-TRITC 70 KD (Invitrogen, D1819) 20 min before sacrifice. Colon samples were extracted and frozen in OCT, and 30-μm-thick sections were immunostained and visualized.

Quantitative real-time PCR

RNA was extracted with the RNeasy Plus Micro Kit (Qiagen, 74034). cDNA was synthesized using the High-Capacity cDNA Reverse Transcription Kit (Applied Biosystems, 4368814). Quantitative PCR was performed using Power SYBR Green PCR Master Mix (Applied Biosystems, 4367659) following the manufacturer's protocol. The primers used in qPCR are listed in Appendix Table S2. GAPDH, 36b4, and TBP were used as internal expression controls. The results (CNRQ; calibrated normalized relative quantity) were analyzed with qbase Plus software (Biogazelle, Gent, Belgium).

Western blot

Cells were lysed in RIPA buffer supplemented with protease and phosphatase inhibitors. Protein samples were separated by 8% SDS–PAGE, transferred to nitrocellulose membranes, blocked with 5% BSA, and incubated sequentially with primary and horseradish peroxidase (HRP)-conjugated secondary antibodies, with washes. The primary antibodies used were anti-MT1-MMP (LEM-2/15) (Galvez *et al*, 2001), anti-eNOS (BD Bioscience, 610297), anti-GFP (Abcam, ab13970), anti-GAPDH (Sigma-Aldrich, G9545), and anti-β-actin (Sigma-Aldrich, A5441). All primary antibodies were used at a dilution of 1:1,000. The secondary antibodies used were HRP goat anti-mouse and HRP goat anti-rabbit (Jackson), and bound secondary antibodies were visualized with Luminata Classico Western HRP Substrate (Millipore, WBLUC0500) in ImageQuant LAS 4000 (GE Healthcare Life Sciences, Massachusetts, USA). Western blots were quantified using ImageJ software (https://imagej.nih.gov/ij/).

In vitro digestion assay

Human TSP1 purified from plasma (a gift from Dr. G. Taraboletti, Istituto di Ricerche Farmacologiche Mario Negri IRCCS, Bergamo, Italy) was incubated with increasing amounts of the catalytic domain of human recombinant MMP14 (hrMMP14, ref. 475935; Calbiochem, San Diego, USA) in digestion buffer (50 mM Tris–HCl, 10 mM CaCl2, 80 mM NaCl [pH 7.4]) for 2 h at 37°C. Samples were separated by 10% SDS–PAGE and transferred to nitrocellulose membranes (Bio-Rad, 45 μm). Full-length TSP1 and fragments were detected with an anti-TSP1 antibody recognizing an epitope nearby the N-terminus (Lee *et al*, 2006). An anti-rabbit HRP secondary antibody (Jackson) was used and the bound proteins developed with Luminata Classico Western HRP Substrate (Millipore, WBLUC0500) in ImageQuant LAS 4000 (GE Healthcare Life Sciences, Massachusetts, USA).

Whole-mount staining

For cremaster muscle, anesthetized mice were intravenously injected with 100 μl of 100 μM acetylcholine 15 min before sacrifice and with 100 μl of 100 μM sodium 2-(N,N-diethylamino)-diazenolate-2-oxide (DEANO) 5 min before sacrifice; saline was used as a control for both injections. For VEGF administration to the distal colon, 20 ng of VEGF (PeproTech, 450-32) in a final volume of 50 μl was delivered into anesthetized mice via a rectal cannula, 10 min before sacrifice. Cremaster muscle or distal colon was then removed, cleaned, flat-mounted, and fixed with 4% PFA overnight at 4°C. Mouse and human whole-mount samples were blocked and permeabilized in blocking solution (PBS 5% BSA, 5% normal goat serum, and 0.3% Triton X-100). Primary antibodies were diluted 1:100 in blocking solution, and samples were incubated on a shaker at 4°C overnight. Vessels were stained with anti-CD31 (Millipore, MAB1398Z), anti-ICAM2 (BD Pharmingen, 553325), and anti-ERG 647 (Abcam, ab196149). The following day, the samples were washed 3 × 1 h in PBS and 0.1% Triton X-100 and incubated overnight at 4°C with the appropriate secondary fluorescent antibodies (goat anti-Armenian hamster IgG, anti-mouse IgG, anti-rabbit IgG, or anti-rat IgG, all from Jackson ImmunoResearch) and Hoechst 33342 (Invitrogen, H1399). The next day, samples were washed 3 × 1 h in PBS and 0.1% Triton X-100 and mounted in glycerol. Fluorescence microscopy images were acquired with a Zeiss LSM 700 confocal microscope at 21–23°C using Plan-Apochromat, 25 × 0.8 or 63× glycerol DIC M27, and z-stacks were captured every 1.5 or 1 μm, respectively. Confocal images were imported into Imaris (version 7.7.2; Bitplane AG, Switzerland) to obtain a precise 3D reconstruction generated by the program's iso-surface rendering function of this software. In 3D images of the mucosal vasculature, we evaluated vascular volume, intussusception events (holes, loops, and duplications), and vascular perfusion, and in 3D images of the cremaster muscle, capillary diameters were quantitated. Intercapillary angles in the mucosa vascular plexus were measured by ImageJ software. Capillary diameters in CD31-stained whole-mount colons after VEGF rectal administration were quantified by an ImageJ *ad-hoc* plugin (http://adm.irbbarcelona.org/image-j-fiji#TOC-Blood-vessel-segmentation-and-network-analysis).

Second-harmonic generation multi-photon microscopy

Autofluorescence of fibrillar collagen (425- to 465-nm filter) was visualized in flat-mounted fixed colon from $MT1^{f/f}$ and $MT1^{i\Delta EC}$ mice with a Zeiss LSM 780 microscope coupled to a Spectra-Physics Mai Tai DS Laser, using an 800 nm excitation wavelength, which resulted in the SHG signal detectable at 400 nm (emission fluorescence range 388–408 nm).

Endothelial cell immunofluorescence staining

Confluent ECs on glass coated with 1% gelatin were fixed with 4% PFA during 8 min at RT. The cells were stained with anti-MT1-MMP (LEM-2/15) and anti-TSP1 (Thermo Fisher, MA5-13398) primary antibodies diluted 1:100. Cells were incubated with appropriate secondary fluorescent antibodies (anti-mouse IgG, anti-rabbit IgG from Jackson ImmunoResearch), phalloidin FITC (Life Technologies, F432), and Hoechst 33342 (Invitrogen, H1399) for 30 min at 37°C. Fluorescence microscopy images were acquired with a Zeiss LSM 700 confocal microscope at 21–23°C using Plan-Apochromat, 40 × 0.8 oil DIC M27, and *z*-stacks were captured every 1 μm. Images were analyzed using ImageJ software (https://imagej.nih.gov/ij/).

Cell sorting

Freshly isolated mouse lung endothelial cells (MLECs) were obtained from lungs as described (Oblander *et al*, 2005). Red blood cells were removed by incubating the lung cell suspension for 5 min in ACK buffer (150 mM NH_4Cl, 0.1 mM Na_2EDTA, 10 mM $KHCO_3$, pH = 7.4). The cells were then resuspended in sorting buffer (PBS + 1% FBS + 10 mM HEPES) and incubated for 10 min at 4°C with an Fc-block anti-CD16/CD32 mAb (Pharmingen) to block non-antigen-specific binding of immunoglobulins to the Fcγ receptors. This was followed by staining with Alexa Fluor 488-conjugated anti-mouse CD31 (Mec13.3) and V405-conjugated anti-mouse CD45.1 (all from BD Bioscience Pharmingen). The endothelial cell population defined as $CD31^+/CD45^-$ was sorted in a Synergy 4L Cell Sorter (Sony Biotechnology Inc.), and MT1-MMP deletion efficiency was analyzed by qPCR.

Enzyme-linked immunosorbent assay

C57BL/6 mice were administered 1% DSS for 7 days; blood was collected by cardiac puncture, and serum was separated and stored at −80°C. Soluble TSP1 was measured in serum by enzyme-linked immunosorbent assay (Mouse TSP1 ELISA kit; Cusabio, CSB-E08765m). Soluble TSP1 in serum from human control individuals and IBD patients was measured by ELISA (Human TSP1 DuoSet ELISA; R&D Systems, DY3074). Mean optical density (OD) at 450 nm was calculated from triplicate readings per sample, and OD values at 570 nm were subtracted to correct for optical imperfections in the plate reading. A 4-parameter logistic (4-PL) curve fit was generated using Benchmark Plus Microplate Spectrophotometer (BIO-RAD) coupled to Microplate Manager 5.2.1.

Colon immunofluorescence staining

Paraffin-embedded colonic mouse experimental colitis samples were cut into 5-μm sections, deparaffinized, hydrated through an alcohol series of decreasing concentration, and treated with sodium citrate buffer (10 mM sodium citrate, 0.05% Tween-20, pH 6.0) for 20 min at 95°C and then cooled for 2 h at room temperature for antigen retrieval. Sections were permeabilized with PBS containing 0.3% Triton X-100 for 10 min at room temperature and blocked with Image-iT™ FX signal enhancer (Invitrogen, 36933) for 30 min at room temperature and with blocking buffer (PBS with 5% BSA and 5% goat serum) for 1 h at room temperature. Sections were incubated with the following primary antibodies overnight at 4°C in blocking buffer: anti-CD31 (DIANOVA, DIA310) anti-MT1-MMP (LEM-2/15) and anti-TSP1 (provided by Dr M. L. Iruela-Arispe, University of California, Los Angeles, CA, USA, 10 μg/ml). Subsequently, samples were washed with PBS and 0.1% Triton X-100 and incubated for 2 h at room temperature with the corresponding conjugated secondary antibodies and Hoechst 33342. Samples were mounted in Fluoromount-G imaging medium (4958-02, Affymetrix eBioscience).

Samples included in OCT were permeabilized and blocked in PBS containing 0.3% Triton X-100, 5% BSA, 5% goat serum, and anti-CD16/CD32 (clone 24g2, 1:100) for 1 h at room temperature. Samples were then incubated overnight at 4°C with anti-CD11b Alexa 647 (clone M1/70, eBiosciences, 51-0112-82), anti-Erg, anti-β-galactosidase, and anti-ICAM2. Samples were then incubated with the corresponding secondary antibodies and Hoechst 33342 for 2 h at room temperature. Finally, samples were mounted in Fluoromount-G, and images were acquired with a Zeiss LSM 700 confocal microscope fitted with a 25× objective and processed and quantified using ImageJ software.

Nitric oxide production

Confluent ECs were seeded in 96-well glass plates coated with 1% gelatin and cultured in EGM2 (Promocell, C-22111). The cells were incubated with 2.5 μM DAF-FM diacetate (Life Technologies, D23842) for 30 min at 37°C and washed with PBS. The DAF-FM fluorescence signal was visualized with a Zeiss LSM 700 confocal microscope (Plan-Apochromat 40 × 1.3 Oil DIC M27), and mean fluorescence intensity (MFI) at single-cell level was analyzed with ImageJ software. HUVEC were treated for 24 h with antibodies to MT1-MMP (LEM-2/15), integrin αv [anti-αv integrins ABA 6D1 (Yanez-Mo *et al*, 1998)], or CD47 (Abcam, ab3283), with a range of concentrations of the peptides RGDS, RADS, cilengitide, TSP1 nonamer GDGRGDACK, or the control GDGRADACK, or with human full-length TSP1 or the human recombinant TSP1 fragment E123GaC-1.

Intravital microscopy in the cremaster muscle

For the analysis of arteriolar vasodilation, mice were anesthetized, and the cremaster muscle was isolated and exposed on the microscope plate as described (Rius & Sanz, 2015). Mice were injected with 100 μl of 100 μM acetylcholine, and arterioles were recorded for at least 15 min using a Leica DM6000-FS intravital microscope fitted with an Apo 40× NA 1.0 water-immersion objective and linked to a DFC350-FX camera. LASAF software was used for image acquisition and processing.

In silico modeling of MT1-MMP dimer

The MT1-MMP monomer was modeled by submitting the Fasta sequence of mature human MT1-MMP protein (UniProt ID: P50281, residues 112–582) to a local implementation of I-Tasser software suite v4.4 (Yang *et al*, 2015) for threading modeling with homology. The selected model was that with minimal energy and correct folding (best structural alignment to templates; PDB ID: 1BQQ for catalytic domain and 3C7X for hemopexin-like domain). In this model, the transmembrane domain (TM) is buried in the protein core. To fix this, this region (transmembrane plus C-term, TMIC) was extracted from the model, angles were fixed according to the predicted secondary structure, and a refinement cycle was performed using the relax tool (Nivon *et al*, 2013; Conway *et al*, 2014) in Rosetta suite v3.5 release 2015.38.58158 (www.rosettacommons.org). The best model for TMIC (lower energy and best stability) was selected and aligned with the previous MT1-MMP model, and the new model composed of MT1-MMP without TMIC domains and the new TMIC model was used as the template; the gap between them was closed using the loopmodel tool (Mandell & Kortemme, 2009; Stein & Kortemme, 2013) in Rosetta suite. The most stable model was selected as the final model for the MT1-MMP monomer. To

The paper explained

Problem

Human inflammatory bowel disease (IBD) is a chronic inflammatory disease of the intestine comprising ulcerative colitis and Crohn's disease and characterized by phases of remission and relapse. IBD is a multifactorial disease featuring a primary defect in intestinal epithelial barrier integrity and an exacerbated immune response to the microbiota. The use of immunomodulators, new biologics, and small molecules has improved IBD treatment in the recent years, but non-responder patients and the unpredicted nature of relapses make necessary to expand our knowledge about other processes influencing IBD pathophysiology. Colitis progression seems to involve angiogenesis, the formation of new vessels from pre-existing ones, which is regarded as a potential therapeutic target but with limited success in animal models. A better understanding of the molecular pathways behind colitis-associated angiogenesis will help designing more efficient and tailor-based therapies for this complex disease.

Results

In this study, we implemented confocal microscopy and 3D image reconstruction tools to investigate intussusceptive (or splitting) angiogenesis (IA), a poorly characterized mode of angiogenesis, in a mouse model of IBD. After induction of mild colitis, we detected an increased number of vascular events, all hallmarks of IA. We next explored the role of the matrix metalloproteinase MT1-MMP in IA and we demonstrated that the selective absence of MT1-MMP from endothelial cells decreased IA events and led to improved vascular perfusion, milder clinical score, and better-preserved intestine morphology during mouse colitis.

Vasodilation is an obliged prerequisite to IA, and we demonstrated that endothelial MT1-MMP absence decreased capillary vasodilation induced by VEGF in the intestine and by acetylcholine in the muscle. We showed *in vivo* and *in vitro* that MT1-MMP catalytic activity was required for nitric oxide production and for the induction of IA. *In vitro* digestion assays, *in silico* protein modeling, and endothelial cell culture identified the cleavage of the matricellular protein thrombospondin-1 (TSP1) by MT1-MMP as responsible for nitric oxide production. Finally, we found higher levels of TSP1 in serum from low active IBD patients, and we reduced IA during mouse colitis progression via anti-MT1-MMP antibody injection or delivery of a blocking TSP1 peptide.

Impact

We propose that our findings have both diagnostic and therapeutic clinical impacts for patients with IBD. Indeed, our data from IBD-affected patients suggest that MT1-MMP and TSP1 could serve as surrogate biomarkers of disease activity. Moreover, our findings identify the MT1-MMP/TSP1/αvβ3 integrin/nitric oxide pathway as a novel actor in IA whose targeting ameliorates colitis progression. We have demonstrated this therapeutic application by blocking this axis with anti-MT1-MMP inhibitory antibodies, and through selective competition of TSP1 binding to αvβ3 integrin by continuous peptide delivery. Since we found elevated serum TSP1 in patients with low active colitis and MT1-MMP endothelial deletion protected mainly from mild colitis, these therapeutic options may be of special value in early stages or mild forms of IBD. Finally, the *in silico* docking of the TSP1 cleavage sites with MT1-MMP could lead to small-molecule screening and to new cell-specific strategies involving peptide-directed delivery, nanoparticles, or other modes of tissue-tailored therapeutic intervention.

model dimeric MT1-MMP, two of these monomers were positioned according to the published MT1-MMP dimer interface using PyMOL v1.8 (www.pymol.org), and the new dimer model was used as the initial template. A new PDB file was generated for the model, in which the membrane protein structure is transformed into PDB coordinates (with the *z*-axis normal to the membrane) using the PPM server (http://opm.phar.umich.edu/server.php). A full spanfile was generated from the PDB structure using the spanfile_from_pdb application in the membrane framework in Rosetta suite v3.5 release 2015.38.58158. An initial relax cycle was performed using the relax application in Rosetta suite to minimize energy and clashes using the initial template and the full spanfile (Conway *et al*, 2014). The lowest scoring refined model (lowest energy) was selected as the input model, and a new dimer model was generated using the mp_dock application in the Rosetta suite membrane framework (Alford *et al*, 2015). All models with TM embedded in the membrane clustered together. The best model, with lowest energy, was selected as the final dimer. This homodimer meets the previously described binding interface constraints, with docking via the hemopexin-like domains, and has quasi-C2 symmetry. We next positioned the MT1-MMP dimer model together with the reported crystal structure of the TSP1 type 1 repeat (PDB ID: 1LSL) using PyMOL and evaluated the global topography and accessibility of the complex.

Statistics

Protein expression on Western blots was quantified densitometrically using ImageJ software (NIH, Bethesda, USA) and normalized to the corresponding loading control. Data were tested for normal distribution by D'Agostino–Pearson test and compared with non-parametric or parametric statistical tests as appropriate (see figure legends for details). Graphs were prepared and statistical analysis performed using GraphPad Prism 5.0 (GraphPad Software, La Jolla, USA). Data are presented as mean ± standard error of the mean (SEM). Differences were considered significant at $^{*}P < 0.05$, $^{**}P < 0.01$, $^{***}P < 0.001$, and $^{****}P < 0.0001$.

Study approval

Animal procedures were approved by the Committee on the Ethics of Animal Experiments of the CNIC (Permit Number: CNIC-01/13) and by the corresponding legal authority of the local government "Comunidad Autónoma" of Madrid (Permit Number: PROEX 34/13). Animal studies were conformed to directive 2010/63EU and recommendation 2007/526/EC regarding the protection of animals used for experimental and other scientific purposes, enforced in Spanish law under RD1201/2005. Human samples were obtained with informed consent after ethical approval by the Hospital de La Princesa Ethics Committee. Informed consent was obtained from all subjects, and the experiments conformed to the principles set out in the WMA Declaration of Helsinki and the Department of Health and Human Services Belmont Report.

Expanded View for this article is available online.

Acknowledgements

We thank Ralf Adams (Max Planck Institute for Molecular Biomedicine, Germany) and Carlos López-Otín for providing the *Cdh5*(BAC)Cre^{ERT2} and *Mmp14*$^{floxed/floxed}$ mouse lines, respectively; María José Calzada for providing anti-CD47 antibody and human TSP1; Giulia Taraboletti and Deane F. Mosher for providing full-length TSP1 and the E123CaG-1 fragment, respectively;

Ángela Pollán, Ángel Colmenar, and Alberto Jiménez-Montiel for technical support; and Simon Bartlett for English editing. This study was supported by grants from the Spanish Ministerio de Ciencia, Innovación y Universidades (SAF2014-52050-R and SAF2017-83229-R to A.G.A). S.E. was recipient of a FPI-Severo Ochoa fellowship. The CNIC is supported by the Instituto de Salud Carlos III, the Spanish Ministry of Ciencia, Innovación y Universidades, and the Pro-CNIC Foundation and is a Severo Ochoa Center of Excellence (SEV-2015-0505).

Author contributions

SE performed and analyzed HUVEC experiments and most colitis experiments; CC performed histology, immunofluorescence, *in vitro* digestion assay, some colitis experiments, and image quantification; AK and PG performed and analyzed initial colitis experiments; CR and VA performed and analyzed intravital microscopy experiments; FM performed *in silico* protein modeling; AU provided DSS-model expertise; MS provided the $MT1^{lacz/+}$ mouse line; PML, MC, and JPG provided human samples from IBD patients; and AGA designed and supervised the research and wrote the manuscript.

Conflict of interest

M Chaparro has served as a speaker for or has received research or education funding from MSD, Abbvie, Hospira, Pfizer, Takeda, Janssen, Ferring, Shire Pharmaceuticals, Dr Falk Pharma, and Tillotts Pharma. JP Gisbert has served as a speaker, a consultant, and advisory member for or has received research funding from MSD, Abbvie, Hospira, Pfizer, Kern Pharma, Biogen, Takeda, Janssen, Roche, Sandoz, Celgene, Ferring, Faes Farma, Shire Pharmaceuticals, Dr. Falk Pharma, Tillotts Pharma, Chiesi, Casen Fleet, Gebro Pharma, Otsuka Pharmaceutical, and Vifor Pharma. The rest of the authors declare no conflict of interest.

References

Ackermann M, Tsuda A, Secomb TW, Mentzer SJ, Konerding MA (2013) Intussusceptive remodeling of vascular branch angles in chemically-induced murine colitis. *Microvasc Res* 87: 75 – 82

Alford RF, Koehler Leman J, Weitzner BD, Duran AM, Tilley DC, Elazar A, Gray JJ (2015) An integrated framework advancing membrane protein modeling and design. *PLoS Comput Biol* 11: e1004398

Alvarado J, del Castillo JR, Thomas LE (2008) Modulation of membrane type 1 matrix metalloproteinase by LPS and gamma interferon bound to extracellular matrix in intestinal crypt cells. *Cytokine* 41: 155 – 161

Annis DS, Murphy-Ullrich JE, Mosher DF (2006) Function-blocking antithrombospondin-1 monoclonal antibodies. *J Thromb Haemost* 4: 459 – 468

Aoi Y, Terashima S, Ogura M, Nishio H, Kato S, Takeuchi K (2008) Roles of nitric oxide (NO) and NO synthases in healing of dextran sulfate sodium-induced rat colitis. *J Physiol Pharmacol* 59: 315 – 336

Armstrong LC, Bornstein P (2003) Thrombospondins 1 and 2 function as inhibitors of angiogenesis. *Matrix Biol* 22: 63 – 71

Beck PL, Xavier R, Wong J, Ezedi I, Mashimo H, Mizoguchi A, Mizoguchi E, Bhan AK, Podolsky DK (2004) Paradoxical roles of different nitric oxide synthase isoforms in colonic injury. *Am J Physiol Gastrointest Liver Physiol* 286: G137 – G147

Burri PH, Hlushchuk R, Djonov V (2004) Intussusceptive angiogenesis: its emergence, its characteristics, and its significance. *Dev Dyn* 231: 474 – 488

Chernoguz A, Crawford K, Vandersall A, Rao M, Willson T, Denson LA, Frischer JS (2012) Pretreatment with anti-VEGF therapy may exacerbate inflammation in experimental acute colitis. *J Pediatr Surg* 47: 347 – 354

Chidlow JH Jr, Langston W, Greer JJ, Ostanin D, Abdelbaqi M, Houghton J, Senthilkumar A, Shukla D, Mazar AP, Grisham MB *et al* (2006) Differential angiogenic regulation of experimental colitis. *Am J Pathol* 169: 2014 – 2030

Chung J, Gao AG, Frazier WA (1997) Thrombspondin acts via integrin-associated protein to activate the platelet integrin alphaIIbbeta3. *J Biol Chem* 272: 14740 – 14746

Conway P, Tyka MD, DiMaio F, Konerding DE, Baker D (2014) Relaxation of backbone bond geometry improves protein energy landscape modeling. *Protein Sci* 23: 47 – 55

Cooke JP, Losordo DW (2002) Nitric oxide and angiogenesis. *Circulation* 105: 2133 – 2135

D'Alessio S, Correale C, Tacconi C, Gandelli A, Pietrogrande G, Vetrano S, Genua M, Arena V, Spinelli A, Peyrin-Biroulet L *et al* (2014) VEGF-C-dependent stimulation of lymphatic function ameliorates experimental inflammatory bowel disease. *J Clin Invest* 124: 3863 – 3878

Danese S (2007) Inflammation and the mucosal microcirculation in inflammatory bowel disease: the ebb and flow. *Curr Opin Gastroenterol* 23: 384 – 389

Danese S, Sans M, Spencer DM, Beck I, Donate F, Plunkett ML, de la Motte C, Redline R, Shaw DE, Levine AD *et al* (2007a) Angiogenesis blockade as a new therapeutic approach to experimental colitis. *Gut* 56: 855 – 862

Danese S, Scaldaferri F, Vetrano S, Stefanelli T, Graziani C, Repici A, Ricci R, Straface G, Sgambato A, Malesci A *et al* (2007b) Critical role of the CD40 CD40-ligand pathway in regulating mucosal inflammation-driven angiogenesis in inflammatory bowel disease. *Gut* 56: 1248 – 1256

Danese S (2008) Mechanisms of action of infliximab in inflammatory bowel disease: an anti-inflammatory multitasker. *Dig Liver Dis* 40(Suppl 2): S225 – S228

De Bock K, Cauwenberghs S, Carmeliet P (2011) Vessel abnormalization: another hallmark of cancer? Molecular mechanisms and therapeutic implications. *Curr Opin Genet Dev* 21: 73 – 79

De Paepe ME, Benny MK, Priolo L, Luks FI, Shapiro S (2017) Florid intussusceptive-like microvascular dysangiogenesis in a preterm lung. *Pediatr Dev Pathol* 20: 432 – 439

Di Lorenzo A, Lin MI, Murata T, Landskroner-Eiger S, Schleicher M, Kothiya M, Iwakiri Y, Yu J, Huang PL, Sessa WC (2013) eNOS-derived nitric oxide regulates endothelial barrier function through VE-cadherin and Rho GTPases. *J Cell Sci* 126: 5541 – 5552

Djonov V, Schmid M, Tschanz SA, Burri PH (2000) Intussusceptive angiogenesis: its role in embryonic vascular network formation. *Circ Res* 86: 286 – 292

Eder P, Korybalska K, Linke K, Witowski J (2015) Angiogenesis-related proteins–their role in the pathogenesis and treatment of inflammatory bowel disease. *Curr Protein Pept Sci* 16: 249 – 258

Egginton S (2011) *In vivo* shear stress response. *Biochem Soc Trans* 39: 1633 – 1638

Filipovic N, Tsuda A, Lee GS, Miele LF, Lin M, Konerding MA, Mentzer SJ (2009) Computational flow dynamics in a geometric model of intussusceptive angiogenesis. *Microvasc Res* 78: 286 – 293

Galvez BG, Matias-Roman S, Albar JP, Sanchez-Madrid F, Arroyo AG (2001) Membrane type 1-matrix metalloproteinase is activated during migration of human endothelial cells and modulates endothelial motility and matrix remodeling. *J Biol Chem* 276: 37491 – 37500

Galvez BG, Genis L, Matias-Roman S, Oblander SA, Tryggvason K, Apte SS, Arroyo AG (2005) Membrane type 1-matrix metalloproteinase is regulated by chemokines monocyte-chemoattractant protein-1/ccl2 and interleukin-8/CXCL8 in endothelial cells during angiogenesis. *J Biol Chem* 280: 1292 – 1298

Genis L, Gonzalo P, Tutor AS, Galvez BG, Martinez-Ruiz A, Zaragoza C, Lamas S, Tryggvason K, Apte SS, Arroyo AG (2007) Functional interplay between endothelial nitric oxide synthase and membrane type 1 matrix metalloproteinase in migrating endothelial cells. *Blood* 110: 2916 – 2923

Giacomini A, Ackermann M, Belleri M, Coltrini D, Nico B, Ribatti D, Konerding MA, Presta M, Righi M (2015) Brain angioarchitecture and intussusceptive microvascular growth in a murine model of Krabbe disease. *Angiogenesis* 18: 499 – 510

Gonzalo P, Guadamillas MC, Hernandez-Riquer MV, Pollan A, Grande-Garcia A, Bartolome RA, Vasanji A, Ambrogio C, Chiarle R, Teixido J *et al* (2010) MT1-MMP is required for myeloid cell fusion via regulation of Rac1 signaling. *Dev Cell* 18: 77 – 89

van Groningen JP, Wenink AC, Testers LH (1991) Myocardial capillaries: increase in number by splitting of existing vessels. *Anat Embryol (Berl)* 184: 65 – 70

Groppa E, Brkic S, Uccelli A, Wirth G, Korpisalo-Pirinen P, Filippova M, Dasen B, Sacchi V, Muraro MG, Trani M *et al* (2018) EphrinB2/EphB4 signaling regulates non-sprouting angiogenesis by VEGF. *EMBO Rep* 19: e45054

Gutierrez LS, Ling J, Nye D, Papathomas K, Dickinson C (2015) Thrombospondin peptide ABT-898 inhibits inflammation and angiogenesis in a colitis model. *World J Gastroenterol* 21: 6157 – 6166

Gutierrez-Fernandez A, Soria-Valles C, Osorio FG, Gutierrez-Abril J, Garabaya C, Aguirre A, Fueyo A, Fernandez-Garcia MS, Puente XS, Lopez-Otin C (2015) Loss of MT1-MMP causes cell senescence and nuclear defects which can be reversed by retinoic acid. *EMBO J* 34: 1875 – 1888

Gyires K, Toth EV, Zadori SZ (2014) Gut inflammation: current update on pathophysiology, molecular mechanism and pharmacological treatment modalities. *Curr Pharm Des* 20: 1063 – 1081

Hlushchuk R, Styp-Rekowska B, Dzambazi J, Wnuk M, Huynh-Do U, Makanya A, Djonov V (2017) Endoglin inhibition leads to intussusceptive angiogenesis via activation of factors related to COUP-TFII signaling pathway. *PLoS ONE* 12: e0182813

Iruela-Arispe ML (2008) Regulation of thrombospondin1 by extracellular proteases. *Curr Drug Targets* 9: 863 – 868

Isenberg JS, Frazier WA, Roberts DD (2008a) Thrombospondin-1: a physiological regulator of nitric oxide signaling. *Cell Mol Life Sci* 65: 728 – 742

Isenberg JS, Roberts DD, Frazier WA (2008b) CD47: a new target in cardiovascular therapy. *Arterioscler Thromb Vasc Biol* 28: 615 – 621

Isenberg JS, Martin-Manso G, Maxhimer JB, Roberts DD (2009) Regulation of nitric oxide signalling by thrombospondin 1: implications for anti-angiogenic therapies. *Nat Rev Cancer* 9: 182 – 194

Karthik S, Djukic T, Kim JD, Zuber B, Makanya A, Odriozola A, Hlushchuk R, Filipovic N, Jin SW, Djonov V (2018) Synergistic interaction of sprouting and intussusceptive angiogenesis during zebrafish caudal vein plexus development. *Sci Rep* 8: 9840

Kevil CG, Orr AW, Langston W, Mickett K, Murphy-Ullrich J, Patel RP, Kucik DF, Bullard DC (2004) Intercellular adhesion molecule-1 (ICAM-1) regulates endothelial cell motility through a nitric oxide-dependent pathway. *J Biol Chem* 279: 19230 – 19238

Klose A, Zigrino P, Mauch C (2013) Monocyte/macrophage MMP-14 modulates cell infiltration and T-cell attraction in contact dermatitis but not in murine wound healing. *Am J Pathol* 182: 755 – 764

Kolluru GK, Sinha S, Majumder S, Muley A, Siamwala JH, Gupta R, Chatterjee S (2010) Shear stress promotes nitric oxide production in endothelial cells by sub-cellular delocalization of eNOS: a basis for shear stress mediated angiogenesis. *Nitric Oxide* 22: 304 – 315

Konerding MA, Turhan A, Ravnic DJ, Lin M, Fuchs C, Secomb TW, Tsuda A, Mentzer SJ (2010) Inflammation-induced intussusceptive angiogenesis in murine colitis. *Anat Rec (Hoboken)* 293: 849 – 857

Konerding MA, Gibney BC, Houdek JP, Chamoto K, Ackermann M, Lee GS, Lin M, Tsuda A, Mentzer SJ (2012) Spatial dependence of alveolar angiogenesis in post-pneumonectomy lung growth. *Angiogenesis* 15: 23 – 32

Koutroubakis IE, Tsiolakidou G, Karmiris K, Kouroumalis EA (2006) Role of angiogenesis in inflammatory bowel disease. *Inflamm Bowel Dis* 12: 515 – 523

Koziol A, Gonzalo P, Mota A, Pollan A, Lorenzo C, Colome N, Montaner D, Dopazo J, Arribas J, Canals F *et al* (2012a) The protease MT1-MMP drives a combinatorial proteolytic program in activated endothelial cells. *FASEB J* 26: 4481 – 4494

Koziol A, Martin-Alonso M, Clemente C, Gonzalo P, Arroyo AG (2012b) Site-specific cellular functions of MT1-MMP. *Eur J Cell Biol* 91: 889 – 895

Kumar S, Ratnikov BI, Kazanov MD, Smith JW, Cieplak P (2015) CleavPredict: a platform for reasoning about matrix metalloproteinases proteolytic events. *PLoS ONE* 10: e0127877

Lawler PR, Lawler J (2012) Molecular basis for the regulation of angiogenesis by thrombospondin-1 and -2. *Cold Spring Harb Perspect Med* 2: a006627

Leavesley DI, Schwartz MA, Rosenfeld M, Cheresh DA (1993) Integrin beta 1- and beta 3-mediated endothelial cell migration is triggered through distinct signaling mechanisms. *J Cell Biol* 121: 163 – 170

Lee NV, Sato M, Annis DS, Loo JA, Wu L, Mosher DF, Iruela-Arispe ML (2006) ADAMTS1 mediates the release of antiangiogenic polypeptides from TSP1 and 2. *EMBO J* 25: 5270 – 5283

Lindberg FP, Gresham HD, Reinhold MI, Brown EJ (1996) Integrin-associated protein immunoglobulin domain is necessary for efficient vitronectin bead binding. *J Cell Biol* 134: 1313 – 1322

Lopez-Dee Z, Pidcock K, Gutierrez LS (2011) Thrombospondin-1: multiple paths to inflammation. *Mediators Inflamm* 2011: 296069

Lopez-Ramirez MA, Fonseca G, Zeineddine HA, Girard R, Moore T, Pham A, Cao Y, Shenkar R, de Kreuk BJ, Lagarrigue F *et al* (2017) Thrombospondin1 (TSP1) replacement prevents cerebral cavernous malformations. *J Exp Med* 214: 3331 – 3346

Mandell DJ, Kortemme T (2009) Computer-aided design of functional protein interactions. *Nat Chem Biol* 5: 797 – 807

Margosio B, Rusnati M, Bonezzi K, Cordes BL, Annis DS, Urbinati C, Giavazzi R, Presta M, Ribatti D, Mosher DF *et al* (2008) Fibroblast growth factor-2 binding to the thrombospondin-1 type III repeats, a novel antiangiogenic domain. *Int J Biochem Cell Biol* 40: 700 – 709

Martin-Alonso M, Garcia-Redondo AB, Guo D, Camafeita E, Martinez F, Alfranca A, Mendez-Barbero N, Pollan A, Sanchez-Camacho C, Denhardt DT *et al* (2015) Deficiency of MMP17/MT4-MMP proteolytic activity predisposes to aortic aneurysm in mice. *Circ Res* 117: e13 – e26

Monvoisin A, Alva JA, Hofmann JJ, Zovein AC, Lane TF, Iruela-Arispe ML (2006) VE-cadherin-CreERT2 transgenic mouse: a model for inducible recombination in the endothelium. *Dev Dyn* 235: 3413 – 3422

Mori M, Stokes KY, Vowinkel T, Watanabe N, Elrod JW, Harris NR, Lefer DJ, Hibi T, Granger DN (2005) Colonic blood flow responses in experimental colitis: time course and underlying mechanisms. *Am J Physiol Gastrointest Liver Physiol* 289: G1024 – G1029

Nivon LG, Moretti R, Baker D (2013) A Pareto-optimal refinement method for protein design scaffolds. *PLoS ONE* 8: e59004

Noiri E, Lee E, Testa J, Quigley J, Colflesh D, Keese CR, Giaever I, Goligorsky MS (1998) Podokinesis in endothelial cell migration: role of nitric oxide. *Am J Physiol* 274: C236 – C244

Nowak-Sliwinska P, Alitalo K, Allen E, Anisimov A, Aplin AC, Auerbach R, Augustin HG, Bates DO, van Beijnum JR, Bender RHF *et al* (2018) Consensus guidelines for the use and interpretation of angiogenesis assays. *Angiogenesis* 21: 425 – 532

Oblander SA, Zhou Z, Galvez BG, Starcher B, Shannon JM, Durbeej M, Arroyo AG, Tryggvason K, Apte SS (2005) Distinctive functions of membrane type 1 matrix-metalloprotease (MT1-MMP or MMP-14) in lung and submandibular gland development are independent of its role in pro-MMP-2 activation. *Dev Biol* 277: 255 – 269

Parma L, Baganha F, Quax PHA, de Vries MR (2017) Plaque angiogenesis and intraplaque hemorrhage in atherosclerosis. *Eur J Pharmacol* 816: 107 – 115

Pender SL, Salmela MT, Monteleone G, Schnapp D, McKenzie C, Spencer J, Fong S, Saarialho-Kere U, MacDonald TT (2000) Ligation of alpha4ss1 integrin on human intestinal mucosal mesenchymal cells selectively Up-regulates membrane type-1 matrix metalloproteinase and confers a migratory phenotype. *Am J Pathol* 157: 1955 – 1962

Podolsky DK (2002) Inflammatory bowel disease. *N Engl J Med* 347: 417 – 429

Potente M, Gerhardt H, Carmeliet P (2011) Basic and therapeutic aspects of angiogenesis. *Cell* 146: 873 – 887

Punekar S, Zak S, Kalter VG, Dobransky L, Punekar I, Lawler JW, Gutierrez LS (2008) Thrombospondin 1 and its mimetic peptide ABT-510 decrease angiogenesis and inflammation in a murine model of inflammatory bowel disease. *Pathobiology* 75: 9 – 21

Rafii S, Cao Z, Lis R, Siempos II, Chavez D, Shido K, Rabbany SY, Ding BS (2015) Platelet-derived SDF-1 primes the pulmonary capillary vascular niche to drive lung alveolar regeneration. *Nat Cell Biol* 17: 123 – 136

Rajavashisth TB, Liao JK, Galis ZS, Tripathi S, Laufs U, Tripathi J, Chai NN, Xu XP, Jovinge S, Shah PK *et al* (1999) Inflammatory cytokines and oxidized low density lipoproteins increase endothelial cell expression of membrane type 1-matrix metalloproteinase. *J Biol Chem* 274: 11924 – 11929

Ravnic DJ, Konerding MA, Tsuda A, Huss HT, Wolloscheck T, Pratt JP, Mentzer SJ (2007) Structural adaptations in the murine colon microcirculation associated with hapten-induced inflammation. *Gut* 56: 518 – 523

Resovi A, Pinessi D, Chiorino G, Taraboletti G (2014) Current understanding of the thrombospondin-1 interactome. *Matrix Biol* 37: 83 – 91

Ribatti D, Djonov V (2012) Intussusceptive microvascular growth in tumors. *Cancer Lett* 316: 126 – 131

Risher WC, Kim N, Koh S, Choi JE, Mitev P, Spence EF, Pilaz LJ, Wang D, Feng G, Silver DL *et al* (2018) Thrombospondin receptor alpha2delta-1 promotes synaptogenesis and spinogenesis via postsynaptic Rac1. *J Cell Biol* 217: 3747 – 3765

Rius C, Sanz MJ (2015) Intravital microscopy in the cremaster muscle microcirculation for endothelial dysfunction studies. *Methods Mol Biol* 1339: 357 – 366

Robinson SD, Hodivala-Dilke KM (2011) The role of beta3-integrins in tumor angiogenesis: context is everything. *Curr Opin Cell Biol* 23: 630 – 637

Rogers NM, Sharifi-Sanjani M, Csanyi G, Pagano PJ, Isenberg JS (2014) Thrombospondin-1 and CD47 regulation of cardiac, pulmonary and vascular responses in health and disease. *Matrix Biol* 37: 92 – 101

Sasaki M, Bharwani S, Jordan P, Elrod JW, Grisham MB, Jackson TH, Lefer DJ, Alexander JS (2003) Increased disease activity in eNOS-deficient mice in experimental colitis. *Free Radic Biol Med* 35: 1679 – 1687

Scaldaferri F, Vetrano S, Sans M, Arena V, Straface G, Stigliano E, Repici A, Sturm A, Malesci A, Panes J *et al* (2009) VEGF-A links angiogenesis and inflammation in inflammatory bowel disease pathogenesis. *Gastroenterology* 136: 585 – 595 e585

Stein A, Kortemme T (2013) Improvements to robotics-inspired conformational sampling in rosetta. *PLoS ONE* 8: e63090

Styp-Rekowska B, Hlushchuk R, Pries AR, Djonov V (2011) Intussusceptive angiogenesis: pillars against the blood flow. *Acta Physiol (Oxf)* 202: 213 – 223

Tang Y, Rowe RG, Botvinick EL, Kurup A, Putnam AJ, Seiki M, Weaver VM, Keller ET, Goldstein S, Dai J *et al* (2013) MT1-MMP-dependent control of skeletal stem cell commitment via a beta1-integrin/YAP/TAZ signaling axis. *Dev Cell* 25: 402 – 416

Taraboletti G, Rusnati M, Ragona L, Colombo G (2010) Targeting tumor angiogenesis with TSP-1-based compounds: rational design of antiangiogenic mimetics of endogenous inhibitors. *Oncotarget* 1: 662 – 673

Thibeault S, Rautureau Y, Oubaha M, Faubert D, Wilkes BC, Delisle C, Gratton JP (2010) S-nitrosylation of beta-catenin by eNOS-derived NO promotes VEGF-induced endothelial cell permeability. *Mol Cell* 39: 468 – 476

Tolstanova G, Khomenko T, Deng X, Chen L, Tarnawski A, Ahluwalia A, Szabo S, Sandor Z (2009) Neutralizing anti-vascular endothelial growth factor (VEGF) antibody reduces severity of experimental ulcerative colitis in rats: direct evidence for the pathogenic role of VEGF. *J Pharmacol Exp Ther* 328: 749 – 757

te Velde AA, de Kort F, Sterrenburg E, Pronk I, ten Kate FJ, Hommes DW, van Deventer SJ (2007) Comparative analysis of colonic gene expression of three experimental colitis models mimicking inflammatory bowel disease. *Inflamm Bowel Dis* 13: 325 – 330

Vimalraj S, Bhuvaneswari S, Lakshmikirupa S, Jyothsna G, Chatterjee S (2018) Nitric oxide signaling regulates tumor-induced intussusceptive-like angiogenesis. *Microvasc Res* 119: 47 – 59

Wang Y, Nakayama M, Pitulescu ME, Schmidt TS, Bochenek ML, Sakakibara A, Adams S, Davy A, Deutsch U, Luthi U *et al* (2010) Ephrin-B2 controls VEGF-induced angiogenesis and lymphangiogenesis. *Nature* 465: 483 – 486

Williams JL, Cartland D, Hussain A, Egginton S (2006) A differential role for nitric oxide in two forms of physiological angiogenesis in mouse. *J Physiol* 570: 445 – 454

Yana I, Sagara H, Takaki S, Takatsu K, Nakamura K, Nakao K, Katsuki M, Taniguchi S, Aoki T, Sato H *et al* (2007) Crosstalk between neovessels and mural cells directs the site-specific expression of MT1-MMP to endothelial tip cells. *J Cell Sci* 120: 1607 – 1614

Yanez-Mo M, Alfranca A, Cabanas C, Marazuela M, Tejedor R, Ursa MA, Ashman LK, de Landazuri MO, Sanchez-Madrid F (1998) Regulation of endothelial cell motility by complexes of tetraspan molecules CD81/TAPA-1 and CD151/PETA-3 with alpha3 beta1 integrin localized at endothelial lateral junctions. *J Cell Biol* 141: 791 – 804

Yang J, Yan R, Roy A, Xu D, Poisson J, Zhang Y (2015) The I-TASSER Suite: protein structure and function prediction. *Nat Methods* 12: 7 – 8

Yurdagul A Jr, Chen J, Funk SD, Albert P, Kevil CG, Orr AW (2013) Altered nitric oxide production mediates matrix-specific PAK2 and NF-kappaB activation by flow. *Mol Biol Cell* 24: 398 – 408

Zhou A, Egginton S, Hudlicka O, Brown MD (1998) Internal division of capillaries in rat skeletal muscle in response to chronic vasodilator treatment with alpha1-antagonist prazosin. *Cell Tissue Res* 293: 293 – 303

SCIENTIFIC REPORTS
nature research

OPEN

PKM2 regulates endothelial cell junction dynamics and angiogenesis via ATP production

Jesús Gómez-Escudero[1,2], Cristina Clemente[1,3], Diego García-Weber[4], Rebeca Acín-Pérez[5], Jaime Millán[4], José A. Enríquez[5], Katie Bentley[6,7], Peter Carmeliet[8,9,10] & Alicia G. Arroyo[1,3*]

Angiogenesis, the formation of new blood vessels from pre-existing ones, occurs in pathophysiological contexts such as wound healing, cancer, and chronic inflammatory disease. During sprouting angiogenesis, endothelial tip and stalk cells coordinately remodel their cell-cell junctions to allow collective migration and extension of the sprout while maintaining barrier integrity. All these processes require energy, and the predominant ATP generation route in endothelial cells is glycolysis. However, it remains unclear how ATP reaches the plasma membrane and intercellular junctions. In this study, we demonstrate that the glycolytic enzyme pyruvate kinase 2 (PKM2) is required for sprouting angiogenesis *in vitro* and *in vivo* through the regulation of endothelial cell-junction dynamics and collective migration. We show that PKM2-silencing decreases ATP required for proper VE-cadherin internalization/traffic at endothelial cell-cell junctions. Our study provides fresh insight into the role of ATP subcellular compartmentalization in endothelial cells during angiogenesis. Since manipulation of EC glycolysis constitutes a potential therapeutic intervention route, particularly in tumors and chronic inflammatory disease, these findings may help to refine the targeting of endothelial glycolytic activity in disease.

Angiogenesis, the formation of new blood vessels from pre-existing ones, occurs in pathophysiological contexts such as wound healing, cancer and chronic inflammatory disease. In sprouting angiogenesis, endothelial cells (ECs) receive a stimulus (usually VEGFA) which triggers the angiogenic response by the selection and specification of the endothelial tip cell[1]. This cell migrates toward the stimulus followed by the stalk cells, defined by a balanced Dll4/VEGFA signaling[2]. A fine-tuned coordination of diverse cellular responses is necessary at this initial step, including reorganization of endothelial cell junctions, tip-cell migration to generate characteristic cytoskeletal protrusions called filopodia, and proliferation and lumenization by stalk cells. Impairment in any of these processes prevents productive angiogenesis and the formation of a functional vascular plexus[3–5]. A shared feature of all these endothelial cell responses is the need for energy in the form of ATP[6,7].

The predominant ATP generation route in ECs is glycolysis[8], providing both the ATP required for cell function and the intermediate metabolites that feed into other metabolic pathways for macromolecule biosynthesis[9,10]. During sprouting angiogenesis, glycolysis is boosted in the endothelial tip cell, and angiogenesis is blunted by the genetic deletion or pharmacological inhibition of glycolytic enzymes like PFKFB3[11–13]. Recent dissection of the impact of distinct metabolic routes in endothelial cells has revealed that glycolysis impacts endothelial

[1]Vascular Pathophysiology, Centro Nacional de Investigaciones Cardiovasculares (CNIC). Melchor Fernández Almagro 3, 28029, Madrid, Spain. [2]Tumour Biology Department, Barts Cancer Institute, John´s Vane Centre, Queen Mary´s University of London. Charterhouse Sq, EC1M 6BQ, London, UK. [3]Centro de Investigaciones Biológicas (CIB-CSIC). Ramiro de Maeztu 9, 28040, Madrid, Spain. [4]Centro de Biología Molecular Severo Ochoa, Consejo Superior de Investigaciones Científicas (CSIC), Universidad Autónoma de Madrid, 28049, Madrid, Spain. [5]Myocardial Pathology Areas, Centro Nacional de Investigaciones Cardiovasculares (CNIC). Melchor Fernández Almagro 3, 28029, Madrid, Spain. [6]Computational Biology Laboratory, Beth Israel Deaconess Medical Center, Harvard Medical School, Boston, MA, USA. [7]Cellular Adaptive Behaviour Laboratory, Rudbeck Laboratories, Department of Immunology, Genetics and Pathology, Uppsala University, Uppsala, Sweden. [8]Laboratory of Angiogenesis and Vascular Metabolism, Center for Cancer Biology, Vlaams Instituut voor Biotechnologie (VIB), B-3000, Leuven, Belgium. [9]Laboratory of Angiogenesis and Vascular Metabolism, Center for Cancer Biology, Department of Oncology, University of Leuven, B-3000, Leuven, Belgium. [10]State Key Laboratory of Ophthalmology, Zhongsan Ophthalmic Center, Sun Yat-Sen University, Guangzhou, China. *email: agarroyo@cib.csic.es

cell migration (in addition to proliferation), whereas fatty-acid oxidation and amino-acid metabolism support nucleotide and protein synthesis[14]. These recent discoveries have opened new avenues for possible therapeutic modulation of EC metabolism in cancer and chronic inflammatory disease[15].

Glycolysis is classically viewed as occurring in the cytosol, with ATP diffusing throughout the cell to reach distant locations such as plasma membrane protrusions and intercellular junctions. ATP diffusion to cell-membrane locations is often limited by the long distances involved and obstruction by the packed cytoskeleton[16,17]. Pioneering studies showed the anchoring of glycolytic enzymes to the erythrocyte plasma membrane[18], and more recent evidence supports the subcellular compartmentalization of glycolytic and ATP-producing enzymes in other cell types[19]. Examples of this type of local ATP production include the regulation of vesicle traffic along microtubules in neurons by GAPDH[20], actin cytoskeleton reorganization at lamellipodia by PFKFB3[11], and the establishment and stability of endothelial cell-cell contacts by the nucleoside-diphosphate kinase (NDPK) NM23[6]. These findings indicate that compartmentalization of ATP-producing enzymes is a general mechanism governing spatio-temporal cellular events[21]. How this ATP compartmentalization occurs is, however, incompletely understood.

During glycolysis, the enzyme pyruvate kinase (PK) is in charge of catalyzing the last step, which converts phosphoenolpyruvate to pyruvate with the generation of one molecule of ATP. PK has three forms: L (liver), R (erythrocytes), and M (muscle). The M form is expressed in most human organs and has two isoforms, M1 and M2, regulated by alternative splicing of the PKM gene[22]. The M1 and M2 isoforms differ in the regulation of their catalytic activity, with PKM1 constitutively active and PKM2 subject to regulation[22–25]. PKM2 function has mainly been analyzed in cancer and inflammation[26,27]. Although PKM2 was considered a master regulator of proliferation, particularly in tumor cells, recent studies have established that the primary cause of cell-cycle arrest in PKM2-null mice or PKM2-depleted cells is compensatory overexpression of PKM1[27,28]. Protein kinase actions have also been linked to PKM2, although the direct contribution of PKM2 and the importance of this activity remain unresolved[29,30]. In the context of angiogenesis, soluble PKM2 dimers released by tumor cells have been reported to increase endothelial cell-tube formation by increasing cell proliferation, migration, and extracellular matrix adhesion; however, the mechanisms of these PKM2 extracellular actions remain unclear[31]. More recently, JMDM8 was shown to regulate human EC sprouting and metabolism through its association with PKM2, but the impact of JMDM8 silencing was only analyzed in the sprout spheroid assay, and no mechanisms were defined[32]. In this study, we explore PKM2 actions in sprouting angiogenesis *in vitro* and *in vivo* and decipher the role of PKM2 subcellular compartmentalization in this process.

Results

PKM2 is required for sprouting angiogenesis *in vitro* and *in vivo*. To characterize the role of PKM2 in ECs during sprouting angiogenesis, we specifically silenced PKM2 expression in human umbilical vein ECs (HUVEC) with an isoform-specific siRNA that decreased PKM2 expression without affecting PKM1 levels (Fig. 1A). In the spheroid culture system used to study sprouting angiogenesis, suppression of PKM2 expression was maintained up to the final time point (day 7) (Supplementary Figure S1A,B). Although sprouts developed a proper lumen in both groups (Supplementary Figure S1C), PKM2-silenced EC spheroids produced fewer and shorter sprouts than spheroids formed by control siRNA-transfected ECs (Fig. 1B–D). Silencing PKM2 also resulted in reduced number and shorter endothelial tubes in the 'hanging drop' assay, which runs for 24 hours (Supplementary Figure S1D,E). Moreover, sprouts formed by control and PKM2-silenced EC spheroids contained similar proportions of Ki67+ proliferating cells, and tip cells in these spheroids produced fewer filopodia (Fig. 1E–H). Silencing PKM2 with an independent siRNA in mouse lung ECs also impaired sprout formation in the spheroids confirming the need of PKM2 for *in vitro* sprouting angiogenesis (Supplementary Figure S1F,G).

To determine whether PKM2 was also required for sprouting angiogenesis *in vivo*, P6 mice were given an intravitreal injection of PKM2 siRNA, and we examined the retinal vasculature after 72 h. Western blot of retina extracts showed reduced PKM2 protein expression, and immunofluorescence analysis confirmed decreased PKM2 in the vasculature (Fig. 2A,B). PKM2-silencing in retina diminished radial vascular growth with no impact on vascular density (Fig. 2C–E). This prompted us to analyze EC number and proliferation. PKM2-silenced and control-siRNA treated retinas had similar densities of ERG+ cells and the same proportion of Ki67+ ECs (Fig. 2F–I). Matching the *in vitro* analysis, filopodia number was lower in PKM2-silenced retinas (Fig. 2J,K). Together, these observations show that PKM2 is required for sprouting angiogenesis *in vitro* and *in vivo* by mechanisms that do not seem to involve EC proliferation.

PKM2 is located at VE-cadherin-expressing endothelial cell junctions. Although PKM2 was mostly found in the cytoplasm of ECs, high-resolution confocal microscopy images, image deconvolution and profile intensity analysis revealed however that a pool of PKM2 localized close to VE-cadherin and cortical F-actin at the junctions (Fig. 3A,B). We confirmed PKM2 vicinity to VE-cadherin at the endothelial junctions by proximity ligation assays (Fig. 3C). Moreover, in spite of similar PKM2 protein levels, PKM2 was barely observed at the junctions of VE-cadherin-null endothelial cells compared to VE-cadherin-positive ones (Fig. 3D,E). PKM2 was also found nearby the junctions of ECs stimulated with sphingosine-1-phosphate (S1P), an inducer of EC junction remodeling and reinforcement[33] (Supplementary Figure S2A), and of 3D EC sprouts *in vitro* (Fig. 3F), without significant differences in PKM2 presence at the junctions of tip and stalk cells (PKM2 $MFI_{tip} = 144.4 \pm 22.82$ and $MFI_{stalk} = 156.3 \pm 20.3$, $n = 19$ sprouts). PKM2 was also detected at F-actin-rich filopodia and lamellipodia of migrating ECs in 3D and 2D respectively (Supplementary Figure S2B,C), in line with the reported PKM2/F-actin association[34].

In accordance with the immunofluorescence data, PKM2 was found by western blot in both cytosolic and membrane EC fractions and the specificity of this compartmentation was shown by reduced PKM2 abundance in the membrane fraction of PKM2-silenced ECs (Fig. 3G). Cell membrane subfractionation further revealed that PKM2 was present in low-density fractions containing plasma membrane and in endosomes (Fig. 3H).

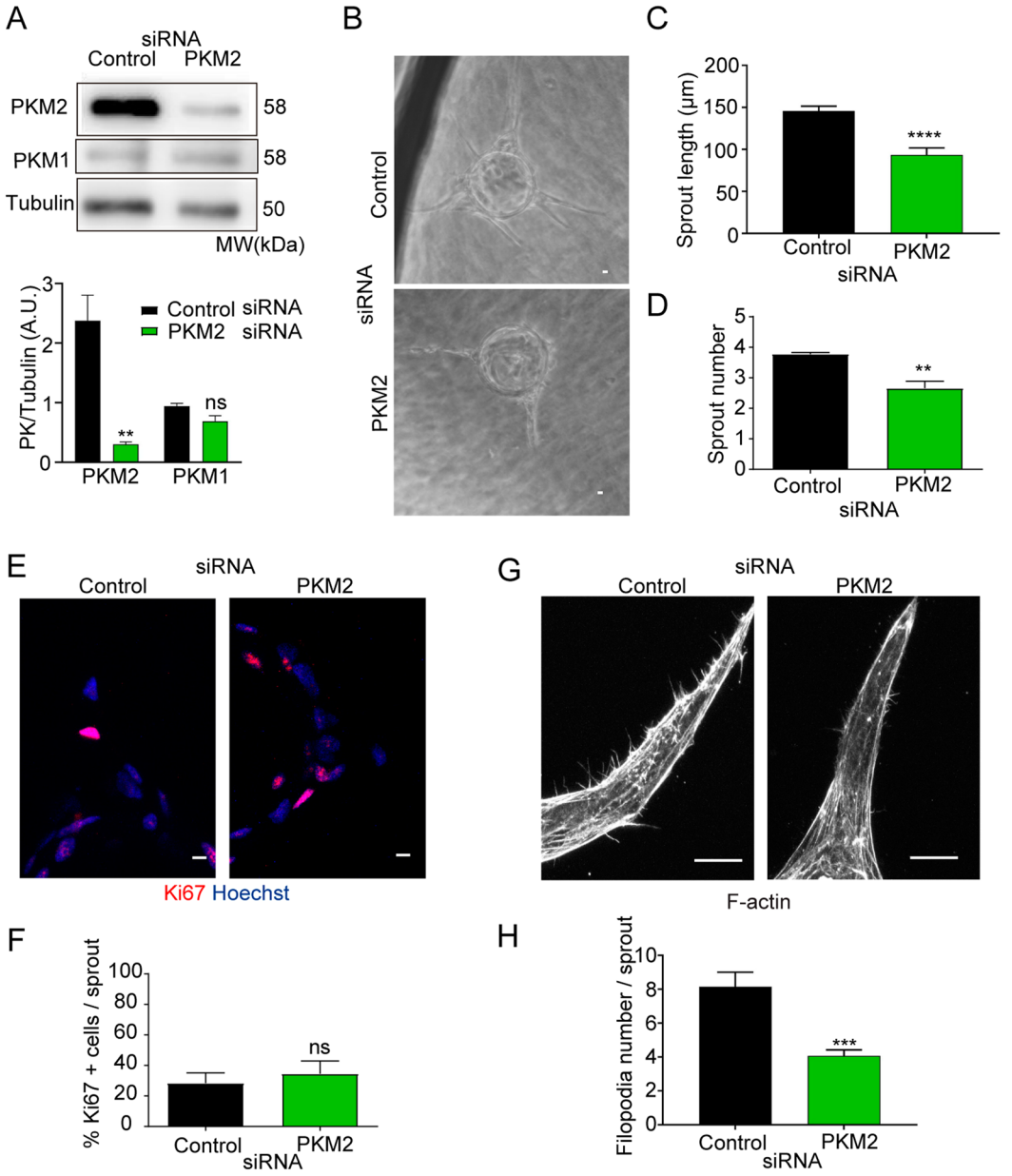

Figure 1. PKM2 is required for *in vitro* endothelial cell sprouting. (**A**) Western blot of PKM2 and PKM1 expression 72 hours after siRNA silencing in HUVECs and quantification versus tubulin included as a loading control; means ± SEM, n = 3, ns non-significant, **p < 0.01 by unpaired Student t-test. (**B**) Bright-field microscopy images of spheroids coated with HUVECs transfected with control or PKM2 siRNA and embedded in fibrin gels for 7 days. Scale bar, 10 µm. (**C**) Sprout length in 3D spheroids; means ± SEM, n = 103 and 38 spheroids formed by control and PKM2 siRNA-silenced cells from one representative experiment of five performed, ****p < 0.0001 by unpaired Student t-test. (**D**) Sprout numbers in 3D spheroids; means ± SEM, n = 27 and 14 spheroids formed by control and PKM2 siRNA-silenced cells from one experiment representative of five performed, **p < 0.01 by unpaired Student t-test. (**E**) Immunofluorescence of Ki67 (red, proliferation) and Hoechst (blue, nuclei) in 3D spheroid sprouts. Scale bar, 10 µm. (**F**) Percentage of Ki67-positive cells per sprout in 3D spheroids; means ± SEM, n = 3 independent experiments, ns non-significant by paired Student t-test. (**G**) Immunofluorescence of F-actin in 3D spheroid sprouts. Scale bar, 10 µm. (**H**) Filopodia number in 3D spheroids; means ± SEM, n = 13 and 15 filopodia in sprouts formed by control and PKM2 siRNA-silenced cells from one representative experiment of five performed, ***p < 0.0001 by Welch´s test. MW, molecular weight. See also Figure S1.

PKM2-silencing destabilizes junctions and impairs EC collective migration. Productive angiogenesis depends on VE-cadherin-mediated EC junction stability and dynamics[35,36]. We therefore investigated the influence of PKM2 on EC-junctional VE-cadherin at baseline and upon junction remodeling induced by S1P.

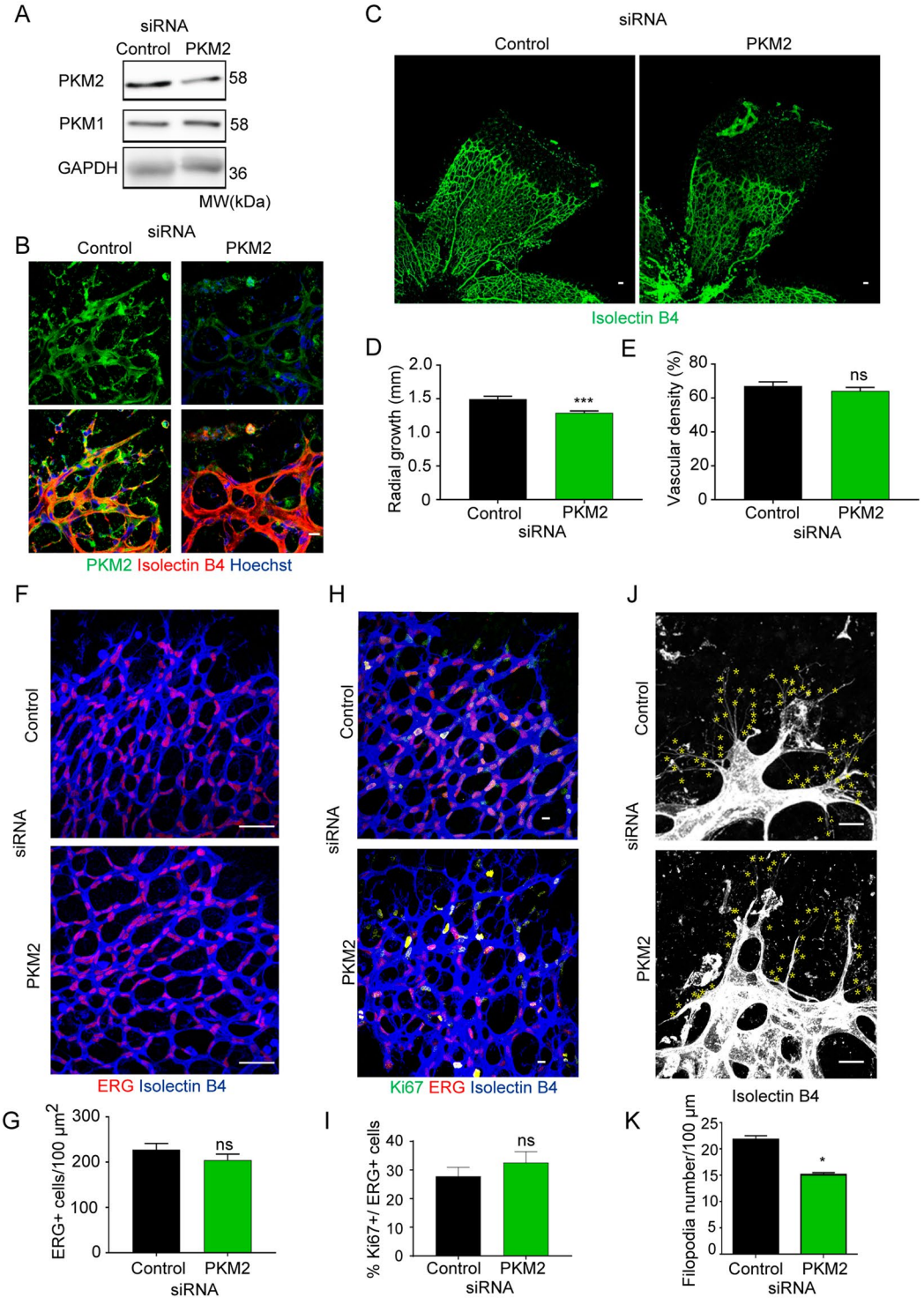

Figure 2. PKM2 silencing results in reduced vascular growth and filopodia number in the postnatal mouse retina. (**A**) Western blot of PKM2 and PKM1 expression in protein extracts from mouse retinas obtained 72 hours after intravitreal siRNA-injection. GAPDH is included as a loading control; n = 3 mice per condition. (**B**) Immunofluorescence of isolectin B4 (red, vessels), PKM2 (green), and nuclei (blue, Hoechst) in whole-mount P6 mouse retinas 72 hours after intravitreal siRNA-injection. Scale bar, 10 µm. (**C**) Immunofluorescence of isolectin B4 (green, vessels) in whole-mount P6 mouse retinas 72 hours after intravitreal siRNA-injection. Scale bar, 50 µm. Disconnected Erg/IB4-positive structures correspond to rests of hyaline membrane fragments. (**D**) Radial vascular growth in mouse retinas (P6) 72 hours after intravitreal siRNA-injection, means ± SEM, n = 8 mice per condition, ***$p < 0.001$ by Mann-Whitney test. (**E**) Vascular density in mouse retinas (P6) 72 hours after intravitreal siRNA-injection, means ± SEM, n = 4 mice per condition, ns non-significant by unpaired Student t-test. (**F**) Immunofluorescence ERG (white, endothelial cell nuclei) in whole-mount P6 mouse retinas 72 hours after intravitreal siRNA-injection. Scale bar, 50 µm. (**G**) ERG positive cells per vessel

area in P6 mouse retinas 72 hours after intravitreal siRNA-injection, means ± SEM, n = 4 mice per condition, ns non-significant by unpaired Student t-test. (**H**) Immunofluorescence of isolectin B4 (blue, vessels), Ki67 (green, proliferation), and ERG (red, endothelial cell nuclei) in whole-mount P6 mouse retinas 72 hours after intravitreal siRNA-injection. Scale bar, 10 μm. (**I**) Percentage of Ki67-positive cells per total ERG-positive cells in P6 mouse retinas 72 hours after intravitreal siRNA-injection; means ± SEM, n = 4 mice per condition, ns non-significant by unpaired Student t-test. (**J**) Immunofluorescence of isolectin B4 (white, vessels) in whole-mount P6 mouse retinas 72 hours after intravitreal siRNA-injection. Each yellow asterisk marks one filopodia. Scale bar, 10 μm. (**K**) Number of filopodia per 100 μm of vascular front in P6 mouse retinas 72 hours after intravitreal siRNA-injection; means ± SEM, n = 4 mice per condition, *$p < 0.05$ by unpaired Student t-test. MW, molecular weight.

In spite of no change in total VE-cadherin protein expression, PKM2-silenced ECs showed lower cell-junction VE-cadherin intensity than control ECs, together with a higher proportion of discontinuous junctions at baseline and after S1P treatment (Fig. 3I–M and Supplementary Figure S2D–F). Junctions formed by PKM2-silenced ECs also showed a clear decrease in plakoglobin, a marker of stable VE-cadherin cell-cell contacts (Fig. 3N and Supplementary Figure S2G). Indeed, PKM2-silencing with an independent siRNA confirmed a similar altered junctional VE-cadherin pattern in mouse lung ECs (Supplementary Figure 2H–J). Finally, PKM2-silenced cells showed a weakened response to S1P-driven reinforcement of the EC barrier, as indicated by lower transendothelial electrical resistance (TEER) values (Fig. 3O). These data indicate defects in VE-cadherin–mediated EC barrier in the absence of PKM2 in remodeling conditions.

A recognized function of VE-cadherin at cell-cell junctions is to conduct polarity signals while maintaining barrier integrity during collective migration[36]. In line with the observed junctional defects, PKM2-silenced HUVECs were significantly less efficient than control siRNA-transfected ECs at closing the wound area in the scratch assay without showing differences in cell proliferation (Fig. 4A–D). Accordingly, inhibition of proliferation did not change the defective wound closure and PKM2 silencing did not affect EC basal growth and proliferation (Supplementary Figure S3A–D). We next assessed the role of PKM2 in the orientation and directionality of migrating EC cells by quantifying Golgi apparatus polarization and by time-lapse microscopy[37,38]. PKM2-silenced migrating EC cultures showed more discontinuous junctions and this correlated with a higher proportion of cells polarized against the wound than control cultures (Fig. 4E–G). Time-lapse recording and single-cell track analysis confirmed that PKM2-silenced ECs migrated faster and for longer linear (Euclidean) distances opposite to the wound but for shorter distances and less directional toward the wound compared with controls (Fig. 4H–J and Movies S1–S2). Moreover, PKM2 silencing impaired collective migration of adjacent endothelial cells (Fig. 4K).

PKM2 is required for endothelial cell junction remodeling during angiogenic sprouting *in vitro* and *in vivo*. In addition to maintenance of junction stability and to collective migration in 2D, VE-cadherin dynamics are also essential for functional EC arrangements during 3D sprouting angiogenesis, and this manifests as a balanced distribution of stable and unstable EC junctions[35]. To determine the role of PKM2 in regulating this mosaicism, we quantified the distribution of EC junction patches by classifying the morphology of EC junctions based on their VE-cadherin pattern, from discontinuous (active/unstable) to continuous (inactive/stable) according to the reported 'patching algorithm'[35]. The 3D sprouts formed *in vitro* by PKM2-silenced human ECs showed an altered EC-junction patch distribution, with a higher abundance of patches containing active/unstable junctions than 3D sprouts formed by control siRNA-transfected ECs; this was reflected by a change in the active/unstable:inactive/stable patch ratio (Fig. 5A–D). This phenotype was also confirmed *in vivo* in the vasculature of PKM2-silenced postnatal retinas (Fig. 5E–G).

PKM2 activity is involved in the regulation of EC junctions and sprouting angiogenesis. In addition to its action in glycolysis, PKM2 has been linked to non-glycolytic functions[29,30]. To determine whether the effects of PKM2 absence on EC junctions and sprouting angiogenesis are related to pyruvate kinase activity, we treated ECs with shikonin, a specific inhibitor of the PKM2 isoform[39]. Pharmacological inhibition of PKM2 activity increased the number of discontinuous junctions in basal and S1P-treated human ECs (Supplementary Figure S4A,B) and recapitulated the rest of effects of PKM2-silencing. Shikonin reduced the number and length of sprouts in the 3D spheroid assay and impaired wound closure and EC collective migration without influencing EC proliferation (Supplementary Figure S4C–G and Movies S3-S4). In contrast, the general glycolysis inhibitor 2-deoxyglucose (2-DG), in addition to impairing junction stability and EC migration, also decreased EC proliferation (Supplementary Figure S4H–K). PKM2 activity was also required *in vivo* since intravitreal injection of shikonin reduced vascular radial growth and filopodia number in P6 mice while having no effect on vascular density, EC number, or the percentage of proliferating ECs, thus reproducing the phenotype observed in the vasculature of PKM2-silenced retinas (Supplementary Figure S5A–I). Intravitreal shikonin injection also shifted the active/unstable:inactive/stable junction ratio by increasing the proportion of active junctions in the P6 retinal vasculature (Supplementary Figure S5J–L).

PKM2-silencing decreases ATP nearby EC junctions. Given the requirement of PKM2 kinase activity for its actions on EC junctions and sprouting angiogenesis, we next assessed the impact of PKM2 on EC ATP production. Analysis of the global metabolic state revealed that PKM2-silenced ECs had a lower glycolysis flux than control siRNA-transfected cells, revealed by a relative ~20% drop in the extracellular acidification ratio (ECAR) (Fig. 6A). This was reflected in significantly lower total ATP production (Fig. 6B). Mitochondrial

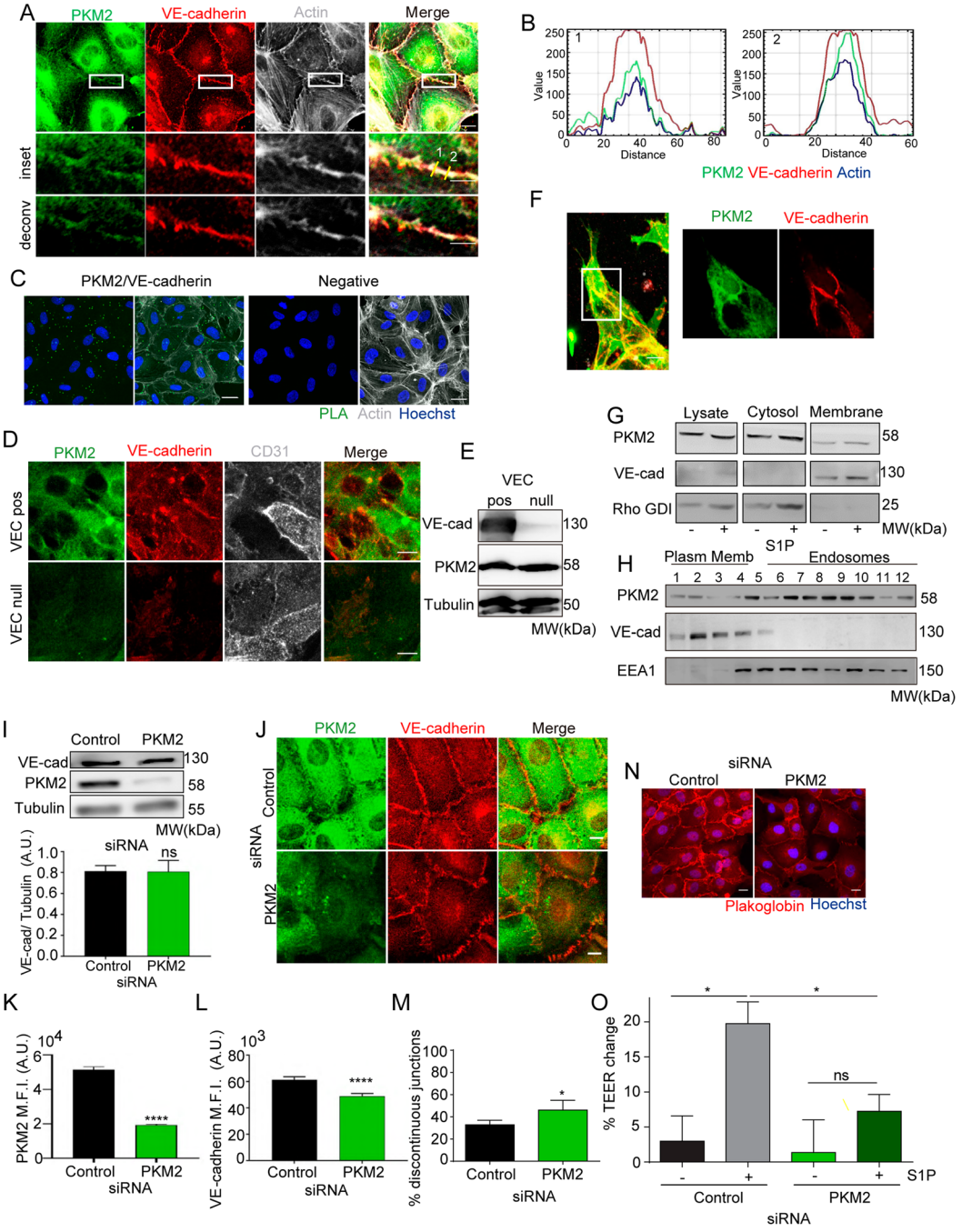

Figure 3. PKM2 is localized at VE-cadherin junction compartment. (**A**) Immunofluorescence of PKM2 (green), VE-cadherin (red) and F-actin (grey) in confluent HUVECs; single color and merged images are shown. Magnified views and de-convolved images of boxed areas below. Scale bars, 10 µm and 5 µm in the magnified views. (**B**) RGB (red, green, blue) profile of PKM2 (green), VE-cadherin (red) and F-actin (blue) intensity at areas of the endothelial cell junction marked by the yellow lines in A. (**C**) Representative merged images of Hoechst (blue) and proximity ligation assay (PLA, green) for PKM2 and VE-cadherin (left) and together with F-actin (grey; right) in HUVECs. PLA of rabbit and goat IgGs is also shown (negative). Scale bar, 10 µm. (**D**) Immunofluorescence of PKM2 (green), VE-cadherin (red) and CD31 (grey) in confluent VE-cadherin-expressing (VEC-pos) and VE-cadherin–deficient (VEC-null) mouse endothelial cells; single color and merged images of green and red channels are shown. Scale bar, 10 µm. (**E**) Western blot of VE-cadherin and PKM2 in lysates from VEC-pos and VEC-null endothelial cells. Tubulin is included as a loading control. MW, molecular weight. (**F**) Immunofluorescence of PKM2 (green), VE-cadherin (red) and F-actin (grey) in 3D spheroid sprouts. Scale bar, 10 µm. (**G**) Western blot of PKM2 in total lysate and in cytosol and membrane fractions of confluent HUVECs treated with S1P or vehicle (left) and transfected with control or PKM2. VE-cadherin and Rho-GDI are included as markers of plasma membrane and cytosol. MW, molecular weight. (**H**) Western blot of PKM2 in membrane subfractions obtained from confluent HUVECs by density gradient centrifugation. VE-cadherin and EEA1 are included as markers of plasma membrane and endosomes. MW,

molecular weight. (**I**) Western blot and quantification of VE-cadherin in HUVECs transfected with control or PKM2 siRNA. Tubulin is included as a loading control. Means ± SEM, n = 3 independent experiments, ns non-significant by unpaired Student t-test. (**J**) Immunofluorescence of VE-cadherin (red) and PKM2 (green) in siRNA-silenced confluent HUVECs. Scale bar, 10 µm. (**K** and **L**) Mean fluorescent intensity (M.F.I.) of PKM2 (K) and VE-cadherin (L) at the junctions of siRNA-silenced confluent HUVECs; means ± SEM, n = 5 independent experiments, ****$p < 0.0001$ by Mann-Whitney test. (**M**) Percentage of discontinuous VE-cadherin-junctions; means ± SEM, n = 3 independent experiments, *$p < 0.05$ by unpaired Student t-test. (**N**) Immunofluorescence of plakoglobin (red) and nuclei (blue, Hoechst) in siRNA-silenced confluent HUVECs. Scale bar, 10 µm. (**O**) Change in trans-endothelial electrical resistance (TEER) across monolayers of siRNA-silenced HUVECs left untreated or treated with 1 µM S1P for 3 hours; means ± SEM, n = 3 independent experiments, ns non-significant, *$p < 0.05$ by one-way ANOVA with Sidak post-test. See related Figure S2.

activity remained intact, with similar basal and maximal oxygen consumption ratios (OCR) in PKM2 and control siRNA-silenced human ECs (Fig. 6C,D).

Following the protocol reported for other glycolytic enzymes[16,20], we next performed sequential cell lysis with increasing proportions of saponin to allow the extraction of two fractions, one enriched for cytosol and the other less soluble for cytoskeleton and EC junctions (CSK-junction enriched) (Fig. 6E,F). Pyruvate kinase activity was ~1.8-fold higher in the CSK-junction enriched sub-fraction than in the cytosol; specificity for PKM2 was confirmed by decreased PK activity in both compartments when PKM2 expression was silenced (Fig. 6G).

To assess whether PKM2-silencing impaired local ATP levels, particularly at CSK-junction compartment, we quantitated ATP in saponin-extracted sub-fractions. PKM2-silencing in mouse and human ECs significantly decreased ATP production in the cytosol, by ~50%, and the CSK-junction enriched sub-fraction, by ~40% (Supplementary Figure S6A and Fig. 6H), in accordance with the reduced PK activity (Fig. 6G). To ensure quantification of ATP levels nearby EC junctions, we transduced HUVECs with lentivirus encoding the FRET-based ATP sensor GO-ATeam1[40]. PKM2 silencing resulted in a significant reduction in the GO-ATeam1 FRET signal at both cytosol and junctions (as in subcellular fraction analysis), but the ratio of ATP levels at junctions versus cytosol was significantly decreased indicating a major impact of PKM2 absence on ATP levels at the junctional region of 2D human EC monolayers (Fig. 6I,J). We observed similar results in GO-ATeam1-transduced HUVEC when PKM2 activity was inhibited by shikonin in line with the reduction of ATP levels in the CSK-junction fraction (Supplementary Figure S6B,C). These findings indicate that PKM2-silencing reduces ATP levels nearby EC junctions.

PKM2 and local ATP regulate VE-cadherin dynamics and internalization at EC junctions. We next explored whether reduced ATP production in the CSK-junction compartment in PKM2 absence/inhibition may affect VE-cadherin turnover[41]. Gradient sub-fractionation experiments revealed that PKM2 inhibition by shikonin increased the proportion of VE-cadherin present at the plasma membrane versus endosomes compared to control ECs (Supplementary Figure S6D).

Live imaging of HUVEC transduced with lentivirus coding for VE-cadherin-EGFP or LifeAct-EGFP in basal conditions and after stimulation with VEGFA allowed us to analyze VE-cadherin, and F-actin dynamics at EC junctions[42]. Time-lapse microscopy of VE-cadherin-EGFP-expressing HUVEC showed that PKM2 inhibition by shikonin led to increased numbers of inter-cellular gaps mostly after VEGFA treatment compared to control ECs (Fig. 7A,C; Movies S5–S8); similar gaps were observed in VE-cadherin-EGFP-transduced HUVEC silenced for PKM2 (Supp Figure S6E and Movies S9–S10). These data confirmed the enhanced junction instability observed in 2D endothelial monolayers in static conditions (Fig. 3H–M). In LifeAct-EGFP-expressing ECs, we visualized small active F-actin protrusions in the lateral border preceding VE-cadherin 'plaques' and corresponding to 'junction-associated intermittent lamellipodia' (JAIL), which increased in size and persistence after VEGFA stimulation in control cells as reported[42] (Movies S11–S14). Notably, PKM2 inhibition by shikonin significantly reduced the number of JAIL and VE-cadherin plaques in untreated and VEGFA-stimulated cells compared to controls (Fig. 7A,B,D,E).

We next investigated directly the impact of PKM2 inhibition on VE-cadherin internalization in basal conditions and after stimulation with VEGFA. VEGFA-triggered VE-cadherin internalization is a classic clathrin-dependent/ATP-consuming event[43,44]. Notably, PKM2 silencing in ECs led to a significant reduction of VEGFA-induced VE-cadherin internalization compared to controls (Fig. 7F,G), arguing for decreased local ATP level as a mediator of such effect. We obtained a similar phenotype in human ECs treated with shikonin (Supplementary Figure S6F).

Our data support a model in which PKM2 absence/inhibition reduces ATP levels nearby endothelial junctions thus hindering VE-cadherin clathrin-mediated internalization and JAIL formation and overall resulting in impaired junction remodeling, collective migration, and angiogenic sprouting.

Discussion

This study presents the first description of the impact of subcellular compartmentalization of PKM2 on ATP levels, VE-cadherin internalization and EC junction rearrangements, and sprouting angiogenesis *in vitro* and *in vivo*.

PKM2 expression has been correlated with cell proliferation, particularly in tumor cells[26]. Our data establish that PKM2 is not required for EC proliferation, since PKM2-silenced and shikonin-treated ECs showed no differences from controls *in vitro* or *in vivo*. Despite the proposed role of PKM2 in cancer-cell proliferation, recent findings from Vander Heiden's group and others indicate that cell-cycle arrest in the absence of PKM2 is likely driven by compensatory PKM1 upregulation[27]. In this study, PKM2-null mice displayed distinct patterns of

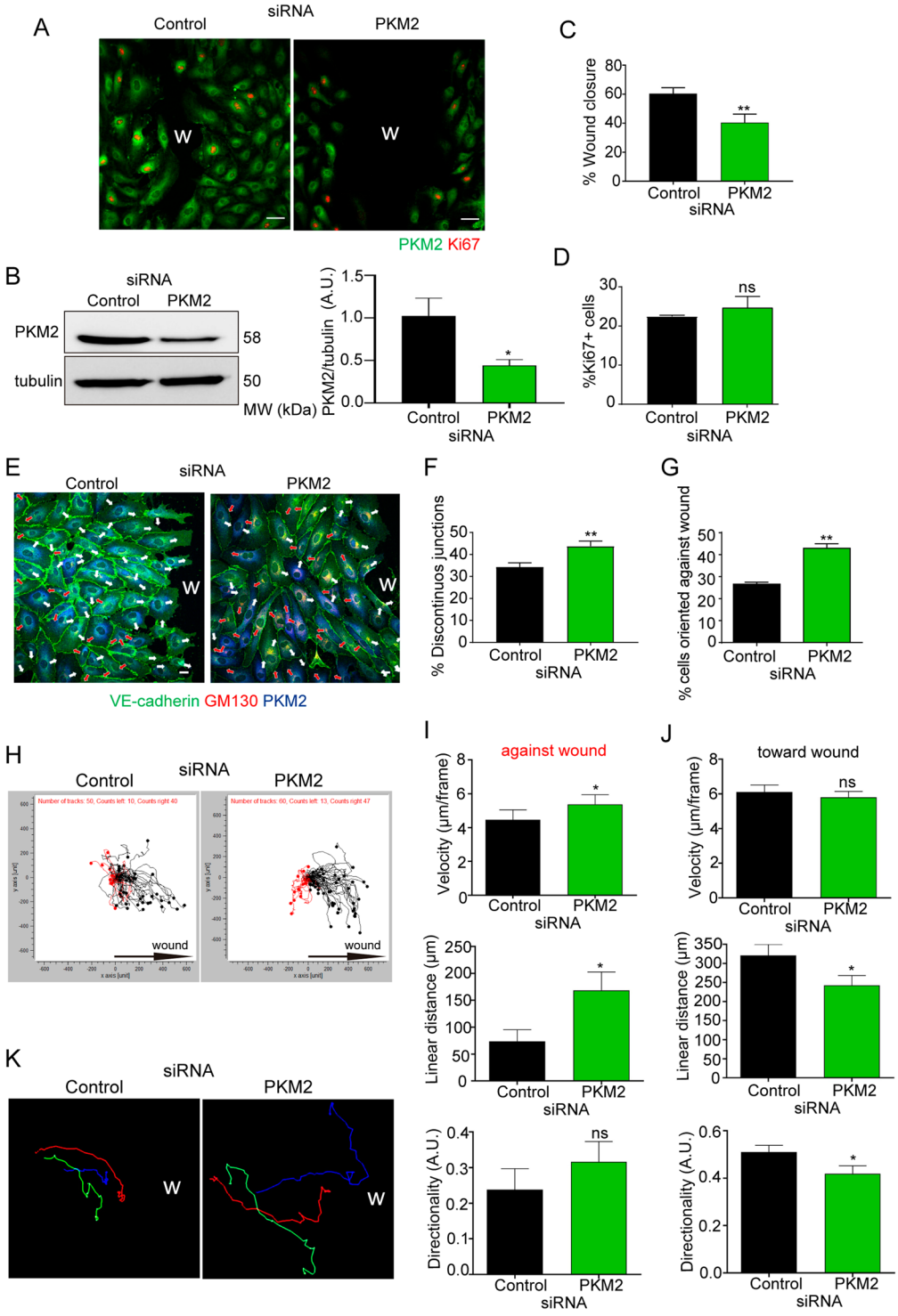

Figure 4. PKM2 silencing leads to misorientation and impaired collective migration of ECs. (**A**) Immunofluorescence of PKM2 (green) and Ki67 (red, proliferation) in siRNA-silenced HUVECs 16 hours after scratch wounding. Scale bar, 50 µm. W, wound. (**B**) Western blot and quantification of PKM2 expression in silenced-HUVEC cells at the end of the scratch assay; means ± SEM, n = 3 independent experiments, *$p < 0.05$ by Mann-Whitney test. MW, molecular weight (**C** and **D**) Percentage of wound closure (**C**) and of Ki67-positive cells (**D**) 16 hours after scratch wounding; means ± SEM, n = 3 independent experiments, ns non-significant and **$p < 0.01$ by unpaired Student t-test. (**E**) Immunofluorescence of VE-cadherin (green), PKM2 (blue), and GM130 (red) in siRNA-silenced HUVECs 16 hours after scratch wounding. W, wound. White and red arrows indicate cell polarization toward and away from the wound, respectively; Scale bar, 10 µm. (**F** and **G**) Percentage of discontinuous junctions (**F**) and of endothelial cells oriented against the wound (**G**) in siRNA-silenced HUVECs 16 hours after scratch wounding; means ± SEM, n = 3 independent experiments, **$p < 0.01$ by unpaired Student t-test. (**H**) Single-cell track analysis of siRNA-silenced HUVECs in the scratch assay; n = 3

independent experiments. Black and red tracks indicate cells migrating toward and against the wound. (**I** and **J**) Velocity, linear (Euclidean) distance and directionality of single cells moving against (**I**) and toward the wound (**J**); means ± SEM, n = 50–60 cells from 3 independent experiments, ns non-significant and *$p < 0.05$ by Mann-Whitney test. (**K**) Representative single-cell tracks of three adjacent siRNA-silenced ECs migrating during the scratch assay. See related Figure S3 and Movies S1 and S2.

tumor-cell proliferation depending on PKM1 expression, such that if PKM1 was expressed, proliferation capacity was reduced[27]. Moreover, PKM2-deficient primary cells derived from this mouse model also showed compensatory PKM1 upregulation, leading to impaired cell proliferation[28]. Corroborating this, proliferating embryo regions which would normally express PKM2 have been shown to initiate PKM1 expression in PKM2-null embryos, which is accompanied by a slowing of cell division and unexpected normal embryonic development[45]. In our experiments, PKM1 expression did not increase in PKM2-silenced ECs, possibly explaining the lack of any impact on EC proliferation. This is in contrast with recent reports claiming that PKM2 knockout reduced EC proliferation in which the compensatory increase of PKM1 might be a confounding factor to interpret direct PKM2 effects in EC proliferation[46,47]. Our findings further support the functional segregation of metabolic enzymes in regulating the spectrum of EC responses required for angiogenesis[14].

PKM2 has been reported to both favor and decrease cancer cell migration[48–50]. Our study is in line with recent reports on the requirement of PKM2 for endothelial cell migration[46,47]. Other glycolytic enzymes have been shown to positively regulate cell migration, for example PGK1 in tumor cells[51], PFKFB3 in ECs[11], and HK2 in lymphatic ECs[13]. Our findings show that PKM2 activity is required for EC collective migration, evidenced by impaired EC orientation and migration in the scratch assay and by the reduced 3D sprout-length and retinal vascular radial outgrowth without changes in proliferation.

Our findings also provide insight into how differential VE-cadherin dynamics and mosaic junction activity influence productive angiogenesis. PKM2 loss reduced junctional VE-cadherin and increased the proportion of active/unstable junctions, thus compromising the balance between inactive/stable and active/unstable junctions and destabilizing the endothelial barrier. These findings thus indicate that PKM2 is primarily required for proper VE-cadherin–mediated endothelial cell-junction stability. The 'patching algorithm' developed by Bentley[35] has been especially useful in gaining insight into this process because it gives not only absolute numbers of stable and unstable junctions but also their clustered distribution. Recent studies into the role of EC junctions in angiogenesis provide evidence that they not only constitute a barrier and a signaling platform but also fine-tune cellular processes of paramount importance for efficient directionality and expansion of capillary sprouts. For example, VE-cadherin fingers from the pulling EC are essential for collective and cohesive EC migration during sprout extension[36]; we confirm that defective VE-cadherin at junctions by PKM2 absence or inhibition results in impaired collective migration. Our findings also demonstrate that VE-cadherin internalization which is required for EC junction stability and remodeling, depends on PKM2 activity, likely through the provision of ATP for vesicle movement[20] since VEFGA-induced VE-cadherin endocytosis is clathrin-dependent and thus ATP-consuming[52]. PKM2-generated ATP at junctions could additionally favor actomyosin contractility or the phosphorylation of enzymes implicated in cell-cell junction stabilization or remodeling[6,53,54].

PKM2 silencing also led to reduced numbers of filopodia in the endothelial tip cells. Since filopodia positively regulate cell motile velocity, they ultimately affect sprouting[55,56]. This phenotype could be related to the reported association of PKM2 with F-actin[34] since although our live imaging data favor the hypothesis of a primary impact of PKM2 inhibition on VE-cadherin internalization and JAIL formation, we cannot rule out an additional action on F-actin dynamics. Thus, PKM2 could provide ATP near to dynamic membrane protrusions such as filopodia and lamellipodia, and together with other enzymes such as PKFB3 form the actin-bound 'glycolytic hub' proposed by Carmeliet's group[19,57]. Whether a similar complex also forms at EC junctions deserves however further analysis.

VE-cadherin is the master regulator of EC junction formation and stability, but recently new players have been identified. For example, vinculin restrains junctions during remodeling and pacsin2 inhibits asymmetric VE-cadherin internalization, protecting EC-junction integrity from mechanical forces; moreover, the YAP/TAZ pathway increases VE-cadherin turnover, promoting cell migration while maintaining barrier function[58–60]. EC junctions, and particularly VE-cadherin, are thus dynamically and exquisitely remodeled during angiogenesis. Nevertheless, in spite of the recognized importance of metabolic pathways in EC responses, very little is known about how metabolism impacts EC junction stability and dynamics. Only the glycolytic enzyme PFKBF3 has been shown to modulate EC junctions, by an as-yet unknown mechanism[61]. Although PKM2 loss has been claimed to alter EC junction stability by non-enzymatic actions[46,47], to our knowledge the present report is the first to demonstrate the presence of a pool of a glycolytic enzyme nearby the junctions of confluent ECs by immunostaining and biochemical approaches. Moreover, we show that PKM2 is required for ATP-dependent processes as VEFGA-induced clathrin-mediated VE-cadherin endocytosis[44] and thus for junction stability[41]. The fact that PKM2 at the CSK-junction enriched compartment has higher pyruvate kinase activity than cytosolic PKM2 suggests that the activity of the CSK-junction–associated PKM2 is positively regulated by mechanisms that may involve tetramer stabilization upon F-actin binding, similar to what occurs with PFKFB3 at lamellipodia[57]. The activity of PKM2 tetramers at cell-cell junctions may also be regulated by local interaction with allosteric activators or posttranslational modifications[62]. This also raises the question of how PKM2 traffics toward and locates at the plasma membrane. PKM2 interacts with huntingtin[63], which associates with GAPDH in vesicles traveling along microtubules in neurons[20], and it has recently been found enriched at these motile vesicles[64]. It is therefore possible that PKM2 also traffics on microtubules alone or together with GAPDH in ECs. Furthermore, we demonstrate that VE-cadherin is required for PKM2 localization at the endothelial junctions. Whether PKM2/VE-cadherin association is direct or mediated by an intermediate protein as β-catenin, a renowned VE-cadherin partner also shown to interact with PKM2 in other contexts[65], deserves further investigation.

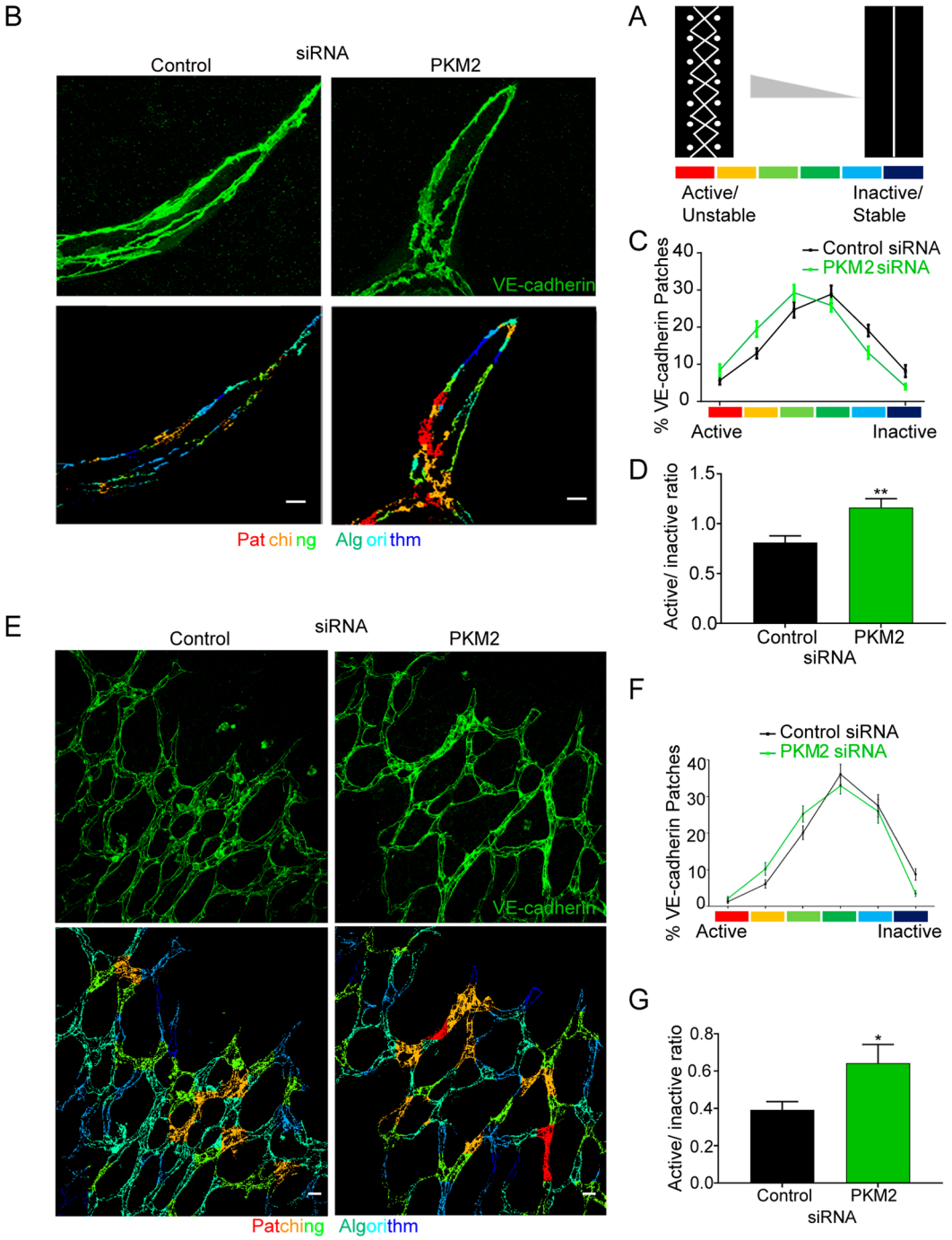

Figure 5. PKM2 is required for endothelial-cell junction remodeling during sprouting angiogenesis *in vitro* and *in vivo*. (**A**) Scheme illustrating the patching algorithm classification of VE-cadherin active (unstable)/ inactive (stable) junctions adapted from Bentley *et al.*, 2014. (**B**) Immunofluorescence of VE-cadherin (green, top) in 3D spheroid sprouts. Pseudo-colored images according to the patching algorithm classification are shown below. Scale bar, 10 µm. (**C** and **D**) Percentage of VE-cadherin active and inactive junction patches (**C**) and their ratio (**D**) in 3D spheroid formed by siRNA-silenced HUVECs; means ± SEM, n = 3 independent experiments. $^{**}p < 0.01$ by Mann-Whitney test. (**E**) Immunofluorescence of VE-cadherin (green, top) in P6 mouse whole-mount retinas 72 hours after intraocular siRNA injection. Pseudo-colored images according to the patching algorithm classification are shown below. Scale bar, 10 µm. (**F** and **G**) Percentage of VE-cadherin active and inactive junction patches (**F**) and their ratio (**G**) in P6 mouse retinas 72 hours after siRNA injection; means ± SEM, n = 4 mice, $^{*}p < 0.05$ by Welch's test.

The defective vasculature of PKM2-silenced and shikonin-treated retinas in postnatal mice supports the recent evidences of a requirement for PKM2 in angiogenesis *in vivo*[46,47]. In our context, the vascular impairment affected radial growth and filopodia number without influencing EC proliferation, and the phenotype correlates

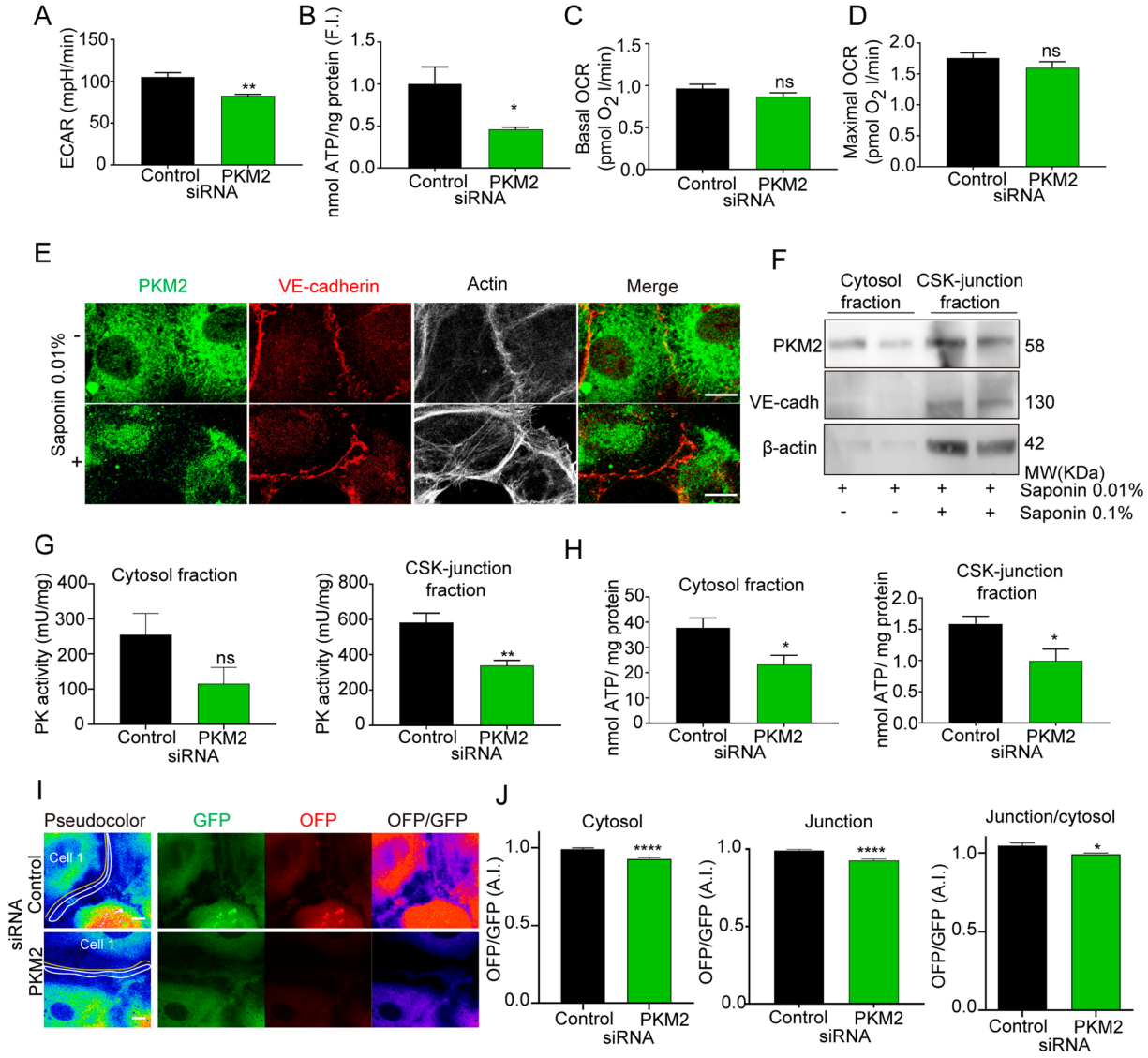

Figure 6. PKM2 activity is required for ATP levels at EC junctions. (**A**) Extracellular acidification ratio (ECAR) in HUVECs transfected with control or PKM2 siRNA; means ± SEM, n = 3 independent experiments.**$p < 0.01$ by Mann-Whitney t-test. (**B**) Total ATP per ng protein in HUVECs transfected with control or PKM2 siRNA, quantified as fold induction (F.I.) versus control; means ± SEM, n = 8 independent samples analyzed in 2 sets of experiments. *$p < 0.05$ by Mann-Whitney t-test. (**C** and **D**) Baseline (**C**) and maximum (**D**) oxygen consumption ratio (OCR) in HUVECs transfected with control or PKM2 siRNA; means ± SEM, n = 3 independent experiments, ns non-significant by Mann-Whitney t-test. (**E**) Immunofluorescence of PKM2 (green), VE-cadherin (red) and F-actin (grey) in HUVECs permeabilized or not with 0.01% saponin. Merged image of green and red channels is also shown. Scale bar, 10 µm. (**F**) Western blot of PKM2 in fractions extracted from HUVECs with 0.01% saponin (cytosol enriched) or 0.01% + 0.1% saponin (cytoskeleton (CSK)-junction enriched). VE-cadherin and β-actin are included as markers of cell junctions and cytoskeleton. MW, molecular weight. (**G** and **H**) Pyruvate kinase activity (**G**) and ATP amount (**H**) normalized to protein content in fractions extracted as in F from HUVECs transfected with control or PKM2 siRNA; means ± SEM, n = 8 independent samples analyzed in 2 sets of experiments, ns non-significant, *$p < 0.05$ and **$p < 0.001$ by unpaired Student t-test. (**I**) Images of the GFP, OFP and OFP/GFP channels from live microscopy of GO-ATeam1-transduced HUVECs silenced with control or PKM2 siRNA. The yellow and white lines mark in the GFP channel the cytosol and EC junction areas for OFP/GFP quantification. Scale bar, 10 µm. (**J**) OFP/GFP intensity ratio at cytosol, EC junctions and EC junction/cytosol of GO-ATeam1-transduced HUVECs transfected with control or PKM2 siRNA as fold induction respect control siRNA cells in each experiment, means ± SEM, n = 100–109 cells from 5 independent experiments analyzed per condition, ****$p < 0.0001$ by unpaired Student t-test. See related Figures S4, S5 and S6.

with the altered ratio of stable and unstable EC junctions. The possible clinical application of these findings to stimulate or inhibit PKM2 activity in disease needs to be carefully considered. In pathological angiogenesis, the proportion of active junctions increases (with a discontinuous pattern)[35], and sprouting defects are related to

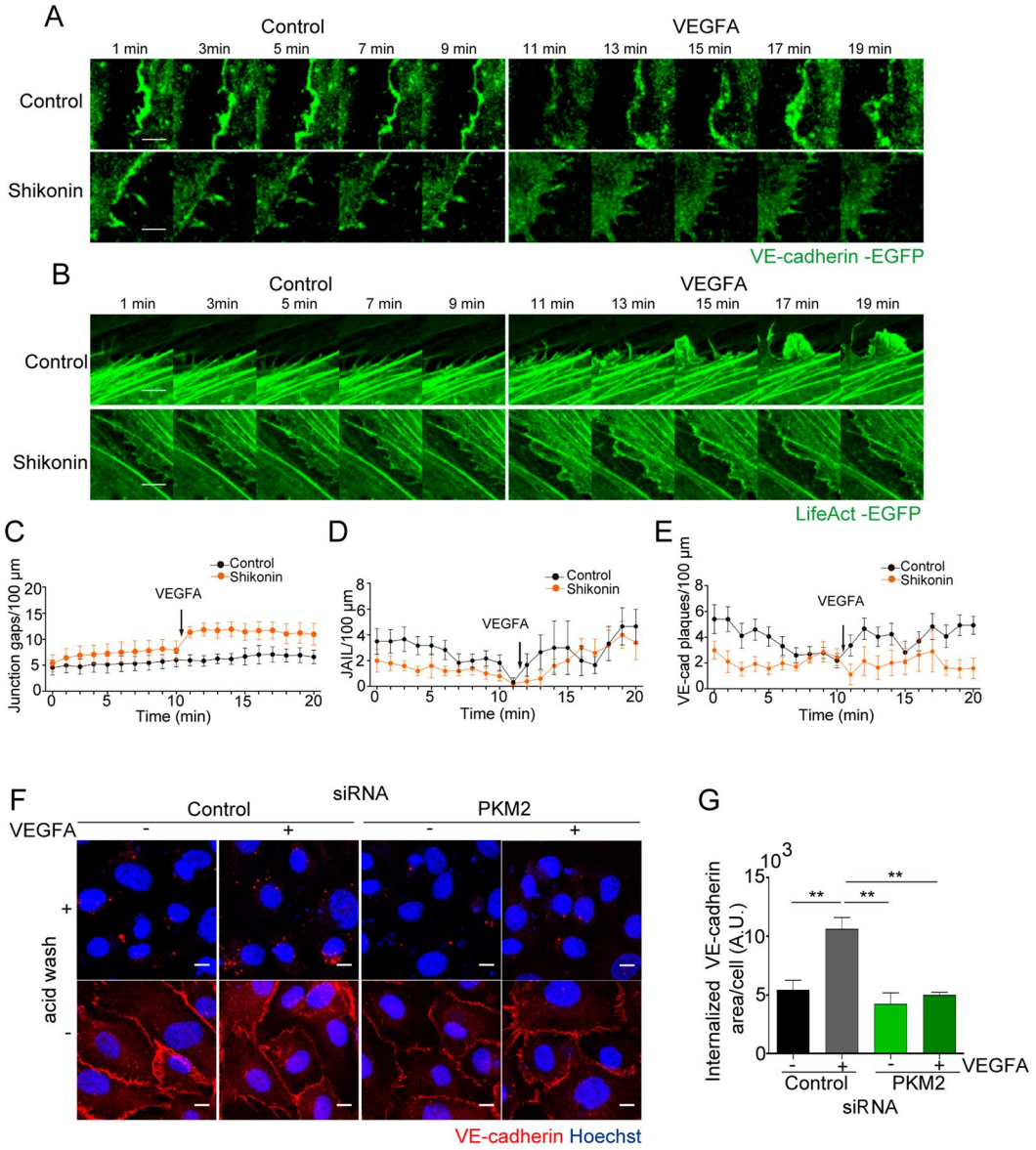

Figure 7. PKM2 is required for junction dynamics and VE-cadherin internalization. (**A** and **B**) Still images from live microscopy of HUVECs transduced with lentivirus coding for VE-cadherin-EGFP (**A**) or LifeAct-EGFP (**B**) for 10 min prior and after addition of 20 ng/ml of VEGFA; untreated and shikonin-treated cells are shown. Scale bar, 5 µm. (**C**) Number of inter-cellular gaps at junctions of VE-cadherin-transduced HUVEC along time. (**D** and **E**) Number of JAIL and of VE-cadherin plaques at the lateral junctions of LifeAct-EGFP and VE-cadherin-EGFP-transduced HUVECs, respectively; means ± SEM, n = 6 junctions for 2 independent experiments. (**F**) Immunofluorescence of VE-cadherin (red) and Hoechst (blue, nuclei) before or after acid wash in HUVECs transfected with control or PKM2 siRNA and treated with 20 ng/ml VEGFA for 15 minutes. Scale bar, 10 µm. (**G**) Internalized VE-cadherin positive area per number of cells in arbitrary units (A.U.); n = 3 independent experiments, $^{**}p < 0.01$ by one-way ANOVA with Sidak post-test. See related Figure S6 and Movies S5–S8 and S11–S14.

impaired endothelial junctions[66,67]. In contrast, there is no evidence that an increased proportion of inactive junctions (with a continuous pattern) has any effect on angiogenesis[68]. PFKFB3, a key glycolysis regulator, has been proposed as a target for inducing normalization of EC junctions[61,69]. In a model of high-dose-VEGFA–induced pathological retinal angiogenesis[35,70], the PFKFB3 inhibitor 3PO decreased glycolysis by 15% and normalized the vasculature[69]. This effect was also observed in 3PO-treated tumor ECs[61]. However, treatment of ECs with higher 3PO concentrations, inhibiting glycolysis by 40%, induced an increase in discontinuous junctions rather than vessel normalization[71]. This finding underlines the importance of the level of glycolysis inhibition in determining the final angiogenic outcome. In line with this, we observed increased instability of VE-cadherin EC junctions upon PKM2-silencing, which also decreases glycolysis by 40%, and with the global glycolysis inhibitor 2-DG, which almost abolishes glycolysis. Moreover, high concentrations of exogenous ATP also increase discontinuous

junctions and decrease TEER in brain endothelial cells[72]. Together, these observations suggest a dual effect of ATP, with a precisely adjusted level required for proper dynamic EC junction rearrangement. Metabolic regulation of EC junctions thus appears to be a complex process that depends on the quantity of ATP produced, the step in the glycolytic pathway involved, and where the implicated enzyme is located. Given the likelihood that glycolysis inhibition will have a 'dose response' effect on angiogenesis, studies are warranted to address the impact of PKM2 silencing or inhibition on pathological angiogenesis.

Our findings show that PKM2 makes an essential contribution to angiogenesis *in vitro* and *in vivo* by providing ATP for the regulation of VE-cadherin internalization and EC junctions. In light of the importance of PKM2 in cancer and other diseases such as diabetes, our findings provide information relevant to the development of PKM2-based therapeutic strategies.

Experimental Procedures

Antibodies and reagents. The following antibodies were used: PKM2 (#4053) and PKM1 (#7067) from Cell Signaling; β-actin (A441) and GAPDH (G9545) from Sigma; Rho-GDI (sc-360) and VE-cadherin (sc-6458) from Santa Cruz Biotechnologies; VE-cadherin (555289), plakoglobin (610254), GM130 (610605), and EEA1 (610685) from BD Pharmingen; Ki67 (IR626) from DAKO; and Ki67 (ab16667) from Abcam. F. Sánchez-Madrid (Centro Nacional de Investigaciones Cardiovasculares, CNIC, Madrid) kindly provided the anti-VE-cadherin TEA1/31 antibody[73]. IsolectinB4 (B-1205) was from Vector. Phalloidin, streptavidin, and Alexa Fluor secondary antibodies and Hoechst were from Life Technologies, and HRP secondary antibodies were from Jackson Immunoresearch Laboratories.

2-DG, ATP, FCCP, EDTA, glucose, luciferin, luciferase, mitomycin C, saponin, and shikonin were from Sigma Aldrich; cytodex3 from Amersham; fibrinogen, thrombin, and methylcellulose from Merck-Millipore; fluoromount-G from Southern Biotech; Ibidi chambers from Ibidi; phosphatase and proteinase inhibitors from Roche; Optiprep from AxisShield; and S1P from Cayman.

Cell cultures. HUVECs (Lonza) were cultured in plastic dishes (Falcon and Ibidi) coated with 0.5% gelatin and were used for experiments at P3-P4. HUVECs were grown and maintained in 199 cultured medium (Lonza) supplemented with 20% FBS (Gibco), 100 U/ml penicillin, 100 µg/ml Streptomycin, 2 mM L-Glutamine, and 10 mM Hepes (all from Lonza), and ECGS-heparin factors (Promocell). For angiogenesis experiments, EGM-2 medium (Promocell) was used. HUVECs were serum-starved for at least 3 hours before experiments, and maintained without FBS throughout treatments.

Fibroblasts were provided by M. A. del Pozo (Centro Nacional de Investigaciones Cardiovasculares, CNIC, Madrid) and were cultured in IMDM medium supplemented with 10% FBS,100 U/ml penicillin, 100 µg/ml streptomycin, 1mM L-glutamine, 10 mM Hepes and 1 mM Na-pyruvate.

Mouse lung endothelial cells (MLECs) isolated from C57BL/6 mice and VE-cadherin-null mouse endothelial cells provided by E. Dejana (FIRC Institute of Molecular Oncology, Italy) were cultured as described previously[6].

Mouse retinal vasculature model. Retinal angiogenesis was assessed in C57BL/6 mice. Mice were housed and animal experiments performed under specific pathogen-free conditions at the Animal facility of Centro Nacional de Investigaciones Cardiovasculares Carlos III (CNIC), and in strict accordance with the institutional guidelines. Animal procedures were approved by the Committee on the Ethics of Animal Experiments of the CNIC (Permit Number: CNIC-01/13) and by the corresponding legal authority of the local government 'Comunidad Autónoma' of Madrid (Permit Number: PROEX 34/13). Animal studies were conformed to directive 2010/63EU and recommendation 2007/526/EC regarding the protection of animals used for experimental and other scientific purposes, enforced in Spanish law under RD1201/2005. Mice were fed ad libitum with standard chow (2108 Teklad global, Harlan Interfauna Iberica S.L.).

Animals were intravitreally injected with 1 µg of siRNA in Lipofectamine RNAimax at P3 and sacrificed at P6. For pharmacological inhibition of PKM2 activity, 100 µM of shikonin (or DMSO control) were injected at P5, and the mice were sacrificed at P6. Eyes were fixed overnight in 2% paraformaldehyde (PFA) and then enucleated, and retina was isolated as reported[74].

siRNA interference and plasmid and lentivirus transfection. Silencer™ Select siRNA oligonucleotides against isoform M2 of pyruvate kinase (Thermo Fisher) were transfected using Lipofectamine RNAimax (Thermo Fischer) in Optimem medium (Lonza) at a final siRNA concentration of 10 nM. Oligonucleotide sequences were 5′CCAUAAUCGUCCUCACCAA dTdT 3′ for human PKM2 and 5′ GUGCGAGCCUCCAGUCACU dTdT 3′ Ambion™ *In Vivo* for mouse PKM2. Control siRNA was from Ambion™ *In Vivo*.

Lentivirus containing Go-ATeam1[40] was generated at VRC in Leuven Belgium or at the CNIC Viral Vectors Unit using the particles provided by Esteban Veiga-Chacón (Centro Nacional de Biotecnologia, CNB-CSIC, Madrid). Lentiviruses were added to cells at a M.O.I. of 10.

Lentivirus containing VE-Cadherin-EGFP and LifeAct-EGFP (kindly provided by Prof. Hans Schnittler from the Universität of Münster, Germany) was generated at the CNIC Viral Vectors Unit. Lentiviruses were added to cells at a M.O.I. of 10.

Scratch assays. Confluent HUVECs were serum-starved for 3 hours and a wound was made with a plastic pipette tip. After washing the cells with PBS, migration was stimulated by adding medium containing 5% FBS. In the experiments in which proliferation was inhibited, cells were treated before and throughout the experiment with 2 µg ml^{-1} mitomycin C, 1 µM Shikonin or corresponding vehicle control. Migration was quantified as the proportion of the initial wound area remaining uncovered at the end of the experiment.

For collective migration, time-series pictures were taken every 20 minutes during 16 hours; only those experiments in which the endothelial monolayer remained confluent >80% after siRNA silencing or shikonin treatment were included in the analysis.

Cell count assay. Cells were seeded at equal density in P96 wells. On each day of the experiment, cells in individual wells were detached and counted.

Microbead spheroid assay. Cytodex3 microbeads were purchased from Amersham, and the protocol was performed as previously described[75].

Transendothelial electrical resistance (TEER). TEER assays with an electric cell-substrate impedance sensing system (ECIS 1600R; Applied Biophysics[76];) were performed as described[77,78]. The S1P-induced TEER increase was expressed as the percentage difference in resistance between unstimulated ECs and ECs stimulated with S1P for 3 hours.

Immunofluorescence. Cells were fixed for 15 min in 4% PFA, blocked and permeabilized in 0.01% Triton X-100 2% BSA in PBS. Primary antibodies were incubated overnight in a cold room and secondary antibodies for 1 hour at 37 °C. Cell orientation was quantitated according to the relative position of Golgi versus nucleus toward or against the wound (±180°).

Fibrin gels were fixed in 1% PFA PBS for 30 minutes and washed. Gels were then permeabilized and blocked for 2 hours in blocking and permeabilization (BP) buffer (2% BSA, 0.3% Triton X-100, 0.3 M glycine, 0.2% azide, and 1% goat serum in PBS). Gels were incubated with primary antibodies overnight in the same buffer. The next day, gels were post-fixed in 4% PFA for 15 minutes. After a wash and 30 minutes in BP buffer, gels were incubated with secondary antibodies.

Retinas were blocked and fixed overnight in 2% BSA, 1% goat serum, 0.2% deoxycholate, 0.5% Triton X-100, and 0.2% azide in PBS. The next day, primary antibodies were added and incubations were maintained overnight. Retinas were then incubated overnight with Isolectin B4 in PBLEC buffer (1 mM $MgCl_2$, 1 mM $CaCl_2$, and 0.1 mM MnCl in PBS pH 6.8). Finally, secondary antibodies were added and incubations were maintained overnight. All preparations were mounted in Fluoromount-G.

Proximity ligation assay (PLA). HUVECs were grown to confluence, fixed and permeabilized. PLA was performed next day following the manufacturer's instructions (Duolink PLA, Sigma Aldrich). Briefly, samples were blocked with the blocking solution for 30 min at 37 °C and incubated overnight with the primary antibodies, rabbit anti-PKM2 (#4053, Cell Signalling) and goat anti-VE-cadherin (sc-6458, Santa Cruz biotechnology), at 4 °C. The following day, the samples were washed and incubated for 1 h at 37 °C with PLA probes for rabbit and goat antibodies. After washing, samples were incubated with the ligase for 30 min at 37 °C, washed again and incubated with the polymerase for 100 min at 37 °C. Finally, the samples were washed, dried completely and mounted in Duolink *In Situ* Mounting Medium with Hoechst. Rabbit and goat IgGs were used as negative control.

Cell live imaging. Live imaging was performed with a LSM700 Zeiss confocal microscope (Carl Zeiss) at a constant temperature of 37 °C and 5% CO_2. PKM2-GFP was detected with 488 nm excitation and 510 nm emission. Go-ATeam1 was detected with 488 nm excitation and emission at 510 nm and 560 nm. VE-cadherin-GFP and LifeAct-GFP were detected with 488 nm excitation and 510 nm emission, time-series images were taken every minute for 15 minutes and after addition of 50 ng/ml of VEGFA for a further 15 min. Image analysis was performed using Fiji software.

Membrane subfractionation. The membrane subfractionation protocol was performed as previously described[79]. Briefly, HUVEC membrane fractions were obtained and separated by ultracentrifugation on a discontinuous Optiprep density gradient (AxisShield). Protein fractions were precipitated, resuspended in Laemmli buffer, resolved by SDS-PAGE, and analyzed by western blot.

Western blotting. Cells were lysed in RIPA buffer as described[6]. Retinas were isolated as reported[80], and then RIPA buffer was added to the exposed vessels. Centrifugation was performed after 1 hour of incubation, and supernatant was recovered. Protein lysates were separated by 8% SDS-PAGE under reducing conditions. After transfer to a nitrocellulose membrane (Bio-Rad), blots were blocked with 5% BSA-PBS and incubated for 1 hour at room temperature (RT) with primary antibody diluted in 2% BSA-PBS. Membranes were then washed in 0.2% Tween 20-PBS and incubated for 1 hour at RT with horseradish peroxidase-conjugated secondary antibody. Protein bands were visualized by enhanced chemiluminescence (ECL; GE Healthcare). Band intensities were analyzed with Fiji software.

Glucose and oxygen consumption. The extracellular acidification and oxygen consumption ratios (ECAR and OCR) were obtained in a Seahorse XF96 (Agilent), using glucose, oligomycin, FCCP and 2-DG, as described[81].

ATP levels. ATP production in saponin-enriched fractions was measured by a kinetic luciferin-luciferase luminescence assay, and normalized to the protein concentration in each sample[6]. Briefly, fractions were diluted in buffer A (150 mM KCl, 25 mM Tris-HCl pH 7.4, 2 mM EDTA, 0.1% BSA, 10 mM KPO4, 0.1 mM MgCl2) with

0.15 mM diadenosine pentaphosphate and then buffer B (0.5 M Tris–acetate pH 7.75, 0.8 mM luciferin, 20 μg/ml luciferase) and 0.1 mM ADP were added before recording light emission in the luminometer.

Pyruvate kinase assay. PK activity was measured in saponin-permeabilized HUVEC fractions using a commercial kit from Biovision.

VE-cadherin internalization. Internalization assays were performed as previously described[82]. Briefly, to measure internalization of endogenous VE-cadherin, confluent HUVEC were incubated with the VE-cadherin antibody (TEA1/31) at 4 °C for 1 h in 1% BSA medium. Then, we rinsed the cells in cold culture medium to remove unbound antibody and treated them with 50 ng/ml of VEGFA for 30 min at 37 °C to allow the internalization. Cells were acid-washed (2 mM PBS-glycine, pH 2.0) or washed with cold PBS 3 times for 10 min each (used as control) and fixed and processed for immunofluorescence.

Confocal image quantification. Images were obtained with a Zeiss LSM700 confocal microscope (Carl Zeiss Microscopy) and maximum intensity projections are shown in all figures unless otherwise indicated. For analysis of mean fluorescence intensity, regions of interest (ROIs) were selected around junctions with Fiji software. For junction morphology analysis, we used reported criteria to distinguish discontinuous and continuous junctions[83]. For spheroid assays, mean length of sprouts and sprout number were analyzed in bright-field images with Fiji. Filopodia number was determined using phalloidin-stained F-actin. Data were normalized to cell length. For Go-aTeam1 analysis, the region of interest (ROI) for EC junctions was drawn $\leq$5 μm width around the cell-cell contacts defined by a 16 colors-pseudocolor plugin of Fiji software (validated by VE-cadherin staining). The cytosol ROI was defined as the rest of the cell.

Retinal parameters were quantified as described[74,84]. Radial growth was calculated as the average length in each lobule of one eye, from the optic nerve to the vascular front. Vascular density was calculated as the percentage of total area occupied by isolectin B4. Ki67 positive ECs were calculated as the percentage of Ki67 + ERG + cells of total ERG + cells, and normalized by Isolectin B4 area. Junction morphology was analyzed using the 'patching algorithm' implemented in MATLAB software[35].

For VE-cadherin internalization experiments, images were taken using Nikon A1R confocal microscopy with a 40x objective and image analysis were performed using Fiji software.

For time-lapse scratch assay, images were taken with a Nikon time-lapse microscope with a 10x objective. Analysis of the tracking was done using Fiji with manual tracking plugin and Chemotaxis tool from ibidi.

Statistical analysis. Absolute values were represented for most of the quantitated parameters. In cases of high variability in such values among experiments, fold induction versus control was calculated for each experiment as indicated in the corresponding legend. All values were analysed with Prism GraphPad. First all values were subjected to Grubbs's outlier test ($p < 0.05$), and then D'Agostino-Pearson test for analysis of normal distribution was performed. The proper tests to compare samples were used as indicated in each figure legend. In general, for comparison of two samples, unpaired Student t-test was used in normal (Gaussian) data with equal variance, Welch's test was used in normal (Gaussian) data with no equal variance and Mann-Whitney test for non-normal data; for comparison of three or more conditions, One-way ANOVA with Sidak-post test was used. Differences were considered significant at $p < 0.05$.

Data availability

All relevant data are available from the authors upon request.

Received: 14 June 2019; Accepted: 19 September 2019;

Published online: 21 October 2019

References

1. Carmeliet, P. & Jain, R. K. Molecular mechanisms and clinical applications of angiogenesis. *Nature* **473**, 298–307, https://doi.org/10.1038/nature10144 (2011).
2. Tung, J. J., Tattersall, I. W. & Kitajewski, J. Tips, stalks, tubes: notch-mediated cell fate determination and mechanisms of tubulogenesis during angiogenesis. *Cold Spring Harb. Perspect. Med.* **2**, a006601, https://doi.org/10.1101/cshperspect.a006601 (2012).
3. Carmeliet, P., De Smet, F., Loges, S. & Mazzone, M. Branching morphogenesis and antiangiogenesis candidates: tip cells lead the way. *Nat. Rev. Clin. Oncol.* **6**, 315–326, https://doi.org/10.1038/nrclinonc.2009.64 (2009).
4. Serra, H. *et al.* PTEN mediates Notch-dependent stalk cell arrest in angiogenesis. *Nat Commun* **6**, 7935, https://doi.org/10.1038/ncomms8935 (2015).
5. Vitorino, P. *et al.* MAP4K4 regulates integrin-FERM binding to control endothelial cell motility. *Nature* **519**, 425–430, https://doi.org/10.1038/nature14323 (2015).
6. Moreno, V. *et al.* An EMMPRIN-gamma-catenin-Nm23 complex drives ATP production and actomyosin contractility at endothelial junctions. *J. Cell Sci.* **127**, 3768–3781, https://doi.org/10.1242/jcs.149518 (2014).
7. Van Daele, P., Van Coevorden, A., Roger, P. P. & Boeynaems, J. M. Effects of adenine nucleotides on the proliferation of aortic endothelial cells. *Circ. Res.* **70**, 82–90 (1992).
8. Polet, F. & Feron, O. Endothelial cell metabolism and tumour angiogenesis: glucose and glutamine as essential fuels and lactate as the driving force. *J. Intern. Med.* **273**, 156–165, https://doi.org/10.1111/joim.12016 (2013).
9. DeBerardinis, R. J. & Cheng, T. Q's next: the diverse functions of glutamine in metabolism, cell biology and cancer. *Oncogene* **29**, 313–324, https://doi.org/10.1038/onc.2009.358 (2010).
10. Eelen, G., de Zeeuw, P., Simons, M. & Carmeliet, P. Endothelial cell metabolism in normal and diseased vasculature. *Circ. Res.* **116**, 1231–1244, https://doi.org/10.1161/CIRCRESAHA.116.302855 (2015).

11. De Bock, K. *et al*. Role of PFKFB3-driven glycolysis in vessel sprouting. *Cell* **154**, 651–663, https://doi.org/10.1016/j.cell.2013.06.037 (2013).
12. Verdegem, D., Moens, S., Stapor, P. & Carmeliet, P. Endothelial cell metabolism: parallels and divergences with cancer cell metabolism. *Cancer Metab* **2**, 19, https://doi.org/10.1186/2049-3002-2-19 (2014).
13. Yu, P. *et al*. FGF-dependent metabolic control of vascular development. *Nature* **545**, 224–228, https://doi.org/10.1038/nature22322 (2017).
14. Eelen, G. *et al*. Endothelial Cell Metabolism. *Physiol. Rev.* **98**, 3–58, https://doi.org/10.1152/physrev.00001.2017 (2018).
15. Rohlenova, K., Veys, K., Miranda-Santos, I., De Bock, K. & Carmeliet, P. Endothelial Cell Metabolism in Health and Disease. *Trends Cell Biol.* **28**, 224–236, https://doi.org/10.1016/j.tcb.2017.10.010 (2018).
16. Hu, H. *et al*. Phosphoinositide 3-Kinase Regulates Glycolysis through Mobilization of Aldolase from the Actin Cytoskeleton. *Cell* **164**, 433–446, https://doi.org/10.1016/j.cell.2015.12.042 (2016).
17. Jones, D. P. Intracellular diffusion gradients of O_2 and ATP. *Am. J. Physiol.* **250**, C663–675, https://doi.org/10.1152/ajpcell.1986.250.5.C663 (1986).
18. Green, D. E. *et al*. Association of integrated metabolic pathways with membranes. I. Glycolytic enzymes of the red blood corpuscle and yeast. *Arch. Biochem. Biophys.* **112**, 635–647 (1965).
19. Menard, L., Maughan, D. & Vigoreaux, J. The structural and functional coordination of glycolytic enzymes in muscle: evidence of a metabolon? *Biology (Basel)* **3**, 623–644, https://doi.org/10.3390/biology3030623 (2014).
20. Zala, D. *et al*. Vesicular glycolysis provides on-board energy for fast axonal transport. *Cell* **152**, 479–491, https://doi.org/10.1016/j.cell.2012.12.029 (2013).
21. Seidler, N. W. Compartmentation of GAPDH. *Adv. Exp. Med. Biol.* **985**, 61–101, https://doi.org/10.1007/978-94-007-4716-6_3 (2013).
22. Noguchi, T., Inoue, H. & Tanaka, T. The M1- and M2-type isozymes of rat pyruvate kinase are produced from the same gene by alternative RNA splicing. *J. Biol. Chem.* **261**, 13807–13812 (1986).
23. Anastasiou, D. *et al*. Inhibition of pyruvate kinase M2 by reactive oxygen species contributes to cellular antioxidant responses. *Science* **334**, 1278–1283, https://doi.org/10.1126/science.1211485 (2011).
24. Mazurek, S. Pyruvate kinase type M2: a key regulator of the metabolic budget system in tumor cells. *Int. J. Biochem. Cell Biol.* **43**, 969–980, https://doi.org/10.1016/j.biocel.2010.02.005 (2011).
25. Yamada, K. *et al*. Tissue-specific expression of rat pyruvate kinase L/chloramphenicol acetyltransferase fusion gene in transgenic mice and its regulation by diet and insulin. *Biochem. Biophys. Res. Commun.* **171**, 243–249 (1990).
26. Christofk, H. R. *et al*. The M2 splice isoform of pyruvate kinase is important for cancer metabolism and tumour growth. *Nature* **452**, 230–233, https://doi.org/10.1038/nature06734 (2008).
27. Israelsen, W. J. *et al*. PKM2 isoform-specific deletion reveals a differential requirement for pyruvate kinase in tumor cells. *Cell* **155**, 397–409, https://doi.org/10.1016/j.cell.2013.09.025 (2013).
28. Lunt, S. Y. *et al*. Pyruvate kinase isoform expression alters nucleotide synthesis to impact cell proliferation. *Mol. Cell* **57**, 95–107, https://doi.org/10.1016/j.molcel.2014.10.027 (2015).
29. Hosios, A. M., Fiske, B. P., Gui, D. Y. & Vander Heiden, M. G. Lack of Evidence for PKM2 Protein Kinase Activity. *Mol. Cell* **59**, 850–857, https://doi.org/10.1016/j.molcel.2015.07.013 (2015).
30. Lu, Z. & Hunter, T. Metabolic Kinases Moonlighting as Protein Kinases. *Trends Biochem. Sci.* **43**, 301–310, https://doi.org/10.1016/j.tibs.2018.01.006 (2018).
31. Li, L., Zhang, Y., Qiao, J., Yang, J. J. & Liu, Z. R. Pyruvate kinase M2 in blood circulation facilitates tumor growth by promoting angiogenesis. *J. Biol. Chem.* **289**, 25812–25821, https://doi.org/10.1074/jbc.M114.576934 (2014).
32. Boeckel, J. N. *et al*. JMJD8 Regulates Angiogenic Sprouting and Cellular Metabolism by Interacting With Pyruvate Kinase M2 in Endothelial Cells. *Arterioscler. Thromb. Vasc. Biol.* **36**, 1425–1433, https://doi.org/10.1161/ATVBAHA.116.307695 (2016).
33. Lee, O. H. *et al*. Sphingosine 1-phosphate induces angiogenesis: its angiogenic action and signaling mechanism in human umbilical vein endothelial cells. *Biochem. Biophys. Res. Commun.* **264**, 743–750, https://doi.org/10.1006/bbrc.1999.1586 (1999).
34. Puchulu-Campanella, E. *et al*. Identification of the components of a glycolytic enzyme metabolon on the human red blood cell membrane. *J. Biol. Chem.* **288**, 848–858, https://doi.org/10.1074/jbc.M112.428573 (2013).
35. Bentley, K. *et al*. The role of differential VE-cadherin dynamics in cell rearrangement during angiogenesis. *Nat. Cell Biol.* **16**, 309–321, https://doi.org/10.1038/ncb2926 (2014).
36. Hayer, A. *et al*. Engulfed cadherin fingers are polarized junctional structures between collectively migrating endothelial cells. *Nat. Cell Biol.* **18**, 1311–1323, https://doi.org/10.1038/ncb3438 (2016).
37. Martin, M., Veloso, A., Wu, J., Katrukha, E. A. & Akhmanova, A. Control of endothelial cell polarity and sprouting angiogenesis by non-centrosomal microtubules. *Elife* **7**, https://doi.org/10.7554/eLife.33864 (2018).
38. Millarte, V. & Farhan, H. The Golgi in cell migration: regulation by signal transduction and its implications for cancer cell metastasis. *ScientificWorldJournal* **2012**, 498278, https://doi.org/10.1100/2012/498278 (2012).
39. Chen, J. *et al*. Shikonin and its analogs inhibit cancer cell glycolysis by targeting tumor pyruvate kinase-M2. *Oncogene* **30**, 4297–4306, https://doi.org/10.1038/onc.2011.137 (2011).
40. Nakano, M., Imamura, H., Nagai, T. & Noji, H. Ca(2)(+) regulation of mitochondrial ATP synthesis visualized at the single cell level. *ACS Chem. Biol.* **6**, 709–715, https://doi.org/10.1021/cb100313n (2011).
41. Cavey, M. & Lecuit, T. Molecular bases of cell-cell junctions stability and dynamics. *Cold Spring Harb. Perspect. Biol.* **1**, a002998, https://doi.org/10.1101/cshperspect.a002998 (2009).
42. Cao, J. & Schnittler, H. Putting VE-cadherin into JAIL for junction remodeling. *J. Cell Sci.* **132**, https://doi.org/10.1242/jcs.222893 (2019).
43. West, J. J. & Harris, T. J. Cadherin Trafficking for Tissue Morphogenesis: Control and Consequences. *Traffic* **17**, 1233–1243, https://doi.org/10.1111/tra.12407 (2016).
44. Xiao, K. *et al*. p120-Catenin regulates clathrin-dependent endocytosis of VE-cadherin. *Mol. Biol. Cell* **16**, 5141–5151, https://doi.org/10.1091/mbc.e05-05-0440 (2005).
45. Dayton, T. L. *et al*. Germline loss of PKM2 promotes metabolic distress and hepatocellular carcinoma. *Genes Dev.* **30**, 1020–1033, https://doi.org/10.1101/gad.278549.116 (2016).
46. Kim, B. *et al*. Endothelial pyruvate kinase M2 maintains vascular integrity. *J. Clin. Invest.* **128**, 4543–4556, https://doi.org/10.1172/JCI120912 (2018).
47. Stone, O. A. *et al*. Loss of pyruvate kinase M2 limits growth and triggers innate immune signaling in endothelial cells. *Nat Commun* **9**, 4077, https://doi.org/10.1038/s41467-018-06406-8 (2018).
48. Chen, Y. L. *et al*. Mechanisms of pyruvate kinase M2 isoform inhibits cell motility in hepatocellular carcinoma cells. *World J. Gastroenterol.* **21**, 9093–9102, https://doi.org/10.3748/wjg.v21.i30.9093 (2015).
49. Wang, C. *et al*. PKM2 promotes cell migration and inhibits autophagy by mediating PI3K/AKT activation and contributes to the malignant development of gastric cancer. *Sci. Rep.* **7**, 2886, https://doi.org/10.1038/s41598-017-03031-1 (2017).
50. Yang, P. *et al*. Secreted pyruvate kinase M2 facilitates cell migration via PI3K/Akt and Wnt/beta-catenin pathway in colon cancer cells. *Biochem. Biophys. Res. Commun.* **459**, 327–332, https://doi.org/10.1016/j.bbrc.2015.02.112 (2015).
51. Ding, H. *et al*. Phosphoglycerate kinase 1 promotes radioresistance in U251 human glioma cells. *Oncol. Rep.* **31**, 894–900, https://doi.org/10.3892/or.2013.2874 (2014).

52. Delva, E. & Kowalczyk, A. P. Regulation of cadherin trafficking. *Traffic* **10**, 259–267, https://doi.org/10.1111/j.1600-0854.2008.00862.x (2009).
53. Huang, R. L. *et al*. ANGPTL4 modulates vascular junction integrity by integrin signaling and disruption of intercellular VE-cadherin and claudin-5 clusters. *Blood* **118**, 3990–4002, https://doi.org/10.1182/blood-2011-01-328716 (2011).
54. Onodera, Y., Nam, J. M. & Bissell, M. J. Increased sugar uptake promotes oncogenesis via EPAC/RAP1 and O-GlcNAc pathways. *J. Clin. Invest.* **124**, 367–384, https://doi.org/10.1172/JCI63146 (2014).
55. Fantin, A. *et al*. NRP1 Regulates CDC42 Activation to Promote Filopodia Formation in Endothelial Tip Cells. *Cell Rep* **11**, 1577–1590, https://doi.org/10.1016/j.celrep.2015.05.018 (2015).
56. Phng, L. K., Stanchi, F. & Gerhardt, H. Filopodia are dispensable for endothelial tip cell guidance. *Development* **140**, 4031–4040, https://doi.org/10.1242/dev.097352 (2013).
57. De Bock, K., Georgiadou, M. & Carmeliet, P. Role of endothelial cell metabolism in vessel sprouting. *Cell Metab* **18**, 634–647, https://doi.org/10.1016/j.cmet.2013.08.001 (2013).
58. Dorland, Y. L. *et al*. The F-BAR protein pacsin2 inhibits asymmetric VE-cadherin internalization from tensile adherens junctions. *Nat Commun* **7**, 12210, https://doi.org/10.1038/ncomms12210 (2016).
59. Huveneers, S. *et al*. Vinculin associates with endothelial VE-cadherin junctions to control force-dependent remodeling. *J. Cell Biol.* **196**, 641–652, https://doi.org/10.1083/jcb.201108120 (2012).
60. Neto, F. *et al*. YAP and TAZ regulate adherens junction dynamics and endothelial cell distribution during vascular development. *Elife* **7**, https://doi.org/10.7554/eLife.31037 (2018).
61. Cantelmo, A. R. *et al*. Inhibition of the Glycolytic Activator PFKFB3 in Endothelium Induces Tumor Vessel Normalization, Impairs Metastasis, and Improves Chemotherapy. *Cancer Cell* **30**, 968–985, https://doi.org/10.1016/j.ccell.2016.10.006 (2016).
62. Israelsen, W. J. & Vander Heiden, M. G. Pyruvate kinase: Function, regulation and role in cancer. *Semin. Cell Dev. Biol.* **43**, 43–51, https://doi.org/10.1016/j.semcdb.2015.08.004 (2015).
63. Kaltenbach, L. S. *et al*. Huntingtin interacting proteins are genetic modifiers of neurodegeneration. *PLoS Genet* **3**, e82, https://doi.org/10.1371/journal.pgen.0030082 (2007).
64. Hinckelmann, M. V. *et al*. Self-propelling vesicles define glycolysis as the minimal energy machinery for neuronal transport. *Nat Commun* **7**, 13233, https://doi.org/10.1038/ncomms13233 (2016).
65. Yang, W. *et al*. Nuclear PKM2 regulates beta-catenin transactivation upon EGFR activation. *Nature* **480**, 118–122, https://doi.org/10.1038/nature10598 (2011).
66. Fraccaroli, A. *et al*. Endothelial alpha-parvin controls integrity of developing vasculature and is required for maintenance of cell-cell junctions. *Circ. Res.* **117**, 29–40, https://doi.org/10.1161/CIRCRESAHA.117.305818 (2015).
67. Wimmer, R., Cseh, B., Maier, B., Scherrer, K. & Baccarini, M. Angiogenic sprouting requires the fine tuning of endothelial cell cohesion by the Raf-1/Rok-alpha complex. *Dev. Cell* **22**, 158–171, https://doi.org/10.1016/j.devcel.2011.11.012 (2012).
68. Li, J. *et al*. The Poly-cistronic miR-23-27-24 Complexes Target Endothelial Cell Junctions: Differential Functional and Molecular Effects of miR-23a and miR-23b. *Mol Ther Nucleic Acids* **5**, e354, https://doi.org/10.1038/mtna.2016.62 (2016).
69. Cruys, B. *et al*. Glycolytic regulation of cell rearrangement in angiogenesis. *Nat Commun* **7**, 12240, https://doi.org/10.1038/ncomms12240 (2016).
70. Ubezio, B. *et al*. Synchronization of endothelial Dll4-Notch dynamics switch blood vessels from branching to expansion. *Elife* **5**, https://doi.org/10.7554/eLife.12167 (2016).
71. Conradi, L. C. *et al*. Tumor vessel disintegration by maximum tolerable PFKFB3 blockade. *Angiogenesis* **20**, 599–613, https://doi.org/10.1007/s10456-017-9573-6 (2017).
72. Maeda, T. *et al*. ATP increases the migration of microglia across the brain endothelial cell monolayer. *Biosci. Rep.* **36**, https://doi.org/10.1042/BSR20160054 (2016).
73. Galvez, B. G., Matias-Roman, S., Albar, J. P., Sanchez-Madrid, F. & Arroyo, A. G. Membrane type 1-matrix metalloproteinase is activated during migration of human endothelial cells and modulates endothelial motility and matrix remodeling. *J. Biol. Chem.* **276**, 37491–37500, https://doi.org/10.1074/jbc.M104094200 (2001).
74. Pitulescu, M. E., Schmidt, I., Benedito, R. & Adams, R. H. Inducible gene targeting in the neonatal vasculature and analysis of retinal angiogenesis in mice. *Nat. Protoc.* **5**, 1518–1534, https://doi.org/10.1038/nprot.2010.113 (2010).
75. Nakatsu, M. N. *et al*. Angiogenic sprouting and capillary lumen formation modeled by human umbilical vein endothelial cells (HUVEC) in fibrin gels: the role of fibroblasts and Angiopoietin-1. *Microvasc. Res.* **66**, 102–112 (2003).
76. Tiruppathi, C., Malik, A. B., Del Vecchio, P. J., Keese, C. R. & Giaever, I. Electrical method for detection of endothelial cell shape change in real time: assessment of endothelial barrier function. *Proc. Natl. Acad. Sci. USA* **89**, 7919–7923 (1992).
77. Aranda, J. F. *et al*. MYADM controls endothelial barrier function through ERM-dependent regulation of ICAM-1 expression. *Mol. Biol. Cell* **24**, 483–494, https://doi.org/10.1091/mbc.E11-11-0914 (2013).
78. Fernandez-Martin, L. *et al*. Crosstalk between reticular adherens junctions and platelet endothelial cell adhesion molecule-1 regulates endothelial barrier function. *Arterioscler. Thromb. Vasc. Biol.* **32**, e90–102, https://doi.org/10.1161/ATVBAHA.112.252080 (2012).
79. Manickam, V. *et al*. Regulation of vascular endothelial growth factor receptor 2 trafficking and angiogenesis by Golgi localized t-SNARE syntaxin 6. *Blood* **117**, 1425–1435, https://doi.org/10.1182/blood-2010-06-291690 (2011).
80. Choi, J. H. *et al*. mTORC1 accelerates retinal development via the immunoproteasome. *Nat Commun* **9**, 2502, https://doi.org/10.1038/s41467-018-04774-9 (2018).
81. Rose, S. *et al*. Oxidative stress induces mitochondrial dysfunction in a subset of autism lymphoblastoid cell lines in a well-matched case control cohort. *PLoS One* **9**, e85436, https://doi.org/10.1371/journal.pone.0085436 (2014).
82. Orsenigo, F. *et al*. Phosphorylation of VE-cadherin is modulated by haemodynamic forces and contributes to the regulation of vascular permeability *in vivo*. *Nat Commun* **3**, 1208, https://doi.org/10.1038/ncomms2199 (2012).
83. Millan, J. *et al*. Adherens junctions connect stress fibres between adjacent endothelial cells. *BMC Biol.* **8**, 11, https://doi.org/10.1186/1741-7007-8-11 (2010).
84. Wilhelm, K. *et al*. FOXO1 couples metabolic activity and growth state in the vascular endothelium. *Nature* **529**, 216–220, https://doi.org/10.1038/nature16498 (2016).

Acknowledgements

We thank Ángel Colmenar for technical support and Simon Bartlett (CNIC) for English editing. We are grateful to Prof. Schnittler by his gift of VE-cadherin-EGFP and LifeAct-EGFP reporter lentivirus and Prof. Dejana by providing VE-cadherin-null cells. We also thank Prof. Hodivala-Dilke for her generous support. This study was supported by grants from the Spanish Ministerio de Ciencia, Innovación y Universidades (SAF2014-52050-R and SAF2017-83229-R to A.G.A). J.G.E. and D.G.W. were recipients of FPI fellowships from the Ministerio de Economía, Industria y Competitividad. K.B. research is supported by Knut and Alice Wallenberg foundation and the Beijer Institute. The CNIC is supported by the Instituto de Salud Carlos III (ISCIII), the Ministerio de Ciencia, Innovación y Universidades and the Pro CNIC Foundation, and is a Severo Ochoa Center of Excellence (SEV-2015-0505).

Author contributions

J.G.E. performed and analyzed most of the experiments and wrote the paper; C.C. performed and analysed time-lapse recording of scratch assays and lentivirus transduced-endothelial cells, and VEGFA-induced VE-cadherin internalization, and helped with intraocular siRNA experiments and western blotting; D.G.W. and J.M. performed TEER experiments; R.A.-P. and J.A.E. performed Seahorse metabolism experiments; K.B. provided the 'patching algorithm' MATLAB code; P.C. provided GO-ATeam1 lentivirus and critical suggestions; and A.G.A. designed and supervised the research and wrote the paper.

Competing interests

The authors declare no competing interests.

Additional information

Supplementary information is available for this paper at https://doi.org/10.1038/s41598-019-50866-x.

Correspondence and requests for materials should be addressed to A.G.A.

Reprints and permissions information is available at www.nature.com/reprints.

Publisher's note Springer Nature remains neutral with regard to jurisdictional claims in published maps and institutional affiliations.

Sequential Bone-Marrow Cell Delivery of VEGFA/S1P Improves Vascularization and Limits Adverse Cardiac Remodeling After Myocardial Infarction in Mice

Magdalena M. Żak,[1] Polyxeni Gkontra,[1] Cristina Clemente,[1] Mario Leonardo Squadrito,[2] Alessia Ferrarini,[3] Rubén A. Mota,[4] Eduardo Oliver,[5] Susana Rocha,[1] Jaume Agüero,[5,6] Jesús Vázquez,[3,6] Michele De Palma,[2] Borja Ibáñez,[5,6] and Alicia G. Arroyo[1,*,†]

[1]*Vascular Pathophysiology Area,* [3]*Proteomics Unit,* [4]*Animal Facility, and* [5]*Myocardial Pathology Area, Centro Nacional de Investigaciones Cardiovasculares (CNIC), Madrid, Spain;* [2]*École Polytechnique Federale de Lausanne (EPFL), ISREC-Swiss Institute for Experimental Cancer Research, Lausanne, Switzerland; and* [6]*CIBER-CV, Madrid, Spain.*

[†]*Present address: Centro de Investigaciones Biológicas (CIB-CSIC), Madrid, Spain.*

Microvascular dysfunction and resulting tissue hypoxia is a major contributor to the pathogenesis and evolution of cardiovascular diseases (CVD). Diverse gene and cell therapies have been proposed to preserve the microvasculature or boost angiogenesis in CVD, with moderate benefit. This study tested *in vivo* the impact of sequential delivery by bone-marrow (BM) cells of the pro-angiogenic factors vascular endothelial growth factor (VEGFA) and sphingosine-1-phosphate (S1P) in a myocardial infarction model. For that, mouse BM cells were transduced with lentiviral vectors coding for *VEGFA* or sphingosine kinase (*SPHK1)*, which catalyzes S1P production, and injected them intravenously 4 and 7 days after cardiac ischemia–reperfusion in mice. Sequential delivery by transduced BM cells of VEGFA and S1P led to increased endothelial cell numbers and shorter extravascular distances in the infarct zone, which support better oxygen diffusion 28 days post myocardial infarction, as shown by automated 3D image analysis of the microvasculature. Milder effects were observed in the remote zone, together with increased proportion of capillaries. BM cells delivering VEGFA and S1P also decreased myofibroblast abundance and restricted adverse cardiac remodeling without major impact on cardiac contractility. The results indicate that BM cells engineered to deliver VEGFA/S1P angiogenic factors sequentially may constitute a promising strategy to improve microvascularization and oxygen diffusion, thus limiting the adverse consequences of cardiac ischemia.

Keywords: VEGFA, S1P, gene–cell angiotherapy, myocardial infarction, oxygen diffusion, cardiac remodeling

INTRODUCTION

CARDIOVASCULAR DISEASE (CVD) has been the leading cause of death in the United States since the beginning of the 20th century, with almost half of those deaths caused by coronary heart disease.[1,2] The most common long-term consequence of coronary heart disease is heart failure (HF), and its prevalence increased between 2009 and 2014, in part due to the improvement in acute treatment of CVD.[2] One of the clinical manifestations of coronary heart disease is myocardial infarction (MI), which is the sudden death of myocardial tissue from ischemia caused by a blockage of a coronary artery, usually from the rupturing of an atherosclerotic plaque.[3] MI causes cardiomyocyte death, which triggers acute inflammation, angiogenesis, and finally scar formation.[4] Fibrotic scar formation is the main healing mechanism after MI due to the limited ability of the adult mammalian heart to regenerate.[3] Fibrosis causes abnormalities in both relaxation and contractility of the heart muscle, which causes ventricular remodeling, a mechanism of heart adaptation to adverse stimuli.[5] Remodeling includes left ventricular wall thinning, ventricle

*Correspondence: Dr. Alicia G. Arroyo, Vascular Pathophysiology Area, Centro Nacional de Investigaciones Cardiovasculares (CNIC), Melchor Fernández Almagro 3, 28029 Madrid, Spain. E-mail agarroyo@cnic.es

DOI: 10.1089/hum.2018.194

dilation, and changes in its shape from ellipsoid to more spherical.[6] At the cellular level, cardiomyocytes in the viable myocardium undergo hypertrophy triggered by increased load. These malformations create increasing wall stress, which causes higher myocardial oxygen demand and could cause further enlargement of the area at risk for ischemia.[7] Pathological heart remodeling caused by MI and secondary hypoxia induces HF and high mortality in the long term.[8] Indeed, HF becomes the main cause of death of patients >65 years old within 6 years after MI.[9] HF can also derive from other CVD involving microvascular dysfunction and tissue hypoxia as hypertensive cardiac hypertrophy and diabetic coronary microangiopathy.[10] For that reason, prevention and ameliorating effects of HF are of great importance.

Over the past decades, a need for an effective therapy to prevent and limit hypoxia-related cardiac adverse remodeling and as a consequence HF, particularly after MI, remains unmet. Since the introduction of fibrinolysis and angioplasty in the late 1970s, acute treatment of MI has improved dramatically, although the mortality rate caused by CVD remains high.[11] Trying to overcome the inability of adult cardiac muscle to regenerate, many therapies were implemented, including cell and gene therapies and delivery of cytokines and soluble factors. One of the aims of these therapies has been modulating angiogenesis,[12–18] since by preserving the microvasculature or boosting the formation of new vessels, tissue oxygenation would improve, alleviating adverse consequences of acute or chronic ischemia. In recent years, importance has also been given to modulating immune response after MI for its beneficial effect on heart repair.[19–22]

One of the main unsolved questions in these studies was the optimal delivery route for the factors with strategies including delivery of the recombinant protein,[23,24] gene delivery using plasmids[16,17] and modified RNA,[25] and virus-based approaches, mostly using adeno-associated virus (AAV).[14,26,27] On the other hand, cell therapies, whose main effect is believed to be based on secreting factors such as vascular endothelial growth factor A (VEGFA) and PDGF showed limited long-term improvement in cardiac vascularization.[28–30] It was hypothesized that combining two approaches by delivering cells but also transducing them to overexpress proangiogenic factors may bring an improvement in cardiac vascularization after ischemia. In the field of proangiogenic therapies, the strong proangiogenic factor VEGFA generated promising results in animal models but showed no sustained improvement in myocardial perfusion measured in the NORTHERN clinical trial.[13] However, co-delivery of VEGFA and sphingosine-1-phosphate (S1P) by AAV promoted angiogenesis and reduced cell apoptosis in a pig model of MI.[14] Of note, sequential instead of simultaneous exposure to VEGFA and S1P led to the formation of more stable vessels in scaffolds *in vitro*, but this approach has never been tested *in vivo*.[31]

This study investigated the effect of bone-marrow (BM) cells engineered to produce VEGFA or S1P and injected sequentially in improving vascularization in a preclinical mouse model of acute ischemic heart disease. Indeed, it is demonstrated that lentiviral vector (LV)-transduced BM cells injected intravenously (i.v.) in mice to deliver the pro-angiogenic factors VEGFA and S1P sequentially resulted in sustained increased vascularization 28 days after MI assessed by a newly implemented pipeline for automatized 3D image analysis of the microvasculature[32] and in contrast to the transient effect reported for non-transduced BM cells. As a consequence, the strategy also limited fibrosis and adverse cardiac remodeling. This study may offer new therapeutic possibilities for patients suffering cardiac ischemic disease.

METHODS

All experimental procedures are explained in detail in the Supplementary Methods.

LV construction and evaluation

Human *VEGFA* and *SPHK1* and *GFP* cDNAs were amplified by polymerase chain reaction and inserted downstream to the SFFV promoter of the SFFV.insert.WPRE LV backbone described in Squadrito *et al*.[33] Enzyme-linked immunosorbent assay kits were used to quantify VEGFA protein level in cell supernatants. LV transduction of BM cells was performed overnight at a multiplicity of infection of 50. The collection of cell supernatant was performed 48 and 72 h after transduction. S1P expression was measured by mass spectrometry 48 h after transduction with LV_SPHK1. For further details, see the Supplementary Methods.

Flow cytometry

BM cells were stained with antibodies against CD11b-AF647, F4/80-PE-Cy7, Ly6C-FITC, CCR2-PE, and CX_3CR1-Pacific Blue and 7-AAD live/death dye. Sample acquisition was performed using a BD LSRFortessa flow cytometer (BD Biosciences) and analyzed using FlowJo software (FlowJo LLC). Detailed staining procedure and a

list of antibodies is available in the Supplementary Methods.

Aortic ring assay

Aortic ring assay was performed, as described in Baker *et al.*[34] Mouse aortic rings were cultured in the presence of various combinations of soluble factors (rhVEGFA 30 ng/mL, S1P 1 μM) or mouse BM cells previously transduced with LVs (BM^{hVEGF}, BM^{hSPHK1}). On day 8, rings were fixed in 1.6% paraformaldehyde, and incubated overnight at 4°C with the following antibodies/reagents: IB4 or anti-CD31 (1:150) for endothelial cells and anti-smooth-muscle actin (SMA; 1:400) for mural cells. Images were acquired with a Nikon A1R confocal system coupled to a Nikon Ti-Eclipse microscope using a 10× objective and capturing 400 μm in depth with a z-stack every 3 μm. Analysis of aortic ring images was performed using Imaris software and a Matlab-based method for 3D-microvasculature developed in the lab. Reagents, antibodies, and detailed procedures are described in the Supplementary Methods.

In vivo mouse ischemia–reperfusion experiment protocol

Mice were kept at the animal facility of the Centro Nacional de Investigaciones Cardiovasculares under specific pathogen-free conditions and in accordance with the institutional guidelines. Animal procedures were approved by the corresponding legal authority of the local government of Madrid (reference number of approval PROEX/ 34/ 13). Ischemia–reperfusion (I/R) was performed in 10- to 12-week-old male BL6 mice by ligation of the left anterior descendent coronary artery for 45 min of ischemia followed by reperfusion. Echocardiography was performed 3 days after to confirm MI, and mice with a left ventricular ejection fraction (LVEF) between 20% and 40% were randomly assigned to control and treated groups. Four days post I/R, mice were injected i.v. with 5×10^6 BM^{hVEGF} in 100 μL of phosphate-buffered saline (PBS) or with PBS only as a control. Seven days post I/R, a second injection was performed with 5×10^6 BM^{hSPHK1} or PBS. On day 28, after endpoint echocardiography, hearts were weighed and collected. Echocardiography was performed using Vevo 2100 ultra high frequency ultrasound to assess cardiac parameters (end-diastolic and end-systolic volumes, stroke volume (SV), LVEF and left ventricular posterior wall thickness). Analysis of heart roundness (*i.e.*, sphericity) was performed on macroscopic images of the dissected hearts using ImageJ[35] software. Fibrosis was assessed based on Masson's trichrome staining of a series of seven levels of tissue cuts, starting from the apex to the base of the heart and visualized using NanoZoomer-2.ORS® (Hamamatsu); scar area is represented as the percentage of left-ventricular area using ImageJ software. To quantify cardiomyocyte size, an ImageJ-based semi-automated macro was designed where cardiomyocytes were recognized by laminin staining and their area and perimeter quantified. Detailed experimental procedures are described in the Supplementary Methods.

Microvasculature analysis

Sections (15 μm thick) were stained with anti-CD31, anti-PDGFRβ, and anti-SMA antibodies and with Hoechst for nuclear staining. Images were acquired with a Leica SP5 confocal microscope using a 40× objective (NA 1.25) with oil immersion with z-stacks captured every 1 μm. Analysis of the microvasculature was based on the fully automatic image analysis pipeline developed in the authors' laboratory to analyze microvascular data. The pipeline permits the calculation of a pool of parameters that quantify all major features of the vascular network. It has been described in detail in Gkontra *et al.*,[32] while a brief overview of necessary adaptations is provided in the Supplementary Methods.

Statistics

Statistical analysis was performed using GraphPad Prism v6/7. Distribution of the data sets was checked with D'Agostino–Pearson and Shapiro–Wilk normality tests, and then parametric or nonparametric tests were performed as indicated in the legends. Outliers were identified using the ROUT method ($Q = 1.000\%$).

RESULTS

Experimental design for *in vivo* sequential VEGF/S1P gene–cell angiotherapy in a MI mouse model

Sequential delivery of VEGFA (VEGF hereafter) and S1P has been shown to increase the formation of mature vessels in *in vitro* scaffolds compared to the effect of single or combined factors.[31] It was confirmed in the mouse aortic ring assay that sequential delivery of S1P after VEGF or combined delivery of the two factors induced a significantly higher proportion of sprouts, covered by SMA+ cells and a more complex vascular network than VEGF alone (Supplementary Fig. S1A and B). A decision was therefore made to test the effects of a combined gene–cell therapy in which BM cells were

boosted to produce VEGF and S1P by LV transduction and to deliver these factors sequentially. For that, LVs were generated encoding for the human *VEGF*, or *SPHK1* (sphingosine-kinase 1), the enzyme that catalyzes the conversion of the precursor sphingolipid sphingosine to the active form S1P (herein LV_ hVEGF and LV_hSPHK1, respectively). Then, the efficacy of the LV was validated in HEK and mouse BM cells transduced with LV_hVEGF and LV_hSPHK1, which indeed overexpressed VEGF and produced S1P (Supplementary Fig. S2). The proposed strategy was tested in the mouse model of acute cardiac I/R, which is closer to the human MI clinical practice. Before proceeding with the *in vivo* approach, the ability of i.v. injected BM cells to migrate to the infarcted myocardium was confirmed. Histological analysis performed 24 h after Tomato$^+$ BM cell i.v. injection confirmed the presence of red round cells in the infarct zone of hearts 4 days after I/R. Only an unspecific non-membrane-associated red signal was detected in the hearts from PBS-injected mice (Supplementary Fig. S3A).

Prior to their i.v. injection, the study also analyzed whether LV transduction and culture in the presence of stem-cell factor (SCF) and macrophage colony-stimulating factor *in vitro* impacted on the phenotype of BM cells. Following the flow cytometry gating strategy detailed in the Methods (Supplementary Fig. S3B and C), it was observed that after LV transduction with LV_hVEGF or LV_hSPHK1, the amount of neutrophils increased, macrophages decreased, and the scarce myeloid progenitors remained unchanged (Supplementary Fig. S3D–F). Notably, although no differences in the percentage of monocytes ($\sim$60%) were observed, after LV transduction, there was an increase in their CX_3CR1 cell surface expression, particularly after LV_hSPHK1 transduction with milder changes in CCR2 levels (Supplementary Fig. S3G).

BM cell-mediated delivery of VEGF and S1P improves vascularization and reduces intercapillary distances in the post-infarcted heart

Next, the study tested the *in vivo* impact of boosting BM cell sequential secretion of VEGF and S1P in a mouse model of cardiac I/R (Supplementary Fig. S4A). MI was confirmed by echocardiography 3 days post I/R, and mice with a LVEF of 20–40% were included in the study. Mice were afterwards randomly assigned to control and treated groups and then injected i.v. on day 4 post I/R with PBS or with 5×10^6 of BM^{hVEGF} followed on day 7 by PBS or 5×10^6 of BM^{hSPHK1} similar to the time points tested in the *in vitro* aortic ring assay (Supplementary Fig. S1).

Sequential VEGF/S1P angiotherapy by BM cells was primarily designed to enhance angiogenesis and increase the functional microvasculature after I/R, which may secondarily reduce post-MI adverse effects. In an effort to quantify the effect of the proposed treatment to the microvasculature in an unbiased and reproducible manner, images of transverse slices of cardiac tissue from treated and untreated subjects were analyzed by means of a 3D fully automated image analysis pipeline developed at the authors' lab.[32] The tissue was labeled for blood vessels, in particular for endothelial cells (CD31) and for SMA and PDGFRβ+ cells, and then imaged by confocal microscopy. The automated analysis approach allowed the post-MI changes of the microvasculature of the control and BM cell-delivered VEGF/S1P hearts to be compared in terms of all major microvascular characteristics: morphology, topology, angio-architecture, efficiency for oxygen diffusion, as well as its relation with SMA$^+$ and PDGFRβ^+ cells. A summary of all quantified parameters and their changes are provided in Table 1. Reference values for the parameters extracted from microvascular tissues of basal mice are also given.

Among fractal parameters, lacunarity, a parameter measuring the heterogeneity in the distribution of the size of the gaps in the tissue, significantly decreased in the infarcted area of the hearts in the treated group. This indicates a smaller dispersion of non-vascularized areas, implying a better-organized microvasculature (Table 1). Although no significant differences were observed in the overall vascular volume density 28 days after I/R, after decomposing the microvasculature into its components, that is, capillaries ($CD31^+SMA^-$, $<5\,\mu$m), enlarged capillaries ($CD31^+SMA^-$, $>5.1\,\mu$m), and arterioles ($CD31^+SMA^+$), a trend to increased capillary volume density and decreased enlarged capillaries was noticed in the infarcted zone of hearts from mice injected with BM cells delivering VEGF/S1P compared to controls (Fig. 1A–C and Table 1). There were, however, no changes in the volume density and the percentage of arterioles (Fig. 1B and C). Accordingly, treatment also resulted in significantly more abundant endothelial cells in the vasculature of the infarcted zone (Fig. 1A). Interestingly, in the remote zone, a significant increase in the volume and percentage of capillaries and a decrease in the percentage of enlarged capillaries were also observe in hearts from the VEGF/S1P-treated group, in spite of the lack of statistically significant between-group differences

Table 1. *Quantitative analysis of microvasculature parameters in the cardiac tissue from treated and non-treated mice after myocardial infarction*

	Infarct untreated	*Infarct treated*	*Remote untreated*	*Remote treated*	*Basal*
Fractal-based metrics					
Fractal dimension	1.79 ± 0.04	1.78 ± 0.03 ↓	1.86 ± 0.04	1.85 ± 0.04 ↓	1.91 ± 0.01
Lacunarity ($\times 10^{-2}$)	96.42 ± 0.84	95.84 ± 1.16 ↓	92.34 ± 0.94	91.46 ± 0.83 ↓*	90.93 ± 0.15
Minkowski-based metrics					
Vascular volume density (%)	2.62 ± 0.38	2.46 ± 0.26 ↓	3.66 ± 1	3.44 ± 0.8 ↓	3.48 ± 0.21
Vascular surface area density ($\times 10^{-3}$; $\mu m^2/\mu m^3$)	23.79 ± 1.51	24.86 ± 3.13 ↑	41.72 ± 6.31	43.08 ± 5.15 ↑	40.17 ± 1.91
Breadth density ($\times 10^{-3}$; $\mu m/\mu m^3$)	0.97 ± 0.06	1.08 ± 0.23 ↑	2.23 ± 0.31	2.38 ± 0.22 ↑	2.05 ± 0.22
Euler characteristic density ($\times 10^{-5}$; $1/\mu m^3$)	−1.7 ± 3.09	−1.2 ± 2.87 ↑	1.6 ± 6.89	3.49 ± 9.56 ↑	5.89 ± 1.76
Capillary volume density (%)	0.66 ± 0.15	0.76 ± 0.17 ↑	2.31 ± 0.39	2.65 ± 0.31 ↑*	2.36 ± 0.13
Capillary surface area density ($\times 10^{-3}$; $\mu m^2/\mu m^3$)	9.94 ± 2.5	11.24 ± 2.75 ↑	32.49 ± 4.57	37.1 ± 2.69 ↑**	32.47 ± 2.08
Enlarged capillary volume density (%)	0.58 ± 0.34	0.34 ± 0.21 ↓	0.81 ± 0.63	0.4 ± 0.43 ↓	0.3 ± 0.16
Enlarged capillary surface area density ($\times 10^{-3}$; $\mu m^2/\mu m^3$)	4.84 ± 2.55	2.93 ± 1.7 ↓	6.69 ± 5.11	3.47 ± 3.68 ↓	2.51 ± 1.45
SMA+ vessel volume density (%)	1.37 ± 0.24	1.35 ± 0.16 ↓	0.53 ± 0.27	0.39 ± 0.26 ↓	0.82 ± 0.1
SMA+ vessel surface area density ($\times 10^{-3}$; $\mu m^2/\mu m^3$)	10.21 ± 1.73	11.67 ± 1.67 ↑	4.12 ± 1.78	3.55 ± 2.6 ↓	6.18 ± 0.33
Capillary (%)	26.42 ± 9.74	31.11 ± 7.53 ↑	66.19 ± 15.86	78.94 ± 10.78 ↑*	67.92 ± 3.57
Enlarged capillary (%)	21.05 ± 10.45	13.6 ± 6.98 ↓	19.95 ± 13.19	9.95 ± 8.48 ↓*	8.53 ± 4.54
SMA+ vessel (%)	52.52 ± 6.81	55.29 ± 5.89 ↑	13.86 ± 4.84	11.11 ± 6.6 ↓	23.55 ± 2.56
Graph-based metrics					
Vascular segment diameter (μm)	4.23 ± 0.7	3.96 ± 0.6 ↓	3.76 ± 0.62	3.43 ± 0.37 ↓	3.91 ± 0.25
Vascular segment length (μm)	8.58 ± 1.55	8.58 ± 1.4 ↓	9.67 ± 1.23	10.06 ± 1.06 ↑	12.24 ± 1.62
Vascular segment surface (μm^2)	119.08 ± 38.82	112.19 ± 30.08 ↓	121.14 ± 31.15	114.62 ± 18.95 ↓	153.61 ± 26.72
Vascular segment volume (μm^3)	149.58 ± 67.97	132.71 ± 48.83 ↓	135.32 ± 52.18	113.56 ± 27.61 ↓	175.04 ± 37.32
Tortuosity ($\mu m/\mu m$)	1.5 ± 0.06	1.54 ± 0.06 ↑	1.51 ± 0.08	1.54 ± 0.06 ↑	1.47 ± 0.01
SMA+ and Pdgfrb-related metrics					
Myofibroblasts abundance	0.5 ± 0.06	0.43 ± 0.09 ↓*	0.04 ± 0.03	0.03 ± 0.02 ↓	0.02 ± 0.01
Vessels covered with Pdgfrb (%)	76.95 ± 8.09	76.59 ± 11.75 ↓	87.07 ± 7.1	87.21 ± 5.71 ↑	88.75 ± 2.85
Vessels covered with SMA (%)	38.19 ± 4.82	40.98 ± 5.7 ↑	15.98 ± 6.07	12.26 ± 6.01 ↓	24.18 ± 3.27
SMA+ layer thickness (μm)	3.72 ± 0.82	3.68 ± 0.51 ↓	3.85 ± 0.39	3.7 ± 0.79 ↓	4.5 ± 0.52
SMA+ perivascular cells[a]	16.19 ± 3.65	18.33 ± 4.39 ↑	6.1 ± 2.78	4.93 ± 2.56 ↓	8.33 ± 0.66
Efficiency in oxygen diffusion					
Median extravascular distance (μm)	13.38 ± 1.52	11.76 ± 2.21 ↓	5.68 ± 0.51	5.34 ± 0.28 ↓	5.63 ± 0.35
Maximal extravascular distance (μm)	43.63 ± 7.04	36.02 ± 8.59 ↓*	12.53 ± 1.2	11.69 ± 0.76 ↓	13.19 ± 1
Additional cell-related metrics					
Endothelial cells ($\times 10^5$)[b]	26.71 ± 2.37	30.31 ± 4.28 ↑*	35.43 ± 5.83	39.79 ± 6.04 ↑	31.63 ± 4.75

The mean ± standard deviation of all parameters for cardiac tissue from treated (BM^{hVEGF} + BM^{hSPHK1}) and non-treated (phosphate-buffered saline) mice along with pairwise comparisons among the different tissue conditions. Capillaries correspond to CD31+ and SMA– vessels of diameter <5 μm, enlarged capillaries to CD31+ and SMA– vessels of diameter ≥5 μm, and SMA+ vessels to CD31+ and SMA+ vessels regardless their diameter. Up and down arrows indicate increase and decrease, respectively, of the parameter value for (1) tissue from infarcted areas of subjects treated with BM^{hVEGF} + BM^{hSPHK1} compared to tissue from infarcted areas of untreated subjects, and (2) tissue from remote areas of subjects treated with BM^{hVEGF} + BM^{hSPHK1} compared to tissue from remote areas of untreated subjects.

[a]Number per mm vascular length.

[b]Number per mm^3 vascular volume.

*$p < 0.05$; **$p < 0.01$. The p-values were calculated by means of a two-sample t-test.

BM, bone marrow; VEGF, vascular endothelial growth factor; SPHK1, sphingosine kinase; SMA, smooth-muscle actin.

in overall vascular volume density. Concomitantly, endothelial cell abundance in the remote zone was slightly increased in the treated group (Fig. 1D–F). These findings indicate that combined delivery of VEGF/S1P impacted mostly on the capillaries, increasing their volume density and the endothelial cell content while decreasing their remodeling/enlargement in both the infarcted and the remote zones.

The main function of the microvasculature is to provide nutrients and oxygen to the heart, particularly after ischemia, to preserve cell viability and promote repair. Thus, toward obtaining insights into the efficiency of the network for oxygen diffusion, traditional indicators of oxygen diffusion (*i.e.*, maximal extravascular distances) were studied by means of the automated pipeline. According to the larger proportion of capillaries and higher endothelial cell numbers, maximal extravascular distances were significantly reduced in the infarct zone of hearts from mice injected with BM cells producing VEGF and S1P 28 days after I/R compared to the controls, indicating better oxygen diffusion. A similar trend to reduced extravascular distances was observed in the remote zone of treated mice (Fig. 2).

Next, the study sought to decipher the contribution of VEGF and S1P overexpression versus

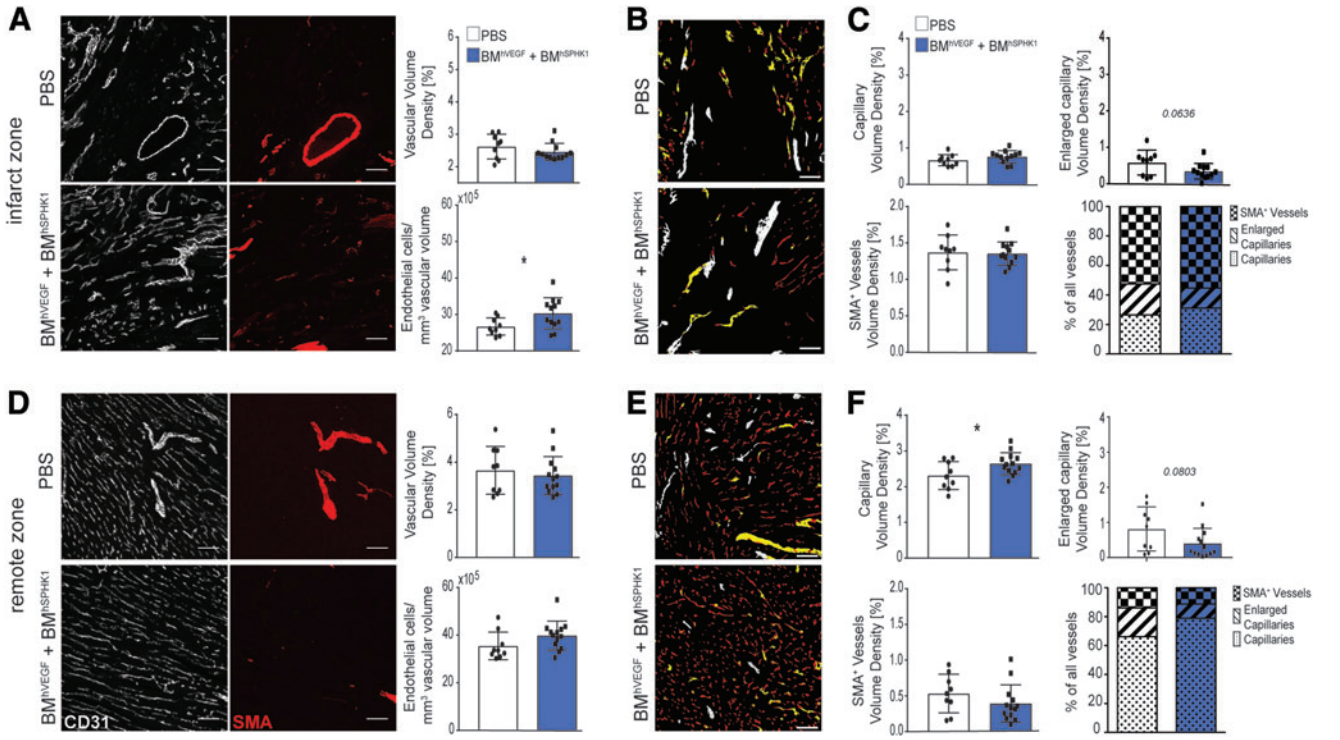

Figure 1. Sequential bone marrow (BM) cell delivery of vascular endothelial growth factor (VEGF) and sphingosine-1-phosphate (S1P) increases capillary volume density and endothelial cell number on the infarcted heart post myocardial infarction (MI). **(A)** *Left panels*: representative maximal intensity projections from confocal microscopy images of transverse sections of mouse hearts stained for endothelial cells (CD31, *gray*) and smooth-muscle cells (SMA, *red*). *Right panels*: bar graphs showing total vascular volume density and the number of endothelial cells per vascular volume in the infarct zone of treated and non-treated mice 28 days post ischemia–reperfusion (I/R). Scale bar: 50 μm. **(B)** Representative images of segmented vessels in three categories: capillaries ($CD31^+SMA^-$, <5 μm diameter, *red*), enlarged capillaries ($CD31^+SMA^-$, >5.1 μm diameter, *yellow*), and arterioles/SMA+ vessels ($CD31^+SMA^+$, *white*) in the infarct zone of treated and non-treated hearts. Scale bar: 50 μm. **(C)** Bar graphs showing volume densities for the three-vessel categories, as well as percentage representation of each vessel type out of the total vasculature. **(D–F)** Representative images and bar graphs, as described in **(A–C)**, corresponding to the remote zone of hearts from treated and non-treated mice 28 post I/R. Data represent the mean ± *SD* of 9 and 12 mice for non-treated and treated groups, respectively, analyzed in two independent experiments. A parametric *t*-test was used for statistical comparison. *$p<0.05$; **$p<0.01$; ***$p<0.001$. Color images are available online.

endogenous secretion of factors by BM cells to the myocardial angiogenic phenotype, since PBS was used as *in vivo* control. Non-transduced BM cells did not increase vascular sprouting versus control medium in the aortic ring in contrast to sequential exposure to BM cells secreting VEGF and S1P, which induced a significant increase in vascular sprouts with a good proportion covered by SMA+ cells, indicative of stable vessels, and a more complex vascular network (Supplementary Fig. S4B). These findings argue in favor of overexpressed VEGF and S1P by LV-transduced BM cells as the factors responsible for boosting capillarization post MI.

Sequential BM cell delivery of VEGF and S1P diminishes post-infarction tissue fibrosis with no impact on cardiac contractility

After MI, dead cardiomyocytes are mostly replaced by fibrotic tissue, reducing cardiac pump function. The study analyzed whether improved capillarization and oxygen diffusion by BM cell sequential delivery of VEGF/S1P had any impact on cardiomyocyte survival and thus in cardiac performance. Despite the presence of isolated clusters of viable cardiomyocytes within the scar of infarcted hearts from VEGF/S1P-treated mice but not in untreated controls 28 days post-I/R (Supplementary Fig. S5A), echocardiography analysis showed no significant between-group differences in the reduced LVEF and the SV (Supplementary Fig. S5B and C).

Regardless the ejection fraction values, fibrosis extent and tissue stiffness are the major factors driving post-MI progression to HF. Therefore, although a major impact of the BM cell-VEGF/S1P therapy could not be observed on cardiac contractility, next fibrosis-related parameters were assessed, since cardiac injury and hypoxia are enhancers of the myofibroblast-driven fibrotic program.[36,37] Between-group differences could not be detected in the total scar volume of the left ventricular free wall calculated from serial Masson-stained sections

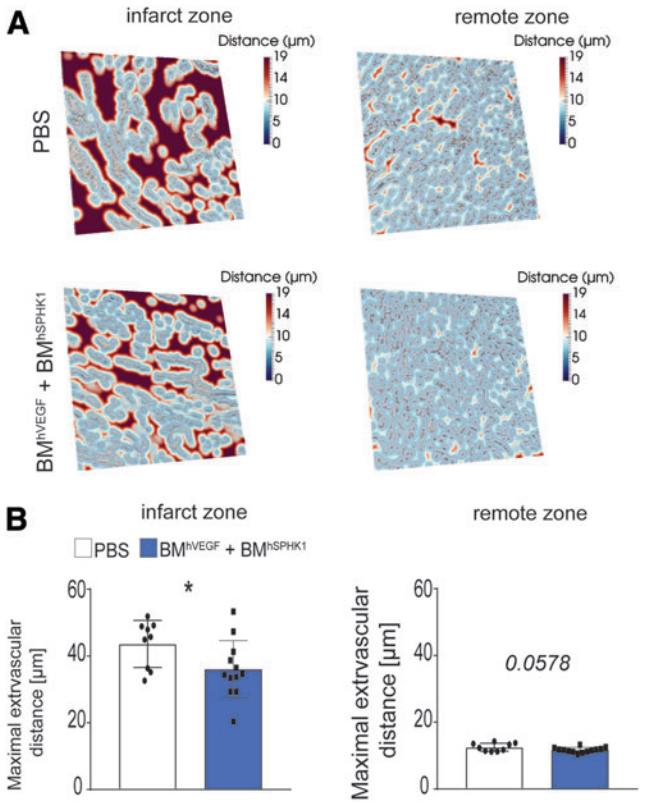

Figure 2. BM cell sequential delivery of VEGF and S1P reduces intercapillary distances in the post-infarcted heart. **(A)** Representative images of extravascular distance maps from the infarct and remote zone of treated and control mice 28 days post MI. **(B)** Bar graphs show the quantification of maximal extravascular distances in the conditions shown in **(A)**. Data are represented as the mean ± standard deviation (*SD*) of 9 and 12 mice for non-treated and treated groups, respectively, analyzed in two independent experiments. A parametric *t*-test was used for statistical comparison. $*p<0.05$; $**p<0.01$; $***p<0.001$. Color images are available online.

spanning the whole heart 28 days post I/R (Fig. 3A and B). However, the cardiac section closest to the valves consistently showed a significantly reduced scar area in the BM cell VEFG/S1P-treated group (Fig. 3C). Complementarily, using the images of mouse cardiac tissues stained for PDGFRβ and CD31, the myofibroblast abundance were also automatically quantitated as the ratio of the volume of myofibroblasts over the volume of all PDGFRβ+ cells. In this approach, myofibroblasts are considered PDGFRβ+ areas that are not in touch with the vessels.[32,38] Following this approach, significantly reduced myofibroblast abundance was noticed in the infarct zone of hearts from BM cell VEGF/S1P-treated mice compared to untreated controls. Myofibroblasts were barely detected, but there were fewer in the remote zone of the treated group (Fig. 3D and E and Table 1). Since myofibroblasts are in charge of secreting and remodeling extracellular matrix proteins, particularly collagens, to form the scar, myofibroblast reduction prompted collagen fiber organization and condensation to be analyzed, in spite of no significant differences observed in overall scar area. Analysis of first-order features of collagen fibrils in second harmonic generation microscopy images revealed increased skewness and kurtosis in the collagen fibers of the scar from infarcted hearts of the BM cell VEGF/S1P-treated group compared to controls (Fig. 3F and G). These values would indicate thinner and underdeveloped collagen fibers and thus lower tissue stiffness.[39]

VEGF and S1P sequential delivery by BM cells limits adverse cardiac remodeling post MI

One of the consequences of MI is cardiac remodeling defined as the post-damage alterations that result in acute and chronic changes of heart size, mass, geometry, and function, which may finally lead to cardiac dysfunction and HF.[40] First, ventricle cavity size and wall thickness were quantitated, and a trend was observed of reduced dilatation and thickening of the left ventricle in the VEGF/S1P-treated mice 28 days post I/R (Fig. 4A and B). Since volume and thickness changes are not fully developed 4 weeks after I/R in mice,[41] global cardiac geometry was also analyzed, which is modified more acutely.[40] It was found that hearts from BM cell VEGF/S1P-treated mice kept their ellipsoid-like shape in contrast to those from untreated control mice that became significantly rounder at 28 days post I/R, as expected (Fig. 4C). Moreover, analysis of cardiomyocytes in the remote zone, which usually become hypertrophic in response to post-MI left ventricular stiffness and volume overload,[40] showed that cardiomyocytes in the remote zone of hearts from BM cell VEGF/S1P-treated mice became less hypertrophic, with significantly smaller area and perimeter compared to control mice 28 days post I/R (Fig. 4D and E). Finally, cardiac remodeling also results in changes at the molecular level, with proteins increasing (collagen type I) or decreasing (Atpa2a/Serca2a) during the process.[40] Notably, VEGF/S1P treatment led to decreased collagen type I and increased Atp2a2 (Serca2) protein levels in heart extracts compared to untreated mice 28 days post I/R (Fig. 4F and G), confirming that the angiotherapy ameliorated adverse cardiac remodeling.[40]

Collectively, these findings indicate that sequential VEGF/S1P gene–BM cell therapy limits post-MI adverse cardiac remodeling consistent with the enhanced capillarization and oxygen diffusion effects and reduced myofibroblast abundance in the infarcted tissue.

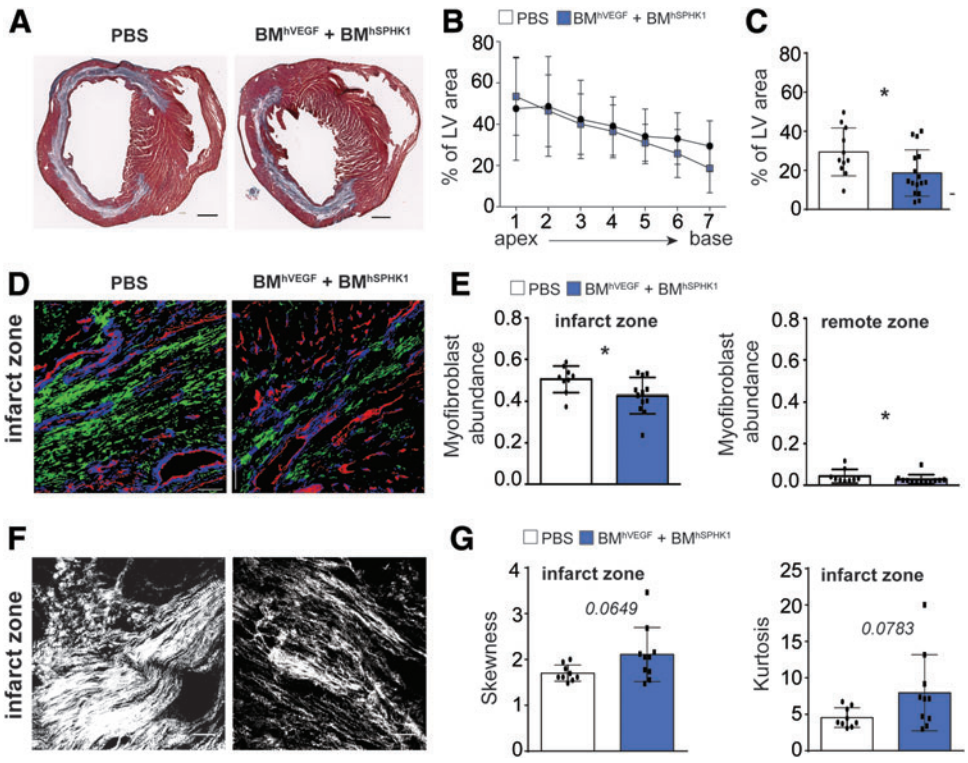

Figure 3. Sequential BM cell-secreted VEGF and S1P angiotherapy reduces myofibroblast abundance and collagen fiber compaction in the infarcted heart post I/R. **(A)** Representative images from Masson's trichrome-stained transverse sections of hearts from treated and control groups 28 days post I/R. **(B)** Graphs shows the percentage of the left ventricular area covered by scar tissue in serial cuts spanning the whole heart from the apex (1) to the base (7). **(C)** Bar graph shows the percentage of left ventricular scar area in the transverse section of the base of the heart (closest to the valves). **(D)** Pseudo-colored representation of confocal microscopy images of transverse sections from the infarct zone of treated and control hearts stained for CD31 and PDGFRβ in which vessels (CD31$^+$) are shown in *red*, perivascular cells (PDGFRβ^+ cells touching vessels) in *blue*, and myofibroblasts (PDGFRβ^+ cells distant from the vessels) in *green*. **(E)** Bar graphs represent myofibroblast abundance in the infarct and remote zones. **(F)** Representative images of collagen fibers obtained by second harmonic generation (SHG) multiphoton microscopy in transverse sections of hearts from treated and control groups 28 days post I/R. **(G)** Bar graphs show the quantitation of the first-order parameter skewness (asymmetry of pixel distribution) and kurtosis (gray-tone spread-out distribution) in SHG images. Data are represented as the mean $\pm$ *SD*. $n=11$ and 16 **(B** and **C)**, $n=9$ and 12 **(D** and **E)**, and $n=9$ and 10 **(F** and **G)** mice of non-treated and treated groups, respectively, analyzed in three **(B** and **C)** and two **(D–G)** independent experiments. Data were statistically compared by **(B)** two-way analysis of variance (ANOVA), **(C)** parametric *t*-test, and **(D–G)** nonparametric Mann–Whitney *U*-test. $*p<0.05$; $**p<0.01$; $***p<0.001$. Color images are available online.

DISCUSSION

This study tested the effect of sequential delivery by BM cells of the proangiogenic factors VEGF and S1P on boosting angiogenesis and/or preserving the microvasculature after MI *in vivo*. The intervention succeeded in increasing endothelial cell numbers and capillaries and diminishing adverse angioadaptation, thus improving oxygen diffusion 4 weeks after the ischemic event. In spite of no major effect on cardiac contractility, BM cell

Figure 4. Sequential delivery of VEGF and S1P by lentiviral vector (LV)-transduced BM cells limits adverse cardiac remodeling post MI. **(A)** Graphs show the left ventricular end-systolic (LVESV) and end-diastolic (LVEDV) volumes of hearts from basal (no I/R) and from control (PBS) or VEGF/S1P-treated mice at 3 and 28 days post I/R. **(B)** Graph shows the left ventricular posterior wall end-diastolic thickness calculated in M-mode ultrasound images in hearts from control (PBS) or VEGF/S1P-treated mice at 28 days post I/R. **(C)** Bar graphs show the heart roundness coefficient quantitated in macroscopic images from hearts of treated and non-treated mice 28 days post I/R. **(D)** Maximal intensity projections from confocal microscopy images of the remote area from pan-laminin (green)-stained transverse sections of hearts from treated and non-treated mice 28 days post I/R. Scale bar: 50 μm. **(E)** Bar graphs show the quantification of cardiomyocyte area and perimeter from pan-laminin-stained images **(D)**. **(F)** Representative Western blots for Col1a1 and Atp2a2 protein expression in hearts from treated and non-treated mice 28 days post I/R (*top*) and graphs with the quantification expressed as fold change (F.C., *bottom*). Tubulin is included as loading control. $n=6$ mice from non-treated (PBS) and treated (BM^{hVEGF}+BM^{hSPHK1}) groups. Data are shown as the mean $\pm$ standard error of the mean and were statistically compared with a parametric *t*-test ($*p<0.05$). **(G)** Representative maximal intensity projections from confocal microscopy images of heart sections from treated and non-treated mice 28 days post I/R stained for cardiomyocytes (α-actinin, *gray*) and Atp1a2 (*red*). *Yellow squares* indicate the magnified areas. Scale bar: 100 and 50 μm in the magnified views. Data represent the mean $\pm$ *SD*. $n=6$ mice for non-I/R and $n=11$–12 and 16–18 mice for non-treated and treated groups, respectively, analyzed in three independent experiments **(A–E)**. $n=6$ mice for non-treated and treated groups, respectively, analyzed in two independent experiments **(F)**. Data were statistically compared with one-way ANOVA **(A)** and a parametric *t*-test **(B–F)**. $*p<0.05$; $**p<0.01$; $***p<0.001$. Color images are available online.

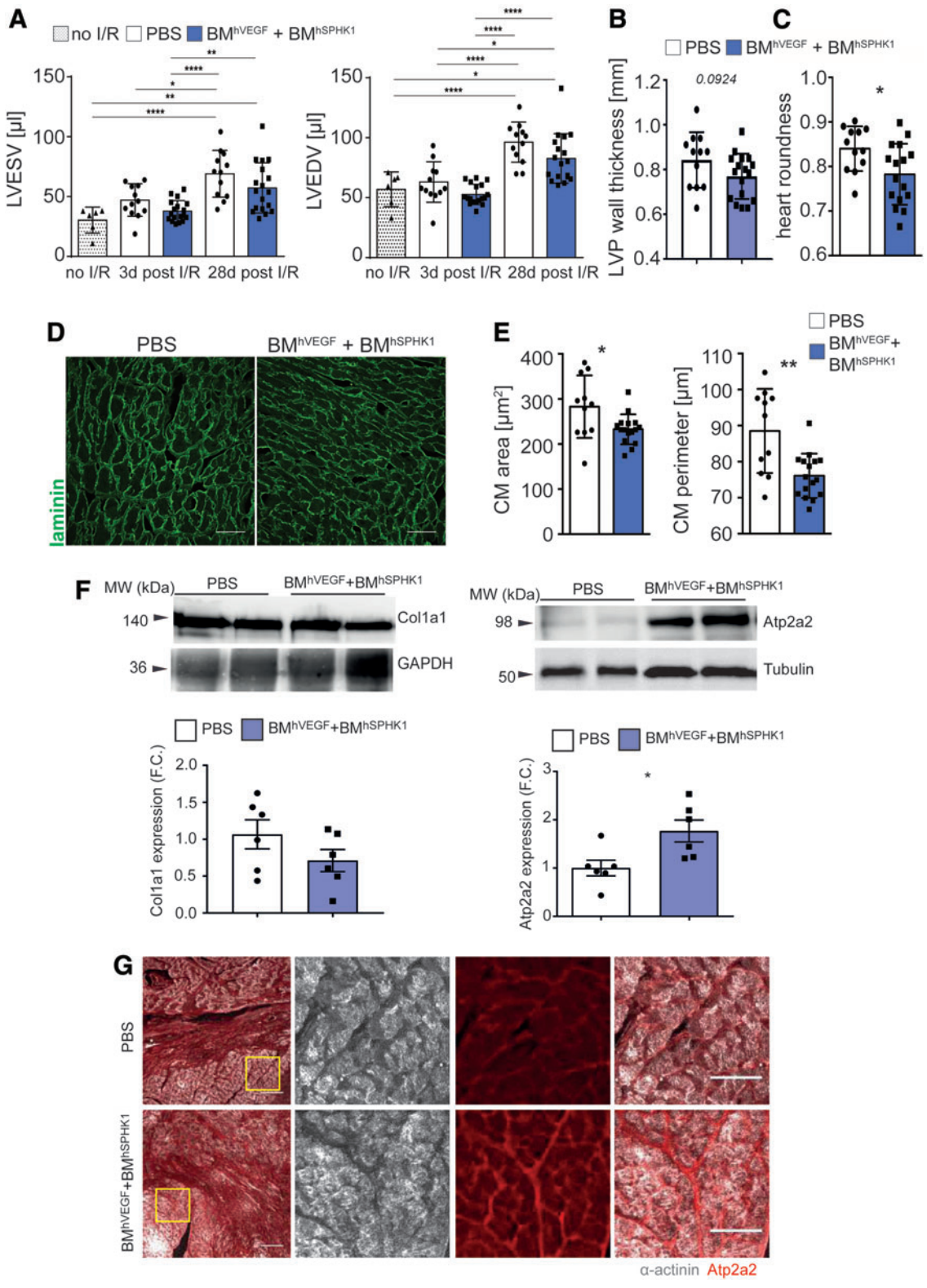

sequential VEGF/S1P therapy also reduced myofibroblast-driven tissue fibrosis and limited adverse post-MI cardiac remodeling.

In terms of safety and possible translation of this therapy, LV transduction is performed *ex vivo*, and the injected cells are mostly differentiated. This would limit the possibility of transferring the LV to other cell types in the organism and reduce risks of genetic alterations in the hematopoietic progenitors and their progeny by LV insertion. Previous analysis in the pig infarcted heart showed that on day 3 post MI, the 3D structure of the microvasculature is mostly preserved, but its function starts to decline, as manifested by the larger extravascular distances causing disturbed oxygen diffusion.[32] Endogenous angiogenesis after MI occurs during the first 2 weeks after the ischemic event. Thus, detailed kinetics of the endothelial cell marker PECAM1/CD31 in a mouse model of permanent coronary artery ligation showed an increase in endothelial cells at 2 days with a maximum at 4 days and then a decline and return to baseline levels 7 days after MI.[4,36,42,43] These findings support the vascular boosting intervention 4 days post MI.

This study analyzed the impact of the BM cell VEGF/S1P therapy at the 28-day endpoint post I/R. Notably, persistent benefits were observed from this strategy in contrast to previously reported therapeutic approaches in which effects on the vasculature were often transient. For example, the intramyocardial injection of mesenchymal stem cells showed benefits in perfusion on the infarcted area at the first week but not after 4 weeks.[44] This newly implemented BM cell VEGF/S1P therapy mainly induced an increase in the abundance of endothelial cells and reduced extravascular distances in the infarcted area of hearts from treated mice. Concomitantly, trends toward decreased presence of enlarged capillaries were observed. These effects might indicate reduced angioadaptation, which normally occurs in response to capillary loss and flow redistribution in the remaining vessels.[32,45] Previous proangiogenic therapies, including AAV-mediated overexpression of VEGF and ANG1 in a pig model of MI,[14] plasmid-mediated overexpression of bFGF and PDGF in a rat model of MI,[46] and microcapsule release of FGF2 and HGF in a rat model of HF,[47] improved the cardiac vasculature by increasing both capillary and arteriole/large-vessel content. As it is becoming recently accepted, interventions in the cardiac stroma[48] as the microvasculature may secondarily lead to reduced CM death, tissue damage, and fibrosis, since this is often triggered by tissue hypoxia.[37]

The intervention was based on previous reports showing that sequential VEGF and S1P actions were of benefit to induce stable vessels in scaffolds *in vitro*.[31] VEGF is a proangiogenic factor, which induces endothelial cell migration, proliferation, and survival, depending on the endothelial cell context, and at high persistent levels may induce vascular leakiness and regression.[49,50] The increase in endothelial cell number in the infarcted area of hearts from treated mice suggests an overall effect of VEGF in endothelial cell proliferation and/or survival. Moreover, stimulation of endothelial cells with VEGF causes overexpression of S1P1 receptors on these cells and, in isolated arteries, enhances S1P-mediated vasorelaxation and eNOS phosphorylation.[31] This effect may contribute further to pro-survival and proangiogenic programs in the capillary endothelium. It is worth mentioning that although VEGF and S1P are endogenously produced in the heart, cell-type transcriptomics analysis in the pig heart revealed decreased mRNA levels of *VEGF* and *SPHK1* 3 days post I/R (unpublished data), supporting the rationale of boosting VEGF/S1P tissue levels by LV-BM delivery. S1P itself is considered a master regulator of signaling pathways involved in cardiac improvement after MI, and it has lately attracted attention as a possible target.[51] It cannot be ruled out that S1P secreted locally by the transduced BM cells in the infarcted area could have, in addition to enhanced capillarization, some direct impact on cardiomyocyte survival and thus on reducing cardiac damage. Nonetheless, the lack of major differences in the infarct size argues against a major role of this protection mechanism. Furthermore, in contrast to the reported S1P effect on myofibroblasts,[51] reduced myofibroblast abundance is observed, suggesting that S1P paracrine effects on cell types other than endothelial cells seem unlikely. Autocrine effects, however, may still be possible, since transduction with LV_hVEGF or LV_hSPHK1 resulted in BM-derived monocytes with higher CX_3CR1 levels, which may enhance their early traffic to the damaged heart.[52] In this line, higher expression of the CX_3CR1 receptor on circulating $Ly6C^{low}$ monocytes has been shown to induce a positive effect on their recruitment and the promotion of angiogenesis in the injury site in hind-limb ischemia[53] and carotid injury[54] models. Moreover, S1P can promote an anti-inflammatory phenotype in macrophages through activation of their S1P1 receptor after damage and contribute to macrophage-mediated cardiac repair.[55] This pos-

sibility merits further analysis with macrophage specific markers. Of note, significantly increased capillaries and a trend to diminished extravascular distances were also observed in the remote zone of BM cell VEGF/S1P-treated infarcted mice, suggesting that LV-BM cells can also induce vascular effects in that area.[56]

VEGF/S1P gene–cell therapy did not improve post-MI cardiac contractility in accordance with other previously reported strategies. Nevertheless, in spite of no major impact on contractility, VEGF/S1P combined angiotherapy limited post-MI adverse cardiac remodeling, as demonstrated by the preserved cardiac geometry and cardiomyocyte morphology in the remote zone, as well as the higher Atp2a2 protein levels. The reduced cardiac sphericity induced by the angiotherapy supports its clinical relevance, since it has been related to post-MI long-term survival.[57] This improvement may be related to the reduced collagen stiffness and myofibroblast abundance in the infarcted area but also in the remote zone of hearts from the treated mice.[58] Whether remote changes are directly related to the therapy or indirectly as a consequence of the effects on the scar properties (better perfusion, lower stiffness) in the infarcted area remains to be elucidated. Moreover, since cardiac macrophages proliferate in response to mechanical stretching caused by stiffer failing myocardium,[20] the reduced collagen stiffness in treated mice may also explain the trend to lower amount of macrophages in the remote zone observed in these mice (unpublished data).

There were fewer functional beneficial effects of the angiotherapy than expected, despite a consistent biological effect on histology endpoints. This may be related to insufficient factor concentration in the *in vivo* experiments, and more dramatic effect needs to be induced to elicit relevant functional changes. In this regard, future studies with higher transgene overexpression, or more effective gene–cell delivery systems (intracoronary, trans-endocardial) may overcome the limitations observed in the murine model.[59]

This work presents some limitations, which require future studies. First, in this study, gene–cell therapy was compared to a placebo to acquire a clear determination of its efficacy. Although the absence of angiogenic effects induced by non-transduced BM cells on the mouse aortic rings argue in favor of specific effects of sequential delivery of VEGF plus S1P on the phenotype observed in the microvasculature 28 days post MI, comparison with injection of wild-type or LV mock-transduced BM cells would help establish the precise contribution of paracrine signaling by the BM cells versus the delivered VEGF/S1P *in vivo*. Second, deciphering the actual impact of the combined gene–cell VEGF and S1P therapy on the microvasculature, cardiomyocyte survival, and/or monocyte/macrophage subsets will require deeper analysis at earlier time points after ischemia. Third, the benefits of this strategy have only been tested in the I/R model by its proximity to clinical practice. It will also be of interest to evaluate the impact of combined VEGF/S1P gene–cell therapy in the extensively used permanent left anterior descending coronary artery ligation in which arterialization is relevant for revascularization, as well as in CVD involving chronic cardiac ischemia. Forth, in terms of global cardiac function, clinical trials using intracoronary injection of whole BM showed no long-term improvement in LVEF after MI,[60,61] despite promising short-term effects.[62,63] Therefore, analysis of the impact of BM cell VEGF/S1P therapy at longer time points after cardiac ischemia is guaranteed to elucidate whether the beneficial effects on cardiac remodeling persist in time.

In sum, this study offers a novel therapeutic strategy based on sequential BM cell delivery of angiogenic factors to enhance micro-vascularization and oxygen diffusion, thus limiting the adverse consequences of cardiac ischemic diseases.

ACKNOWLEDGMENTS

We thank Mónica Gómez for her help with I/R surgery, Lorena Flores and Ana Vanessa Alonso López for performing and analyzing echocardiography, Dr. Manuel Lobo for ultrasound image analysis, Drs. Borreguero and Maria Villalba for their help in interpreting the results, and Verónica Labrador and CNIC's Microcopy Unit for their expertise and help with image analysis.

This study was supported by grants from the Spanish Ministerio de Ciencia, Innovación y Universidades SAF2014-52050-R and SAF2017-83229-R to A.G.A. and BIO2015-67580-P to J.V. and the Carlos III Institute of Health-Fondo de Investigación Sanitaria (PRB2, IPT13/0001-ISCIII-SGEFI/FEDER, ProteoRed). The research leading to these results received funding from the People Programme (Marie Curie Action) of the European Union's Seventh Framework Programme (FP7/2007-2013) under REA grant Agreement 608027. The CNIC is supported by the Spanish Ministerio de Ciencia, Innovación y Universidades and the Pro-CNIC Foundation, and is a Severo Ochoa Center of Excellence (award SEV-2015-0505).

AUTHOR DISCLOSURE

No competing financial interests exist.

SUPPLEMENTARY MATERIAL

Supplementary Methods

Supplementary Fig. S1
Supplementary Fig. S2
Supplementary Fig. S3
Supplementary Fig. S4
Supplementary Fig. S5

REFERENCES

1. Mendis S, Puska P, Norrving B, et al. Global Atlas on Cardiovascular Disease Prevention and Control. Geneva, Switzerland: World Health Organization in collaboration with the World Heart Federation and the World Stroke Organization, 2011.
2. Benjamin EJ, Blaha MJ, Chiuve SE, et al. Heart disease and stroke statistics—2017 update: a report from the American Heart Association. Circulation 2017;135:e146–e603.
3. Frangogiannis NG. Pathophysiology of myocardial infarction. Compr Physiol 2015;5:1841–1875.
4. Matsui Y, Morimoto J, Uede T. Role of matricellular proteins in cardiac tissue remodeling after myocardial infarction. World J Biol Chem 2010;1:69–80.
5. Schirone L, Forte M, Palmerio S, et al. A review of the molecular mechanisms underlying the development and progression of cardiac remodeling. Oxid Med Cell Longev 2017;2017:3920195.
6. Jessup M, Brozena S. Heart failure. N Engl J Med 2003;348:2007–2018.
7. Bhatt AS, Ambrosy AP, Velazquez EJ. Adverse remodeling and reverse remodeling after myocardial infarction. Curr Cardiol Rep 2017;19:71.
8. Taimeh Z, Loughran J, Birks EJ, et al. Vascular endothelial growth factor in heart failure. Nat Rev Cardiol 2013;10:519–530.
9. Torabi A, Cleland JG, Rigby AS, et al. Development and course of heart failure after a myocardial infarction in younger and older people. J Geriatr Cardiol 2014;11:1–12.
10. Pieske B, Wachter R. Impact of diabetes and hypertension on the heart. Curr Opin Cardiol 2008; 23:340–349.
11. Bennett J, Dubois C. Percutaneous coronary intervention, a historical perspective looking to the future. J Thorac Dis 2013;5:367–370.
12. Doppler SA, Deutsch MA, Lange R, et al. Cardiac regeneration: current therapies—future concepts. J Thorac Dis 2013;5:683–697.
13. Stewart DJ, Kutryk MJ, Fitchett D, et al. VEGF gene therapy fails to improve perfusion of ischemic myocardium in patients with advanced coronary disease: results of the NORTHERN trial. Mol Ther 2009;17:1109–1115.
14. Tao Z, Chen B, Tan X, et al. Coexpression of VEGF and angiopoietin-1 promotes angiogenesis and cardiomyocyte proliferation reduces apoptosis in porcine myocardial infarction (MI) heart. Proc Natl Acad Sci U S A 2011;108:2064–2069.
15. Hedman M, Hartikainen J, Syvanne M, et al. Safety and feasibility of catheter-based local intracoronary vascular endothelial growth factor gene transfer in the prevention of postangioplasty and in-stent restenosis and in the treatment of chronic myocardial ischemia: Phase II results of the Kuopio Angiogenesis Trial (KAT). Circulation 2003;107:2677–2683.
16. Kastrup J, Jorgensen E, Ruck A, et al. Direct intramyocardial plasmid vascular endothelial growth factor-A165 gene therapy in patients with stable severe angina pectoris A randomized double-blind placebo-controlled study: the Euroinject One trial. J Am Coll Cardiol 2005;45:982–988.
17. Vera Janavel GL, De Lorenzi A, Cortes C, et al. Effect of vascular endothelial growth factor gene transfer on infarct size, left ventricular function and myocardial perfusion in sheep after 2 months of coronary artery occlusion. J Gene Med 2012;14: 279–287.
18. Ieda M, Fu JD, Delgado-Olguin P, et al. Direct reprogramming of fibroblasts into functional cardiomyocytes by defined factors. Cell 2010;142: 375–386.
19. Nahrendorf M, Swirski FK, Aikawa E, et al. The healing myocardium sequentially mobilizes two monocyte subsets with divergent and complementary functions. J Exp Med 2007;204:3037–3047.
20. Sager HB, Hulsmans M, Lavine KJ, et al. Proliferation and recruitment contribute to myocardial macrophage expansion in chronic heart failure. Circ Res 2016;119:853–864.
21. van den Akker F, Deddens JC, Doevendans PA, et al. Cardiac stem cell therapy to modulate inflammation upon myocardial infarction. Biochim Biophys Acta 2013;1830:2449–2458.
22. Hamid T, Prabhu SD. Immunomodulation is the key to cardiac repair. Circ Res 2017;120:1530–1532.
23. Lopez JJ, Laham RJ, Stamler A, et al. VEGF administration in chronic myocardial ischemia in pigs. Cardiovasc Res 1998;40:272–281.
24. Henry TD, Annex BH, McKendall GR, et al. The VIVA trial: vascular endothelial growth factor in ischemia for vascular angiogenesis. Circulation 2003;107:1359–1365.
25. Zangi L, Lui KO, von Gise A, et al. Modified mRNA directs the fate of heart progenitor cells and induces vascular regeneration after myocardial infarction. Nat Biotechnol 2013;31:898–907.
26. Pacak CA, Mah CS, Thattaliyath BD, et al. Recombinant adeno-associated virus serotype 9 leads to preferential cardiac transduction *in vivo*. Circ Res 2006;99:e3–9.
27. Vassalli G, Bueler H, Dudler J, et al. Adeno-associated virus (AAV) vectors achieve prolonged transgene expression in mouse myocardium and arteries *in vivo*: a comparative study with adenovirus vectors. Int J Cardiol 2003;90:229–238.
28. Kocher AA, Schuster MD, Szabolcs MJ, et al. Neovascularization of ischemic myocardium by human bone-marrow-derived angioblasts prevents cardiomyocyte apoptosis, reduces remodeling and improves cardiac function. Nat Med 2001;7:430–436.
29. Bartunek J, Vanderheyden M, Vandekerckhove B, et al. Intracoronary injection of CD133-positive enriched bone marrow progenitor cells promotes cardiac recovery after recent myocardial infarction: feasibility and safety. Circulation 2005;112: I178–183.
30. Takahashi M, Li TS, Suzuki R, et al. Cytokines produced by bone marrow cells can contribute to functional improvement of the infarcted heart by protecting cardiomyocytes from ischemic injury. Am J Physiol Heart Circ Physiol 2006;291:H886–893.
31. Tengood JE, Kovach KM, Vescovi PE, et al. Sequential delivery of vascular endothelial growth factor and sphingosine 1-phosphate for angiogenesis. Biomaterials 2010;31:7805–7812.
32. Gkontra P, Norton KA, Zak MM, et al. Deciphering microvascular changes after myocardial infarction through 3D fully automated image analysis. Sci Rep 2018;8:1854.
33. Squadrito ML, Pucci F, Magri L, et al. miR-511-3p modulates genetic programs of tumor-associated macrophages. Cell Rep 2012;1:141–154.
34. Baker M, Robinson SD, Lechertier T, et al. Use of the mouse aortic ring assay to study angiogenesis. Nat Protoc 2011;7:89–104.
35. Schindelin J, Arganda-Carreras I, Frise E, et al. Fiji: an open-source platform for biological-image analysis. Nat Methods 2012;9:676–682.
36. Prabhu SD, Frangogiannis NG. The biological basis for cardiac repair after myocardial infarction: from inflammation to fibrosis. Circ Res 2016;119: 91–112.

37. Talman V, Ruskoaho H. Cardiac fibrosis in myocardial infarction—from repair and remodeling to regeneration. Cell Tissue Res 2016;365:563–581.

38. Fan H, Ma L, Fan B, et al. Role of PDGFR-beta/PI3K/AKT signaling pathway in PDGF-BB induced myocardial fibrosis in rats. Am J Transl Res 2014; 6:714–723.

39. Mostaco-Guidolin L, Rosin NL, Hackett TL. Imaging collagen in scar tissue: developments in second harmonic generation microscopy for biomedical applications. Int J Mol Sci 2017;18.

40. Azevedo PS, Polegato BF, Minicucci MF, et al. Cardiac remodeling: concepts, clinical impact, pathophysiological mechanisms and pharmacologic treatment. Arq Bras Cardiol 2016;106: 62–69.

41. De Celle T, Cleutjens JP, Blankesteijn WM, et al. Long-term structural and functional consequences of cardiac ischaemia–reperfusion injury *in vivo* in mice. Exp Physiol 2004;89:605–615.

42. Silvestre JS, Smadja DM, Levy BI. Postischemic revascularization: from cellular and molecular mechanisms to clinical applications. Physiol Rev 2013;93:1743–1802.

43. Dube KN, Thomas TM, Munshaw S, et al. Recapitulation of developmental mechanisms to revascularize the ischemic heart. JCI Insight 2017;2.

44. Schuleri KH, Amado LC, Boyle AJ, et al. Early improvement in cardiac tissue perfusion due to mesenchymal stem cells. Am J Physiol Heart Circ Physiol 2008;294:H2002–2011.

45. Zakrzewicz A, Secomb TW, Pries AR. Angioadaptation: keeping the vascular system in shape. News Physiol Sci 2002;17:197–201.

46. Hao X, Mansson-Broberg A, Gustafsson T, et al. Angiogenic effects of dual gene transfer of bFGF and PDGF-BB after myocardial infarction. Biochem Biophys Res Commun 2004;315:1058–1063.

47. Banquet S, Gomez E, Nicol L, et al. Arteriogenic therapy by intramyocardial sustained delivery of a novel growth factor combination prevents chronic heart failure. Circulation 2011;124:1059–1069.

48. Forte E, Furtado MB, Rosenthal N. The interstitium in cardiac repair: role of the immune-stromal cell interplay. Nat Rev Cardiol 2018;15:601–616.

49. Baluk P, Lee CG, Link H, et al. Regulated angiogenesis and vascular regression in mice overexpressing vascular endothelial growth factor in airways. Am J Pathol 2004;165:1071–1085.

50. Sano H, Hosokawa K, Kidoya H, et al. Negative regulation of VEGF-induced vascular leakage by blockade of angiotensin II type 1 receptor. Arterioscler Thromb Vasc Biol 2006;26:2673–2680.

51. Waeber C, Walther T. Sphingosine-1-phosphate as a potential target for the treatment of myocardial infarction. Circ J 2014;78:795–802.

52. Jung K, Kim P, Leuschner F, et al. Endoscopic time-lapse imaging of immune cells in infarcted mouse hearts. Circ Res 2013;112:891–899.

53. Park Y, Lee J, Kwak JY, et al. Fractalkine induces angiogenic potential in CX3CR1-expressing monocytes. J Leukoc Biol 2018;103:53–66.

54. Getzin T, Krishnasamy K, Gamrekelashvili J, et al. The chemokine receptor CX3CR1 coordinates monocyte recruitment and endothelial regeneration after arterial injury. EMBO Mol Med 2018;10: 151–159.

55. Hughes JE, Srinivasan S, Lynch KR, et al. Sphingosine-1-phosphate induces an antiinflammatory phenotype in macrophages. Circ Res 2008;102:950–958.

56. Sager HB, Hulsmans M, Lavine KJ, et al. Proliferation and recruitment contribute to myocardial macrophage expansion in chronic heart failure. Circ Res 2016;119:853–864.

57. Wong SP, French JK, Lydon AM, et al. Relation of left ventricular sphericity to 10-year survival after acute myocardial infarction. Am J Cardiol 2004; 94:1270–1275.

58. van den Borne SW, Diez J, Blankesteijn WM, et al. Myocardial remodeling after infarction: the role of myofibroblasts. Nat Rev Cardiol 2010;7:30–37.

59. Aguero J, Lobo Gonzalez M, Ishikawa K. Route TESI: main street for MSC? Circ Res 2017;120: 1055–1056.

60. Meyer GP, Wollert KC, Lotz J, et al. Intracoronary bone marrow cell transfer after myocardial infarction: 5-year follow-up from the randomized-controlled BOOST trial. Eur Heart J 2009;30: 2978–2984.

61. Assmus B, Rolf A, Erbs S, et al. Clinical outcome 2 years after intracoronary administration of bone marrow-derived progenitor cells in acute myocardial infarction. Circ Heart Fail 2010;3:89–96.

62. Wollert KC, Meyer GP, Lotz J, et al. Intracoronary autologous bone-marrow cell transfer after myocardial infarction: the BOOST randomised controlled clinical trial. Lancet 2004;364:141–148.

63. Schachinger V, Erbs S, Elsasser A, et al. Intracoronary bone marrow-derived progenitor cells in acute myocardial infarction. N Engl J Med 2006;355:1210–1221.

Received for publication September 21, 2018; accepted after revision February 12, 2019.

Published online: February 15, 2019.

SCIENTIFIC REPORTS

Correction: Author Correction

OPEN

Deciphering microvascular changes after myocardial infarction through 3D fully automated image analysis

Received: 29 August 2017
Accepted: 8 January 2018
Published online: 30 January 2018

Polyxeni Gkontra[1,5], Kerri-Ann Norton[2,7], Magdalena M. Żak[1], Cristina Clemente[1], Jaume Agüero[1,3], Borja Ibáñez[1,3,4], Andrés Santos[5,6], Aleksander S. Popel[2] & Alicia G. Arroyo[1]

The microvasculature continuously adapts in response to pathophysiological conditions to meet tissue demands. Quantitative assessment of the dynamic changes in the coronary microvasculature is therefore crucial in enhancing our knowledge regarding the impact of cardiovascular diseases in tissue perfusion and in developing efficient angiotherapies. Using confocal microscopy and thick tissue sections, we developed a 3D fully automated pipeline that allows to precisely reconstruct the microvasculature and to extract parameters that quantify all its major features, its relation to smooth muscle actin positive cells and capillary diffusion regions. The novel pipeline was applied in the analysis of the coronary microvasculature from healthy tissue and tissue at various stages after myocardial infarction (MI) in the pig model, whose coronary vasculature closely resembles that of human tissue. We unravelled alterations in the microvasculature, particularly structural changes and angioadaptation in the aftermath of MI. In addition, we evaluated the extracted knowledge's potential for the prediction of pathophysiological conditions in tissue, using different classification schemes. The high accuracy achieved in this respect, demonstrates the ability of our approach not only to quantify and identify pathology-related changes of microvascular beds, but also to predict complex and dynamic microvascular patterns.

Cardiovascular diseases (CVDs) are the leading cause of deaths worldwide, despite significant progress having been made in their prognosis, treatment and medical management[1]. The socio-economic burden associated with CVDs, including myocardial infarction (MI) and its complications such as heart failure[2], has led an important amount of research to focus on unravelling its causes and developing therapeutic approaches[3]. In recent decades, dysfunction of the coronary microvasculature has emerged as an additional complication of myocardial ischaemia, and, therefore, as a potential prognostic biomarker and therapeutic target[4,5].

The microvasculature represents the anatomy of microcirculation and comprises the smallest blood vessels of the tissues; capillaries, arterioles and venules. Its architecture is a major determinant of blood flow, oxygen transport, wall shear stress and distribution of pressure in microvessels[6,7]. Nonetheless, its *in vivo* visualization in humans remains a bottleneck. For this reason, *ex vivo* imaging and different animals models have been used[8–13]. Among them, the pig animal model has attracted considerable attention due to the similarity of its coronary network to that of humans. Pioneering work by Kassab[13] in this area has provided a wealth of data regarding diameters, length and topology of the porcine microvascular network, through the use of coronary corrosion casts. These data provided significant insight into porcine microvascular structure and enabled the subsequent modelling of hemodynamics at basal conditions[14,15].

However, the microvasculature is not a static system, but rather a dynamic one and it continuously adapts in order to meet the tissue demands in response to physiological and pathophysiological conditions, such as MI and other CVDs as diabetes or hypertension. Thanks to its dynamic nature, the microvasculature is capable

[1]Centro Nacional de Investigaciones Cardiovasculares Carlos III (CNIC), Madrid, 28029, Spain. [2]Department of Biomedical Engineering, School of Medicine, Johns Hopkins University, Baltimore, MD, 21205, USA. [3]Centro de Investigación Biomédica en Red de Enfermedades CardioVasculares (CIBERCV), Madrid, Spain. [4]IIS-Fundación Jiménez Díaz, Madrid, Spain. [5]Biomedical Image Technologies (BIT), ETSI Telecomunicación, Universidad Politécnica de Madrid, Madrid, 28040, Spain. [6]Centro de Investigación Biomédica en Red de Bioingeniería, Biomateriales y Nanomedicina (CIBERBBN), Madrid, Spain. [7]Present address: Division of Science, Mathematics, and Computing, Bard College, Annandale-on-Hudson, NY, 12504, USA. Correspondence and requests for materials should be addressed to A.G.A. (email: agarroyo@cnic.es)

	Basal	I1MI	I3MI	I7MI	R1MI	R3MI	R7MI
Fractal-Based Metrics							
1. Fractal Dimension	2.22 ± 0.03	2.26 ± 0.05	2.22 ± 0.04	2.15 ± 0.04	2.24 ± 0.04	2.23 ± 0.03	2.22 ± 0.05
2. Lacunarity ($\times 10^{-2}$)	76.92 ± 5.15	72.75 ± 3.85	78.08 ± 5.52	83.98 ± 2.96	76.33 ± 4.58	73.64 ± 2.73	76.1 ± 4.03
3. Succolarity ($\times 10^{-2}$)	0.33 ± 0.14	0.49 ± 0.23	0.28 ± 0.13	0.19 ± 0.11	0.32 ± 0.16	0.3 ± 0.16	0.3 ± 0.2
Minkowski-Based Metrics							
4. Vascular Volume Density (%)	6.75 ± 0.85	8.9 ± 2.82	6.46 ± 1.06	5.04 ± 0.92	7.21 ± 1.34	6.14 ± 1.29	6.64 ± 1.83
5. Surface Area Density ($\times 10^{-3}$) ($\mu m^2/\mu m^3$)	48.36 ± 7.05	55.06 ± 12.86	46.45 ± 6.95	27.15 ± 4.05	48.2 ± 6.25	47.1 ± 6.62	45.04 ± 11.28
6. Breadth Density ($\times 10^{-3}$) ($\mu m/\mu m^3$)	1.47 ± 0.29	1.43 ± 0.27	1.42 ± 0.28	0.64 ± 0.11	1.37 ± 0.19	1.52 ± 0.23	1.27 ± 0.32
7. Euler-Poincaré Characteristic Density ($1/\mu m^3$)	−4.32 ± 1.78	−4.84 ± 3.1	−3.36 ± 1.38	−0.05 ± 1.49	−3.5 ± 1.62	−4.06 ± 1.69	−3.56 ± 2.64
8. Capillary Volume Density (%)	6.07 ± 0.9	8.04 ± 2.63	5.7 ± 1	4.34 ± 0.85	6.55 ± 1.17	5.43 ± 1.22	5.7 ± 1.97
9. Capillary Surface Area Density ($\times 10^{-3}$) ($\mu m^2/\mu m^3$)	46.94 ± 7.15	53.47 ± 12.69	44.5 ± 7.15	25.34 ± 4	46.62 ± 6.19	45.11 ± 6.63	42.5 ± 11.91
Graph-Based Metrics							
10. Vascular length density ($\times 10^{-3}$) ($\mu m/\mu m^3$)	3.51 ± 0.85	4.13 ± 1.43	3.51 ± 0.82	1.65 ± 0.3	3.37 ± 0.58	3.54 ± 0.74	3.18 ± 1.21
11. Vascular surface density ($\times 10^{-3}$) ($\mu m^2/\mu m^3$)	38.87 ± 6.87	51.79 ± 18.71	38.05 ± 7.24	24.37 ± 4.63	40.35 ± 7.75	36.94 ± 8.29	36.94 ± 13.86
12. Vascular volume density ($\times 10^{-2}$) ($\mu m^3/\mu m^3$)	3.94 ± 0.66	6.16 ± 2.75	3.92 ± 0.93	3.33 ± 0.87	4.48 ± 1.3	3.59 ± 1.11	3.94 ± 1.68
13. Vascular segment radius (μm)	2.65 ± 0.31	2.91 ± 0.33	2.62 ± 0.3	3.25 ± 0.29	2.79 ± 0.33	2.48 ± 0.26	2.74 ± 0.26
14. Vascular segment length (μm)	18.85 ± 2.64	16.09 ± 2.83	17.65 ± 2.22	15.74 ± 2.77	18.15 ± 2.96	19.89 ± 3.21	17.59 ± 2.77
15. Vascular segment surface (μm^2)	215.3 ± 49.14	200.75 ± 35.27	193.63 ± 27.74	231.67 ± 35.76	218.53 ± 42.92	207.73 ± 33.87	206.2 ± 34.89
16. Vascular segment volume (μm^3)	224.15 ± 71.59	234.5 ± 54.3	200.87 ± 46.54	313.63 ± 59	241.77 ± 63.37	200.19 ± 42.08	220.22 ± 50.23
17. Tortuosity ($\mu m/\mu m$)	1.39 ± 0.01	1.38 ± 0.02	1.4 ± 0.03	1.38 ± 0.04	1.38 ± 0.02	1.39 ± 0.02	1.39 ± 0.03
18. Vascular segments ($\times 10^5$)[a]	1.91 ± 0.6	2.77 ± 1.48	2.02 ± 0.57	1.09 ± 0.3	1.91 ± 0.49	1.86 ± 0.68	1.9 ± 0.97
19. Vessels of diameter < =6.9 (μm) (%)	94.56 ± 2.94	90.14 ± 5.45	93.02 ± 4.1	83.92 ± 6.01	92.14 ± 5.02	95.56 ± 2.93	92.94 ± 3.03
20. Vessels of diameter between 6.9 and 8.2 (μm) (%)	3.01 ± 1.46	4.88 ± 2.02	3.54 ± 1.83	8.46 ± 2.31	3.92±2.06	2.21 ± 1.38	3.9 ± 1.52
21. Vessels of diameter >8.2 (μm) (%)	2.42 ± 1.57	4.98 ± 3.56	3.44 ± 2.62	7.62 ± 4.21	3.94 ± 3.07	2.23 ± 1.68	3.16 ± 1.74
22. Branching nodes ($\times 10^4$)[a]	10.14 ± 3.43	14.79 ± 8.12	10.74 ± 3.33	5.48 ± 1.58	9.94 ± 2.71	9.79 ± 3.84	9.85 ± 5.31
23. Blind-ends/sprouts ($\times 10^4$)[a]	5.08 ± 1.42	7.47 ± 3.93	5.37 ± 1.3	3.44 ± 0.89	5.64 ± 1.47	4.95 ± 1.75	5.49 ± 2.38
24. Branching nodes[b]	30.02 ± 4.03	35.1 ± 6.26	31.29 ± 4.76	32.91 ± 5.61	30.54 ± 5.22	28.58 ± 4.57	31.11 ± 5.37
25. Blind-ends/sprouts[b]	18.22 ± 5.81	19.46 ± 4.52	16.52 ± 3.41	20.47 ± 4.18	18.99 ± 4.59	16.92 ± 4.32	21.04 ± 6.56
SMA^+ **related metrics**							
26. Vessels covered with SMA (%)	80.05 ± 11.57	67.32 ± 19.45	69.34 ± 7.81	54.03 ± 9.82	73.82 ± 9.71	74.5 ± 15.59	78.01 ± 14.33
27. SMA^+ layer thickness (μm)	2.43 ± 1.15	2.32 ± 0.77	4.13 ± 2.4	10.23 ± 1.76	2.7 ± 0.69	2.75 ± 0.8	3.31 ± 1.37
28. Damage Index	0.01 ± 0.01	0.01 ± 0.01	0.02 ± 0.02	0.14 ± 0.06	0.01 ± 0.01	0.02 ± 0.01	0.02 ± 0.02
29. Myofibroblasts ($\times 10^4$)[a]	1.04 ± 0.51	0.9 ± 0.56	0.96 ± 0.42	2.12 ± 0.77	0.64 ± 0.32	0.77 ± 0.34	0.67 ± 0.44
30. SMA^+ perivascular cells[b]	31.71 ± 11.34	24.58 ± 12.6	24.83 ± 8.48	45.72 ± 17.49	30.95 ± 6.76	22.68 ± 7.48	26.19 ± 10.53
Efficiency in oxygen diffusion							
31. Maximal Extravascular Distance (μm)	27.35 ± 6.76	28.29 ± 4.52	33.72 ± 6.8	46.22 ± 8.26	30.37 ± 5.13	28.32 ± 3.71	29.69 ± 4.42
32. Median Extravascular Distance (μm)	14.57 ± 3.56	15.07 ± 2.38	17.92 ± 3.58	24.51 ± 4.35	16.16 ± 2.7	15.08 ± 1.95	15.8 ± 2.33
33. Capillary Density[c]	1236.16 ± 714.07	1226.84 ± 567.85	1101.16 ± 525.2	394.24 ± 211.98	1091.95 ± 452.94	1053.55 ± 781.83	1059.93 ± 514.7
34. Intercapillary Distance (μm)	16.91 ± 2.08	16.93 ± 1.84	17.44 ± 2.46	25.54 ± 4.44	17.68 ± 1.62	17.17 ± 1.85	19.51 ± 3.64
35. Diffusion Distance (μm)	9.77 ± 1.43	9.1 ± 1.38	9.72 ± 1.17	14.07 ± 1.38	9.83 ± 0.83	9.63 ± 1	10.55 ± 2.17
Additional cell-related metrics							
36. Endothelial cells ($\times 10^5$)[d]	22.85 ± 6.83	19.19 ± 5.19	19.36 ± 3.82	18.31 ± 5.97	19.18 ± 4.5	19.17 ± 3.74	15.12 ± 2.76
37. Endothelial cells[b]	44.14 ± 8.53	40.93 ± 8.16	35.97 ± 5.78	55.47 ± 16.91	40.44 ± 6.09	33.1 ± 4.75	33.13 ± 7.98

Table 1. List of the parameters (mean ± standard deviation) that are extracted automatically for the characterization of the cardiac microvasculature, its interactions with SMA^+ cells and remodelling due to MI. I1MI, I3MI, and I7MI, refer to infarcted areas at 1 day, 3 and 7 days post MI respectively. Similarly, R1MI, R3MI, and R7MI refer to the corresponding remote areas. [a]Number per mm^3 of tissue. [b]Number per mm vascular length. [c]Number per mm^2 of tissue. [d]Number per mm^3 vascular volume.

of adding new vessels by sprouting[16] or intussusceptive angiogenesis[17], altering the structure of existing vessels (remodelling[18]) and pruning of abundant vessels (regression[19]). These processes of vascular patterning, termed angioadaptation[20], affect the architecture of the microvasculature. Despite significant attempts to develop approaches that would promote therapeutic remodelling or revascularization[21], no drug has so been approved for clinical use for MI[22,23]. There is, therefore, a growing quest to develop a better understanding of the microvascular dynamic changes in MI and how to control them. Towards this aim, quantitative data on the anatomy of coronary microcirculation in pathology and not only under basal conditions are essential[24]. These data are the key challenge for understanding structure-function relation through modelling approaches, and thus, developing and

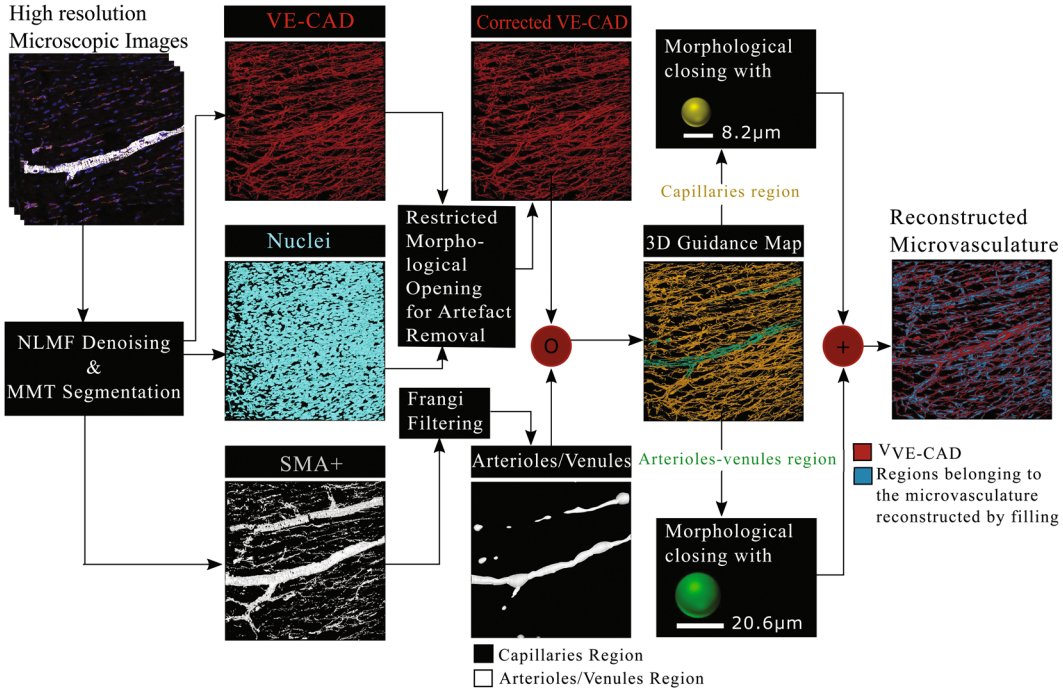

Figure 1. Overview of the proposed approach for the reconstruction of the complete microvasculature from thick sections of pig heart tissue labelled for VE-Cadherin (endothelial junctions).

evaluating more efficient therapeutic approaches. In addition, studies are expected to recognize the inherently three-dimensional (3D) and complex structure of the microvasculature.

Obtaining such data is nowadays more feasible than ever thanks to revolutionary advancements in confocal microscopy that have allowed the acquisition of data in 3D with sub-micrometer resolution, at increasing imaging depths[25]. Furthermore, confocal microscopy, in combination with fluorescent dyes, allows the simultaneous study of the microvasculature in relation to other key players in tissue healing after MI. However, today's imaging systems produce a vast amount of data whose complexity preclude traditional manual and supervised analysis methods[26]. A work-around adapted by the scientific community during several years has been the assessment of the microvasculature from 2D slices or maximum intensity projections produced from 3D volumes. However, it is increasingly apparent that this approach might lead to errors, misinterpretations and loss of important information of biological significance. Therefore, the quest for 3D automated bioimage analysis tools has steadily been increasing[27,28].

In this work, we aim to enrich the knowledge about cardiac microcirculation pathophysiology with quantitative data spanning different stages following MI (1, 3, and 7 days), as well as from basal conditions, in an unbiased manner. We use thick slices of porcine cardiac tissue, label them for cell nuclei, endothelial cell junctions and smooth muscle actin positive (SMA^+) cells and image them by using confocal microscopy. We design a 3D fully automatic bioimage analysis pipeline that firstly allows us to reconstruct the complete microvasculature from stained endothelial junctions and SMA^+ cells. We subsequently extract essential biological information about all major characteristics of the microvasculature, its relation with SMA^+ and capillary diffusion regions, which was not possible in the past when using a single software. We show that using confocal microscopy and our pipeline we are able to unravel fine alterations of the cardiac microvasculature in the aftermath of MI. The fully automatic nature of the approach ensures reproducibility, reliable significance and objectiveness of the findings. Furthermore, we evaluate the potential of the extracted knowledge to be used for predicting the pathophysiological condition of unseen tissue and we achieve high accuracy (higher than 80%) in the task of distinguishing infarcted from basal tissue and in recognizing the stage of the infarcted tissue. Lastly, we also investigate a later time point post MI (45 days) to understand whether early microvascular alterations persist and/or change during cardiac remodelling. Overall, the study allows a deeper understanding of microvascular alterations in MI and marks a step forward towards modelling of microcirculation at different stages after pathology, while it provides an unbiased means in the evaluation of the outcome of potential treatments.

Results

Endothelial cell junction-based 3D reconstruction of the microvasculature from cardiac tissue.

We use thick slices of cardiac tissue (~100 μm) stained with fluorescent markers for cell nuclei (Hoechst), endothelial junctions (anti-VE-Cadherin) and SMA^+ cells (anti-α-SMA) and image them by means of confocal microscopy (see Methods). In the case of subjects that had suffered MI, tissues from both infarcted and non-infarcted (remote) areas are used. Prior to proceeding with the core of the analysis pipeline, non-local means

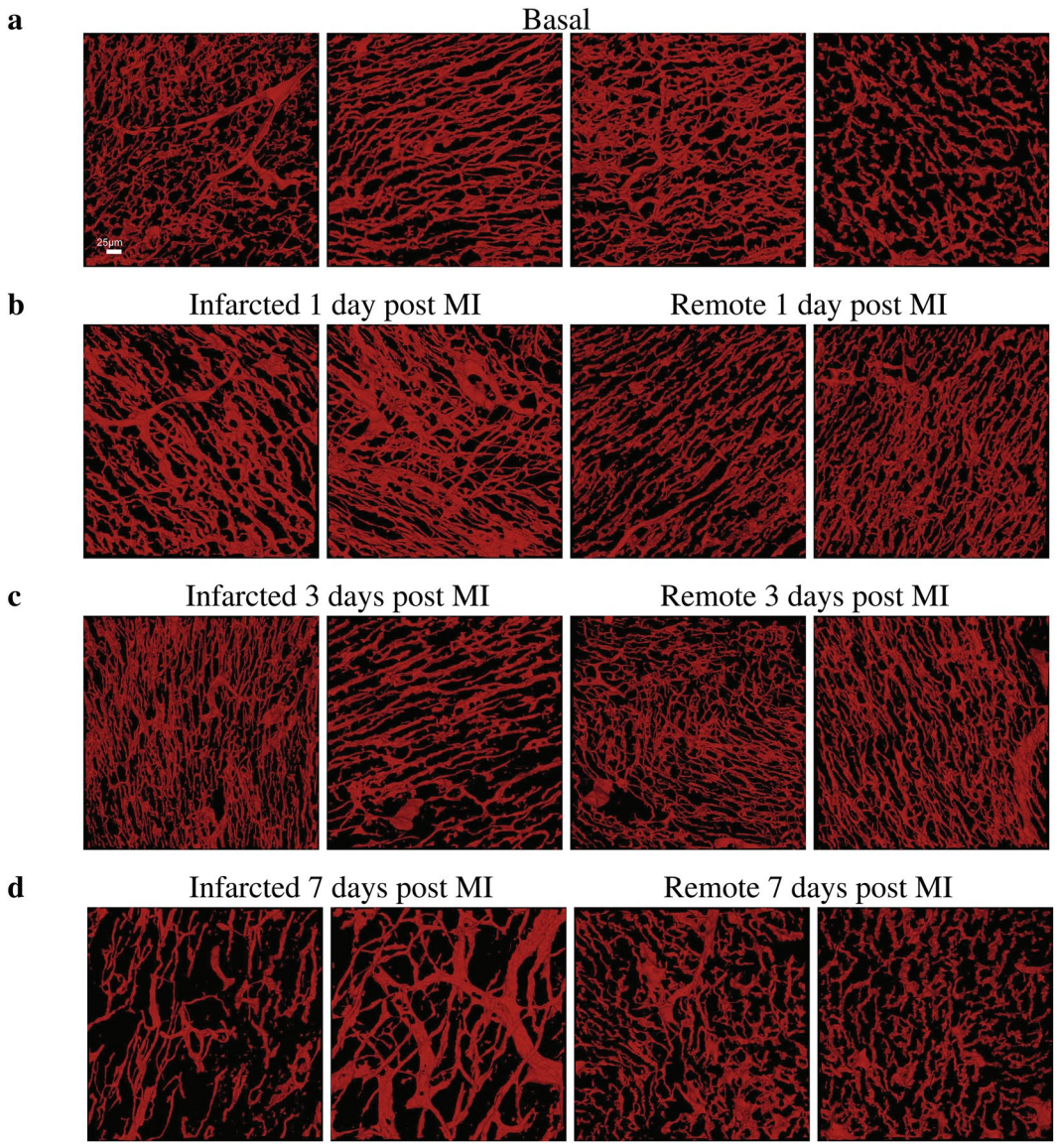

Figure 2. Representative 3D reconstructions of the cardiac microvasculature from tissues at different pathophysiological conditions. **(a)** Microvasculature reconstructed from tissues at basal conditions. **(b)** Microvasculature reconstructed from tissues at 1 day post MI. **(c)** Microvasculature reconstructed from tissues at 3 days post MI. **(d)** Microvasculature reconstructed from tissues at 7 days post MI. In panels (**b**–**d**) the first two volumes correspond to tissues from infarcted areas at the corresponding time-point after MI, while the third and fourth volumes to tissues from remote ones. Scale bar (25 μm) is the same for all images.

filtering (NLMF)[29] was applied with the aim of enhancing the quality of the images while preserving image information.

The first step towards quantifying the microvasculature and its infarction-related dynamic changes is to automatically segment the labelled structures of the VE-Cadherin, SMA and of the Hoechst channels. Towards this aim, the multi-scale multi-level thresholding algorithm (MMT)[30] is applied to every channel of the 3D confocal image. In the case of the VE-Cadherin channel, the segmentation is further improved by excluding possible artefacts, i.e. objects that are smaller than 100 voxels and that do not have a nucleus.

Following the segmentation of structures labelled with VE-Cadherin, major parts of the microvasculature are reconstructed. However, VE-Cadherin is a marker of endothelial junctions and not of the vessel lumen or of the complete endothelial cell (see Methods). As a result, there are gaps in the reconstructed blood vessels. The size of these gaps is not homogeneous but rather depends on the type of microvessels. Smaller gaps are observed in capillaries and larger ones in larger microvessels, i.e. arterioles and venules. A filling method was developed to deal with this limitation. The method is applied on top of the VE-Cadherin segmentation with the aim of reconstructing microvascular parts which had not been labelled with VE-Cadherin.

An overview of the filling algorithm is provided in Fig. 1. The method is based on two types of information; information regarding the spatial relation of the microvessels with SMA^+ cells and information about the

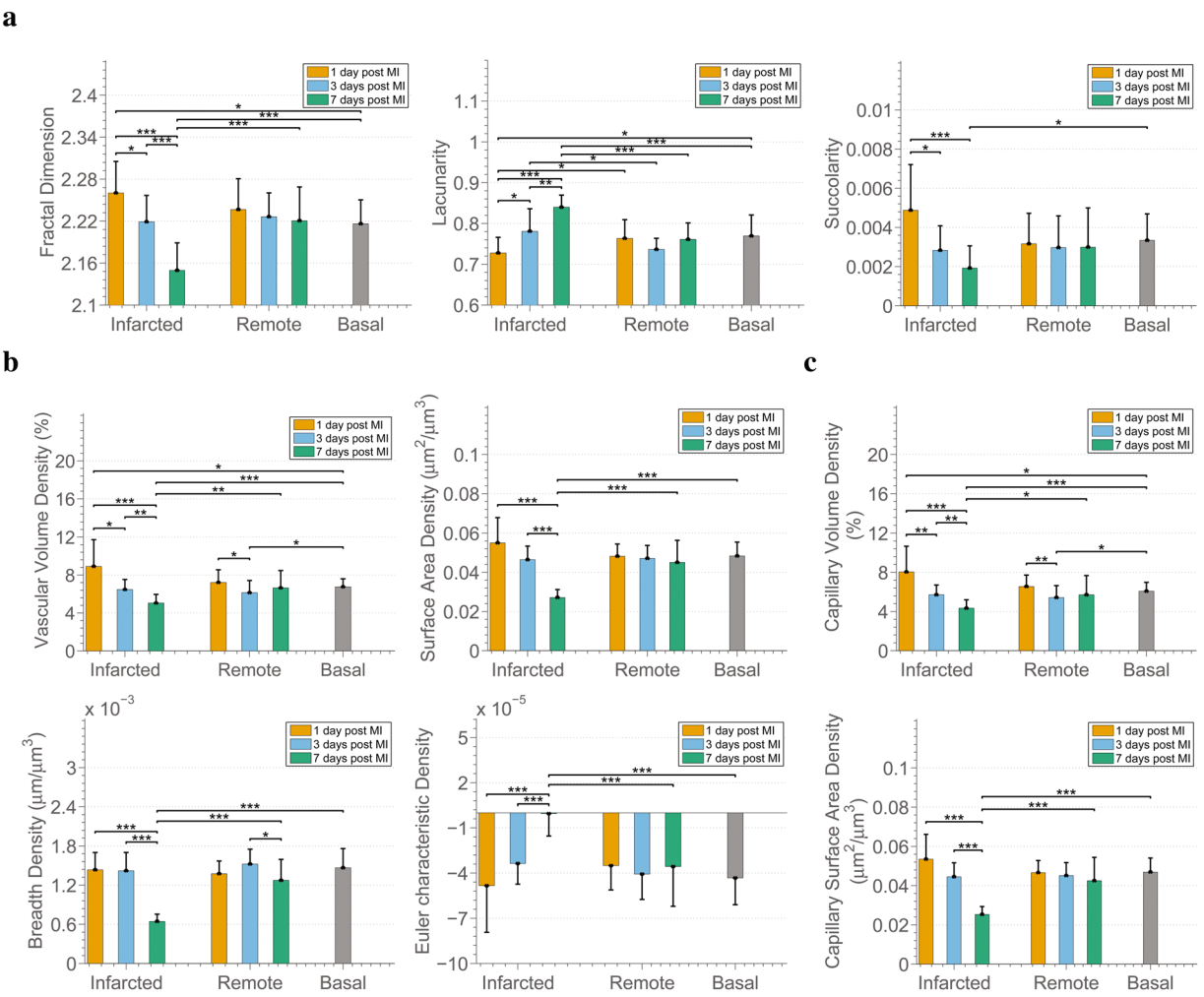

Figure 3. Myocardial infarction decreases 3D complexity, integrity, and connectivity of the coronary microvasculature while it alters heterogeneity in the distribution of non-vascularized areas and capacity for blood flow. **(a)** 3D fractal-based parameters; Fractal Dimension, Lacunarity, and Succolarity. **(b)** Parameters based on the Minkowski functionals calculated for complete microvasculature (capillaries, arterioles, venules); Vascular Density, Surface Area Density, Breadth Density, Euler-Poincaré Characteristic Density. **(c)** Parameters based on the Minkowski functionals calculated for capillaries exclusively; Capillary Volume Density, Capillary Surface Area Density. In all figures of the manuscript, the bars show mean values, while error bars represent standard deviation. Furthermore, *, ** and *** represent p-value < 0.05, 0.01 and 0.001 respectively. The p-values were calculated by means of Wilcoxon rank-sum tests and corrected with the Benjamini-Hochberg procedure for multiple testing. The number of samples compared is 18 per tissue condition.

physiology of the different types of microvessels that form the microvascular network. In particular, taking advantage of the knowledge about the existence of a SMA^+ layer that surrounds arterioles and venules[31], Frangi-based filtering[32] is applied to the SMA^+ segmentation to extract tubular elements whose diameter is in the range of that of arterioles and venules (i.e. larger than the diameter of 7.3 μm of the larger capillary connected directly to an arteriole[13]). This results in a 3D binary image on which regions that might belong to arterioles/venules are on voxels (voxels of value one) and regions belonging to capillaries are off voxels (voxels with value equal to zero). The 3D image is subsequently used to distinguish between microvessels formed by the VE-Cadherin junctions that are capillaries and those that are possible arterioles or venules. For this purpose, element-wise multiplication of the VE-Cadherin segmentation and the 3D image with arterioles and capillaries is performed. The procedure results in the creation of a 3D Guidance Map (Supplementary Fig. S1) containing information about the type of microvessels and therefore of the size of gaps that should be filled.

Morphological closing is performed using structural elements of various sizes based on the vessel type, as defined by the 3D Guidance Map. More precisely, in order to fill gaps in regions of capillaries, a ball structural element is used whose size is equal to the diameter of the largest capillary (8.2 μm) found in the pig animal model[13]. Similarly, in order to fill gaps in the case of arterioles/venules a larger ball structural element is used whose diameter is equal to the largest reported arteriole/venule of order 2 (20.6 μm). The combination of filled capillaries and arterioles/venules produced by means of the aforementioned work-flow results in the reconstruction of the

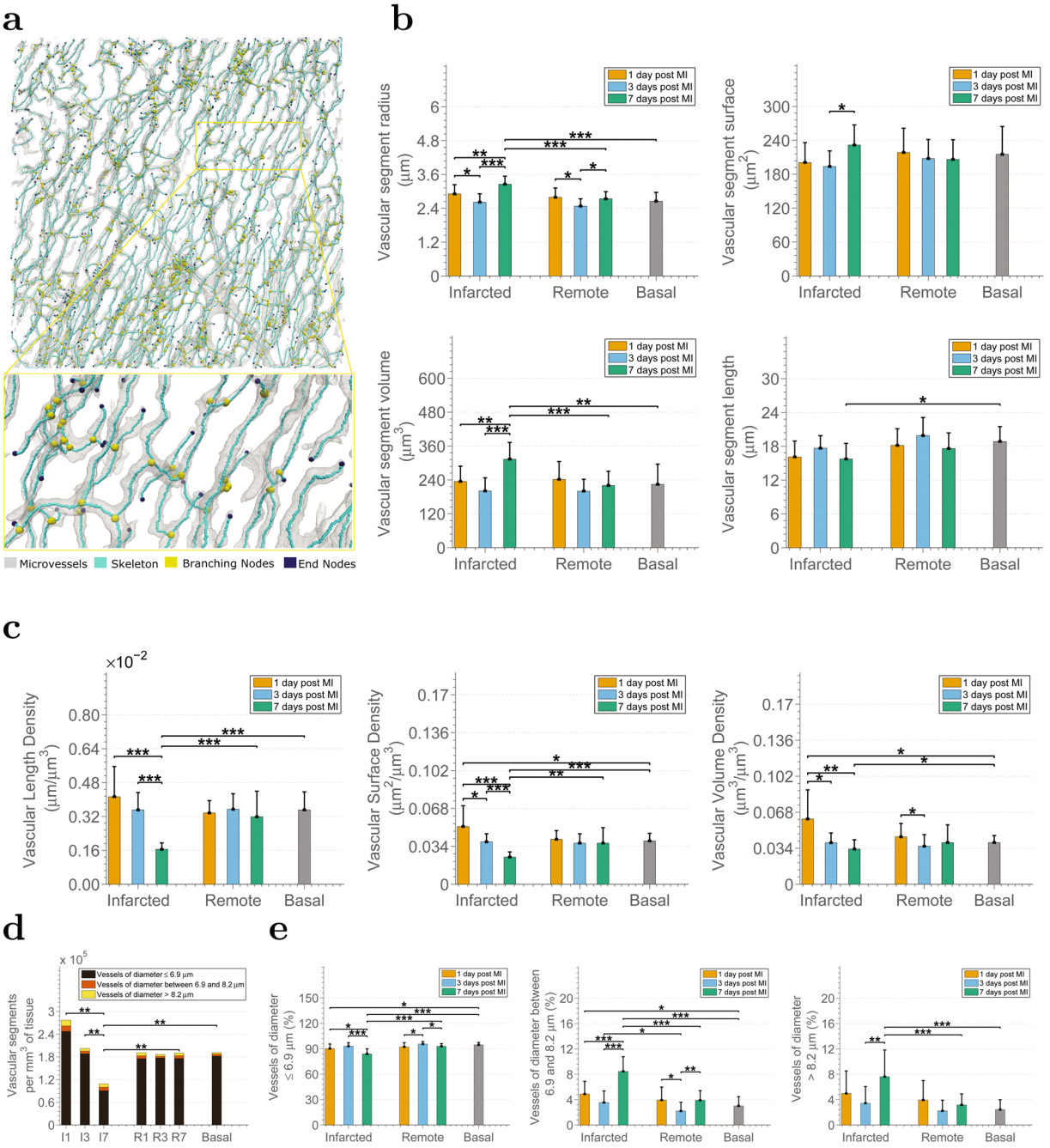

Figure 4. Microvascular angioadaptation occurs in response to MI. (**a**) Example graph-based representation of a microvascular structure. Each microvessel, i.e. segment from branching node to branching/ending node, is considered as a tube of constant radius. **(b)** Analysis of the characteristics of the microvessels in the pig infarcted heart in terms of vascular segment radius, vascular segment length, vascular segment surface, and vascular segment volume. **(c)** Analysis of vascular length density, vascular surface density, and vascular volume density. In panels **(d)** and **(e)**, changes in the number and percentages of microvessels in the infarcted pig heart according to their radius and to the physiological condition of the tissue. In particular, **(d)** analysis of the number of microvascular segments per mm^3 of tissue. **(e)** Analysis of the percentage of vascular segments with radius smaller than 6.9 μm, with radius between 6.9 and 8.2 μm and with radius larger than 8.2 μm. I1, I3, I7, R1, R3, R7 stand for infarcted areas and remote areas at 1, 3, 7 days post MI respectively. Note that statistical hypothesis testing in **(d)** refers to the comparison of the overall number of vascular segments i.e. the sum of the three categories.

complete microvasculature, including regions that might not have been labelled with VE-Cadherin, but nonetheless belong to the microvasculature. Supplementary Fig. S2 allows appreciation of the improved identification of the microvascular network by using the proposed filling approach.

Myocardial infarction decreases 3D complexity, integrity, and connectivity of the coronary microvasculature while it leads to altered capacity and heterogeneity of blood flow. After the VE-Cadherin, as well as SMA^+ cells, and nuclei are segmented, and the 3D microvasculature is reconstructed, the next step is to quantify the parameters that allow description of the characteristics of the microvasculature and assessment of infarction-related changes. Figure 2 provides representative 3D reconstructions of the microvasculature at different conditions under investigation (basal, infarcted and remote at 1, 3, and 7 days following MI respectively) used for the analysis. Table 1 provides a detailed list of the parameters extracted to describe the complex microvascular network described in this and following sections. Statistical analysis of the parameters is performed to identify vital changes that occur at different stages following MI.

Parameters based on fractal analysis and on the Minkowski Functionals (MF) are used for describing the microvasculature as a complete network, and thus, identifying its alterations after MI at a structure-global level. Fractal analysis accounts for the multiscale properties of structures that can be self-similar, such as the vascular networks[33], and it is powerful tool in cardiology[34]. Here, as in[30], we used three fractal parameters calculated directly from the 3D volumes; fractal dimension, lacunarity and succolarity. Fractal dimension provides an estimation of the morphological complexity of structures. Lacunarity describes the heterogeneity in the distribution of gaps sizes. Gaps in the case of cardiac tissue represent non-vascularized areas. Succolarity indicates the capacity of a fluid, i.e. blood in the case of the microvasculature, to flow through the structure. On the other hand, the Minkowski functionals (MF)[35] are morphological descriptors (volume, surface area, mean integral of breadth and Euler-Poincaré characteristic) that encompass standard geometric and topological (connectivity) properties of structures. Thus, a combination of fractal and Minkowski-based parameters, allows obtaining complementary information regarding the microvascular networks.

The fractal parameters demonstrate significant differences in terms of multi-scale characteristics of the microvascular networks in the infarcted areas, over time (Fig. 3a). In particular, when comparing infarcted areas at 1, 3, and 7 days, we noted that the morphological complexity (fractal dimension) and capacity of blood flow (succolarity) of the microvasculature decreased, while the heterogeneity in the distribution of the non-vascularized areas (lacunarity), increased. The reverse relationship between morphological complexity and heterogeneity has been observed in earlier studies[30,36]. Moreover, the distribution of non-vascularized areas affects blood flow. Thus, higher heterogeneity, as observed here, is expected to result in higher heterogeneity in blood flow within the tissue, and could therefore denote the existence of regions with lower perfusion. Furthermore, complexity and heterogeneity in the infarcted areas at 1 and 7 days are statistically different than in the corresponding remote areas (1 and 7 days respectively). In terms of all multi-scale characteristics, the differences of the microvasculature from infarcted areas at 7 days post MI are significant compared with that at basal conditions. It is worth also noting that at infarcted areas 1 day post MI the tendencies compared with basal conditions are opposite to 7 days: higher morphological complexity and blood flow instead of lower, and lower lacunarity instead of higher. This could be linked to the first response of the system to MI and the poorer contractility of cardiomyocytes at day 1. Moreover, in contrast with the changes observed in microvascular networks from infarcted areas, no significant differences are found in the remote areas over time and compared with the basal case.

The reduction in the morphological complexity of the microvasculature in infarcted areas can be further explained by the progressive loss of microvascular volume that occurs in the infarcted areas as revealed by the decreased vascular volume density (Fig. 3b) observed in those areas. Furthermore, the microvasculature appears reduced in the infarcted areas, with less breadth and smaller surface area for the exchange of oxygen and nutrients, while it is progressively converted from a strongly connected network to a less connected one (progressively increasing Euler-Poincaré characteristic). The reduced connectivity and volume are related to the lower capacity of blood flow and probably to its heterogeneity described earlier. An unexpected observation is the significant decrease of the microvascular volume density at remote areas at 3 days post MI compared with remote at 1 day post MI and basal. Further exploration of the lost vascular volume (capillary volume or arteriole/venule volume) led to the observation that the loss is associated with the loss of capillary volume (Fig. 3c). Lastly, as with the fractal parameters, in terms of all metrics the infarcted area 7 days post MI presents significant differences with basal areas, as well as with corresponding remote areas.

Myocardial infarction promotes microvascular angioadaptation. Metrics at the structure-global level provide us with paramount information regarding the whole microvascular plexus, but they do not provide insights into the angioarchitecture, i.e. the morphology and arrangement of the individual microvessels that form the microvasculature, on which the functional properties of microcirculation and their modelling critically depend[37]. For this reason, we perform a quantitative analysis at the segment level using the 3D graph-based representation of the microvasculature (Fig. 4a), complemented with information regarding the radius, length, surface and volume of every segment (see Methods).

The most profound changes are observed at infarcted areas 7 days after MI. By examining Fig. 4b it is obvious that the microvascular segments of those regions present larger radius than those of tissues from infarcted areas at earlier time-points, remote areas at 7 days post MI and at basal conditions, despite the reduction of the overall microvasculature described in the previous subsection. This results in segments with significantly larger volume than segments from the other areas, while their surface area is significantly larger than that of segments from infarcted areas at 3 days post MI and their length is shorter than segments from basal conditions. In contrast, the microvessels in both the infarcted and remote areas 3 days post MI become significantly smaller in terms of radius compared to those of the infarcted areas from earlier and later time-points under investigation, indicating a possible vasoconstriction on this time-point. The radius of microvessels from infarcted and remote tissue 1 day following MI, as well as from remote areas 7 days post MI, seem to remain unaffected. No significant difference among any tissue categories is observed in terms of tortuosity and the relative plot was, therefore, omitted. However, the corresponding mean and standard deviations are provided in Table 1.

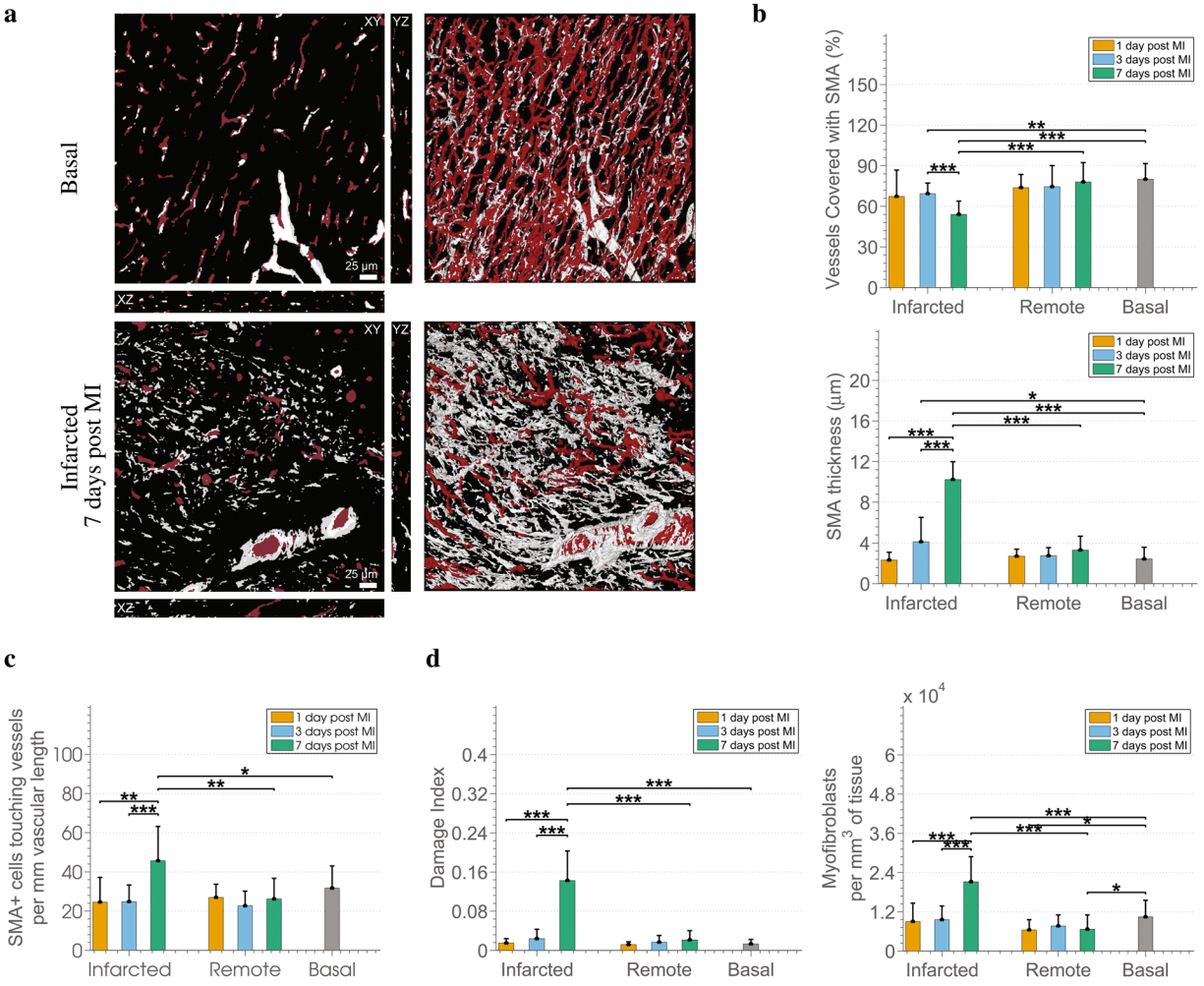

Figure 5. Changes in SMA$^+$ perivascular cells and myofibroblasts in the aftermath of MI. **(a)** Example of 3D reconstructions of the microvasculature (red) merged with the segmentation of the SMA$^+$ cells channel (grey) in a basal and an infarcted 7 days post MI case. **(b)** Changes in SMA$^+$ related metrics, i.e. the percentage of vessels with a SMA$^+$ coat along with the corresponding thickness of the coat. **(c)** Analysis of the number of SMA$^+$ cells of which the SMA$^+$ coat covering the microvessels consists. **(d)** Analysis of the cardiac tissue by means of indicators of tissue fibrosis, i.e. the Damage Index (percentage of SMA$^+$ volume that are not associated with vessels), and number of myofibroblasts per mm^3 of tissue.

Length, surface and volume density (Fig. 4c) calculated by means of the graph-based representation of the microvasculature confirm the microvascular changes revealed by the corresponding Minkowski-based metrics (breadth, surface and volume density). This fact demonstrates that the latter are sufficient in describing those characteristics of microvascular networks and it is therefore feasible to avoid exhaustive extraction of centerlines when characteristics of the individual microvessels are out of interest.

Subsequently, segments were divided into three classes based on the morphological data of[13] in order to study the size of microvessels at each tissue condition. The maximum diameters found in the left ventricle of the pig heart according to the published data are 7.3 μm for capillaries fed directly by arterioles (C_{oa}), 8.2 μm for capillaries drained directly by venules (C_{ov}), and 6.9 μm for cross-connecting capillaries (C_{cc}) and capillaries connected to C_{oa} and C_{ov} types (C_{oo}). Thus, the three classes created are (i) segments with diameter smaller or equal to 6.9 μm corresponding to C_{cc} and C_{oo} capillaries, (ii) segments with diameter between 6.9 and 8.2 μm corresponding to C_{oa} and C_{ov} capillaries, and (iii) segments with diameter larger than 8.2 μm representing arterioles or venules.

A gradual decrease in the overall number of microvascular segments per mm^3 of tissue is observed at the infarcted areas (Fig. 4d). The decrease becomes profound and statistically significant at 7 days post MI compared with all other conditions. The reduced number of segments explains the reduced morphological complexity, vascular volume density, surface area and breadth density of this area expressed by the fractal dimension and the Minkowski metrics (Fig. 3). Furthermore, a higher number of vascular segments can be also observed in the infarcted area 1 day post MI compared to the basal tissue. This difference, although not significant, matches the higher density and morphological complexity on this tissue category described in the previous subsection (Fig. 3).

Looking further into the percentage of vessels in each radius range (Fig. 4e) the percentage of microvessels with diameter larger than 8.2 μm, i.e. arterioles/venules, and "medium"-sized capillaries of the categories C_{oa}

Classifier	1	2	3	Classifier	1	2	3
Infarcted - Basal	77	81	74	**Remote - Basal**	68	72	75
I1MI - Basal	82	75	59	R1MI - Basal	61	70	61
I3MI - Basal	66	77	47	R3MI - Basal	65	63	57
I7MI - Basal	100	100	94	R7MI - Basal	63	59	70
Infarcted over time	75	89	72	**Remote over time**	48	50	40
I1MI - I3MI	71	84	64	R1MI - R3MI	61	66	57
I1MI - I7MI	100	100	97	R1MI - R7MI	53	60	56
I7MI - I3MI	93	97	93	R7MI - R3MI	56	64	56
Infarcted - Remote	67	71	56				
I1MI - R1MI	53	68	69				
I3MI - R3MI	62	60	42				
I7MI - R7MI	97	100	88				

Table 2. Accuracy (%) in classifying the distinct vascular patterns using different classifiers: (1) Knn, (2) SVM, (3) Adaboost, and 9-fold cross-validation, repeated 10 times. Metrics of $1-28$ of Table 1 are used as features for performing the classification.

and C_{ov} (6.9 and 8.2 μm) are increased in infarcted areas 7 days post MI. On the contrary, the smallest vessels (C_{cc} and C_{oo}) are reduced compared to the healthy tissue, infarcted tissue at earlier stages after MI as well as with the corresponding remote area. This fact demonstrates a regression of smaller microvessels and probably dilation or even arterialization of the remaining vessels in infarcted tissues from 7 days following MI. The smallest microvessels from infarcted tissue 1 day post MI are significantly decreased as well, while the percentage of capillaries C_{oa} and C_{ov} (6.9 and 8.2 μm), is increased when comparing to microvessels belonging to basal tissue, which implies a possible vasodilation effect. Interestingly, at remote areas 3 days post MI the number of smallest capillaries is increased compared with the remote areas at other time-points, and in contrast, the percentage of "medium"-sized vessels is reduced.

Information from the α-SMA channel and its relation to the microvasculature (Fig. 5a) is quantified through an additional module of the analysis pipeline in order to study perivascular cells stained by α-SMA, i.e. pericytes and smooth muscle cells. We are particularly interested in the coating of microvessels by layer(s) of α-SMA expressing cells as this could be an indicator of vessel maturation[38,39] and denote the end of a plasticity window for intervention[40]. A significantly lower percentage of vessels coated with α-SMA$^+$ cells is observed in infarcted areas 3 and 7 post MI compared to the basal tissue as well as to the corresponding remote area for the second case (Fig. 5b). However, the layers of α-SMA$^+$ perivascular cells on those days, i.e. 3 and 7 days post MI, are significantly thicker than in the basal case as shown in the same panel. Furthermore, the thick layer of α-SMA$^+$ at the infarcted area 7 days post MI consists of significantly more cells than in the infarcted areas of previous time-points, the basal and remote area 7 days post MI as indicated by the increased number of α-SMA$^+$ perivascular cells per *mm* of vascular length (Fig. 5c). Thus, we have a proliferation of the perivascular α-SMA$^+$, and not a dilation of the cells.

We also noticed, mainly in infarcted areas, α-SMA$^+$ regions that were not associated with microvessels, i.e. they were not localized in the perivascular layers of microvessels. Given that myofibroblasts are non-vascular cells that produce extracellular matrix indispensable for healing after MI and have contractile properties related to their expression of α-SMA[41], we considered those α-SMA$^+$ regions corresponding to myofibroblasts. We further complemented their characterization by their concomitant expression of other markers, such as platelet-derived growth factor receptor beta (PDGFRB)[42], vimentin and collagen I[43] (Supplementary Fig. S4). We then decided to extract quantitative information regarding the myofibroblasts based on the α-SMA$^+$ staining. For this purpose, a damage index was defined for the tissue as an estimator of the presence of myofibroblasts. Precisely, the index is given by the ratio of the volume of myofibroblasts over the volume of all α-SMA$^+$ regions. Furthermore, the number of the myofibroblasts is quantified as the number of simultaneously stained nuclei by Hoechst and α-SMA.

Damage index (Fig. 5d) demonstrates a non-significant increase in the presence of myofibroblasts in infarcted tissues at the first time-points after MI (1 and 3 days) followed by a significant increase at the later time point (7 days post MI). This observation is in accordance with findings in the healing human tissue[44], and rat tissue after MI[45]. A lack of increase in the damage index in the remote areas compared to the basal case denotes no increase of myofibroblasts, and thus, no inappropriate deposition of extracellular matrix in remote areas[41]. As far as the absolute number of myofibroblasts per mm^3 of tissue is concerned, the trends presented in infarcted areas are similar with that of the damage index. However, additionally a decrease of myofibroblasts in remote areas at 1 and 7 days post MI compared with the basal case can be observed.

3D microvascular characteristics predict the healthy or diseased status of the cardiac tissue. The quantitative information about the cardiac microvasculature and SMA$^+$ cells obtained by our pipeline was evaluated with the task of predicting the condition of previously unseen tissue based on the characteristics of the microvascular bed. Towards this aim, we incorporated the parameters at structure level, at segment level as well SMA$^+$ related metrics (metrics 1–28 of Table 1) into a classification scheme using three different classifiers; (i) K-nearest neighbours classifier (Knn), (ii) Support Vector Machines (SVM), and (iii) Adaboost[46]. In all cases, 9-fold cross validation repeated 10 times was used. Accuracy rates (%) are presented in Table 2.

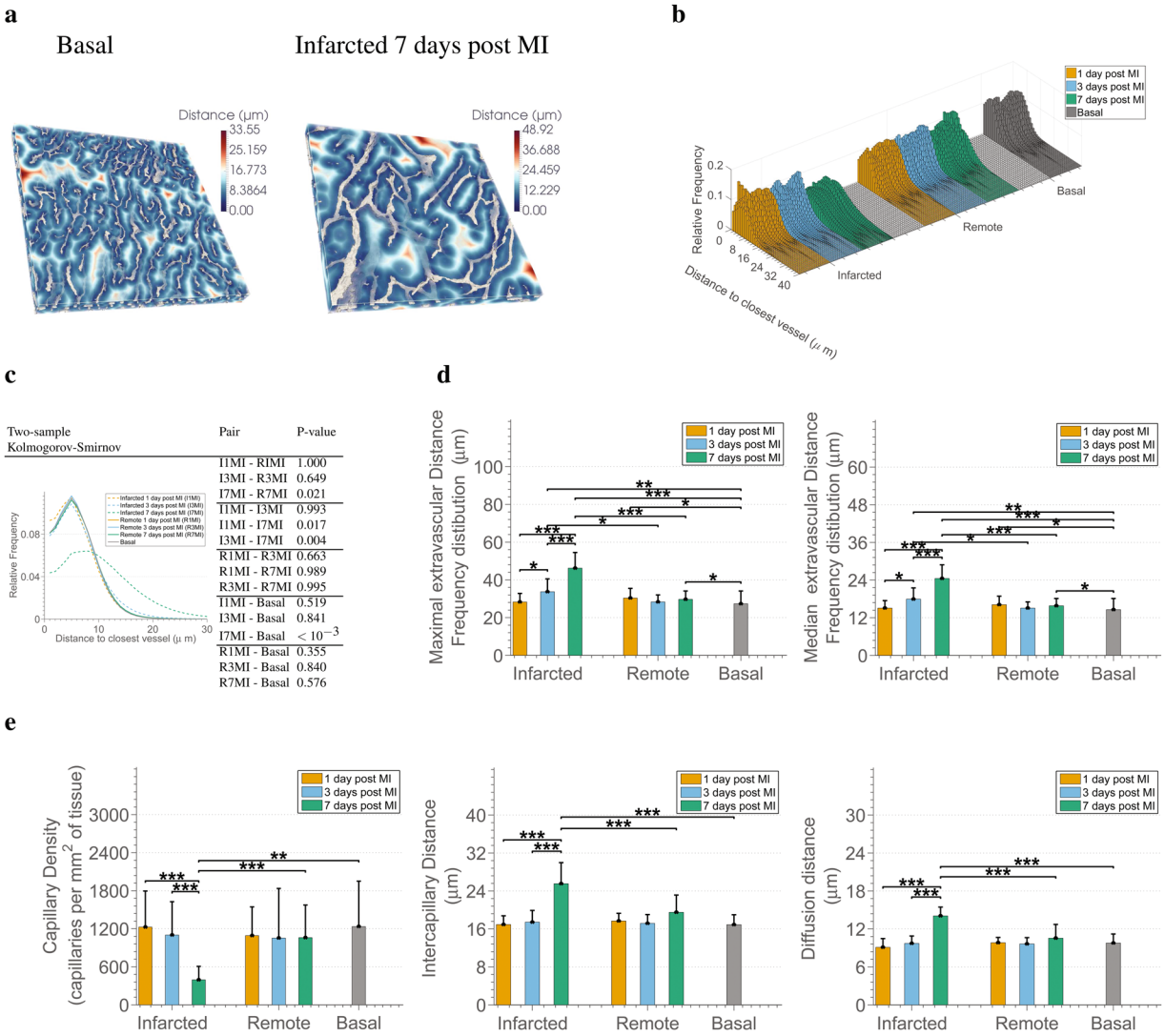

Figure 6. Capillary diffusion distances support altered oxygen diffusion in the infarcted cardiac tissue. **(a)** Example of 3D extravascular distance maps for a basal and a 7 days post MI case. **(b)** Histograms of the extravascular diffusion distances for all volumes of the dataset colour-coded according to the tissue condition. **(c)** Kolmogorov-Smirnov statistical tests for identifying significant differences in the mean relative frequencies of diffusion distances between the different tissue categories. **(d)** Analysis of the maximum and median extravascular diffusion distances at the different tissue conditions based on all volumes of the dataset. **(e)** Analysis of metrics traditionally related to oxygen-diffusion distances, i.e. capillary density, and inter-capillary distance calculated from 2D slices of the 3D volume, and of the diffusion distance calculated by using the length density, instead of the detailed 3D maps of panel.

The proposed approach achieves high accuracy in the range 74–81% in differentiating between infarcted and basal tissue, as well as in recognizing the day after MI that the infarcted tissue belongs to (72–89%). The accuracy in classification drops to levels of 68–75% and 56–71% in differentiating between remote and basal tissue, and between remote and infarcted tissue respectively. This is expected taking into account the lack of significant differences in the majority of metrics between those categories. It is worth noting that, for the same reason, the worst levels of accuracy in classification (40–50%) are achieved in terms of recognizing which day following MI the remote tissue belongs to.

Structural changes of the microvasculature support altered oxygen diffusion in the post-infarcted cardiac tissue. The diffusion of oxygen from the microvascular network to the tissue critically depends on the density and the arrangement of the microvascular bed[47]. Simple metrics, such as capillary density, intercapillary distance, diffusion distance as derived from vascular length density, and 3D extravascular distances (EDs), have been proposed in the literature as indices of oxygen diffusion, with the latter having been proven more efficient[48].

In this work, 3D maps of EDs were calculated by getting the distance of every point to the closest vessel (Fig. 6a) and they were used to calculate the relative frequency distributions (Fig. 6b). From the comparative

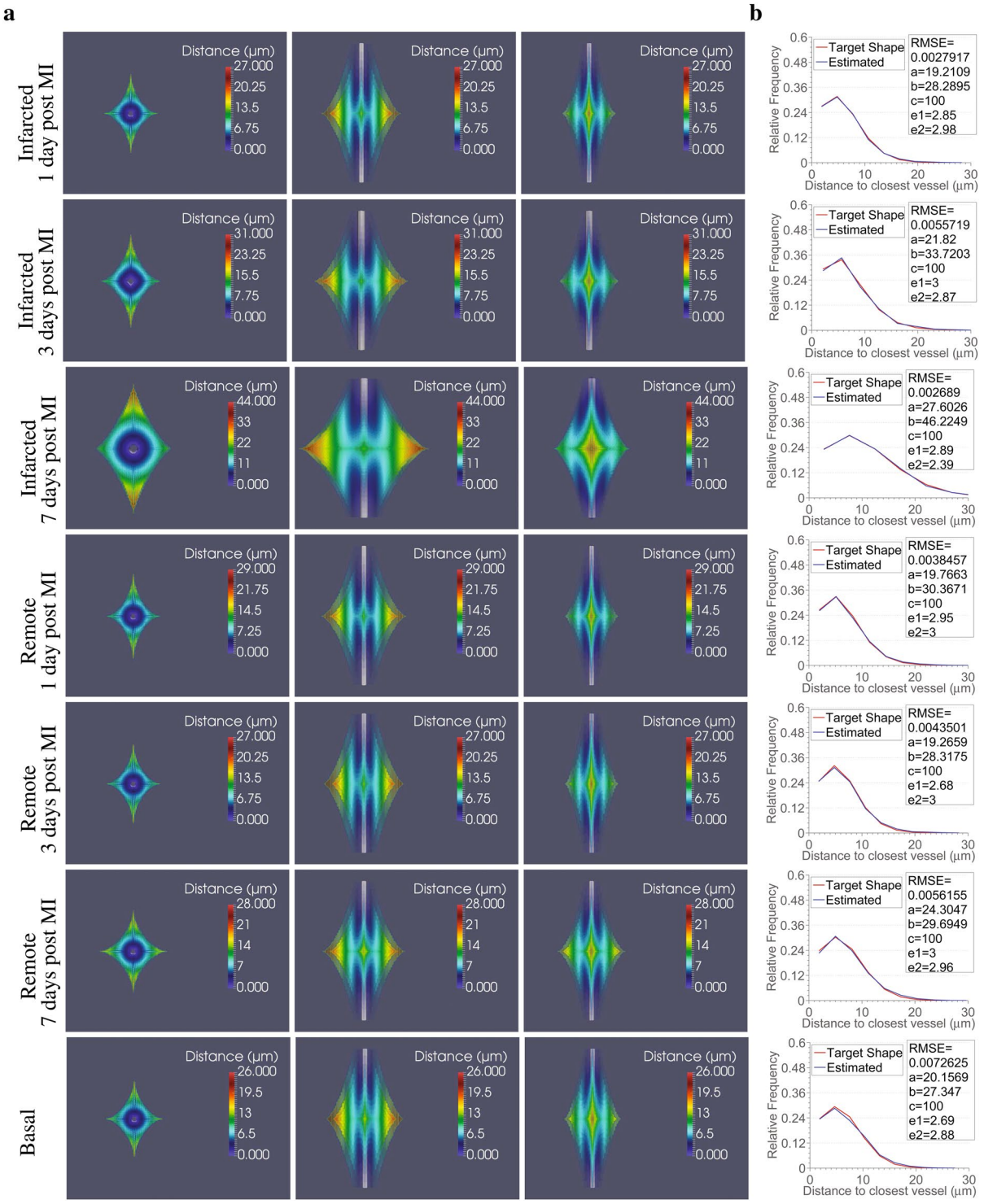

Figure 7. 3D super-ellipsoids are adequate geometrical models to represent the capillary diffusion area. **(a)** 3D super-ellipsoids estimated to best fit the mean distributions of extravascular distances extracted from histograms of 10 bins for the different tissue conditions (one per row; basal, infarcted and remote 1, 3, 7 days following MI) from x-y (first column), x-z (second column) and y-z views (third column). The tissue points inside the 3D shapes are pseudo-coloured according to the distance to the central capillary (represented with grey in all sub-figures). The radius of the central capillary for each tissue condition was set equal to the minimum extravascular distance found for the particular case. **(b)** Accuracy of the fitting between the mean distributions of extravascular distances for the different tissue conditions (target represented with red) and the distributions produced using the estimated 3D super-ellipsoids of panel a to best fit them (represented with blue). RMSE stands for the root mean square error, while a, b, c, e_1, e_2 are the estimated parameters that define the 3D super-ellipsoids. In particular, a, b, c, are the scale factors for axis x, y and z respectively, and e_1, e_2 control the shape of the super-ellipsoid.

plot, the most striking difference that we can observe among the different tissue conditions is a long-tail in the distribution of EDs at the infarcted areas 7 days following MI. This tail implies longer diffusion distances, which are associated with longer diffusion times, and thus worst oxygenation[47]. Two sample Kolmogorov-Smirnov tests were used to compare the mean relative frequencies of each tissue category (Fig. 6c). The outcome verified the statistical significance of the difference in the shape of the distributions. The median and maximal EDs, calculated as the 50% and 95% quartile respectively[48], also confirm significantly increased diffusion distances in the infarcted areas 7 days post MI. However, significant differences in both metrics in the infarcted areas 3 days following MI, compared to the basal and corresponding remote tissue, highlight that the increase in the EDs had already started in the infarcted areas from day 3 following MI. Moreover, the EDs at remote areas at 1 and 7 days after MI are also affected and are significantly different from that of the basal tissue.

EDs calculated directly from the complete 3D volumes are expected to be more accurate than capillary density and intercapillary distance which are calculated in 2D, or the diffusion distance which is derived from the vascular length density. However, for the sake of completeness and for facilitating comparison with past and future works, these metrics are provided in Fig. 6d. According to the plots, the capillary density is affected and reduced in infarction, with the reduction becoming significant at 7 days post MI in infarcted area. On the other hand, the intercapillary distance which is associated with an inverse relationship with capillary density, is increased in the infarcted areas at 7 days following MI. The diffusion distance calculated directly from the length density follows the same trend as the EDs calculated from the 3D distance maps, although an underestimation of the distances can be observed.

Lastly, we contrasted the mean relative frequency distributions of 3D EDs for each tissue category with the ones that would be provided by equivalent Krogh cylinder models[49]. The Krogh cylinder model assumes the supply of oxygen by every capillary to a cylindrical region whose radius equals half the intercapillary distance. As a result, the relative frequency distributions in the Krogh cylinder model are monotonically increasing to the maximum distance to the closest vessel (Supplementary Fig. S3) and are far from describing the distributions observed in the cardiac tissue studied in this work. In an effort to identify a geometric pattern that would describe the area of capillary diffusion so that it closely matches the relative frequency distributions observed in our volumes, we used a super-ellipsoid model. Super-ellipsoids allow description of a variety of shapes, ranging from cylinders (such as in the Krogh model) to more complex ones, by varying only a small number of parameters (see Methods). Thus, we formulated a question of finding a set of parameters that would define super-ellipsoids that match simplified versions of our distributions (10 bins) as an error minimization problem between the observed relative frequency distributions and the ones corresponding to different super-ellipsoids (Fig. 7). Root mean squared error in the range of 0.0027–0.0073 between the relative frequency distributions of extravascular distances in the super-ellipsoid models and the target ones demonstrate the superiority of the super-ellipsoid model over the Krogh cylinder model to represent the region of capillary diffusion in the cardiac tissue studied here.

Changes in the microvasculature and in the diffusion of oxygen persist and intensify at later time-points post MI. We next analyzed, by means of our image analysis pipeline, the microvascular characteristics of porcine tissues from infarcted and remote areas 45 days post MI (Supplementary Fig. S5) to examine whether the observed microvascular alterations during the first week post MI persisted at later time-points and whether additional changes occurred. The results, which have been summarized in Supplementary Table S1 point to the persistent nature of the extensive microvascular remodelling that takes place 7 days post MI in infarcted areas together with a deterioration in certain metrics at 45 days post MI. Changes, which had been slightly observed at remote areas 7 days post MI, also intensified and became evident at remote areas 45 days post MI.

Both infarcted and remote areas at 45 days post MI present the same increasing or decreasing trends in those parameters which describe the microvasculature (fractal-, minkowski- and graph-based metrics) as the corresponding tissue 7 days post MI compared to earlier time-points post MI and basal conditions. There are several metrics, however, where increases or decreases are so prominent that statistically significant differences are observed between the tissues examined 7 and 45 days post MI. More precisely, infarcted areas at 45 days post MI have less vascular surface, breadth and length density, while they present a higher heterogeneity in distribution of non-vascularized areas compared to 7 days post MI. Concomitantly, there were fewer smaller and more medium and larger microvessels with increased intercapillary and diffusion distances at 45 days. Altogether this remodelling indicates worse vascular perfusion and oxygen supply in infarcted areas at late time-points. In the remote areas at 45 days similar changes were observed for the microvasculature which was characterized by a further loss of its morphological complexity, breadth and connectivity. These changes are accompanied again by enlarged vessels, reduction in smaller and increase in larger microvessels along with higher heterogeneity in the distribution of non-vascular areas as well as a trend to poorer diffusion. Moreover, the SMA^+ perivascular layer is thinner, while the number of myofibroblasts decreases in both remote and infarcted areas compared to day 7 post MI. This suggests deceleration or termination of extracellular cardiac remodelling at this late stage.

Discussion

The link between the anatomy of microcirculation and CVDs' onset and progression had led to considerable efforts in unravelling the fine perturbations of the microvascular networks. This is particularly true in the case of MI were an amount of important works had been performed prior to our work[38,40,50–56]. However, there is a high variability among the quantification methods used in those studies, with each study reporting a different set of parameters to characterize the anatomy of microcirculation and some of them being based on the 2D analysis. Works more closely related to ours[56] do not provide the wealth of data which are indispensable in describing the complications of MI, but are rather based on only a few traditional metrics.

This work was designed to deal with these shortcomings by allowing the in-depth study of all major characteristics of the microvasculature in 3D through a single pipeline. Our pipeline consists of modules that permit translation of image information to quantitative biological knowledge regarding (i) the multiscale and geometric properties of the microvasculature, (ii) topological characteristics and biologically important morphological information about the segments the microvascular structure consists of, (iii) the microstructural relationship with SMA^+ cells, which are key players in tissue healing after MI (myofibroblasts), as well as in vessel maturation and stabilization (SMA^+ perivascular cells), and (iv) diffusion efficiency of the microvascular bed and adequate geometric models of the capillary supply region. We show that each class of parameters offers complementary information in understanding the effects of MI and that it is indispensable to study all classes in order to understand changes to a system as complex as the microvasculature.

Furthermore, we provide a novel method for accurately reconstructing the complete microvasculature from VE-Cadherin-labelled endothelial junctions. This approach will enable the use of VE-Cadherin, an endothelial marker with high specificity even in infarction, to reconstruct microvessels and it will allow the simultaneous study of endothelial junctions, SMA^+ and microvessels through the use of two fluorescent markers (VE-Cadherin, SMA^+ cells) instead of three. The latter is noteworthy given that the number of fluorochromes that can be imaged simultaneously is limited[57]. Lastly, a simple, yet efficient, approach in distinguishing between capillaries and arterioles/venules was incorporated in the pipeline. The importance of identifying the type of microvessels is not solely limited to the definition of the 3D guidance map for filling (and pruning), but it is also crucial in the implementation of theoretical modelling approaches[58]. The approach could be further extended to separate arterioles from venules, given their morphological characteristics such as branching patterns and tortuosity.

Among the main findings is an intensive structural remodelling of the microvasculature at 7 days post MI, which persists and even deteriorates 45 days post MI, in combination with an abundant presence of myofibroblasts, a higher percentage of microvessels which lacked a SMA^+ coating, but with the coated ones having a thick SMA^+ layer. The latter might mark the end of the plasticity window for intervention[40]. By quantifying the effect of the structural remodelling in functional terms, we were able to identify a low capacity for blood flow (succolarity) and long diffusion distances which is linked with worse oxygenation. This might be related to the regression of vessels non-coated with SMA^+ resulting in a less complex and connected network that, as a result, requires longer diffusion times. Moreover, despite the decrease in the capacity of blood flow at the tissue level, observed also at organ level (Supplementary Table S2) at infarcted areas 7 days post MI, the larger diameter of the individual microvessels and the SMA^+ hyperplasia, together with increased number of endothelial cells per length (Table 1), likely reflects adaptation to persistent/chronic high flow in these remaining vessels. Interestingly, in terms of structural characteristics (density, size of microvessels) the infarcted area at 3 days post MI, seems closer to the basal one than at 1 or 7 days post MI. This could indicate a normalization of the effect of infarction 3 days following MI after a first inflammatory response at day 1 and, therefore, denote a time window for therapeutic intervention around day 3 post MI when the microvasculature is not structurally so different from the basal but functionally already starts the misadaptation as implied by the larger extravascular distances and higher heterogeneity in non-vascularized areas observed in infarcted areas 3 days post MI. Moreover, our results imply a connection between the appearance of constriction or dilation and the time which elapsed following MI. In particular, we observed a tendency for an initial dilation of the vessels in infarcted area at 1 day post MI, a subsequent constriction at 3 days, followed by possible pruning of microvessels, and maybe dilation/arterialization of the remaining microvessels at day 7. It is also worth noting that apart from the vasodilation effect the structural changes at infarcted areas at 1 day post MI are opposite to that of 7 days. Specifically, an increased number of microvessels, vascular density and complexity at infarcted areas at 1 day post MI were described. Thus, we cannot rule out angiogenesis (either sprouting or intussusceptive) at that time-point but it is clear that there is an overall loss of microvasculature afterwards, mostly of capillaries. In addition, as expected[59], changes at remote areas are not significant or they are milder than the ones found in the infarcted areas, but they are not entirely absent as pathology progresses.

Despite the importance of our findings, there are some limitations to the current work. One of the strengths of this study is the choice of the highly translational porcine animal model. However, due to the cost and difficulty in handling large animals, we were able to use a limited number of subjects. Furthermore, the chosen ischaemia model might influence the microvascular changes described in this study. This means that the same changes may not be necessarily anticipated in other ischaemia models, such as permanent coronary artery ligation. This limitation could motivate future research as the presented approach paves the way to standardized analysis and future comparison of different experimental ischaemia setups. Another limitation of the present work is the loss of precise topological information at the organ level during tissue processing and confocal microscopy imaging. Also, in spite of the fully automated and un-biased analysis pipeline, human bias might be potentially introduced in the selection of the areas to be imaged by confocal microscopy and in the adjustment of the microscope settings. In addition, since no automated method can ensure 100% accuracy in terms of segmentation, the exact metric numbers might deviate slightly from reality, although the trends would remain uninfluenced given that the same method was applied to all images. Lastly, running the complete pipeline on large images can be computationally and time demanding, but this can be balanced by the fact that requires no human intervention, therefore, minimizing costs and labor requirements, while facilitating the calculation of complex metrics.

In conclusion, our fully automated image analysis pipeline permitted the accurate reconstruction of the 3D microvasculature and subsequent acquisition of novel, quantitative insights into its structure and changes at different stages after MI. The study was performed in the pig model, whose coronary microvasculature bears strong similarities to that of humans. Our method also provides an automated and unbiased means of evaluating therapeutic approaches and of diagnostic classification of unseen cardiac tissue. Furthermore, the wealth of quantitative data on the anatomy of microcirculation provided can serve as reference for comparisons for future studies in the field of cardiac microvascular research as well as enable modelling microcirculation at different stages

of pathology. Lastly, the open-source nature of our approach makes it reusable in future studies of the cardiac microvasculature, but also in the study of other diseases and tissue types for which the microvascular structure and its changes are in focus.

Methods

Animals and Myocardial Infarction. All experiments were approved by the Ethical Committee for Animal Experimentation of CNIC and the Comunidad Autónoma de Madrid in accordance with the Guide for the Care and Use of Laboratory Animals. Six adult male Large-White pigs weighting 30–40 kg were anaesthetized with a ketamine/xyzaline/midazolam mixture in continuous intravenous infusion. Subsequently, acute myocardial infarction was percutaneously induced using an angioplasty balloon with 30-minute occlusion of the left anterior descending coronary artery (distal to the first diagonal branch) followed by reperfusion. The pigs were sacrificed one, three and seven days after infarction, respectively. A similar procedure with 40-minute occlusion was followed for three additional pigs that were sacrificed forty-five days following infarction. Furthermore, two more pigs under basal conditions were sacrificed to serve as the control subjects of the present study. The subjects' structural and functional characteristics are provided in Supplementary Table S2.

Tissue preparation and Immunofluorescence histochemistry. The porcine hearts were extracted immediately after euthanasia, cleaned with saline and cut into three thick cross-sections, at the basal, mid-ventricular (papillary muscle) and apical levels. Left ventricle tissue samples from both infarcted and remote areas were collected and used for the purposes of this study. Samples were fixed overnight with 0.4% PFA at 4 °C, washed with PBS, cryoprotected with 30% sucrose and embedded in OCT with transmural orientation kept. Thick slices of 100 μm were cut using Leica AM1950 automated cryostat. Immunostaining was performed in flotation using the following procedure; 2 hours permeabilization in 0.3% Triton-X 100, 0.1% Tween in PBS at RT followed by 1 hour blocking with 0.3% Triton-X 100, 4% FBS in PBS at 4 °C. For the staining of the microvasculature, the slices were incubated in blocking buffer with primary antibodies anti-VE-Cadherin (Santa Cruz) and α-SMA (Sigma) with dilution 1:100 and 1:200 respectively, overnight at 4 °C. After washing with 0.3% Triton-X 100 in PBS, incubation with secondary antibodies donkey anti-goat Alexa Fluor-568, chicken anti-mouse Alexa Fluor-647, 1:500 (Molecular probes) and Hoechst 33342, 1:10000 (Life Technologies) was performed for 2 hours in blocking buffer at RT. After washing, slices were mounted on the glass using Fluoromount G (Southern Biotech). All incubations were performed on a nutator.

VE-Cadherin stains the endothelial junctions and not the complete endothelial cell, resulting in gaps in the reconstructed blood vessels. However, it has been chosen in this work as a vasculature marker over other commonly used endothelial markers, such as Isolectin B4 or CD31 (PECAM-1), due to its specificity even in infarction. Isolectin tends to stain not only endothelial cells, but also macrophages[60]. Therefore, its use in infarcted tissue is not appropriate, especially at early time-points, when the inflammation process occurs. In our samples large contamination of macrophage staining was observed in infarct zones when Isolectin was used. A similar problem was presented in the case of CD31 marker, which is present in endothelial cell junctions but it is also expressed in other cell types, e.g. platelets, monocytes and macrophages[61]. For those reasons, the use of VE-Cadherin that is exclusively an endothelial cell marker[62], was preferred.

A similar protocol was followed in the case of tissue used to study the co-expression of α-SMA with other markers. More precisely, 15 μm slices of tissue from infarcted areas from the pigs sacrificed at 7 days following MI were used. After fixation and cutting, the slices were incubated in blocking buffer with primary antibody anti-CD31 (Abcam) with dilution 1:100 and one of the following primary antibodies: (i) anti-Vimentin (Sigma) with dilution 1:100, (ii) anti-Collagen I (Santa-Cruz) with dilution 1:50, or (iii) anti-PDGFRB (eBioscience) with dilution 1:100, overnight at 4 °C. After washing with 0.3% Triton-X 100 in PBS, incubation with secondary antibodies goat anti-rabbit Alexa Fluor-488 (Life Technologies) with dilution 1:500, chicken anti-mouse Alexa Fluor-647, 1:500 (Life Technologies) and Hoechst 33342, 1:10000 (Invitrogen) was performed for 2 hours in blocking buffer at RT. After washing with 0.3% Triton-X 100 in PBS, the slices were incubated in blocking buffer with 5% mouse serum for 1 hour at RT. Subsequently, they were incubated with anti-α-SMA-Cy3 (Sigma) with dilution 1:300 for an additional hour at RT. After a final wash with 0.3% Triton-X 100 in PBS, the slices were mounted on the glass using Fluoromount G. In this case CD31 was used as a marker of the microvasculature instead of VE-Cadherin due to compatibility issues of the species of primary antibody host.

Image acquisition. Spectral imaging was performed by means of Leica SP5 confocal microscopy using a 40 × oil immersion lens of numerical aperture 1.25. Emissions of 405 *nm*, 561 *nm*, and 633 *nm* laser lines were used to excite the Hoechst, VE-Cadherin and SMA fluorophores respectively. Z-stack slices (1024 × 1024 pixels) were acquired every 1 μm and by applying the deepness correction set-up provided by the microscope. The final number of slices acquired depended on particular antibody penetration and ranged between 54 and 95 μm. The resulting voxel size was 0.3785 μm × 0.3785 μm × 1.007 μm, or 0.3142 μm × 0.3142 μm × 1.007 μm in a few cases. In total, 126 multichannel images, 18 per tissue condition (9 per subject), were acquired and they were used for the analysis at time-points 1, 3, 7 days post MI and under basal conditions. Additionally, 36 images, 18 from infarcted (6 per subject) and 18 from remote areas (6 per subject), were acquired in the same manner and they were used for investigating microvascular characteristics and changes at 45 days following MI.

The same imaging system and procedure were also used to acquire images from tissue simultaneously labelled using anti-CD31, anti-SMA and anti-PDGFRB/anti-vimentin. However, emissions of 405 *nm*, 488 *nm*, 561 *nm*, and 633 *nm* laser lines were used to excite the Hoechst, CD31, SMA and PDGFRB or vimentin fluorophores, respectively. In the case of tissue simultaneously labelled with anti-CD31, anti-SMA and anti-collagen I, the image acquisition process followed was the same, with the difference that the Nikon A1R confocal microscopy was used.

Multi-scale Multi-level Thresholding (MMT). The first step towards quantifying the microvasculature and its infarction-related dynamic changes is to automatically segment the labelled structures of the VE-Cadherin, SMA and of the Hoechst channels. Towards this aim, the multi-scale multi-level thresholding algorithm[30] is applied to every channel of the 3D confocal image.

Multi-scale multi-level thresholding has been previously described in detail[30]. In essence, grids of boxes of various sizes $e = 1, .., N$ were applied to the original de-noised image I. For every grid size e, a candidate segmentation (V_e) was produced by applying Otsu's multi-level thresholding[63] to each box comprising the grid in order to separate I into M intensity levels. Subsequently, only the two highest intensity levels were retained as part of the structure under investigation. Final segmentation was produced by using the majority rule on candidate segmentations.

In the case of the VE-Cadherin channel, the segmentation is further improved by excluding possible artefacts, i.e. objects that are smaller than 100 voxels and that do not have a nucleus.

Fractal-based Metrics. Fractal dimension was calculated by applying the box-counting method in the 3D volume of the reconstructed microvasculature. In brief, grids of boxes of different sizes were overlaid on the microvasculature. Fractal dimension was estimated by

$$Fd = -lim\frac{ln(n(e))}{ln(e)} \tag{1}$$

where $n(e)$ is the number of boxes of size e needed to cover the object under investigation. We subsequently identify the cut-off scales over which the microvascular structures no longer present self-similarity[64], i.e. can not be considered as fractals. This additional step was considered necessary because real-life objects, such as the vascular patterns, might not present self-similarity over an infinite range of scales but rather over finite scales. However, no statistically significant difference was observed between the calculation of fractal dimension with and without cut-offs. This might be explained by the limited physical scales of the microvascular patterns in our dataset. Consequently, the fractal dimension presented in this manuscript is without cut-offs.

Lacunarity was calculated by using the gliding box method[36]. Boxes of various sizes e were glided over the 3D binary volume of the segmented microvasculature by 1 voxel. For every box size e, the total number of boxes of size e ($N(e)$) and the number of vascular voxels ($P(n,e)$) inside every box $n = 1, .., N(e)$ were taken into account. The sum of the number of voxels belonging to the microvasculature in every box $n = 1, ..., N(e)$ was calculated ($Q_1 = \sum_{n=1, .., N(e)} P(n, e)$), as well as the sum of the square number of vascular voxels ($Q_2 = \sum_{n=1, .., N(e)} P(n, e)^2$). Lacunarity for box size e was then given by

$$L(e) = \frac{N(e) \times Q_2}{{Q_1}^2} \tag{2}$$

In order to tackle the dependence of lacunarity on image density and to be able to compare images of various densities as the ones comprising our dataset, lacunarity was subsequently normalized using the lacunarity of the complementary image ($cL(e)$) by $L_{norm}(e) = 1 - \frac{1}{L(e)} - \frac{1}{cL(e)}$. Lacunarity over all scales, i.e. all box sizes, is finally defined as the mean of the normalized lacunarity of individual scales.

Succolarity was calculated according to previous study[65]. The areas where blood can flow through the microvasculature are the vascularized areas, while the non-vascularized were considered to be obstructing the flow. There are six possible directions of flow in the case of the 3D microvasculature: horizontal flow from left to right and vice versa, vertical flow from top to bottom and vice versa, and in-depth blood flow from the upper to the lower slices and vice versa. The volume of the 3D microvasculature was decomposed in six 3D images, one per flow direction. Each of those images contained only microvascular parts that would allow a continuous flow, if blood was to enter from that particular direction.

Grids of boxes of different sizes, as in the case of the box counting method, were applied on the decomposed images. The occupation percentage of vascular voxels ($O(n,e)$) inside each box n of size e, as well as an indicator of pressure ($PR(e)$), were calculated. $PR(e)$ was calculated based on the coordinates of the centroid of the box along the direction under investigation. Therefore, in the cases of horizontal, vertical and in depth directions of blood flow respectively, the pressure was given by the x, y and z coordinates respectively. A normalized version of succolarity was given by dividing the pressure in the case of 100% occupation with vascular voxels for all boxes. Therefore,

$$S(e, d) = \frac{\sum_{n=1, ..., N(e)} OP(n, e) \times PR(e)}{\sum_{n=1, .., N(e)} PR(e)} \tag{3}$$

Taking into account all 6 directions, the overall succolarity was approximated as

$$S = \frac{1}{6} \sum_{d=1, ..., 6} \sum_{e} \frac{S(d, e)}{N(e)} \tag{4}$$

where $N(e)$ refers to the total number of boxes of size e comprising the grid.

Minkowski Metrics. For an arbitrary object A in the d-dimensional Euclidean space $\mathbb{R}^d$, there exist $d+1$ Minkowski Functionals (MF) $M_n(A)$ with $n = 1, .., d+1$. Therefore, in $3-D$ space, there exist four MF, which are

proportional to the commonly known properties volume (M_1), surface area (M_2), mean integral of breadth (M_3) and Euler-Poincaré characteristic (M_4). The MFs for the 3D microvasculature are calculated by[35]:

$$\begin{aligned} M_1(V) &= n_c \\ M_2(V) &= -6n_c - 2n_f \\ M_3(V) &= 3n_c - 2n_f + n_e \\ M_4(V) &= -n_c + n_f - n_e + n_v \end{aligned} \tag{5}$$

where n_c is the total number of voxels that the microvasculature consists of, n_f is the number of open faces, n_e the number of edges and n_v the number of vertices.

In the present work, we normalize the MFs by the volume of the tissue from which the microvasculature was reconstructed to obtain density, surface area density, breadth density and Euler-Poincaré characteristic density. Normalization was performed in order to allow the comparative analysis of the MFs among different images. This would otherwise have not been possible due to the variability found in tissue volume among the images of our dataset.

Graph-based representation and related metrics. In order to convert the microvasculature to a 3D graph that encompasses the topological information of the network, the reconstructed microvasculature is firstly skeletonized through the use of a thinning algorithm[66]. The skeleton is converted to a graph consisting of nodes that represent the branching or end nodes that could be possible sprouts (mean and standard deviations presented in Table 1) of the microvascular network and the edges (i.e. segments) that represent the skeleton parts between two consecutive nodes[67]. Subsequently, to eliminate false short spurs produced by the thinning procedure, the 3D image volume with possible areas of arterioles/venules obtained after Frangi filtering (G) introduced previously, is used. G allows us to guide a local, pruning process during which end segments (segments defined between a branching node and an ending node) are pruned based on their length and type (capillaries or arterioles/venules). More precisely, segments whose length is smaller than one-and-a-half times the diameter of the smallest capillary ($4.1\,\mu m$), found in the LV of the pig heart according to[13], are used in areas that the 3D G indicated that corresponded to capillaries. On the other hand, on those areas that correspond to arterioles/venules according to G, the segments are pruned when their length is smaller than one-and-a-half times the diameter of the smallest arteriole/venule of order 1 ($8.96\,\mu m$)[13]. The pruning procedure is repeated twice to ensure that spur "Y"-shaped segments, resulting from the thinning process, are entirely pruned. The branching and end-nodes of the skeleton are extracted as nodes with more than one and only one neighbouring point respectively by convolving the 3D skeleton of the image with a $3 \times 3 \times 3$ sized mask of ones. Bubble-like nodes resulting as an artefact of the skeletonization process are replaced by the central node. The radius of each segment is calculated using the distance of the points on the skeleton to the closest non-vascular element. Among the distances, the radius is set equal to the largest one. Every segment of microvasculature between two nodes i,j is subsequently considered a tube of constant diameter (d_{ij}), length (L_{ij}) and the following metrics at segment level are calculated as in[68]:

$$\begin{aligned} \textit{Vascular segment volume } (V_{ij}) &= \frac{\pi \times d_{ij}^2 \times L_{ij}}{4} \\ \textit{Vascular segment surface } (S_{ij}) &= \pi \times d_{ij} \times L_{ij} \\ \textit{Tortuosity} &= \frac{L_{ij}}{\textit{Euclidean distance between i and j}} \\ \textit{Vascular length density } (L_d) &= \frac{1}{V} \times \sum_{ij=1,\ldots,N} L_{ij} \\ \textit{Vascular surface density} &= \frac{1}{V} \times \sum_{ij=1,\ldots,N} S_{ij} \\ \textit{Vascular volume density } (V_d) &= \frac{1}{V} \times \sum_{ij=1,\ldots,N} V_{ij} \\ \textit{Diffusion distance } (D) &= \frac{1}{\sqrt{\pi \times L_d}} \end{aligned} \tag{6}$$

where V is the volume of the tissue and N is the total number of segments that form part of the microvasculature.

Nuclei counting. The number of nuclei first had to be calculated in order to calculate the number of α-SMA$^+$ and endothelial cells. For this purpose, 3D watershed transformation[69] was applied to the segmentation of the Hoechst channel in order to separate merged nuclei. Nuclei belonging to α-SMA$^+$ were considered to be the ones with simultaneous staining of α-SMA and Hoechst. Nuclei belonging to endothelial cells were considered to be then ones that were overlapping with the surface of microvessels.

It should be noted that although watershed transformation is a popular approach for nuclei segmentation, it also tends to produce errors, such as over-estimation of nuclei. However, as development of novel tools for nuclei segmentation was beyond the scope of this work, watershed performed reasonably well for our approach and we, therefore, just adapted it for the task at hand. Nonetheless it is noted that the number of nuclei in this work might, therefore, not be precise.

Super-ellipsoids & Optimization. Super-ellipsoids are a type of 3D geometric shape that belongs to the same, more general family of geometric shapes named superquadrics[70]. Super-ellipsoids are implicitly defined by

$$\left[\left(\frac{|x - Cx|}{a}\right)^{\frac{2}{e_2}} + \left(\frac{|y - Cy|}{b}\right)^{\frac{2}{e_2}}\right]^{\frac{e_2}{e_1}} + \left(\frac{|z - Cz|}{c}\right)^{\frac{2}{e_1}} <= 1 \tag{7}$$

where a, b, c are scale factors for axis x, y and z respectively, Cx, Cy, Cz represent the centre of the super-ellipsoid, and e_1, e_2 control the shape of the super-ellipsoid. e_1 controls the squareness along z-axis and e_2 the squareness along plane x-y. Therefore, a variety of shapes can be determined by varying e_1 and e_2; $e_1 < 1$, $e_2 < 1$ result in cuboids, $e_2 = 1$ and $e_1 < 1$ in cylindroids, $e_1 = 1$, $e_2 < 1$ in pillow shapes, e_1 or e_2 larger than 2 in pinched shapes, e_1 or e_2 equal 2 in flat-beveled shapes.

Our aim was to identify a shape that the frequency distribution of distances of points inside the shape to the closest capillary (estimated distribution) best matches a given frequency distribution of maximum extravascular distances (target distribution). Toward this aim, the capillary was first approximated by a cylinder whose diameter was considered equal to the minimum extravascular distance observed. The length of the vessel was arbitrary chosen (100 μm). We subsequently set Cx, Cy, Cz as the coordinates of the centre of the vessel, b as the maximum extravascular distance observed, and c as length of the capillary, while the set of parameters a, e_1, and e_2 as the unknowns to be defined through optimization. The target of optimization was to minimize the mean square error between estimated and target distributions. The parameters were initialized so as to produce a cylinder (i.e. $e_1 = 1$, $e_2 = 0.2$) whose length is equal to that of the vessel ($c = 100\,\mu m$) and whose diameter (i.e. a,b) is equal to that of the maximum extravascular distance. In each step of the minimization procedure, a new set of parameters and, therefore, a new shape was defined by varying the unknown parameters in predefined ranges. In particular, parameter a was allowed to vary in the range between the minimum and maximum extravascular distance of the target distribution. Parameters e_1, and e_2 were allowed to vary between [0,3] and, therefore, cover all ranges of possible shapes. The minimization procedure stopped after a minimum was achieved in the root mean square error. It should be noted that a simplified version of the target distribution (10 bins) was used. Optimization is based on *fmincon* MATLAB (Mathworks) solver and sequential quadratic programming.

Machine learning. Multi-class classification was performed to predict the time that elapsed since the onset of MI for infarcted tissue and remote tissue ("Infarcted over time", and "Remote over time" respectively in Table 2). In all other cases, binary classifications were performed. 9-fold cross-validation repeated 10 times was used. k-fold validation is a common model approach in machine learning that helps to avoid overfitting the training set and it is usually repeated a multitude of times to ensure different separation of folds. The idea behind k-fold cross-validation is to divide the sample in k equal folds of which k-1 are used for training and one is kept for testing.

In this work, three different classifiers were employed. K-nearest neighbours classifier (Knn) assigns an unseen object to a class, based on the labels of the k-nearest training objects that are closest (or more similar) to the object under investigation. Here, we used 1-Knn classifier, e.g. the tissue is classified according to the label of the closest training tissue. The distance metric used was euclidean distance.

Support vector machines (SVMs) are inherently binary classifiers. Standard SVMs define a hyperplane function that guaranties optimum separation, e.g. largest margin, between the (training) data of the two classes. A new object is subsequently assigned to one or the other class based on whether the predefined hyperplane function is positive or negative for that particular object. The idea of reducing the multiclass classification problem to binary classification problems has been introduced and different approaches have been developed in order to perform multi-class classification with SVMs. In this work, we adapted the one-versus-one strategy according to which SVMs are built for all possible pairwise comparisons. Each class is, therefore, compared to each other separately.

Adaboost is based on a cascade of weak classifiers (learners) used to create a strong classifier which has higher accuracy that single classifiers. During each iteration of the training procedure, a learner is added so as to weight higher misclassified examples of the previous iteration and, therefore, to redirect the focus of subsequent weak learners in those examples. The strong classifier produced by a weighted sum of the weak learners is responsible for the assignment of labels to unseen objects. In this paper, we used Knn weak classifiers.

Statistical analysis. Statistical significance of differences in medians for pairwise comparisons was assessed by non-parametric, two-sided Wilcoxon rank sum tests. P-values were corrected for multiple testing with the Benjamini-Hochberg false discovery rate procedure which was applied to the fifteen pairwise tests performed per each quantified parameter. The number of samples per tissue category remained the same throughout this work and it equals to 18. Two sample Kolmogorov-Smirnov tests were performed to evaluate the statistical significance of differences in distributions.

3D Visualization. Visualization of 3D volumes (reconstructions, skeletons, distance maps) was performed with open-source softwares Paraview (http://www.paraview.org/) and ITK-SNAP (http://www.itksnap.org/).

Code availability. The code for all modules of the image processing pipeline presented in this work is open-source, along with the supporting documentation to run the modules separately or the complete pipeline at once. The statistical analysis and the creation of the comparative plots per metric was performed with an additional module of our pipeline, which is also available. Code/libraries from previous works necessary to run the pipeline are also provided and the creators have been credited accordingly. The code was written in MATLAB (Mathworks).

References

1. Fuster, V. & Kelly, B. *Promoting Cardiovascular Health in the Developing World: A Critical Challenge to Achieve Global Health. Institute of Medicine (US) Committee on Preventing the Global Epidemic of Cardiovascular Disease: Meeting the Challenges in Developing Countries* (National Academies Press (US), Washington (DC) 2010).
2. Finegold, J. A., Asaria, P. & Francis, D. P. Mortality from ischaemic heart disease by country, region, and age: Statistics from world health organisation and united nations. *International Journal of Cardiology* **168**, 934–945 (2013).
3. Ziaeian, B. & Fonarow, G. C. Epidemiology and aetiology of heart failure. *Nat Rev Cardiol* **13**, 368–378 (2016).
4. Petersen, J. W. & Pepine, C. J. Microvascular coronary dysfunction and ischemic heart disease: Where are we in 2014? *Trends Cardiovasc Med* **25**, 98–103 (2015).
5. Camici, P. G., d'Amati, G. & Rimoldi, O. Coronary microvascular dysfunction: mechanisms and functional assessment. *Nat Rev Cardiol* **12**, 48–62 (2015).
6. Pries, A. R. *et al*. Resistance to blood flow in microvessels *in vivo*. *Circ. Res.* **75**, 904–915 (1994).
7. Popel, A. S. & Johnson, P. C. Microcirculation and hemorheology. *Annu Rev Fluid Mech* **37**, 43–69 (2005).
8. Wearn, J. T. The extent of the capillary bed of the heart. *J Exp Med* **47**, 273–290 (1928).
9. Brown, R. The pattern of the microcirculatory bed in the ventricular myocardium of domestic mammals. *Am J Anat* **116**, 355–374 (1965).
10. Bassingthwaighte, J. B., Yipintsoi, T. & Harvey, R. B. Microvasculature of the dog left ventricular myocardium. *Microvasc Res* **7**, 229–249 (1974).
11. Ludwig, G. Capillary pattern of the myocardium. *Methods Achiev Exp Pathol* **5**, 238–271 (1971).
12. Batra, S., Rakusan, K. & Campbell, S. E. Geometry of capillary networks in hypertrophied rat heart. *Microvasc Res* **41**, 29–40 (1991).
13. Kassab, G. S. & Fung, Y. C. Topology and dimensions of pig coronary capillary network. *Am. J. Physiol.* **267**, H319–H325 (1994).
14. Lee, J. C., Pullan, A. J. & Smith, N. P. A computational model of microcirculatory network structure and transient coronary microcirculation. *Conf Proc IEEE Eng Med Biol Soc* **5**, 3808–3811 (2004).
15. Kassab, G. S., Le, K. N. & F. Y., C. A hemodynamic analysis of coronary capillary blood flow based on anatomic and distensibility data. *Am J Physiol* **277**, H2158–H2166 (1999).
16. Carmeliet, P. Angiogenesis in life, disease and medicine. *Nature* **438**, 932–936 (2005).
17. Djonov, V., Baum, O. & Burri, P. Vascular remodeling by intussusceptive angiogenesis. *Cell Tissue Res* **314**, 107–117 (2003).
18. Pries, A. R., Reglin, B. & Secomb, T. W. Remodeling of blood vessels: responses of diameter and wall thickness to hemodynamic and metabolic stimuli. *Hypertension* **46**, 725–731 (2005).
19. Korn, C. & Augustin, H. G. Mechanisms of vessel pruning and regression. *Dev Cell.* **34**, 5–17 (2015).
20. Zakrzewicz, A., Secomb, T. W. & Pries, A. R. Angioadaptation: keeping the vascular system in shape. *News Physiol. Sci.* **17**, 197–201 (2002).
21. van der Laan, A. M., Piek, J. J. & van Royen, N. Targeting angiogenesis to restore the microcirculation after reperfused mi. *Nat Rev Cardiol* **6**, 515–523 (2009).
22. Clegg, L. E. & Mac Gabhann, F. Systems biology of the microvasculature. *Integr. Biol* **7**, 498–512 (2015).
23. Carmeliet, P. & Jain, R. K. Molecular mechanisms and clinical applications of angiogenesis. *Nature* **473**, 298–307 (2011).
24. Waters, S. *et al*. Theoretical models for coronary vascular biomechanics: progress and challenges. *Prog. Biophys. Mol. Biol.* **104**, 49–76 (2011).
25. Pawley, J. B. Handbook of Biological Confocal Microscopy (Springer, 2006).
26. Meijering, E., Carpenter, A. E., Peng, H., Hamprecht, F. A. & Olivo-Marin, J.-C. Imagining the future of bioimage analysis. *Nature Biotechnology* **34**, 1250–1255 (2016).
27. Eliceiri, K. W. *et al*. Biological imaging software tools. *Nature Methods* **9**, 697–710 (2012).
28. Peng, H. Bioimage informatics: a new area of engineering biology. *Bioinformatics* **24**, 1827–1836 (2008).
29. Buades, A., Coll, B. & Morel, J.-M. A non-local algorithm for image denoising. *CVPR* **2**, 60–65 (2005).
30. Gkontra, P. *et al*. A 3d fractal-based approach towards understanding changes in the infarcted heart microvasculature. In *Medical Image Computing and Computer Assisted Intervention (MICCAI), Lecture Notes in Computer Science (LNCS)*, vol. 9351, 173–180 (Springer 2015).
31. Jackson, W. F. Microcirculation. *In* Joseph Hill *&* Eric Olson *(Eds.) Muscle: Fundamental Biology and Mechanisms of Disease* 1197–1206 (2012).
32. Frangi, A., Niessen, W., Vincken, K. & Viergever, M. Multiscale vessel enhancement filtering. In *Medical Image Computing and Computer Assisted Intervention (MICCAI), Lecture Notes in Computer Science (LNCS)*, vol. 1496, 130–137 (Springer 1998).
33. Lorthois, S. & Cassot, F. Fractal analysis of vascular networks: insights from morphogenesis. *J Theor Biol* **262**, 614–633 (2010).
34. Captur, G., Karperien, A. L., Hughes, A. D., Francis, D. P. & Moon, J. C. The fractal heart - embracing mathematics in the cardiology clinic. *Nat Rev Cardiol* **14**, 56–64 (2016).
35. Legland, D., Kiêu, K. & Devaux, M.-F. Computation of minkowski measures on 2d and 3d binary images. *Image Anal. Stereol* **26**, 83–92 (2007).
36. Gould, D., Vadakkan, T., Poché, R. & Dickinson, M. Multifractal and lacunarity analysis of microvascular morphology and remodeling. *Microcirculation* **18**, 136–151 (2011).
37. Pries, A. R. & Secomb, T. W. Modeling structural adaptation of microcirculation. *Microcirculation.* **15**, 753–764 (2008).
38. Dobaczewski, M. *et al*. Vascular mural cells in healing canine myocardial infarcts. *Journal of Histochemistry & Cytochemistry* **52**, 1019–1029 (2004).
39. Frangogiannis, N. G. The immune system and cardiac repair. *Pharmacological Research* **58**, 88–111 (2008).
40. Ren, G., Michael, L. H., Entman, M. L. & Frangogiannis, N. G. Morphological characteristics of the microvasculature in healing myocardial infarcts. *J Histochem Cytochem* **50**, 71–79 (2002).
41. van den Borne, S. W. *et al*. Myocardial remodeling after infarction: the role of myofibroblasts. *Nat Rev Cardiol* **7**, 30–37 (2010).
42. Fan, H. *et al*. Role of pdgfr-b/pi3k/akt signaling pathway in pdgf-bb induced myocardial fibrosis in rats. *Am J Transl Res* **6**, 714–723 (2014).
43. Goldsmith, E. C., Bradshaw, A. D., Zile, M. R. & Spinale, F. G. Myocardial fibroblast-matrix interactions and potential therapeutic targets. *J. Mol. Cell. Cardiol.* **70**, 92–99 (2014).
44. Willems, I. E., Havenith, M. G., De Mey, J. G. & Daemen, M. J. The alpha-smooth muscle actin-positive cells in healing human myocardial scars. *Am J Pathol* **145**, 868–875 (1994).
45. Vracko, R. & Thorning, D. Contractile cells in rat myocardial scar tissue. *Lab Invest* **65**, 214–227 (1991).
46. Wu, X. *et al*. Top 10 algorithms in data mining. *Knowledge and Information Systems* **14**, 1–37 (2008).
47. Pries, A. R. & Secomb, T. W. Making microvascular networks work: Angiogenesis, remodeling, and pruning. *Physiology (Bethesda)* **29**, 446–455 (2014).
48. Cassot, F., Lauwers, F., Fouard, C., Prohaska, S. & Lauwers-Cances, V. A novel three-dimensional computer-assisted method for a quantitative study of microvascular networks of the human cerebral cortex. *Microcirculation* **13**, 1–18 (2006).
49. Krogh, A. The number and distribution of capillaries in muscles with calculations of the oxygen pressure head necessary for supplying the tissue. *J Physiol* **52**, 409–415 (1919).
50. Anversa, P., Ricci, R. & Olivetti, G. Quantitative structural analysis of the myocardium during physiologic growth and induced cardiac hypertrophy: a review. *J Am Coll Cardiol* **7**, 1140–1149 (1986).

51. Watanabe, N. *et al*. Three-dimensional microstructural abnormality of the coronary capillary network after myocardial reperfusion–comparison between 'reflow' and "no-reflow'. *Circ J.* **68**, 868–872 (2004).
52. Brown, M. D., Davies, M. K. & Hudlicka, O. Angiogenesis in ischaemic and hypertrophic hearts induced by long-term bradycardia. *Angiogenesis* **8**, 253–262 (2005).
53. Campbell, D. J. *et al*. Reduced microvascular density in non-ischemic myocardium of patients with recent non-st-segment-elevation myocardial infarction. *Int J Cardiol* **167**, 1027–1037 (2013).
54. Koudstaal, S. *et al*. Assessment of coronary microvascular resistance in the chronic infarcted pig heart. *J Cell Mol Med* **17**, 1128–1135 (2013).
55. Hollander, M. R. *et al*. Dissecting the effects of ischemia and reperfusion on the coronary microcirculation in a rat model of acute myocardial infarction. *PLoS One.* **11**, e0157233 (2016).
56. Seidel, T., Edelmann, J. C. & Sachse, F. B. Analyzing remodeling of cardiac tissue: A comprehensive approach based on confocal microscopy and 3d reconstructions. *Ann Biomed Eng* **44**, 1436–1448 (2016).
57. Eissing, N. *et al*. Easy performance of 6-color confocal immunofluorescence with 4-laser line microscopes. *Immunol. Lett.* **161**, 1–5 (2014).
58. Smith, A. F., Secomb, T. W., Pries, S. N. P. A. R. & Shipley, R. J. Structure-based algorithms for microvessel classification. *Microcirculation* **22**, 99–108 (2014).
59. Cleutjens, J. P., Blankesteijn, W. M., Daemen, M. J. & Smits, J. F. The infarcted myocardium: simply dead tissue, or a lively target for therapeutic interventions. *Cardiovasc Res* **44**, 232–241 (1999).
60. Ismail, J. A. *et al*. Immunohistologic labeling of murine endothelium. *Cardiovascular Pathology* **12**, 82–90 (2003).
61. Pusztaszeri, M. P., Seelentag, W. & Bosman, F. Immunohistochemical expression of endothelial markers cd31, cd34, von willebrand factor, and fli-1 in normal human tissues. *Journal of Histochemistry & Cytochemistry* **54**, 385–395 (2006).
62. Vestweber, D. Ve-cadherin the major endothelial adhesion molecule controlling cellular junctions and blood vessel formation. *Arterioscler Thromb Vasc Biol* **28**, 223–232 (2008).
63. Otsu, N. A. Threshold selection method from gray-level histograms. *IEEE Transactions on Systems, Man, and Cybernetics* **9**, 62–66 (1979).
64. Berntson, G. M. & Stoll, P. Correcting for finite spatial scales of self-similarity when calculating fractal dimensions of real-world structures. *Proceedings of the Royal Society B: Biological Sciences* **264**, 1531–1537 (1997).
65. Melo, A. & Conci, R. H. C. How succolarity could be used as another fractal measure in image analysis. *Telecommunication Systems* **52**, 1643–1655 (2013).
66. Lee, T., Kashyap, R. & Chu, C. Building skeleton models via 3-d medial surface/axis thinning algorithms. *Computer Vision, Graphics, and Image Processing* **56**, 462–478 (1994).
67. Kerschnitzki, M. *et al*. Architecture of the osteocyte network correlates with bone material quality. *J Bone Miner Res* **28**, 1837–1845 (2013).
68. Stamatelos, S., Kim, E., Pathak, A. & Popel, A. A bioimage informatics based reconstruction of breast tumor microvasculature with computational blood flow predictions. *Microvasc Res.* **91**, 8–21 (2014).
69. Meyer, F. Topographic distance and watershed lines. *Signal Processing* **38**, 113–125 (1994).
70. Barr, A. H. Superquadrics and angle-preserving transformations. *IEEE Comput Graph Appl* **1**, 11–23 (1981).

Acknowledgements

The authors would like to thank Ángel Colmenar for staining tissues for four of the subjects. The authors would also like to express their gratitude to Carlos Galán Arriola for providing us with the tissue from infarcted pigs at 45 days post MI along with the characteristics of the corresponding subjects and MRI-based estimations of blood flow. The research leading to these results has received funding from the People Programme (Marie Curie Action) of the European Union's Seventh Framework Programme (FP7/2007-2013) under REA grant Agreement 608027. This work was also supported by grants from the Spanish Ministry of Economy and Competitiveness SAF2014-52050-R to A.G.A., TEC2015-66978-R to A.S. and SAF2013-49663-EXP to B.I., from the Institute of Health Carlos III and the European Regional Development Fund (ERDF/FEDER) PI13/01979 to B.I., from La Marató TV3 Foundation to A.G.A., and from NIH grant R01HL101200 to A.P. The CNIC is supported by the Ministry of Economy, Industry and Competitiveness (MINECO) and the Pro CNIC Foundation, and is a Severo Ochoa Center of Excellence (SEV-2015-0505).

Author Contributions

P.G. designed and developed the pipeline, performed the experiments, analysed the results, and wrote the manuscript. K.A.N. and A.G.A. contributed in the design of the pipeline and analysis of the results. M.M.Z. optimized the protocol for the immunofluorescence staining of the tissue and performed the staining for four of the subjects. P.G. and M.M.Z. acquired the images. C.C. performed the stainings from tissues at 45 days post MI, the simultaneous staining of thin tissues with different markers of myofibroblasts, and imaging of tissues labelled with collagen I. J.A. performed the infarction to the pigs. A.G.A. conceived and supervised the project. K.A.N., B.I., A.S., A.S.P. and A.G.A. advised the project. All authors reviewed the manuscript.

Additional Information

Supplementary information accompanies this paper at https://doi.org/10.1038/s41598-018-19758-4.

Competing Interests: The authors declare that they have no competing interests.

Publisher's note: Springer Nature remains neutral with regard to jurisdictional claims in published maps and institutional affiliations.

Chapter 18

3D Image Analysis of the Microvasculature in Healthy and Diseased Tissues

Álvaro Sahún-Español, Cristina Clemente, and Alicia G. Arroyo

Abstract

The vasculature ensures optimal delivery of nutrients and oxygen throughout the body. The ability to respond to changing tissue demands requires constant reshaping of the vascular network through modulation of its density, diameter, or patterning. These processes are especially prominent after tissue damage or in tumors. The matrix metalloproteinase (MMP) family of endopeptidases are key contributors to vascular remodeling, able to cleave all extracellular matrix components and also soluble factors and membrane receptors. Observations recorded over several decades have established that the vasculature changes in pathological contexts, and this has formed the basis for developing angiotherapies as a novel approach to treating disease. For example, inhibition of angiogenesis or normalization of the vasculature has been proposed as treatment for cancer and chronic inflammatory diseases. In contrast, boosting angiogenesis may be helpful in ischemic conditions such as myocardial infarction and in regenerative medicine. Classical histological methods for the analysis of tissue vasculature have relied on thin sections that do not capture the complex 3D structure of the vascular network. Given the importance of understanding disease-associated vascular changes for the development of rational angiotherapeutic interventions, we present a protocol for thick section-based 3D image analysis of vasculature structure and function.

Key words Vasculature, Thick section, Volumetric, Three-dimensional, Mouse, Confocal microscope, Quantification

1 Introduction

The vasculature must continually adapt to tissue demands in order to ensure optimal delivery of nutrients and oxygen throughout the body, particularly after tissue damage or in tumors. This adaptation requires constant reshaping of the vascular network by modulating its density, diameter, and/or complexity. Being aware of the vasculature changes in pathological contexts, researchers have proposed angiotherapies as a feasible treatment strategy.

When activated, the normally quiescent vasculature promotes the formation of new vessels from pre-existing ones in a process called angiogenesis. Angiogenic vascularization is a critical step in tumor growth, with tumors reportedly unable to grow in the

Santiago Cal and Alvaro J. Obaya (eds.), *Proteases and Cancer: Methods and Protocols*, Methods in Molecular Biology, vol. 1731, https://doi.org/10.1007/978-1-4939-7595-2_18,

absence of proper vascularization to more than 2–3 mm in diameter [1]. In addition, vascularization not only provides the tumor with nutrients but is also necessary for metastasis to occur [2, 3]. Because of this, some therapies are focused on abrogating tumor angiogenesis by depriving the tumor of oxygen and nutrients, causing a reduction in tumor growth. This therapeutic approach is very common for some types of cancer, such as breast cancer [4]. However, vascular architecture in the tumor is chaotic and tortuous, with vessels having irregular diameters and poor functionality due to improper lumen formation. Tumor vasculature also has defects in pericyte coverage and in endothelial cell junctions, making it highly permeable to nutrients and metastatic cells [5]. This extremely complex and abnormal vasculature has raised questions about drug delivery and efficacy of anti-angiogenic therapies [6]. An alternative approach is to normalize the aberrant vasculature to make the tumor more accessible to drugs, which has proved successful with some types of cancer [7]. In other cancers, such as pancreatic cancer, tumor growth and spread are reduced by strategies to increase vascular development [8]. These examples demonstrate the importance of a thorough understanding of the vascular plexus when deciding on the appropriate therapeutic approach.

Understanding the vascular architecture is essential not only for tumor angiotherapies but also for other pathological settings. A prominent example is regenerative medicine. An injured tissue needs to be revascularized in order to obtain oxygen and nutrients and to allow infiltration by effector immune cells for proper repair and regeneration [9]. Much of the attention in this area is focused on heart repair after myocardial infarction, and boosting angiogenesis after an ischemic event is considered one of the most promising approaches to improving cardiac repair and avoiding negative postinfarction effects [10, 11]. In the case of the injured heart, it is also important to understand the process of arteriogenesis, the growth of functional collateral arteries from pre-existing arterio-arteriolar anastomoses.

Angiotherapies are thus relevant to a broad spectrum of pathologies, including tumors and chronic inflammatory diseases that could benefit from angiogenesis inhibition or normalization of the aberrant vasculature. Ischemic disorders such as myocardial infarction by its part can benefit from boosting the vascularization as a promising strategy to promote tissue repair and regeneration. Angiotherapies have classically targeted angiogenic factors such as VEGFA and related receptors; however, other potential targets are the matrix metalloproteinases (MMPs), a family of proteolytic enzymes that make a varied contribution to angiogenesis and vasculature remodeling. MMPs are endopeptidases that play an important role in extracellular matrix (ECM) degradation and also modulate the bioactivity of soluble factors and membrane receptors. There are currently 25 metalloproteinases characterized in

mammals [12–14]. MMPs such as MT1-MMP (MMP14) directly degrade the ECM, allowing ECs to migrate and form the vascular net in vitro and in vivo [15, 16]. In addition, the degradation of their substrates releases peptidic fragments that modulate angiogenesis. Examples include the proangiogenic C-terminal noncollagenous 1 domains produced by the degradation of collagen [17] and the VEGFA inhibitor endostatin, generated by the activity of MMP3, MMP9, MMP12, MMP13, and MMP20 [18]. MMPs can also process other proteins related to angiogenesis. For example, MMP9 can release VEGFA from the ECM, allowing its binding to VEGFR and thus promoting the angiogenic switch in tumors [19]. In addition, MMP9 and MMP14 (MT1-MMP) can both release and activate TGF-β [19, 20].

Quantitative assessment of the structure and function of the vasculature is thus of key importance (1) to increase knowledge about the basic mechanisms by which the vasculature contributes to tissue damage and repair and (2) for the implementation of rational angiotherapies adapted to specific pathophysiological contexts.

When studying the vasculature under pathological conditions, it is important to address parameters related to the abundance, function, and pattern of the vasculature. This is achieved by quantitating endothelial cell (EC) content, vascular volume fraction or density, vessel number and length, and also other parameters such as pattern and order (tortuosity, thickness), maturation (perivascular coverage), and functionality (vascular perfusion, vascular stability, and leakage). All these parameters are essential indicators of vasculature status [21], and a precise understanding should be considered together with the three-dimensional (3D) structure of the vascular network, a feature of the vascular architecture that has been often dismissed. Tissue vasculature is conventionally analyzed by histology and immunohistochemistry for specific markers on 5–10 μm sections. These approaches have yielded crucial information about the number and density of capillaries, EC content, and perivascular coverage. Moreover, analysis of sections from tissue perfused with antibodies or dextran has allowed partial functional analysis [22]. However, in recent years, the need to understand the vasculature as a connected network has prompted researchers to move from the use of thin sections that provide 2D information to thicker sections that allow 3D volumetric studies (Table 1). Some specific vascular plexus have a flattened structure, such as the superficial vascular plexus of the postnatal retina [23, 24]; however, many other vascular nets develop in 3D, with vessels sprouting in all directions [25]. Because of this, 3D image acquisition and analysis is becoming an essential requirement for vascular biology researchers [26]. To reconstruct the vascular tree and enable reliable data quantification, we and others [26] specifically recommend the use of 40- to 50-μm-thick sections or whole-mount

Table 1
Pros and cons of 2D vs 3D imaging

Method	Advantages	Limitations
2D	Low sample requirements	Loss of structural network
	Quick (staining protocol, image acquisition, quantification)	Only able to quantify vascular area or endothelial cell number
	Low tool requirements (standard fluorescence microscope, widely used analysis software)	Difficult to visualize rare events (tip cells or intussusception)
		Loss of tissue integrity even in serial slicing, you can lose some material because of the cut
3D	Visualization of structural network	More sample requirements
	Visualization of rare events (tip cells or intussusception)	Time consuming (staining protocol, image acquisition, quantification)
	Possibility to quantify parameters such as branching points or tortuosity	Specific tool requirements (mandatory use of confocal microscope and 3D analysis software)
	Maintenance of tissue integrity	Depth limitation for antibody penetration
	Parameters with direct biological meaning (true vessel length)	

samples of thin tissues (such as skin or gut); this task may be facilitated by new optimized clearing protocols [27].

New or improved protocols for the study of the vascular network in tissues are of great interest to scientists working in fields from oncology to regenerative medicine. Here we present a protocol for 3D analysis of the vascular plexus architecture and its functionality. This protocol can be used for the in-depth study of changes to the vasculature in pathologies such as cancer and myocardial infarction among others as well as the impact of specific molecular pathways or angiotherapies.

2 Materials

2.1 Mouse Injection for Functional In Vivo Analysis

1. Homemade restraining device. For IV injection, the mouse must be immobilized. This restraining accessory, made by 3D printing, allows the researcher to restrict mouse movement, leaving the tail exposed in the correct position for IV injection. Both ends of the device are open, one to allow the mouse to breathe and the other to leave the tail exposed. If this device is unavailable, a conical centrifuge tube open at both ends can be used instead.
2. Warming chamber.
3. 70% ethanol.
4. 1 mL syringe.
5. 25 G needles.
6. Dextran tetramethylrhodamine 70,000 MW (dextran-TRITC).
7. *Griffonia simplicifolia* lectin I/isolectin B4 (IB4).
8. Anesthesia: Medeson 1 mL (medetomidine/Domtor), Zoletil 100 mg (tiletamine + zolazepam).
9. Dextran-TRITC preparation: Dissolve lyophilized dextran-TRITC in PBS at 71.5 μM (5 mg/mL), aliquot, and store at −20 °C in the dark.
10. Anesthesia preparation: To prepare Zoletil, add 5 mL of solvent liquid to the lyophilized reagent and mix, and then add 20 mL of saline solution and mix. To prepare Domtor, add 9 mL of saline solution to 1 mL of reagent and mix. For anesthesia, mix the Zoletil and Domtor preparations 1:1, prepare 1 mL aliquots, and store at −20 °C until use.

2.2 Tissue Dissection and Processing

1. CO_2 chamber.
2. Dissection material: Forceps, scissors.
3. Phosphate-buffered saline (PBS): Dissolve 8 g of NaCl (final 137 mM), 1.78 g Na_2HPO_4 dihydrate (final 10 mM), 0.2 g KCl (final 2.7 mM), and 0.24 g KH_2PO_4 (final 1.8 mM) in 500 mL Milli-Q water. Sterilize at 121 °C for 20 min and adjust to pH 7.4. Store at room temperature.
4. 10 mL syringe.
5. 30 G needles.
6. Paraformaldehyde powder (PFA): Warm 400 mL PBS to 60 °C. Next, add 16 g of PFA (highly toxic! Use a biohazard hood and prepare in the dark). When dissolved, filter with a 0.22 μm filter and adjust to pH 7.4. Store in the dark at 4 °C for up to a week; for longer periods, store 10–13 mL aliquots at −20 °C.

7. Sucrose.
8. Intermediate Cryomold.
9. Optimal cutting temperature compound (OCT, Tissue-Tek O.C.T. Compound).
10. Sucrose solution preparation: 0.44 and 0.88 M (15% and 30%, respectively) sucrose solutions are prepared by dissolving 1.5 or 3 g of sucrose in 10 mL PBS. Stir until sucrose is totally dissolved. Solutions are best prepared fresh for every experiment but can be stored for short periods at 4 °C.

2.3 Tissue Cutting

1. Cryostat.
2. Cutting material: Blades, forceps.
3. 48-well flat-bottom cell culture plates.

2.4 Staining

1. Methanol.
2. Hydrogen peroxide, 30% w/v.
3. Triton X-100.
4. Normal goat serum (NGS). Dissolve the vial in Milli-Q water, aliquot, and store at −20 °C.
5. Rocker.
6. Blocking solution: 0.3% Triton X-100 + 2% NGS in PBS. Store at 4 °C.
7. Washing solution: 0.15% Triton X-100 in PBS.
8. Primary antibodies: Anti-CD31, anti-Erg, and anti-smooth muscle actin (anti-SMA) (Table 2).
9. Secondary antibodies: Alexa-647-conjugated goat anti-hamster, Alexa-488-conjugated goat anti-rabbit, Alexa-488-conjugated streptavidin (Table 2).
10. Hoechst 33342, trihydrochloride, trihydrate (Table 2).

2.5 Mounting

1. Paintbrush.
2. Petri dish.
3. Superfrost slides.
4. Coverslips.
5. Mounting medium (Fluoromount-G).

2.6 Image Acquisition

1. Confocal microscopy: For reliable 3D image acquisition, confocal microscopy with an automatized plate should be available, as well as the possibility for intensity adjustment through Z stacks during acquisition. In addition, a set of at least four wavelength channels is required: an ultraviolet laser (excitation ~352 nm, for Hoechst), a blue laser (excitation ~490 nm,

Table 2
List of antibodies and reagents used in this protocol

Marker	Supplier	Ref.	Dilution/ concentration	Staining	Comments
CD31	Millipore	MAB1398Z	1/200 2.5 µg/mL	ECs from blood and lymphatic vessels (membrane)	–
Erg	Abcam	ab92513	1/100 5 µg/mL	ECs (nuclear)	–
SMA	Sigma	C6198	1/300 5 µg/mL	VSMCs (cytoplasmatic)	Cy3 directly labeled
Dextran-TRITC	Invitrogen	D1819	100 µL of 5 mg/ mL	Permeability	i.v. injection
Isolectin B4 (IB4)	Vector	B-1205	100 µL of 0.5 mg/ mL	Perfusion	i.v. injection
2.4G2 (CD16/CD32)	BD Pharmingen	553142	1/100 5 µg/mL	Fc receptors	Blocking antibody
Alexa Fluor 647 goat α-hamster	Jackson ImmunoResearch	127-605-160	1/500 1 µg/mL	--	CD31 secondary antibody
Alexa Fluor 488 goat α-rabbit	Life Technologies	A11034	1/500 4 µg/mL	--	Erg secondary antibody
Alexa Fluor 488 streptavidin	Life Technologies	S32354	1/500 4 µg/mL	--	IB4 secondary antibody
Hoechst 33342	Invitrogen	H1399	1/5.000 2 µg/mL	Nuclei	--

for FITC and Alexa-488), a green laser (excitation ~556 nm, for dextran-TRITC and Cy3), and an infrared laser (excitation ~649 nm, for Alexa-647). We acquire images using a Nikon A1R confocal microscope with NIS-Elements software.

2.7 Image Quantification

1. Image analysis requires dedicated 3D software tools. Although 3D data can be processed with standard programs such as ImageJ with the use of specific plugins, we recommend the use of specialized software. Most of these programs use the voxel as the basic unit instead of the pixel (the homologous basic unit in two-dimensional images). They are generally able to perform analyses such as delimitation of a volumetric region, masking fluorescence in order to generate an individual mask containing the specific fluorescent signal of the raw channel, and 3D co-localization assays to detect structures that share the same location or are in close apposition. Volocity, Amira, or Bioimage 3D are all examples. Vaa3D, although more suitable for larger volumes (SPIM data), may be another option. Furthermore, computer programming in MATLAB can be used to generate specific plugins for these programs for improved 3D analysis. Here, analysis and semiautomatic quantifications are performed using Imaris 7.7.2 (Bitplane).

3 Methods

3.1 Mouse Procedures (Only for In Vivo Staining)

For in vivo staining, we use C57BL6 adult mice (15 weeks old):

1. Warm the mice to 39 °C in a warming chamber for 5–10 min to dilate the tail vein and flush with 70% ethanol (*see* **Note 1**).
2. Using a 25 G needle, inject 100 μL of 71.5 μM (5 mg/mL) of dextran-TRITC (70 kDa) intravenously 30 min previous to the sacrifice.
3. Using a 25 G needle, intravenously inject 100 μL of IB4 20 min before sacrifice (*see* **Note 2**).

3.2 Sample Collection

3.2.1 For In Vivo Staining

1. After dextran-TRITC and IB4 administration, mice were anesthetized by intraperitoneal injection with 200 μL of Zoletil/Domtor (Z/D).
2. Check the anesthesia with the plantar reflex.
3. Flush the animal with 70% ethanol and open the thoracic cavity without cutting large vessels.
4. Remove the lungs.
5. Perfuse the animal with 20 mL of 1% PFA by direct injection through the aorta (*see* **Note 3**).
6. Extract the tissue and place it in cold PBS.

7. Postfix the tissue with 4% PFA 2 h at 4 °C.
8. Place the samples in 30% (w/v) sucrose in PBS at 4 °C overnight (o/n).

3.2.2 For Ex Vivo Staining

1. Sacrifice mice in a CO_2 chamber.
2. Using a 10 mL syringe with a 30 G needle, perfuse the mice through the aorta with cold PBS until all blood is washed out.
3. Dissect the organ/tissue of interest and place it in 4% PFA o/n at 4 °C (*see* **Note 4**).
4. Wash the organ three times with PBS for 10 min each (*see* **Note 5**).
5. In order to preserve tissue structure when freezing, the sample must be embedded in sucrose. Place the sample in 15% (w/v) sucrose in PBS until it sinks at 4 °C. Then transfer it to 30% (w/v) sucrose in PBS again until it sinks at 4 °C.

3.3 Tissue Freezing and Sectioning

1. Put some drops of OCT in the Cryomold. Then, dry the sample gently with a piece of paper, and place it over the OCT drops in the correct orientation. Then fill the Cryomold with OCT and freeze and store the sample at −80 °C.
2. Take the OCT block from the Cryomold, and use a drop of OCT to attach it to the cryostat adapter in the desired orientation.
3. Take a 48-well plate and fill as many wells as staining panels you have with 300 μL PBS.
4. For 3D analysis, cut sections at around 40–50 μm thick. At this thickness, cutting along the OCT block produces a roll of OCT. This roll contains the thick tissue section and so must be gently collected using tweezers and placed in the well containing PBS. We recommend adding two to three sections per well in order to have technical replicates for each staining.

3.4 Immunostaining

1. Replace the PBS, and agitate the samples for 5 min at room temperature (RT) to eliminate residual OCT (*see* **Note 6**).
2. Add blocking solution to the wells and incubate for 1 h at RT (*see* **Note 7**).
3. Prepare the primary antibodies in fresh blocking solution. Each well requires 100 μL final volume to cover the sections. We recommend the following dilutions, although antibodies should be correctly titrated: 1/200 for CD31 (used for in vivo and ex vivo staining) and 1/100 for Erg (used for ex vivo staining).
4. Add the diluted primary antibodies to the sections and incubate at 4 °C o/n with gentle agitation.

5. The next day, wash the sections three times for 30 minutes in washing solution followed by a further wash for 1 h.
6. To the washed sections, add directly labeled anti-SMA antibody (used in ex vivo staining) at 1/300 in blocking solution and also add the secondary-labeled antibodies diluted 1/500. We recommend goat anti-hamster 647 for CD31 and goat anti-rabbit 546 for Erg. For in vivo IB4 staining, add Alexa-488-conjugated streptavidin at 1/500. Finally, add also Hoechst for nuclear staining at 1/5000 (*see* **Note 8**).
7. Incubate secondary antibodies o/n at 4 °C with gentle agitation (*see* **Note 9**).
8. The next day, wash the sections four times in washing solution for 30 min each. Finally, wash the sections for 1 h in PBS without detergent.
9. Mount the sections on slides. Remove the sections from the wells using a paintbrush, and place them in a PBS-filled petri dish. Using the paintbrush, pick sections up one at a time and place them on the slide.
10. Once the sections are attached to the slide, remove the PBS and dry the surface thoroughly. Fluoromount-G or other mounting medium can then be added and a coverslip placed over the sections.

3.5 Image Acquisition

1. Place the slide on the confocal microscope stage and use the 10× objective to find the tissue section of interest. Change the objective depending on the requirements (for general visualization of the vascular plexus, 10× should be enough; when studying cells, 20× is recommended). Finally, adjust the focus to examine the sample.
2. Once a representative area for analysis has been located, acquire confocal sections every 1 μm through the entire sample depth. If possible, maintain a constant temperature in order to avoid loss of focus, and try to adjust the intensity along Z stack acquisition. If tile scanning, set up the overlay at 10%. Laser parameters should be adjusted according to the staining performance; however, the intensity should be set at 20–30% of the total laser intensity for all markers except for Hoechst (nuclear signal) and the anti-SMA and anti-CD31 antibodies, whose bright signal will require 12–15% laser intensity. Offset should not exceed −15, and gain should be set at around 110–130, except for anti-SMA and anti-CD31, for which gain should be no more than 100. We recommend a resolution of 1024 × 1024. With these settings, a four laser 3 × 3 tile scan with 45 stacks (45 images) will require approximately 1 h of acquisition (*see* **Note 10**).

3. A stack of sequential images will be obtained covering the full thickness of the sample. Maximal intensity projection (MIP) generates a consensus image to present the volumetric information in 2D. Nevertheless, MIP may overestimate some parameters such as vessel density [21] (*see* **Note 11**). In the current protocol, we therefore propose analysis and quantification of the 3D composition provided by the image stack without a preprocessing step that eliminates 3D properties.

As an example, we show representative images of CD31 staining obtained in thick sections (xenograft tumor) and whole mount (skin wound healing) (Fig. 1a). The same figure shows representative images of cardiac injury (neonatal cryoinjury and adult permanent ligation of the left anterior descending [LAD] artery) obtained with different antibodies (Fig. 1b, ex vivo, and Fig. 1c, in vivo).

3.6 Image Quantification

3.6.1 Generation of Volumes of Interest (VOI)

When the image contains healthy and injured areas (Figs. 1 and 2) or any regions of specific interest, these areas should be selected and isolated so that they can be analyzed separately. The first step is thus to extract 3D regions containing the information you want to quantify:

1. To generate the volume of interest (VOI), a region of interest (ROI) is drawn in a section in the middle of the stack. The same ROI is then copied to the other images in the stack (*see* **Note 12**).
2. The 3D software will connect these ROIs to create a 3D mask. This mask is a volumetric selection containing the whole volume of interest. This volume can be analyzed independently, allowing injured and healthy regions to be analyzed separately.

The mask contains the fluorescence channels of every antibody used, enabling analysis of different parameters. For a first screening, the structural parameters of the vascular plexus can be analyzed, including the number of endothelial cells, perivascular coverage, general vascular density, and even volumetric parameters specifically related to capillary structure or to the presence of arterioles. A functional analysis can then be used to calculate number of perfused (functional) vessels or dextran extravasation (vascular leakage). Other analysis options include calculation of arteriolar thickness or further analysis of the leakiness of the vascular net. We use cardiac injury (both cryoinjury and LAD ligation) as a model for all these analyses because it provides a vascular plexus containing capillary and arteriolar structures and showing impaired function.

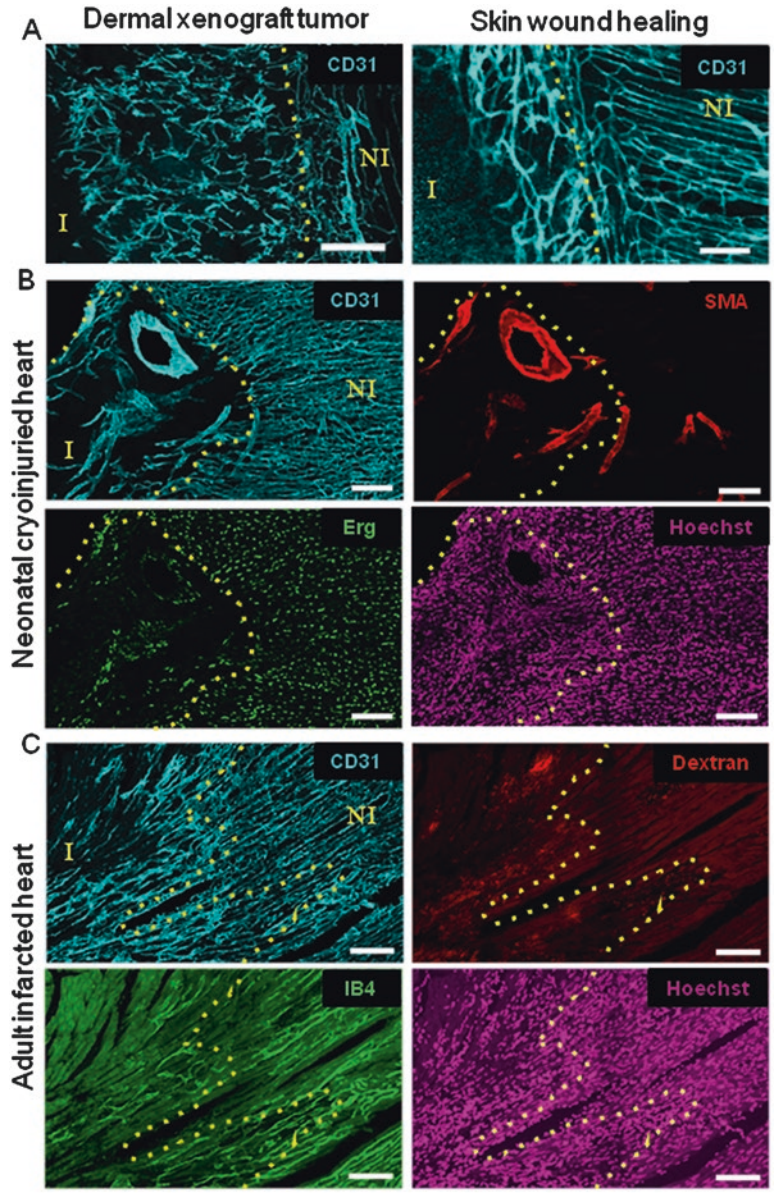

Fig. 1 Examples of immunostaining in thick sections (50 μm). (**a**) CD31 staining in a thick section of a dermal xenograft tumor (left) and a whole mount of wounded skin on day 6 post wound (right). (**b**) Sections of neonatal heart cryoinjured (CI) at P1, dissected at 14 days post-CI and stained for Hoechst, Erg, CD31, and SMA. (**c**) Sections of adult heart infarcted by left anterior descending (LAD) artery ligation, dissected 3 days post-injury and stained for Hoechst, isolectin B4, CD31, and dextran (70 kDa). Dotted lines separate the healthy region (right) from the injured area (left). *I* injured, *NI* noninjured; Scale bar: 200 μm in **a** left and 100 μm in **a** right, **b** and **c**

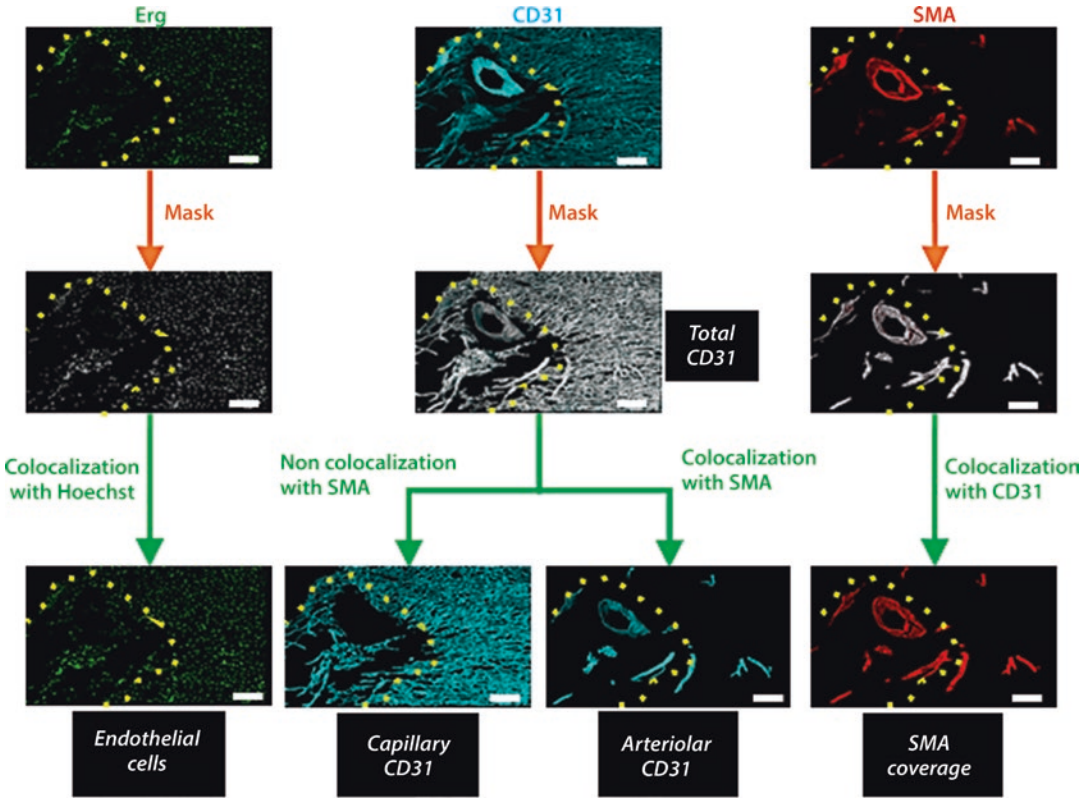

Fig. 2 3D image quantification workflow: vascular architecture quantification. From the masks for CD31, SMA, and Erg, we obtain volumetric three-dimensional information about the endothelial arteriolar and capillary structures as well as about SMA coverage and endothelial cell number. Scale bar: 100 μm

3.6.2 Structural Parameters (Fig. 2)

Here we provide guidelines for analyzing vasculature-associated cellular components as well as the basic structural parameters related to volumetric quantitation of the vasculature and its coverage by SMA^+ perivascular cells. As an example, we use the cryoinjury model in a P1 postnatal heart 14 days after cryoinjury.

1. One of the most important components of the vascular plexus is the population of endothelial cells (ECs) forming the vascular net. Before extracting volumetric information about the vascular plexus, EC content can be measured by generating a mask from the Erg^+ fluorescence channel. This mask identifies each of the Erg^+ nuclei, and dedicated 3D software quantifies the number of Erg^+ nuclei.
2. A more precise measure of EC number requires a refining step. Since Erg is a nuclear marker, the Erg signal should co-localize with Hoechst (nuclei). Therefore, after generating the Erg mask (**step 1**), a Hoechst co-localization assay should be performed and only cells doubly positive for Erg and Hoechst

considered as ECs. In the co-localization analysis, the 3D software takes each positive Erg unit and checks if the associated voxels (volumetric information homologous to the pixels in 2D images) are also positive for the Hoechst fluorescence signal. If voxels for a cell in the Erg mask also show an intense Hoechst signal, the software will mark the double-positive cell as a genuine EC.

3. The 3D analysis software will provide an absolute number of ECs present in the tissue, and this number can be normalized to the total number of cells, determined as the total number of Hoechst-positive elements (Table 3).
4. Another important parameter is the volume that the vascular net occupies within the tissue; and to obtain a precise picture of the state of the vascular plexus, information about EC number must be combined with volumetric data. General vascular volume is quantified by generating a volumetric mask from the fluorescence channel corresponding to the $CD31^+$ vascular signal. This mask will be a volumetric net containing all $CD31^+$ fluorescent signals. Dedicated 3D software quantifies the number of positive voxels inside the mask, thereby obtaining a volumetric measure of the CD31 signal. This $CD31^+$ volume can then be normalized to the total region volume, thus yielding the vascular volume density, which can also be expressed as a percentage (Table 3).
5. Vascular smooth muscle cells (VSMCs) are perivascular cells that surround the endothelial layer, providing contractility to large arterioles and arteries and mechanical stability to some capillaries of the microvasculature. VSMC coverage of the endothelium provides crucial information about the arteriolar plexus. VSMCs can be specifically identified from the expression of SMA. A mask of the SMA fluorescent signal provides volumetric information about VSMC coverage.
6. Injured tissue can contain SMA-positive nonvascular elements (e.g., myofibroblasts within infarcted regions) [22], and this can lead to these structures being erroneously identified as VSMCs. Non-VSMC SMA^+ cells can be eliminated from the mask by considering only SMA^+ structures in close apposition to the $CD31^+$ EC signal. The co-localization assay checks which SMA^+ structures (**step 5**) are in close apposition to $CD31^+$ voxels, and only these structures are retained as genuine VSMCs (*see* **Notes 13** and **14**).
7. The 3D software then calculates the number of voxels inside this refined SMA^+ volumetric mask, providing the volume associated with the VSMC signal. Normalizing to the total region volume gives a measure of the presence of arterioles and the percentage of SMA^+ volume (Table 3).

Table 3
Quantification of vascular structural parameters in neonatal cryoinjured heart

	Infarcted region	Non-infarcted region
CD31 volume (%)	7.3	13.8
SMA volume (%)	3.5	0.8
Arteriolar volume (%)	37.1	2.9
Capillary volume (%)	62.8	97.0
Number of ECs (%)	13.9	36.4

Images shown in Fig. 1b were quantified according to the protocol and pipeline described in Fig. 2

8. Phenotypic analysis may require separation of the capillary plexus from arterioles. Again, this is achieved by co-localization analysis. In this case, from the CD31$^+$ volumetric mask (**step 4**), you retain only those CD31$^+$ structures in close apposition with the SMA$^+$ fluorescence channel. The selected CD31$^+$ vessels will correspond to VSMC-covered CD31$^+$ endothelium, classified as arteriolar endothelium (*see* **Note 15**). Again, using the 3D analysis software to quantify voxels inside the generated mask, we can provide volumetric information about this specific endothelium. We recommend normalization to the total CD31$^+$ volume (**step 4**) to obtain the final percentage of arteriolar endothelium in the analyzed vasculature (Table 3).
9. The same analysis will yield a mask of CD31$^+$ structures that are not in close apposition to SMA, corresponding to the capillary endothelium. The specific volumetric mask will give a 3D measure that can be normalized to the total vascular CD31$^+$ volume to determine the capillary plexus as a percentage of the total vasculature (Table 3).

3.6.3 Functional Parameters (Fig. 3)

Analyzing the performance of vascular structures in vivo is a crucial part of 3D vasculature analysis. Staining for functional parameters can provide information about the vasculature perfusion (identifying lumenized vessels that are receiving blood flow) and also about the leakage of the vascular plexus (an index of the stability of the vascular net). For this analysis, we show an example of artery ligation in adult mice at 3 days post infarction.

1. First, generate a volumetric mask from the fluorescence channel for the IB4$^+$ vascular signal. This mask will reveal the volumetric net of perfused vessels. These vessels, which have taken

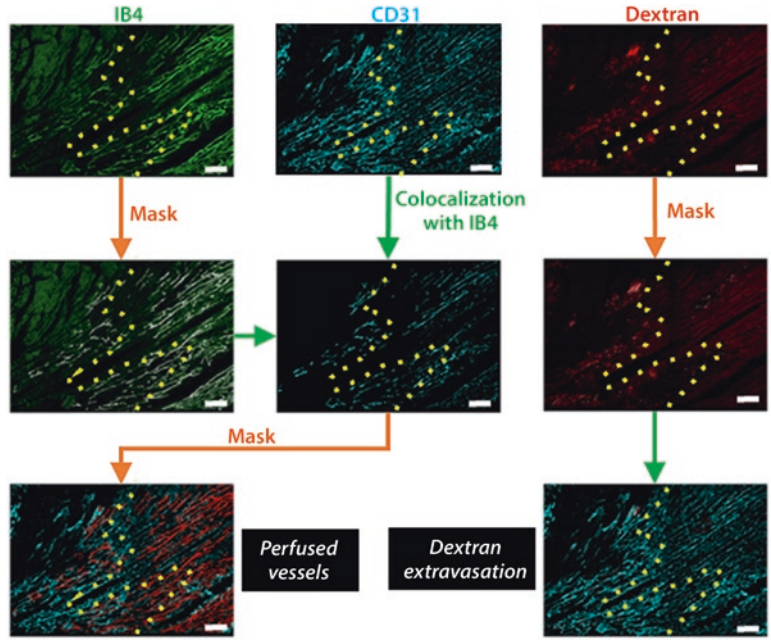

Fig. 3 3D image quantification workflow: functional quantification. From the Isolectin B4, CD31, and dextran masks, we can obtain information about the perfusion and leakage of the vascular net. Scale bar: 100 μm

up the IV-injected IB4 and are thus competent for blood flow, should be considered functional.

2. Select the $CD31^+$ fluorescence signal from within the IB4 mask (**step 1**). Rather than positively selecting that part of a fluorescence channel showing co-localization, as in previous examples (Subheading 3.6.2 **step 2**, **6**, and **8**), here the procedure involves elimination of $CD31^+$ fluorescence that is not inside the mask voxels, thus leaving only the fluorescent signal associated with the mask. In this specific case, CD31 fluorescence that does not co-localize with the voxels in the IB4 mask (**step 2**) is eliminated, yielding a CD31 fluorescence channel of double-positive ($CD31^+$ and $IB4^+$) vessels.
3. Using the 3D software, a volumetric mask can then be generated over the IB4-co-localized $CD31^+$ fluorescence signal, enabling determination of the volume of correctly perfused vasculature.
4. The perfused vasculature (**step 3**) can be normalized to the whole vascular plexus, obtained from the general mask of the $CD31^+$ vascular signal (Subheading 3.6.2 **step 4**) (*see* Table 4).
5. Following the same principle, a volumetric mask can be generated of the dextran surface and normalized to the vascular

Table 4
Quantification of vascular functional parameters in adult infarcted heart

	Infarcted region	Non-infarcted region
CD31 volume (%)	9.9	11.4
Perfused vessel volume (%)	11.2	47.6
Extravasated dextran volume	1.5	0.1

Images shown in Fig. 1c were quantified according to the protocol and pipeline described in Fig. 3

plexus volume. This reveals the volume of extravasated dextran, giving a measure of the stability and leakage of the vascular plexus (Table 4).

These masking and co-localization functions are integral to all 3D programs; however, individual programs can also include specific tools that allow a more detailed analysis. For example, Imaris 7.7.2 includes the distance transformation map, which can substitute the co-localization assays and determine structures by simply checking the distance between them. There are also customized algorithms (MATLAB programming) that allow quantification of other structural parameters such as number of segments, vessel radius, branching nodes, etc. (*see* **Note 16**).

4 Notes

1. Tail vein dilatation is crucial when working with dark strains (such as C57BL6), in which the tail is darker and the vein difficult to see. For white strains (such as BALB/c), this is less important because the vein is clearly visible.
2. The first tail injection should be distal to the second. Alternatively inject each component in different veins.
3. From here on, samples are maintained and manipulated in the dark to prevent loss of dextran fluorescence.
4. Some antibodies may require a milder fixation, and PFA concentrations from 0.4% to 2% can be used.
5. For whole-mount staining, go directly to the step 3.4 (immunostaining). Whole-mount samples can be stored for up to a month in PBS at 4 °C.
6. During staining, liquids should be removed with care, using a p200 pipette. Avoid suction to prevent sample damage.

7. Anti-CD16/CD32 antibodies should be included when staining samples with high numbers of inflammatory cells in order to avoid the possible non-specific reactions of their FcR receptors.
8. DAPI (4′,6-diamidino-2-phenylindole, dihydrochloride) or Hoechst can be added for nuclear staining indistinctly.
9. From here on, samples are maintained and manipulated in the dark to preserve the fluorescence signal.
10. For the 3D acquisition of full structures, such as tumors or hearts, a 512 × 512 pixel resolution should be enough for quantification of vessel density, perfusion, and extravasation, making it possible to reduce microscopy acquisition time, obtain smaller files, and thus speed up analysis. Acquisition time can also be reduced by acquiring optical sections in the Z stacks at 1.5–2 μm intervals.
11. Maximal intensity projections are useful for rapid visualization of the sample, giving an initial idea of the parameters that may be of interest for 3D quantification.
12. The region of interest in damaged tissue can be delineated by selecting the aberrant $CD31^+$ vasculature; however, other markers such as the macrophage marker CD68 can also be used.
13. The endothelial cells and VSMC layers are closely apposed but do not coincide exactly. Co-localization analysis can be used to specifically select VSMCs because the endothelial and perivascular cell fluorescence signals are superimposed. However, some 3D analysis programs (e.g., Imaris version 7.7.2) can perform distance transformation maps that examine the inter-signal distance instead of co-localization. This tool, although not included in every 3D software package, can be more specific, and we encourage its use when available.
14. Any remaining anomalous SMA structure should be eliminated manually.
15. In the heart model, most SMA^+-covered vessels correspond to arterioles. However, in other contexts such as tumors, SMA^+-covered vessels may not correspond to arterioles but to more mature or stabilized vessels; the immature vessels will be those with less or no SMA coverage.
16. With this kind of 3D images, it is possible to analyze other structural parameters, such as tortuosity and number of branch points, providing information about how the vessel network is structured. This kind of analysis can be done with programs like Imaris (the one that we use here) and also with customized software implemented in MATLAB, for example [28].

Acknowledgments

We thank Simon Bartlett for English editing. This work was supported by grant SAF2014-52050R from the Spanish Ministry of Economy and Competitiveness. A.S-E. is funded by a fellowship from Obra Social "La Caixa." The CNIC is supported by the Ministry of Economy, Industry and Competitiveness and the Pro-CNIC Foundation and is a Severo Ochoa Center of Excellence (SEV-2015-0505).

References

1. Greenblatt M, Shubi P (1968) Tumor angiogenesis: transfilter diffusion studies in the hamster by the transparent chamber technique. J Natl Cancer Inst 41(1):111–124
2. Parangi S, O'Reilly M, Christofori G et al (1996) Antiangiogenic therapy of transgenic mice impairs de novo tumor growth. Proc Natl Acad Sci U S A 93(5):2002–2007
3. Folkman J (2002) Role of angiogenesis in tumor growth and metastasis. Semin Oncol 29(6 Suppl 16):15–18. https://doi.org/10.1053/sonc.2002.37263
4. Fakhrejahani E, Toi M (2014) Antiangiogenesis therapy for breast cancer: an update and perspectives from clinical trials. Jpn J Clin Oncol 44(3):197–207. https://doi.org/10.1093/jjco/hyt201
5. Weis SM, Cheresh DA (2005) Pathophysiological consequences of VEGF-induced vascular permeability. Nature 437(7058):497–504. https://doi.org/10.1038/nature03987
6. Bae YH, Park K (2011) Targeted drug delivery to tumors: myths, reality and possibility. J Control Release 153(3):198–205. https://doi.org/10.1016/j.jconrel.2011.06.001
7. Carmeliet P, Jain RK (2011) Principles and mechanisms of vessel normalization for cancer and other angiogenic diseases. Nat Rev Drug Discov 10(6):417–427. https://doi.org/10.1038/nrd3455
8. Wong PP, Demircioglu F, Ghazaly E et al (2015) Dual-action combination therapy enhances angiogenesis while reducing tumor growth and spread. Cancer Cell 27(1):123–137. https://doi.org/10.1016/j.ccell.2014.10.015
9. Madeddu P (2005) Therapeutic angiogenesis and vasculogenesis for tissue regeneration. Exp Physiol 90(3):315–326. https://doi.org/10.1113/expphysiol.2004.028571
10. Zhang H, van Olden C, Sweeney D et al (2014) Blood vessel repair and regeneration in the ischaemic heart. Open Heart 1(1):e000016. https://doi.org/10.1136/openhrt-2013-000016
11. Porrello ER, Olson EN (2014) A neonatal blueprint for cardiac regeneration Stem Cell Res 13 (3 Pt B):556-570. doi:https://doi.org/10.1016/j.scr.2014.06.003
12. Rundhaug JE (2005) Matrix metalloproteinases and angiogenesis. J Cell Mol Med 9(2):267–285
13. Siefert SA, Sarkar R (2012) Matrix metalloproteinases in vascular physiology and disease. Vascular 20(4):210–216. https://doi.org/10.1258/vasc.2011.201202
14. Zhou Z, Apte SS, Soininen R et al (2000) Impaired endochondral ossification and angiogenesis in mice deficient in membrane-type matrix metalloproteinase I. Proc Natl Acad Sci U S A 97(8):4052–4057. https://doi.org/10.1073/pnas.060037197
15. Galvez BG, Genis L, Matias-Roman S et al (2005) Membrane type 1-matrix metalloproteinase is regulated by chemokines monocyte-chemoattractant protein-1/ccl2 and interleukin-8/CXCL8 in endothelial cells during angiogenesis. J Biol Chem 280(2):1292–1298. https://doi.org/10.1074/jbc.M408673200
16. Galvez BG, Matias-Roman S, Albar JP et al (2001) Membrane type 1-matrix metalloproteinase is activated during migration of human endothelial cells and modulates endothelial motility and matrix remodeling. J Biol Chem 276(40):37491–37500. https://doi.org/10.1074/jbc.M104094200
17. Koziol A, Gonzalo P, Mota A et al (2012) The protease MT1-MMP drives a combinatorial proteolytic program in activated endothelial cells. FASEB J 26(11):4481–4494. https://doi.org/10.1096/fj.12-205906
18. Sudhakar A, Sugimoto H, Yang C et al (2003) Human tumstatin and human endostatin exhibit distinct antiangiogenic activities mediated by alpha v beta 3 and alpha 5 beta 1 integrins.

Proc Natl Acad Sci U S A 100(8):4766–4771. https://doi.org/10.1073/pnas.0730882100

19. Bergers G, Brekken R, McMahon G et al (2000) Matrix metalloproteinase-9 triggers the angiogenic switch during carcinogenesis. Nat Cell Biol 2(10):737–744. https://doi.org/10.1038/35036374
20. Mu D, Cambier S, Fjellbirkeland L et al (2002) The integrin alpha(v)beta8 mediates epithelial homeostasis through MT1-MMP-dependent activation of TGF-beta1. J Cell Biol 157(3):493–507. https://doi.org/10.1083/jcb.200109100
21. Walchli T, Mateos JM, Weinman O et al (2015) Quantitative assessment of angiogenesis, perfused blood vessels and endothelial tip cells in the postnatal mouse brain. Nat Protoc 10(1):53–74. https://doi.org/10.1038/nprot.2015.002
22. Cunha SI, Pardali E, Thorikay M et al (2010) Genetic and pharmacological targeting of activin receptor-like kinase 1 impairs tumor growth and angiogenesis. J Exp Med 207(1):85–100. https://doi.org/10.1084/jem.20091309
23. Pitulescu ME, Schmidt I, Benedito R et al (2010) Inducible gene targeting in the neonatal vasculature and analysis of retinal angiogenesis in mice. Nat Protoc 5(9):1518–1534. https://doi.org/10.1038/nprot.2010.113
24. Tual-Chalot S, Allinson KR, Fruttiger M et al (2013) Whole mount immunofluorescent staining of the neonatal mouse retina to investigate angiogenesis in vivo. J Vis Exp 77:e50546. https://doi.org/10.3791/50546
25. Walls JR, Coultas L, Rossant J et al (2008) Three-dimensional analysis of vascular development in the mouse embryo. PLoS One 3(8):e2853. https://doi.org/10.1371/journal.pone.0002853
26. Jester JV, Ho-Chang J (2003) Modulation of cultured corneal keratocyte phenotype by growth factors/cytokines control in vitro contractility and extracellular matrix contraction. Exp Eye Res 77(5):581–592
27. Richardson DS, Lichtman JW (2015) Clarifying tissue clearing. Cell 162(2):246–257. https://doi.org/10.1016/j.cell.2015.06.067
28. Gkontra P, Żak MM, Norton K-A et al (2015) A 3D fractal-based approach towards understanding changes in the infarcted heart microvasculature. Springer 9351:173–180. https://doi.org/10.1007/978-3-319-24574-4_21

PLOS ONE

RESEARCH ARTICLE

Developmental expression of membrane type 4-matrix metalloproteinase (Mt4-mmp/Mmp17) in the mouse embryo

María José Blanco[1☯], Iván Rodríguez-Martín[1☯], Ana I. R. Learte[1☯], Cristina Clemente[2], María Gregoria Montalvo[3], Motoharu Seiki[4], Alicia G. Arroyo[2], Cristina Sánchez-Camacho[2,3]*

1 Basic Biomedical Sciences Department, Universidad Europea de Madrid, Villaviciosa de Odón, Madrid, Spain, **2** Centro Nacional de Investigaciones Cardiovasculares Carlos III (CNIC), Madrid, Spain, **3** Doctoral Studies and Research School, Universidad Europea de Madrid, Villaviciosa de Odón, Madrid, Spain, **4** Institute of Medical Science, University of Tokyo, Minato-ku, Tokyo, Japan

☯ These authors contributed equally to this work.
* cristina.sanchez-camacho@universidadeuropea.es

Citation: Blanco MJ, Rodríguez-Martín I, Learte AIR, Clemente C, Montalvo MG, Seiki M, et al. (2017) Developmental expression of membrane type 4-matrix metalloproteinase (Mt4-mmp/Mmp17) in the mouse embryo. PLoS ONE 12(9): e0184767. https://doi.org/10.1371/journal.pone.0184767

Editor: Michael Schubert, Laboratoire de Biologie du Développement de Villefranche-sur-Mer, FRANCE

Received: April 10, 2017

Accepted: August 30, 2017

Published: September 19, 2017

Data Availability Statement: All relevant data are within the paper and its Supporting Information files.

Funding: This work was supported by a grant from the Universidad Europea de Madrid (2016UEM04) to C.S.C. and grant SAF2014-20520R from the Ministry of Economy, Industry and Competitiveness (MIEC) to A.G.A. The CNIC is supported by the MIEC and the Pro-CNIC

Abstract

Matrix metalloproteinases (MMPs) constitute a large group of endoproteases that play important functions during embryonic development, tumor metastasis and angiogenesis by degrading components of the extracellular matrix. Within this family, we focused our study on Mt4-mmp (also called Mmp17) that belongs to a distinct subset that is anchored to the cell surface via a glycosylphosphatidylinositol (GPI) moiety and with the catalytic site exposed to the extracellular space. Information about its function and substrates is very limited to date, and little has been reported on its role in the developing embryo. Here, we report a detailed expression analysis of Mt4-mmp during mouse embryonic development by using a LacZ reporter transgenic mouse line. We showed that Mt4-mmp is detected from early stages of development to postnatal stages following a dynamic and restricted pattern of expression. Mt4-mmp was first detected at E8.5 limited to the intersomitic vascularization, the endocardial endothelium and the dorsal aorta. Mt4-mmp$^{LacZ/+}$ cells were also observed in the neural crest cells, somites, floor plate and notochord at early stages. From E10.5, expression localized in the limb buds and persists during limb development. A strong expression in the brain begins at E12.5 and continues to postnatal stages. Specifically, staining was observed in the olfactory bulb, cerebral cortex, hippocampus, striatum, septum, dorsal thalamus and the spinal cord. In addition, LacZ-positive cells were also detected during eye development, initially at the hyaloid artery and later on located in the lens and the neural retina. Mt4-mmp expression was confirmed by quantitative RT-PCR and western blot analysis in some embryonic tissues. Our data point to distinct functions for this metalloproteinase during embryonic development, particularly during brain formation, angiogenesis and limb development.

Foundation, and is a Severo Ochoa Center of Excellence (SEV-2015-0505).

Competing interests: The authors have declared that no competing interests exist.

Introduction

Matrix metalloproteinases (MMPs) constitute a large group of endoproteases that are mainly aimed to degrade and modify distinct components of the extracellular matrix (ECM). These enzymes play also a key role as regulators for tumor invasion and vascular formation [1]. The MMPs are mostly secreted, although there is a subgroup that are tethered to the cell membrane (MT-MMPs), either by a single transmembrane domain or by a glycophosphatidyl inositol (GPI) anchor, and with the catalytic site exposed to the extracellular space [2,3]. The membrane anchored MT-MMPs are relevant modifiers of the immediate cellular microenvironment, which modulates cellular functions [4]. This subgroup includes Mt4-mmp, also known as Mmp17, which is a relatively new member of the MMP family and has been poorly characterized to date [5,6]. Mt4-mmp exhibits unique structural and functional characteristics since it has the least degree of sequence identity to the other family members, presenting no shared enzymatic properties with them [1,7]. For instance, its proteolytic activity against ECM proteins is limited, suggesting a certain degree of specificity against its substrates, possibly located in the pericellular space as well as in the plasma membrane associated to lipid rafts [5,6,8].

Mt4-mmp physiological role remains unclear: its loss of function seems to trigger no apparent defects in gestation, growth, morphology, fertility and behavior, and mice showed no apparent abnormal developmental phenotypes [9]. However, it is known that Mt4-mmp is highly expressed in the kidney papilla as well as in the anterior hypothalamus, and null mice have decreased intake of water and daily urine output, suggesting a role for this enzyme in water homeostasis and regulation of the thirst center in mice [10]. The expression pattern of Mt4-mmp appears to be restrained to certain tissues such as the brain, testis, ovaries, leukocytes and colon in humans [2,5,8,11,12], where it may play specific roles [13]. Although the possibility that Mt4-mmp may contribute to development and organogenesis in these tissues seems feasible, likely through the regulation of cell migration, very little is known about its role during development.

Regarding the formation of the brain, the role of Mt4-mmp during the development of the central nervous system (CNS) is not yet clear. It is known that metalloproteinases are generally implicated in neurogenesis, axonal growth and myelin formation, as well as recovery from injury to the nervous system [14]. Indeed Mt4-mmp may be important during brain development, since it is known that it exhibits high levels of expression in the normal brain tissue, being localized in the cerebral cortex and hippocampus at postnatal stages, and the adult hypothalamus [9,10]. It also displays an intense expression pattern in the dorsal cortical plate at late embryonic stages [15–17]. Despite a previous report in zebrafish that shows that its ortholog mmp17b, is required for the proper migration of neural crest cells [17], almost nothing has been reported on the function and expression of membrane type MMPs during embryonic development.

Our previous work has recently revealed a specific function for Mt4-mmp in the proper organization of the aortic wall. Mt4-mmp is detected in the dorsal aorta from early stages of embryonic development, and its loss of function in mice results in the presence of immature vascular smooth muscle cells (VSMCs) and altered ECM, indicating its essential role in arterial vessel wall development and function [18].

It is known that Mt-mmps are also relevantly involved in pathological conditions regulating vascular stability and permeability [1]. Besides, Mt4-mmp has been identified in cancer tissues and previous studies have brought up potential roles for it in cancer progression [4,19–22]. Interestingly, one key aspect of the role of Mt4-mmp in tumor physiology is that it contributes to vessel maturation and stabilization during tumor angiogenesis [1]. This enzyme displays high levels of expression in transformed cells and not in normal epithelium, and it has been

shown to display a tumor-promoting activity [4,12,23]. These evidences provide a link between its role in vessel formation and tumorigenesis.

Since to date, little is known about the precise contribution of Mt4-mmp during CNS and blood vessel development, to determine the function of Mt4-mmp during these processes seems paramount to gain further knowledge on its role in pathological phenomena. By using the LacZ reporter under the control of the Mt4-mmp promoter [9] we have detailed that Mt4-mmp is expressed in a specific regionally and timely controlled manner. During early stages of development, Mt4-mmp expression is clearly related to vascular development. Our study reveals that Mt4-mmp is also expressed in distinct brain regions at later stages. Thus, our data suggest important activities of this metalloproteinase during brain formation as well as during vasculogenesis and angiogenesis.

Material and methods

Animals

Mutant mice that express LacZ reporter under the control of the endogenous Mt4-mmp promoter were generated by gene-targeting and genotyped as previously described [9]. Mt4-mmp deficient mice were maintained in a C57/Bl6 genetic background. Wild type and Mt4-mmp$^{LacZ/+}$ littermate embryos from pregnant mice were collected between embryonic stages E8.5–18.5 (E0.5 correspond to the day of the vaginal plug) and at postnatal stages P0-P1. Mice were housed in the Centro Nacional de Investigaciones Cardiovasculares Carlos III (CNIC) Animal Facility under pathogen-free conditions and in strict accordance with the institutional guidelines. The protocol was approved by the Committee on the Ethics of Animal Experiments of the CNIC (Permit Number: CNIC-01/13) and the Comunidad Autónoma de Madrid (Permit Number: PROEX 34/13). All animals were sacrificed by cervical dislocation, and all efforts were made to minimize suffering. Animal studies were conformed to directive 2010/63EU and recommendation 2007/526/EC regarding the protection of animals used for experimental and other scientific purposes, enforced in Spanish law under RD1201/2005.

β-galactosidase staining

Mt4-mmp distribution was determined by using X-gal histochemistry in Mt4-mmp$^{LacZ/+}$ embryos. Small mouse embryos, from E8.5 to E12.5, were fixed by immersion in 0,125% glutaraldehyde in phosphate buffer saline 0.1M pH 7.2 (PBS) for 3h at room temperature and processed for *in toto* LacZ staining according to standard protocols [24]. Briefly, the whole embryo was incubated in X-gal buffer (5mM potassium ferrocyanide, 5mM potassium ferricyanide, 2 mM $MgCl_2$, 0.01% deoxycholate acid, 0.02% NP-40 and 0.1% X-gal) at 37˚C overnight. Following PBS washing, embryos were fixed in 4% paraformaldehyde (PFA), and then paraffin-embedded and sectioned in the frontal plane at 7 μm thickness. Sections were counterstained with Fast Red to better define distinct embryonic structures. For those embryos older than E12.5 and postnatal stages, animals were transcardially perfused with 0,125% glutaraldehyde in PBS and post-fixed for 2-12h at 4˚C. Then, they were cryoprotected in 30% sucrose solution in PBS, embedded in OCT and sectioned in the frontal plane with a cryostat (Leica). Coronal sections of 20-μm thickness were collected and then processed for LacZ staining as described above.

Protein extraction and western-blot analysis

Protein extracts were obtained from E14.5 wildtype (WT, n = 4), heterozygous (HT, n = 3), and knockout (KO, n = 3) embryonic mouse tissues (forelimb, cerebral cortex and spinal

cord), using a cold lysis buffer (20 mM Tris pH 7.5, 2% SDS) and protease inhibitors (Complete, Mini, EDTA-free, Roche). Proteins (30 μg) were resolved by 10% SDS-PAGE in reducing conditions and transferred onto nitrocellulose membranes (0.45 μm, Bio-Rad, Hercules). Membranes were blocked with 5% non-fat milk. Antibodies against polyclonal MMP17 rabbit (EP1270Y clone, ab51075, Abcam), and monoclonal α-tubulin mouse (T6074, SIGMA-Aldrich) were used at 1:1000 and 1:5000 dilution overnight, respectively. Membranes were developed using goat anti-rabbit HRP (1:10000; 111-035-003, Jackson Immunoresearch) and goat anti-mouse HRP (1:10000; 115-035-003, Jackson Immunoresearch) antibodies, recorded by ImageQuant LAS 4000 (GE healthcare Life Sciences) or goat anti-mouse 800 (1:10000; ODYSSEY IRDye®) and recorded by LI-COR Odyssey technology.

Immunohistochemistry

For immunohistochemical procedures, embryos were fixed in 4% PFA in PBS 0.1M pH 7.2 by immersion or perfusion depending on the developmental stage, cryoprotected in a 30% sucrose solution, and then embedded in OCT and sectioned in the cryostat at 20 μm thickness in the transverse plane. Immunohistochemistry was performed following standard protocols. Primary antibodies used include: polyclonal anti-CD31 hamster (1:1000; MAB1398Z, Millipore), anti-β-galactosidase rabbit (1:1000; ab4761, Abcam), anti-FoxA2 mouse (1:250; F55A10, DSHB), anti-Nkx6.1 mouse (1:1000; 4C7, DSHB), anti-Olig2 rabbit (1:1000; AB9610, Chemicon), anti-ERG-647 rabbit (1:500; ab196149, Abcam) and anti-WT-1 mouse (Wilms´ Tumor-1; 1:50; M3516, Dako). Sections were incubated with the primary antibody diluted in PBS containing 0.1% Triton X-100 and 1% bovine serum albumin (BSA), for 48 h at 4˚C. Subsequently, the sections were rinsed in PBS and incubated for 2 hours at room temperature with 488 or 594-Alexa™-conjugated fluorescent antibodies (Molecular Probes, 1:1000). Sections were counterstained with Hoechst (Molecular Probes, 1:1000) for 5 min at room temperature to visualize nuclei.

RNA purification and quantitative real-time PCR

For RT-PCR analysis, total RNA was extracted from distinct wildtype (WT), heterozygous (HT) and knockout (KO) mouse embryonic tissues at three developmental stages: cerebral cortex, tail, forelimb and heart from E10.5 and E12.5 embryos; cerebral cortex, tail, forelimb, heart, eye, olfactory bulb, spinal cord, mesencephalon and hindbrain from E14.5 embryos (n = 3 for each embryonic stage and genotype). Total RNA was extracted with Tri-Reagent® (Sigma-Aldrich) and purified by using RNeasy Mini Kit (Qiagen Sciences). First-strand cDNA was synthesized with ImProm-II™ Reverse Transcriptase (Promega) according to manufacturer's instructions. In all cases, a reverse transcriptase negative control was used for testing genomic DNA contamination. Quantitative RT-PCR was conducted with the iQ™ SYBR® Green Supermix (BIO-RAD) on a CFX96 Real-Time System (BIO-RAD), with following conditions: initial denaturation at 95˚C for 10 min, followed by 40 cycles of denaturation at 95˚C for 15 sec, annealing and extension at 60˚C for 1 min. Melt curve analysis from 60˚C to 95˚C was performed at the end of each run as a quality-control step. The following specific primers were used: for *Mt4-mmp*: `5´-GACCTTCCGTTCCTCAGATG-3´` (F) and `5´-CCTGGTAGTACGGTTGCATG-3´` (R); for *Gapdh*: `5´-AATGCATCCTGCACCACCAA-3´` (F) and `5´-GTGGCAGTGATGGATGGA-3´` (R). Quantitative data were examined using the comparative Ct method [25]. Mt4-mmp expression levels were normalized to the house-keeping GAPDH and presented as a fold increase or decrease relative to the expression levels in the adult cerebral cortex. In all cases, data were plotted as the mean ± standard error of the mean (SEM) derived from duplicate experiments ($n \geq 3$).

Statistics

Statistical differences in protein expression and mRNA levels among different tissues and embryonic stages were assessed by one-way ANOVA followed by post-hoc Student-Newman-Keuls (SNK) multiple comparison test and Student's t test. Analysis was performed using Graphpad Prism 6.0 and IBM SPSS Statistics v21. Significance was assigned at $p<0.05$. For Western blot analysis, relative intensity of the bands were quantified by Image J software (https://imagej.nih.gov/ij/) and normalized to α-tubulin ones.

Data availability

All relevant data are within the paper and its Supporting Information files.

Results

Mt4-mmp is expressed at the early embryo and during cardiovascular development

The expression pattern of Mt4-mmp was examined at early stages of development by means of β-galactosidase staining using the activity of the LacZ reporter transgene under the endogenous Mt4-mmp promoter in whole mouse heterozygous embryos (Figs 1 and 2) [9]. A consistent staining and distribution of β-gal positive cells was observed among the analysed embryos. LacZ-positive cells were first detected at 4–6 somite embryos (E8.5) in the neural folds corresponding to premigratory neural crest cells as well as in the somites and the mesenchymal presomitic tissue (Fig 1C and 1G). The premigratory and migratory neural crest cells also express Mt4-mmp in 10 somite-stage embryos (Fig 1D). Between 8 and 10 somite embryos, Mt4-mmp expression was primarily associated to the vasculature. Thus, expression was detected in the intersomitic vascularization and the endocardial endothelium of the primitive heart tube (Fig 1A and 1B) and other vascular structures such as the allantois, the umbilical vessels, the vitellin artery and vein and the posterior branch of the primary head vein (Fig 3). Somites also show β-gal positive cells in a pattern compatible with intersomitic arteries beginning to branch from the dorsal aorta (Fig 1E and 1I). In fact, β-gal positive cells are apparent along the entire rostro-caudal extension of the dorsal aorta, particularly in the ventral aortic wall, which possibly correspond to the hemogenic endothelium at these stages. E9.5 embryos showed a similar reporter expression in the intersomitic arteries sprouting from the dorsal aorta and in the posterior and ventral portions of the somites (Fig 1J and Fig 2A–2C). Indeed, double-labelled cells for ERG, an endothelial transcription factor, or CD31 (PECAM-1), an early membrane marker for endothelial cells, and β-gal demonstrate that Mt4-mmp is expressed in these vascular cells. This vascular pattern of expression persists during somite development and begins at the head and the branchial arch vessels. In fact, by E10.5 and E11.5, LacZ staining also localizes mainly in endothelial cells of the dorsal aorta, the branch from the internal carotid artery, and persists in the allantoic vascular plexus (Fig 3D and 3F). By means of double labelling immunohistochemistry for anti-β-gal and the early endothelial marker CD31, we confirmed that Mt4-mmp$^{LacZ/+}$ expression in the dorsal aorta correspond to endothelial cells at E10.5 (Fig 3J–3L). As previously reported, we also found a strong labelling in the dorsal aorta at E14.5 around the whole wall of the vessel (Fig 3I), including endothelial and vascular smooth muscle cells (VSMCs), and persists from E16.5 to E18.5 although the labelling was weaker [18].

Apart from the aorta, expression in VSMCs was also detected in other large blood vessels as the pulmonary or the common carotid arteries at later stages of development (Fig 3E). In addition, β-gal positive cells were disposed surrounding the neural tube, in the perineuronal vascular plexus (PNVP) at E9.5 (Fig 1I). This labelling persists later in development including blood

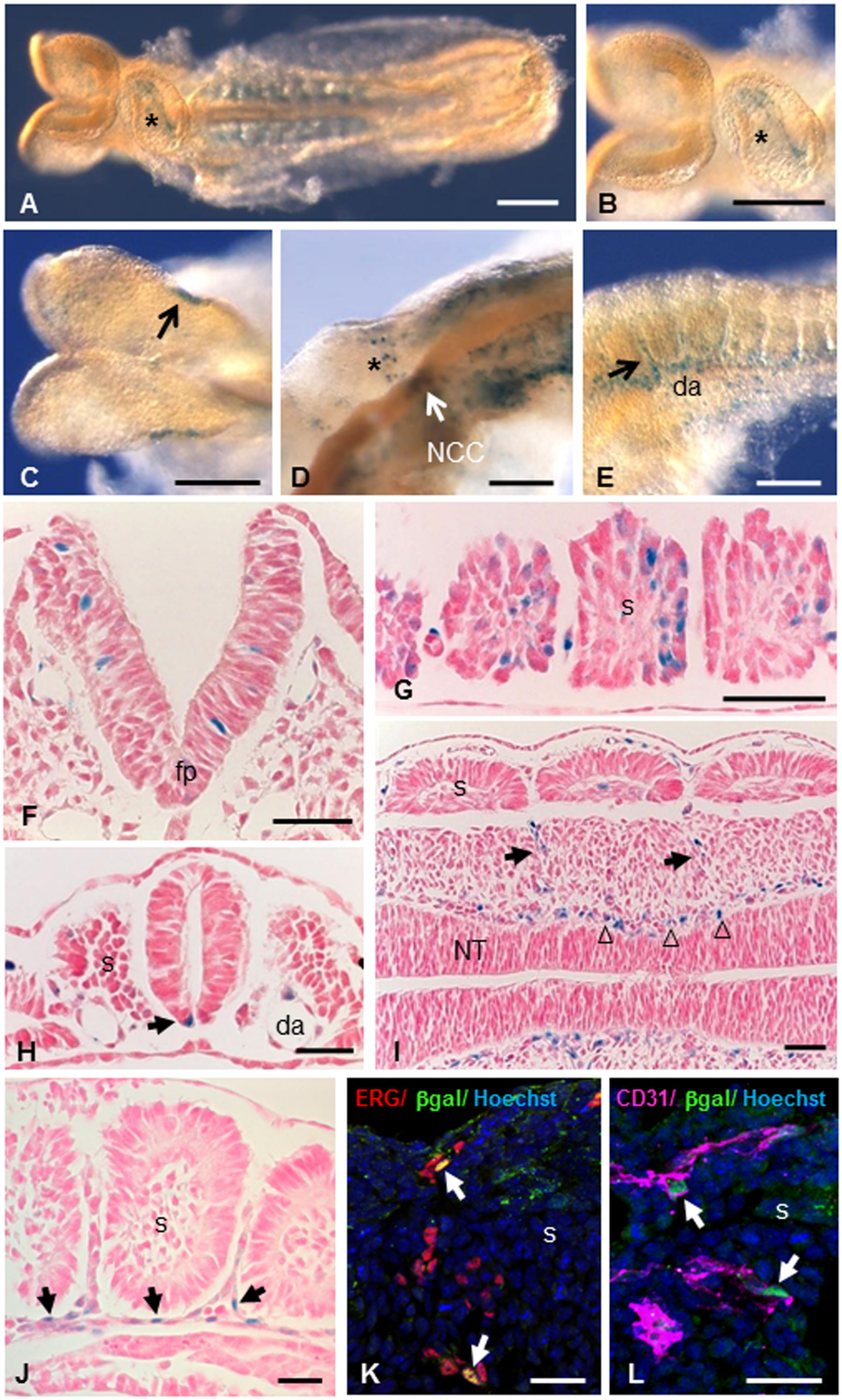
A
*
B
*
C
D
*
NCC
E
da
F
fp
G
s
H
s
da
I
s
NT
J
s
K
ERG/ βgal/ Hoechst
s
L
CD31/ βgal/ Hoechst
s

Fig 1. Mt4-mmp expression during early mouse embryonic development. (A-E) Whole-mount β-gal staining in 6–10 somite stage Mt4-mmp$^{LacZ/+}$ embryos. In a ventral view of an 8 somite-stage embryo, it becomes apparent the staining in the endocardial tissue of the primitive heart tube (asterisks in A, B). Staining is observed in the premigratory neural crest cells of a 6 somite-stage embryo (arrow in C). The premigratory and migratory neural crest cells (arrow and asterisk in D) express Mt4-mmp in 10 somite-stage embryos. Somites also show β-gal positive cells (E) in a pattern compatible with intersomitic arteries (arrow in E) beginning to branch from the dorsal aorta. (F-I) β-Gal staining of coronal sections from Mt4-mmp$^{LacZ/+}$ embryos highlights Mt4-mmp distribution in neuroepithelial cells of the neural tube (F), somites (G), floor plate (arrow in H) and dorsal aorta (H) at E8.5 embryos (n = 8). Localization of β-galactosidase was detected in the intersomitic vasculature (arrow in I) and in the perineuronal vascular plexus (arrowheads in I). Detail of LacZ staining in the intersomitic blood vessels (arrows in J). Double-labelled cells for the endothelial markers ERG (red, arrows in K) or CD31 (magenta, arrows in L) and β-gal (green) demonstrate that cells expressing Mt4-mmp in this location are endothelial cells. Abbreviations: da, dorsal aorta; fp, floor plate; s, somite; NCC, neural crest cells; NT, neural tube. Scale bars: 200 μm (A-C), 100 μm (D, E), 50 μm (F-I), 30 μm (J-L).

https://doi.org/10.1371/journal.pone.0184767.g001

vessel branches from this plexus that enter into the brain parenchyma. Mt4-mmp was also detected during the development of the heart. Thus, Mt4-mmp$^{LacZ/+}$ cells were first detected by E8.5 in the endocardial endothelium of the atrial and ventricular chambers of the primitive heart tube (Figs 1A, 1B and 3A). From E12.5 to E18.5, a similar labeling was found mainly located in the epicardium of the atrium and ventricles (Fig 3B and 3C). We could no detect the expression of Mt4-mmp in the proepicardium nor in the epicardium at earlier stages of development (S1 Fig).

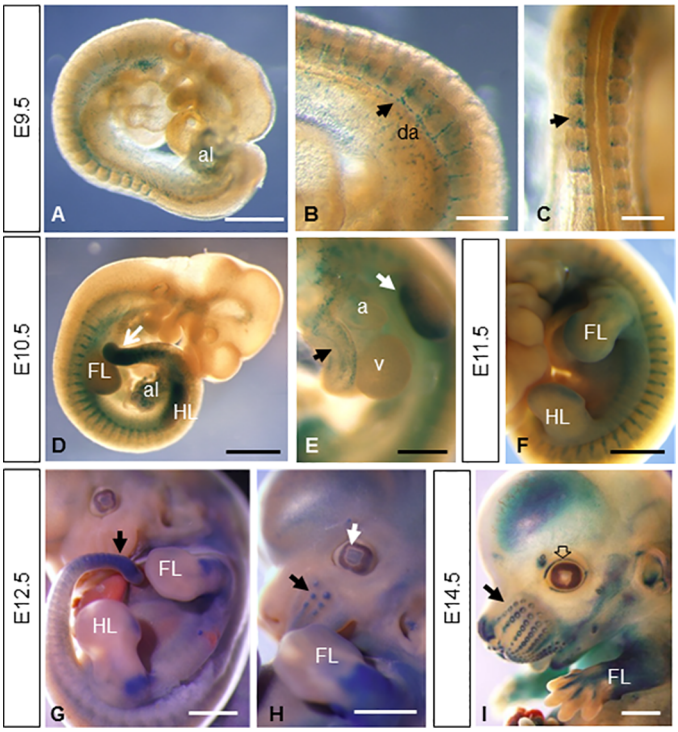

Fig 2. Whole-mount β-gal stained embryos from E9.5 to E14.5. (A-C) E9.5 embryos (n = 7) show reporter expression in the allantois (A), the intersomitic arteries sprouting from the dorsal aorta (arrow in B) and in the posterior portion of the somites (arrow in C). (D-F) This vascular pattern of expression persists during somite development as shown in D and F. Other embryonic tissues like the limb buds, the mesenchymal tail tip (arrow in D and G), the allantois, the atrium and aorta (E) show β-gal staining at E10.5 (n = 5) and E11.5 (n = 3). At later stages of development, expression persists in the limbs (G-I) and appears in the primordium of follicle of vibrissa (arrows in H and I), lens (white arrow in H), eyelid (empty arrow in I), nose, pinna of the ear and brain (n = 6 for E12.5 and E14.5 embryos). Abbreviations: a, atrium; al, allantois; da, dorsal aorta; FL, forelimb; HL hindlimb; v, ventricle. Scale bars: 1 mm (D, F-I), 500 μm (A, E) and 250 μm (B, C).

https://doi.org/10.1371/journal.pone.0184767.g002

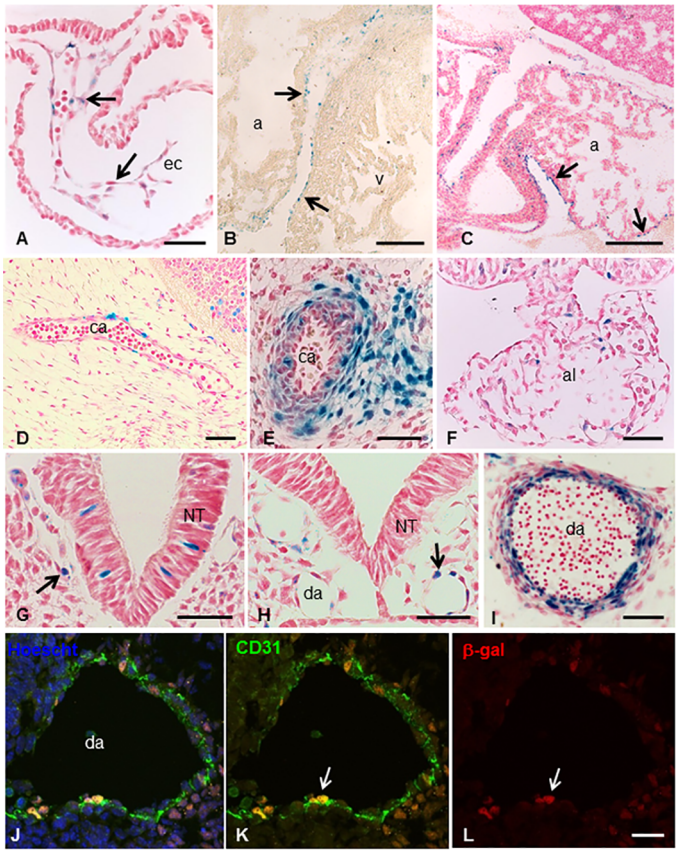

Fig 3. Mt4-mmp$^{LacZ/+}$ expression during cardiovascular development. (A-C) β-gal staining at distinct stages of heart development reveals the expression of Mt4-mmp in the endocardial endothelium of the primitive heart tube at E8.5 (arrows in A) and the epicardium of the atrium and ventricle (arrows in B and C) at E14.5 (B) and E18.5 (C). Expression was also detected in other vascular structures as the branch from internal carotid artery at E11.5 (D) and E14.5 (E) and the allantois at E9.5 (F). By E8.5 β-gal positive cells were detected in the posterior branch of primary head vein (arrow in G) and the dorsal aorta (arrow in H). Labelling in the dorsal aorta persists later in development and by E14.5 Mt4-mmp expression is not only restricted to the endothelium but also located in smooth muscle cells of the aortic wall (I). Double labelling immunohistochemistry for CD31 (J,K) and β-gal (J,L) confirmed the expression of Mt4-mmp in endothelial cells of the dorsal aorta at E10.5 (arrows in K and L). Abbreviations: a, atrium; al, allantois; ca, carotid artery; da, dorsal aorta; ec, endothelial cells; NT, neural tube; v, ventricle. Scale bars: 200 μm (B, C), 50 μm (A, E-H, J-L) and 20 μm (D, I).

https://doi.org/10.1371/journal.pone.0184767.g003

Apart from the cardiovascular system, other embryonic tissues like the mesenchymal tail tip, cells migrating into the branchial arches, premuscle mesodermal condensation/myotome-derived premuscle mass and the rib primordium showed β-gal staining from E10.5 to E12.5 (Fig 2D–2H). As development proceeded, β-gal positive cells were observed in other structures of the embryo such as the cartilage primordium of the body of hyoid bone at E14.5.

To confirm our results based on the LacZ reporter expression of Mt4-mmp gene, we performed quantitative RT-PCR analysis in distinct tissues at three developmental stages. Levels of Mt4-mmp expression in the embryonic tissues were always normalized to RNA levels of the enzyme in the adult cerebral cortex according to the high expression reported in this region in previous studies [9,10,15]. Low levels of RNA were detected at E10.5, E12.5 and E14.5 in the tail and the heart of the wild type (WT) embryos, whereas as expected, expression was reduced in the heterozygous (HT) and absent in the knockout (KO) tissues (Fig 4A).

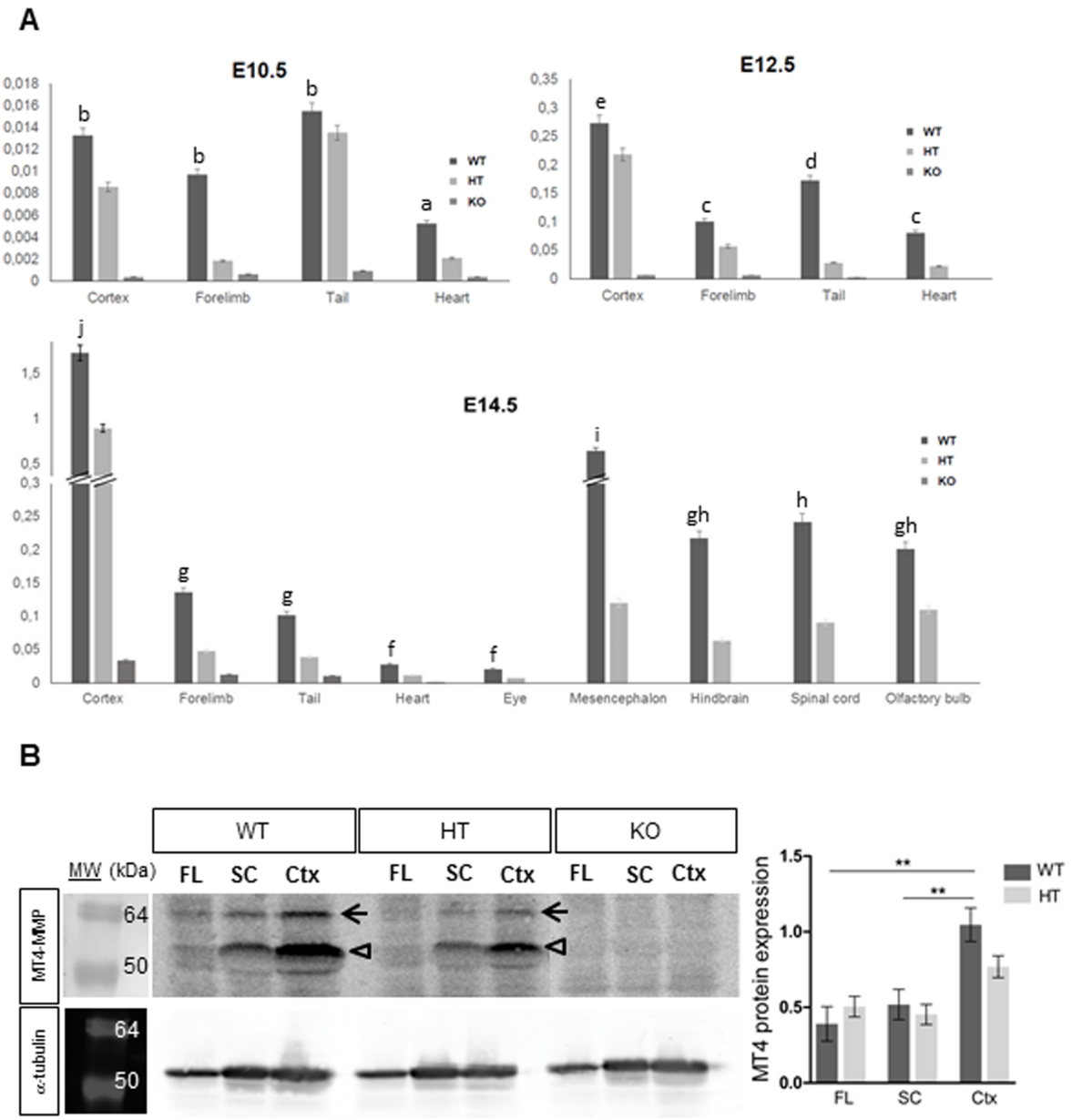

Fig 4. Real-time PCR and western blot analysis of Mt4-mmp expression in mouse embryonic tissues. (A) Real-time PCR analysis was performed using cDNA prepared from E10.5, E12.5 and E14.5 WT, HT and KO mouse embryonic tissues. Mt4-mmp expression increases as development proceeds and particularly, high RNA levels were detected at E14.5 in distinct brain regions as the cerebral cortex, olfactory bulb, mesencephalon, hindbrain and spinal cord. Mt4-mmp RNA levels of were normalized to the housekeeping GAPDH levels and relative to expression levels in the adult cerebral cortex. Data shown are representative of three independent experiments and expressed as the mean ± SEM. In all cases, mRNA levels were significantly reduced in the HT compared to the WT tissues at the distinct embryonic stages analysed. Different letters indicate significant differences ($p < 0.05$) among distinct tissues of the same embryonic stage by ANOVA and post-hoc analysis (SNK). (B) Total cell lysates from forelimbs (FL), spinal cord (SC) and cerebral cortex (Ctx) of E14.5 WT, HT and KO embryos were analysed by western blotting with the anti-MT4-MMP antibody and anti-α-tubulin antibody for loading control. Specific bands correspond to the precursor of the GPI-anchored form (63 kDa, closed arrow) and the GPI-anchored latent and active forms (55 and 50 kDa, opened arrow) of MT4-MMP. Quantification of Western blot shows significant higher levels of protein expression in the cerebral cortex compared to the spinal cord and the forelimb of WT embryos. MT4-MMP protein levels were significantly decreased in the HT cerebral cortex compared to the WT embryos and were totally absent in all KO embryonic tissues analysed (**, indicates significant differences at $p < 0.01$).

https://doi.org/10.1371/journal.pone.0184767.g004

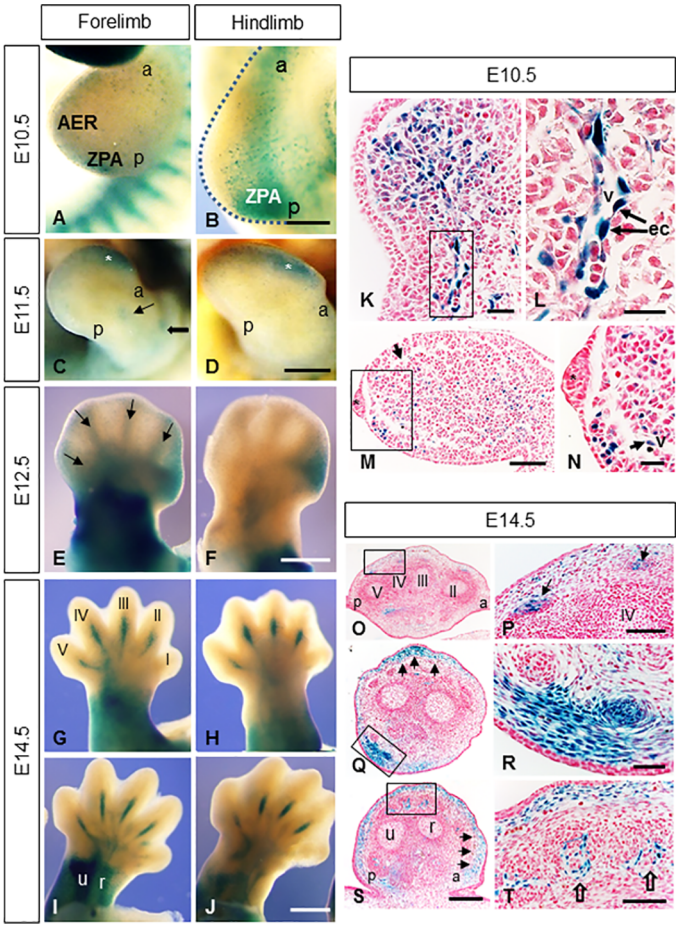

Fig 5. Mt4-mmp$^{LacZ/+}$ distribution during mouse limb development. Mt4-mmp$^{LacZ+/-}$ expression pattern was studied in whole mount limbs at distinct embryonic stages. (A, B) Distal (A) and proximal regions (B) of the limb buds as well the ZPA region show β-gal staining at E10.5. (C, D) Mt4-mmp expression was detected in distal regions of the hand and footplate (asterisks in C,D) as well as in the developing stylopodial and zeugopodial segments (thick and thin arrows in C). (E-J) β-gal staining from E12.5 to E14.5 appears in the stylopodium, zeugopodium and proximal regions of the handplate (E, G-J). In addition, anterior mesenchymal expression is observable in the E12.5 footplate (F). Mt4-mmp expression was first observed in digits at E12.5 (arrows in E) evolving to a pattern restricted to metacarpals and metatarsals of digits II, III, IV and V, either in dorsal (G, H) and ventral side (I, J) at E14.5. (K-N) Paraffin cross sections though hindlimb (K, L) and forelimb (M, N) showed β-gal positive cells in the mesenchyme (arrow in N) and in endothelial cells (ec) of blood vessels entering the limbs (L). The asterisk corresponds to the AER. (O-T) E14.5 limb crossed-sections from distal (O, P) to proximal (Q-T) levels evidence β-gal staining in the tendon blastemas (arrows in P), in subepidermal mesenchymal cells (arrows in Q, S) and in ventral muscle blocks (R) as well as in blood vessels entering the muscles (empty arrows in T). In all sections dorsal is up; ventral is down. Abbreviations: a, anterior; AER, apical ectodermal ridge; ec, endothelial cells; p, posterior; r, radius; u, ulna; v, blood vessel; ZPA, zone of polarizing activity. Scale bars: 500 μm (C-J), 250 μm (A, B, O, Q, S), 100 μm (M, P, T), 50 μm (K, R) and 25 μm (L, N).

https://doi.org/10.1371/journal.pone.0184767.g005

Dynamic expression of Mt4-mmp during limb development

Mt4-mmp distribution was also analyzed during mouse limb development showing a very dynamic pattern of expression. Therefore, Mt4-mmp$^{LacZ/+}$ expression was detected by means of β-gal staining during limb development from E10.5 to E16.5 (Fig 5). At early stages of development (E10.5), positive cells were found in distal (forelimb) and proximal (hindlimb) areas as well as in the posterior part of the limbs, particularly in the Zone of Polarizing Activity (ZPA) (Fig 5A and 5B). Paraffin sections at this stage also evidenced positive cells in the

mesenchyme (Fig 5K, 5M and 5N) in a pattern compatible with vascular networks established within the limb bud. In addition, endothelial cells were observed in blood vessels entering the hindlimb (Fig 5K and 5L). No expression was detected in the apical ectodermal ridge (AER) by this stage (Fig 5M and 5N). At E11.5, β-gal staining persisted in distal areas of hand and footplate (Fig 5C and 5D). Expression in the zeugopodium and stylopodium (Fig 5C) begins to be observed at this stage, becoming stronger at E12.5. Also, proximal regions of the handplate and developing digits appear strongly stained (Fig 5E). The footplate is less developed than the handplate, showing an interdigital anterior mesenchymal staining (Fig 5F). At E14.5, the stylopodial and zeugopodial regions showed a strong expression, probably related to the establishment of the earliest muscle blocks (Fig 5G–5J). Mt4-mmp expression extended along the metatarsals and metacarpals, either in the dorsal or ventral side (Fig 5E and 5G–5J). This pattern corresponds to the tendon blastemas as it is evidenced by the β-gal positive cells observed in the paraffin crossed-sections though the digits (Fig 5O and 5P). A strong and consistent expression is observed at E14.5 in subepidermal mesenchymal cells and in ventral muscle groups (Fig 5Q, 5R and 5S). Limb sections at the level of proximal radius and ulna, revealed that LacZ expressing cells are related to the developing vascular network irrigating the dorsal muscleskeletal elements (i.e. tendons/ligaments) (Fig 5R, 5S and 5T).

To confirm our results, we performed RT-PCR analysis that revealed Mt4-mmp expression in the WT forelimbs at E10.5, E12.5 and E14.5 whereas RNA levels were reduced in the HT and absent in the KO forelimbs (Fig 4A). As shown by means of β-gal staining, Mt4-mmp RNA levels significantly increase during development ($p < 0.05$; Fig 4A). In addition, analysis by western-blot confirmed the expression of the protein in the forelimbs of E14.5 WT and HT embryos while it is absent in the KO embryo (Fig 4B).

Mt4-mmp is highly expressed during brain development

Mt4-mmp expression has been previously reported in the brain at late embryonic and postnatal stages [9,10,15]. Here, we demonstrate that Mt4-mmp is located in the nervous system from the early embryo to postnatal stages of development. Thus, Mt4-mmp expression was first detected associated to blood vessels in the neural parenchyma, the notochord, the floor plate and the neural tube at early embryonic stages as shown in transverse sections (Fig 1F, 1H and 1I) (from E9.5 to E11.5). By E11.5, a strong expression was found in the ventral column of motoneurons of the spinal cord (Fig 6A). We could not find phenotypic differences in the distribution of two transcription factors, Nkx6.1 and Olig2, both involved in the ventral patterning of the neural tube, when comparing the percentage of positive cells between the WT and HT embryos, nor when we analysed the KO embryos (S1A–S1C and S1G Fig). Also, we have reported LacZ staining in the floor plate and immunohistochemistry for FoxA2 revealed that the formation of the floor plate is normally specified and developed in the WT, HT and KO embryos (S1D–S1F Fig). Positive cells for LacZ were also observed in the floor plate of the rhombencephalon and mesencephalon at this stage (Fig 6C). By E14.5, LacZ-positive cells were detected in the olfactory bulb (Fig 6D) and the mantle zone of the cerebral cortex (Fig 6H). Notably, expression of Mt4-mmp was found in the spinal cord, particularly stronger at the cervical and lumbar intumescence levels. Other structures in the brain were also labelled at this stage as the dorsal thalamus (Fig 6H), the dorsal hypothalamus, the rhombic lip and the primordium of the cerebellum (Fig 6J and 6K). Mt4-mmp$^{LacZ/+}$ cells were observed in the choroid plexus of the IV ventricle as well as in the blood vessels in the cerebral parenchyma by this stage.

Later in development, the pattern of expression of Mt4-mmp was similar from E18.5 to postnatal stages P0 and P1. Expression restricted to the motoneuron pool in the spinal cord is maintained at E18.5 (Fig 6B). The β-gal staining of coronal sections from postnatal Mt4-mmp$^{LacZ/+}$

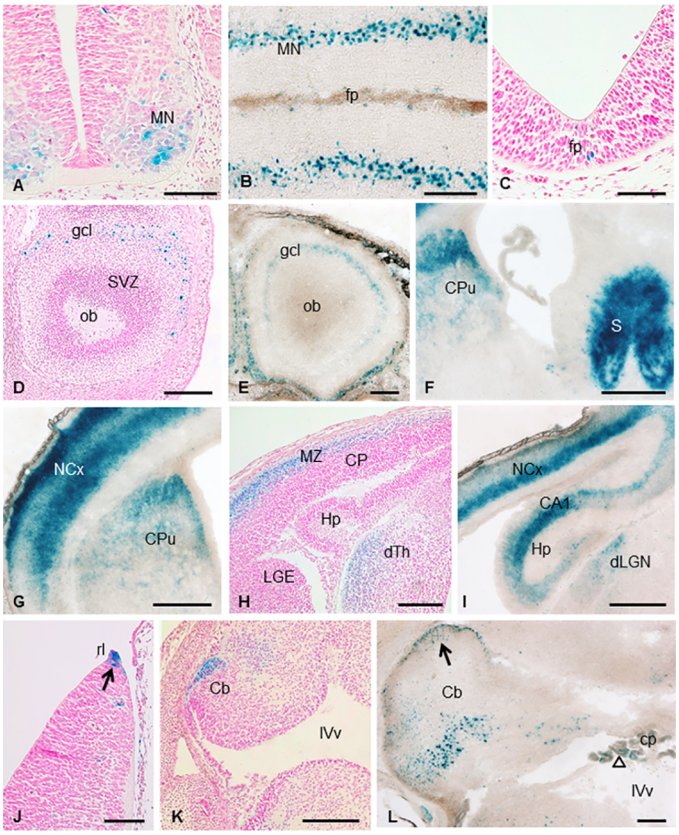

Fig 6. Expression of Mt4-mmp in the developing mouse brain. β-gal staining of coronal sections of embryonic E11.5 (A) and longitudinal sections of E18.5 Mt4-mmp$^{LacZ/+}$ embryos (B) (n = 3) revealed expression of Mt4-mmp in the ventral column of motoneurons in the spinal cord. In addition, β-gal positive cells were detected in the floor plate of the mesencephalon at E11.5 (C). LacZ-positive cells were located in the granular cell layer of the olfactory bulb at embryonic stage E14.5 (D) and postnatal stages (E). Reporter expression was also detected in the septum, striatum, at deep and superficial layers of the cerebral cortex, the hippocampus and the dorsal thalamus and dorsal lateral geniculate nucleus at E14.5 (H) and P1 (F,G,I; n = 3). Mt4-mmp expression was located at the rhombic lip at E12.5 (arrow in J) and the cerebellum primordium at E14.5 (K). By postnatal stages, many β-gal-positive cells were located at the cerebellum possibly corresponding to Purkinje cells and in the external granule layer (arrow in L). At this level, staining was also detected in the choroid plexus of the IV ventricle (empty arrow in L). Abbreviations: Cb, cerebellum; cp, choroid plexus; CP, cortical plate; CPu, caudate putamen; gcl, granular cell layer; dLGN, dorsal lateral geniculate nucleus; dTh, dorsal thalamus; Hp, hippocampus; MZ, mantle zone; NCx, neocortex; ob, olfactory bulb; rl, rhombic lip; S, septum; SVZ, subventricular zone; IVv, IV ventricle. Scale bars: 500 μm (F, G, I), 200 μm (B, D, E, H, K, L) and 100 μm (A, C, J).

https://doi.org/10.1371/journal.pone.0184767.g006

mice revealed expression of Mt4-mmp in the granular layer of the olfactory bulb (Fig 6E). A strong reporter expression was also detected in the septum, caudate-putamen (striatum), at deep and superficial layers of the cerebral cortex and the hippocampus (Fig 6F, 6G and 6I). Many β-gal-positive cells were located at the cerebellum possibly corresponding to Purkinje cells and in the external granule layer (Fig 6L). At this level, staining was also detected in the choroid plexus of the IV ventricle (Fig 6L).

Quantitative RT-PCR analysis confirmed increasing RNA levels of Mt4-mmp as brain development proceeds. Thus, expression of the enzyme was low in the cerebral cortex of E10.5 WT embryos but highly increased at E14.5 (significance at $p < 0.001$) (Fig 4A). At this stage, Mt4-mmp expression was also detected in other brain regions, as the olfactory bulb, spinal cord, mesencephalon and hindbrain. Supporting these data, the expression of the protein

MT4-MMP in the brain was confirmed by western blot analysis in the cerebral cortex and the spinal cord of E14.5 WT and HT embryos while no protein levels were detected in the KO. As shown in Fig 4B, the quantity of the enzyme is significantly higher in the cerebral cortex as compared with protein levels detected in the spinal cord and forelimb at this embryonic stage. These results are consistent with our data on the LacZ reporter expression of our gene in these brain regions.

Mt4-mmp expression in sensory organs and during eye development

Mt4-mmp expression was also detected related to the development of distinct sensory organs (Fig 7). Thus, from E12.5 some dispersed LacZ-positive cells were detected dorsally in the olfactory epithelium at the entrance to the primitive nasal cavity (Fig 7A). This expression persists and increases later in development and by E14.5 βgal-positive cells are located in the dorsal part of the olfactory epithelium and the surrounding mesenchyme (Fig 7B and 7D). At E10.5, scattered LacZ-positive cells were found at the otic vesicle (Fig 7I) and this expression is restricted to the caudal portion of the saccule and the associated vestibulocochlear (VIII) ganglia complex at later stages of development (Fig 7J). In addition, some β-gal positive cells were distributed in the semicircular canal from E11.5 embryonic stage (Fig 7K). Sections through the external ear of E14.5 and E16.5 embryos revealed Mt4-mmp labeling in proliferating cells at the base of the developing pinna as well as in mesenchymal cells (Fig 7G and 7H). By E14.5 Mt4-mmp$^{LacZ/+}$ cells were located in the ventral extremity of the lower and upper jaws (Fig 7E) and the epithelium of nose (Figs 2I and 7E). In addition, high levels of expression were found in the mesenchymal layer immediately surrounding the hair follicles primordium of vibrissa and the dermal papilla in the hair bulb (Figs 2H, 2I and 7B and 7C), as well as in the precursor of median fibrous septum and intrinsic muscles of the tongue (Fig 7F) from E12.5 to E16.5.

Finally, we examined Mt4-mmp$^{Lacz/+}$ expression at distinct stages of the eye development. Expression within the optic cup was restricted and first detected by E10.5 in the hyaloid artery (Fig 8A). This pattern of expression in the blood vessels within the eye is maintained throughout development (Fig 8B and 8C) and persists in the central retinal artery entering through the optic disc by E18.5 and postnatal stages (Fig 8E). In addition, cells positive for LacZ were also detected in the lens at E12.5 with a stronger expression at E14.5 (Fig 8C and 8D). Mt4-mmp expression was also observed in scattered cells of the neural retina at E14.5 (Fig 8D). These results are consistent with the detection of the Mt4-mmp RNA levels as demonstrated by RT-PCR in the eye at this embryonic stage (Fig 4A). As development proceeds, the labelling was stronger and mainly restricted to the retinal ganglion cell layer in the postnatal neural retina (Fig 8E and 8F). Notably, a strong expression was also detected in the eyelids from E14.5 to postnatal stages (Figs 2I, 8D and 8E).

Discussion

The present data reports for the first time that Mt4-mmp expression in the mouse embryo is developmentally controlled and tissue specific, which suggest important roles for this metalloproteinase during brain formation as well as during cardiovascular and limb development.

Previous attempt to analyze Mt4-mmp developmental function were hampered partially due to the lack of apparent abnormal developmental phenotypes in Mt4-mmp null mice, which have been suggestive of redundant roles for this enzyme with other MMPs [9]. To date, only one study has pointed out the requirement of mmp17b, the ortholog of Mmp17 in zebrafish, during cardiovascular development, contributing to vascular smooth muscle cells (VSMCs) in certain aortic regions [17]. Supporting these data, we have recently shown that the

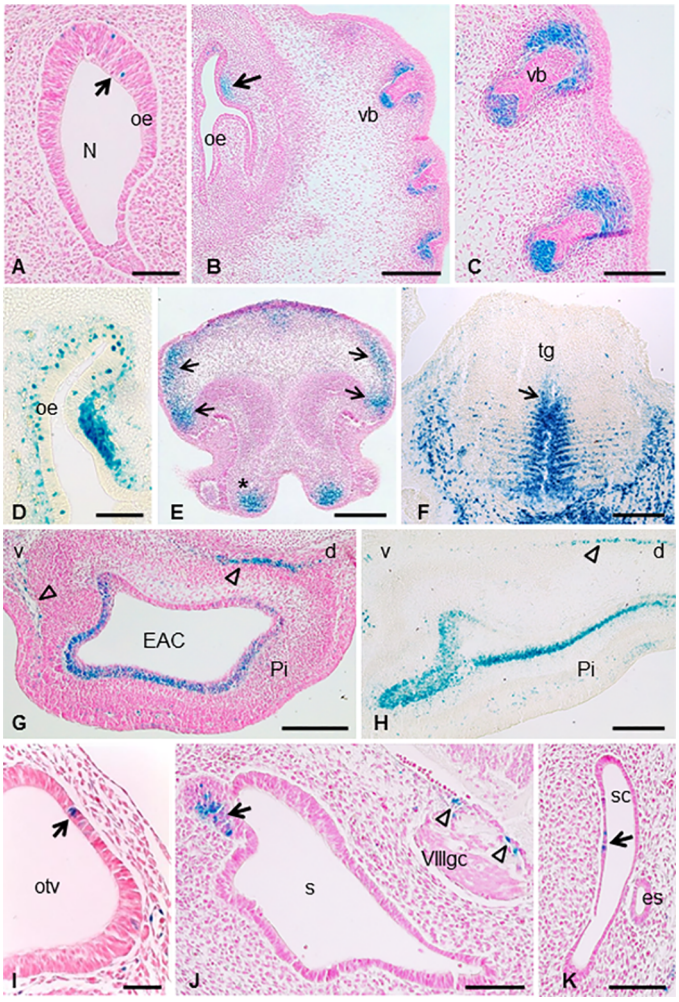

Fig 7. Mt4-mmp expression in sensory organs of the developing mouse embryo. (A-D) Coronal sections through the embryo show the expression of scattered β-gal positive cells dorsally in the olfactory epithelium at the entrance to the nasal cavity at E12.5 (A) and E14.5 (B,D) as well as in the surrounding mesenchyme (arrow in B). High expression of Mt4-mmp was also detected in mesenchymal cells adjacent to the primordium of the follicle of vibrissae (B,C). (E-F) At this embryonic stage, Mt4-mmp expression was also detected in the ventral extremity of the upper jaw (asterisk in E), epithelium of the nose (arrows in E) and median fibrous septum (arrow) and intrinsic muscle of the tongue (F). (G-H) LacZ-positive cells were distributed in the pinna of the ear at E14.5 and E16.5 stages. Empty arrows indicate mesenchymal cells in the pinna. (I-K) From E10.5, the first Mt4-mmp$^{lacZ/+}$ cells were detected in the otic vesicle (arrow in I) and persists at E12.5, in the caudal portion of the saccule (arrow in J), the vestibulocochlear (VIII) ganglion complex (arrowheads in J) as well as in the semicircular canal (arrow in K). Abbreviations: d, dorsal; EAC, external auditory canal; es, endolymphatic sac; N, nasal cavity; oe, olfactory epithelium; otv, otic vesicle; Pi, pinna; s, saccule; sc, semicircular canal; tg, tongue; v, ventral; vb, sensory vibrissae; VIIIgc, vestibulocochlear (VIII) ganglion complex. Scale bars: 200 μm (B, E, F, G, H), 100 μm (A, C, D, J, K) and 50 μm (I).

https://doi.org/10.1371/journal.pone.0184767.g007

activity of this enzyme is essential for arterial vessel wall development and function in adult mice. Thereby, the lack of Mt4-mmp results in the presence of immature VSMCs and altered ECM in the vessel wall leading to a dilative arterial disorder and hypotension. Maturation of VSMCs during aortic wall development involves the c-Jun N-terminal kinase (JNK) intracellular signaling pathway [18]. Notably, the Wnt/planar cell polarity (PCP) pathway involves downstream activation of JNK in the embryo to mediate cytoskeletal rearrangement and cell movement. Our present data prove Mt4-mmp expression in the dorsal aorta and in premigratory and

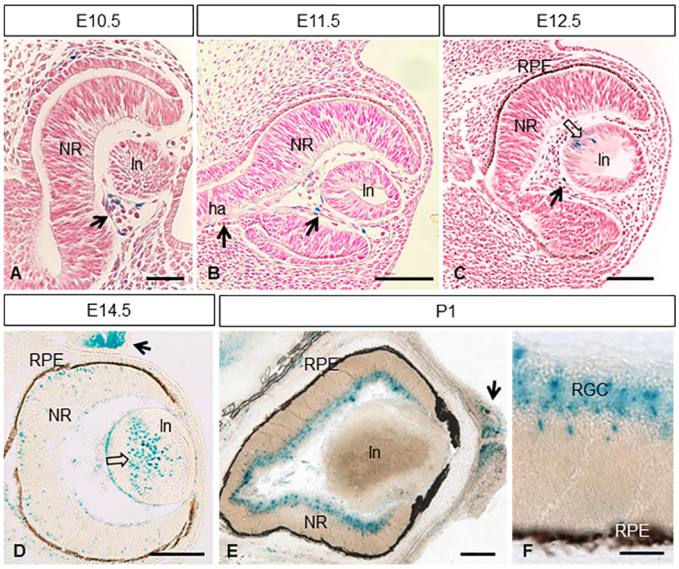

Fig 8. Expression of Mt4-mmp$^{LacZ/+}$ during mouse eye development. β-gal staining of coronal sections through the eye at different stages of development revealed Mt4-mmp expression in the hyaloid artery from E10.5 to E12.5 embryos (arrows in A-C). Scattered LacZ-positive cells were first detected in the lens by E12.5 and persist at E14.5 (opened arrows in C, D). A strong Mt4-mmp expression in the eyelids (arrow in D) and some β-gal positive cells was shown in the neural retina at E14.5 (D). At postnatal stages, expression of Mt4-mmp was distributed particularly in the retinal ganglion cell layer (E, F) of the neural retina and persists in the eyelids (arrow in E). Abbreviations: ha, hyaloid artery; ln, lens; NR, neural retina; RGC, retinal ganglion cells; RPE, retinal pigmented epithelium. Scale bars: 200 μm (D, E), 100 μm (B, C) and 50 μm (A, F).

https://doi.org/10.1371/journal.pone.0184767.g008

migratory neural crest cells at early stages of development. Thereby, it is possible that Mt4-mmp participates during cell migration in the mouse embryo in a similar manner as described in zebrafish [17].

Expression of MT4-MMP was initially reported in several adult human tissues such as the brain, leukocytes, colon, ovary, testis [5] and the amniochorion [26]. Similarly in mice, Mt4-mmp was detected in distinct organs such as the lung, uterus, spleen, stomach, intestine, testis, ovary, liver, kidney, skeletal muscle and heart [9]. Also high Mt4-mmp expression was described in the cerebrum, particularly in the dorsal cortical plate at late mouse embryonic stages, and the cerebral cortex, hippocampus, caudate-putamen and hypothalamus in the postnatal brain [9,10,15]. However, no detailed expression analysis for this enzyme has been published during early CNS development before. Our study confirms previous data and reports for the first time the detection of Mt4-mmp from early stages of the embryonic brain. As development proceeds, the enzyme localized in other structures, such as the olfactory bulb, mantle zone of the cerebral cortex, septum, hippocampus or the striatum. Even though the role of Mt4-mmp in the brain is not yet clear, our results hint for important functions of its activity during CNS development. Expression from early embryonic stages may involve the activity of the enzyme in neural proliferation and migration, whereas later in development Mt4-mmp may participate in other functions such as synaptic transmission and plasticity due to its expression in the cerebral cortex and hippocampus. Despite to date only one study has proposed a physiological role for Mt4-mmp in the CNS [9], we hypothesize that Mt4-mmp may contribute to these functions by remodeling the ECM locally or interacting with other cell signaling pathways.

We have also shown that, during eye development, Mt4-mmp expression is initially restricted to blood vessels of the hyaloid artery at early stages and it can also be detected in the

lens and retinal ganglion cell (RGC) layer in later stages. Supporting our data, it has been reported that Mt4-mmp is selectively expressed in starburst amacrines and in a subset of ON-OFF direction-selective RGCs at postnatal stages, particularly in those RGCs that prefer nasal motion [27]. Moreover, we found that Mt4-mmp is expressed in the dorsal thalamus by E14.5 and in the dorsal lateral geniculate nucleus postnatally, one of the major central targets for retinal axons. These data suggest the involvement of this protease during axon guidance of visual axons. In fact, there are some evidence for the requirement for MMPs in the development of the retinotectal projections. Thus, broad inhibition of MMP activity in *in vivo* exposed preparations of *Xenopus* brain resulted in misguidance of RGC axons at the level of the optic chiasm and the optic tectum [28,29]. Furthermore, it was demonstrated that Mmp14a, one paralog of another membrane-anchored MMP (Mmp14/Mt1-mmp), is necessary for retinal neurogenesis and differentiation and RGC axon innervation of the optic tectum in zebrafish larvae [30]. Also another transmembrane MMP, Mt5-mmp, which is highly expressed in the hippocampus and cerebellum, has been directly involved in axon growth and detected at the growth cone [31,32]. Nevertheless, it remains to be determined if Mt4-mmp also participates in axon guidance and growth of retinal projections and if it is involved during the proliferation and maturation of the retina.

As shown in our study, Mt4-mmp is highly and dynamically expressed during the formation of the mouse embryonic limb since early developmental stages, being detected in the zone of polarizing activity (ZPA) and the mesenchyme underlying the apical ectodermal ridge (AER), respectively. Notably, cells in the ZPA secrete the morphogen Sonic Hedgehog (Shh) which regulates digit fate and is crucial to establish the anterior-posterior skeletal pattern of the limb at these stages [33,34]. In the proximo-distal axis, outgrowth of digits requires fibroblast growth factor (FGF) signaling emanating from the AER [35]. Since the appropriate limb development requires the coordination of both signaling pathways in the anterior-posterior and proximo-distal axis, it is likely that Mt4-mmp associates with both. Regarding this idea, a recent study has pointed out that the activity of the membrane-anchored metalloproteinase-regulator RECK is essential for limb development, directing the expression of genes in three signaling centers essential for limb growth and patterning: DE (producing Wnt7a), ZPA (producing Shh), and AER (producing Fgfs) [36]. Whether the expression of these morphogens is altered in the Mt4-mmp mutant embryonic limb has not been addressed so far, although limb development seems to be normal in the mutant embryo.

In addition to the latter, our data shows Mt4-mmp expression in ZPA cells at E10.5, suggesting that Mt4-mmp might be related to the role proposed for Shh on the anterior-posterior organization of muscles acting through migrating progenitors coming from the somites. These cells, once in the limb bud, will respond to Shh signal from the posterior part of the limb [37]. As limb development proceeds and the skeletal elements differentiate, Mt4-mmp is expressed in the tendons of digits and in developing muscle blocks in the stylopodium and zeugopodium confirming previous evidence [38–40]. Moreover, limb expression of Mt4-mmp between E12.5 and E14.5 mimics that of Scleraxis (Scx), a highly specific marker for tendons [41].

We have also demonstrated that the expression of Mt4-mmp is linked to the vascularization of the limb buds between E10.5-E11.5. At these stages, angiogenesis initiates as sprouts from the dorsal aorta, invading the limb and forming a vascular plexus within the limb mesenchymal core [42]. In addition, concomitant vasculogenesis occurs by migration of somite-derived angioblasts to be integrated into the developing vascular plexus [43]. Both events can be recognized in the limbs included in this study. Thus, β-gal positive cells are found in the mesenchyme extending along the network of microvessels throughout the limb. Also, Mt4-mmp was expressed in the blood vessels entering the limb buds at E10.5 in a pattern compatible with that reported by [44]. Regarding limb development, Mt4-mmp expression also seems to be

related to muscle progenitors in the embryonic limb bud by E10.5. Thus, Mt4-mmp expression is observed in cells at the base of the hindlimb, compatible with migrating myogenic and angioblastic cells as described by [45]. Indeed, expression of the enzyme is associated to the initial formation of blood vessels in other structures and organs of the embryo, such as the eye, heart or the nervous system. From our data, Mt4-mmp expression is also located in distinct blood vessels (carotid artery, umbilical vein, vitellin artery an vein, primary head vein, PNVP) at early stages, when the first vascular system start to develop. Mt4-mmp expression in the dorsal aorta has been reported as early as E10.5 in periaortic progenitors and in the adult mouse [10,18], but here we report that Mt4-mmp is detected even earlier in development (from E8.5), possibly related to the hemogenic endothelium. Altogether, our data reveal that Mt4-mmp is located in endothelial cells (EC) of blood vessels of distinct organs at early embryonic development, which contrasts with the fact that its expression seems to be downregulated in EC of more mature blood vessels [9]. The role of Mt4-mmp in blood vessel formation during embryogenesis remains unknown, since only in pathological conditions, Mt4-mmp has been involved in angiogenesis by contributing to vessel maturation and stabilization during tumor progression [1]. For instance, in breast cancer, MT4-MMP induces tumor growth and metastasis by stimulating angiogenesis in the tumor [23,46]. Notably, this angiogenic response requires its proteolytic activity in the tumor compartment but not from the host-derived stroma [46]. Thus, MT4-MMP expression in host cells does not affect angiogenesis. Therefore, it is conceivable that as occurs during metastatic dissemination, Mt4-mmp also contributes to create a permissive microenvironment that favors cell migration in the embryo.

Regarding the proteolytic activity of Mt4-mmp, only few substrates have been identified so far, including pro-TNFα, α-macroglobulin [47], low density lipoprotein receptor related protein (LRP) [48] and aggrecanase (ADAMTS-4) [49] Recently, the matricellular glycoprotein osteopontin (OPN) has been also confirmed as another substrate cleaved by Mt4-mmp and essential during the formation of the aortic wall [18]. Interestingly, OPN is expressed in other tissues during embryonic development where Mt4-mmp also localizes, as the kidney, cartilage and brain. Thus, OPN is expressed in several neural nuclei of the developing rat brainstem and cerebellum [50] as well as in active macrophages in the embryonic and early rat postnatal brain [51]. Previous data suggest that OPN may contribute to the migration and phagocytic function of brain macrophages in the developing rat brain. In fact, OPN functions as a potent chemoattractant that promotes the migration of cells of monocyte/macrophage lineage [52]. However, if OPN has a specific function dependent on Mt4-mmp proteolytic activity during embryogenesis as in the aortic development, remains unknown. It should be mentioned that apart from its proteolytic function, Mt4-mmp is also able to modify intracellular response through the activation of the growth receptor EGFR. Thus, Mt4-mmp positively promotes cancer cell proliferation by enhancing the EGFR signaling pathway independently on the catalytic site of the enzyme [53].

In summary, in this study we reported the spatiotemporal expression of Mt4-mmp during mouse embryonic development. The present data reveals that this GPI-anchored metalloproteinase is expressed in a dynamic pattern of expression from early stages of development to postnatal stages with a high expression of this enzyme during vascular development and brain formation. Our results point for key functions of Mt4-mmp during the CNS and limb development as well as in angiogenesis. If similarly to cancer cells, non-catalytic and catalytic functions of Mt4-mmp can be required for proliferation and for angiogenesis and cell migration in the embryo requires further research. In these processes, both ECM remodeling at pericellular level and activation of distinct intracellular signaling pathways to direct cell movement are crucial events that may involve Mt4-mmp activity.

Supporting information

S1 Fig. Mt4-mmp is not expressed in the proepicardium and epicardium at early developmental stages. (A-B) LacZ staining of sagital sections from E9.5 Mt4-mmp$^{LacZ/+}$ embryos illustrating the lack of βgal-positive cells in the region of the proepicardium. (C-H) Double labelling immunohistochemistry for anti-WT-1 (arrows in red) and anti-βgal (green). No doubled-positive cells were detected in the region of the epicardium nor in the proepicardium of E10.5 heterozygous embryos. Abbreviations: EC, epicardium; PE, proepicardium; V, ventricle. Scale bars = 50 μm (A,B); 40 μm (C-H).
(TIF)

S2 Fig. Ventral patterning and specification of the embryonic neural tube. (A-C) Double-labelling immunohistochemistry for the transcription factors Nkx6.1 (red) and Olig2 (green) in the neural tube of E10.5 WT, HT and KO embryos. (D-F) Immunostaining for FoxA2 (red) demonstrated that the floor plate is properly specified in the WT, HT and KO neural tubes. Sections were incubated with Hoechst for nuclear staining (blue). (F) Quantification of the percentage of Nkx6.1 and Olig2-positive cells relative to the total area of the neural tube in the WT, HT and KO embryos. Data are presented as mean ± SD (n = 3 per each genotype). One-way ANOVA analysis revealed no statistical differences in the percentage of positive cells among the WT, HT and KO neural tubes. Abbreviations: fp, floor plate. Scale bars: 50 μm (A-C); 20 μm (D-F).
(TIF)

S3 Fig. Database containing quantified data from real-time PCR and western blot analysis (in Fig 4) and ventral neural tube patterning (in S2 Fig).
(XLSX)

Acknowledgments

We would like to thank to Roisin Brid Doohan for her technical assistance at the Histopathological Service and Laura Balonga and Ángel Colmenar for mouse genotyping at the Centro Nacional de Investigaciones Cardiovasculares (CNIC).

Author Contributions

Conceptualization: Alicia G. Arroyo, Cristina Sánchez-Camacho.

Funding acquisition: Alicia G. Arroyo, Cristina Sánchez-Camacho.

Investigation: María José Blanco, Iván Rodríguez-Martín, Ana I. R. Learte, Cristina Clemente, María Gregoria Montalvo, Cristina Sánchez-Camacho.

Methodology: María José Blanco, Iván Rodríguez-Martín, Ana I. R. Learte.

Project administration: Cristina Sánchez-Camacho.

Resources: Motoharu Seiki.

Writing – original draft: María José Blanco, Ana I. R. Learte, Alicia G. Arroyo, Cristina Sánchez-Camacho.

References

1. Sounni N. E., Paye A., Host L., & Noël A. MT-MMPS as regulators of vessel stability associated with angiogenesis. Front Pharmacol. 2011; 2, 111. https://doi.org/10.3389/fphar.2011.00111 PMID: 21687519

2. Itoh Y., Kajita M., Kinoh H., Mori H., Okada A., & Seiki M. Membrane type 4 matrix metalloproteinase (MT4-MMP, MMP-17) is a glycosylphosphatidylinositol-anchored proteinase. J Biol Chem 1999; 274 (48):34260–34266. PMID: 10567400
3. Seiki M. Membrane-type 1 matrix metalloproteinase: a key enzyme for tumor invasion. Cancer Lett. 2003; 194(1):1–11. PMID: 12706853
4. Itoh Y. Membrane-type matrix metalloproteinases: their functions and regulations. Matrix Biol. 2015; 44:207–223. https://doi.org/10.1016/j.matbio.2015.03.004 PMID: 25794647
5. Puente X. S., Pendás A. M., Llano E., Velasco G., & López-Otín C. Molecular cloning of a novel membrane-type matrix metalloproteinase from a human breast carcinoma. Cancer Res. 1996; 56(5): 944–949. PMID: 8640782
6. Kajita M., Kinoh H., Ito N., Takamura A., Itoh Y., Okada A. et al. Human membrane type-4 matrix metalloproteinase (MT4-MMP) is encoded by a novel major transcript: isolation of complementary DNA clones for human and mouse mt4-mmp transcripts. FEBS Lett. 1999; 457(3):353–356. PMID: 10471807
7. Kolkenbrock H., Essers L., Ulbrich N., & Will H. Biochemical characterization of the catalytic domain of membrane-type 4 matrix metalloproteinase. Biol Chem. 1999; 380(9):1103–1108. https://doi.org/10.1515/BC.1999.137 PMID: 10543448
8. Mittal R., Patel A. P., Debs L. H., Nguyen D., Patel K., Mittal J. et al. Intricate functions of matrix metalloproteinases in physiological and pathological conditions. J Cell Physio. 2016; 231(12):2599–2621. https://doi.org/10.1002/jcp.25430 PMID: 27187048
9. Rikimaru A., Komori K., Sakamoto T., Ichise H., Yoshida N., Yana I. et al. Establishment of an MT4-MMP-deficient mouse strain representing an efficient tracking system for MT4-MMP/MMP-17 expression in vivo using β-galactosidase. Genes Cells. 2007; 12(9):1091–1100. https://doi.org/10.1111/j.1365-2443.2007.01110.x PMID: 17825051
10. Srichai M. B., Colleta H., Gewin L., Matrisian L., Abel T. W., Koshikawa N. et al. Membrane-type 4 matrix metalloproteinase (MT4-MMP) modulates water homeostasis in mice. PloS ONE, 2011; 6(2): e17099. https://doi.org/10.1371/journal.pone.0017099 PMID: 21347258
11. Verma R. P., & Hansch C. Matrix metalloproteinases (MMPs): chemical–biological functions and (Q) SARs. Bioorg Med Chem. 2007; 15(6): 2223–2268. https://doi.org/10.1016/j.bmc.2007.01.011 PMID: 17275314
12. Sohail A., Sun Q., Zhao H., Bernardo M. M., Cho J. A., & Fridman R. MT4-(MMP17) and MT6-MMP (MMP25), a unique set of membrane-anchored matrix metalloproteinases: properties and expression in cancer. Cancer Metastasis Rev. 2008; 27(2):289–302. https://doi.org/10.1007/s10555-008-9129-8 PMID: 18286233
13. Curry T. E., Dean D. D., Sanders S. L., Pedigo N. G., & Jones P. B. The role of ovarian proteases and their inhibitors in ovulation. Steroids. 1989; 54(5): 501–521. PMID: 2559499
14. Yong V. W. Metalloproteinases: mediators of pathology and regeneration in the CNS. Nat Rev Neurosc. 2005; 6(12): 931–944. https://doi.org/10.1038/nrn1807 PMID: 16288297
15. Funatsu N., Inoue T., & Nakamura S. Gene expression analysis of the late embryonic mouse cerebral cortex using DNA microarray: identification of several region-and layer-specific genes. Cereb Cortex. 2004; 14(9):1031–1044. https://doi.org/10.1093/cercor/bhh063 PMID: 15142957
16. McFarlane S. Metalloproteases: carving out a role in axon guidance. Neuron. 2003; 37(4):559–562. PMID: 12597854
17. Leigh N. R., Schupp M. O., Li K., Padmanabhan V., Gastonguay A., Wang L. et al. Mmp17b is essential for proper neural crest cell migration in vivo. PloS ONE 2013; 8(10):e76484. https://doi.org/10.1371/journal.pone.0076484 PMID: 24098510
18. Martin-Alonso M., Garcia-Redondo A. B., Guo D., Camafeita E., Martínez F., Alfranca A. et al. Deficiency of MMP17/MT4-MMP proteolytic activity predisposes to aortic aneurysm in mice. Circ Res. 2015; CIRCRESAHA-114. https://doi.org/10.1161/CIRCRESAHA.117.305108 PMID: 25963716
19. Zucker S., Pei D., Cao J., & Lopez-Otin C. Membrane type-matrix metalloproteinases (MT-MMP). Curr Top Dev Biol 2003; 54: 1–74. PMID: 12696745
20. Hotary K., Li X. Y., Allen E., Stevens S. L., & Weiss S. J. A cancer cell metalloprotease triad regulates the basement membrane transmigration program. Genes Dev. 2006; 20(19):2673–2686. https://doi.org/10.1101/gad.1451806 PMID: 16983145
21. Itoh Y., & Seiki M. MT1-MMP: A potent modifier of pericellular microenvironment. J Cell Physio. 2006; 206(1):1–8. https://doi.org/10.1002/jcp.20431 PMID: 15920734
22. Arroyo A. G., Genis L., Gonzalo P., Matias-Roman S., Pollan A., & Galvez B. G. Matrix metalloproteinases: new routes to the use of MT1-MMP as a therapeutic target in angiogenesis-related disease. Curr Pharm Des. 2007; 13(17):1787–1802. PMID: 17584108

23. Chabottaux V., & Noel A. Breast cancer progression: insights into multifaceted matrix metalloproteinases. Clin Exp Metastasis. 2007; 24(8):647–656. https://doi.org/10.1007/s10585-007-9113-7 PMID: 17968664

24. Sánchez-Camacho C., Ortega J. A., Ocaña I., Alcántara S., & Bovolenta P. Appropriate Bmp7 levels are required for the differentiation of midline guidepost cells involved in corpus callosum formation. Dev Neurobiol. 2011; 71(5), 337–350. https://doi.org/10.1002/dneu.20865 PMID: 21485009

25. Schmittgen T. D., & Livak K. J. Analyzing real-time PCR data by the comparative CT method. Nat Protoc. 2008; 3(6):1101–1108. PMID: 18546601

26. Fortunato S. J., & Menon R. Screening of novel matrix metalloproteinases (MMPs) in human fetal membranes. J Assist Reprod Genet. 2002; 19(10):483–486. https://doi.org/10.1023/A:1020362519981 PMID: 12416653

27. Kay J. N., De la Huerta I., Kim I. J., Zhang Y., Yamagata M., Chu M. W. et al. Retinal ganglion cells with distinct directional preferences differ in molecular identity, structure, and central projections. J Neurosc. 2011; 31(21): 7753–7762. https://doi.org/10.1523/JNEUROSCI.0907-11.2011 PMID: 21613488

28. Webber C. A., Hocking J. C., Yong V. W., Stange C. L., & McFarlane S. Metalloproteases and guidance of retinal axons in the developing visual system. J Neurosc. 2002; 22(18):8091–8100. PMID: 12223563

29. Hehr C. L., Hocking J. C., & McFarlane S. Matrix metalloproteinases are required for retinal ganglion cell axon guidance at select decision points. Development. 2005; 132(15):3371–3379. https://doi.org/10.1242/dev.01908 PMID: 15975939

30. Janssens E., Gaublomme D., De Groef L., Darras V. M., Arckens L., Delorme N. et al. Matrix metalloproteinase 14 in the zebrafish: an eye on retinal and retinotectal development. PloS ONE. 2013; 8(1): e52915. https://doi.org/10.1371/journal.pone.0052915 PMID: 23326364

31. Hayashita-Kinoh H., Kinoh H., Okada A., Komori K., Itoh Y., Chiba T. et al. Membrane-type 5 matrix metalloproteinase is expressed in differentiated neurons and regulates axonal growth. Cell Growth Differ. 2001; 12(11): 573–580. PMID: 11714638

32. Monea S., Jordan B. A., Srivastava S., DeSouza S., & Ziff E. B. Membrane localization of membrane type 5 matrix metalloproteinase by AMPA receptor binding protein and cleavage of cadherins. J Neurosc. 2006; 26(8):2300–2312. https://doi.org/10.1523/JNEUROSCI.3521-05.2006 PMID: 16495457

33. Marigo V., Davey R. A., Zuo Y., Cunningham J. M., & Tabin C. J. Biochemical evidence that patched is the Hedgehog receptor. Nature. 1996; 384(6605):176. https://doi.org/10.1038/384176a0 PMID: 8906794

34. Chiang C., Litingtung Y., Harris M. P., Simandl B. K., Li Y., Beachy P. A. et al. Manifestation of the limb prepattern: limb development in the absence of sonic hedgehog function. Dev Biol. 2001; 236(2):421–435. https://doi.org/10.1006/dbio.2001.0346 PMID: 11476582

35. Mao J., McGlinn E., Huang P., Tabin C. J., & McMahon A. P. Fgf-dependent Etv4/5 activity is required for posterior restriction of Sonic Hedgehog and promoting outgrowth of the vertebrate limb. Dev Cell. 2009; 16(4):600–606. https://doi.org/10.1016/j.devcel.2009.02.005 PMID: 19386268

36. Yamamoto M., Matsuzaki T., Takahashi R., Adachi E., Maeda Y., Yamaguchi S., et al. The transformation suppressor gene Reck is required for postaxial patterning in mouse forelimbs. Biol Open. 2012; 1 (5):458–466. https://doi.org/10.1242/bio.2012638 PMID: 23213437

37. Hu J. K. H., McGlinn E., Harfe B. D., Kardon G., & Tabin C. J. Autonomous and nonautonomous roles of Hedgehog signaling in regulating limb muscle formation. Genes Dev. 2012; 26(18):2088–2102. https://doi.org/10.1101/gad.187385.112 PMID: 22987639

38. McCulloch D. R., Le Goff C., Bhatt S., Dixon L. J., Sandy J. D., & Apte S. S. Adamts5, the gene encoding a proteoglycan-degrading metalloprotease, is expressed by specific cell lineages during mouse embryonic development and in adult tissues. Gene Expr Patterns. 2009; 9(5):314–323. https://doi.org/10.1016/j.gep.2009.02.006 PMID: 19250981

39. Watson S. S., Riordan T. J., Pryce B. A., & Schweitzer R. Tendons and muscles of the mouse forelimb during embryonic development. Dev Dynam. 2009; 238(3):693–700. https://doi.org/10.1002/dvdy.21866 PMID: 19235726

40. Huang A. H., Lu H. H., & Schweitzer R. Molecular regulation of tendon cell fate during development. Journal Orthop Res. 2015; 33(6):800–812. https://doi.org/10.1002/jor.22834 PMID: 25664867

41. Murchison N. D., Price B. A., Conner D. A., Keene D. R., Olson E. N., Tabin C. J. et al. Regulation of tendon differentiation by scleraxis distinguishes force-transmitting tendons from muscle-anchoring tendons. Development. 2007; 134(14), 2697–2708. https://doi.org/10.1242/dev.001933 PMID: 17567668

42. Seichert V., & Rychter Z. Vascularization of the developing anterior limb of the chick embryo. 111. Developmental changes in the perimctacarpal capillary network. Folia Morphol (Warsz), 1972; 20, 397405. PMID: 4637581

43. Ambler C. A., Nowicki J. L., Burke A. C., & Bautch V. L. Assembly of trunk and limb blood vessels involves extensive migration and vasculogenesis of somite-derived angioblasts. Dev Biol. 2001; 234 (2):352–364. https://doi.org/10.1006/dbio.2001.0267 PMID: 11397005

44. Eshkar-Oren I., Viukov S. V., Salameh S., Krief S., Akiyama H., Gerber H. P. et al. The forming limb skeleton serves as a signaling center for limb vasculature patterning via regulation of Vegf. Development. 2009; 136(8):1263–1272. https://doi.org/10.1242/dev.034199 PMID: 19261698

45. Yvernogeau L., Auda-Boucher G., & Fontaine-Perus J. Limb bud colonization by somite-derived angioblasts is a crucial step for myoblast emigration. Development. 2012; 139(2):277–287. https://doi.org/10.1242/dev.067678 PMID: 22129828

46. Host L., Paye A., Detry B., Blacher S., Munaut C., Foidart J. M. et al. The proteolytic activity of MT4-MMP is required for its pro-angiogenic and pro-metastatic promoting effects. Int J Cancer. 2012; 131 (7):1537–1548. https://doi.org/10.1002/ijc.27436 PMID: 22262494

47. English W. R., Puente X. S., Freije J. M., Knäuper V., Amour A., Merryweather A. et al. Membrane type 4 matrix metalloproteinase (MMP17) has tumor necrosis factor-α convertase activity but does not activate pro-MMP2. J Biol Chemi. 2000; 275(19):14046–14055. PMID: 10799478

48. Rozanov D. V., Hahn-Dantona E., Strickland D. K., & Strongin A. Y. The low density lipoprotein receptor-related protein LRP is regulated by membrane type-1 matrix metalloproteinase (MT1-MMP) proteolysis in malignant cells. Journal of Biol Chem. 2004; 279(6):4260–4268. https://doi.org/10.1074/jbc.M311569200 PMID: 14645246

49. Clements K. M., Flannelly J. K., Tart J., Brockbank S. M., Wardale J., Freeth J. et al. Matrix metalloproteinase 17 is necessary for cartilage aggrecan degradation in an inflammatory environment. Ann Rheum Dis. 2011; 70(4):683–689. https://doi.org/10.1136/ard.2010.130757 PMID: 21216815

50. Lee M. Y., Choi J. S., Lim S. W., Cha J. H., Chun M. H., & Chung J. W. Expression of osteopontin mRNA in developing rat brainstem and cerebellum. Cell Tissue Res. 2001; 306(2):179–185. https://doi.org/10.1007/s004410100456 PMID: 11702229

51. Choi J. S., Cha J. H., Park H. J., Chung J. W., Chun M. H., & Lee M. Y. Transient expression of osteopontin mRNA and protein in amoeboid microglia in developing rat brain. Exp Brain Res. 2004; 154 (3):275–280. https://doi.org/10.1007/s00221-003-1657-4 PMID: 14557908

52. Giachelli C. M., Lombardi D., Johnson R. J., Murry C. E., & Almeida M. Evidence for a role of osteopontin in macrophage infiltration in response to pathological stimuli in vivo. Am J Pathol. 1998; 152(2):353. PMID: 9466560

53. Paye A., Truong A., Yip C., Cimino J., Blacher S., Munaut C. et al. EGFR activation and signaling in cancer cells are enhanced by the membrane-bound metalloprotease MT4-MMP. Cancer Res. 2014; 74 (23),6758–6770. https://doi.org/10.1158/0008-5472.CAN-13-2994 PMID: 25320013

European Journal of Cell Biology 91 (2012) 889–895

Contents lists available at SciVerse ScienceDirect

European Journal of Cell Biology

journal homepage: www.elsevier.com/locate/ejcb

Review

Site-specific cellular functions of MT1-MMP

Agnieszka Koziol[1], Mara Martín-Alonso[1], Cristina Clemente, Pilar Gonzalo, Alicia G. Arroyo*

Vascular Biology and Inflammation Department, Centro Nacional de Investigaciones Cardiovasculares (CNIC), 28029 Madrid, Spain

ARTICLE INFO

Article history:
Received 6 June 2012
Received in revised form 18 July 2012
Accepted 19 July 2012

Keywords:
MT1-MMP
Subcellular location
Cell migration
Cell metabolism
Hypoxia
Chromatin remodeling
Macrophages
Inflammation
Endothelial cells
Angiogenesis

ABSTRACT

The response to environmental cues such as inflammatory stimuli requires coordinated cellular functions. Certain proteins have functions on both sides of the plasma membrane to allow coordination between the extracellular and intracellular milieus. The membrane-anchored matrix metalloproteinase MT1-MMP is well positioned to sense and modify the extracellular environment by processing matrix components, transmembrane proteins and soluble factors. Recent findings show, however, that MT1-MMP also plays unexpected intracellular roles in macrophages through its location at the plasma membrane, the Golgi or the nucleus, impacting cell motility, metabolism and gene transcription. MT1-MMP is thus an example of the evolutionary diversification of protein function, allowing optimal coordination between extracellular stimuli and cellular responses. It remains to be determined whether these new MT1-MMP functions are specific to macrophages, professional phagocytes involved in inflammation, or are present in other inflammation-responsive cells. In this review, we will summarize these site-specific MT1-MMP functions in macrophages and comment on the possible conservation of these functions in endothelial cells.

Introduction

Cells explore their microenvironment to sense cues that activate appropriate adaptive responses. Different evolutionary mechanisms have expanded the functional repertoire of certain proteins to allow coordination between their functions on both sides of the plasma membrane, the extracellular and intracellular milieus. These mechanisms include unconventional secretion of proteins with dual topology, such as syntaxin 2, HGMB1 and tissue transglutaminase, and interdependence of function and location for membrane-anchored proteins, such as β-catenin, which was the first individual protein shown to have distinct but linked functions related to its subcellular compartmentalization (Radisky et al., 2009).

Matrix metalloproteinases (MMPs) can sense and induce environmental modifications since they are secreted enzymes able to degrade a battery of extracellular matrix (ECM) components (Page-McCaw et al., 2007). A subfamily of MMPs is anchored to the membrane instead of being secreted, and this fact positions these MT-MMPs as prime candidates to coordinate extracellular cues with cellular responses. MT1-MMP is especially suited for pericellular proteolysis through its ability to process ECM components, transmembrane proteins and soluble factors (Itoh and Seiki, 2006). Moreover, it has been proposed that MT1-MMP might also be involved in processing of intracellular substrates such as pericentrin, pro-αv integrin and focal adhesion kinase (Golubkov et al., 2005; Ratnikov et al., 2002; Shofuda et al., 2004) (Fig. 1). Accordingly, as with other MMPs, recent proteomics approaches have identified intracellular proteins as possible MT1-MMP substrates; for example, HGMB1 (one of the unconventional dual topology proteins just mentioned), DJ-1, hsp90α, and γ-enolase, although it is not clear if processing would occur in the extracellular or intracellular compartments (Butler et al., 2008; Cauwe and Opdenakker, 2010) (Fig. 1). These findings indicate that under certain circumstances MT1-MMP might unexpectedly be proteolytically active inside cells, through as-yet unclear mechanisms. Regulated compartmentalization of MT1-MMP is essential for this diversity of proteolytic actions; in this regard, the presence of MT1-MMP at caveolae/lipid raft domains – apart from their role in its internalization – often dictates protease location and function in different cell contexts (Frittoli et al., 2011; Poincloux et al., 2009). As an example, forced location of MT1-MMP to lipid rafts by deletion of its cytosolic tail limited its access and processing of E-cadherin and thereby tumor cell locomotion and growth (Rozanov et al., 2004). Moreover, MT1-MMP co-localizes and co-traffics with caveolin-1 to invadopodia, actin-rich invasive protrusions, resulting in matrix degradation in several tumor cell types (Grass et al., 2012; Yamaguchi et al., 2009).

* Corresponding author at: Matrix Metalloproteinases Lab, Centro Nacional de Investigaciones Cardiovasculares (CNIC), Melchor Fernández Almagro 3, 28029 Madrid, Spain. Tel.: +34 91 4531200x1159; fax: +34 91 4531265.
E-mail address: agarroyo@cnic.es (A.G. Arroyo).
[1] These authors contributed equally to this work.

0171-9335/$ – see front matter © 2012 Elsevier GmbH. All rights reserved.
http://dx.doi.org/10.1016/j.ejcb.2012.07.003

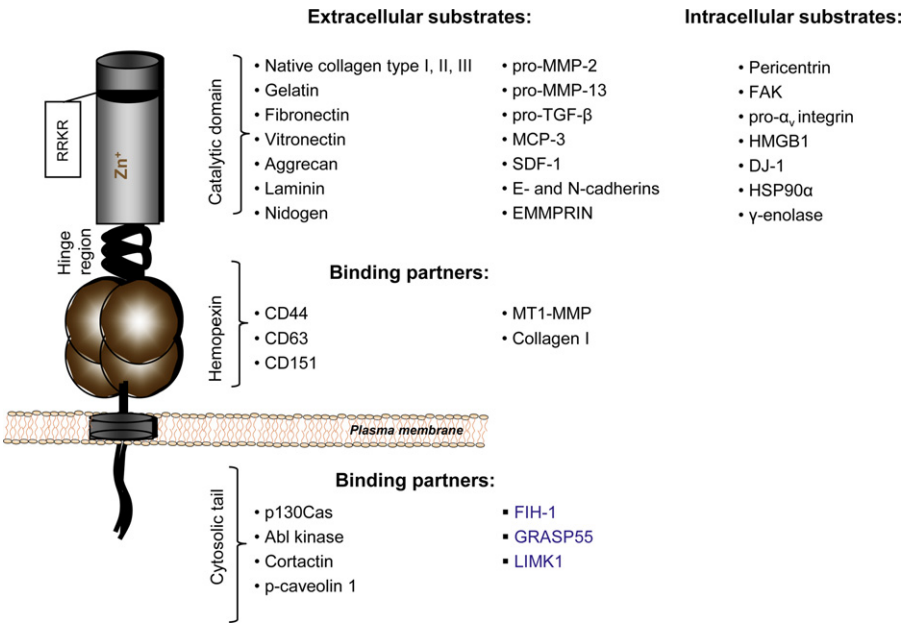

Fig. 1. Extracellular and intracellular substrates and partners of MT1-MMP. The domain structure of MT1-MMP is shown together with lists of selected extracellular and intracellular substrates and binding partners associated with each domain. Intracellular binding partners that interact with MT1-MMP at the Golgi apparatus are indicated in blue text.

But in addition to its proteolytic activities, MT1-MMP can also modulate intracellular responses through molecular interactions of its cytosolic tail leading to induction of signaling pathways such as ERK (Gingras and Beliveau, 2010). Most identified molecular partners interact with the MT1-MMP cytosolic tail at the plasma membrane; however, associations at other cell compartments such as the Golgi have been reported (Fig. 1) (Artym et al., 2006; Cauwe et al., 2007; Gingras et al., 2008; Gonzalo et al., 2010; Labrecque et al., 2004; Roghi et al., 2010; Sakamoto and Seiki, 2010; Smith-Pearson et al., 2010; Tapia et al., 2011).

This information suggests that the compartmentalization of MT1-MMP is linked to proteolytic-dependent and proteolytic-independent functions, through which it can coordinate extracellular cues with cellular responses. We will summarize recent data about new functions of MT1-MMP in macrophages linked to its location at the plasma membrane, the Golgi and the nucleus and discuss the possible conservation of these functions in endothelial cells, another cell type relevant to inflammation.

Site-specific functions of MT1-MMP in macrophages

Macrophages, which derive from myeloid progenitors/monocytes, are phagocytes with a high phenotypic plasticity associated with their essential role in inflammation. MT1-MMP is expressed and active at the plasma membrane of monocyte/macrophages (Matias-Roman et al., 2005), and also of hematopoietic progenitors whose G-CSF-induced mobilization involves enhanced MT1-MMP location at lipid rafts (Shirvaikar et al., 2010). Moreover, MT1-MMP is a component of the podosome machinery in macrophages and of the sealing zone of osteoclasts (macrophage-derived cells), and is involved in matrix degradation at these specialized membrane protrusions (Nusblat et al., 2011). Recent data from our group and others have, however, challenged this paradigm, and shown that MT1-MMP can also exert non-catalytic functions at the macrophage plasma membrane, and more importantly has unexpected functions at other cell compartments, including the Golgi/trans-Golgi network (TGN) and the nucleus.

We showed that the absence of MT1-MMP results in a defect in the fusion of macrophages to form multinucleate osteoclasts and giant cells, and that this defect is related to deficient motility and membrane protrusive activity of MT1-MMP null bone marrow-derived myeloid progenitors/macrophages (Gonzalo et al., 2010). Interestingly, normal progenitor motility and fusion was rescued by re-expression of a catalytically dead mutant, pointing to a proteolysis-independent mechanism. Further analysis showed that MT1-MMP associates with the adapter protein p130Cas at the plasma membrane, promoting optimal recruitment and activity of the small GTPase Rac1 (Gonzalo et al., 2010). Association with p130Cas involves MT1-MMP cytosolic tail Tyr^{573} which had previously been proposed to be phosphorylated by Src kinase (Nyalendo et al., 2007). This study established that the MT1-MMP/p130Cas/Rac1 molecular complex thus coordinates proper macrophage cell motility, migration and fusion both in vitro and in vivo (Fig. 2).

In an independent study, Seiki's group reported that, unlike macrophage invasion (which requires MT1-MMP catalytic activity), migration of mouse bone marrow-derived macrophages is also dependent on the MT1-MMP cytosolic tail (Sakamoto and Seiki, 2009). Macrophages are metabolically unusual in that, to enable migration into hypoxic inflamed tissues, they use glycolysis rather than oxidative phosphorylation for ATP production constitutively, even during normoxia. Seiki's group found that MT1-MMP regulated macrophage motility by increasing hypoxia inducible factor (HIF)-1α-mediated glycolysis and thus production of energy (ATP) by these cells; previous transcriptomic analysis in tumor cells had suggested regulation of energy metabolism by MT1-MMP, but the mechanism was undefined (Rozanov et al., 2008). Dissection of the mechanism by which the MT1-MMP cytosolic tail regulates macrophage metabolism revealed that this action relies on MT1-MMP localization to the Golgi apparatus, where its cytosolic tail retains factor inhibiting HIF (FIH)-1. FIH-1 acts by hydroxylating a conserved asparagine residue in HIF-1α thus impairing its interaction with its transcriptional co-activator p300 and abrogating

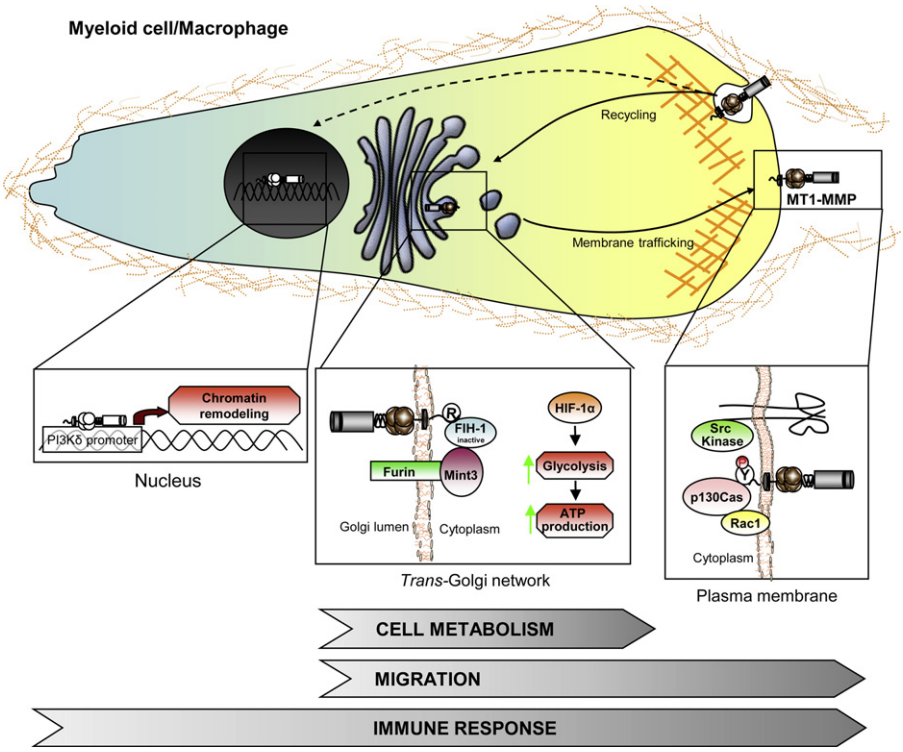

Fig. 2. Site-specific functions of MT1-MMP in macrophages. MT1-MMP is involved in macrophage migration and the immune response in a catalytic-independent manner through at least three site-specific pathways linked to distinct MT1-MMP traffic routes. At the plasma membrane, MT1-MMP can modulate Rac1 activity through binding to p130Cas, thereby regulating migration. The formation of this complex can be regulated by tyrosine phosphorylation of MT1-MMP cytosolic Y^{573} by Src kinase. At the Golgi apparatus, MT1-MMP, through the Arg^{576} in its cytoplasmic tail, binds FIH-1, keeping it close to Mint-3. This inactivation of FIH-1 stabilizes HIF-1α, resulting in the activation of glycolytic ATP production needed for macrophage migration and the immune responses. Upon translocation to the nucleus through as-yet undefined mechanisms, MT1-MMP induces PI3Kδ expression and regulates the transcription of genes critical for the inflammatory response.

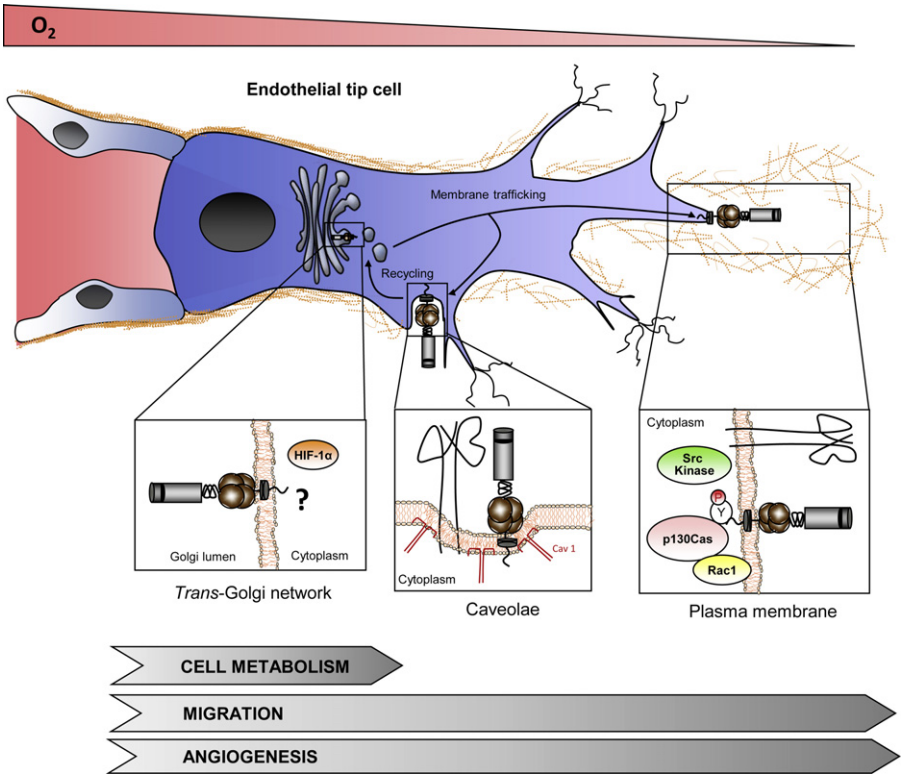

Fig. 3. Site-specific functions of MT1-MMP in endothelial cells. MT1-MMP can affect endothelial cell migration, metabolism and therefore angiogenesis through different pathways involving distinct cytosolic tail interactions and subcellular locations. These actions could be especially relevant in endothelial tip cells, which are exposed to low O_2 levels. In endothelial cells, MT1-MMP association to caveolae can regulate its traffic and function at different cellular locations. In addition, interaction of the MT1-MMP cytosolic tail with p130Cas at the plasma membrane might regulate Rac1 membrane targeting and migration, similar to the situation in macrophages. At the Golgi apparatus, the MT1-MMP cytosolic tail might interact with FIH-1 as reported for macrophages, thereby promoting HIF-1α-mediated cell metabolism.

induction of HIF-1α-dependent genes (Fraisl et al., 2009). MT1-MMP is normally processed by the pro-convertase furin at the Golgi. In macrophages, MT1-MMP at the Golgi interacts through its cytosolic tail Arg^{576} with FIH-1, thereby favoring FIH-1 proximity to Mint-3/APBA3 (another furin partner). Mint-3 in turn forms a complex with FIH-1, retaining it at this site and reducing its available cytoplasmic levels. In the presence of the MT1-MMP/FIH-1/Mint-3 complex at the Golgi, HIF-1α will be free and stabilized, and thus able to induce glycolysis and final production of ATP (Sakamoto and Seiki, 2010). In this manner MT1-MMP might coordinate its pro-invasive activity with the HIF machinery and thereby the cellular metabolism that is also required for migration (Fig. 2); in fact, it is possible that a feedback loop might be operative between hypoxia and MT1-MMP in macrophages since at least in tumor cells both MT1-MMP transcription and mobilization to the plasma membrane can in turn be regulated by HIF-2 and by hypoxia, respectively (Li et al., 2012; Munoz-Najar et al., 2006; Petrella et al., 2005). Points that remain to be defined include whether MT1-MMP exerts this function at the Golgi during its secretory path to the plasma membrane or upon its recycling from the plasma membrane after clathrin or caveolae-mediated endocytosis (Poincloux et al., 2009). Support for the idea that MT1-MMP localization at the Golgi modulates or provides additional MT1-MMP functions is given by the recently reported interactions of MT1-MMP with other Golgi proteins. In tumor cells the peripheral Golgi matrix protein GRASP55 associates with the LLY^{573} motif in the MT1-MMP cytoplasmic domain and favors its furin-dependent activation (Kuo et al., 2000; Roghi et al., 2010). LIM kinase 1 (LIMK1), a modulator of actin dynamics, also co-localizes and associates with MT1-MMP at the Golgi vesicles, facilitating its transport to the plasma membrane in tumor cells (Tapia et al., 2011).

More recently, Weiss's group has uncovered a novel MT1-MMP function in macrophages, dependent on its translocation to the nucleus by an as-yet undefined mechanism (Shimizu-Hirota et al., 2012). MT1-MMP traffics to the nucleus and triggers the activation of the promoter of phosphoinositide 3-kinase δ (PI3Kδ), thus activating the Akt/GSK3β signaling cascade (Fig. 2). This in turn controls the immunoregulatory Mi-2/NuRD complex of nucleosome remodeling enzymes responsible for limiting the transcription of genes involved in the immune response. In this manner, in the absence of MT1-MMP genes belonging to the Mi-2/NuRD complex like *Mi-2β*, *HDAC2* and *MBD3* are down-regulated and genes related to pro-inflammatory responses like *Mx1*, *Mx2*, *Saa3*, *CXCL10* and *CCL5* are up-regulated. The mechanism of MT1-MMP translocation to the nucleus remains unclear, although transfection with various MT1-MMP constructs points to a requirement for MT1-MMP anchorage to the membrane but not for its cytosolic or hemopexin domains or for its catalytic activity (Shimizu-Hirota et al., 2012). The possible role of MT1-MMP in ATP production may also contribute to its transcriptional function, since the Mi-2/NuRD axis is an ATP-dependent nucleosome remodeling complex.

Thus in macrophages, a highly plastic cell type with special metabolic features, the functional repertoire of MT1-MMP has expanded to adapt its functions to cellular responses required for optimal cell function during inflammation and its resolution.

Site-specific functions of MT1-MMP in endothelial cells

During an inflammatory response macrophages constitute the first-line sensors of damage, producing a number of soluble factors, including TNF-α. TNF-α in turn can activate endothelial cells to engage in an angiogenic program aimed at forming new vessels and resolving the inflammation. MT1-MMP, in addition to its important functions in macrophages, is also a key protease in endothelial cells that plays important roles in various steps of the angiogenic response. MT1-MMP proteolytic activity in endothelial cells is closely linked to its regulated presence at specific domains of the plasma membrane, in particular at lamellipodia and filopodia protrusions in which MT1-MMP associates with caveolin-1 and integrin αvβ3 and is catalytically active (Galvez et al., 2002, 2004; Fig. 3). Caveolae constitute the main route for MT1-MMP internalization in endothelial cells but they might also contribute to its mobilization to invadopodia as reported for tumor cells (Frittoli et al., 2011; Galvez et al., 2004; Poincloux et al., 2009). Consistently, MT1-MMP is expressed in endothelial tip cells, specialized cells at the nascent vascular sprout that contain many filopodia, are highly migratory and invasive and are enriched in caveolin-1 and αvβ3 integrin expression as shown by recent transcriptomic analysis (Aplin et al., 2009; del Toro et al., 2010; Gerhardt et al., 2003; Kachgal et al., 2012; Strasser et al., 2010; Yana et al., 2007).

The possibility that MT1-MMP might play additional site-specific functions in endothelial cells is supported by several observations. First, MT1-MMP deficiency reduces the targeting of p130Cas and Rac1 to the plasma membrane, similar to previous findings in myeloid progenitors (Fig. 2; Gonzalo et al., 2010). In endothelial cells, the MT1-MMP/p130Cas/Rac1 complex might contribute to migration, especially in endothelial tip cells, where Rac1 activity has been shown to be relevant (De Smet et al., 2009;

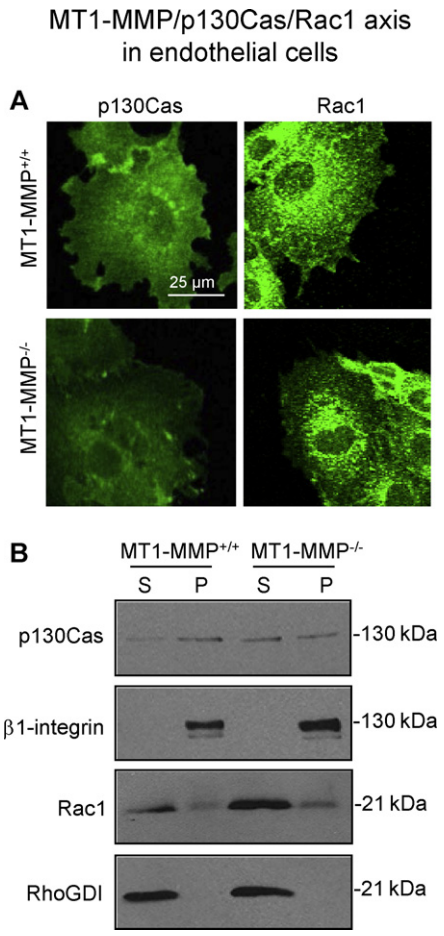

Fig. 4. p130Cas and Rac1 membrane levels are reduced in MT1-MMP null endothelial cells. (A) Mouse lung endothelial cells (MLEC) from wild type or MT1-MMP deficient mice were cultured to 70% confluence and after serum deprivation for 16 h were stained for p130Cas and Rac1 (green). Images show representative confocal microscopy maximal projections. (B) MLEC cultured as in A were separated into particulate (P) and soluble (S) fractions, and analyzed by Western blot for p130Cas and Rac1 expression. β1 integrin and RhoGDI are included as controls of particulate and soluble fractions. A representative blot is shown ($n = 5$).

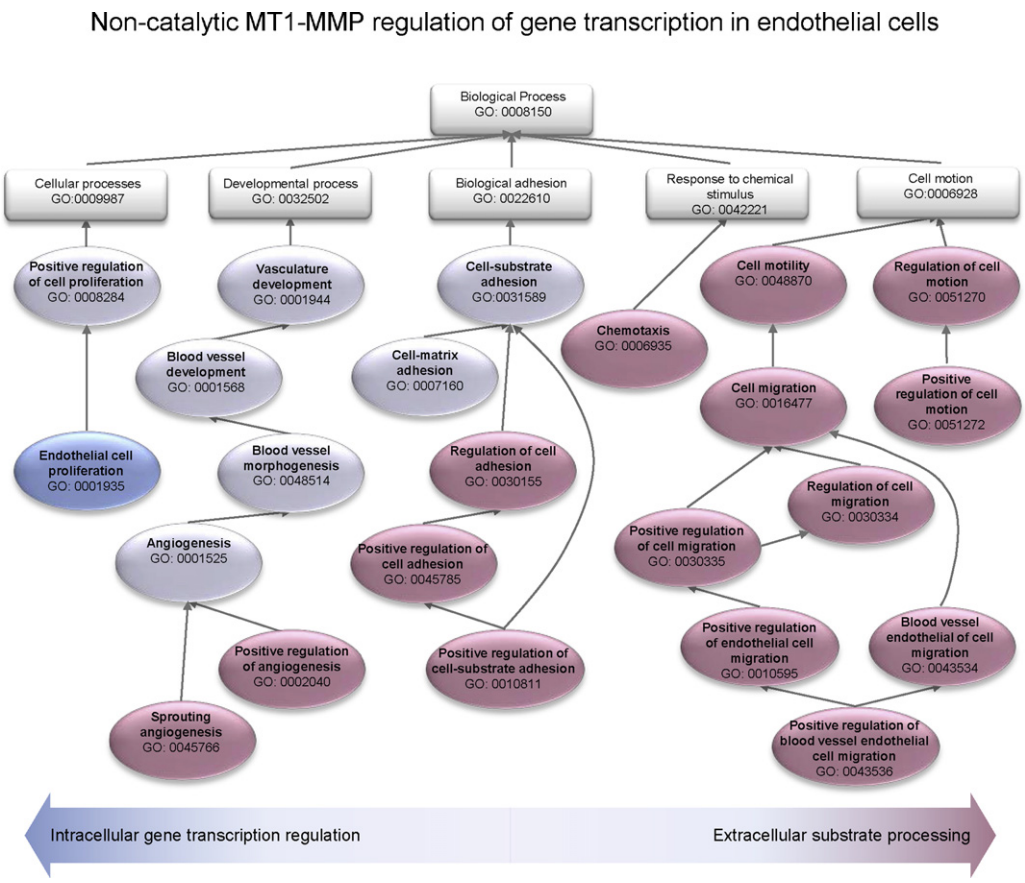

Fig. 5. Selected biological processes (GO annotations) regulated by MT1-MMP. Transcriptome and degradome analysis of inflammatory-activated mouse primary endothelial cells identified genes and proteins positively regulated by MT1-MMP that can affect a number of biological processes related to angiogenesis. Upregulated genes in the transcriptome analysis were predominantly enriched in processes related to proliferation, vasculature development and adhesion, while proteins identified in the MT1-MMP degradome mostly affect processes related to extracellular matrix degradation during neovessel formation (cell motility, adhesion, chemotaxis and vessel morphogenesis). Processes regulated only by intracellular transcription are shown in blue, those regulated only by extracellular processing (degradome) are in red, and processes regulated by both routes are in gray.

Figs. 3 and 4). This new MT1-MMP function might also be conserved in other cell types; for example, MT1-MMP has been shown to associate with a p130Cas/focal adhesion kinase complex upon Src kinase-dependent Tyr^{573} phosphorylation, thus favoring degradation of the matrix at focal adhesions in tumor cells (Wang and McNiven, 2012).

Second, MT1-MMP could be expected to regulate HIF-1 machinery in endothelial cells. The MT1-MMP/HIF-1 axis is active in tumor cells, which also use 'aerobic' glycolysis (the Warburg effect) (Hara et al., 2011), and more recently this axis was reported in bone marrow hematopoietic progenitors exposed to low oxygen tension (Nishida et al., 2012). Like these cell types, endothelial cells are equipped with metabolic mechanisms to enable survival in highly hypoxic conditions, including deriving most of their energy anaerobically through glycolysis (Fraisl et al., 2009). Moreover, the HIF-1α inhibitor FIH-1 is expressed in certain endothelial cells and might inhibit Notch activity, which is critical for endothelial tip cell fate specification. It will be interesting to explore whether MT1-MMP can also associate with FIH-1/Mint-3 in endothelial tip cells, thereby modulating FIH-1 availability and regulating HIF-1α-dependent genes such as Dll4 and Notch signaling (Fig. 3).

Finally, bioinformatics analysis of the MT1-MMP transcriptome and degradome (the collection of its substrates) in cytokine-activated primary mouse lung endothelial cells points to a role of MT1-MMP in regulating gene transcription in endothelial cells in a proteolytic-independent manner. Although most of the Gene Ontology Biological Processes related to angiogenesis, such as chemotaxis, motility, migration, adhesion or vasculature development, are enriched in MT1-MMP degradome or in both MT1-MMP degradome and transcriptome, endothelial cell proliferation was only enriched in the transcriptome. This analysis indicates that there is a minor contribution from non-catalytic MT1-MMP-driven gene regulation to angiogenesis (Fig. 5). MT1-MMP nuclear translocation is not exclusive of macrophages since it has also been observed in hepatocellular carcinoma cells in which caveolin-mediated endocytosis was proposed as the underlying mechanism (Ip et al., 2007). Moreover, MT1-MMP can modulate the expression of components of chromatin remodeling complexes in several cell types including HMGA2 in tumor cells through ERK signaling and Mi-2/NuRD in macrophages through the PI3Kδ/Akt/GSK3 pathway (Dangi-Garimella et al., 2011; Shimizu-Hirota et al., 2012). Although MT1-MMP nuclear translocation has not been confirmed in endothelial cells, we can thus speculate that MT1-MMP might directly or indirectly regulate chromatin remodeling, and thereby gene transcription, in endothelial cells. It will be important to investigate this point further given the current interest in epigenetic regulation in vascular biology and angiogenesis (Aurora et al., 2010; Yan et al., 2010).

Concluding remarks and future perspectives

Interdependence between location and function has been claimed as a mechanism for diversification of protein functions and improvement of their ability to coordinate extracellular cues and intracellular responses. MT1-MMP has become a

prime example of such a site-specific, multi-task protein, able to coordinate extracellular proteolytic modification with non-proteolytic-mediated cellular responses including cell motility and metabolism, ultimately leading to inflammatory responses and angiogenesis.

Open questions remain about the mechanisms by which cells and their metabolic needs regulate the distinct subcellular locations and functions of MT1-MMP. There are several possibilities; for example different metabolic or inflammatory conditions might trigger distinct traffic routes of MT1-MMP. Thus, environmental metabolic needs might change the manner in which MT1-MMP is endocytosed, steering its fate away from degradation to active roles in the Golgi or other compartments such as the nucleus; alternatively, MT1-MMP and its partners might meet at the Golgi/TGN as a result of altered synthesis and secretion. In support of regulated traffic of MT1-MMP under metabolic stress, in addition to transcriptional regulation of MT1-MMP by HIF-2 in tumor cells (Petrella et al., 2005), hypoxia can also promote the mobilization of MT1-MMP from cytosolic storage pools to the plasma membrane involving different molecular mechanisms such as RhoA activation (Li et al., 2012; Munoz-Najar et al., 2006). Interestingly, RhoA activation induced MT1-MMP location at cell-cell contacts and inhibited its caveolae-mediated traffic in endothelial cells (Galvez et al., 2004); it will be interesting to explore whether hypoxia in a RhoA-dependent or independent manner, can impact caveolae traffic routes since at least in tumor cells HIF-1 and -2 induce caveolin-1 transcription and caveolae formation (Wang et al., 2012). Notably, hypoxia also stimulates the formation of invadopodia in tumor cells (Lucien et al., 2011; Munoz-Najar et al., 2006) supporting the concept that a decrease in oxygen availability might trigger a coordinated cellular response involving increased MT1-MMP traffic to the plasma membrane together with induction of caveolae and invadopodia formation resulting in higher levels of MT1-MMP at these invasive structures. This response might be relevant not only in the tumor context but also in hypoxic inflammatory foci leading to endothelial tip cell and macrophage invasion. Moreover, in pathological contexts such as pulmonary arterial hypertension, hypoxia can also lead to trapping of vesicle tethers (SNAREs and SNAPs) in the Golgi (Sehgal and Lee, 2011); it is tempting to speculate that inflammatory hypoxic environments could also regulate Golgi-dependent MT1-MMP traffic to endow cells with appropriate adaptive responses. Understanding these new mechanisms of action of MT1-MMP has the potential to provide further insights into the complex networks activated under stressful inflammatory conditions and open new avenues for therapeutic intervention.

Acknowledgments

We thank S. Bartlett for English editing. This work was supported by grants from the Ministerio de Economia y Competitividad (MINECO; SAF2008-02104, SAF2011-25619 and RD06/0014/1016) and the Fundación Genoma España to A.G.A. AK and MMA are funded by fellowships from the Spanish Ministry of Education and Science and MINECO, respectively. The CNIC is supported by the MINECO and the Pro-CNIC Foundation.

References

Aplin, A.C., Zhu, W.H., Fogel, E., Nicosia, R.F., 2009. Vascular regression and survival are differentially regulated by MT1-MMP and TIMPs in the aortic ring model of angiogenesis. Am. J. Physiol. Cell Physiol. 297, C471–C480.

Artym, V.V., Zhang, Y., Seillier-Moiseiwitsch, F., Yamada, K.M., Mueller, S.C., 2006. Dynamic interactions of cortactin and membrane type 1 matrix metalloproteinase at invadopodia: defining the stages of invadopodia formation and function. Cancer Res. 66, 3034–3043.

Aurora, A.B., Biyashev, D., Mirochnik, Y., Zaichuk, T.A., Sanchez-Martinez, C., Renault, M.A., Losordo, D., Volpert, O.V., 2010. NF-kappaB balances vascular regression and angiogenesis via chromatin remodeling and NFAT displacement. Blood 116, 475–484.

Butler, G.S., Dean, R.A., Tam, E.M., Overall, C.M., 2008. Pharmacoproteomics of a metalloproteinase hydroxamate inhibitor in breast cancer cells: dynamics of membrane type 1 matrix metalloproteinase-mediated membrane protein shedding. Mol. Cell. Biol. 28, 4896–4914.

Cauwe, B., Opdenakker, G., 2010. Intracellular substrate cleavage: a novel dimension in the biochemistry, biology and pathology of matrix metalloproteinases. Crit. Rev. Biochem. Mol. Biol. 45, 351–423.

Cauwe, B., Van den Steen, P.E., Opdenakker, G., 2007. The biochemical, biological, and pathological kaleidoscope of cell surface substrates processed by matrix metalloproteinases. Crit. Rev. Biochem. Mol. Biol. 42, 113–185.

Dangi-Garimella, S., Krantz, S.B., Barron, M.R., Shields, M.A., Heiferman, M.J., Grippo, P.J., Bentrem, D.J., Munshi, H.G., 2011. Three-dimensional collagen I promotes gemcitabine resistance in pancreatic cancer through MT1-MMP-mediated expression of HMGA2. Cancer Res. 71, 1019–1028.

De Smet, F., Segura, I., De Bock, K., Hohensinner, P.J., Carmeliet, P., 2009. Mechanisms of vessel branching: filopodia on endothelial tip cells lead the way. Arterioscler. Thromb. Vasc. Biol. 29, 639–649.

del Toro, R., Prahst, C., Mathivet, T., Siegfried, G., Kaminker, J.S., Larrivee, B., Breant, C., Duarte, A., Takakura, N., Fukamizu, A., Penninger, J., Eichmann, A., 2010. Identification and functional analysis of endothelial tip cell-enriched genes. Blood 116, 4025–4033.

Fraisl, P., Mazzone, M., Schmidt, T., Carmeliet, P., 2009. Regulation of angiogenesis by oxygen and metabolism. Dev. Cell 16, 167–179.

Frittoli, E., Palamidessi, A., Disanza, A., Scita, G., 2011. Secretory and endo/exocytic trafficking in invadopodia formation: the MT1-MMP paradigm. Eur. J. Cell Biol. 90, 108–114.

Galvez, B.G., Matias-Roman, S., Yanez-Mo, M., Sanchez-Madrid, F., Arroyo, A.G., 2002. ECM regulates MT1-MMP localization with beta1 or alphavbeta3 integrins at distinct cell compartments modulating its internalization and activity on human endothelial cells. J. Cell Biol. 159, 509–521.

Galvez, B.G., Matias-Roman, S., Yanez-Mo, M., Vicente-Manzanares, M., Sanchez-Madrid, F., Arroyo, A.G., 2004. Caveolae are a novel pathway for membrane-type 1 matrix metalloproteinase traffic in human endothelial cells. Mol. Biol. Cell 15, 678–687.

Gerhardt, H., Golding, M., Fruttiger, M., Ruhrberg, C., Lundkvist, A., Abramsson, A., Jeltsch, M., Mitchell, C., Alitalo, K., Shima, D., Betsholtz, C., 2003. VEGF guides angiogenic sprouting utilizing endothelial tip cell filopodia. J. Cell. Biol. 161, 1163–1177.

Gingras, D., Beliveau, R., 2010. Emerging concepts in the regulation of membrane-type 1 matrix metalloproteinase activity. Biochim. Biophys. Acta 1803, 142–150.

Gingras, D., Michaud, M., Di Tomasso, G., Beliveau, E., Nyalendo, C., Beliveau, R., 2008. Sphingosine-1-phosphate induces the association of membrane-type 1 matrix metalloproteinase with p130Cas in endothelial cells. FEBS Lett. 582, 399–404.

Golubkov, V.S., Boyd, S., Savinov, A.Y., Chekanov, A.V., Osterman, A.L., Remacle, A., Rozanov, D.V., Doxsey, S.J., Strongin, A.Y., 2005. Membrane type-1 matrix metalloproteinase (MT1-MMP) exhibits an important intracellular cleavage function and causes chromosome instability. J. Biol. Chem. 280, 25079–25086.

Gonzalo, P., Guadamillas, M.C., Hernandez-Riquer, M.V., Pollan, A., Grande-Garcia, A., Bartolome, R.A., Vasanji, A., Ambrogio, C., Chiarle, R., Teixido, J., Risteli, J., Apte, S.S., del Pozo, M.A., Arroyo, A.G., 2010. MT1-MMP is required for myeloid cell fusion via regulation of Rac1 signaling. Dev. Cell 18, 77–89.

Grass, G.D., Bratoeva, M., Toole, B.P., 2012. Regulation of invadopodia formation and activity by CD147. J. Cell Sci. 125, 777–788.

Hara, T., Mimura, K., Seiki, M., Sakamoto, T., 2011. Genetic dissection of proteolytic and non-proteolytic contributions of MT1-MMP to macrophage invasion. Biochem. Biophys. Res. Commun. 413, 277–281.

Ip, Y.C., Cheung, S.T., Fan, S.T., 2007. Atypical localization of membrane type 1-matrix metalloproteinase in the nucleus is associated with aggressive features of hepatocellular carcinoma. Mol. Carcinog. 46, 225–230.

Itoh, Y., Seiki, M., 2006. MT1-MMP: a potent modifier of pericellular microenvironment. J. Cell. Physiol. 206, 1–8.

Kachgal, S., Carrion, B., Janson, I.A., Putnam, A.J., 2012. Bone marrow stromal cells stimulate an angiogenic program that requires endothelial MT1-MMP. J. Cell. Physiol.

Kuo, A., Zhong, C., Lane, W.S., Derynck, R., 2000. Transmembrane transforming growth factor-alpha tethers to the PDZ domain-containing, Golgi membrane-associated protein p59/GRASP55. EMBO J. 19, 6427–6439.

Labrecque, L., Nyalendo, C., Langlois, S., Durocher, Y., Roghi, C., Murphy, G., Gingras, D., Beliveau, R., 2004. Src-mediated tyrosine phosphorylation of caveolin-1 induces its association with membrane type 1 matrix metalloproteinase. J. Biol. Chem. 279, 52132–52140.

Li, J., Zucker, S., Pulkoski-Gross, A., Kuscu, C., Karaayvaz, M., Ju, J., Yao, H., Song, E., Cao, J., 2012. Conversion of stationary to invasive tumor initiating cells (TICs): role of hypoxia in membrane type 1-matrix metalloproteinase (MT1-MMP) trafficking. PLoS One 7, e38403.

Lucien, F., Brochu-Gaudreau, K., Arsenault, D., Harper, K., Dubois, C.M., 2011. Hypoxia-induced invadopodia formation involves activation of NHE-1 by the p90 ribosomal S6 kinase (p90RSK). PLoS One 6, e28851.

Matias-Roman, S., Galvez, B.G., Genis, L., Yanez-Mo, M., de la Rosa, G., Sanchez-Mateos, P., Sanchez-Madrid, F., Arroyo, A.G., 2005. Membrane type 1-matrix metalloproteinase is involved in migration of human monocytes and is regulated through their interaction with fibronectin or endothelium. Blood 105, 3956–3964.

Munoz-Najar, U.M., Neurath, K.M., Vumbaca, F., Claffey, K.P., 2006. Hypoxia stimulates breast carcinoma cell invasion through MT1-MMP and MMP-2 activation. Oncogene 25, 2379–2392.

Nishida, C., Kusubata, K., Tashiro, Y., Gritli, I., Sato, A., Ohki-Koizumi, M., Morita, Y., Nagano, M., Sakamoto, T., Koshikawa, N., Kuchimaru, T., Kizaka-Kondoh, S., Seiki, M., Nakauchi, H., Heissig, B., Hattori, K., 2012. MT1-MMP plays a critical role in hematopoiesis by regulating HIF-mediated chemo-/cytokine gene transcription within niche cells. Blood 119, 5405–5416.

Nusblat, L.M., Dovas, A., Cox, D., 2011. The non-redundant role of N-WASP in podosome-mediated matrix degradation in macrophages. Eur. J. Cell Biol. 90, 205–212.

Nyalendo, C., Michaud, M., Beaulieu, E., Roghi, C., Murphy, G., Gingras, D., Beliveau, R., 2007. Src-dependent phosphorylation of membrane type I matrix metalloproteinase on cytoplasmic tyrosine 573: role in endothelial and tumor cell migration. J. Biol. Chem. 282, 15690–15699.

Page-McCaw, A., Ewald, A.J., Werb, Z., 2007. Matrix metalloproteinases and the regulation of tissue remodelling. Nat. Rev. Mol. Cell Biol. 8, 221–233.

Petrella, B.L., Lohi, J., Brinckerhoff, C.E., 2005. Identification of membrane type-1 matrix metalloproteinase as a target of hypoxia-inducible factor-2 alpha in von Hippel–Lindau renal cell carcinoma. Oncogene 24, 1043–1052.

Poincloux, R., Lizarraga, F., Chavrier, P., 2009. Matrix invasion by tumour cells: a focus on MT1-MMP trafficking to invadopodia. J. Cell Sci. 122, 3015–3024.

Radisky, D.C., Stallings-Mann, M., Hirai, Y., Bissell, M.J., 2009. Single proteins might have dual but related functions in intracellular and extracellular microenvironments. Nat. Rev. Mol. Cell Biol. 10, 228–234.

Ratnikov, B.I., Rozanov, D.V., Postnova, T.I., Baciu, P.G., Zhang, H., DiScipio, R.G., Chestukhina, G.G., Smith, J.W., Deryugina, E.I., Strongin, A.Y., 2002. An alternative processing of integrin alpha(v) subunit in tumor cells by membrane type-1 matrix metalloproteinase. J. Biol. Chem. 277, 7377–7385.

Roghi, C., Jones, L., Gratian, M., English, W.R., Murphy, G., 2010. Golgi reassembly stacking protein 55 interacts with membrane-type (MT) 1-matrix metalloprotease (MMP) and furin and plays a role in the activation of the MT1-MMP zymogen. FEBS J. 277, 3158–3175.

Rozanov, D.V., Deryugina, E.I., Monosov, E.Z., Marchenko, N.D., Strongin, A.Y., 2004. Aberrant, persistent inclusion into lipid rafts limits the tumorigenic function of membrane type-1 matrix metalloproteinase in malignant cells. Exp. Cell Res. 293, 81–95.

Rozanov, D.V., Savinov, A.Y., Williams, R., Liu, K., Golubkov, V.S., Krajewski, S., Strongin, A.Y., 2008. Molecular signature of MT1-MMP: transactivation of the downstream universal gene network in cancer. Cancer Res. 68, 4086–4096.

Sakamoto, T., Seiki, M., 2009. Cytoplasmic tail of MT1-MMP regulates macrophage motility independently from its protease activity. Genes Cells 14, 617–626.

Sakamoto, T., Seiki, M., 2010. A membrane protease regulates energy production in macrophages by activating hypoxia-inducible factor-1 via a non-proteolytic mechanism. J. Biol. Chem. 285, 29951–29964.

Sehgal, P.B., Lee, J.E., 2011. Protein trafficking dysfunctions: role in the pathogenesis of pulmonary arterial hypertension. Pulm. Circ. 1, 17–32.

Shimizu-Hirota, R., Xiong, W., Baxter, B.T., Kunkel, S.L., Maillard, I., Chen, X.W., Sabeh, F., Liu, R., Li, X.Y., Weiss, S.J., 2012. MT1-MMP regulates the PI3Kdelta.Mi-2/NuRD-dependent control of macrophage immune function. Genes Dev. 26, 395–413.

Shirvaikar, N., Marquez-Curtis, L.A., Shaw, A.R., Turner, A.R., Janowska-Wieczorek, A., 2010. MT1-MMP association with membrane lipid rafts facilitates G-CSF-induced hematopoietic stem/progenitor cell mobilization. Exp. Hematol. 38, 823–835.

Shofuda, T., Shofuda, K., Ferri, N., Kenagy, R.D., Raines, E.W., Clowes, A.W., 2004. Cleavage of focal adhesion kinase in vascular smooth muscle cells overexpressing membrane-type matrix metalloproteinases. Arterioscler. Thromb. Vasc. Biol. 24, 839–844.

Smith-Pearson, P.S., Greuber, E.K., Yogalingam, G., Pendergast, A.M., 2010. Abl kinases are required for invadopodia formation and chemokine-induced invasion. J. Biol. Chem. 285, 40201–40211.

Strasser, G.A., Kaminker, J.S., Tessier-Lavigne, M., 2010. Microarray analysis of retinal endothelial tip cells identifies CXCR4 as a mediator of tip cell morphology and branching. Blood 115, 5102–5110.

Tapia, T., Ottman, R., Chakrabarti, R., 2011. LIM kinase1 modulates function of membrane type matrix metalloproteinase 1: implication in invasion of prostate cancer cells. Mol. Cancer 10, 6.

Wang, Y., McNiven, M.A., 2012. Invasive matrix degradation at focal adhesions occurs via protease recruitment by a FAK–p130Cas complex. J. Cell Biol. 196, 375–385.

Wang, Y., Roche, O., Xu, C., Moriyama, E.H., Heir, P., Chung, J., Roos, F.C., Chen, Y., Finak, G., Milosevic, M., Wilson, B.C., Teh, B.T., Park, M., Irwin, M.S., Ohh, M., 2012. Hypoxia promotes ligand-independent EGF receptor signaling via hypoxia-inducible factor-mediated upregulation of caveolin-1. Proc. Natl. Acad. Sci. U.S.A. 109, 4892–4897.

Yamaguchi, H., Takeo, Y., Yoshida, S., Kouchi, Z., Nakamura, Y., Fukami, K., 2009. Lipid rafts and caveolin-1 are required for invadopodia formation and extracellular matrix degradation by human breast cancer cells. Cancer Res. 69, 8594–8602.

Yan, M.S., Matouk, C.C., Marsden, P.A., 2010. Epigenetics of the vascular endothelium. J. Appl. Physiol. 109, 916–926.

Yana, I., Sagara, H., Takaki, S., Takatsu, K., Nakamura, K., Nakao, K., Katsuki, M., Taniguchi, S., Aoki, T., Sato, H., Weiss, S.J., Seiki, M., 2007. Crosstalk between neovessels and mural cells directs the site-specific expression of MT1-MMP to endothelial tip cells. J. Cell Sci. 120, 1607–1614.

eLIFE elifesciences.org

RESEARCH ARTICLE

Pivotal role for skin transendothelial radio-resistant anti-inflammatory macrophages in tissue repair

Olga Barreiro[1*†], Danay Cibrian[1,2,3], Cristina Clemente[1], David Alvarez[4], Vanessa Moreno[1], Íñigo Valiente[5], Antonio Bernad[5], Dietmar Vestweber[6], Alicia G Arroyo[1], Pilar Martín[1], Ulrich H von Andrian[4,7], Francisco Sánchez Madrid[1,2,3*]

[1]Department of Vascular Biology and Inflammation, Centro Nacional de Investigaciones Cardiovasculares, Madrid, Spain; [2]Servicio de Inmunología, Hospital de la Princesa, Universidad Autónoma de Madrid, Madrid, Spain; [3]Instituto Investigación Sanitaria Princesa, Universidad Autónoma de Madrid, Madrid, Spain; [4]Department of Microbiology and Immunobiology, Harvard Medical School, Boston, United States; [5]Department of Cardiovascular Development and Repair, Centro Nacional de Investigaciones Cardiovasculares, Madrid, Spain; [6]Max Planck Institute of Molecular Biomedicine, Münster, Germany; [7]Ragon Institute of MGH, MIT and Harvard, Cambridge, United States

***For correspondence:** olga_barreiro@hms.harvard.edu (OB); fsmadrid@salud.madrid.org (FSM)

Present address: †Department of Microbiology and Immunobiology, Harvard Medical School, Boston, United States

Competing interests: The authors declare that no competing interests exist.

Funding: See page 29

Received: 16 February 2016
Accepted: 13 June 2016
Published: 15 June 2016

Reviewing editor: Satyajit Rath, National Institute of Immunology, India

Abstract Heterogeneity and functional specialization among skin-resident macrophages are incompletely understood. In this study, we describe a novel subset of murine dermal perivascular macrophages that extend protrusions across the endothelial junctions in steady-state and capture blood-borne macromolecules. Unlike other skin-resident macrophages that are reconstituted by bone marrow-derived progenitors after a genotoxic insult, these cells are replenished by an extramedullary radio-resistant and UV-sensitive Bmi1^{+} progenitor. Furthermore, they possess a distinctive anti-inflammatory transcriptional profile, which cannot be polarized under inflammatory conditions, and are involved in repair and remodeling functions for which other skin-resident macrophages appear dispensable. Based on all their properties, we define these macrophages as Skin Transendothelial Radio-resistant Anti-inflammatory Macrophages (STREAM) and postulate that their preservation is important for skin homeostasis.
DOI: 10.7554/eLife.15251.001

Introduction

Macrophages are myeloid cells highly specialized in pathogen clearance and antigen capture in lymphoid tissues, where they participate in the first line of immune defense against exogenous threats, extending a bridge between innate and adaptive immunity (***Varol et al., 2015***). Homeostasis is also maintained in a number of peripheral non-lymphoid tissues by the phagocytic, anti-microbial and tissue remodeling activities of specialized resident macrophages, including alveolar macrophages in lungs, interstitial histiocytes in connective tissue, osteoclasts in bone, microglia in brain, Kupffer cells in liver, peritoneal, intestinal and adipose tissue macrophages (***Murray and Wynn, 2011***). Likewise, macrophages contribute to the barrier function of the skin. Unlike migratory epidermal Langerhans cells and dermal dendritic cells, which are mobilized after topical antigen uptake to perform their tolerogenic or immunogenic role within the draining lymph nodes (***Henri et al., 2010***), skin-resident

eLife digest The skin forms an essential barrier that defends our body from external damage. For this reason, it is important to understand the complex mechanisms involved in healing wounds and maintaining healthy skin. This could allow us to find effective treatments for skin diseases such as atopic dermatitis and psoriasis.

Immune cells called macrophages can protect the body in different ways depending on the signals they receive. Their protective roles include killing microbes that may cause disease, and helping to repair damaged tissues. Barreiro et al. have now investigated the roles of the macrophages in the skin by means of a number of complementary techniques, including a method called intravital microscopy that can image cells in a living organism.

The experiments revealed that a division of labor exists among the macrophages that reside in the skin of mice. Some macrophages help to trigger inflammatory responses in the skin. These immune cells disappear after being exposed to ionizing radiation (such as that used to treat cancer) but can be replaced via a bone marrow transplant. Other macrophages that help to repair tissues can survive being exposed to ionizing radiation but cannot resist high levels of ultraviolet light. Both types of macrophages perform unique and essential roles, and both types are necessary for maintaining healthy skin.

Barreiro et al. also discovered that the skin macrophages that help to repair tissues have the ability to move into blood vessels and take up substances from the blood. A question for future investigation is whether the macrophages perform this scavenging process to trigger a protective immune response in the nearby skin.

DOI: 10.7554/eLife.15251.002

macrophages remain in the dermis, contributing to pathogen clearance, tissue repair and the resolution of inflammation (***Pasparakis et al., 2014***).

A certain degree of heterogeneity among skin-resident macrophages has been previously reported relative to their ontogeny as well as to the functional specialization of specific subsets (***Abtin et al., 2014***; ***Hoeffel et al., 2015***; ***Schulz et al., 2012***; ***Tamoutounour et al., 2013***). Herein, we define for the first time a clear dichotomy among the skin-resident macrophages based on their differential sensitivity to γ-irradiation. Radio-resistant and radio-sensitive skin macrophages are distinctively polarized already in steady state as revealed by transcriptional analysis. Consequently, these two macrophage subsets are functionally specialized in a cell-autonomous manner even though both subsets are exposed to mostly shared environmental cues. In particular, the radio-resistant macrophage subset comprises a novel type of perivascular macrophages that gain access to the vascular lumen, are highly phagocytic and possess anti-inflammatory properties even in the presence of pro-inflammatory stimuli. Moreover, they are renewed from a local Bmi1^{+} progenitor and become outcompeted over time by bone marrow-derived resident macrophages. Finally, the preferential depletion of these skin transendothelial radio-resistant anti-inflammatory macrophages (STREAMs) using diphtheria toxin-OVA nanoparticles evidences their involvement in tissue repair and remodeling, as well as the inability of their radio-sensitive counterparts to act as functional surrogates.

Results

Dermal perivascular macrophages protrude into microvessels at steady-state

To visualize the microvascular network of the skin, we performed intravital imaging of the upper dermis of the mouse ear under steady-state conditions using a minimally invasive model based on confocal microscopy (***Auffray et al., 2007***). The vasculature was highlighted by injecting i.v. a non-permeable vascular tracer, high molecular weight (HMw; 2 MDa) TRITC-dextran. Remarkably, a population of perivascular cells became readily visible during the first hours after HMw dextran injection, suggesting that these mostly sessile cells were constantly taking up intravascular dextran (***Figure 1A*** and ***Video 1***). This observation was further confirmed by monitoring the uptake of two differently labeled HMw dextrans injected with a lapse of 24 hr (***Figure 1—figure supplement 1A***). Dextran

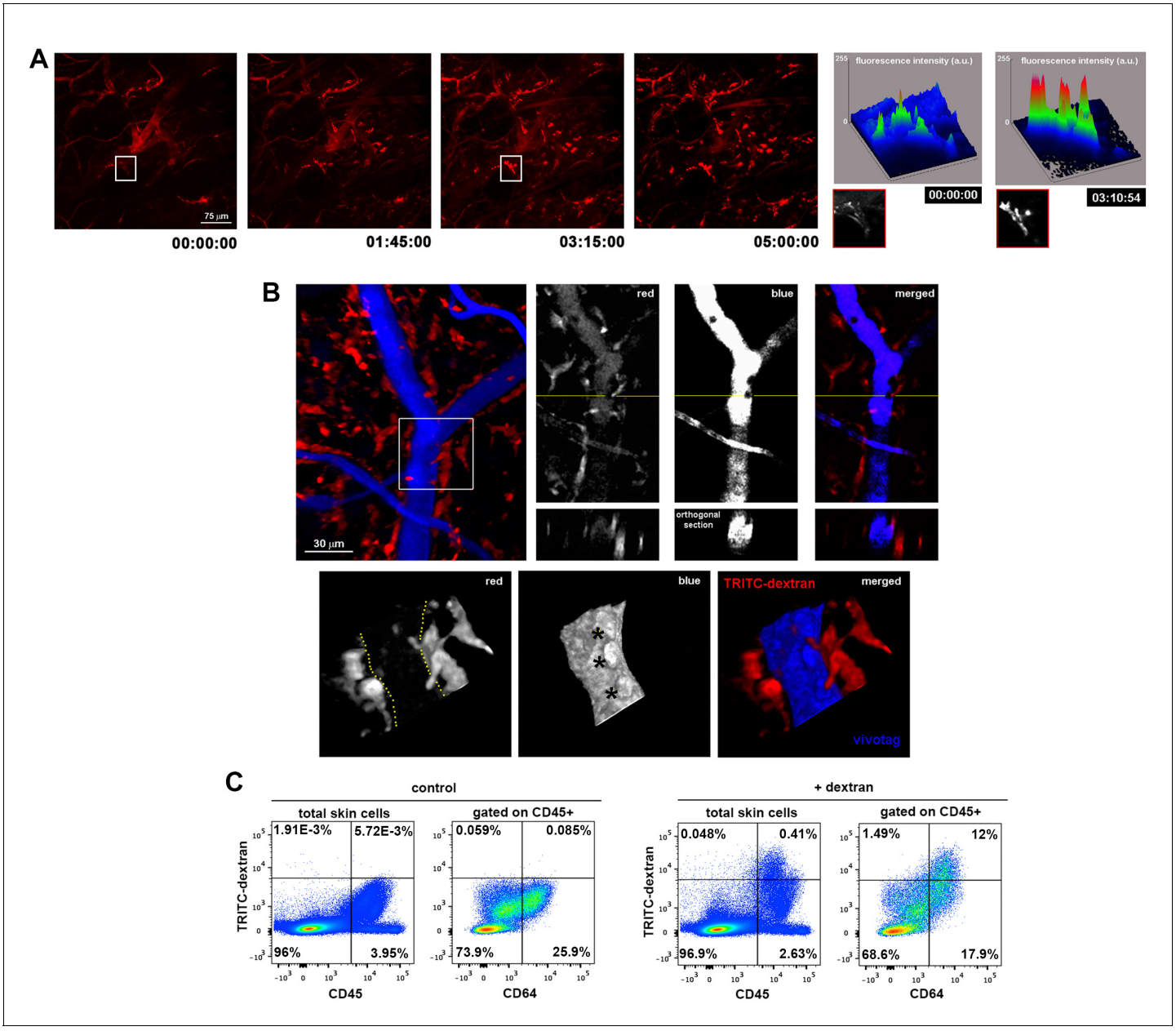

Figure 1. Dermal perivascular macrophages capture intraluminal dextran. (**A**) (Left) Representative frames from ***Video 1*** are shown. Briefly, image acquisition of ear mouse dermis started 30 min after i.v. injection of HMw TRITC-dextran and lasted for 5 hr. (Right) The surface plots show the fluorescence intensity of a representative cell at the starting time and 3 hr 15 min later (white insets in corresponding video frames; a.u., arbitrary units). (**B**) (Upper left) Three-dimensional (3D) rendering of the fluorescence signals obtained in a C57BL/6 ear dermis after i.v. administration of HMw TRITC-dextran (red, injected 16 hr before imaging) and vivotag (blue, injected at the time of imaging). (Upper right) The panels show a representative xy plane split into the different channels with an orthogonal section beneath, obtained along the yellow cross-section line. (Lower) The boxed region in the 3D rendering is shown tilted and at higher magnification. Yellow-dotted line marks endothelial perimeter in the red channel. Black asterisks mark void spaces corresponding to intravascular cells in the blue channel. (**C**) Phenotypic analysis of the dextran^{+} cells in the ear skin using the pan-leukocyte marker CD45 and the macrophage marker CD64. Representative FACS dot plots of control and HMw TRITC-dextran-injected mice are shown (n = 4).
DOI: 10.7554/eLife.15251.003
The following figure supplement is available for figure 1:

Figure supplement 1. Spatio-temporal analysis of endothelial-protruding macrophages under steady-state conditions.
DOI: 10.7554/eLife.15251.004

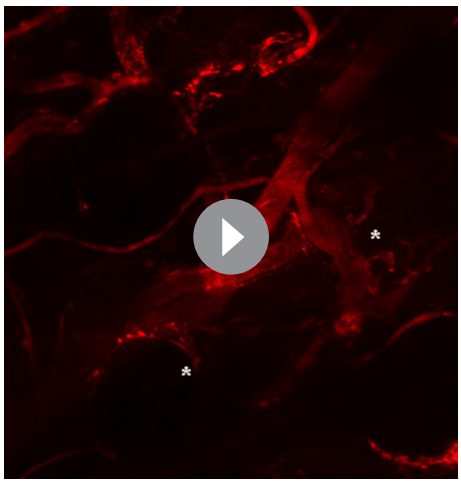

Video 1. Observation of intravascular dextran uptake by dermal non-migratory perivascular cells. Video sequence illustrating the progressive phagocytosis of intravascular dextran by perivascular cells (mostly sessile) under homeostatic conditions. A C57BL/6 animal was injected i.v. with HMw TRITC-dextran and immobilized by means of long-term anesthesia. Intravital imaging started 30 min after injection. The frames in the video sequence are maximal projections of a confocal z-stack (207 planes, 129.66 µm in depth) acquired every 5 min over 5 hr (only shown first 3 hr 15 min). White asterisks highlight cells of particular interest. The video also shows the clearance of dextran from the bloodstream and the absence of paravascular permeability under homeostatic conditions.
DOI: 10.7554/eLife.15251.005

administration followed by the subsequent injection of a non-phagocytosable tracer (vivotag) revealed the presence of dextran$^+$ protrusions as non-stained regions in the vivotag channel projecting into the vessel lumen (***Figure 1B***). The protrusions were flapping inside the vessels, presumably deflected by the vascular flow, and even contacting circulating cells (***Figure 1—figure supplement 1B*** and ***Videos 2–4***). The phenotypic characterization of the TRITC-dextran$^+$ perivascular cells identified them mostly as macrophages (i.e., they were either CD45$^+$ F4/80^{high} CD11c$^-$ CD11b$^+$ or CD45$^+$ F4/80^{high} CD11c$^-$ CD64$^+$ cells by FACS [***Figure 1C*** and ***Figure 1—figure supplement 1C***] and CD68$^+$ cells by whole-mount immunofluorescence staining [***Figure 1—figure supplement 1D***]). Flow cytometry analysis of skin single-cell suspensions from 12-week-old animals showed that the 96.67% ± 1.02% of all TRITC-dextran$^+$ cells were CD45$^+$ and the 90.41% ± 2.06% of CD45$^+$ TRITC-dextran$^+$ cells corresponded to macrophages (CD64$^+$). In addition, TRITC-dextran$^+$ macrophages represented 41.28% ± 5.66% of total skin macrophages. Next, we performed a mesoscopic analysis of murine ears to characterize the spatial distribution of skin macrophages. This analysis revealed their preferential localization around dermal blood microvessels rather than lymphatics (***Figure 2—figure supplement 1A*** and ***Video 5***). Interestingly, TRITC-dextran$^+$ macrophages were mostly apposed to capillaries and venules, possibly because the dense smooth muscle layer wrapping arterioles prevented the access of macrophages to the arteriolar lumen (*data not shown*). Moreover, endothelial cells did not detectably capture dextran under our experimental conditions, ruling out the possibility of the endothelium making accessible the intravascular dextran to the perivascular macrophages by transcytosis (***Figure 2—figure supplement 1B***).

We next studied how the macrophage protrusions gain access to the vascular lumen. We detected dextran$^+$ macrophages embracing vessels from outside the pericyte sheath (visualized as GFP$^+$ cells around vessels using a nestin-eGFP reporter mouse), whereas their protrusions extended across the basement membrane (stained with anti-collagen IV) and between pericytes to reach the endothelial wall (whole-mount immunofluorescence stainings in ***Figure 2A*** and ***Figure 2—figure supplement 1C***). We also visualized dextran$^+$ macrophage protrusions aligned with endothelial junctions in vivo by intravital microscopy by injecting i.v. an anti-CD31 antibody to stain the luminal surface of dermal microvasculature (***Figure 2—figure supplement 1D*** and ***Video 6***). Further analysis using orthogonal sectioning of whole-mount immunofluorescence stainings indicated that the macrophages insert their protrusions in the intravascular space through endothelial intercellular junctions (***Figure 2B***). Interestingly, TRITC-dextran uptake was minimal in VE-cadherin-α-catenin knock-in mice (***Figure 2C***). In these animals, endothelial adherens junctions are stabilized (***Schulte et al., 2011***), which prevents paravascular permeability and leukocyte paracellular but not transcellular diapedesis. The ability of dermal macrophages to access the intraluminal space is restricted in these animals, supporting the observation that macrophages can reach the vascular lumen crossing the endothelial junctions and excluding the possibility that their protrusions reach the vessel lumen via a transcellular route through endothelial cells. Finally, since the capture of dextran by skin myeloid cells is mediated by the mannose receptor (CD206) (***Wollenberg et al., 2002***), we could selectively stain the intraluminal protrusions of these dermal perivascular macrophages in vivo by injecting i.v. anti-CD206 and

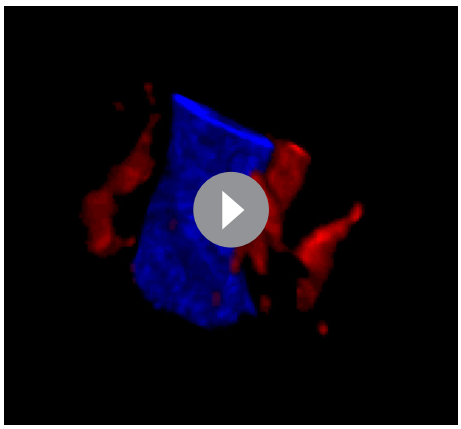

Video 2. Dermal perivascular cells protrude into dermal microvessels and contact intravascular leukocytes. Video animation of a 3D rendering from a z-stack acquired in vivo in the dermis of a mouse ear. The mouse was injected i.v. with HMw TRITC-dextran 16 hr before microscopic observation and injected i.v. with vivotag (as vascular tracer) just before the experiment. Intravital imaging with confocal sectioning (1 z-stack, 65 planes, 40.28 µm in depth) was performed. The image shows several perivascular dextran$^+$ cells around a vessel highlighted in blue (vivotag staining). Remarkably, two adjacent perivascular cells introduce their protrusions into the vascular lumen to contact intravascular leukocytes, seen as holes not filled with the vascular tracer.
DOI: 10.7554/eLife.15251.006

quantified the amount of endothelial-protruding macrophages by FACS (***Figure 2D***). Altogether these data indicate the existence of hitherto unidentified dermal perivascular macrophages able to protrude across endothelial junctions to reach the vascular lumen in homeostatic conditions.

Dermal dextran$^+$ macrophages are a radio-resistant subset of tissue-resident macrophages

In an attempt to visualize endothelial-protruding macrophages without dextran labeling, we first analyzed whether these macrophages selectively expressed CX3CR1, a marker associated to certain tissue-resident macrophage subsets including intestinal macrophages and microglia (***Varol et al., 2015***). However, dextran$^+$ macrophages did not express fluorescent reporter protein in *Cx3cr1$^{gfp/+}$* mice, neither in other myeloid reporter strains such as *Lyz2Cre:Rosa26YFP* and *Langerin-eGFP* (***Figure 3—figure supplement 1A***). Then, we generated chimeric animals by reconstituting lethally irradiated C57BL/6 mice with β-actin-GFP$^+$ hematopoietic progenitors, since it has been previously reported the absence of radio-resistant macrophages in the skin (***Bogunovic et al., 2006***). Unexpectedly, dextran$^+$ dermal macrophages did not express GFP in these chimeras (***Figure 3A*** and ***Video 7***), indicating that they were not replaced by BM-derived macrophages after irradiation and suggesting that they could be a specialized radio-resistant subset of skin-resident macrophages never characterized before. In fact, we monitored the presence of perivascular macrophages able to phagocytose intravascular HMw dextran 7d after lethal γ-irradiation without BM reconstitution (***Figure 3—figure supplement 1B***). To further assess their radio-resistant nature, we reconstituted lethally irradiated CD45.2 host mice with CD45.1 BM progenitors. Reconstitution of the hematopoietic system in blood and lymphoid organs was complete after 12 weeks, with a negligible residual contribution of host cells to the myeloid compartment. In contrast, the chimerism rate in the skin myeloid subsets exhibited a higher contribution of the host populations, which could not be ascribed to blood reconstitution (***Figure 3—figure supplement 1C–D***). The host radio-resistant CD45.2$^+$ macrophages efficiently captured HMw dextran under steady-state conditions and were found mostly positioned around microvessels (***Figure 3B*** and ***Figure 3—figure supplement 1E***). To validate this observation in a homeostatic context devoid of irradiation, the uptake of intravascular dextran was also analyzed in

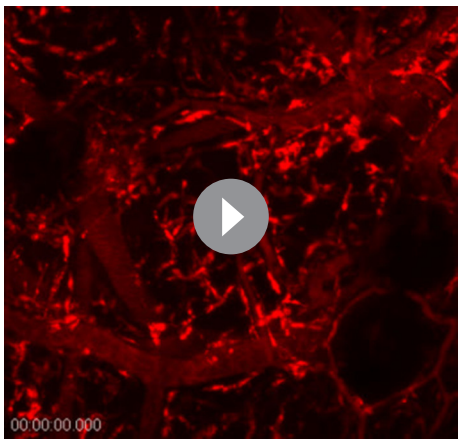

Video 3. Scanning movement of the protrusions of dermal perivascular cells. Frames represent maximal projections of a z-stack (9 sections acquired every 10 µm) obtained repeatedly (delay time 7 s 89 ms) over a short time period (9 min 30 s). The video shows the scarce motility of dextran-capturing cells.
DOI: 10.7554/eLife.15251.007

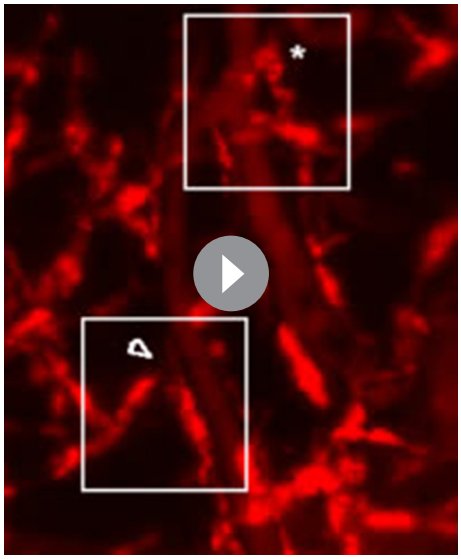

Video 4. Magnified detail from ***Video 3***. Crop and zoom from ***Video 3*** for detailed observation. The white asterisk marks a cell with an intravascular protrusion that flaps inside the vessel due to blood flow and the arrowhead points to the rearward movement of a dextran-loaded phagocytic vesicle from the vessel and along the protrusion towards the perivascular cell body.
DOI: 10.7554/eLife.15251.008

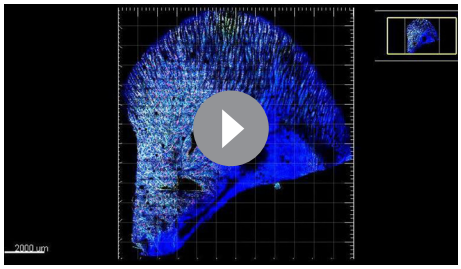

Video 5. Mesoscopic analysis of macrophage organization in relation to lymphatic and blood vessels. A whole mount-staining of a C57BL/6 ear dermis followed by tiled z-stack acquisition of the whole organ were performed. The video animation progresses from the mesoscopic analysis of the whole organ (ear) towards the detailed microscopic organization of lymphatics (LYVE-1$^+$, red), vascular endothelium (CD31$^+$, green) and tissue resident macrophages (CD68$^+$, white). Note the evident organization of macrophages around the complex endothelial network formed around hair follicles (minimal units of the skin) instead of around lymphatics. Blue corresponds to DAPI staining of nuclei, to facilitate observation of ear anatomy.
DOI: 10.7554/eLife.15251.009

parabiotic mice maintained for 6 months with a shared circulation. The results obtained were similar to those of chimeric animals, inasmuch as only host macrophages captured intraluminal dextran (***Figure 3C***).

Interestingly, a recent study described the existence of a subset of GFP$^+$ perivascular macrophages in the DPE-GFP mouse strain, in which GFP is driven under the control of the distal and proximal CD4 enhancers and CD4 promoter (details on the generation of this mouse line described in [***Mempel et al., 2006***]). These GFP$^+$ macrophages provide guidance cues for the recruitment of inflammatory cells such as neutrophils during intradermic bacterial infection (***Abtin et al., 2014***). To analyze whether the dermal endothelial-protruding macrophages correspond to the GFP$^+$ macrophages described above, we injected HMw TRITC-dextran in DPE-GFP animals. Remarkably, ~80% of cells that acquired circulating HMw dextran were GFP$^-$ in the skin of DPE-GFP mice (***Figure 4A***). Furthermore, chimerism experiments in which we reconstituted lethally irradiated CD45.2 DPE-GFP hosts with CD45.1 hematopoietic progenitors revealed a dramatic decrease in the number of GFP$^+$ dermal macrophages one month after the genotoxic insult, indicating their radio-sensitive nature (***Figure 4B***). Altogether these results allow us to establish a clear dichotomy between DPE-GFP$^+$ and dextran-capturing perivascular macrophages.

Radio-resistant macrophages derive from an extramedullary UV-sensitive source

In order to find the source for the skin-resident radio-resistant macrophages described in this work, we explored whether they are long-lived, endowed with self-renewal capacity, or derived from an extramedullary progenitor as alternative possibilities. We first tackled their sensitivity to UV irradiation, since other radio-resistant immune subset in the skin, the Langerhans cells (LC), is UV-sensitive (***Merad et al., 2002***). Chimeric CD45.1/CD45.2 (donor/host) animals were exposed to UVA-B irradiation (5 J/cm^2), and ear skin was analysed after one month. UV irradiation had a clearly negative effect on the survival and renewal of host compared with donor macrophages (***Figure 5A***), indicating that radio-resistant macrophages are UV-sensitive. However, the radio-resistant macrophages did not

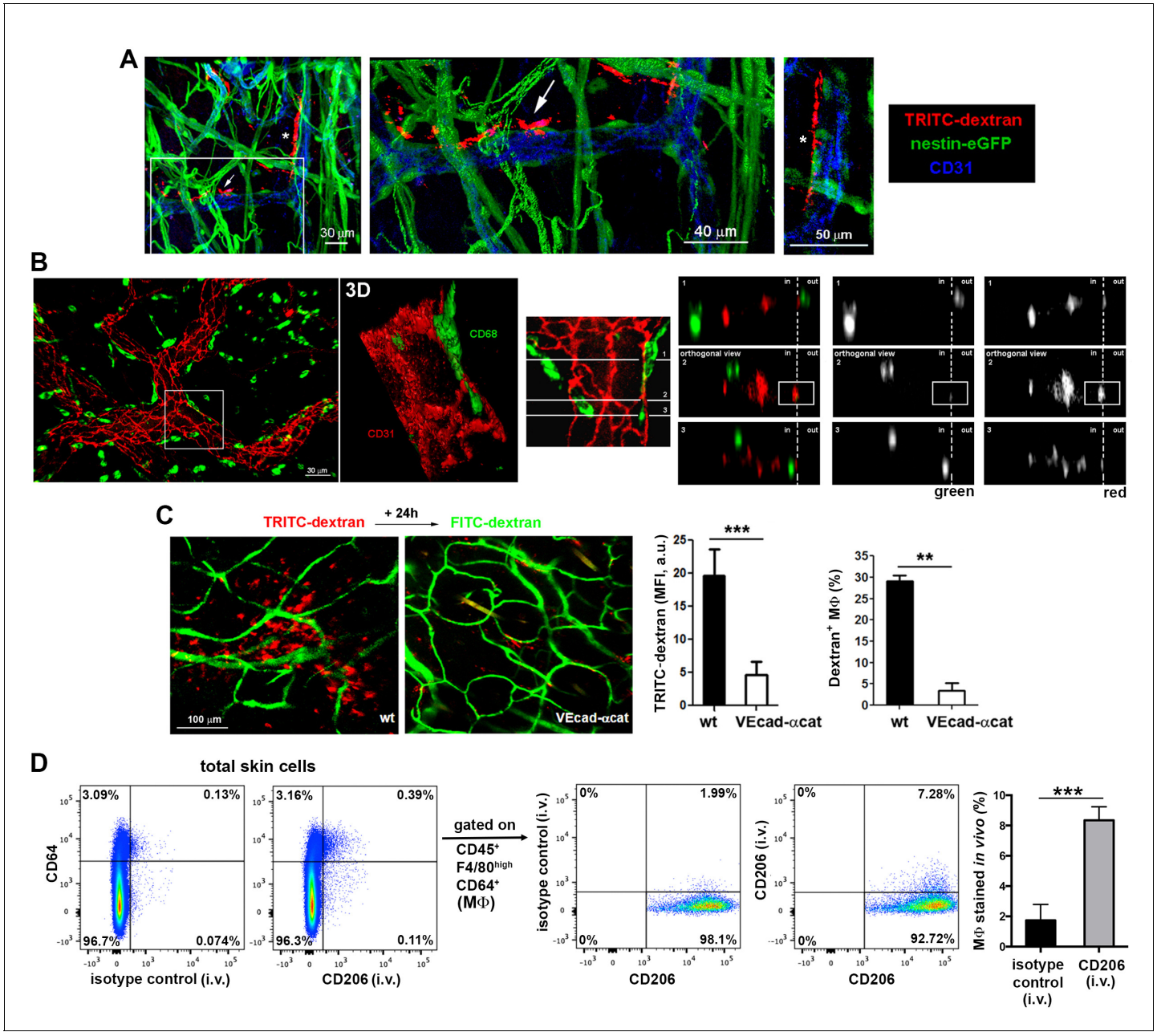

Figure 2. Dermal perivascular macrophages protrude across endothelial junctions into microvessels. (**A**) (Left) 3D reconstruction combining fluorescence signal and isosurface rendering of the ear dermis of a nestin-eGFP animal injected i.v. with HMw dextran. The inset is shown magnified in the central panel with a dextran^{+} macrophage protruding into the vascular lumen highlighted with a white arrow. Another protruding macrophage, marked with an asterisk in the 3D reconstruction image, is shown in a zoomed single confocal plane on the right. (**B**) (Left) Whole-mount staining of a C57BL/6 ear using anti-CD31 (red) and anti-CD68 (green) antibodies. (Center) The inset is shown as a 3D rendering with higher magnification. (Right) The same inset was tilted and further analyzed by orthogonal sectioning. The white cross-section lines are localized along the cell body and the intravascular protrusion of the macrophage on the right side. (in, intraluminal; out, extravascular). (**C**) Comparison of dextran capture in wt vs. VE-cadherin-α-cat mice under steady-state conditions. Animals were injected i.v. with HMw TRITC-dextran and with HMw FITC-dextran 24 hr later, before imaging. (Left) Representative intravital images show the dermis of each phenotype, containing dextran^{+} cells (red) and vasculature (green). (Center) The bar histogram represents the mean fluorescence intensity (MFI) of the TRITC-dextran signal ± SD obtained from five 20x fields of view of 2 animals of each phenotype (a.u., arbitrary units). (Right) Flow cytometry analysis of dextran capture by macrophages in wt and VE-cad-α-cat mice. Statistical significance was assessed by unpaired two-tailed Student's t-test (**p-value < 0.005, ***p-value < 0.001). (**D**) In vivo staining of the intraluminal protrusions of endothelium-protruding macrophages. Mice were injected i.v. with either an antibody against CD206 (mannose receptor, involved in dextran uptake) or an isotype control antibody and sacrificed 3 min later. Then, animals were perfused with PBS and ears were processed for FACS analysis. Single-cell suspensions were stained with anti-CD45, anti-F4/80, anti-CD64 and a different anti-CD206 clone. Representative FACS dot plots

Figure 2 continued on next page

Figure 2 continued

are depicted and the bar histogram shows the specific detection of macrophage staining in vivo (MΦ: macrophages). Data are mean values ± SD (n = 4). Statistical significance was assessed by unpaired two-tailed Student's t-test (***p<0.001).

DOI: 10.7554/eLife.15251.010

The following figure supplement is available for figure 2:

Figure supplement 1. Spatial organization of skin macrophages relative to lymphatic and blood vessels.

DOI: 10.7554/eLife.15251.011

express langerin and are clearly distinguishable from epidermal and dermal langerin$^+$ dendritic cells (***Figure 3—figure supplement 1A***).

Next, we explored whether the radio-resistant macrophages proliferate in situ. We first treated chimeric animals intradermally with clodronate liposomes to deplete skin macrophages. Monitoring at 24 hr after injection showed depletion of both macrophage subsets, whereas after 7d we observed selective partial recovery of host macrophages, consistent with an in situ renewal of these cells (***Figure 5—figure supplement 1***). Then, we performed Ki-67 staining in the skin of host and donor macrophages from chimeric animals using LC as control cells endowed with self-renewal potential (***Chorro et al., 2009***) (***Figure 5B***). The results point out to host macrophages as the only cell type assayed unable to proliferate by itself in steady-state. We complemented the study analysing the incorporation of BrdU administered ad libitum during 8d in these subsets (***Figure 5C***). The results indicate that host radio-resistant macrophages have a slower turnover compared to BM-derived donor macrophages and LC. Altogether these findings suggest that skin radio-resistant macrophages are a long-lived differentiated population that originates from an in situ proliferating progenitor. Interestingly, the relative content of resident macrophages from donor and host changed dynamically over time in favor of the dominant BM-derived pool, which exhibits higher proliferative capacity (***Figure 5D***).

To identify the extramedullary source for dermal radio-resistant macrophages, we performed a fate mapping analysis in adult skin. First, we performed an analysis of the expression of a panel of stemness-related genes demonstrating that skin-resident macrophages possess no pluripotent potential per se in steady-state (***Figure 5—figure supplement 2A***). Then, we employed a reporter mouse (*Bmi1*-IRES-Cre-ERT2 Rosa26 YFP) driven by the promoter of *Bmi1*, gene involved in the maintenance of adult stemness (***Sangiorgi and Capecchi, 2008***), which enabled us to trace adult stem cells and their progeny in skin (***Figure 5—figure supplement 2B***). Macrophages contain very low levels of the *Bmi1* transcript (***Figure 5—figure supplement 2C***) and are devoid of *Bmi1* protein in steady-state (***Sienerth et al., 2011***). However, YFP$^+$ CD45$^+$ F4/80^{high} CD11b$^+$ CD11c$^-$ macrophages were detected in the homeostatic skin of *Bmi1* reporter animals not earlier than 5d after i.p. injection of tamoxifen, suggesting that they are indeed derived from a Bmi1$^+$ progenitor (***Figure 5E***). Generation of YFP$^+$ macrophages was increased during macrophage replenishment after depletion with s.c. clodronate treatment (***Figure 5—figure supplement 2D***). Moreover, microscopy analysis of the dermis of these reporter animals detected perivascular YFP$^+$ cells protruding into vessels (***Figure 5F***). To exclude the contribution of BM-derived hematopoietic stem cells in this system, we generated chimeric CD45.1 C57BL/6 wt//*Bmi1*-IRES-Cre-ERT2

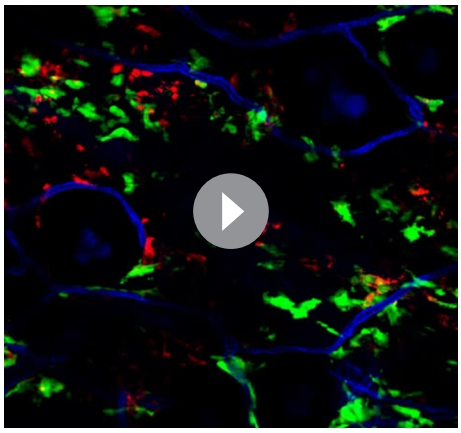

Video 6. In vivo imaging of dextran$^+$ macrophages aligned with endothelial junctions. The video sequence shows a confocal z-stack of the dermis of a mouse ear (65 planes, 40.28 µm in depth). The animal was chimeric (reconstitution with B6 ACTB-eGFP BM cells (green) in a C57BL/6 host) and was injected i.v. with HMw TRITC-dextran (red) 16 hr before imaging. For in vivo staining of endothelial junctions, an anti-CD31 antibody coupled to Alexa 647 (blue) was injected i.v. at the beginning of the experiment. The white circle and arrowheads highlight the area of interest, where the macrophage protrusions are posed in close contact with endothelial junctions.

DOI: 10.7554/eLife.15251.012

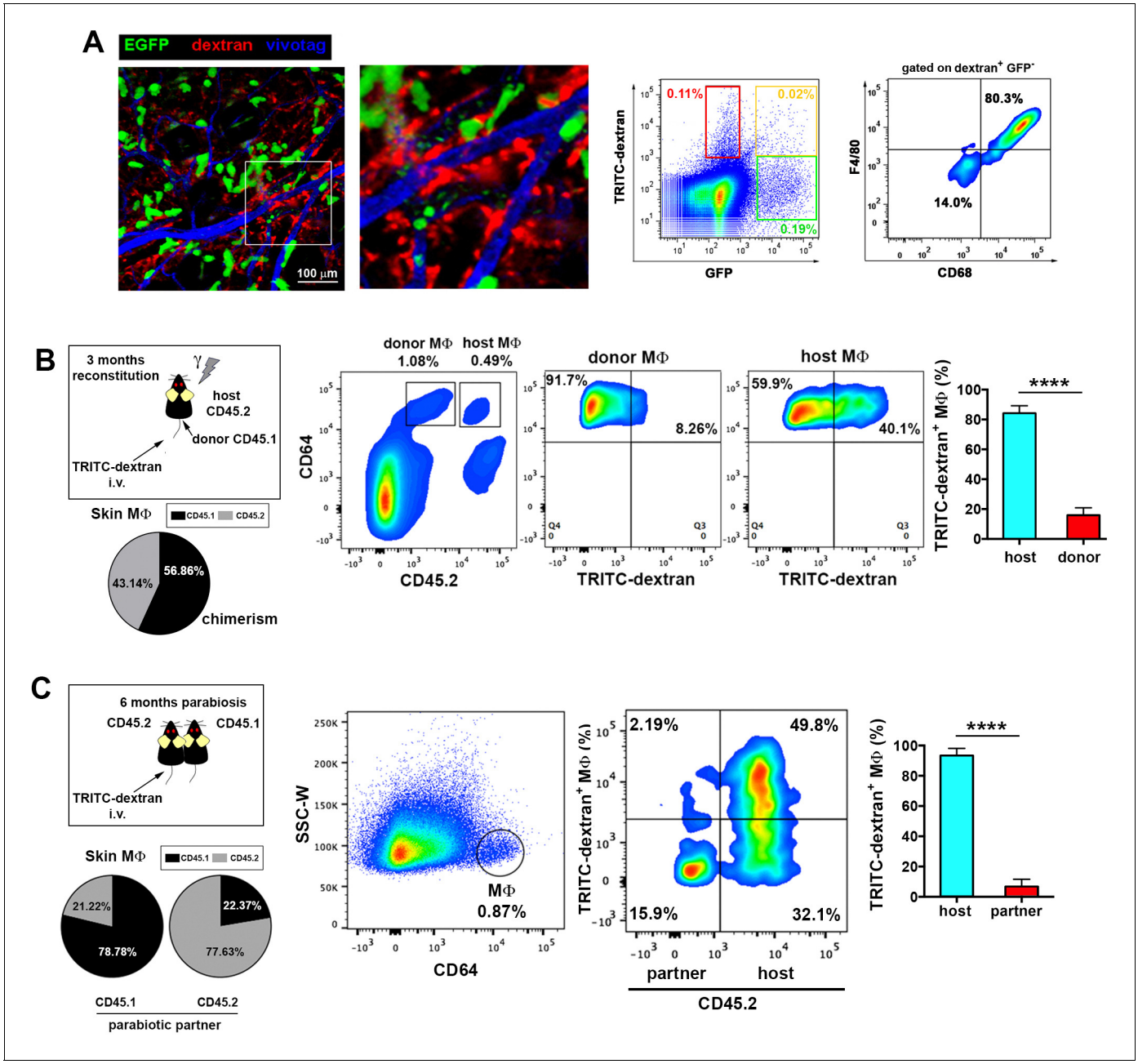

Figure 3. Endothelium-protruding macrophages are radio-resistant macrophages independent of BM supply. (**A**) (Left) Representative intravital image (maximal projection of a z-stack), with zoomed view aside, of the ear dermis of a chimeric B6 ACTB-eGFP (donor, green)/C57BL/6 (host) animal pre-treated with HMw TRITC-dextran (red) and injected with vivotag (blue) at the time of imaging. The 3D colocalization analysis between green and red signals was estimated (Pearson's coefficient in colocalized volume = 0.1074). (Right) Representative FACS dot plots showing the analysis of the TRITC-dextran$^+$ (red), the GFP$^+$ (green) and the double positive subsets in these chimeric animals as well as the macrophage content in the TRITC-dextran$^+$ subset. (**B**) (Left) Averaged frequency of CD45.1$^+$ (donor) and CD45.2$^+$ (host) skin-resident macrophages in chimeric animals reconstituted for 3 months. (Right) Representative FACS analysis of the dextran$^+$ subset in chimeric CD45.1 (donor)/CD45.2 (host) animals treated with HMw TRITC-dextran. The bar histogram shows the contribution of host and donor macrophages to the pool of dextran$^+$ macrophages in the skin. Values are mean ± SD (n=4). Statistical significance was assessed by unpaired two-tailed Student's t-test (****p<0.0001). (**C**) Parabionts were injected i.v. with HMw TRITC-dextran and sacrificed 3d later. Ears were harvested and processed for FACS analysis. (Left) Averaged frequency of CD45.1$^+$ and CD45.2$^+$ skin-resident macrophages in each partner of the parabiotic pairs (n = 4) after 6 months of parabiosis. (Right) Representative dot plots and bar histogram showing the contribution of host macrophages and macrophages derived from partner to the pool of dextran$^+$ macrophages in the skin. Values are mean ± SD (n = 4). Statistical significance was assessed by unpaired two-tailed Student's t-test (****p<0.0001).

DOI: 10.7554/eLife.15251.013

Figure 3 continued on next page

Figure 3 continued

The following figure supplement is available for figure 3:

Figure supplement 1. Analysis of tissue-resident macrophage subsets in reporter and chimeric animals.

DOI: 10.7554/eLife.15251.014

Rosa26 YFP CD45.2 (donor/host) mice. YFP$^+$ dextran$^+$ macrophages were detected in the skin of tamoxifen-treated HMw dextran-injected chimeric mice by FACS analysis (***Figure 5G–H***). Intravital experiments confirmed the existence of YFP$^+$ dextran$^+$ macrophages under steady-state conditions in chimeras lacking tamoxifen-inducible hematopoietic cells of BM origin (***Figure 5I***). Together these results confirm the in situ generation of radio-resistant macrophages from a skin pluripotent progenitor independent of BM.

Phenotypic differences among skin-resident macrophage subsets

Our results strongly imply the coexistence of two distinct skin-resident macrophage pools in homeostasis based on their differential capacity to uptake circulating macromolecules, sensitivity to γ-irradiation and progenitor source. To further characterize these two populations, we performed a detailed phenotypic characterization of host radio-resistant and donor BM-derived macrophages in chimeric mice after 3 months of reconstitution. Both subsets were F4/80^{high}, CD11b$^+$ and expressed similar levels of other myeloid markers such as Ly6C and CD115, as well as of the prototypic macrophage markers CD68 and CD64-MertK (whose combined expression is associated with mature tissue macrophages [***Gautier et al., 2012***]) (***Figure 6A*** and ***Figure 6—figure supplement 1A***). Moreover, both subsets were CD11c$^-$ and Ly6G$^-$ (***Figure 6—figure supplement 1A***). There was also no consistent or sizeable difference in the expression of the angiogenesis-related receptor Tie-2, the costimulatory molecules CD40 and CD70 or MHC-I. However, we found a higher mean expression of the costimulatory molecule CD86 and the mannose receptor (CD206) in the host radio-resistant subset, whereas MHC-II was elevated in the donor BM-derived subset (***Figure 6A***). Nevertheless, the broad range of expression of these differential markers within each macrophage subset precluded their use to dissect accurately the heterogeneity found among the skin-resident macrophages (example provided for MHC-II in ***Figure 6—figure supplement 1B***).

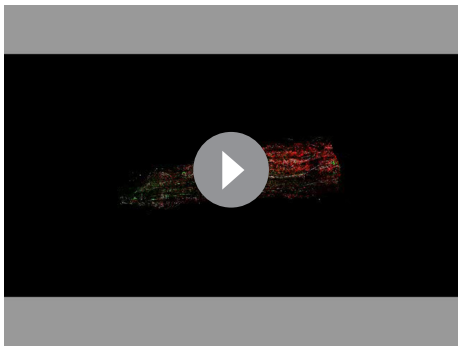

Video 7. Dextran$^+$ macrophages are not from BM origin. Video animation showing the maximal projection of a confocal z-stack obtained from the tail skin of a chimeric animal (B6 ACTB-eGFP(donor)/C57BL6 (host)) injected i.v. with HMw TRITC-dextran. The animation alternatively shows the position of dextran$^+$ macrophages (red) and BM-derived hematopoietic cells (GFP$^+$, green) relative to vessels (CD31$^+$ in white, whole-mount staining) and finally highlights the lack of colocalization of red and green channels.

DOI: 10.7554/eLife.15251.015

Radio-resistant macrophages possess a distinctive anti-inflammatory gene expression profile

To find a specific marker for radio-resistant macrophages and gain further insight into the differences between the two tissue-resident macrophage subsets, we sorted donor and host macrophages from the skin of chimeric animals for high-resolution transcriptome profiling, using deep-sequencing technology (RNA sequencing (RNA-Seq)) (***Wang et al., 2009***). Of 17,741 genes compiled, we found significant differences in 744, 135 corresponding to protein coding sequences with similar normalized expression levels across replicates (***Figure 6B–C***, and ***Supplementary file 1***). A comprehensive Gene Set Enrichment Analysis (GSEA) of all genes expressed in at least one cell type showed 36 Kegg pathways upregulated in host radio-resistant macrophages (14 of them enriched at a nominal p-value < 1%) vs. 149 in donor macrophages (26 pathways enriched at a nominal p-value < 1%). The GSEA analysis confirmed striking differences in metabolism between the

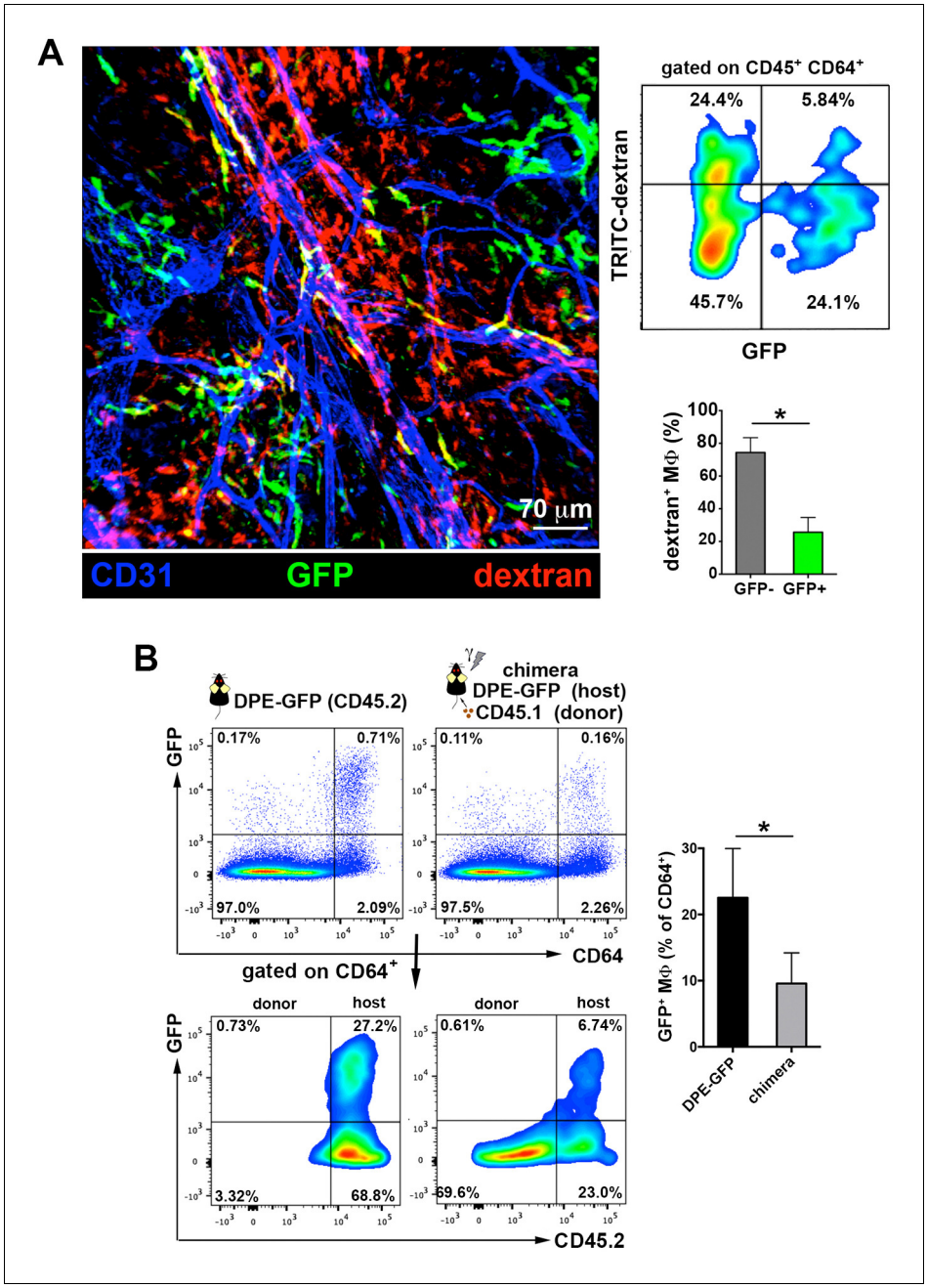

Figure 4. The perivascular endothelium-protruding macrophages are distinct from the perivascular DPE-GFP$^+$ macrophages. (**A**) (Left) Maximal projection of the ear dermis of a DPE-GFP animal injected i.v. with HMw TRITC-dextran, fixed and stained with anti-CD31. The 3D colocalization analysis of the green (GFP$^+$ perivascular MΦ) and red (dextran$^+$ perivascular MΦ) signals was estimated (Pearson's coefficient in colocalized volume = 0.1901). (Upper right) FACS analysis of macrophages in ear skin from DPE-GFP animals injected i.v. with HMw TRITC-dextran. (Lower right) Bar histogram showing contribution of GFP$^-$ and $^+$ subsets to the pool of dextran$^+$ macrophages. Values are mean ± SD (n = 3). Statistical significance was assessed by unpaired two-tailed Student's t-test (* $p<0.05$). (**B**) DPE-GFP CD45.2 animals were lethally irradiated and reconstituted with wt congenic CD45.1 BM. Animals were sacrificed 1 month later and the content of skin GFP$^+$ MΦ in their skin was analyzed by FACS and compared with untreated DPE-GFP CD45.2 animals. The bar histogram on the right shows the % of GFP$^+$ macrophages out of total skin macrophages. Data are mean ± SD (n = 4). Statistical significance was assessed by unpaired two-tailed Student's t-test (* $p<0.05$).

DOI: 10.7554/eLife.15251.016

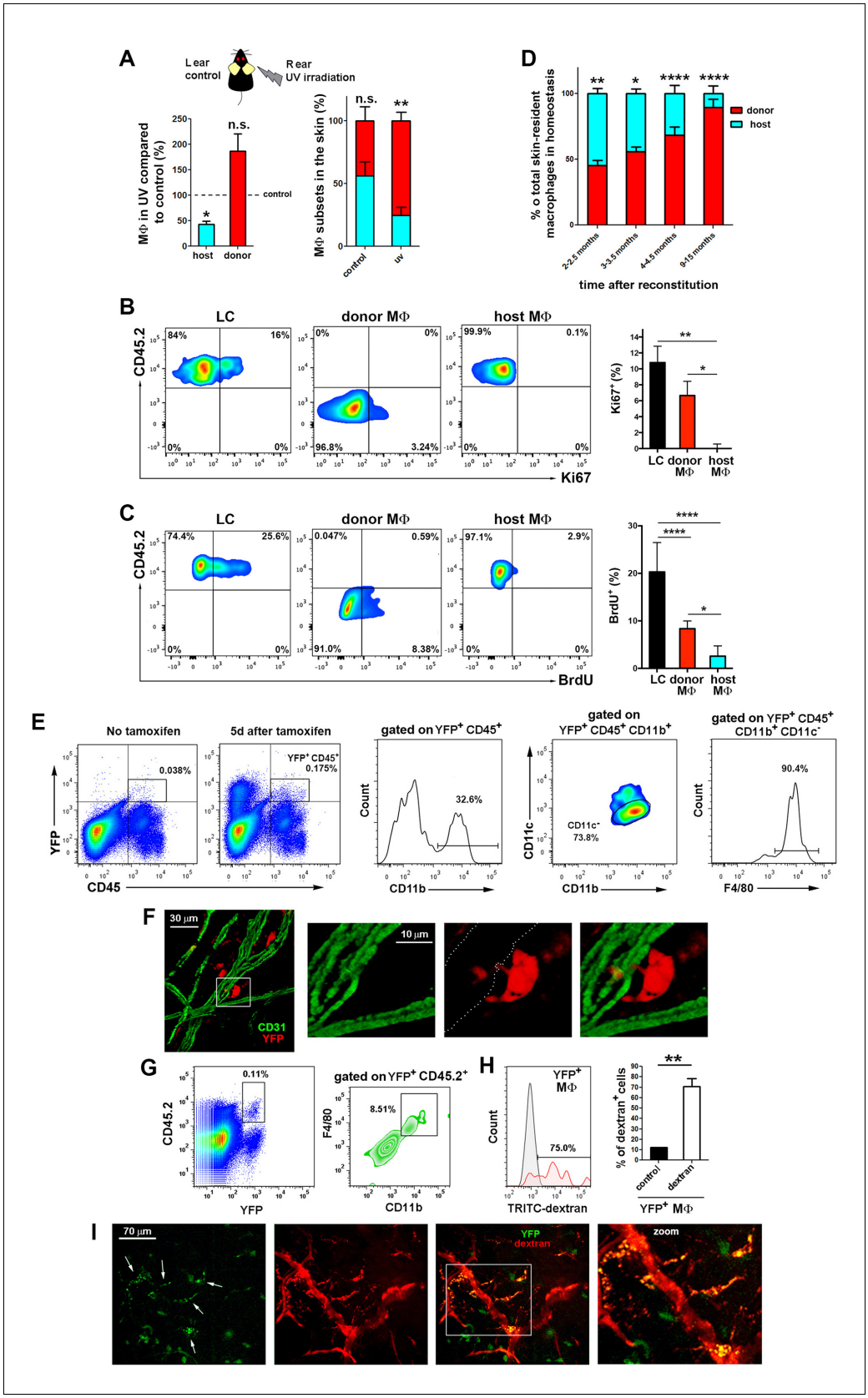

Figure 5. The skin radioresistant macrophages are an UV-sensitive population endowed with in situ renewal potential from an extramedullary progenitor. (**A**) Ears from chimeric animals (CD45.1(donor)/CD45.2(host)) were

Figure 5 continued on next page

Figure 5 continued

analyzed by flow cytometry 4 weeks after irradiation with UV-A/B or no irradiation. The left bar histogram shows the percentage of remaining macrophages of each haplotype after UV irradiation relative to untreated controls (n = 3/group). The second bar histogram depicts the relative content of each subset out of the total pool of tissue-resident macrophages in treated and non-treated animals. Data are means ± SEM. Statistical significance was assessed by two-way ANOVA analysis with Sidak's post-test (left) and one-sample t-test referred to value = 100 (right) (n.s. not significant, **p-value < 0.01). (**B**) Ki-67 staining reveals the lack of self-renewal capacity of radioresistant host macrophages in steady-state. Chimeric mice (CD45.1-donor/CD45.2-host) reconstituted for 3 months were sacrificed and skin processed and stained with anti-Ki-67 for FACS analysis. Tissue-resident macrophages from host ($CD45.2^+$ and $CD64^+$) and donor ($CD45.1^+$ and $CD64^+$) as well as Langerhans cells (LC, $CD45.2^+$ $CD326^+$ and $MHC\text{-}II^+$, used as control subset endowed with self-renewal capacity) were analyzed. Values are mean ± SEM (n = 4). Statistical significance was assessed by one-way ANOVA with Dunnett's post-test (*p-value < 0.05, **p-value < 0.005). (**C**) BrdU tracing revealed the slower turnover rate of host radioresistant macrophages. Chimeric mice (CD45.1-donor/CD45.2-host) were treated with BrdU in drinking water ad libitum. Animals were sacrificed 8 d later and skin processed for BrdU staining. Tissue-resident macrophages from host and donor as well as Langerhans cells were analyzed. Values are mean ± SD (n = 4). Statistical significance was assessed by one-way ANOVA with Tukey's post-test (**p-value < 0.005, ****p-value < 0.0001). (**D**) Fluctuations over time in the relative content of host and donor macrophages in the homeostatic skin of chimeric animals (n = 5/group). Data are mean ± SD. Statistical significance was assessed by two-way ANOVA with Sidak's post-test (*p-value < 0.05, **p-value < 0.01, ***p-value < 0.005, ****p-value < 0.0001). (**E**) Ears from tamoxifen-treated *Bmi1*-IRES-Cre-ERT2 Rosa26 YFP reporter mice were analyzed by flow cytometry 5d after treatment. Representative FACS analysis of the identified YFP^+CD45^+ fraction is shown. (**F**) Whole-mount staining of an ear from a tamoxifen-treated *Bmi1*-IRES-Cre-ERT2 Rosa26 YFP mouse. The boxed area highlights a YFP^+ perivascular cell protruding into a vessel, shown at high magnification in the accompanying panels. The white-dotted line marks the vasculature in the red channel. (**G**) *Bmi1*-IRES-Cre-ERT2 Rosa26 YFP CD45.2 host mice were chimerized with bone marrow from CD45.1 wt donors. Ears of these chimeric mice were analyzed by FACS and a subset of $YFP^+CD11b^+F4/80^{high}$ myeloid cells was detected. (**H**) FACS analysis of *Bmi1*-IRES-Cre-ERT2 Rosa26 YFP chimeric mice injected with HMw dextran. The bar histogram represents the percentage of YFP^+ $dextran^+$ macrophages respect to untreated control (n = 4). Data are mean ± SD. Statistical significance was assessed by unpaired two-tailed Student's t-test (**p-value < 0.01). (**I**) Representative intravital images of the ear of a chimeric mouse generated as in G, and injected with HMw TRITC-dextran. White arrows in the green channel mark $YFP^+dextran^+$ perivascular cells.

DOI: 10.7554/eLife.15251.017

The following figure supplements are available for figure 5:

Figure supplement 1. Selective recovery of host macrophages in chimeric animals treated with clodronate liposomes intradermally.

DOI: 10.7554/eLife.15251.018

Figure supplement 2. Absence of stemness gene expression in skin resident macrophages in steady-state.

DOI: 10.7554/eLife.15251.019

two resident macrophage populations in homeostatic skin (***Figure 6—figure supplement 2A*** and ***Supplementary file 2***). Host radio-resistant macrophages displayed a metabolic gene profile based on fatty acid oxidation and oxidative phosphorylation, whereas donor BM-derived macrophages showed a glycolytic gene profile. Such metabolic differences found at the gene expression level were confirmed by assessing mitochondrial activity ex vivo. Direct staining of the skin with an indicator of mitochondrial membrane potential (MitoTracker Orange CMTMRos) revealed elevated mitochondrial function in host radio-resistant macrophages, although both macrophage subsets contained comparable amounts of mitochondria per cell (as indicated by similar levels of Tomm20, a translocase of the outer mitochondrial membrane) (***Figure 6—figure supplement 2B***). Thus, the metabolic profiles of donor and host macrophages in homeostatic skin mirrored the metabolic reprogramming of pro-inflammatory classically activated and anti-inflammatory alternatively activated macrophages (***Galvan-Pena and O'Neill, 2014***), respectively.

In addition to metabolic differences, we further validated the differential expression observed for several immune-related genes using a microfluidic-based multiplex qRT-PCR. Donor-derived macrophages showed increased expression of genes such as *H2-Eb1* (coding for MHC-II), *Ccr2, Il*β*, Il6* and *Il10*. Importantly, the latest three genes code for cytokines related to the pro-inflammatory response in macrophages (***Rodriguez-Prados et al., 2010***). Host macrophages showed upregulated

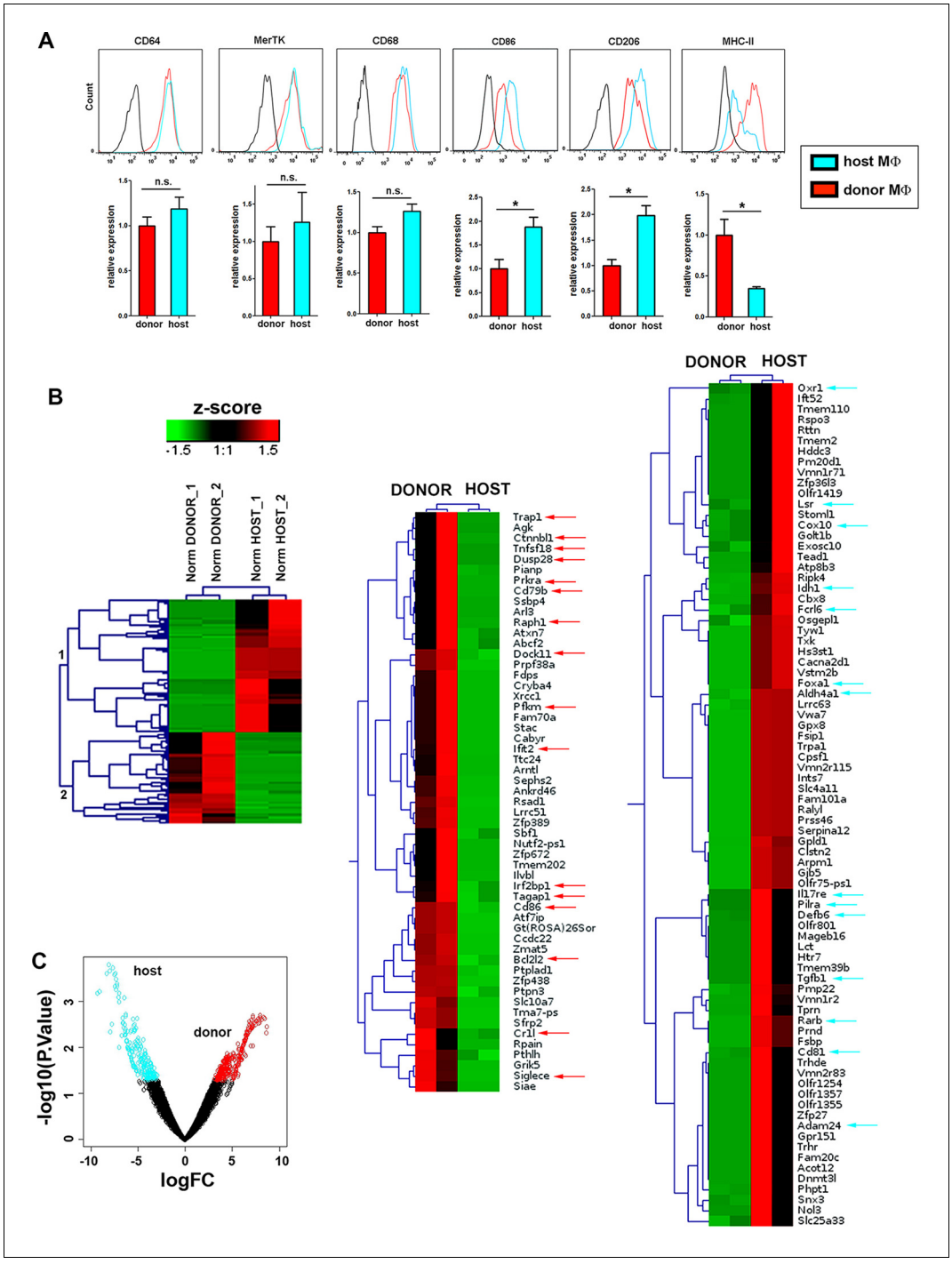

Figure 6. Phenotypic and RNASeq analyses of donor and host skin-resident macrophages from chimeric animals. (**A**) Flow cytometry analysis of the surface expression of macrophage-specific markers (CD64, MerTK, CD68), as well as CD86, CD206 and MHC-II in donor and host macrophages from chimeric animals in steady-state. Values correspond to the normalized average GeoMean ± SD (n = 3). Statistical significance was assessed by unpaired two-tailed Student's t-test (n.s. not significant, *p-value < 0.05, **p-value < 0.01). (**B**) (Left) Compact view of the hierarchical clustering of the normalized expression profiles of the protein coding sequences with p-value <= 0.05 and consistent expression levels across replicates. (Center and right) Detailed view of the hierarchical clustering showing gene annotation. Arrows highlight relevant genes upregulated in host (blue) and donor (red). (**C**) Vulcano plot representing the log2FC vs –log10 p-value transformation. Highlighted points correspond to genes with a p-value smaller than 0.05 (blue for genes more expressed in host than donor and red for genes with the opposite expression profile).

Figure 6 continued on next page

Figure 6 continued

DOI: 10.7554/eLife.15251.020

The following figure supplements are available for figure 6:

Figure supplement 1. Extended phenotypic analysis of host and donor skin-resident macrophages.

DOI: 10.7554/eLife.15251.021

Figure supplement 2. GSEA of the RNASeq data.

DOI: 10.7554/eLife.15251.022

expression of *Cd86, Il15 and Hmox* among others (***Figure 7A***). Accordingly, we detected elevated protein expression of heme oxigenase-1 (encoded by *Hmox*) and of other anti-inflammatory markers such as arginase I (***Figure 7B***) as well as higher production of TGF-β (***Figure 7C***) in host macrophages in resting conditions.

Importantly, the immune gene signatures of the dermal macrophages expressing low MHC-II and never exposed to γ-irradiation and of the remaining dermal macrophages in the skin 7d after lethal γ-irradiation showed lack of upregulation of proinflammatory genes (***Figure 7—figure supplement 1A***), correlating with the observations made in radio-resistant host macrophages in chimeric animals. In contrast, dermal macrophages expressing high MHC-II and never exposed to γ-irradiation possess a pro-inflammatory profile as observed for donor BM-derived macrophages in chimeric animals (***Figure 7—figure supplement 1A***). These results suggest that the prior lethal irradiation to generate BM chimeras did not alter the immune gene expression profiles studied herein.

Hence, our results indicate that the radio-resistant subset of skin-resident macrophages is skewed towards an anti-inflammatory phenotype already in steady-state and predict a certain degree of functional specialization for them. We have coined this novel subset of macrophages as Skin Trans-endothelial Radio-resistant Anti-inflammatory Macrophages (STREAM) based on all the specific hallmarks found in our study.

Skin anti-inflammatory macrophages are refractory to inflammatory stimuli

The divergent immune-related transcriptional profiles observed in the two distinct macrophage subsets coexisting in homeostatic skin prompted us to investigate whether they are committed to specific pro- or anti-inflammatory functions in a cell-autonomous manner and independently of polarizing stimuli. To examine this possibility, we isolated both macrophage subsets treated them ex vivo with LPS, a stimulus for which both subsets expressed the prerequisite receptors (***Figure 7—figure supplement 1B***). Interestingly, the pro-inflammatory macrophages became activated and produced substantial levels of CCL4, CCL5, CXCL1, TNF-α and IL-6 (among other pro-inflammatory mediators examined) in comparison to control conditions, whereas the anti-inflammatory subset did not produce significant amounts of these cytokines and chemokines in response to LPS (***Figure 7D***). However, the anti-inflammatory macrophages produced IL-10 in response to IL-4 stimulation (***Figure 7E***). These results suggest that the anti-inflammatory macrophages have a dearth of functional plasticity, being refractory to pro-inflammatory challenges but responsive to anti-inflammatory stimuli. They also emphasize the fact that the different subsets of skin-resident macrophages could be already committed even since steady-state to perform non-redundant functions.

Selective depletion of STREAMs impairs skin repair

To explore the function of STREAMs, we searched for a method to deplete them selectively from the skin. For this purpose, we studied the capacity of STREAMs to capture nanoparticles coated with ovalbumin (OVA), another ligand for the mannose receptor (***Burgdorf et al., 2006***) that is highly expressed on their surface. In this manner, we ensured the active capture of the particulate OVA (OVA-coated fluorescent nanoparticles (FITC fluospheres), Φ=0.2 μm) from the bloodstream, preventing its passive diffusion into the perivascular tissue that could allow for extravascular phagocytosis. We first observed that OVA fluospheres injected i.v. were specifically captured by skin macrophages (***Figure 8A***), and this process was abrogated after the depletion of skin macrophages by s.c. clodronate treatment (***Figure 8B***). Intravital imaging followed by flow cytometry evaluation confirmed that the macrophages able to capture OVA fluospheres were dextran^{+} in C57BL/6 wt animals (***Figure 8C***, ***Figure 8—figure supplement 1A*** and ***Videos 8–9***) as well as radio-resistant in

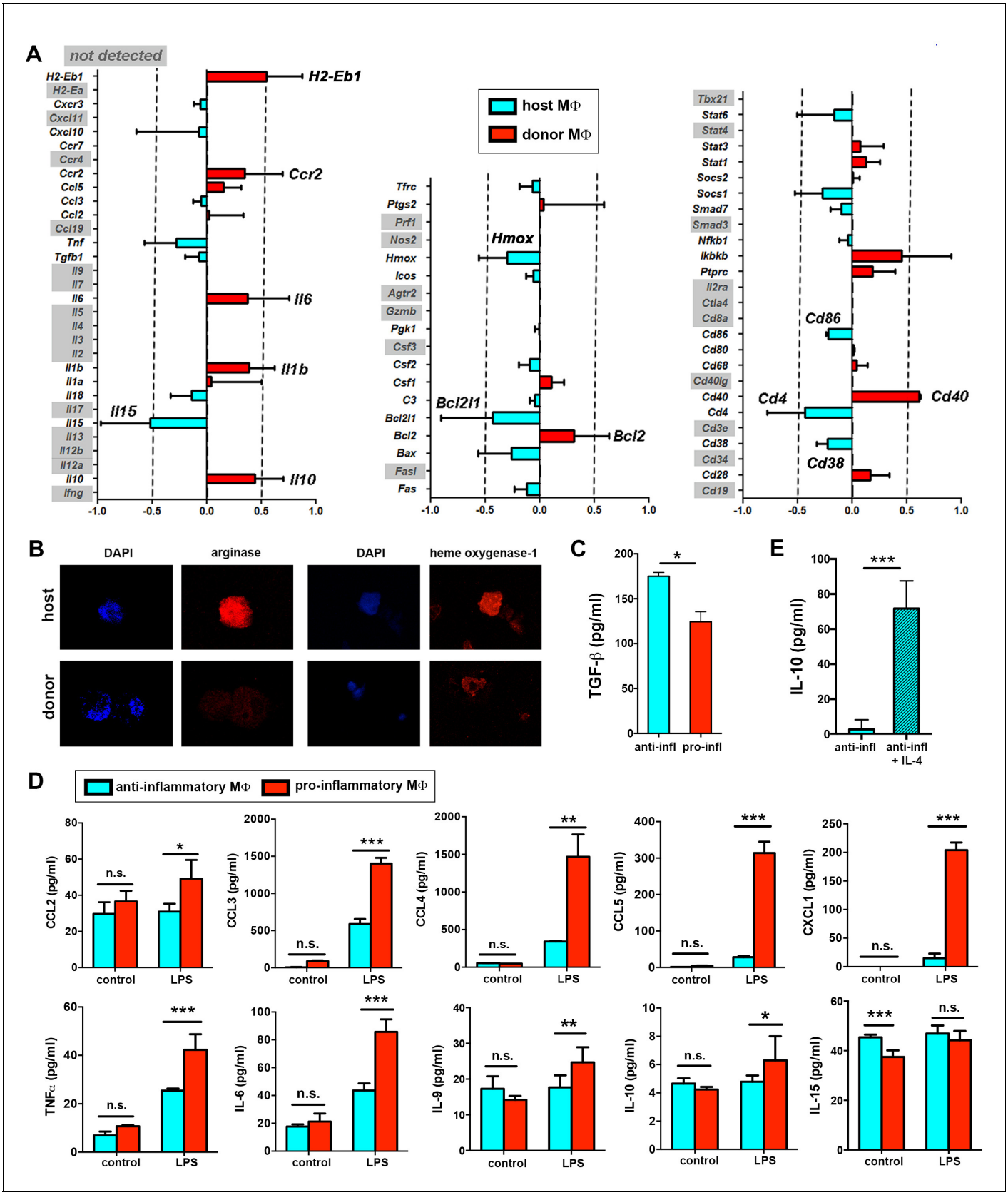

Figure 7. Immune transcriptional profile and polarization potential of STREAMs. (**A**) Comparative qPCR analysis of immune response-related genes in donor and host skin macrophages from chimeric mice. Data represent average logFC values ± SEM (n = 4). (**B**) Immunostaining of anti-inflammatory

Figure 7 continued on next page

Figure 7 continued

markers arginase I and heme oxygenase-1 in cytospin samples of isolated macrophage subsets (donor and host from chimeric animals). (**C**) ELISA quantification of TGF-β secretion by anti-inflammatory and pro-inflammatory macrophages at steady-state. Data are mean value ± SD (n = 4). Statistical significance was assessed by unpaired two-tailed Student's t-test (*p<0.05). (**D**) Sorted pro-inflammatory and anti-inflammatory MΦ were left untreated or treated with 1 ng/ml LPS for 24 hr. Then, a multiplex flow cytometry-based analysis of culture supernatants was performed. Data are mean ± SD (n = 3–5). Statistical significance was assessed by two-way ANOVA with Bonferroni's post-test (n.s. not significant, *p-value < 0.05, ** p-value < 0.01, ***p-value < 0.005). (**E**) ELISA quantification of IL-10 secretion by anti-inflammatory macrophages (50.000 cells/100 µl RPMI medium) at steady-state and after IL-4 stimulation (20 ng/ml) for 24 hr. Data are mean value ± SD (n = 4). Statistical significance was assessed by unpaired two-tailed Student's t-test (***p-value < 0.005).

DOI: 10.7554/eLife.15251.023

The following figure supplement is available for figure 7:

Figure supplement 1. Gene profile of skin macrophages from non-treated and γ-irradiated animals.

DOI: 10.7554/eLife.15251.024

CD45.1/CD45.2 (donor/host) C57BL/6 chimeras (***Figure 8D–E***). The availability of blood-borne nanoparticles in peripheral circulation is limited by the filtering action of mainly the liver and spleen, and therefore the amount of OVA-coated beads captured by skin STREAMs was low compared with that of splenic macrophages (***Figure 8—figure supplement 1B***); however, this amount was increased in γ-irradiated and splenectomized animals (***Figure 8—figure supplement 1A***).

Based on the specific ability of STREAMs to capture OVA nanoparticles, we next set up a method to deplete them selectively by administering i.v. OVA-coated nanoparticles (NP) adsorbed with diphtheria toxin (DT). In contrast to the i.v. administration of clodronate liposomes, which failed to eradicate skin STREAMs (*data not shown*), this tailored experimental strategy depleted preferentially STREAMs preserving most of the other skin macrophages that had no access to the blood-borne toxin-coated NPs (***Figure 9—figure supplement 1***). Then, the potential anti-inflammatory function of STREAMs in tissue repair was interrogated using a model of wound healing in combination with DT-OVA-NP treatment. Animals were treated either with OVA-NP or DT-OVA-NP (2.5 µl/g per dose) 1d before and 2d after wounding and were sacrificed at d5, observing a clear decrease in the macrophage population (***Figure 9A,D***). At this mid-stage of repair, macrophage depletion was associated with a significant delay in the healing process (measured as % of area of initial wound) (***Figure 9B***) and the histological analyses revealed a marked reduction in the formation of granulation tissue, concomitant reduced angiogenesis as well as delayed re-epithelialization (***Figure 9C–D***). Next, we administered a sole dose (2.5 µl/g) of DT-OVA-NP 2d after wounding and monitored wound closure till d9. In this manner, the macrophage depletion was attained after the initial inflammatory phase of wound healing (***Gurtner et al., 2008***). The Masson trichrome staining demonstrated a clear defect in collagen deposition in the animals treated with DT-OVA-NP (***Figure 10A***). This defect correlated with the disordered distribution of myofibroblasts in these animals observed with the α-smooth muscle actin (SMA) staining (***Figure 10B***). These results contrasted with the abundant collagen deposition and the parallel organization of myofibroblasts in OVA-NP-treated animals (***Figure 10A–B***). This noticeable phenotype observed in macrophage function-related parameters indicates that STREAMs could exert a prominent role as the macrophages involved in orchestrating tissue remodeling and repair in skin, as anticipated by their anti-inflammatory gene and protein expression profile.

Next, we performed wound healing experiments abrogating monocyte infiltration in the skin and depleting the radiosensitive subset of skin macrophages to further study the role of STREAMs in such scenario. We first analyzed the healing process in *Ccr2*$^{-/-}$ animals, wherein the repopulation of skin from blood monocytes is compromised (***Boring et al., 1997***; ***Serbina and Pamer, 2006***). Interestingly, STREAMs are CCR2^{-} (***Figure 10—figure supplement 1A***) and are normally localized around dermal vessels in *Ccr2*$^{-/-}$ mice (***Figure 10—figure supplement 1B***). Importantly, we did not observe substantial differences in wound closure, collagen deposition, and myofibroblast distribution in *Ccr2*$^{-/-}$ mice compared to *Ccr2*$^{+/+}$ animals (***Figure 10—figure supplement 1C–D***). Next, we benefited from the radio-resistant nature of STREAMs to deplete skin radio-sensitive macrophages by lethal γ-irradiation and prevented their replenishment by limiting the affluence of peripheral blood monocytes after reconstitution with *Ccr2*$^{-/-}$ hematopoietic progenitors (***Willenborg et al., 2012***) (***Figure 10—figure supplement 1E***). We could not find differences in the healing capacity of

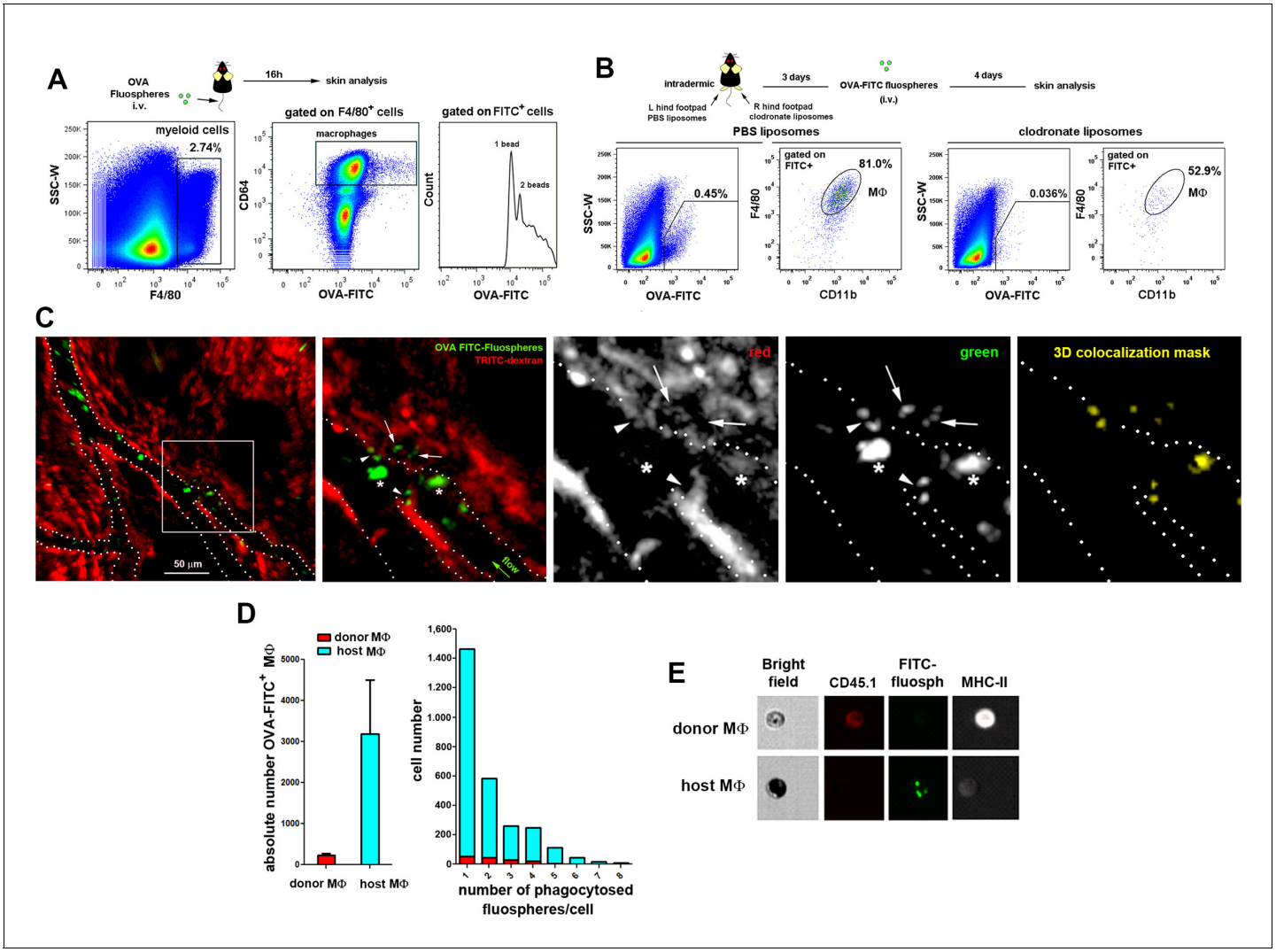

Figure 8. STREAMs capture blood-borne OVA nanoparticles at steady-state. (**A**) Representative flow cytometry analysis of OVA-FITC fluosphere capture by skin macrophages in C57BL/6 mice. The peaks observed in the histogram correspond to the number of fluospheres uptake per cell. (**B**) Mice were intradermally injected with PBS (control) or clodronate liposomes in the hind footpads and were injected i.v. with OVA-adsorbed FITC fluospheres 72 hr later, followed by analysis after 4d. Representative dot plots show the amount of FITC$^+$ cells for each treatment and histograms show the proportion of MΦ in the FITC$^+$ fraction. (**C**) (Left) A C57BL/6 mouse was first injected i.v. with HMw TRITC-dextran and with OVA-FITC fluospheres 16 hr later. Imaging began 24 hr after the last injection. A representative frame of the experiment extracted from ***Video 8*** with zoomed detail aside is shown. White dotted lines depict vessel walls. White asterisks mark FITC$^+$ intravascular monocytes that have phagocytosed OVA fluospheres. White arrowheads point to intraluminal particles retained by dextran$^+$ STREAMs and white arrows point to extravascular particles already phagocytosed by STREAMs. (Center and right) Split channels are shown with higher magnification as well as a 3D colocalization mask of both channels. (**D**) (Left) Absolute number of macrophages of each haplotype (CD45.1 (donor) or CD45.2 (host)) that have captured OVA-coated fluospheres in treated chimeric animals (n = 4). Data are means ± SEM. (Right) Representative per-cell uptake of fluospheres by macrophages of each haplotype. (**E**) Single-cell images of sorted skin macrophage subsets of a chimeric mouse (CD45.1/CD45.2, donor/host) injected i.v. with OVA-FITC fluospheres. Images were obtained using an imaging flow cytometer. Notably, host macrophages were mostly filled with melanin as confirmed with Fontana-Masson staining (*data not shown*).

DOI: 10.7554/eLife.15251.025

The following figure supplement is available for figure 8:

Figure supplement 1. Comparison of OVA-FITC fluosphere uptake either by skin dextran$^+$ macrophages in control, γ-irradiated and splenectomized animals or by spleen macrophages and skin macrophage subsets in chimeric mice.

DOI: 10.7554/eLife.15251.026

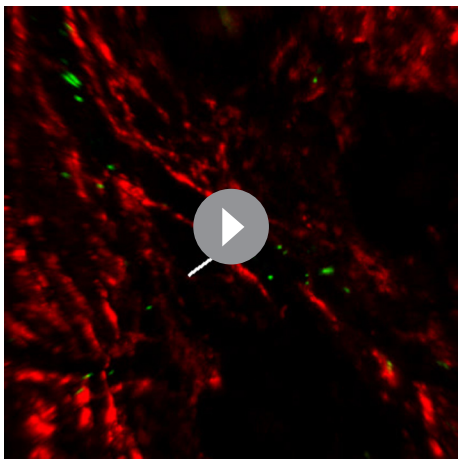

Video 8. In vivo uptake of blood-borne OVA-FITC fluospheres by STREAMs, example 1. A C57BL/6 mouse was first injected i.v. with HMw TRITC-dextran and with OVA-FITC fluospheres 16 hr later. Imaging began 24 hr after the last injection. The frames in the video sequence correspond to a z-stack (4 sections acquired every 10 μm) obtained every 3.300 s over a total period of 16 min. Interestingly, an intravascular STREAM's protrusion is detected at the beginning of the video sequence (white arrow). The video sequence shows free-flowing FITC-fluospheres as well as the intravascular cells that have phagocytosed them (most probably monocytes). Some of the FITC$^+$ cells transiently interact with endothelium at sites coinciding with STREAM's intravascular protrusions. Intraluminal FITC-fluospheres retained in such intravascular protrusions can be also observed. Furthermore, FITC-fluospheres that have been previously phagocytosed by dextran$^+$ STREAMs are detected in the extravascular tissue.

DOI: 10.7554/eLife.15251.027

the *Ccr2*$^{-/-}$/*Ccr2*$^{+/+}$ (donor/host) chimeras (whose skin was defective in radio-sensitive macrophages, the repopulation from BM was prevented but the pool of STREAMs was intact) compared to that of control *Ccr2*$^{+/+}$/*Ccr2*$^{+/+}$ chimeras, using all parameters assayed previously (***Figure 10—figure supplement 1F–G***). Altogether these results strengthen the idea of the selective role for STREAMs in tissue repair.

Discussion

In this study we have identified a unique subset of dermal perivascular macrophages, skin transendothelial radio-resistant anti-inflammatory macrophages (STREAM), which capture blood-borne macromolecules by extending protrusions into the vascular lumen at steady-state. The observation of this phenomenon in chimeric animals allowed us to further characterize STREAMs as a radio-resistant subset of skin macrophages, whose turnover is ensured by an extramedullary source. We could also determine that STREAMs are committed to perform anti-inflammatory functions, lacking the plasticity to be reprogrammed in the presence of a potent pro-inflammatory stimulus. Finally, the selective depletion of STREAMs highlighted their function in tissue repair and remodeling processes to regain skin homeostasis.

It is well established that specialized macrophage subtypes, such as subcapsular sinus macrophages in lymph nodes and Kupffer cells in liver, can traverse fenestrated endothelial sinusoids to capture lymph- or blood-borne particulate antigens and participate in the initiation of innate and adaptive immunity (***Huang et al., 2013***; ***Junt et al., 2007***; ***Lee et al., 2010***; ***Wong et al., 2013***). Dendritic cells are also able to extend transepithelial projections to capture foreign particulate antigens from airways and gut mucosa, or traverse the vasculature in pancreatic islets of Langerhans (***Calderon et al., 2008***; ***Chang et al., 2013***; ***Farache et al., 2013***; ***Hammad et al., 2009***; ***Rescigno et al., 2001***). However, some of these specialized dendritic cells have been redefined as macrophages (***Calderon et al., 2014***; ***Mazzini et al., 2014***). CX3CR1$^+$ myeloid cells in the central nervous system could also gain access to vasculature (***Barkauskas et al., 2013***) and mast cells were recently reported to capture blood-borne IgE, albeit the underlying mechanism remains unknown (***Cheng et al., 2013***). Herein, we report that STREAMs are unique macrophages in that they traverse the endothelial junctions of non-fenestrated dermal vasculature to take up circulating macromolecules under homeostatic conditions. STREAM's protrusions only emerge through the endothelial cell-cell junctions and do not use a transcellular route, as illustrated using a genetic approach (the VE-cad-α-cat transgenic mouse line, which display impregnable, highly stable adherens junctions). Moreover, unlike subcapsular sinus macrophages in lymph nodes, which act like fly paper retaining lymph-borne viral particles on their surface for subsequent transfer to B cells (***Junt et al., 2007***), STREAMs internalize particulate antigens, such as OVA-FITC Fluospheres, and might play a role in their cross-presentation to tissue-resident memory CD8$^+$ T cells.

The existence of radio-resistant dendritic cells in the skin has been previously reported (***Bogunovic et al., 2006***; ***Merad et al., 2002***), whereas the presence of radio-resistant dermal macrophages has remained elusive hitherto. This study reveals that STREAMs are a radio-resistant subset

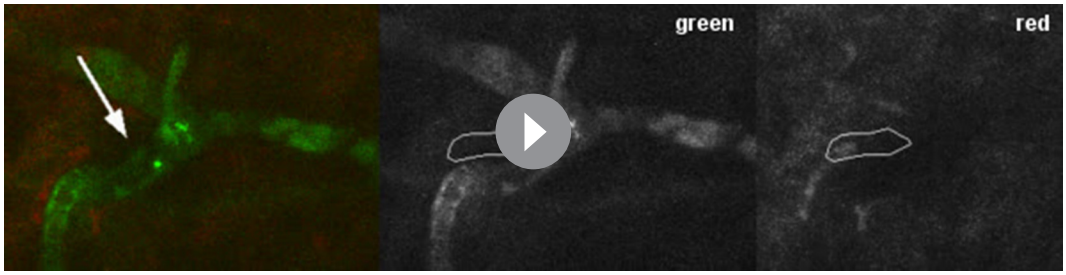

Video 9. In vivo uptake of blood-borne OVA-FITC fluospheres by STREAMs, example 2. The i.v. injection of HMw TRITC-dextran was carried out 16 hr prior to the experiment and the i.v. injection of OVA-FITC fluospheres preceded the beginning of imaging acquisition. The frames from the video sequence are maximal projections of a z-stack (4 sections acquired every 10 μm, 30 μm in depth) obtained every 2.27 sec over a total period of 11 min 30 s. The video shows a dextran^{dim} STREAM that simultaneously phagocytoses several OVA-coated FITC fluospheres. The subsequent retrograde transport of phagosomes from the vessel towards the cell body is also shown. The white arrow in the merged image points to the place where fluospheres are captured from vasculature and the cell area is depicted in green and red channels for clarity.
DOI: 10.7554/eLife.15251.028

that coexists in steady state with other skin macrophages of radio-sensitive nature. In this regard, the radio-resistant macrophages described in (***Haniffa et al., 2009***) might be the human homolog of this mouse subset, extending the generality and impact of our findings. The chimerism, parabiosis and fate mapping experiments also indicate that STREAMs are maintained locally in the skin throughout adult life independently of circulatory precursors, as opposed to radio-sensitive macrophages that are renewed at a low rate from blood in steady state and replaced by donor BM progenitors after a genotoxic insult. Thus, our data further extent the previous knowledge on the minimal blood exchange experienced by tissue-resident macrophages in other tissues (***Hashimoto et al., 2013***; ***Yona et al., 2013***).

The renewal potential and the lifespan of tissue-resident macrophages are still controversial. Somes studies have described the potential of macrophages to be self-perpetuated under certain conditions (for example, in the presence of IL-4 during a parasitic infection [***Jenkins et al., 2011***] or in a M-CSF- or GM-CSF-dependent manner after macrophage depletion [***Hashimoto et al., 2013***]). STREAMs are unable to self-renew in steady-state and their turnover from a Bmi1^{+} adult progenitor occurs at a low basal rate, becoming outcompeted over time by other skin-resident macrophages with faster turnover. Hence, our results concur with previous studies reporting a dual origin for skin macrophages with a prenatally-derived CCR2-independent subset and a postnatal BM-derived CCR2-dependent subset, being the prenatally-derived subset displaced by the BM-derived subset with age (***Jakubzick et al., 2013***; ***Tamoutounour et al., 2013***). Interestingly, this dual origin has been also observed in other tissues such as heart (***Molawi et al., 2014***).

Unraveling the ontogenetic source for tissue-resident macrophages is another complex matter. There are several landmark studies describing the existence of different macrophage precursors during development. The yolk sac-derived Myb-independent F4/80^{bright} macrophages seeded in the embryonic skin prior to birth and renewed independently of definitive hematopoiesis (***Schulz et al., 2012***) might correspond to the developmental precursor for STREAMs and the c-Myb dependent fetal liver monocytes that give rise to macrophages with self-renewal capacity (***Hoeffel et al., 2015***) might be the precursors of the radiosensitive macrophages (those susceptible of replenishment by BM precursors after a genotoxic insult). However, the elucidation of skin macrophage ontogeny deserves further thorough investigation in future studies.

Regarding phenotypic characterization, a classification of the skin mononuclear phagocyte system based on phenotypic markers has recently identified heterogeneity among the skin-resident macrophages, although not related to radio-sensitivity. These authors distinguish two distinct skin-resident macrophage subsets defined both as CD11b^{+} CD11c^{-} CD64^{+} MerTK^{+} Ly6C^{low} CCR2^{-} but differing on the expression of MHC-II (***Tamoutounour et al., 2013***). They suggest that both subsets possess analogous transcriptional profiles, share functions, are radio-sensitive and equally dependent on BM supply, and could represent sequential stages of differentiation (the MHC-II^{low} subset (P4) maturing into MHC-II^{high} (P5) macrophages). As demonstrated in ***Figure 6A*** and ***Figure 6—figure***

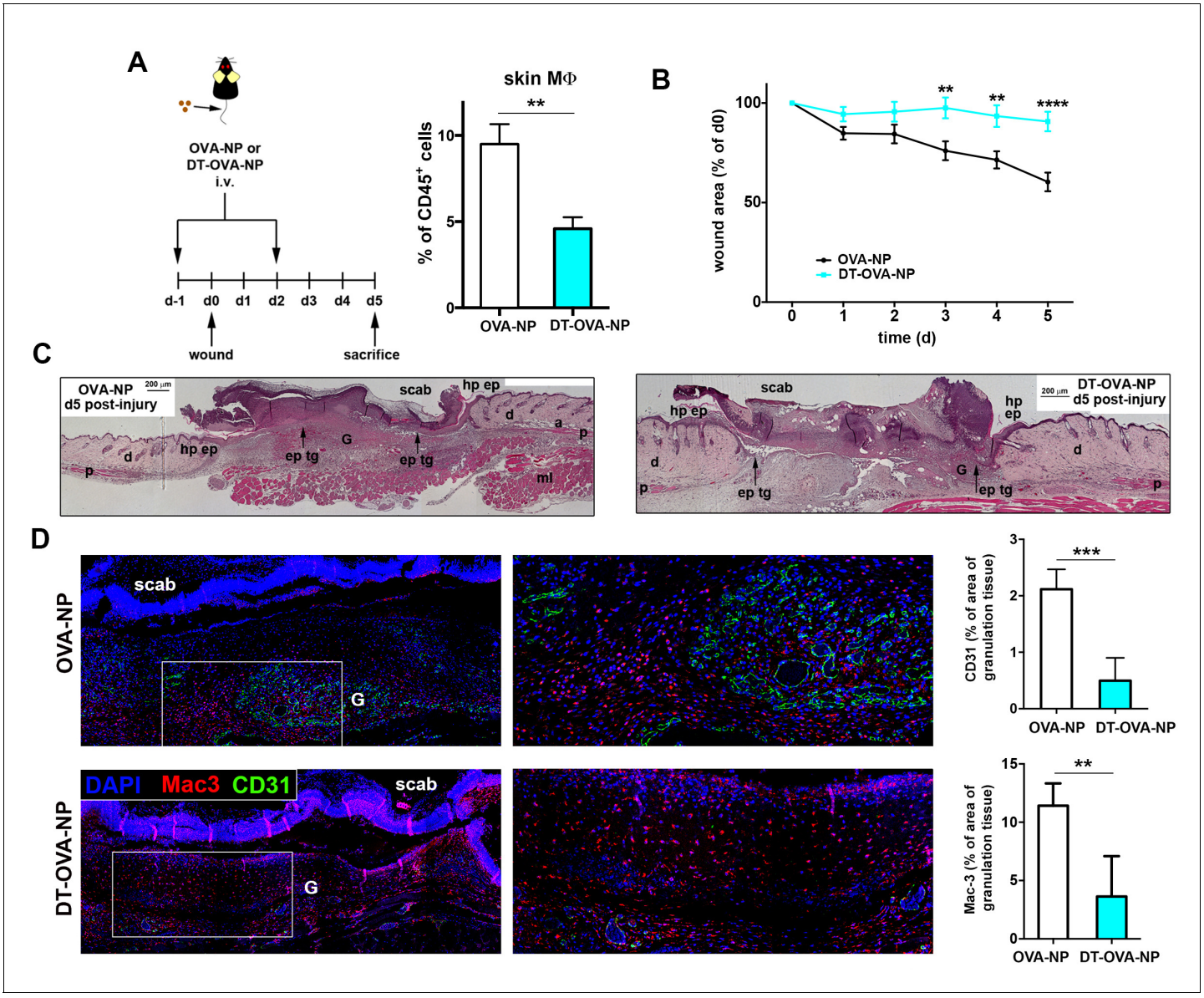

Figure 9. Macrophage depletion using DT-OVA-NP hampered wound healing. (**A**) (Left) Animals were first injected i.v. with either OVA-NP or DT-OVA-NP (2.5 µl/g) and, 1d later, the wound healing assay began. Two days after wounding, animals were treated with another similar dose of OVA-NP (control) or DT-OVA-NP. Then, mice were sacrificed 3d later (mid-stage repair) and their ears were collected to analyze skin macrophages. (Right) Bar histogram showing the percentage of MΦs out of total $CD45^+$ cells in the ears of OVA-NP- or DT-OVA-NP-treated animals. Data are mean ± SEM (n = 4–7). Statistical significance was assessed by unpaired two-tailed Student's t-test (**p-value < 0.01). (**B**) Analysis of mid-stage repair (5d after wounding). The plot illustrates the decrease of the wound area over time expressed as percentage of the initial wound. Data are mean SEM, n = 32 wounds/group. Statistical significance was assessed by two-way ANOVA analysis with Sidak's post-test (**p-value < 0.01, ****p-value < 0.0001) (**C**) Histological analysis of wounds at mid-stage of repair from OVA-NP- and DT-OVA-NP-treated animals. Hematoxylin-eosin staining of representative samples is shown. (Hp ep: hyperproliferative epithelium, ep tg: epithelial tongue, G: granulation tissue, d: dermis, p: panniculus carnosus, a: adipose tissue, ml: muscle layer). (**D**) (Left) Representative immunofluorescence staining of vessels (CD31 staining) and macrophages (Mac-3 staining) in tissue sections of wounds at mid-stage (5d) from OVA-NP- or DT-OVA-NP-treated animals. (Right) Quantification of CD31 and Mac-3 stained area within the granulation tissue is shown. Data are mean ± SD (n = 4–6). Statistical significance was assessed by unpaired two-tailed Student's t-test (**p<0.01, ***p<0.005).

DOI: 10.7554/eLife.15251.029

The following figure supplement is available for figure 9:

Figure supplement 1. Selective deletion of STREAMs after DT-OVA-NP treatment.

DOI: 10.7554/eLife.15251.030

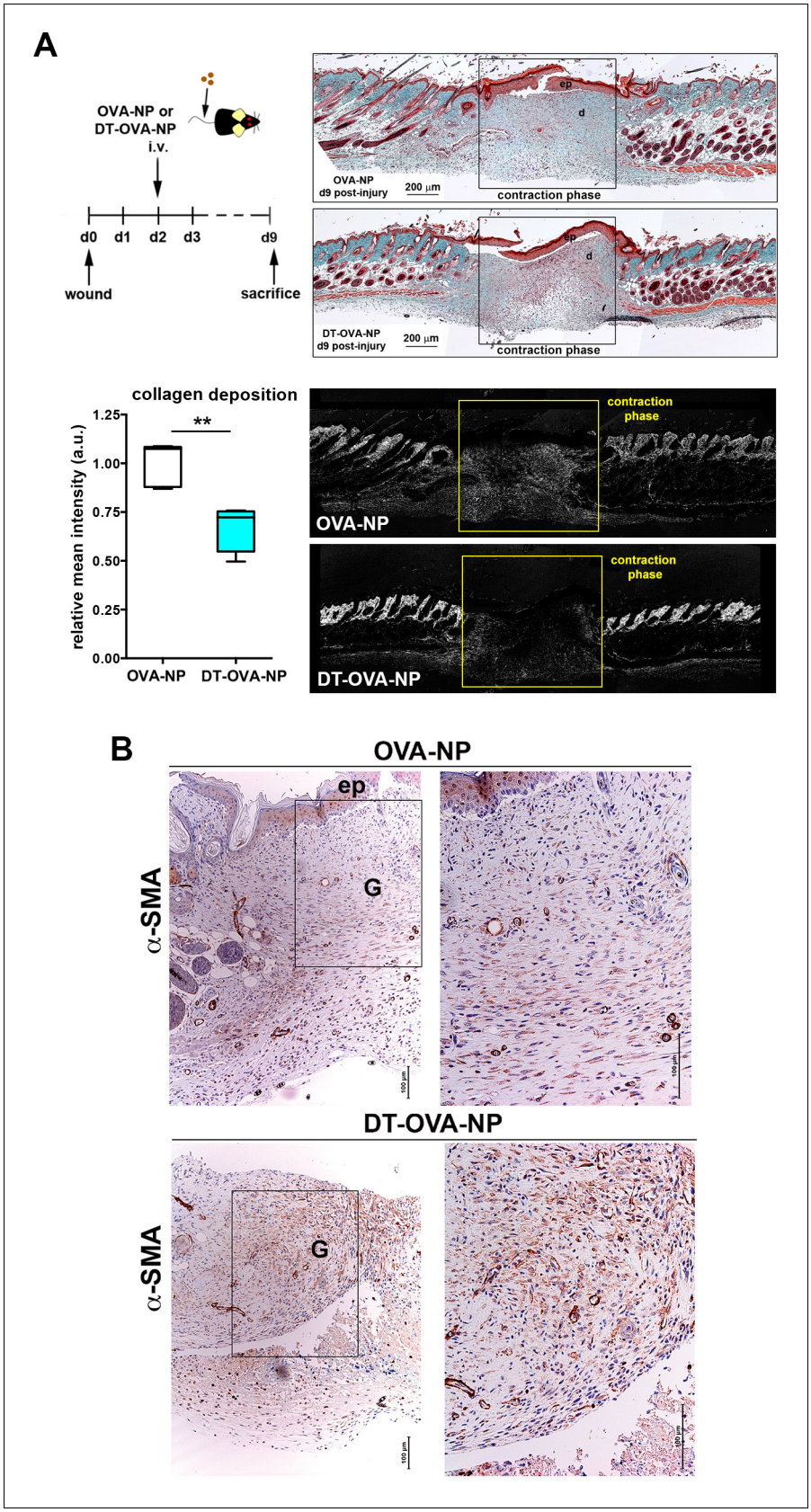

Figure 10. Macrophage depletion using DT-OVA-NP impaired collagen deposition and myofibroblast organization within the wound. (**A**) Wound healing assay until closure with administration of DT-OVA-NP or OVA-

Figure 10 continued on next page

Figure 10 continued

NP 2d after injury. After sacrifice, tissue was stained with hematoxylin-eosin (upper right) or analyzed for its content in collagen using Masson trichrome staining (lower right) followed by relative intensity quantification (n = 6/group) (lower left). Statistical significance was assessed by an unpaired two-tailed Student's t-test (**p<0.01). (Ep: epidermis, d: dermis). (**B**) Analysis of the myofibroblast distribution in the wound area at the time of closure (contraction phase) in OVA-NP and DT-OVA-NP mice. Immunohistochemical staining of α-SMA was performed. (Left) View of the complete wound, (right) zoom in the granulation tissue.

DOI: 10.7554/eLife.15251.031

The following figure supplement is available for figure 10:

Figure supplement 1. Skin-resident macrophages different from STREAMs are not critically involved in tissue repair.

DOI: 10.7554/eLife.15251.032

supplement 1B, the expression of MHC-II in skin macrophages cannot precisely discriminate the two independent subsets of macrophages with distinct radio-sensitivity, different polarization profiles and non-overlapping functions described in our work. Therefore, the classification criteria used in this work allows better resolution of the skin macrophage subsets, compared to classifications relying on subset-defining markers that might not adequately reflect the existing heterogeneity within the skin niche.

Metabolic adaptation is a key feature in macrophage activation, instrumental for their function in homeostasis, immunity, and inflammation (***Martinez et al., 2013***). In this regard, the GSEA of our RNASeq data highlight clear differences in the metabolic gene profiles of host radio-resistant and BM-derived macrophages. We found an enrichment in genes involved in glycerolipid, glycerophospholipid and linoleic acid metabolism, as well as in glycosphingolipid biosynthesis in the gene profile of radio-resistant macrophages. These results are compatible with the energetic requirements and the regulation of membrane fluidity needed for phagocytosis and are also crucial for tissue remodeling (***Biswas and Mantovani, 2012***). Other genes enriched in this subset are related to fibrogenesis and tissue repair such as *Tgfb1* and genes of the Hedgehog signaling pathway, as well as genes related to taurine and hypotaurine metabolism, being consistent this with an antioxidant protective role. Conversely, the transcriptional profile of the BM-derived macrophages includes an over-representation of genes associated with the carbohydrate and retinol metabolisms such as the pentose phosphate pathway, with the ABC transporters and the JAK-STAT and WNT signaling pathways, in accordance with their pro-inflammatory potential. Moreover, a gene encoding a regulator of the metabolic switch from oxidative phosphorylation to aerobic glycolysis (*Trap1*) (***Yoshida et al., 2013***) is specifically expressed in BM-derived macrophages.

Our study in the homeostatic skin along with others describing the existence of polarized macrophages already in steady state in heart, testis and pancreas (***Calderon et al., 2015***; ***DeFalco et al., 2014***; ***Pinto et al., 2012***) help to reformulate the long-held paradigm of macrophage polarization, which defined the functional specialization of macrophages from a steady-state non polarized status mainly as a consequence of integrating external stimuli (***Gordon and Pluddemann, 2013***; ***Sica and Mantovani, 2012***). Interestingly, the study by Calderon and colleagues (***Calderon et al., 2015***) highlights the imprinting of distinct features in macrophages by their anatomical localization within the steady-state pancreas. The macrophages in the islets possess a pro-inflammatory M1 phenotype and protrude into the fenestrated vessels, whereas the stromal milieu sets the response of the macrophages in favor of the M2 phenotype. This pattern of regional specialization might not be applicable to the skin where, e.g., perivascular macrophages with pro-inflammatory (***Abtin et al., 2014***) and anti-inflammatory (STREAMs) phenotypes coexist in the same areas. However, although both subsets mostly share environmental stimuli, STREAMs can get access to the intravascular milieu and might receive selective signals that could contribute to maintain their phenotype. Therefore, the essential role of the environment in controlling tissue-specific macrophage identities cannot be dismissed as highlighted in recent epigenetics studies (***Gosselin et al., 2014***; ***Lavin et al., 2014***).

The preferential depletion of anti-inflammatory STREAMs has a deleterious impact in the wounded skin, indicating that they could participate in orchestrating the pro-reparative functions traditionally associated to the so-called alternatively activated (M2) macrophages (***Das et al., 2015***). Conversely, we observed that the rate of wound closure was neither affected in the *Ccr2*$^{-/-}$ animals

(as previously reported by **Willenborg et al., 2012**) nor in chimeric *Ccr2*$^{-/-}$/*Ccr2*$^{+/+}$ mice, indicating that infiltrating monocytes and radiosensitive tissue-resident macrophages could be mostly dispensable for the reparative phase of the healing process in the skin. Thus, the coexistence of macrophage subsets performing non-redundant roles in homeostatic skin highlights the need of maintaining equilibrium between both pools to preserve the skin fitness. The lack of functional redundancy could be of clinical significance, and may contribute to better understand concomitant skin pathologies arising from radio-induced bone marrow ablation therapies and certain inflammatory skin disorders, particularly those aggravated with age.

Materials and methods

Mice

Male either littermates or age-matched (8-to-12-week-old) mice on the C57BL/6J background were used for intravital imaging, phenotypic characterization, transcriptional analysis and functional experiments. Chimeric animals were generated as follows: 8-to-12-week-old C57BL/6 wt male mice (CD45.2 haplotype), were lethally γ-irradiated with 2 doses of 6.5 Gy and transplanted with a mixture of 5 x 10^6 BM cells from either B6 SJL mice (CD45.1 haplotype), or B6 ACTB-eGFP mice. Alternatively, irradiated B6 SJL mice (CD45.1$^+$) were reconstituted with BM from *Ccr2*$^{+/+}$ or *Ccr2*$^{-/-}$ (CD45.2$^+$) mice. Animals were used for experimental procedures after 12 to 18 weeks of reconstitution. Details of the generation and characterization of the gene-targeted mouse expressing VE-cadherin-α-catenin protein can be found in (**Schulte et al., 2011**). Inducible *Bmi1*-IRES-Cre-ERT2 Rosa26 YFP mice were generated by crossing the *Bmi1*$^{CreER/+}$ strain (**Sangiorgi and Capecchi, 2008**) with Rosa26$^{YFP/+}$ reporter mice. *Bmi1*-IRES-Cre-ERT2 Rosa26 YFP double heterozygous mice were injected with tamoxifen 5d prior to analysis. Tamoxifen (Sigma-Aldrich [St Louis, MO]) was dissolved in corn oil (Sigma-Aldrich) to a final concentration of 20 mg/ml, and mice were i.p. injected every 24 hr on three consecutive days with tamoxifen at a concentration of 9 mg per 40 g body weight. The nestin-eGFP reporter strain was a kind gift from Dr. G. Enikolopov (**Mignone et al., 2004**). DPE-GFP mice were generated as described in (**Mempel et al., 2006**). *Langerin*-eGFP, *Cx3cr1*-GFP, *Lyz2*-Cre:Rosa26YFP and *Ccr2*$^{-/-}$ mice were kindly provided by Dr. B. Malissen, Dr A. Hidalgo, Dr. M. Ricote and Dr. C. Ardavin, respectively. Mice were kept in pathogen-free conditions in the CNIC Animal Unit, Madrid. Animal studies were approved by the local ethics committee and by the Division of Animal Protection of Comunidad de Madrid (approved protocols PROEX 159/15 and 160/15). All animal procedures conformed to EU Directive 2010/63EU and Recommendation 2007/526/EC regarding the protection of animals used for experimental and other scientific purposes, enforced in Spanish law under Real Decreto 1201/2005.

Intravital imaging

Ears were taped to the center of a coverslip and attached with high vacuum grease. Hairless areas were examined using a HCX PL APO lambda blue 20.0X 0.70 IMM UV objective (multi-immersion, glycerol) coupled to an inverted microscope (DMI6000; Leica Microsystems GmbH [Wetzlar, Germany]) equipped with a confocal laser-scanning unit (TCS-SP5; Leica). Non-invasive intravital imaging procedures were carried out in a thermostatic chamber at 37°C. For short-term studies (1–2 hr), animals were first anesthetized by i.p. injection of ketamine (50 mg/kg), xylazine (10 mg/kg), and acepromazine (1.7 mg/kg), and repeated half-doses were administered when needed over the course of the experiments. For long-term studies (time-lapse imaging > 2 hr), animals were first anesthetized by i.p. injection of urethane (1.2 gr/kg) dissolved in PBS, followed by s.c. injection of 1/10 of the initial dose dissolved in 200 µl PBS for rehydration after several hours. As vascular tracers, 100 µl of 2 MDa FITC- or TRITC-dextran (1% w/v, which corresponds to a concentration of 5 µM; anionic lysine fixable [Molecular Probes, Thermo Fisher Scientific, Waltham, MA]), or 25 µg Vivotag (VisEn Medical, PerkinElmer [Waltham, MA]) dissolved in PBS were i.v injected. For in vivo staining of the vasculature, an anti-CD31 antibody (Fitzgerald Industries [North Acton, MA]) was labeled in house with an Alexa Fluor 647 monoclonal antibody labeling kit (Molecular Probes), and 25 µg were injected i.v. 16 hr after dextran administration. Images were obtained using bidirectional scanning mode and the acquisition of the different channels was sequential to avoid fluorescence bleed-through artifacts. Z-stack images were acquired with optimal confocal sectioning (spaced 0.63 µm along the z-axis).

For time-lapse acquisition, z-sections were obtained at 10 µm intervals up to a depth of 70–100 µm, using a pinhole aperture > airy 1 (confocal acquisition). The acquisition rate was ~2–3 sec/z-stack.

Whole-mount staining of skin samples

Live mice anesthetized with a mixture of zoletil and dontor were surgically opened and perfused with 1% paraformaldehyde (PFA) in PBS at a continuous infusion rate of 7 ml/min, using a programmable syringe (Harvard Aparatus). Different parts of the skin were collected and post-fixed in 1% PFA for 1 hr at room temperature (RT). Tissues were stained as described in (***Baluk et al., 2007***). Briefly, tissues were incubated overnight (O/N) at RT with PBS containing 0.3% Triton X-100, 5% goat serum (Jackson ImmunoResearch Europe Ltd. [Suffolk, UK]) and primary antibodies. The anti-murine primary antibodies used were hamster anti-CD31 clone 2H8 (Chemicon, EMD Millipore [Billerica, MA]), rat anti-CD68 clone FA-11 and polyclonal rabbit anti-collagen IV (Abd Serotec, Bio-rad [Hercules, CA]), polyclonal rabbit anti-CD31 and polyclonal chicken anti-GFP (Abcam [Cambridge, UK]), polyclonal rabbit anti-LYVE-1 (ReliaTech [Wolfenbüttel, Germany]), and biotin-conjugated CD45.2 clone 104 (BD Pharmingen, BD Biosciences [San Diego, CA]). Samples were then thoroughly washed with 0.3% Triton X-100 in PBS and stained with appropriate secondary antibodies O/N at RT. Secondary antibodies used were DyLight 405 donkey anti-rat, Cy3 donkey anti-chicken and Alexa Fluor 647 or 488 goat anti-armenian hamster (Jackson Immunoresearch), Rhodamine-X goat anti-rabbit, Alexa 647 goat anti-rabbit, Alexa 647 chicken-anti-rat, Alexa 488 donkey-anti-rat and Alexa 647 or 488 goat-anti-mouse (Molecular Probes). After the last round of washing, labeled samples were fixed in 1% PFA for 30 min and mounted for microscopy analysis in Prolong Gold antifade reagent (Molecular Probes). Confocal z-stacks up to a depth of 100 µm (including epidermis and upper dermis) were obtained using a LSM 700 laser scanning microscope equipped with a LD LCI Plan/Apochromat 25x/0.8 Imm Korr DIC M27 objective (Carl Zeiss AG [Oberkochen, Germany]).

Image processing and analysis

Confocal z-stack images from fixed samples or intravital experiments were processed to obtain maximal projections, orthogonal sectionings, 3D reconstructions or isosurface renderings, fluorescence intensity profiles, colocalization analyses and 3D computational analyses of distances using Imaris 7.3.1 (Bitplane [Belfast, UK]), Volocity 5.5.1 (PerkinElmer), and ImageJ 1.42q (NIH, [Bethesda, MD]). Images from in vivo time-lapse acquisitions were analyzed and videosequences set up and edited either with Imaris or Volocity softwares.

Dextran 'pulse-chase' assay

Animals were injected i.v. with 100 µl 1% HMw TRITC-dextran and, after a lapse of 24 hr, with 100 µl 1% HMw FITC-dextran. Animals were sacrificed 24 hr after the last injection and ears were processed for imaging.

In vivo staining of intraluminal protrusions of macrophages

Mice were injected retro-orbitally with 10 µg of Alexa 488 anti-CD206 (clone C068C2, BioLegend [San Diego, CA]) or Alexa 488 control isotype antibody (rat IgG2b, κ) and sacrificed 3 min later. Then, animals were perfused with PBS and ear skin was processed for flow cytometry. Counter-staining of CD206 was performed with Alexa 647 anti-CD206 clone MR5D3 (BioLegend).

Flow cytometry analysis and sorting strategies

Skin samples (ears and hind footpads) were digested either with 2 mg/ml crude collagenase type IA (Gibco, Thermo Fisher Scientific [Waltham, MA]) in PBS for 2 hr or with 0.25 µg/ml Liberase TM Research Grade (Roche Holding AG [Basel, Switzerland]) in RPMI medium for 1 hr at 37°C. Samples were then mechanically disrupted, washed and filtered. Single-cell suspensions were incubated with anti-mouse FcRII/III (clone 2.4G2) for 10 min at 4°C in PBS containing 0.05% BSA and 0.05 mM EDTA, and then stained with the following antibodies: Pecy7 anti-F4/80 clone BM8, APC or APC-eFluor 780 anti-CD45.2 clone 104, PE anti-CD115 clone AFS98, PE anti-Tie-2 clone Tek4, and APC-eFluor 780 Streptavidin (eBioscience [San Diego, CA]); v450 Horizon anti-CD45 Clone 30-F11, v450 Horizon or PerCP-Cy5.5 anti-CD45.1 clone A.20, PE anti-CD11c clone HL3, FITC or APC or APCCy7

anti-MHC-II clone M5/114.15.2, APC anti-MHC-I clone AF6-88.5, PE anti-Ly6C clone HK1.4, PECy7 or Alexa Fluor 647 anti-CD64 clone X54-5/7.1, PE anti-CD70 clone FR70, PE anti-CD86 clone GL-1, FITC anti-CD40 clone 3/23, and FITC anti-CD11b clone M1/70 (BD Pharmingen); APC anti-CCR2 and biotinylated MertK (R&D Systems Inc. [Minneapolis, MN]); Streptavidin Alexa Fluor 350 (Molecular Probes); APC or PerCP-Cy5.5 anti-CD68 clone FA-11, and Alexa Fluor 647 CD326 clone G8.8 (BioLegend); Alexa Fluor 647 anti-CD206 (AbD serotec); and rabbit polyclonal anti-Tomm20 clone FL-145 (Santa Cruz Biotechnology [Dallas, Tx]). For intracellular staining, samples were first fixed and permeabilized with Fix & Perm before antibody incubations in Wash & Perm buffer (BD Biosciences [San Diego, CA]). For Ki-67 staining, samples were treated following manufacturer's protocol (Alexa Fluor 647 anti-Ki-67, BD Pharmingen). Single-cell suspensions were analyzed with a FACSCanto II HTS cytometer or a FACSAria II SORP sorter (BD Biosciences), and data were processed with FlowJo 7.6.3 and BD FACSDiva v.6.1.3. softwares. In some cases, sorted samples were further analyzed by combining flow cytometry and imaging with Flowsight (Amnis, EMD Millipore [Billerica, MA]).

Parabiosis surgery

For parabiosis, gender- and weight-matched mice were anesthetized i.p. with a mixture of ketamine (100 mg/kg), xylazine (10 mg/kg), and acepromazine (3 mg/kg). Hair was removed from the lateral aspects of the mice by shaving and hair removal cream. A longitudinal skin incision was made from the olecranon to the knee joint on opposing sides of each mouse of the parabiotic pair. Animals were placed side-by-side and the right olecranon of one animal was attached to the left olecranon of the other by a double suture. The equivalent procedure was performed for the knee joints to further secure the parabiotic pair. The dorsal and ventral skins were then approximated continuous 6–0 suture and by staples along the lateral abdominal aspect of the mice. Parabiosis was maintained for 6 months and, then, one of the partners in the parabiotic pair was injected retro-orbitally with 200 µl of HMw TRITC-dextran (5 µM) and animals were sacrificed 3d later. Chimerism in skin-resident macrophages was determined as well as the capture of intraluminal dextran by host and partner macrophages.

Solar-simulated UV radiation

Animals were exposed to UV irradiation using a 1000 watt xenon arc solar simulator (Oriel by Newport [Irvine, CA]) equipped with an Oriel 81,017 filter (Colipa [Oudergem, Belgium]). UVB and UVA irradiance measurements were performed using an IL-1700 radiometer (International Light Technologies Inc. [Peabody, MA]) equipped with SED240/UVB-1/TD and SED033/UVA/TD photodetectors. The radiometer was calibrated with a Solar-Scope spectroradiometer (Solatell [Croydon, UK]). Animals were irradiated with 5 J/cm^2 UVA-UVB except for their left ear that was covered to be used as non-treated control. Then, they were allowed to recover for 1 month before sacrifice.

Clodronate liposome-mediated depletion of skin macrophages

Clodronate (Roche) or PBS liposomes were injected s.c. (20 µl/hind footpad). Skin samples were processed for flow cytometry analysis after 24 hr or 7d.

In vivo BrdU treatment

Mice were allowed to drink BrdU-treated water (0.8 mg/ml) for 8d and then were sacrificed. BrdU incorporation in skin cell subsets was analyzed by flow cytometry (FITC BrdU Flow Kit, BD Pharmingen).

Measurement of mitochondria function

Ex vivo staining of mitochondria activity was conducted by flow cytometry following a previous protocol (***Johnson and Rabinovitch, 2012***). Briefly, ears were excised and split in half. The tissue was immediately incubated in the staining solution (20 nM of MitoTracker Orange CMTMRos [Molecular Probes] diluted in HBSS1X with 5% FBS) for 20 min at 37°C, 5% CO2. Then tissues were digested and dye was maintained at 10 nM in all the following steps before FACS analysis.

RNA-Seq library production

cDNA was synthesized and amplified directly from cells using the Smarter Ultra Low RNA kit (Clontech Laboratories Inc. [Mountain View, CA]). Amplified cDNAs (10 ng) were fragmented using Covaris E220 (Covaris [Woburn, MA]) to an average fragment size of approximately 150 pb. Index-tagged sequencing libraries were generated from the fragmented cDNAs using the TruSeq RNA Sample Preparation v2 Kit (Illumina Inc. [San Diego, CA]), starting from the End Repair step. Libraries were quantified using a Nanodrop spectrophotometer (Thermo Fisher Scientific [Waltham, MA]) and their size distributions were determined using the Bioanalyzer DNA-1000 Kit (Agilent). Libraries were sequenced on the Genome Analyzer IIx (Illumina) following the standard sequencing protocol with the TruSeq SBS Kit v5 (Illumina). Fastq files containing the sequencing reads for each library were extracted and demultiplexed using Casava v1.8.2 (Illumina).

RNA-Seq analysis

Reads were pre-processed with Cutadapt (***Martin, 2011***), to remove both TruSeq adaptor and SMARTer primer sequences. The resulting reads were mapped on the mouse transcriptome (Ensembl gene-build GRCm38.v70) and genome, using RSEM v1.2.3 (***Li and Dewey, 2011***) and Bowtie2 v2.0.6 (***Langmead and Salzberg, 2012***), respectively. The observation that a significant fraction of reads could be mapped on the genome, but not on the transcriptome, in close proximity to dA/dT-rich sequences, suggested that traces of contaminant genomic DNA could have been artifactually amplified by poly (A) priming. To avoid overestimation of transcript read counts, read clusters mapped on the genome at less than 50 bp downstream of dT-rich or upstream dA-rich regions were discarded. Filtered reads were mapped again on the transcriptome, and quantified, with RSEM. Only genes with at least 2 counts per million in at least 2 samples were considered for statistical analysis. Data were then normalized and differential expression tested using the Bioconductor package EdgeR (***Robinson et al., 2010***). Hierarchical Clustering was run using Genesis Software (***Sturn et al., 2002***) on the normalized expression profiles of the subset of genes with a p-value smaller than 0.05 and similar behavior in the two replicates of each cell type. Gene Set Enrichment Analysis (GSEA) (***Subramanian et al., 2005***) was run on the list of genes expressed in at least one cell type. The RNASeq dataset is available at http://www.ncbi.nlm.nih.gov/geo/query/acc.cgi?token=gzijkssyjraldqd&acc=GSE50566 (authors: Francisco Sanchez-Madrid and Olga Barreiro; year of publication: Sep 4th 2013; title: Homeostatic skin contains two different subsets of resident macrophages with distinct origin and gene profile; GEO Accession Number GSE50566).

RNA extraction and immune gene profile analysis

RNA was extracted from sorted macrophage populations obtained from chimeric CD45.1 (donor)-CD45.2 (host) animals using the Absolutely RNA Nanoprep Kit (Agilent Technologies [Santa Clara, CA]). RNA quantity and quality were determined using a 2100 Bioanalyzer (Agilent Technologies) and a Nanodrop-1000 Spectrophotometer (Thermo Fisher Scientific). Each RNA sample was amplified using the MessageAmp II aRNA Amplification Kit (Ambion). Total amplified mRNA (30 ng) was converted to cDNA and loaded on a TaqMan Array Micro Fluidic Card (Applied Biosystems, Life Technologies, Thermo Fisher Scientific [Foster City, CA]). Relative gene expression was calculated with the ABI Prism 7900 HT Sequence Detection System (Applied Biosystems) and Qbase software (Biogazelle [Gent, Belgium]), using *Actb, B2m*, *Hprt1*, *Gusb* and *Gapdh* genes as reference targets for the analysis of the immune system and inflammation gene signature array and *18S, Raf1, Ctnnb1, Eef1a1* for the analysis of the stem cell gene signature array. A comparative gene expression analysis was carried out by calculating ΔlogCt from the average logCt for every gene from each type of tissue-resident macrophages.

Analysis of cytokine secretion by FACs and ELISA

Sorted skin anti- and pro-inflammatory macrophage populations were obtained from the skin of C57BL6 mice. Cells were seeded (40,000 cells/100 µl RPMI medium) and stimulated in vitro with LPS (1 µg/ml) for 24 hr. Supernatants were used for analysis of cytokine secretion using Mouse Inflammation (17-Plex) multiplex kit (ANTIGENIX AMERICA Inc [Huntington Station, NY]). TGF-β and IL-10 secretion were analyzed with an ELISA kit (eBioscience).

Cytospin and staining

Sorted donor and host skin macrophages of quimeric mice were diluted in PBS containing 0.5% BSA and centrifuged in a cytospin centrifuge for 10 min at 800 rpm. Samples were stained with rabbit polyclonal anti-arginase I clone H-52 (Santa Cruz Biotechnology) or rabbit polyclonal anti-heme oxygenase-1 (Chemicon) following a standard immunofluorescence protocol. Then, samples were analyzed in the LSM 700 laser scanning microscope described above.

In vivo uptake of particulate OVA

FITC fluospheres (Ø 0.2 µm) (Fluospheres, sulfate microspheres, Molecular Probes) were diluted in PBS to a final concentration of 0.5% solids and adsorbed with 1 mg/ml endotoxin-free OVA (Calbiochem, EMD Millipore [Billerica, MA]) following the manufacturer's instructions. Then, 200 µl of the colloidal dissolution were injected i.v. in either untreated, lethally γ-irradiated or splenectomized animals. Seventy-two hours later, animals were sacrificed and manually perfused with PBS to eliminate remaining fluospheres from the vasculature. In some cases, hind footpads were treated with clodronate or PBS liposomes 72 hr before the injection of fluospheres. Clodronate or PBS liposomes (ClodronateLiposomes.org) were injected s.c. (20 µl/hind footpad). For splenectomy, animals were anesthetized with a mixture of ketamine/xylazine (100/10 mg/Kg), the left lateral side was depilated and a small incision was made to remove the organ after ligation of the splenic vessels. Then, animals were allowed to recover from surgery for 1 month before proceeding with experiments.

Selective depletion of STREAMs in skin

Home-made ultrasmall superparamagnetic iron oxide nanoparticles (***Groult et al., 2015***) (abbreviated as NPs, 1 ml, 3 mg Fe/ml) with 10 nm of core, 40 nm of hydrodynamic size and −35 mV of ζ-potential were incubated with endotoxin-free OVA (500 µl, 10 mg/ml) for 1 hr at R.T. Non-adsorbed OVA remnants were washed out and further incubation of OVA-NP with diphtheria toxin (DT) (50 µl, 1 mg/ml) (3 hr at R.T.) were carried out, followed by extensive washing. Then, mice were injected i.v. with 1 dose (2.5 µl/g) or 2 doses (spaced 3d apart) of this colloidal suspension and skin samples were analyzed by FACS and immunohistochemistry at different time-points.

Wound healing assay

The back of mice was depilated and left to recover homeostasis (24 hr). Then, animals were anesthetized with isoflurane by inhalation. Four skin excisions of 5 mm in diameter were carried out using a bio-punch (Kai Industries Co., ltd [Seki, Japan]). Wounds were routinely measured every 24 hr until the sacrifice of the animals. Animals were injected i.v. either DT-OVA-NP or OVA-NP before or during the wound healing assay. After sacrifice, wounded tissue was embedded in paraffin and processed for histological analysis.

Histological analysis

Standard Hematoxylin-Eosin and Masson trichrome stainings were performed in wound sections. Alternatively, samples were processed for standard immunohistochemistry staining using anti-αSMA (clone 1A4, Sigma-Aldrich) or for immunofluorescence using anti-Mac-3 (clone M3/84, Santa Cruz Biotechnology), anti-CD31 (rabbit polyclonal anti-mouse/human, Abcam), and DAPI. Stained samples were analyzed on a Leica DM2500 microscope coupled to a Leica DFC420 camera using 5x, 10x and 20x objectives. Intensity quantification of collagen deposition and quantification of macrophages and vessels in the granulation tissue were performed using ImageJ 1.42q.

Statistical analysis

Normality of data distribution was assessed with the Kolmogorov-Smirnov test. Statistical significance was calculated either with an unpaired two-tailed Student's t-test, one-sample t-test, one-way ANOVA followed by either Tukey's or Dunnett's post-tests or two-way ANOVA followed by Sidak's or Bonferroni post-test as indicated. All statistical analyses were carried out with GraphPad Prism v5 (GraphPad Software Inc. [La Jolla, CA]).

Acknowledgements

We thank Dr. M Vicente-Manzanares and S Bartlett for English editing, and Dr. I Mazo, Dr. Hortensia de la Fuente, Ana Domínguez and Raquel Sánchez for technical assistance. We also thank the Microscopy, Cellomics, Genomics, Bioinformatics, Advanced Imaging and Comparative Medicine Units at CNIC and the HMS Center for Immune Imaging for technical support. This work was funded by grants from the Spanish Ministry of Economy and Competitiveness (SAF2011-27330 to PM; and SAF2011-25834 and SAF 2014-55579-R to FS-M); grant INDISNET-S2011/BMD-2332 from the Comunidad de Madrid to PM and FS-M; Red Cardiovascular RD 12-0042-0056 from Instituto Salud Carlos III (ISCIII), and ERC-2011-AdG294340-GENTRIS to FS-M; and National Institutes of Health grant RO1 AR068383 to UHvA. OB is supported by a fellowship from Fundacion Alfonso Martin Escudero, ERC and RO1 grants. DC is supported by SAF grant. The CNIC is supported by the Spanish Ministry of Economy and Competitiveness and the Pro CNIC Foundation.

Additional information

Funding

Funder	Grant reference number	Author
Fundación Alfonso Martín Escudero		Olga Barreiro
European Research Council	ERC-2011-AdG294340-GENTRIS	Olga Barreiro Francisco Sánchez Madrid
National Institutes of Health	RO1 AR068383	Olga Barreiro Ulrich H von Andrian
Ministerio de Economia y Competitividad España	SAF2011-25834	Danay Cibrian Francisco Sánchez Madrid
Ministerio de Economia y Competitividad España	SAF 2014-55579-R	Francisco Sánchez Madrid Danay Cibrian
Ministerio de Economia y Competitividad España	SAF2011-27330	Pilar Martín
Comunidad de Madrid	INDISNET-S2011/BMD-2332	Pilar Martín Francisco Sánchez Madrid
Instituto Salud Carlos III	Red Cardiovascular RD 12-0042-0056	Francisco Sánchez Madrid

The funders had no role in study design, data collection and interpretation, or the decision to submit the work for publication.

Author contributions

OB, Designed research plan, Performed experiments, Analyzed and interpreted data, Wrote the manuscript; DC, Performed experiments, Collaborated in experimental design, Analysis and interpretation of data, ; CC, Participated in wound healing experiments, Acquisition of data, Drafting or revising the article; DA, Performed parabiosis surgery, Acquisition of data, Drafting or revising the article; VM, Provided technical expertise for whole-mount staining, Drafting or revising the article, Contributed unpublished essential data or reagents; ÍV, AB, DV, Contributed with reagents, Drafting or revising the article; AGA, Helped in designing wound healing experiments, Drafting or revising the article; PM, Helped to plan research and collaborated in some experimental approaches and data analyses, Drafting or revising the article; UHvA, Contributed with reagents, Discussed results, Helped with manuscript writing; FSM, Planned research, Discussed results, Wrote the manuscript

Author ORCIDs

Pilar Martín, http://orcid.org/0000-0002-2392-1764
Francisco Sánchez Madrid, http://orcid.org/0000-0001-5303-0762

Ethics

Animal experimentation: Animal studies were approved by the local ethics committee and by the Division of Animal Protection of Comunidad de Madrid (approved protocols PROEX 159/15 and 160/15). All animal procedures conformed to EU Directive 2010/63EU and Recommendation 2007/526/EC regarding the protection of animals used for experimental and other scientific purposes, enforced in Spanish law under Real Decreto 1201/2005

Additional files

Supplementary files

• Supplementary file 1. List of genes of the RNA-Seq analysis differentially express in host versus donor macrophages in chimeric mice. Those protein coding sequences showing similar normalized expression levels across replicates are highlighted in bold.
DOI: 10.7554/eLife.15251.033

• Supplementary file 2. Comprehensive Gene Set Enrichment Analysis (GSEA) of all genes expressed in at least one cell type comparing Kegg pathways upregulated in host (first datasheet) versus donor macrophages (second datasheet) of chimeric mice. Kegg pathways upregulated at a nominal p-value less than 1% appeared in bold. Among them, those categories with a FDR q-value proximal to 25% are highlighted in grey.
DOI: 10.7554/eLife.15251.034

Major datasets

The following dataset was generated:

Author(s)	Year	Dataset title	Dataset URL	Database, license, and accessibility information
Francisco Sánchez Madrid, Olga Barreiro	2013	Homeostatic skin contains two different subsets of resident macrophages with distinct origin and gene profile	http://www.ncbi.nlm.nih.gov/geo/query/acc.cgi?acc=GSE50566	Publicly available at the NCBI Gene Expression Omnibus (Accession no: GSE50556)

References

Abtin A, Jain R, Mitchell AJ, Roediger B, Brzoska AJ, Tikoo S, Cheng Q, Ng LG, Cavanagh LL, von Andrian UH, Hickey MJ, Firth N, Weninger W. 2014. Perivascular macrophages mediate neutrophil recruitment during bacterial skin infection. *Nature Immunology* **15**:45–53. doi: 10.1038/ni.2769

Auffray C, Fogg D, Garfa M, Elain G, Join-Lambert O, Kayal S, Sarnacki S, Cumano A, Lauvau G, Geissmann F. 2007. Monitoring of blood vessels and tissues by a population of monocytes with patrolling behavior. *Science* **317**:666–670. doi: 10.1126/science.1142883

Baluk P, Fuxe J, Hashizume H, Romano T, Lashnits E, Butz S, Vestweber D, Corada M, Molendini C, Dejana E, McDonald DM. 2007. Functionally specialized junctions between endothelial cells of lymphatic vessels. *Journal of Experimental Medicine* **204**:2349–2362. doi: 10.1084/jem.20062596

Barkauskas DS, Evans TA, Myers J, Petrosiute A, Silver J, Huang AY. 2013. Extravascular CX3CR1+ cells extend intravascular dendritic processes into intact central nervous system vessel lumen. *Microscopy and Microanalysis : The Official Journal of Microscopy Society of America, Microbeam Analysis Society, Microscopical Society of Canada* **19**:778–790. doi: 10.1017/S1431927613000482

Biswas SK, Mantovani A. 2012. Orchestration of metabolism by macrophages. *Cell Metabolism* **15**:432–437. doi: 10.1016/j.cmet.2011.11.013

Bogunovic M, Ginhoux F, Wagers A, Loubeau M, Isola LM, Lubrano L, Najfeld V, Phelps RG, Grosskreutz C, Scigliano E, Frenette PS, Merad M. 2006. Identification of a radio-resistant and cycling dermal dendritic cell population in mice and men. *Journal of Experimental Medicine* **203**:2627–2638. doi: 10.1084/jem.20060667

Boring L, Gosling J, Chensue SW, Kunkel SL, Farese RV, Broxmeyer HE, Charo IF. 1997. Impaired monocyte migration and reduced type 1 (Th1) cytokine responses in C-C chemokine receptor 2 knockout mice. *Journal of Clinical Investigation* **100**:2552–2561. doi: 10.1172/JCI119798

Burgdorf S, Lukacs-Kornek V, Kurts C. 2006. The mannose receptor mediates uptake of soluble but not of cell-associated antigen for cross-presentation. *Journal of Immunology* **176**:6770–6776. doi: 10.4049/jimmunol.176.11.6770

Calderon B, Carrero JA, Ferris ST, Sojka DK, Moore L, Epelman S, Murphy KM, Yokoyama WM, Randolph GJ, Unanue ER. 2015. The pancreas anatomy conditions the origin and properties of resident macrophages. *The Journal of Experimental Medicine* **212**:1497–1512. doi: 10.1084/jem.20150496

Calderon B, Carrero JA, Unanue ER. 2014. The central role of antigen presentation in islets of Langerhans in autoimmune diabetes. *Current Opinion in Immunology* **26**:32–40. doi: 10.1016/j.coi.2013.10.011

Calderon B, Suri A, Miller MJ, Unanue ER. 2008. Dendritic cells in islets of Langerhans constitutively present beta cell-derived peptides bound to their class II MHC molecules. *Proceedings of the National Academy of Sciences of the United States of America* **105**:6121–6126. doi: 10.1073/pnas.0801973105

Chang SY, Song JH, Guleng B, Cotoner CA, Arihiro S, Zhao Y, Chiang HS, O'Keeffe M, Liao G, Karp CL, Kweon MN, Sharpe AH, Bhan A, Terhorst C, Reinecker HC. 2013. Circulatory antigen processing by mucosal dendritic cells controls CD8(+) T cell activation. *Immunity* **38**:153–165. doi: 10.1016/j.immuni.2012.09.018

Cheng LE, Hartmann K, Roers A, Krummel MF, Locksley RM. 2013. Perivascular mast cells dynamically probe cutaneous blood vessels to capture immunoglobulin E. *Immunity* **38**:166–175. doi: 10.1016/j.immuni.2012.09.022

Chorro L, Sarde A, Li M, Woollard KJ, Chambon P, Malissen B, Kissenpfennig A, Barbaroux JB, Groves R, Geissmann F. 2009. Langerhans cell (LC) proliferation mediates neonatal development, homeostasis, and inflammation-associated expansion of the epidermal LC network. *The Journal of Experimental Medicine* **206**:3089–3100. doi: 10.1084/jem.20091586

Das A, Sinha M, Datta S, Abas M, Chaffee S, Sen CK, Roy S. 2015. Monocyte and macrophage plasticity in tissue repair and regeneration. *The American Journal of Pathology* **185**:2596–2606. doi: 10.1016/j.ajpath.2015.06.001

DeFalco T, Bhattacharya I, Williams AV, Sams DM, Capel B. 2014. Yolk-sac-derived macrophages regulate fetal testis vascularization and morphogenesis. *Proceedings of the National Academy of Sciences of the United States of America* **111**:E2384–2393. doi: 10.1073/pnas.1400057111

Farache J, Koren I, Milo I, Gurevich I, Kim KW, Zigmond E, Furtado GC, Lira SA, Shakhar G. 2013. Luminal bacteria recruit CD103+ dendritic cells into the intestinal epithelium to sample bacterial antigens for presentation. *Immunity* **38**:581–595. doi: 10.1016/j.immuni.2013.01.009

Galván-Peña S, O'Neill LA. 2014. Metabolic reprograming in macrophage polarization. *Frontiers in Immunology* **5**:420. doi: 10.3389/fimmu.2014.00420

Gautier EL, Shay T, Miller J, Greter M, Jakubzick C, Ivanov S, Helft J, Chow A, Elpek KG, Gordonov S, Mazloom AR, Ma'ayan A, Chua WJ, Hansen TH, Turley SJ, Merad M, Randolph GJ., Immunological Genome Consortium. 2012. Gene-expression profiles and transcriptional regulatory pathways that underlie the identity and diversity of mouse tissue macrophages. *Nature Immunology* **13**:1118–1128. doi: 10.1038/ni.2419

Gordon S, Plüddemann A. 2013. Tissue macrophage heterogeneity: issues and prospects. *Seminars in Immunopathology* **35**:533–540. doi: 10.1007/s00281-013-0386-4

Gosselin D, Link VM, Romanoski CE, Fonseca GJ, Eichenfield DZ, Spann NJ, Stender JD, Chun HB, Garner H, Geissmann F, Glass CK. 2014. Environment drives selection and function of enhancers controlling tissue-specific macrophage identities. *Cell* **159**:1327–1340. doi: 10.1016/j.cell.2014.11.023

Groult H, Ruiz-Cabello J, Pellico J, Lechuga-Vieco AV, Bhavesh R, Zamai M, Almarza E, Martín-Padura I, Cantelar E, Martínez-Alcázar MP, Herranz F. 2015. Parallel multifunctionalization of nanoparticles: a one-step modular approach for in vivo imaging. *Bioconjugate Chemistry* **26**:153–160. doi: 10.1021/bc500536y

Gurtner GC, Werner S, Barrandon Y, Longaker MT. 2008. Wound repair and regeneration. *Nature* **453**:314–321. doi: 10.1038/nature07039

Hammad H, Chieppa M, Perros F, Willart MA, Germain RN, Lambrecht BN. 2009. House dust mite allergen induces asthma via Toll-like receptor 4 triggering of airway structural cells. *Nature Medicine* **15**:410–416. doi: 10.1038/nm.1946

Haniffa M, Ginhoux F, Wang XN, Bigley V, Abel M, Dimmick I, Bullock S, Grisotto M, Booth T, Taub P, Hilkens C, Merad M, Collin M. 2009. Differential rates of replacement of human dermal dendritic cells and macrophages during hematopoietic stem cell transplantation. *Journal of Experimental Medicine* **206**:371–385. doi: 10.1084/jem.20081633

Hashimoto D, Chow A, Noizat C, Teo P, Beasley MB, Leboeuf M, Becker CD, See P, Price J, Lucas D, Greter M, Mortha A, Boyer SW, Forsberg EC, Tanaka M, van Rooijen N, García-Sastre A, Stanley ER, Ginhoux F, Frenette PS, et al. 2013. Tissue-resident macrophages self-maintain locally throughout adult life with minimal contribution from circulating monocytes. *Immunity* **38**:792–804. doi: 10.1016/j.immuni.2013.04.004

Henri S, Guilliams M, Poulin LF, Tamoutounour S, Ardouin L, Dalod M, Malissen B. 2010. Disentangling the complexity of the skin dendritic cell network. *Immunology and Cell Biology* **88**:366–375. doi: 10.1038/icb.2010.34

Hoeffel G, Chen J, Lavin Y, Low D, Almeida FF, See P, Beaudin AE, Lum J, Low I, Forsberg EC, Poidinger M, Zolezzi F, Larbi A, Ng LG, Chan JK, Greter M, Becher B, Samokhvalov IM, Merad M, Ginhoux F. 2015. C-Myb (+) erythro-myeloid progenitor-derived fetal monocytes give rise to adult tissue-resident macrophages. *Immunity* **42**:665–678. doi: 10.1016/j.immuni.2015.03.011

Huang LR, Wohlleber D, Reisinger F, Jenne CN, Cheng RL, Abdullah Z, Schildberg FA, Odenthal M, Dienes HP, van Rooijen N, Schmitt E, Garbi N, Croft M, Kurts C, Kubes P, Protzer U, Heikenwalder M, Knolle PA. 2013. Intrahepatic myeloid-cell aggregates enable local proliferation of CD8(+) T cells and successful immunotherapy against chronic viral liver infection. *Nature Immunology* **14**:574–583. doi: 10.1038/ni.2573

Jakubzick C, Gautier EL, Gibbings SL, Sojka DK, Schlitzer A, Johnson TE, Ivanov S, Duan Q, Bala S, Condon T, van Rooijen N, Grainger JR, Belkaid Y, Ma'ayan A, Riches DW, Yokoyama WM, Ginhoux F, Henson PM,

Randolph GJ. 2013. Minimal differentiation of classical monocytes as they survey steady-state tissues and transport antigen to lymph nodes. *Immunity* **39**:599–610. doi: 10.1016/j.immuni.2013.08.007

Jenkins SJ, Ruckerl D, Cook PC, Jones LH, Finkelman FD, van Rooijen N, MacDonald AS, Allen JE. 2011. Local macrophage proliferation, rather than recruitment from the blood, is a signature of TH2 inflammation. *Science* **332**:1284–1288. doi: 10.1126/science.1204351

Johnson S, Rabinovitch P. 2012. Ex vivo imaging of excised tissue using vital dyes and confocal microscopy. *Current Protocols in Cytometry* **61**:39.

Junt T, Moseman EA, Iannacone M, Massberg S, Lang PA, Boes M, Fink K, Henrickson SE, Shayakhmetov DM, Di Paolo NC, van Rooijen N, Mempel TR, Whelan SP, von Andrian UH. 2007. Subcapsular sinus macrophages in lymph nodes clear lymph-borne viruses and present them to antiviral B cells. *Nature* **450**:110–114. doi: 10.1038/nature06287

Langmead B, Salzberg SL. 2012. Fast gapped-read alignment with Bowtie 2. *Nature Methods* **9**:357–359. doi: 10.1038/nmeth.1923

Lavin Y, Winter D, Blecher-Gonen R, David E, Keren-Shaul H, Merad M, Jung S, Amit I. 2014. Tissue-resident macrophage enhancer landscapes are shaped by the local microenvironment. *Cell* **159**:1312–1326. doi: 10.1016/j.cell.2014.11.018

Lee WY, Moriarty TJ, Wong CH, Zhou H, Strieter RM, van Rooijen N, Chaconas G, Kubes P. 2010. An intravascular immune response to Borrelia burgdorferi involves Kupffer cells and iNKT cells. *Nature Immunology* **11**:295–302. doi: 10.1038/ni.1855

Li B, Dewey CN. 2011. RSEM: accurate transcript quantification from RNA-Seq data with or without a reference genome. *BMC Bioinformatics* **12**:323. doi: 10.1186/1471-2105-12-323

Martin M. 2011. Cutadapt removes adapter sequences from high-throughput sequencing reads. *EMBnet.journal* **17**:10–12. doi: 10.14806/ej.17.1.200

Martinez FO, Helming L, Milde R, Varin A, Melgert BN, Draijer C, Thomas B, Fabbri M, Crawshaw A, Ho LP, Ten Hacken NH, Cobos Jiménez V, Kootstra NA, Hamann J, Greaves DR, Locati M, Mantovani A, Gordon S. 2013. Genetic programs expressed in resting and IL-4 alternatively activated mouse and human macrophages: similarities and differences. *Blood* **121**:e57–69. doi: 10.1182/blood-2012-06-436212

Mazzini E, Massimiliano L, Penna G, Rescigno M. 2014. Oral tolerance can be established via gap junction transfer of fed antigens from $CX3CR1^{+}$ macrophages to $CD103^{+}$ dendritic cells. *Immunity* **40**:248–261. doi: 10.1016/j.immuni.2013.12.012

Mempel TR, Pittet MJ, Khazaie K, Weninger W, Weissleder R, von Boehmer H, von Andrian UH. 2006. Regulatory T cells reversibly suppress cytotoxic T cell function independent of effector differentiation. *Immunity* **25**:129–141. doi: 10.1016/j.immuni.2006.04.015

Merad M, Manz MG, Karsunky H, Wagers A, Peters W, Charo I, Weissman IL, Cyster JG, Engleman EG. 2002. Langerhans cells renew in the skin throughout life under steady-state conditions. *Nature Immunology* **3**:1135–1141. doi: 10.1038/ni852

Mignone JL, Kukekov V, Chiang AS, Steindler D, Enikolopov G. 2004. Neural stem and progenitor cells in nestin-GFP transgenic mice. *Journal of Comparative Neurology* **469**:311–324. doi: 10.1002/cne.10964

Molawi K, Wolf Y, Kandalla PK, Favret J, Hagemeyer N, Frenzel K, Pinto AR, Klapproth K, Henri S, Malissen B, Rodewald HR, Rosenthal NA, Bajenoff M, Prinz M, Jung S, Sieweke MH. 2014. Progressive replacement of embryo-derived cardiac macrophages with age. *Journal of Experimental Medicine* **211**:2151–2158. doi: 10.1084/jem.20140639

Murray PJ, Wynn TA. 2011. Protective and pathogenic functions of macrophage subsets. *Nature Reviews. Immunology* **11**:723–737. doi: 10.1038/nri3073

Pasparakis M, Haase I, Nestle FO. 2014. Mechanisms regulating skin immunity and inflammation. *Nature Reviews. Immunology* **14**:289–301. doi: 10.1038/nri3646

Pinto AR, Paolicelli R, Salimova E, Gospocic J, Slonimsky E, Bilbao-Cortes D, Godwin JW, Rosenthal NA. 2012. An abundant tissue macrophage population in the adult murine heart with a distinct alternatively-activated macrophage profile. *PLoS One* **7**:e36814. doi: 10.1371/journal.pone.0036814

Rescigno M, Urbano M, Valzasina B, Francolini M, Rotta G, Bonasio R, Granucci F, Kraehenbuhl JP, Ricciardi-Castagnoli P. 2001. Dendritic cells express tight junction proteins and penetrate gut epithelial monolayers to sample bacteria. *Nature Immunology* **2**:361–367. doi: 10.1038/86373

Robinson MD, McCarthy DJ, Smyth GK. 2010. edgeR: a Bioconductor package for differential expression analysis of digital gene expression data. *Bioinformatics* **26**:139–140. doi: 10.1093/bioinformatics/btp616

Rodriguez-Prados J-C, Traves PG, Cuenca J, Rico D, Aragones J, Martin-Sanz P, Cascante M, Bosca L. 2010. Substrate fate in activated macrophages: a comparison between innate, classic, and alternative activation. *Journal of Immunology* **185**:605–614. doi: 10.4049/jimmunol.0901698

Sangiorgi E, Capecchi MR. 2008. Bmi1 is expressed in vivo in intestinal stem cells. *Nature Genetics* **40**:915–920. doi: 10.1038/ng.165

Schulte D, Küppers V, Dartsch N, Broermann A, Li H, Zarbock A, Kamenyeva O, Kiefer F, Khandoga A, Massberg S, Vestweber D. 2011. Stabilizing the VE-cadherin-catenin complex blocks leukocyte extravasation and vascular permeability. *The EMBO Journal* **30**:4157–4170. doi: 10.1038/emboj.2011.304

Schulz C, Gomez Perdiguero E, Chorro L, Szabo-Rogers H, Cagnard N, Kierdorf K, Prinz M, Wu B, Jacobsen SE, Pollard JW, Frampton J, Liu KJ, Geissmann F. 2012. A lineage of myeloid cells independent of Myb and hematopoietic stem cells. *Science* **336**:86–90. doi: 10.1126/science.1219179

Serbina NV, Pamer EG. 2006. Monocyte emigration from bone marrow during bacterial infection requires signals mediated by chemokine receptor CCR2. *Nature Immunology* **7**:311–317. doi: 10.1038/ni1309

Sica A, Mantovani A. 2012. Macrophage plasticity and polarization: in vivo veritas. *The Journal of Clinical Investigation* **122**:787–795. doi: 10.1172/JCI59643

Sienerth AR, Scheuermann C, Galmiche A, Rapp UR, Becker M. 2011. Polycomb group protein Bmi1 negatively regulates IL-10 expression in activated macrophages. *Immunology and Cell Biology* **89**:812–816. doi: 10.1038/icb.2010.160

Sturn A, Quackenbush J, Trajanoski Z. 2002. Genesis: cluster analysis of microarray data. *Bioinformatics* **18**:207–208. doi: 10.1093/bioinformatics/18.1.207

Subramanian A, Tamayo P, Mootha VK, Mukherjee S, Ebert BL, Gillette MA, Paulovich A, Pomeroy SL, Golub TR, Lander ES, Mesirov JP. 2005. Gene set enrichment analysis: a knowledge-based approach for interpreting genome-wide expression profiles. *Proceedings of the National Academy of Sciences of the United States of America* **102**:15545–15550. doi: 10.1073/pnas.0506580102

Tamoutounour S, Guilliams M, Montanana Sanchis F, Liu H, Terhorst D, Malosse C, Pollet E, Ardouin L, Luche H, Sanchez C, Dalod M, Malissen B, Henri S. 2013. Origins and functional specialization of macrophages and of conventional and monocyte-derived dendritic cells in mouse skin. *Immunity* **39**:925–938. doi: 10.1016/j.immuni.2013.10.004

Varol C, Mildner A, Jung S. 2015. Macrophages: development and tissue specialization. *Annual Review of Immunology* **33**:643–675. doi: 10.1146/annurev-immunol-032414-112220

Wang Z, Gerstein M, Snyder M. 2009. RNA-Seq: a revolutionary tool for transcriptomics. *Nature Reviews Genetics* **10**:57–63. doi: 10.1038/nrg2484

Willenborg S, Lucas T, van Loo G, Knipper JA, Krieg T, Haase I, Brachvogel B, Hammerschmidt M, Nagy A, Ferrara N, Pasparakis M, Eming SA. 2012. CCR2 recruits an inflammatory macrophage subpopulation critical for angiogenesis in tissue repair. *Blood* **120**:613–625. doi: 10.1182/blood-2012-01-403386

Wollenberg A, Mommaas M, Oppel T, Schottdorf EM, Günther S, Moderer M. 2002. Expression and function of the mannose receptor CD206 on epidermal dendritic cells in inflammatory skin diseases. *Journal of Investigative Dermatology* **118**:327–334. doi: 10.1046/j.0022-202x.2001.01665.x

Wong CH, Jenne CN, Petri B, Chrobok NL, Kubes P. 2013. Nucleation of platelets with blood-borne pathogens on Kupffer cells precedes other innate immunity and contributes to bacterial clearance. *Nature Immunology* **14**:785–792. doi: 10.1038/ni.2631

Yona S, Kim KW, Wolf Y, Mildner A, Varol D, Breker M, Strauss-Ayali D, Viukov S, Guilliams M, Misharin A, Hume DA, Perlman H, Malissen B, Zelzer E, Jung S. 2013. Fate mapping reveals origins and dynamics of monocytes and tissue macrophages under homeostasis. *Immunity* **38**:79–91. doi: 10.1016/j.immuni.2012.12.001

Yoshida S, Tsutsumi S, Muhlebach G, Sourbier C, Lee MJ, Lee S, Vartholomaiou E, Tatokoro M, Beebe K, Miyajima N, Mohney RP, Chen Y, Hasumi H, Xu W, Fukushima H, Nakamura K, Koga F, Kihara K, Trepel J, Picard D, et al. 2013. Molecular chaperone TRAP1 regulates a metabolic switch between mitochondrial respiration and aerobic glycolysis. *Proceedings of the National Academy of Sciences of the United States of America* **110**:E1604–1612. doi: 10.1073/pnas.1220659110